UNIVERSITY OF SOUTHAMPTON

FACULTY OF PHYSICAL AND APPLIED SCIENCES

Physics & Astronomy

Breaking the quantum limit: the magnetic field of neutron stars in extra-galactic Be X-ray binaries

by

Helen Klus

Thesis for the degree of Doctor of Philosophy

April 2015

UNIVERSITY OF SOUTHAMPTON

ABSTRACT

FACULTY OF PHYSICAL AND APPLIED SCIENCES
Physics & Astronomy

Doctor of Philosophy

BREAKING THE QUANTUM LIMIT: THE MAGNETIC FIELD OF NEUTRON STARS IN EXTRA-GALACTIC BE X-RAY BINARIES

by Helen Klus

Neutron stars are some of the most magnetic objects that have ever been observed, and so they provide physicists with unique environments where fundamental laws of physics can be tested. Neutron stars are typically thought to have magnetic fields between 10^8 and 10^{14} G. The effects of the quantum electrodynamics are important above the quantum critical field (B_{QED}) of 4.4×10^{13} G. In this thesis, I provide evidence that there may be many more neutron stars with $B > B_{QED}$ than previously thought, and that all neutron stars in binary systems that are close to spin equilibrium follow the same relationship between spin period (P) and magnetic field. In Chapter 2, I determine the long-term average X-ray luminosity, spin period, and rate of change of spin period for 42 Be X-ray binaries (BeXB) in the Small Magellanic Cloud (SMC). I use this information, combined with orbital data, to show that the neutron stars in all of these systems are disc-accreting, and that $\sim 85\%$ are close to spin equilibrium. All systems with $P \gtrsim 100$ s are predicted to have $B > B_{QED}$. This applies to $\sim$2/3 systems. These predicted magnetic fields are higher than those of neutron stars in Galactic BeXB that have had their magnetic fields directly measured via cyclotron resonance scattering features (CRSF). I conclude that this is because the CRSF sources are not close to spin equilibrium. In Chapter 3, I look at pulse-profiles for the neutron stars discussed in Chapter 2 and find that they contain an array of features that vary both across and within individual systems. I suggest that BeXB containing neutron stars with relatively longer spin periods transition from a pencil to a fan beam at lower luminosities. In Chapter 4, I apply the methods used in Chapters 2 and 3 to LXP187, a BeXB in the Large Magellanic Cloud (LMC) that is not close to spin equilibrium. Results for LXP187 help confirm the conclusions of Chapter 2 - that $\sim 2/3$ BeXB contain neutron stars with $B > B_{QED}$.

Contents

List of Figures

List of Tables

Declaration of Authorship

I, Helen Klus , declare that the thesis entitled *Breaking the quantum limit: the magnetic field of neutron stars in extra-galactic Be X-ray binaries* and the work presented in the thesis are both my own, and have been generated by me as the result of my own original research. I confirm that:

- this work was done wholly or mainly while in candidature for a research degree at this University;
- where any part of this thesis has previously been submitted for a degree or any other qualification at this University or any other institution, this has been clearly stated;
- where I have consulted the published work of others, this is always clearly attributed;
- where I have quoted from the work of others, the source is always given. With the exception of such quotations, this thesis is entirely my own work;
- I have acknowledged all main sources of help;
- where the thesis is based on work done by myself jointly with others, I have made clear exactly what was done by others and what I have contributed myself;
- parts of this work have been published as: (Klus et al., 2013, 2014; Ho et al., 2014)

Signed:.....

Date:.....

Acknowledgements

First and foremost, I would like to thank my supervisors Prof. Malcolm Coe and Dr. Wynn Ho, without whom this thesis would certainly not exist. I would also like to thank everyone else who has contributed to this thesis, including Jose Galache, Silas Laycock, Robin Corbet, Lee Townsend, Liz Bartlett, and Simon Harris. Finally, thank you to Andrew, my love.

Nomenclature

Galaxies

SMC	Small Magellanic Cloud
LMC	Large Magellanic Cloud

Stellar systems

LMXB	Low mass X-ray binary
HMXB	High mass X-ray binary
SGXB	Supergiant X-ray binary
BeXB	Be X-ray binary
SXP	SMC X-ray binary pulsar
LXP	LMC X-ray binary pulsar

Telescopes

RXTE/PCA	Rossi X-ray Timing Explorer/
	Proportional Counter Array
Swift/XRT	Swift/X-ray Telescope
Swift/BAT	Swift/Burst Alert Telescope
XMM-Newton/	X-ray Multi-Mirror Mission- Newton/
EPIC	European Photon Imaging Camera
INTEGRAL/	INTErnational Gamma-Ray Astrophysics Laboratory/
IBIS	Imager on-Board the INTEGRAL Satellite
OGLE	Optical Gravitational Lensing Experiment
	(Las Campanas Observatory in Chile)
MACHO	MAssive Compact Halo Objects
	(1.27 m telescope in Australia)
ESO	European Southern Observatory
	(3.58 m New Technology Telescope in Chile)
SAAO	South African Astronomical Observatory
	(1.9 m Radcliffe telescope in South Africa)

Chapter 1

Introduction

1.1 Neutron stars in X-ray binaries

Neutron stars are unique and fascinating objects that cause matter to behave in ways we could never replicate on Earth. Neutron stars form when massive (∼8-20 $M_{\odot}$, O-B-type) stars stop fusing matter; they eject most of their mass, and their core collapses under its own gravitational force in a Type II supernova (this is discussed further in Section 1.1.2.1). In a Type II supernova, the force of gravity is strong enough to overcome electron degeneracy pressure. Degeneracy pressure is a manifestation of the Pauli exclusion principle, which states that two fermions cannot simultaneously occupy the same quantum state. When every electron energy level is filled, electron degeneracy pressure prevents the core from becoming any denser. In a Type II supernova, electron degeneracy pressure can be overcome, electrons merge with protons to become neutrons, and an object ∼1.4 $M_{\odot}$ compacts to a radius of ∼10 km. The core is prevented from collapsing further due to neutron degeneracy pressure. This makes neutron stars extremely dense; if the force of gravity were strong enough to overcome neutron degeneracy pressure, and they became any denser, then they would become black holes. Neutron stars are also some of the fastest spinning and most magnetic objects ever observed, with spin periods ranging from ms to thousands of s, and magnetic fields of up to $\sim 10^{15}$ G. All of this means that physicists can use observations of neutron stars in order to test and expand fundamental laws of physics.

Isolated neutron stars can be observed from Earth because they radiate at the expense of their rotational energy (Pacini, 1967). This radiation is emitted from the neutron star's magnetic poles in a broad spectrum, from radio to gamma-rays (Pellizzoni et al., 2009; Takata et al., 2012). If a neutron star's rotational and magnetic axes are misaligned, then this radiation can travel past our line-of-sight as the star rotates. This makes the neutron star appear to pulsate, and so neutron stars that emit beamed radiation are known as pulsars. Some isolated pulsars are powered by ultra-strong magnetic fields

of $\gtrsim 10^{14}$ G (Duncan and Thompson, 1992; Camilo et al., 2006). These pulsars emit bursts of X-ray and gamma-ray radiation. They are known as magnetars, and include soft gamma repeaters (SGR) and anomalous X-ray pulsars (AXP).

Neutron stars may also emit X-ray radiation if they are in a binary system and accrete matter from their companion, where accretion refers to the gradual accumulation of matter under the influence of gravity. Here, matter from the companion falls onto the neutron star's magnetosphere. If the neutron star is spinning too fast, then it will be expelled by the centrifugal force. If matter is able to penetrate the magnetosphere, however, then its trajectory can be controlled by the magnetic field lines, which can transfer it to the magnetic poles (this is discussed further in Section 1.2). Matter is accelerated to free-fall velocities of up to $\sim 0.7\ c$ (Kretschmar et al., 2010). When it hits the surface, most of its kinetic energy is radiated away as heat, which powers the X-ray source (this is discussed further in Sections 1.3 and 1.4). Compact objects in binaries that emit X-ray radiation are known as X-ray binaries, and they are amongst the brightest extra-solar objects in the sky. X-ray binaries can also include systems with black holes or white dwarfs, instead of neutron stars, but these will not be discussed in this work.

Neutron star X-ray binaries can generally be divided into two groups depending on the mass of their companion. Low mass X-ray binaries (LMXB) contain a companion $\lesssim 2$ $M_\odot$, which can be a white dwarf or a luminosity class III-V, K-M-type star. High mass X-ray binaries (HMXB) contain a companion star $\gtrsim 8$ $M_\odot$ (Grimm et al., 2003). This is either a supergiant star (an O-B-type star of luminosity class I-II) - in the case of SGXB - or an OBe star (an Oe-Be-type star of luminosity class III-V) - in the case of BeXB. There are very few intermediate mass X-ray binaries (IMXB), X-ray binaries with a companion $\sim$2-8 $M_\odot$. This is because IMXB have relatively short accretion timescales, quickly losing enough mass to become LMXB (van den Heuvel, 1975; Li, 2010).

1.1.1 Low mass X-ray binaries (LMXB)

LMXB form when a neutron star has slowed enough to stop emitting observable radiation due to the loss of rotational energy, and is spun up again via accretion from a low-mass companion. In LMXB, the low-mass star fills its Roche lobe, the region in which material is gravitationally bound to the star. Material outside of the Roche-lobe can fall onto the binary companion and so accretion can be persistent. An optically-thick accretion disc forms, as too much angular momentum is accreted for the neutron star to accrete spherically (this is discussed further in Section 1.2). The accretion of angular momentum, combined with the relatively low magnetic field of these older neutron stars, can cause the neutron stars in LMXB to have spin periods on the order of ms. LMXB generally have X-ray luminosities of $\sim 10^{35} - 10^{38}$ erg s^{-1}, with $\lesssim$10 keV spectra (Tauris and van den Heuvel, 2006). Since the two stars must be close enough for Roche lobe

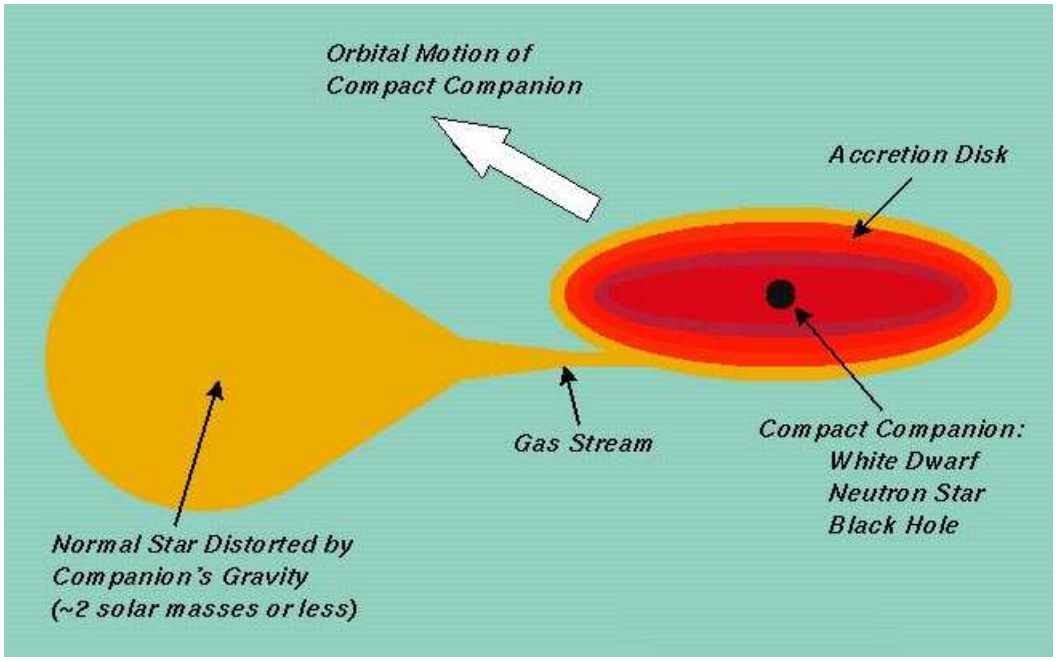

Figure 1.1: Diagram of a LMXB accreting via Roche-lobe overflow (as discussed in Section 1.1.1). Image credit: modified from NASA/Ron Elsner.

overflow to occur, the orbital periods of neutron stars in LMXB depend on the mass of the companion, and typically range from tens of minutes to tens of days (Wu et al., 2010). A diagram of an LMXB is shown in Figure 1.1.

The accretion timescales of LMXB are determined by the mass-transfer process, and LMXB typically accrete for $\sim 10^7 - 10^9$ yr. LMXB are composed of relatively old stars (with ages of $\gtrsim 10^9$ yr), and so are more frequent in the Galactic bulge and in globular clusters (Tauris and van den Heuvel, 2006). They have also been observed outside of the Milky Way, in the Large Magellanic Cloud (LMC), an irregular galaxy that is gravitationally bound to our own (Nazé, 2009), and in M31, the closest spiral galaxy to our own (Peacock et al., 2002).

1.1.2 High mass X-ray binaries (HMXB)

HMXB form from a binary system containing two massive stars. The most massive star evolves fastest, shedding its outer layers, which may be captured by the other star. It then undergoes a supernova, which makes the orbit wider and more eccentric than before.

HMXB are divided into two classes; SGXB and BeXB. SGXB have a massive evolved companion (a luminosity class I-II, O-B-type star). The massive companion of a BeXB is usually a main sequence star (luminosity class III-V), and has a transient circumstellar disc. In Chapter 2, I show that these discs have an average radius of $\sim 20\ R_{OB}$, where R_{OB} is the radius of the massive star. O-B-type stars that have shown evidence for

a circumstellar disc are known as OBe stars, because evidence for the disc comes from hydrogen emission lines in their spectra (discussed further in Section 1.1.2.1). A diagram of a SGXB is shown in Figure 1.2, and diagrams of BeXB are shown in Figures 1.3 and 1.4.

The neutron stars in SGXB tend to accrete persistently from the massive star's stellar wind, either via spherical accretion (with luminosities of $\sim 10^{35} - 10^{36}$ erg s^{-1}) or Roche lobe overflow with an accretion disc (with luminosities of $\sim 10^{35} - 10^{38}$ erg s^{-1}) (Tauris and van den Heuvel, 2006). OBe stars do not fill their Roche lobe, and the velocity of material in the circumstellar disc is both perpendicular to, and far less than, that of a direct stellar wind (in SGXB, a direct stellar wind is thought to reach velocities of up to ∼2000 km s^{-1} (Negueruela, 2010), whereas I show in Chapter 2 that the velocity of material at the edge of the circumstellar disc is ∼150 km s^{-1}). This means that BeXB tend to only accrete from the OBe star's circumstellar disc during periastron (with luminosities of $\sim 10^{35} - 10^{38}$ erg s^{-1}). HMXB generally have harder energy spectra than LMXB (LMXB have spectra $kT \lesssim 10$ keV, whereas HMXB have spectra $kT \gtrsim 15$ keV (Tauris and van den Heuvel, 2006)).

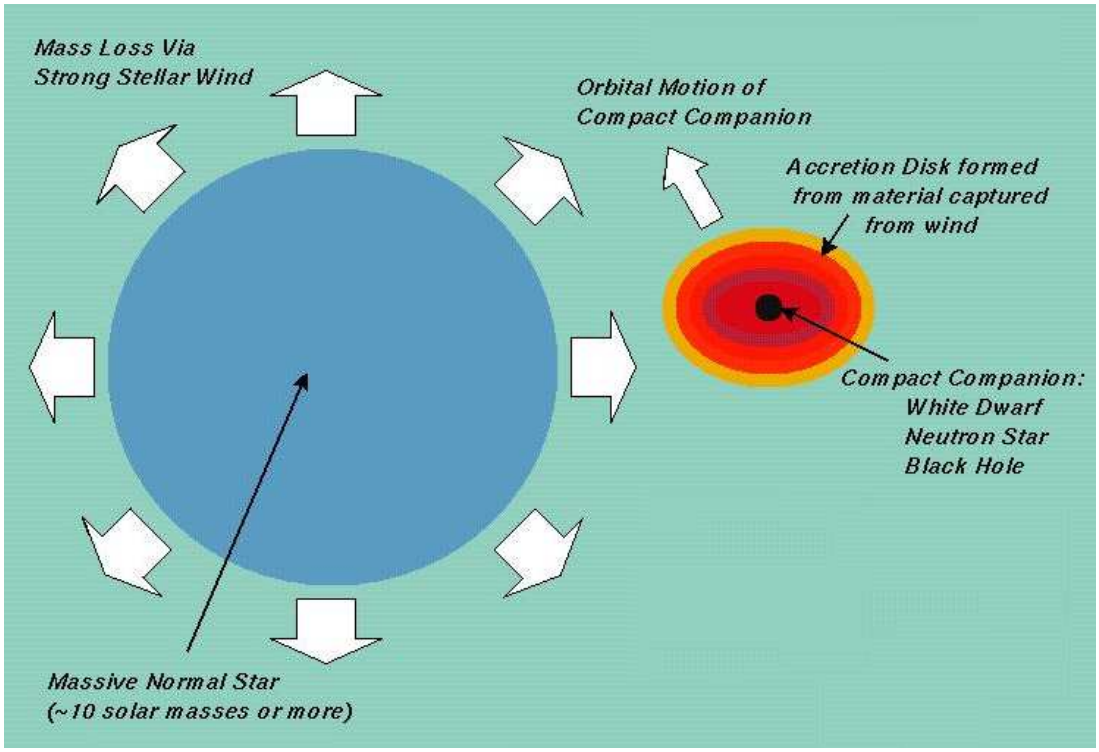

Figure 1.2: Diagram of a wind-fed SGXB (as discussed in Section 1.1.2). Image credit: modified from NASA/Ron Elsner.

The different methods of accretion are reflected in the different positions these systems have on the Corbet (1984) diagram, a plot of spin period as a function of orbital period for HMXB, shown in Figure 1.5. Figure 1.5 shows that disc-fed SGXB have spin periods on the order of ∼1-10 s, and orbital periods of ∼1-3 d. There are only three confirmed

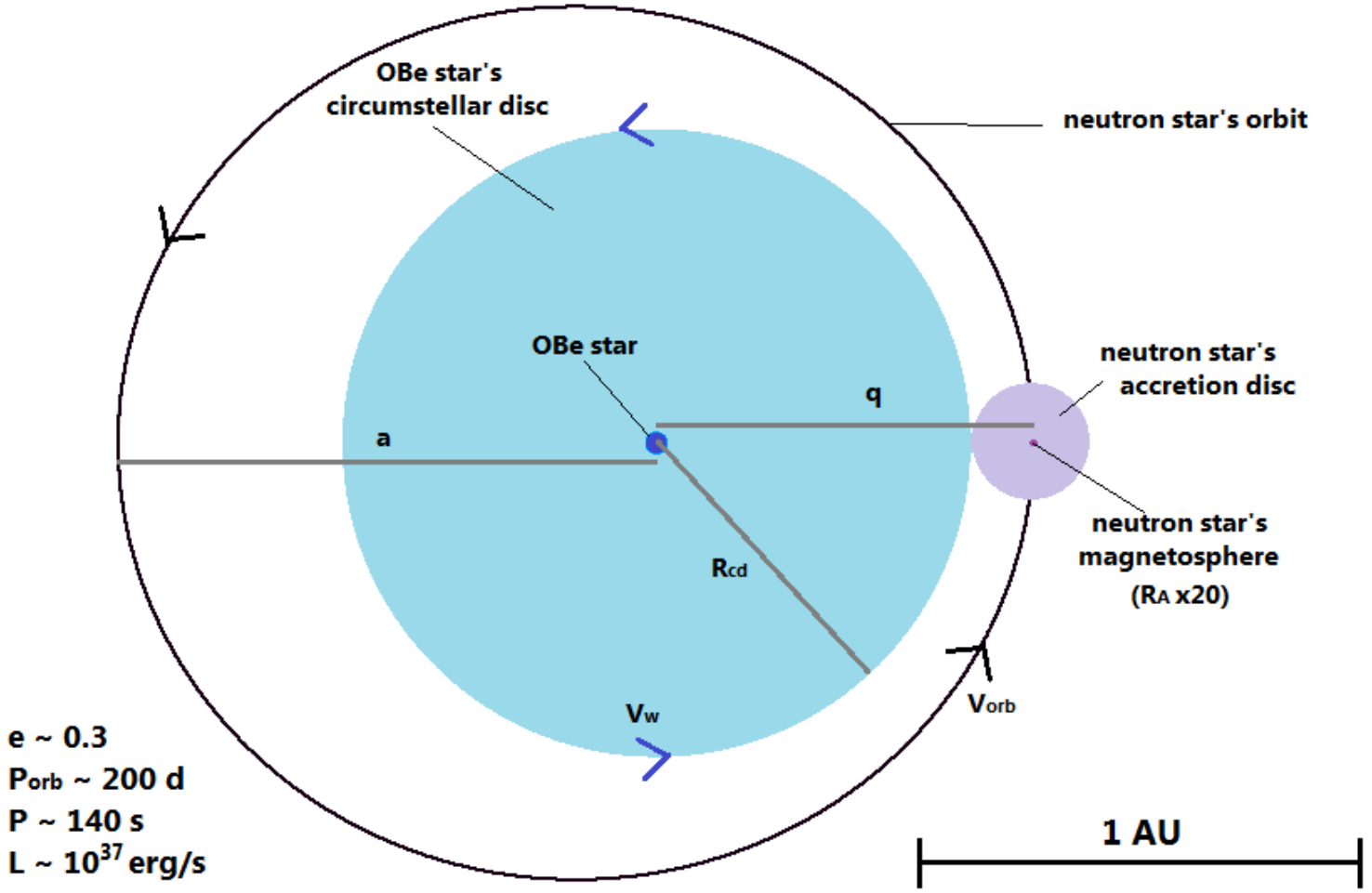

Figure 1.3: Diagram of a typical BeXB to scale (as discussed in Section 1.1.2.1; image viewed from above). The values of a, q, R_{cd}, V_w, and V_{orb} are discussed in Section 2.2.1. Diagrams of specific systems are shown in Appendix B.

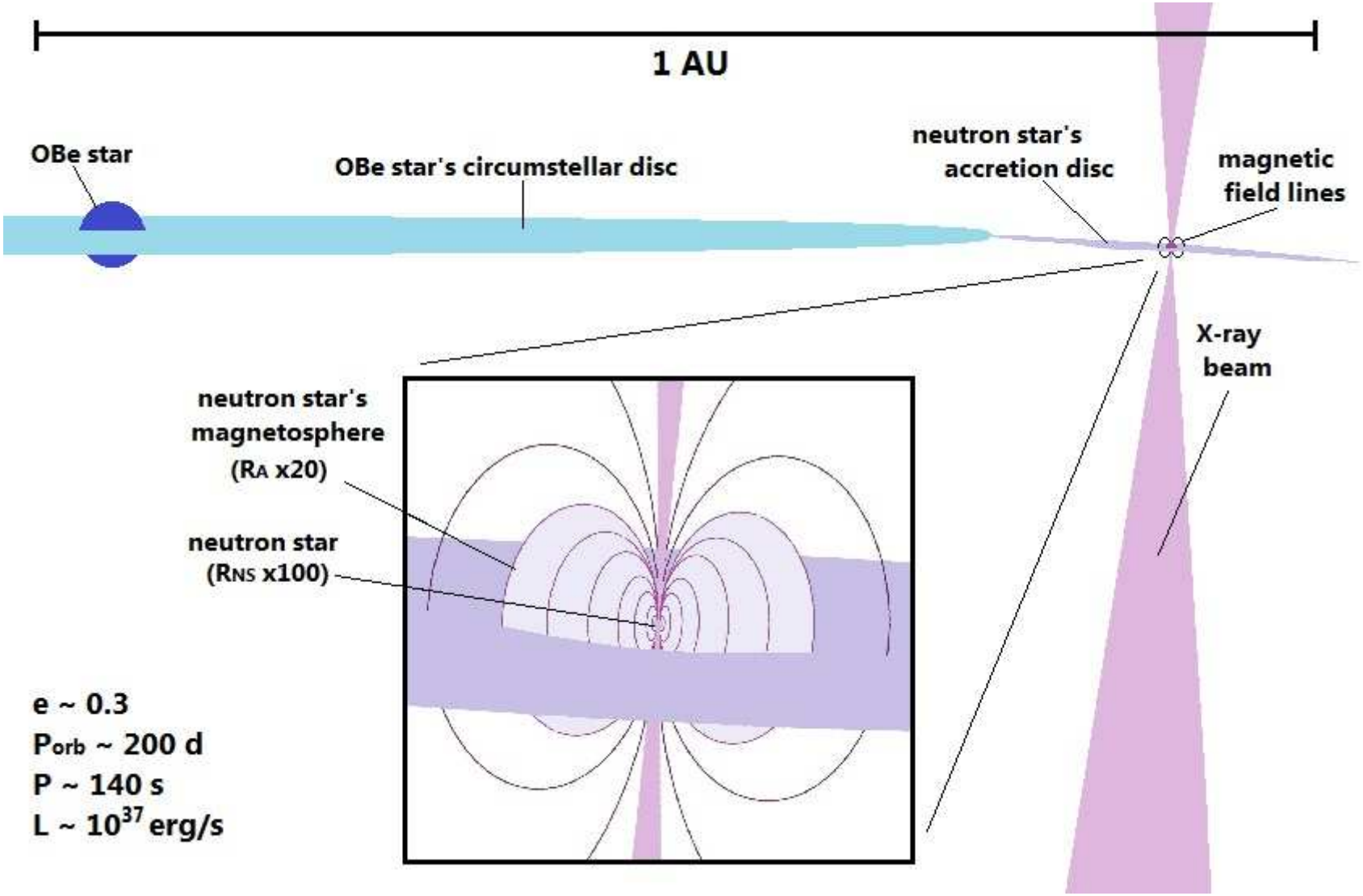

Figure 1.4: Diagram of a typical BeXB to scale (as discussed in Section 1.1.2.1; image viewed from the side).

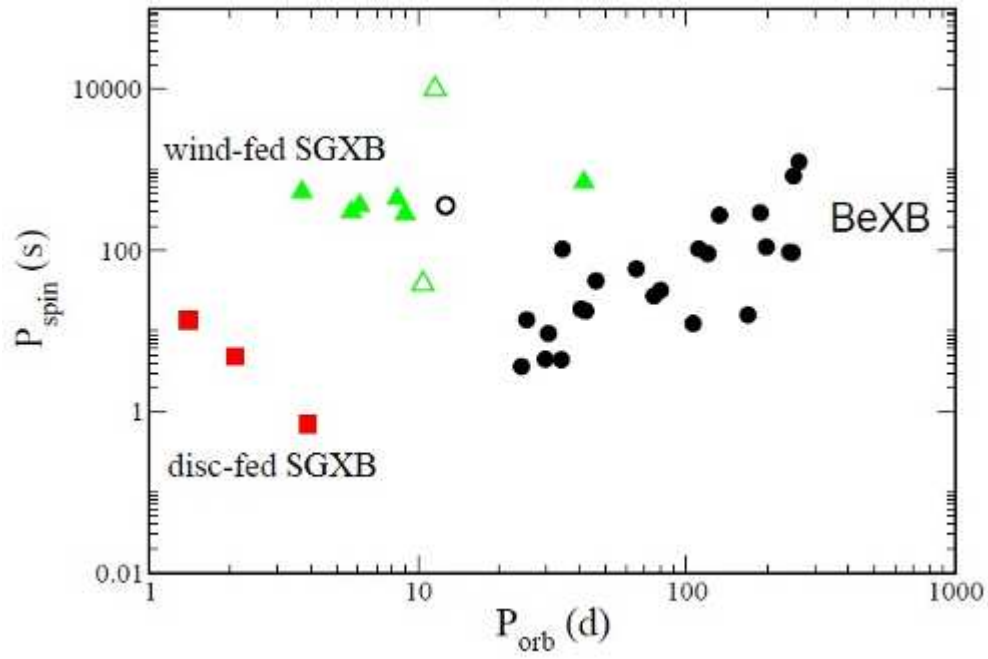

Figure 1.5: The Corbet (1984) diagram for HMXB (as discussed in Section 1.1.2). Wind-fed SGXB (green) do not show a strong correlation between spin period and orbital period because they tend to accrete spherically. Disc-fed SGXB (red) tend to have shorter spin periods if they have longer orbital periods because they are accreting via Roche lobe overflow. BeXB that are spinning at their equilibrium spin period (black) tend to have longer spin periods if they have longer orbital periods because they only accrete during periastron (as discussed in Section 1.2.2). The open triangles correspond to 2S 0114+65 and OAO 1657-41, and the open circle to SAX J2103.5+4545. These are all atypical systems. Image credit: modified from Reig (2011).

disc-fed SGXB, these are most likely accreting persistently via Roche lobe overflow. Wind-fed SGXB have spin periods on the order of ∼200-900 s, and orbital periods of ∼2-40 d. They do not show a clear correlation between orbital period and spin period. This is most likely because they are persistently accreting via a spherical wind. BeXB have spin periods on the order of ∼1-3000 s, and orbital periods of ∼20-400 d. The neutron stars in BeXB have wider, more eccentric orbits than those in SGXB, and they tend to have longer spin periods if they have longer orbital periods. This is because they generally only accrete during periastron, and so systems with longer orbital periods contain neutron stars that accrete less often, and spend longer amounts of time spinning down between accretion events. This means that they spin-down faster than neutron stars with shorter orbital periods. This correlation only holds for prograde systems with neutron stars that are close to spin equilibrium (as discussed in Section 1.2). The majority of neutron stars in BeXB are thought to be in prograde orbits (Brandt and Podsiadlowski, 1995), and in Chapter 2, I argue that most BeXB in the SMC are close to spin equilibrium.

The accretion time-scale and age of the stars in HMXB are dependent on the mass of the

companion star. HMXB generally have shorter accretion timescales than LMXB (LMXB have accretion timescales of $\sim 10^7 - 10^9$ yr, and HMXB have accretion timescales of $\sim 10^5$ yr (Tauris and van den Heuvel, 2006)). Since massive stars have relatively short lifetimes, HMXB are also composed of younger stars than LMXB (LMXB contain stars with ages of $\gtrsim 10^9$ yr and HMXB contain stars with ages of $\lesssim 10^7$ yr (Tauris and van den Heuvel, 2006)). The same correlation holds between SGXB and BeXB, where SGXB are composed of more massive, and therefore younger stars (Binder et al., 2011).

The age of these systems is reflected in their number and location. HMXB are mostly found in star-forming regions in the Galactic plane. To date, there are at least 68 suspected SGXB in the Galaxy, only one of which is disc-fed (Cen X-3). There are only two known SGXB outside of the Galaxy. One in the LMC (LMC X-4), and one (SMC X-1) in the Small Magellanic Cloud (SMC), an irregular dwarf galaxy gravitationally bound to the LMC. These are both disc-fed (Reig, 2011).

There are a roughly even number of SGXB and BeXB in the Galaxy, with at least 63 suspected BeXB (Reig, 2011). There are even more BeXB, however, outside of the Milky Way. There are at least 69 BeXB in the SMC, and at least 14 in the LMC. This number is increasing at a constant rate of ∼2 BeXB per year, while no extra-galactic SGXB have been discovered since the 1970s.

The SMC has a BeXB population that is comparable in number to the Galaxy, despite the fact that it is almost two hundred times less massive. The high number of BeXB in the SMC can be explained by recent bursts of star formation (Antoniou et al., 2010), combined with the low metallicity environment (Russell and Dopita, 1992). A low metallicity means weaker line-driven stellar winds, and so binaries are more likely to remain intact after a supernova (Dray, 2006).

Sub-classes of HMXB include supergiant fast X-ray transients (SFXTs), gamma-ray binaries, and γ Cas-like objects. SFXT are like SGXB, but their outbursts appear only sporadically, and last for only a few hours, reaching luminosities of $\sim 10^{36} - 10^{37}$ erg s^{-1}. These outbursts may result from the accretion of a clump of dense matter from the stellar wind (Romano et al., 2010). They may also be caused by the decay and instabilities of their magnetic field, making them magnetars (Grebenev, 2010). Finally, it is possible that SFXTs are SGXB in highly elliptical orbits, with outbursts occurring at periastron (Reig, 2011).

Gamma-ray binaries are HMXB that emit most of their radiation in the MeV-TeV range. There are currently only four members of this group, only one of which is thought to contain a neutron star and not a black hole, this is PSR B1259-63, although HESS J0632+057 is a possible candidate (Reig, 2011). Both of these systems contain OBe stars.

γ Cas-like objects are BeXB where the OBe star exhibits a series of strong, sharp absorption lines at irregular intervals. This coincides with the OBe star becoming dimmer, and is thought to be due to the OBe star ejecting material, which settles into a ring or a shell around the star (Reig, 2011).

1.1.2.1 Be X-ray binaries (BeXB)

The compact object in the vast majority of BeXB is a neutron star (Reig, 2011), although there are several white dwarf candidates (Haberl, 1995; de Oliveira et al., 2006; Sturm et al., 2012), and a single system containing a black hole, which is X-ray quiescent (Casares et al., 2014; Munar-Adrover et al., 2014). The discovery of this system helps confirm the idea that BeXB containing black holes are difficult to find because they undergo long quiescent states (Zhang et al., 2004). This is contrasted with the idea that there are fewer BeXB containing black holes because they have a lower probability of being formed in the first place (Belczynski and Ziolkowski, 2009).

This work will concentrate on BeXB containing neutron stars, looking at 42 BeXB in the SMC in Chapters 2 and 3, and concentrating on a single system in the LMC in Chapter 4.

Knigge et al. (2011) suggest that BeXB may be split into two populations based on their spin period, which is related to their orbital period via the Corbet (1984) relation (discussed in Section 1.1.2). In Knigge et al. (2011), the authors show that the spin period distribution of 120 confirmed and probable BeXB has two peaks when plotted on a logarithmic scale. The first peak is at $\sim$10 s (corresponding to an orbital period of $\sim$40 d). There is a second, slightly larger peak at $\sim$200 s (corresponding to an orbital period of $\sim$100 d). This is shown in Figure 1.6. The neutron stars in these two populations may be formed by different types of supernova, where neutron stars with relatively long spin periods are created in iron-core-collapse supernovae, and neutron stars with relatively short spin periods are created in electron-capture supernovae (Knigge et al., 2011).

Iron-core-collapse supernovae occur when a high-mass star develops a degenerate iron core before ceasing fusion and collapsing under its own gravity (Woosley and Janka, 2005). Electron-capture supernovae occur when a lower mass star ceases fusion and collapses while it still has an oxygen-neon-magnesium core (Nomoto, 1984, 1987; Heger et al., 2003).

If neutron stars with relatively long spin periods are created in iron-core-collapse supernovae, then they may also have larger masses than those with shorter spin periods. Neutron stars created in iron-core-collapse supernovae are predicted to have masses of $\sim$1.4 $M_{\odot}$, and neutron stars created in electron-capture supernovae are predicted to have masses of $\lesssim$1.3 $M_{\odot}$ (Nomoto, 1984). Iron-core-collapse supernovae also produce more energetic neutron star 'kicks' (iron-core-collapse supernovae produce neutron star kicks

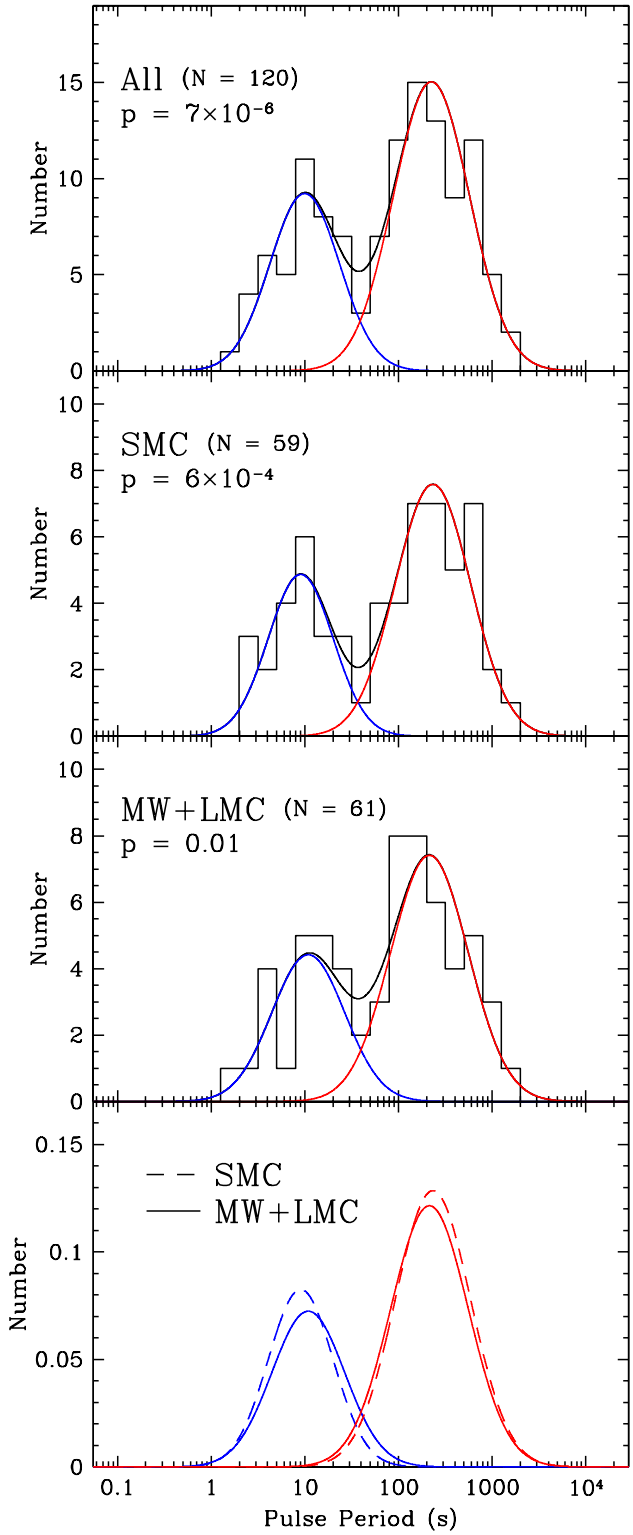

Figure 1.6: Distribution of spin periods for neutron stars in BeXB (as discussed in Section 1.1.2.1). Knigge et al. (2011) suggest that the two populations may be caused by different formation mechanisms, where neutron stars with longer spin periods are created in iron-core-collapse supernovae, and neutron stars with shorter spin periods are created in electron-capture supernovae. Image credit: Knigge et al. (2011).

of $\leq$200 km s^{-1}, whereas electron-capture supernovae are expected to produce neutron star kicks of $\leq$50 km s^{-1} (Podsiadlowski et al., 2004)). A higher velocity kick leads to an increase in the orbital period and eccentricity of the system.

BeXB can also be split into transient and persistent populations. Most BeXB, including all known BeXB with spin periods $\lesssim$150 s, are transient, usually only accreting at periastron, in what are known as Type I outbursts. Transient sources may also emit outbursts at seemingly random times. These are known as Type II outbursts (Stella et al., 1986). Type II outbursts last for longer than Type I outbursts (Type II outbursts can last for longer than the orbital period, whereas Type I outbursts last for $\sim$25% of the orbital period). Type II outbursts also reach higher luminosities, increasing by up to four orders of magnitude, to $\gtrsim 10^{38}$ erg s^{-1}, whereas Type I outbursts coincide with an increase by about an order of magnitude, to $10^{36} - 10^{38}$ erg s^{-1} (Reig, 2011). Type II outbursts are most likely caused by the OBe star, where its circumstellar material or radially driven wind are enhanced so that accretion can occur at a higher rate and at any phase of the orbit (Stella et al., 1986; Negueruela and Okazaki, 2000).

Persistent BeXB tend to accrete throughout their orbital phase. The 6 known persistent BeXB have spin periods of $\gtrsim$150 s, and tend to have lower luminosities than transient BeXB (on the order of $\sim 10^{34} - 10^{35}$ erg s^{-1}). They also sometimes have a blackbody component in their spectra, known as a thermal excess (Bartlett et al., 2013). This allows the radius of the emission region to be determined. In Chapter 4, I provide evidence that LMC source LXP187 (also known as Swift J045106.8-694803) is also a persistent source. Persistent emission is most likely related to the behaviour of the OBe star's circumstellar disc, which may also be persistent in these sources (Bartlett et al., 2013).

The behaviour of an OBe star's circumstellar disc can be observed in the optical and infra-red bands. The presence of a circumstellar disc can be inferred by $H\alpha$ emission lines, which are caused by ionised hydrogen in the circumstellar disc absorbing and re-emitting the optical and ultraviolet light from the OBe star. $H\alpha$ emission lines are shown in Figure 1.7. OBe stars also show more infrared emission than O or B-type stars. This is a result of free-free and free-bound emission from the circumstellar disc (Woolf et al., 1970; Gehrz et al., 1974). The size of the circumstellar disc is directly related to the equivalent-width of the $H\alpha$ emission line (EW $H\alpha$) (Hanuschik, 1989; Huang, 1972).

The circumstellar disc of OBe stars in X-ray binaries are often truncated compared to those of isolated OBe stars due to the tidal interaction of the neutron star. This means that their circumstellar discs are smaller and more compact (Reig et al., 1997; Negueruela and Okazaki, 2001; Okazaki and Negueruela, 2001; Okazaki et al., 2002).

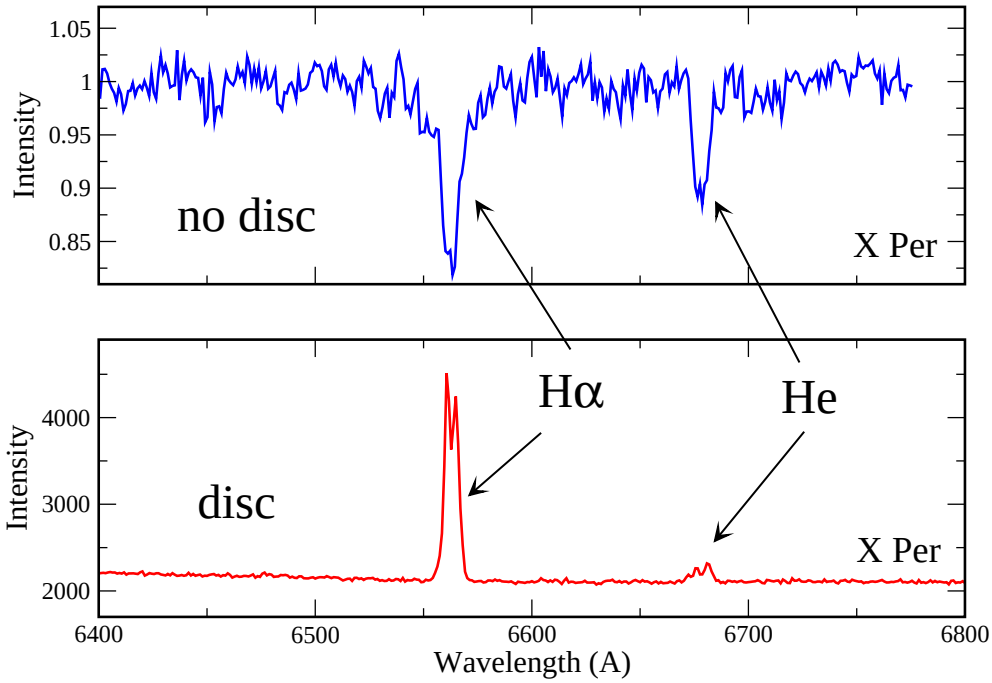

Figure 1.7: The spectra of a BeXB showing emission lines that indicate the presence of a circumstellar disc (as discussed in Section 1.1.2.1). Image credit: Reig (2011).

1.2 Accretion theory for neutron stars in BeXB

The magnetic field of neutron stars in BeXB can be determined directly, from cyclotron resonance scattering features (CRSF) in their spectra (discussed further in Section 1.3.1), or indirectly, using accretion theories. Accretion theories differ, depending on whether accretion is taking place via an accretion disc or a spherical wind.

In BeXB, matter from the OBe star's circumstellar disc begins accreting onto the neutron star's magnetosphere from the gravitational capture or Bondi-Hoyle radius (R_B) (Davidson and Ostriker, 1973; Alpar et al., 1982).

$$R_B = \frac{2GM_{NS}}{V_{rel}^2}, \tag{1.1}$$

where G is the gravitational constant, M_{NS} is the mass of the neutron star, and V_{rel} is the relative velocity of accreted matter (discussed further in Section 2.2.1).

The amount of accreted angular momentum is great enough to cause an accretion disc to form at the circularisation radius (R_{circ}).

$$R_{circ} = \frac{J^2}{GM_{NS}}, \tag{1.2}$$

where J is the net angular momentum (l) per unit mass.

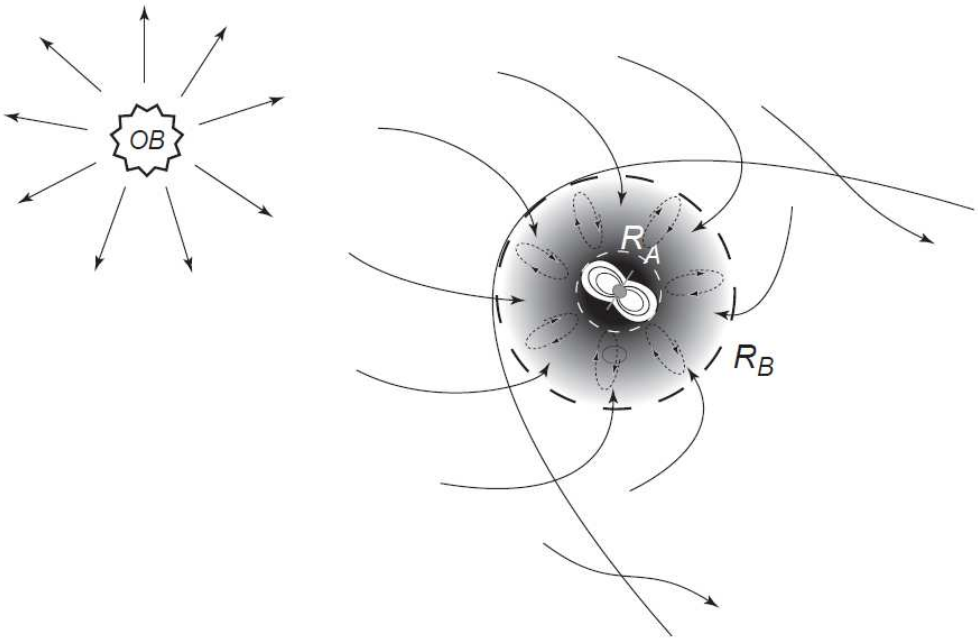

Figure 1.8: Diagram of quasi-spherical accretion in a BeXB. In spherical accretion, matter is accreted from the gravitational capture or Bondi-Hoyle radius (R_B). Within the Alfvén radius (R_A), it can be channelled by the neutron star's magnetic field lines to the magnetic poles. In quasi-spherical accretion, matter first settles down subsonically onto the rotating magnetosphere, forming an extended quasi-static shell extending from R_A to R_B (Postnov et al., 2011; Shakura et al., 2012, 2013) (as discussed in Section 1.2). Image credit: Shakura et al. (2013).

A disc cannot form inside of the neutron star's magnetosphere, however, and so a disc can only form if the circularisation radius is larger than the radius of the neutron star's magnetosphere. The neutron star's magnetosphere is approximately within the Alfvén radius (R_A) (Elsner and Lamb, 1977). Here the ram pressure of accreted matter equals the magnetic pressure, and so the kinetic energy density of accreted matter ($\frac{1}{2}\rho_a V^2$, where ρ_a is the density of the accreted matter, and V is the velocity) equals the magnetic energy density ($B^2/8\pi$, where B is the magnetic field). Assuming that matter falls onto the magnetosphere in spherical radial free fall (ff), then

$$V = V_{ff} = \sqrt{2GM_{NS}/R_A}, \tag{1.3}$$

and,

$$\rho_a = \frac{\dot{M}}{4\pi V_{ff} R_A^2}. \tag{1.4}$$

Assuming the magnetic field is dipolar, then

$$\mu = BR^3, \tag{1.5}$$

where μ is the magnetic dipole moment, and R is the radius. In this case, $R = R_A$, and so,

$$\frac{1}{2}\rho_a V^2 = B^2/8\pi \tag{1.6}$$

giving

$$R_A = \left(\frac{\mu^4}{2GM_{NS}\dot{M}^2}\right)^{1/7}. \tag{1.7}$$

If $R_{circ} < R_A$, then an accretion disc cannot form, and accretion occurs via spherical or quasi-spherical wind accretion. If $R_{circ} > R_A$, then an accretion disc can form, outside of the neutron star's magnetosphere.

R_{circ} depends on the net angular momentum per unit mass, which is related to the mass-accretion rate ($\dot{M}$; equation (2.11)). This is directly related to the X-ray luminosity (L) via

$$L = \frac{dE}{dt} = \frac{GM_{NS}\dot{M}}{R_{NS}} \tag{1.8}$$

where E is energy, and R_{NS} is the radius of the neutron star (Novikov and Thorne, 1973).

Neutron stars in BeXB can sometimes exceed the Eddington luminosity (L_{Edd}). The Eddington luminosity is the maximum luminosity that an object can reach, assuming it is accreting spherically. This occurs when the radiation pressure on in-falling material is equal to the gravitational force of the star,

$$\frac{GM_{NS}m_p}{R^2} = \frac{L_{Edd}\sigma_T}{4\pi cR^2}, \tag{1.9}$$

where m_p is the mass of a proton, σ_T is the Thomson cross section for the electron, and c is the speed of light, and so

$$\begin{aligned} L_{Edd} &= \frac{4\pi cGM_{NS}m_p}{\sigma_T}, \\ &\cong 1.26 \times 10^{38}\frac{M_{NS}}{M_\odot}\ \text{erg s}^{-1}. \end{aligned} \tag{1.10}$$

Neutron stars in BeXB may produce $L > L_{Edd}$ because the accretion is asymmetric, and so radiation may escape from the sides of the accretion column (discussed further in Section 1.3). The opacity may also be less than that given by Thomson scattering due to the relatively high magnetic field (Srinivasan, 2006).

1.2.1 Wind accretion

If there is not enough angular momentum for an accretion disc to form outside of the neutron star's magnetosphere, then matter can fall on to the neutron star's magnetosphere

in all directions, as shown in Figure 1.8. This is known as spherical wind accretion, or Bondi-Hoyle accretion (Illarionov and Sunyaev, 1975; Illarionov and Kompaneets, 1990).

For a neutron star in a prograde orbit, accreting via a spherical wind, the spin-up torque ($\tau_{up\ (wind)}$) is equal to

$$\tau_{up\ (wind)} = 2\pi \dot{M} \eta R_B^2 P_{orb}^{-1}, \tag{1.11}$$

where P_{orb} is the orbital period, and η is a parameter accounting for dissipation of angular momentum in the accreting material, $0 < \eta < 1$, and is assumed in this work to be $0.25 \pm ^{0.75}_{0.15}$ (Ikhsanov and Finger, 2012; Lipunov, 1992). Equation (1.11) shows that the spin-up rate of a wind-accreting neutron star depends on the mass-accretion rate, and hence X-ray luminosity (equation (1.8)), the orbital period, and the relative velocity of accreted matter (equation (1.1)). The spin-up rate is not affected by the neutron star's magnetic field.

The spin-down torque (τ_{down}), caused by the loss of rotational energy, is the same for wind and disc-accreting systems, and is equal to

$$\tau_{down} = \kappa_t \mu^2 / {R_{co}}^3, \tag{1.12}$$

where κ_t is a dimensionless efficiency parameter, accounting for the conductivity, spectrum of turbulence and inhomogeneities of the accreting material, $0 < \kappa_t < 1$, and is assumed in this work to be $1/3 \pm ^{2/3}_{1/3}$ (Lipunov, 1992; Ikhsanov and Finger, 2012; Ikhsanov et al., 2014). R_{co} is the radius at which matter co-rotates with the neutron star and its magnetosphere,

$$R_{co} = \left(\frac{G M_{NS} P^2}{4\pi^2} \right)^{1/3}. \tag{1.13}$$

Equation (1.12) shows that a neutron star in a BeXB spins down at a higher rate the higher the magnetic field, and the shorter the spin period.

When a neutron star is neither spinning up nor down on average, and so has a long-term average $\dot{P}$ of ~ 0, the spin-up torque equals the spin-down torque, and so

$$\tau_{up\ (wind)} = \tau_{down} \tag{1.14}$$

$$2\pi \dot{M} \eta R_B^2 P_{orb}^{-1} = \kappa_t \mu^2 / {R_{co}}^3. \tag{1.15}$$

The magnetic field on the surface of the neutron star can then be found using equation (1.5),

$$B \cong 8.7 \times 10^{13}\ \mathrm{G} \left(\frac{4\eta}{3\kappa_t} \right)^{1/2} R_{NS6}^{-3} \left(\frac{M_{NS}}{M_\odot} \right)^{3/2} \dot{M}_{16}^{1/2} \left(\frac{V_{rel}}{100\ \mathrm{km\ s^{-1}}} \right)^{-2} \frac{P/100}{(P_{orb}/10\ \mathrm{d})^{1/2}}. \tag{1.16}$$

Here V_{rel} is measured in km s^{-1}, P_{orb} is measured in d, and everything else is in cgs units, $R_{NS6} = R_{NS}/10^6$ and $\dot{M}_{16} = \dot{M}/10^{16}$. η and κ_t are normalised to values of 1/4 and 1/3 respectively. Equation (1.16) shows that in wind-accreting systems, with a long-term average $\dot{P}$ of ~ 0, and a set M_{NS} and R_{NS}, B is proportional to P and L, and inversely proportional to V_{rel} and P_{orb}. Here B is most affected by V_{rel}.

Postnov et al. (2011) and Shakura et al. (2012) suggest that these equations need to be adjusted. This is because matter settles down subsonically onto the rotating magnetosphere, forming a quasi-static shell that extends from R_A to R_B, and material must pass through this shell before being accreted (as shown in Figure 1.8). Shakura et al. (2012) find

$$B \cong 6 \times 10^{14} \text{ G } R_{NS6}^{-3} \dot{M}_{16}^{1/3} \left(\frac{V_{rel}}{100 \text{ km s}^{-1}} \right)^{-11/3} \left(\frac{P/100}{P_{orb}/10 \text{ d}} \right)^{11/12}. \quad (1.17)$$

As with equation (1.16), V_{rel} is measured in km s^{-1}, P_{orb} is measured in d, and everything else is in cgs units. Equation (1.17) shows that in wind-accreting systems, with a long-term average $\dot{P}$ of ~ 0, and a set M_{NS} and R_{NS}, B is proportional to P and L, and inversely proportional to V_{rel} and P_{orb}. B is most affected by V_{rel}, and is more affected by this factor in equation (1.17) than in equation (1.16).

1.2.2 Disc accretion

An accretion disc forms if $R_{circ} > R_A$, and, in Chapter 2, I predict that this is the case for most BeXB. Disc accretion brings with it directional angular momentum, which generally causes the neutron star to spin-up. This is only true, however, if the neutron star is in a prograde orbit, meaning that the neutron star orbits in the same direction as material in the OBe star's circumstellar disc. The majority of neutron stars in BeXB are thought to be in prograde orbits (Brandt and Podsiadlowski, 1995), although there may be a misalignment between the spin axis of the OBe star's circumstellar disc and the spin axis of the binary orbit (Martin et al., 2009). This may be due to the supernova kick that occurred when the neutron star was formed (Lai, 1996), or from radiation-induced warping within the OBe star's circumstellar disc (Pringle, 1996).

The spin-up torque of a prograde BeXB accreting via an accretion disc is equal to

$$\tau_{up\ (disc)} = \dot{M} \sqrt{G M_{NS} \epsilon R_A}, \quad (1.18)$$

where ϵ is a numerical coefficient equal to R_0/R_A. R_0 is defined as the radius at which accreted matter is forced to follow the magnetic field lines, $0 < \epsilon < 1$, and is assumed in this work to be $0.5 \pm ^{0.5}_{0.4}$ R_A (Ghosh and Lamb, 1979; Lipunov, 1992). Equation (1.18) shows that in disc-accreting BeXB, the neutron star spins up at a higher rate the higher the mass-accretion rate, and hence X-ray luminosity (equation (1.8)), and the higher

the magnetic field (equation (1.7)). The spin-down torque is the same as in the wind accretion case (equation (1.12)) and has a stronger dependence on μ than the spin-up torque for disc-accreting systems.

The magnetic field of a disc-accreting neutron star with a long-term average $\dot{P}$ of ~ 0 can be calculated by equating the spin-up and spin-down torques (Pringle and Rees, 1972). This gives

$$\tau_{up\ (disc)} = \tau_{down} \tag{1.19}$$

$$\dot{M}\sqrt{GM_{NS}\epsilon R_A} = \kappa_t \mu^2 / {R_{co}}^3, \tag{1.20}$$

and so

$$B \cong 1.9 \times 10^{13}\ \mathrm{G} \left(\frac{2\epsilon}{9\kappa_t^2}\right)^{7/24} R_{NS6}^{-3} \left(\frac{M_{NS}}{M_\odot}\right)^{5/6} \dot{M}_{16}^{1/2} \left(\frac{P}{100}\right)^{7/6}, \tag{1.21}$$

where ϵ and κ are normalised to values of 1/2 and 1/3 respectively. Equation (1.21) shows that in disc-accreting systems, with a long-term average $\dot{P}$ of ~ 0, and a set M_{NS} and R_{NS}, B is proportional to P and L. This means that if these systems have similar luminosities, neutron stars with longer spin periods must have higher magnetic fields. If $L = 10^{37}$ erg s^{-1}, M_{NS}=1.4 $M_\odot$, and R_{NS}=10 km, for example, then neutron stars with spin periods >68 s are predicted to have magnetar-strength magnetic fields ($B > B_{QED}$, where $B_{QED} \cong 4.4 \times 10^{13}$ G is the quantum critical field, discussed in Section 1.3.1).

For disc-accreting neutron stars with a long-term average $\dot{P}$ of ~ 0, the magnetic field can also be calculated by equating R_{co} with R_A (Davidson and Ostriker, 1973; Alpar et al., 1982). This is because matter has no affect on the neutron star's spin period if it is co-rotating with the neutron star's magnetosphere, and so is neither accreted nor expelled (this is discussed further below). If $R_{co} = R_A$, then the magnetic field of a neutron star with a set M_{NS} and R_{NS} is proportional to P and L,

$$R_{co} = R_A \tag{1.22}$$

$$\left(\frac{GM_{NS}P^2}{4\pi^2}\right)^{1/3} = \left(\frac{\mu^4}{2GM_{NS}\dot{M}^2}\right)^{1/7}, \tag{1.23}$$

and so

$$B \cong 1.5 \times 10^{13}\ \mathrm{G}\ R_{NS6}^{-3} \left(\frac{M_{NS}}{M_\odot}\right)^{5/6} \dot{M}_{16}^{1/2} \left(\frac{P}{100}\right)^{7/6}. \tag{1.24}$$

Equation (1.24) gives slightly lower results than equation (1.21). If $L = 10^{37}$ erg s^{-1}, M_{NS}=1.4 $M_\odot$, and R_{NS}=10 km, then neutron stars with spin periods >84 s are predicted to have magnetic fields > B_{QED}.

The neutron stars in BeXB do not always have a long-term average $\dot{P}$ of ~ 0. Neutron stars in BeXB first appear as radio pulsars, during what is known as the ejector phase (Lipunov, 1992; Fu and Li, 2012). During this phase they radiate at the expense of

their rotational energy, and the pressure of outgoing radiation and particles is larger than the pressure of accreted matter at R_B. This means that matter from the OBe star's circumstellar disc cannot pass within this radius. The propeller phase begins when the neutron star has spun down enough for matter to be able to pass within R_B (Shvartsman, 1970; Illarionov and Sunyaev, 1975). A hot, spherical quasi-static envelope can form around the neutron star's magnetosphere, but matter cannot pass within the magnetosphere because R_{co} is within R_A, and so the neutron star is spinning too quickly (Davidson and Ostriker, 1973; Alpar et al., 1982). Instead, the centrifugal force causes matter to accelerate outwards, taking away angular momentum, and causing the neutron star to spin-down further. The neutron star spins down until its magnetosphere is co-rotating with the accreted material ($R_{co} = R_A$). At rotational velocities below this ($R_{co} > R_A$), matter is usually able to penetrate the magnetosphere. If the material is still too hot to be accreted, however, then the neutron star spins down at a subsonic speed, losing further rotational energy until material has cooled enough to be able to penetrate the neutron star's magnetosphere. This is known as the subsonic propeller phase, and is how neutron stars with spin periods $\gtrsim$1000 s are thought to form (Davies and Pringle, 1981; Ikhsanov, 2001a,b, 2007). Accreted material causes the neutron star to spin up, assuming a prograde orbit, but it continues to spin-down between accretion events. The neuron star is said to be close to spin equilibrium when the spin-up rate during accretion is counterbalanced by the spin-down rate between accretion events, and $\dot{P}$ converges on 0 (Davidson and Ostriker, 1973; Alpar et al., 1982). This will happen when the neutron star's spin period converges on the period corresponding to $R_{co} = R_A$, which is known as its equilibrium spin period (P_{eq}).

The magnetic field of a neutron star that is not close to spin equilibrium can be found by considering the total net torque (τ_{tot}).

$$\tau_{tot} = I \times \alpha, \tag{1.25}$$

where α is the angular acceleration

$$\alpha = \dot{\nu} = \frac{-2\pi\dot{P}}{P^2}, \tag{1.26}$$

and I is the moment of inertia,

$$I = 0.4 \times M_{NS} R_{NS}^2. \tag{1.27}$$

This gives

$$\tau_{tot} = \frac{-2\pi I\dot{P}}{P^2}. \tag{1.28}$$

If a system is close to spin equilibrium, then

$$\tau_{tot} = \tau_{up\ (disc)} - \tau_{down} \cong 0. \tag{1.29}$$

If a system is not close to spin equilibrium, then equation (1.29) may be incorrect. Instead, the Ghosh and Lamb (1979) model can be used to determine the neutron star's magnetic field. Here

$$\tau_{tot} = \tau_{up\ (disc)} n(\omega_s), \tag{1.30}$$

where $n(\omega_s)$ varies depending on $\dot{P}$.

For $0 < \omega_s < 0.9$,

$$n(\omega_s) = 1.39(1 - (\omega_s[4.03(1-\omega_s)^{0.173} - 0.878]))(1-\omega_s)^{-1} \tag{1.31}$$

within 5% accuracy, where ω_s is known as the fastness parameter.

$$\omega_s = (\xi_0 R_A / R_{co})^{3/2}, \tag{1.32}$$

where ξ_0 is a numeral coefficient assumed to be 0.38. This gives

$$\omega_s = 1.35 \mu_{30}^{6/7} R_{NS6}^{-3/7} \left(\frac{M_{NS}}{M_\odot}\right)^{-2/7} (P L_{37}^{3/7})^{-1}, \tag{1.33}$$

where $L_{37} = L/10^{37}$.

In the case of spin equilibrium ($\dot{P} = 0,\ R_{co} = R_A$), $\omega_s \cong \xi_0^{3/2}$, and $n(\omega_s) \cong 0$. For systems that are spinning up ($\dot{P} < 0,\ R_{co} > R_A$), $\omega_s < \xi_0^{3/2}$, and $n(\omega_s) > 0$. For systems that are spinning down ($\dot{P} > 0,\ R_{co} < R_A$), $\omega_s > \xi_0^{3/2}$, and $n(\omega_s) < 0$. $\omega_s \cong 0.35$ when $n(\omega_s)$ approaches 0.

Equations (1.30) - (1.33) show that

$$-\dot{P} = 5.0 \times 10^{-5} (\epsilon/0.5)^{1/2} \mu_{30}^{2/7} n(\omega_s) R_{NS6}^{6/7} \left(\frac{M_{NS}}{M_\odot}\right)^{-3/7} I_{45}^{-1} (P L_{37}^{3/7})^2 \text{ s yr}^{-1}, \tag{1.34}$$

where ϵ is assumed to be 0.5. This means that the magnetic field of a disc-accreting neutron star with a set M_{NS} and R_{NS} is dependent only on $\dot{P}$ and $PL^{3/7}$. Results for the Ghosh and Lamb (1979) model for systems that are close to spin equilibrium are ~ 1.4 times lower than those calculated using equation (1.21). A comparison of results from disc accretion models is given in Figure 2.18.

A similar model to the Ghosh and Lamb (1979) model, which we refer to as the Kluzniak and Rappaport (2007) model, uses a different value for ϵ, which is assumed to be 0.52, and ξ_0, which is assumed to be 0.97. Kluzniak and Rappaport (2007) also use a different value for R_A, where $R_{A\ (K\&R)} = 2^{1/7} R_A$, and $n(\omega_s)$, which is designated $g(\omega_s)$.

For $0 < \omega_s < 1$,

$$g(\omega_s) = \frac{10}{9}\left[1 - \frac{1}{20}\frac{\omega_s}{1-\omega_s}\right]. \tag{1.35}$$

In the case of spin equilibrium, ω_s approaches $\xi_0^{3/2}$, and $g(\omega_s)$ approaches 0. With a ξ_0 of 0.97, $\xi^{3/2} \cong 0.95$.

Using the Kluzniak and Rappaport (2007) model,

$$-\dot{P} = 6.2 \times 10^{-5} (\epsilon/0.52)^{1/2} \mu_{30}^{2/7} g(\omega_s) R_{NS6}^{6/7} \left(\frac{M_{NS}}{M_\odot}\right)^{-3/7} I_{45}^{-1} (P L_{37}^{3/7})^2 \text{ s yr}^{-1}, \quad (1.36)$$

where ϵ is assumed to be 0.52. Results from these models can be found assuming the system is close to spin equilibrium (with $\dot{P} = 0$), by working out which value would give a $n(\omega_s)$ of 0, given P and L. Results calculated from the Ghosh and Lamb (1979) model are ∼1.18 times larger than results from the Kluzniak and Rappaport (2007) model for systems that are close to spin equilibrium.

Figures 1.9-1.12 show simulated results for the Ghosh and Lamb (1979) and Kluzniak and Rappaport (2007) models. These were created by assuming values for B, M_{NS}, R_{NS}, and ϵ, and then varying $PL_{37}^{3/7}$ over values of 1-3200. $\dot{P}$ is then determined for each value using equation (1.34) for the Ghosh and Lamb (1979) model, and equation (1.36) for the Kluzniak and Rappaport (2007) model.

Figure 1.9 shows simulated results for neutron stars with $B = 10^{12}$ and $B = 10^{14}$ G, $M_{NS} = 1.4\ M_\odot$, and $R_{NS} = 10$ km, determined using the Ghosh and Lamb (1979) and Kluzniak and Rappaport (2007) models. The difference between spin-up and spin-down results is highlighted. Figure 1.10 shows simulated results for neutron stars with $B = 10^4 - 10^{15}$ G, $M_{NS} = 1.4\ M_\odot$, and $R_{NS} = 10$ km, using the Ghosh and Lamb (1979) model. Figure 1.11 shows simulated results for neutron stars of different masses and radii, with $B = 10^{12}$ and $B = 10^{14}$ G, determined using the Ghosh and Lamb (1979) model. Finally, Figure 1.12 shows simulated results for neutron stars of $M_{NS} = 1.4\ M_\odot$, $R_{NS} = 10$ km, and $B = 10^{12}$ G determined using the Ghosh and Lamb (1979) model, using values of ϵ ranging from 0.1-1. The shape of the simulated results have vertical and diagonal parts. These correspond to the fact that as a system spins up or down, it's P will get shorter or longer until it reaches the equilibrium value. It's $PL_{37}^{3/7}$ will then remain fairly constant. This means that the vertical parts correspond to results for systems that are close to spin equilibrium, and the diagonal parts to results for systems that are not close to spin equilibrium. Many systems will produce results that fall on two different lines, a diagonal line representing the simulated results of a relatively low magnetic field, and a vertical line representing the simulated results of a relatively high magnetic field.

Some accreting pulsars have been found to have magnetar-strength magnetic fields using accretion theories (Fu and Li, 2012; Reig et al., 2012; Ekşi et al., 2014). The first evidence for highly magnetised accreting neutron stars came from Pizzolato et al. (2008), who showed that the X-ray source 1E161348-5055 may be a neutron star with $B \cong 10^{15}$ G. 1E161348-5055 is part of a LMXB system. This was shortly followed by Bozzo et al.

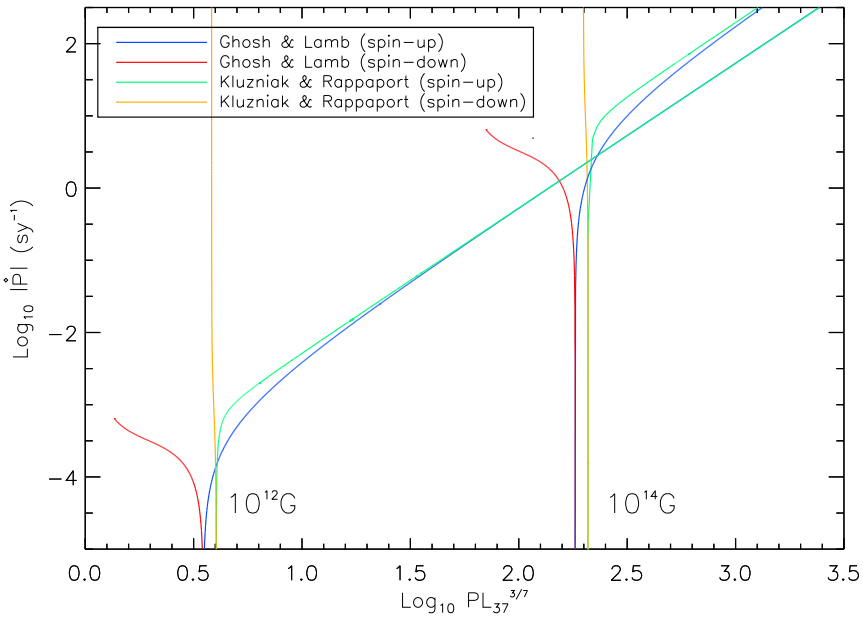

Figure 1.9: Simulated results for neutron stars with $B = 10^{12}$ and $B = 10^{14}$ G, $M_{NS} = 1.4\ M_{\odot}$, and $R_{NS} = 10$ km, determined using the Ghosh and Lamb (1979) (equation (1.34)) model for systems that are spinning up (blue) and down (red) on average. Simulated results determined using the Kluzniak and Rappaport (2007) (equation (1.36)) model for systems that are spinning up (green) and down (orange) on average are also shown.

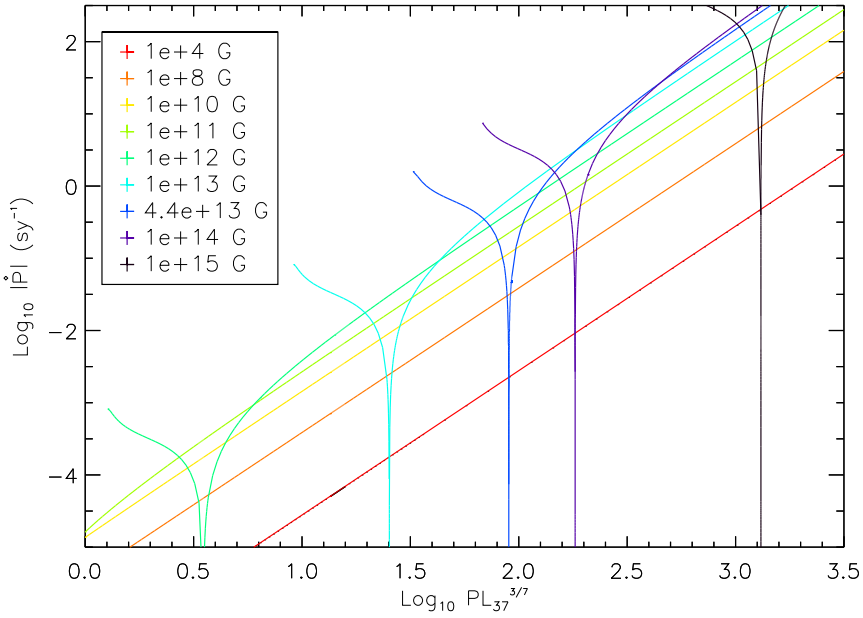

Figure 1.10: Simulated results for neutron stars with $B = 10^4 - 10^{15}$ G, $M_{NS} = 1.4\ M_{\odot}$, and $R_{NS} = 10$ km, determined using the Ghosh and Lamb (1979) (equation (1.34)) model (as discussed in Section 1.2.2).

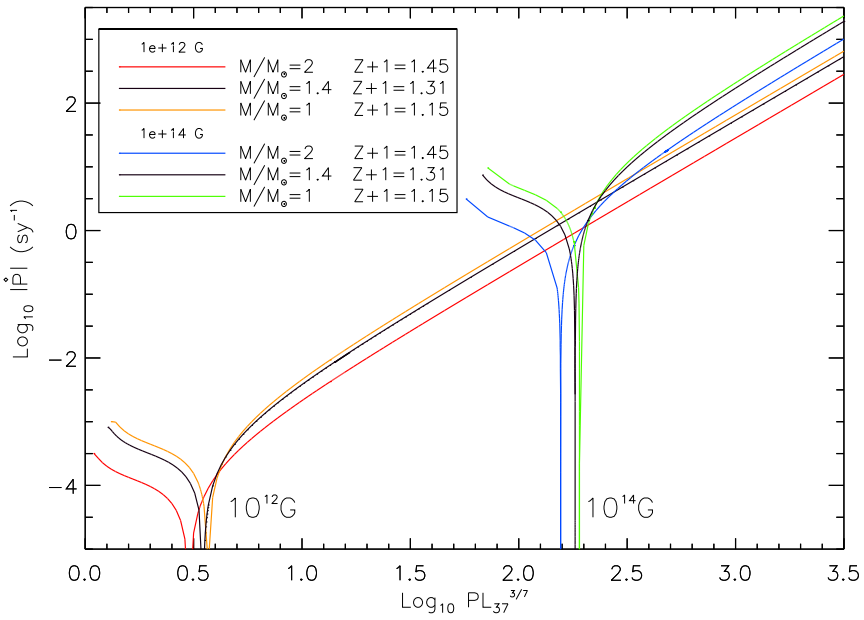

Figure 1.11: Simulated results for neutron stars of different masses and radii ($z+1 = 1.15$-1.45, where z is the gravitational red-shift, equation (1.38)), with $B = 10^{12}$ and $B = 10^{14}$ G, determined using the Ghosh and Lamb (1979) (equation (1.34)) model (as discussed in Section 1.2.2).

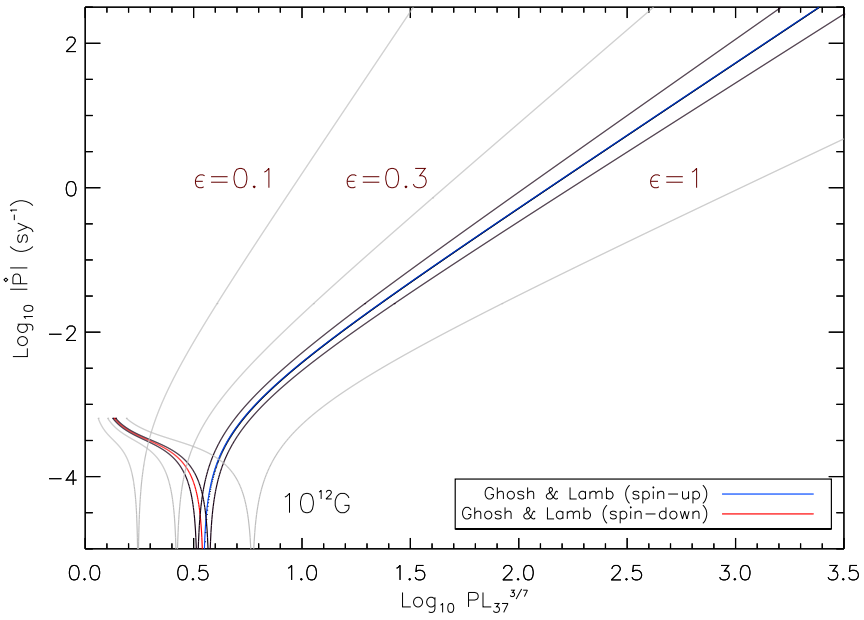

Figure 1.12: Simulated results for neutron stars of $M_{NS} = 1.4\ M_{\odot}$, $R_{NS} = 10$ km, and $B = 10^{12}$ G determined using the Ghosh and Lamb (1979) (equation (1.34)) model (as discussed in Section 1.2.2). The black lines indicate the minimum and maximum results using values of $\epsilon = 0.45$ and $\epsilon = 0.55$ respectively. The grey lines indicate more extreme values, of $\epsilon = 0.10$, $\epsilon = 0.30$, and $\epsilon = 1$.

(2008), who argued that highly magnetised neutron stars may also exist in HMXB. The neutron stars in these systems are not referred to as magnetars because their emission is powered by accretion, rather than the decay and instabilities of their magnetic fields, however they have the potential to become accreting magnetars. LSI+61°303, which is part of a BeXB, previously showed magnetar-like behaviour when it underwent two bursts similar to those of SGR (Torres et al., 2012; Papitto et al., 2012).

In Chapter 2, I apply all of these accretion theories to neutron stars in 42 transient BeXB in the SMC, and in Chapter 4, I do the same with LXP187, a persistent BeXB in the LMC. I show that $\sim 2/3$ BeXB may have $B > B_{QED}$. Accretion theories can be verified by applying them to neutron stars that have had their magnetic fields measured directly via CRSF (discussed in Sections 1.3.1 and 2.4).

1.3 The spectra of neutron stars in BeXB

In BeXB, once matter passes through the neutron star's magnetosphere it is channelled by the magnetic field lines to the neutron star's magnetic polar caps. At relatively low luminosities, and hence low mass-accretion rates (equation (1.8)), a thermal mound of accreted material forms on the surface, which emits blackbody radiation. Due to the flatness of the mound, most radiation is emitted vertically (in the direction of the magnetic field lines). This produces a beam of radiation described as a 'pencil' beam. The thermal mound above the neutron star's polar caps have been measured to be $\lesssim 1$ km^2 for neutron stars in BeXB with $P > 150$ s, where the size of the cap tends to be smaller the longer the neutron star's spin period (Bartlett et al., 2013).

As the mass-accretion rate increases, the amount of radiation emitted from the magnetic poles increases, creating a shock wave. Incoming matter is decelerated by the shock wave, creating an accretion column. The pencil beam is suppressed, and X-rays are emitted from the side of the column (perpendicular to the magnetic field lines) via bremsstrahlung and cyclotron emission. These photons can then be scattered by collisions with high-energy electrons, creating cyclotron resonance scattering features (Becker and Wolff, 2007). Emission from an accretion column produces a beam of radiation described as a 'fan' beam (Basko and Sunyaev, 1975; Wang and Frank, 1981; Wang and Welter, 1981; Parmar et al., 1989). The geometry resulting in pencil and fan beams is shown in Figure 1.13 (and discussed further in Section 1.4.2). Figure 1.14 shows X-ray emission from the accretion column, and Figure 1.15 shows the different spectra produced by the different emission processes.

The spectra of BeXB are dominated by bremsstrahlung, which produces an absorbed power-law spectrum with photon indexes in the range of 0.6-1.4 (Haberl et al., 2008) and high-energy cut-offs in the range of 10-30 keV (Lutovinov et al., 2005; Reig, 2011).

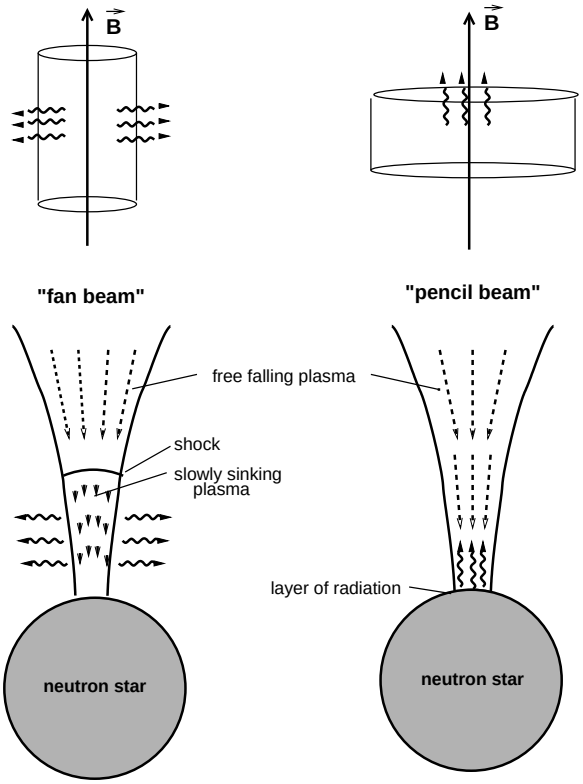

Figure 1.13: Diagram of material accreting onto the magnetic polar cap of a neutron star, showing the geometry resulting in fan (left) and pencil (right) beams (as discussed in Sections 1.3 and 1.4.2). Image credit: Schonherr et al. (2007).

The spectra of BeXB sometimes also exhibit an emission line at 6.4 keV. This occurs when high-energy photons collide with iron ions in the accretion disc.

1.3.1 Cyclotron resonance scattering features

Cyclotron resonance scattering features (CRSF) provide a direct way of measuring a neutron star's magnetic field in the region where the radiation is emitted. CRSF are formed when photons are Compton scattered by electrons that are accelerated by the neutron star's magnetic field. The electron motions are quantised into Landau orbits. These correspond to discrete energy levels, where the energy of each electron is known as its cyclotron energy ($E_{cyc(0)}$) (Daugherty and Harding, 1986). When photons collide with these electrons, they lose an energy equal to $E_{cyc(0)}$, creating broad absorption lines in the X-ray spectrum. The cyclotron energy depends on the strength of the magnetic field via

$$E_{cyc(0)} = n\frac{\hbar eB}{m_e c}, \tag{1.37}$$

where h is Planck's constant and $\hbar = h/2\pi$, e is the elementary charge, m_e is the electron rest mass, and n is the quantum number corresponding to the Landau level, where the lowest energy level is at n=1 (Canuto and Ventura, 1977). The absorption lines are

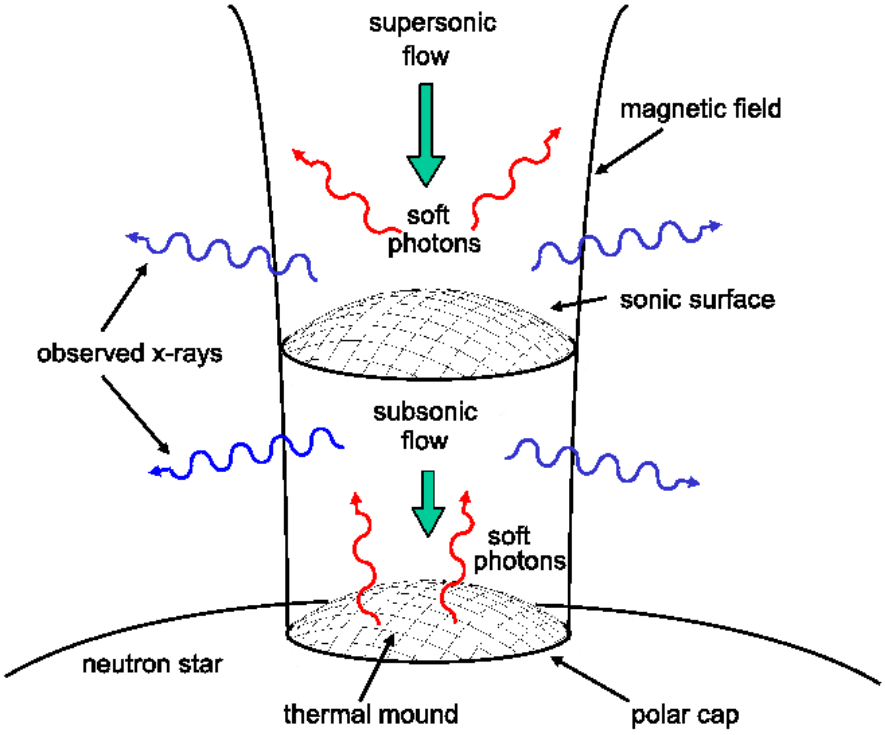

Figure 1.14: Diagram of material accreting onto the magnetic polar cap of a neutron star, resulting in a fan beam (as discussed in Sections 1.3 and 1.4.2). Photons are created via blackbody radiation on the surface of the thermal mound near the base of the column. They are also created above the mound via bremsstrahlung and cyclotron emission. These photons can then be Compton scattered by electrons within the column resulting in CRSF. Image credit: Becker and Wolff (2007).

shifted by a factor of $(1+z)^{-1}$, where z is the gravitational red-shift, due to the neutron star's strong gravitational field. z is related to the mass and radius of the neutron star via

$$1+z = \left(1 - \frac{2G}{c^2}\frac{M_{NS}}{R_{NS}}\right)^{-0.5}, \tag{1.38}$$

as discussed in Section 3.2.1. Neutron stars in X-ray binaries typically have $1+z$ values of 1.25-1.40 (Caballero and Wilms, 2012).

This means that the observed cyclotron energy (E_{cyc}) is

$$\begin{aligned} E_{cyc} &= n\frac{\hbar e B}{m_e c}\,(1+z)^{-1}, \\ &\cong 11.57 \text{ keV } B_{12}\; n\; (1+z)^{-1}. \end{aligned} \tag{1.39}$$

The effects of the quantum electrodynamics (QED) are important above the quantum critical field. This transition occurs when an electron's cyclotron energy equals its rest

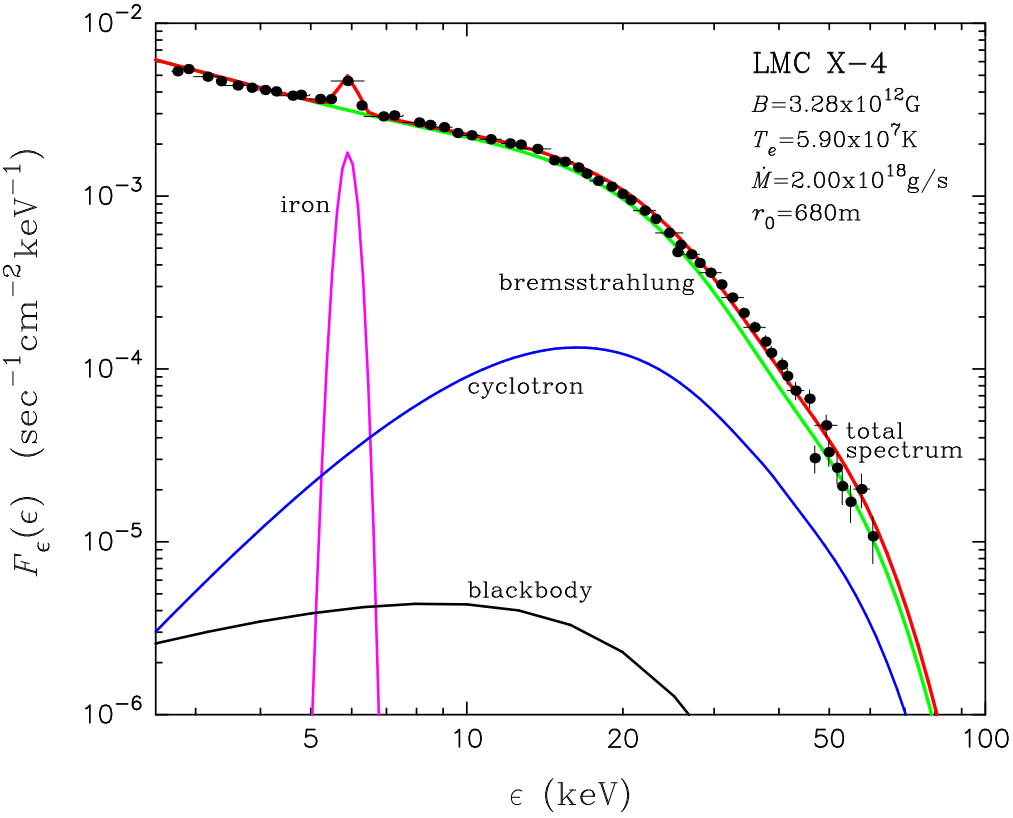

Figure 1.15: The components of the spectra of a HMXB (as discussed in Section 1.3). Image credit: Becker and Wolff (2007).

mass energy ($m_e c^2$), and hence its cyclotron radius is comparable to its de Broglie radius. This change occurs at

$$n\frac{\hbar e B}{m_e c} = m_e c^2, \tag{1.40}$$

and so at n=1,

$$B_{QED} = \frac{m_e^2 c^3}{\hbar e} \cong 4.4 \times 10^{13} \text{ G}. \tag{1.41}$$

It is difficult to find CRSF in the spectra of neutron stars with magnetic fields $\gtrsim 10^{13}$ G. This is because $E_{cyc} \propto B$, and CRSF from electrons are no longer visible in the X-ray spectrum at this magnetic field strength, although lines from protons may be present. Isolated pulsars RXJ0720.43125 and RBS1223 have been determined to have magnetic fields of 2.4×10^{13} G and 3.4×10^{13} G, respectively, using CRSF from protons (Haberl, 2007). Neutron stars in twelve BeXB have had their magnetic fields measured via CRSF, and these fields range from $\sim 10^{12} - 10^{13}$ G. In Chapter 2, I compare the magnetic fields of these systems to those predicted using the accretion theories discussed in Section 1.2.

1.4 Pulse-profiles for neutron stars in BeXB

The geometry of the emission region of an accreting neutron star affects its pulse-profile. If a single magnetic pole were visible, and emitting radiation vertically, in a pencil beam, then we would view it rise in luminosity, as it appears on the neutron star's horizon and rotates towards our line-of-sight. It would then decrease in luminosity as it disappears over the horizon. This would produce a sinusoidal pulse-profile with one peak per phase. The trough of this wave does not reach zero, but settles on a value determined by the pulse-fraction. The pulse-fraction is the fraction of pulsed flux relative to the total flux, where the un-pulsed component of the flux depends on the level of background radiation.

Figure 1.16 shows examples of typical sinusoidal pulse-profiles, which may result from a pencil beam geometry. The structure of the pulse-profiles of neutron stars in BeXB are often more complex than this, with complexities arising for a number of reasons discussed in Sections 1.4.1-1.4.5.

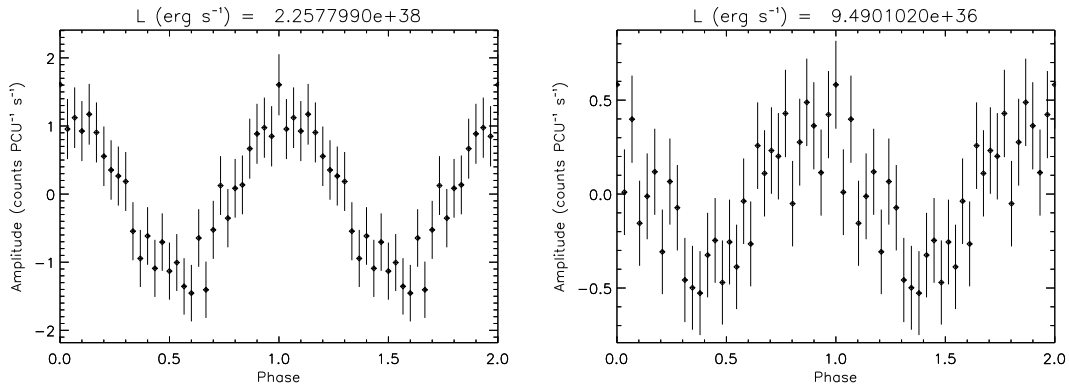

Figure 1.16: Roughly sinusoidal pulse-profiles (as discussed in Section 1.4), as would be expected from a pencil beam geometry (see Figure 1.13, also Sections 1.3 and 1.4.2). The pulse-profiles are normalised to the average count-rate and the phase-shift is arbitrary (pulse-profiles from SXP2.37 (left) and SXP169 (right), also shown in Figures C.2 and C.21).

1.4.1 Number of visible poles

Pulse-profiles may be more complicated than the sinusoidal model discussed above because the secondary pole, the furthest magnetic pole from the observer, may sometimes be visible. This is due to gravitational bending, a classical effect of general relativity caused by the neutron star's strong gravitational field. If the neutron star's magnetic poles are 180° apart, then the secondary pole is at its brightest when the closest magnetic pole to the observer, the primary pole, is not visible. This means that the trough in the sinusoidal profile is filled.

The number of poles that are visible at any one time depends on the angle between the neutron star's rotational axis and the observer's line-of-sight (i), the angle between the neutron star's magnetic axis and its spin axis (θ), and z, the gravitational redshift, which depends on M_{NS} and R_{NS} (equation (1.38)). i and θ are shown in Figure 3.2. A method for modelling pulse-profiles in order to determine i, θ, and z is discussed in Section 3.2.1.

1.4.2 Geometry of the emission region

The structure of pulse-profiles may also vary from a simple sinusoidal model when an accretion column forms, resulting in a fan beam. The geometry resulting in fan and pencil beams is shown in Figure 1.13, and discussed in Section 1.3.

A fan beam produces a peak in the pulse-profile that is out of phase with the peak from the pencil beam by about half a phase. This is because radiation from the fan beam is emitted perpendicular to radiation from the pencil beam. It is also emitted in more than one direction, which may widen the peak. Wang and Welter (1981) show that fan beams can produce sharp features, as the fan beam rotates behind the horizon of the neutron star.

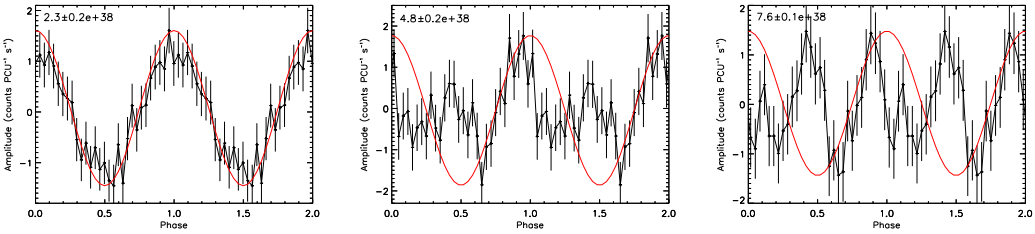

Figure 1.17: Pulse-profiles from SXP2.37 (SMC X-2) showing a transition from a pencil beam to a fan beam at increasing luminosities (as discussed in Sections 1.3 and 1.4.2, luminosity is given in the top left-hand corner in erg s^{-1}, and increases from left to right). The pulse-profiles are normalised to the average count-rate and the phase-shift is arbitrary (these pulse-profiles are also shown in Figure 3.14 and discussed in Section 3.3.2.1).

Double-peaked structure may result from the transition from a pencil beam geometry to a fan beam geometry at increasing mass-accretion rates, and hence luminosities (equation (1.8)) (Wang and Welter, 1981; White et al., 1983; Parmar et al., 1989). At relatively low L, the pencil beam dominates the pulse-profile, with a single magnetic pole producing an approximately sinusoidal peak. As L increases, the fan beam appears, resulting in a secondary peak in the pulse-profile, about half a phase apart from the first. As L increases further, the pencil beam is further suppressed, and the peak from the fan beam becomes dominant, so that the secondary peak is around the same amplitude as the first, resulting in double-peaked structure. Finally, the first peak may disappear completely, as the pencil beam is completely suppressed and radiation is no longer emitted parallel

to the magnetic field lines. Figure 1.17 shows the possible transition from a pencil beam geometry to a fan beam geometry for SXP2.37 (also known as SMC X-2), which is discussed further in Section 3.3.2.1.

This behaviour has previously been observed in pulse-profiles of many BeXB. Bildsten et al. (1997) show that A 0535+ 262, which has a P of 105 s, exhibits single-peaked structure at 4.0×10^{36} erg s^{-1} and double-peaked structure at 9.1×10^{37} erg s^{-1}. Parmar et al. (1989) show that the pulse-profiles of EXO 2030+ 375, which has a P of 42 s, exhibit single-peaked structure at 1.2×10^{36} erg s^{-1}, double-peaked structure at 2.8×10^{37} erg s^{-1}, and single-peaked structure again at 1.0×10^{38} erg s^{-1}. Chen et al. (2008) describe similar behaviour in 4U 1901+ 03, Mukerjee et al. (2000) in V0332+53, Coe et al. (2009) in SXP7.92, and Tsygankov et al. (2006) in Cepheus X-4. Her X-1 has also exhibited double-peaked structure. Trümper et al. (1986) explained this as the result of precession of the magnetic axis, however, Parmar et al. (1989) suggest that this cannot be the case, since Soong et al. (1987) observed these changes in pulse-profiles taken only 20 hours apart. This is too short a time for the magnetic axis to have moved, and so this may also be due to a transition from a pencil beam to a fan beam. The structure of pulse-profiles can be energy dependent. This is because fan and pencil beam components dominate at different energies (Nagel, 1981a,b; White et al., 1983). In Chapter 3, I show that many BeXB in the SMC produce pulse-profiles with double-peaked structure.

1.4.3 Asymmetry

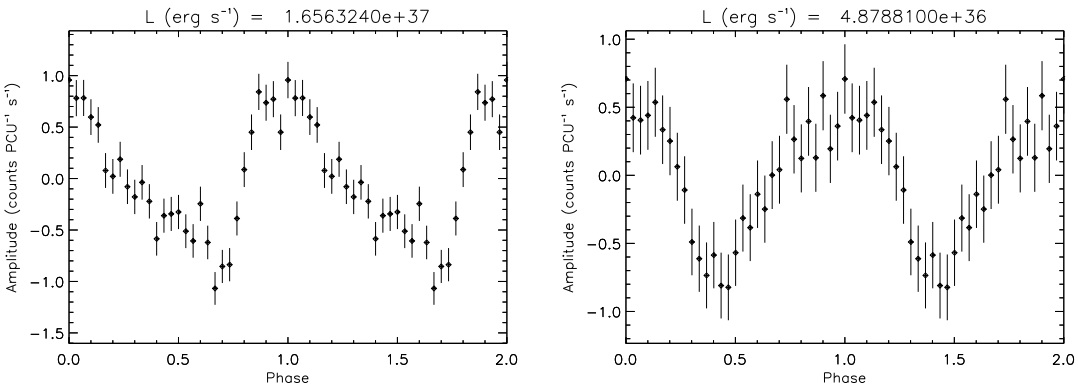

Figure 1.18: Pulse-profiles showing asymmetry (as discussed in Section 1.4.3). The pulse-profiles are normalised to the average count-rate and the phase-shift is arbitrary (pulse-profiles from SXP18.3 (left) and SXP46.6 (right), also shown in Figures C.10 and C.12).

Pulse-profiles may also show peaks that are asymmetric; they may rise sharply and fall gradually, or vice versa. Mytrophanov and Tsygan (1978) suggested that asymmetric pulse-profiles may be formed if photons escape the accretion column in an asymmetric fashion, due to an asymmetry in the magnetic field lines. Wang and Welter (1981) suggested that asymmetries can form when the fan beam is disrupted by asymmetries

in the flow of accreted material through the magnetosphere. This may cause matter to fall on the magnetic pole at different angular velocities, making the accretion column brighter on one side than the other. Figure 1.18 shows examples of pulse-profiles with asymmetry.

1.4.4 Dips

The structure of pulse-profiles may also vary due to dips. These may look like the emergence of double-peaked structure, but are not attributed to the appearance of a fan beam as they do not appear with a peak that is about half a phase from the main peak. This behaviour has been observed in a number of neutron stars within BeXB, including GRO J1008- 57 (Naik et al., 2011), EXO 2030+ 375 (Naik et al., 2013), A0535+ 262 (Naik et al., 2008), and 1A 1118- 61 (Maitra et al., 2012). This behaviour is also energy dependent, with the dips disappearing at higher energies. This may be because the dips are caused by an additional absorption component that obscures the radiation (Galloway et al., 2001). Figure 1.19 shows examples of pulse-profiles with dips.

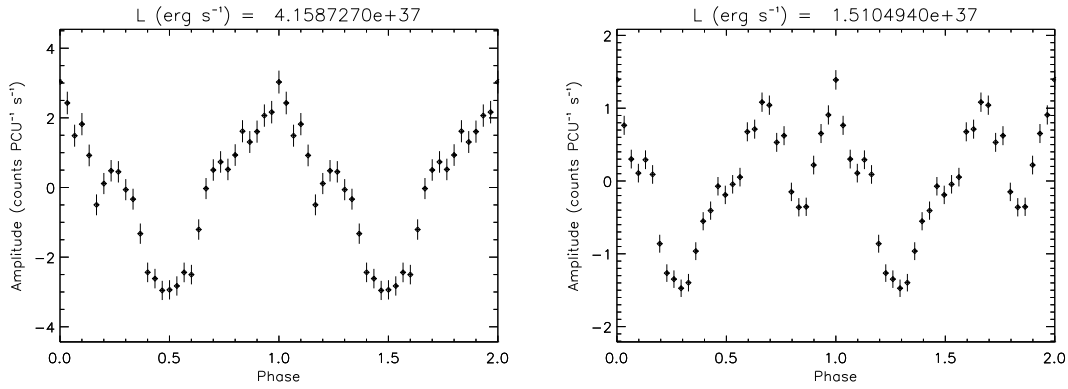

Figure 1.19: Pulse-profiles showing dips (as discussed in Section 1.4.4). The pulse-profiles are normalised to the average count-rate and the phase-shift is arbitrary (pulse-profiles from SXP8.80 and SXP756, also shown in Figures C.6 and C.40).

1.4.5 Magnetic field

Systems with $B > B_{QED}$ may be more likely to have magnetic poles that are not antipodal, and are of different sizes and temperatures. Haberl (2007) shows this to be the case for RX J0720.4 3125 and RBS 1223, where the smaller cap is hotter than the larger cap. The caps may not be antipodal because of an off-centred dipole, or because the neutron star has more than two poles, which can also affect the structure of pulse-profiles. Double-peaked structure may occur in neutron stars with more than two poles

if the flow of accreted material moves to a different magnetic pole, thereby changing trajectory (Parmar et al., 1989).

In Chapter 3, I visually inspect over 1000 pulse-profiles, corresponding to observations of 42 BeXB in the SMC. I show that many contain the features discussed above, which vary within and across individual systems.

1.5 Organisation and content of thesis

In Chapter 2, I use 13 year's worth of Rossi X-ray Timing Explorer (RXTE) data to determine the long-term average L, P, and $\dot{P}$ for 42 transient BeXB in the SMC. Plots of P and L as a function of MJD for all sources are given in Appendix B. I use equations from Section 1.2 to show that all of these systems contain neutron stars that are most likely disc-accreting. Diagrams of each system, composed from their orbital parameters, are also shown in Appendix B. Just over half contain an OBe star with a circumstellar disc that has been truncated by the orbit of the neutron star. I then use the accretion theories discussed in Sections 1.2.1-1.2.2 to determine the possible magnetic fields of the neutron star in each system. These results show that ∼85%, including all systems with $P > 100$ s, are close to spin equilibrium. $\sim 2/3$ systems in this dataset, including all systems with $P > 100$ s, are predicted to have $B > B_{QED}$. Neutron stars in this dataset are predicted to have higher magnetic fields than neutron stars in Galactic BeXB that have had their magnetic fields directly measured via CRSF. I suggest that the neutron stars in this dataset have magnetic fields that are higher than those of the CRSF sources because the latter are not close to spin equilibrium, whereas most of the former are. This is combined with the bias that prevents CRSF from being observed in systems with $B \gtrsim 10^{13}$ G.

In Chapter 3, I use the same data to create pulse-profiles for every observation of every system in this dataset. There are between 5 and 88 pulse-profiles per source, and over 1000 in total. These are shown in Appendix C. I modelled these pulse-profiles in order to determine i, θ, and M_{NS}/R_{NS}, using the model discussed in Section 1.4.1, and visually inspected them, looking for the features discussed in Sections 1.4.1-1.4.5. I find that the pulse-profiles are mostly not well-fit by this model, and contain an array of features that vary both across and within individual systems. I suggest that systems with relatively longer spin periods transition from a pencil beam to a fan beam at relatively lower luminosities, although these results are inconclusive.

In Chapter 4, I apply the methods used in Chapters 2 and 3 to LXP187, a persistent BeXB in the LMC that is not close to spin equilibrium, and is spinning up on average. LXP187 has a longer spin period than all of the BeXB discussed in Chapters 2 and 3 that are not close to spin equilibrium. It is predicted to have a magnetic field similar to those of the CRSF sources, helping confirm the conclusions of Chapter 2 - that CRSF sources

have magnetic fields that differ from those of the sources discussed in Chapter 2 because the CRSF sources are not close to spin equilibrium. The magnetic field of LXP187 is slightly too high for CRSF to be observed using most X-ray telescopes, adding credence to the idea that most BeXB have magnetic fields that are not observable via CRSF.

In Chapter 5, I conclude that evidence from the previous three Chapters suggests that there may be many more neutron stars with $B > B_{QED}$ than previously thought, and that all neutron stars in binary systems that are close to spin equilibrium follow the same relationship between P and B. I also discuss how further evidence for this could be obtained by monitoring CRSF sources in order to determine their long-term average L, P, and $\dot{P}$. This would allow us to see how close they are to spin equilibrium, and to determine their magnetic fields using the Ghosh and Lamb (1979) and Kluzniak and Rappaport (2007) models. Conversely, LXP187, and the sources discussed in Chapters 2 and 3, could be monitored for CRSF, where predictions for the energy of these features are shown in Figure 4.33, and given in Tables 2.9 and 4.2.

Chapter 2

Accretion theories, and the magnetic fields of neutron stars in BeXB in the SMC

2.1 Introduction

In Chapter 2, I use over 13 year's worth of archival Rossi X-ray Timing Explorer/Proportional Counter Array (RXTE/PCA) data to determine the magnetic field of 42 transient BeXB in the SMC, using the accretion theories discussed in Section 1.2.

NASA launched RXTE in December 1995, and it remained active until January 2012. It was composed of the PCA, operating at 2-60 keV, the High Energy X-ray Timing Experiment (HEXTE), operating at 15-250 keV, and the All-Sky Monitor (ASM) operating at 2-10 keV. RXTE did not have focusing X-ray mirrors, and so had no spatial resolution, but its PCA had a timing resolution of $\sim$1 μs.

The SMC contains a relatively large number of BeXB. These are at a well-defined distance, and are located away from the disc of the Milky Way, so they are relatively un-obscured by interstellar dust. RXTE was sensitive to luminosities of just under 10^{36} erg s^{-1} from X-ray binaries in the SMC (at a distance of 60 kpc (Hilditch et al., 2005)), and so the SMC X-ray pulsar (SXP) monitoring campaign began in 1997. This involved monitoring the SMC once or twice a week for durations of $\sim$10,000 s. The SXP monitoring campaign became one of RXTE's 'core programs', and continued from 1997 until RXTE was shut down in 2012.

The long-term pulsed light-curves of 47 BeXB in the SMC were published by Laycock et al. (2005) and Galache et al. (2008) using data from the SXP monitoring campaign. The orbital parameters of these SXP were published by Townsend et al. (2011a) and

Bird et al. (2012), and the optical properties by McBride et al. (2008). Corbet et al. (2001) used RXTE data to study outbursts from SXP2.37 (also known as SMC X-2), and Knigge et al. (2011) used data from RXTE to show that the neutron stars in BeXB may be split into two populations, possibly formed by different types of supernova. I use data from RXTE to determine the long-term average L, P, and $\dot{P}$ for 42 BeXB in the SMC, extending the previous published record by several further years. I then determine the magnetic fields of these SXP using the accretion theories discussed in Section 1.2. In order to know which accretion theories are appropriate, I first determined whether these systems contain neutron stars that are accreting via a spherical wind or an accretion disc using the orbital and optical parameters published by Townsend et al. (2011a), Bird et al. (2012), and McBride et al. (2008). This is discussed in Section 2.2, with plots of P and L as a function of MJD, and diagrams of each system shown in Appendix B. In Chapter 3, I create pulse-profiles for every observation of these systems, looking for the features discussed in Section 1.4. These are shown in Appendix C.

The magnetic field of the neutron stars in these systems have previously been calculated by Chashkina and Popov (2012) using spin equilibrium models. This work differs from theirs as Chashkina and Popov use the values for P and L published in Galache et al. (2008), and estimate V_{rel}, using the same value for each system, whereas I use the raw data, which extends for a few years beyond the published data. I also determine V_{rel} from orbital parameters and take $\dot{P}$ into account, so that I can determine the magnetic field using methods that do not assume spin equilibrium.

Work from this chapter has previously been published as Klus et al. (2014) and Ho et al. (2014). Data used in this chapter was originally extracted by S. Laycock, L.J. Galache, and L.J. Townsend, and equations (2.5)-(2.12) were originally derived by W.C.G. Ho.

An outline of this chapter is as follows: observations are discussed in Section 2.2, with observations regarding accretion methods discussed in Section 2.2.1, and observations regarding accretion theories and magnetic field determination in Section 2.2.2. Results are given in Section 2.3, and possible consequences are discussed in Section 2.4.

2.2 Observations

The observations used in this chapter come from the RXTE SXP monitoring campaign described in Section 2.1. Here, RXTE monitored the SMC once or twice a week, for durations of ∼10,000 s, between 1997 and 2012, and the activity of the neutron stars were determined from timing analysis. See Laycock et al. (2005) and Galache et al. (2008) for detailed reports on this work up until the time of their publication. Here I extend these results, covering a period from 1997-2011 and duration of 13.5 yr in total.

As discussed in Laycock et al. (2005) and Galache et al. (2008), the quality of any single observation depends upon the significance of the detected period combined with the collimator response to the source. Any period detections with a significance $< 99\%$, or a collimator response < 0.2 are removed, as are any datasets with < 5 detections. This leaves results for 42 BeXB, with between 5 and 88 detections per source (see Table 2.1), and over 1000 detections in total. Figure 2.1 shows the location of these sources, where the SXP are labelled by their average pulse period upon detection.

The average count-rate (CR, measured in counts PCU^{-1} s^{-1}) is converted to luminosity using

$$L = 0.4 \times 10^{37} \times \left(\frac{100}{PF}\right) \times CR \times Col^{-1} \text{ erg s}^{-1}, \tag{2.1}$$

where Col is the collimator response, the distance to the SMC is assumed to be 60 kpc (Hilditch et al., 2005), and the average pulse-fraction (PF) is assumed to be 33% (Coe et al., 2009), where the pulse-fraction is the fraction of pulsed flux relative to the total flux. A weighted $\dot{P}$ is calculated by fitting the time evolution of P using MPFITEXPR[1].

P_{orb} is known for 36/42 systems, mostly taken from Bird et al. (2012), and is otherwise assumed to be 262 $\pm$ 258 d (unless otherwise stated) in order to cover the full range of possible values. The eccentricity (e) is known for 6 systems (see Table 2.3) and otherwise assumed to be 0.3 $\pm$ 0.2. EW $H\alpha$ is known for 28 systems and otherwise assumed to be -25 $\pm$ 20 Å (unless otherwise stated). M_{NS} is assumed to be 1.4 $M_{\odot}$ and R_{NS} is assumed to be 10 km (unless otherwise stated). The mass and radius of the OBe star (M_{OB} and R_{OB}) are determined from the spectral type and luminosity class. These are known for 35 systems, mostly taken from McBride et al. (2008), otherwise the average values of $M_{OB}/M_{\odot}$=18.36 $\pm$ 4.42 and $R_{OB}/R_{\odot}$=8.95 $\pm$ 2.08 are assumed. The mass of OBe stars in X-ray binaries can also be measured, in some cases, using dynamical methods. A discrepancy is found between the spectroscopic mass (M_{spec}) and the dynamical mass (M_{dyn}), where M_{dyn} is $\sim$ 20% lower than M_{spec} (Coe et al., 2015a,b). While it is not possible to measure M_{dyn} for any of the systems in this dataset, M_{dyn} is assumed to be 20% lower than M_{spec} in all cases, and results are determined using both values for M_{OB}.

All EW $H\alpha$ measurements were obtained as part of the Southampton SXP optical monitoring campaign that has been running for several years. The data were collected primarily at the South African Astronomical Observatory's (SAAO's) 1.9 m Radcliffe telescope in South Africa, and also at the European Southern Observatory's (ESO's) 3.58 m New Technology Telescope (NTT) in Chile. The instrumental set-ups and the data reduction in both cases are the same as those described in Coe et al. (2012).

The number of observations of each system, the range of data, and the long-term average L, P, and $\dot{P}$ are given in Table 2.1. P_{orb}, EW $H\alpha$ and the spectral type, luminosity

[1] www.physics.wisc.edu/∼craigm/idl/down/mpfitexpr.pro

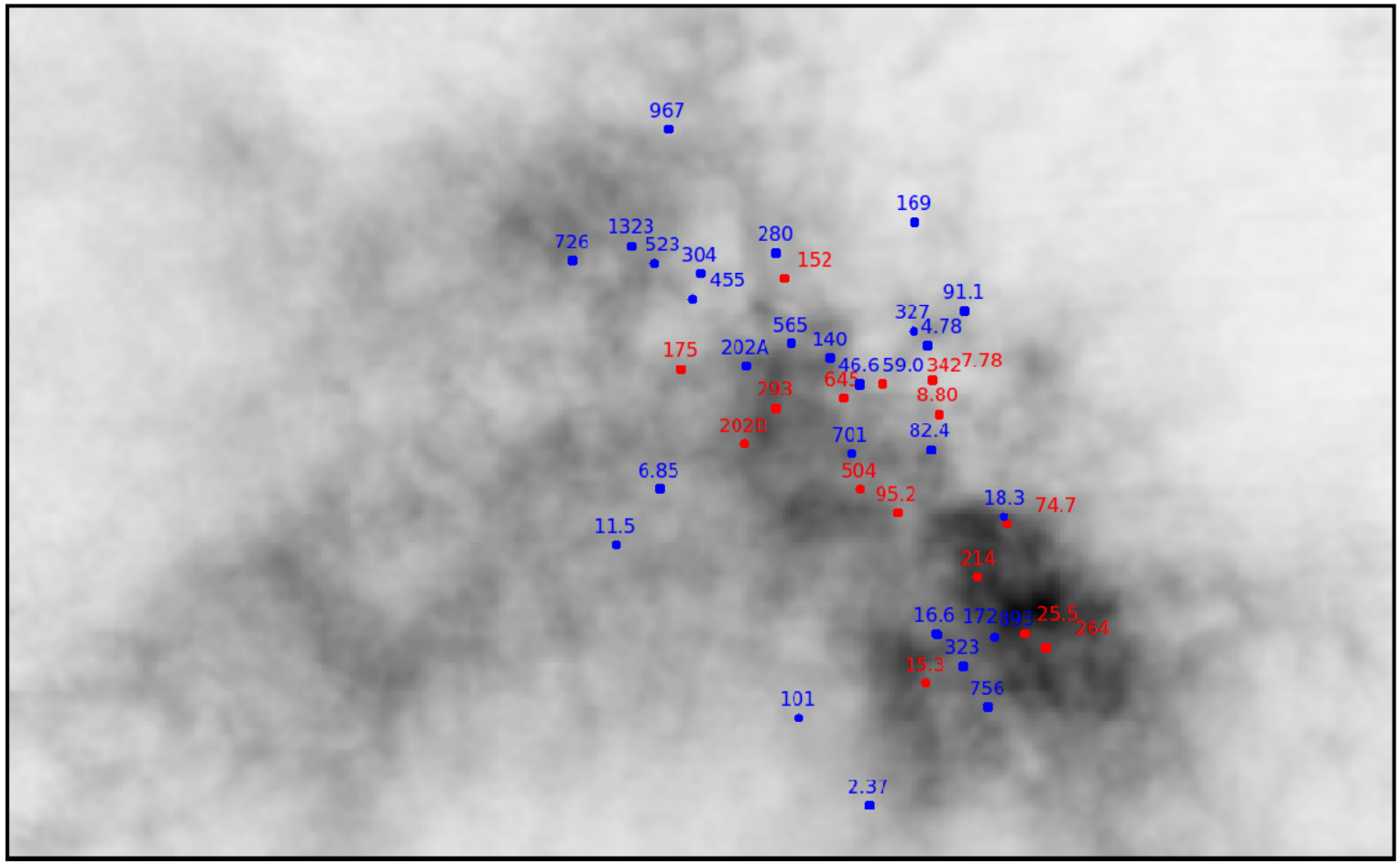

Figure 2.1: Map of the SMC showing the locations of the 42 BeXB in the dataset discussed in Chapters 2 and 3. 27 of these are spinning up on average ($\dot{P} < 0$; blue), and 15 are spinning down ($\dot{P} > 0$; red). Numbers indicate the P of each SXP. The image of the SMC is from Stanimirović et al. (1999), taken by combining Parkes telescope observations of neutral hydrogen with an Australia Telescope Compact Array (ATCA) aperture synthesis mosaic, both in the radio spectrum.

BeXB	No. of obs.	Range of data (yr)	Long-term average L (10^{37} erg s^{-1})	Long-term average P (s)	Long-term average $\dot{P}$ (s yr^{-1})
SXP2.37	23	11.22	12.78 ± 0.95	2.37233 ± 0.00004	-0.0040314 ± 0.0000004
SXP4.78	9	12.70	0.89 ± 0.12	4.78015 ± 0.00012	-0.000851 ± 0.000014
SXP6.85	61	8.03	2.77 ± 0.45	6.85206 ± 0.00037	-0.000221 ± 0.000014
SXP7.78	28	12.30	0.47 ± 0.08	7.78313 ± 0.00062	0.002619 ± 0.000029
SXP8.80	46	11.23	2.55 ± 0.25	8.89961 ± 0.00048	0.001224 ± 0.000007
SXP11.5	16	0.13	1.61 ± 0.17	11.4809 ± 0.0021	-0.04980 ± 0.00670
SXP15.3	10	11.13	0.89 ± 0.11	15.2538 ± 0.0019	0.00700 ± 0.00013
SXP16.6	12	5.46	0.26 ± 0.05	16.5553 ± 0.0028	-0.01307 ± 0.00049
SXP18.3	74	7.39	0.98 ± 0.13	18.3751 ± 0.0020	-0.001178 ± 0.000059
SXP25.5	35	10.56	0.42 ± 0.07	25.5456 ± 0.0041	0.00025 ± 0.00034
SXP46.6	76	13.25	0.69 ± 0.13	46.508 ± 0.021	-0.01549 ± 0.00020
SXP59.0	88	13.10	1.05 ± 0.15	58.859 ± 0.033	-0.02063 ± 0.00047
SXP74.7	28	12.31	1.54 ± 0.22	74.647 ± 0.028	0.02996 ± 0.00042
SXP82.4	21	12.24	0.83 ± 0.17	82.464 ± 0.061	-0.0217 ± 0.0015
SXP91.1	59	13.49	1.38 ± 0.19	88.438 ± 0.065	-0.44195 ± 0.00055
SXP95.2	10	11.01	0.95 ± 0.20	95.21 ± 0.12	0.0267553 ± 0.0054
SXP101	5	7.93	0.90 ± 0.22	101.768 ± 0.088	-0.053 ± 0.013
SXP140	5	6.67	1.17 ± 0.56	140.42 ± 0.87	-0.158 ± 0.099
SXP152	23	11.94	0.80 ± 0.17	151.68 ± 0.25	0.019 ± 0.012
SXP169	35	11.97	1.40 ± 0.27	167.03 ± 0.41	-0.2377889 ± 0.0056
SXP172	42	10.39	0.83 ± 0.23	171.86 ± 0.27	-0.1231 ± 0.0063
SXP175	11	8.50	1.16 ± 0.37	174.95 ± 0.34	0.146 ± 0.011
SXP202A	16	13.28	0.83 ± 0.20	201.47 ± 0.45	-0.130 ± 0.014
SXP202B	5	13.24	0.49 ± 0.21	202.25 ± 0.68	0.209 ± 0.037
SXP214	16	13.26	0.63 ± 0.24	213.68 ± 0.47	0.118 ± 0.018
SXP264	6	10.13	0.32 ± 0.11	262.65 ± 0.89	0.057 ± 0.081
SXP280	6	8.24	0.61 ± 0.24	280.00 ± 0.67	-0.371 ± 0.056
SXP293	12	11.08	0.48 ± 0.12	293.89 ± 0.96	0.025 ± 0.046
SXP304	7	6.09	2.10 ± 0.64	304.11 ± 0.98	-0.50 ± 0.20
SXP323	19	9.42	0.80 ± 0.24	318.53 ± 0.75	-0.946 ± 0.020
SXP327	5	1.76	0.20 ± 0.05	327.53 ± 0.99	-0.82 ± 0.77
SXP342	20	10.29	1.46 ± 0.41	341.0 ± 1.5	0.962 ± 0.062
SXP455	7	12.05	2.69 ± 0.74	452.3 ± 3.2	-0.20 ± 0.32
SXP504	31	13.29	0.69 ± 0.18	502.0 ± 2.5	0.340 ± 0.051
SXP565	8	7.48	0.27 ± 0.15	564.1 ± 3.3	-0.85 ± 0.37
SXP645	13	11.74	0.67 ± 0.28	644.6 ± 6.1	0.31 ± 0.26
SXP701	27	11.71	0.56 ± 0.17	695.8 ± 5.5	-0.03 ± 0.27
SXP726	7	4.20	1.92 ± 0.71	726.3 ± 8.4	-0.8 ± 1.1
SXP756	29	11.20	0.82 ± 0.10	754.6 ± 3.4	-0.011 ± 0.077
SXP893	29	10.44	0.42 ± 0.13	890.8 ± 7.6	-1.89 ± 0.32
SXP967	7	2.85	3.18 ± 1.00	962.9 ± 10.2	-1.1 ± 3.5
SXP1323	25	4.89	2.82 ± 0.49	1322.7 ± 11.6	-7.04 ± 0.67

Table 2.1: Number of observations, range of data, and long-term average L, P, and $\dot{P}$, for 42 BeXB in the SMC (as discussed in Section 2.2). A weighted $\dot{P}$ is found by fitting the time evolution of P, as shown in Figures B.1-B.84 (and discussed in Section 2.3).

BeXB	P_{orb} (d)	$EW\ H\alpha$ (Å)	Spectral type & luminosity class	V
SXP2.37	18.62 ± 0.02 [1]	-7.9 ± 0.6	O9.5 III-V [12]	16.38 ± 0.02 [12]
SXP4.78	23.9 ± 0.06 [3]	-43.7 ± 1.1	B0-B1 V [10]	15.8 [10]
SXP6.85	21.9 ± 0.1 [4]	-3.8 ± 3.7	O9.5-B0 IV-V [12]	14.59 ± 0.02 [12]
SXP7.78	44.93 ± 0.01 [2]	-14.3 ± 2.3	B1-B1.5 IV-V [12]	14.91 ± 0.02 [12]
SXP8.80	28.47 ± 0.04 [7]	-5.1 ± 0.4	O9.5-B0 IV-V [12]	14.87 ± 0.12 [12]
SXP11.5	36.3 ± 0.4 [6]		O9.5-B0 IV-V [11]	
SXP15.3	74.32 ± 0.03 [2]	-25.1 ± 1.5	O9.5-B0 III-V [12]	14.67 ± 0.04 [12]
SXP16.6	33.72 ± 0.05 [7]			
SXP18.3	17.79 ± 0.03 [2]		B1-B3 V [4]	15.6 [10]
SXP25.5	22.53 ± 0.01 [2]			15.2 [10]
SXP46.6	137.4 ± 0.2 [2]	-21.9 ± 0.7	O9.5-B1 IV-V [12]	14.72 ± 0.03 [12]
SXP59.0	122.1 ± 0.38 [7]	-23.4 ± 1.4	O9 V [12]	15.28 ± 0.01 [12]
SXP74.7	33.387 ± 0.006 [2]	-18.3 ± 2.3	B3 V [12]	16.92 ± 0.06 [12]
SXP82.4	362.2 ± 4.1 [7]	-25.9 ± 1.1	B1-B3 III-V [12]	15.02 ± 0.02 [12]
SXP91.1	88.37 ± 0.03 [2]	-26.7 ± 2.6	B0.5 III-V [12]	15.05 ± 0.06 [12]
SXP95.2	280 ± 8 [8]			
SXP101	21.949 ± 0.003 [2]	-7.8 ± 5		15.67 ± 0.15 [12]
SXP140	197 ± 5 [5]	-47.3 ± 3.1	B1 V [12]	15.88 ± 0.03 [12]
SXP152		-17.3 ± 1.7	B1-B2.5 III-V [12]	15.69 ± 0.03 [12]
SXP169	68.37 ± 0.07 [2]	-29.2 ± 2.6	B0-B1 III-V [12]	15.53 ± 0.02 [12]
SXP172	68.78 ± 0.08 [2]	-15 ± 1.3	O9.5-B0 V [12]	14.45 ± 0.02 [12]
SXP175	87.2 ± 0.2 [9]		B0-B0.5 III [9]	14.6 [9]
SXP202A	71.98 ± 5 [10]	-18.1 ± 5	B0-B1 V [12]	14.82 ± 0.02 [12]
SXP202B	224.6 ± 0.3 [2]		B0-5 III [10]	15.6 ± [10]
SXP214			B2-B3 III [13]	
SXP264	49.12 ± 0.03 [2]	-30.1 ± 1.7	B1-B1.5 V [12]	15.85 ± 0.01 [12]
SXP280	127.62 ± 0.25 [2]	-42 ± 3.1	B0-B2 III-V [12]	15.64 ± 0.03 [12]
SXP293	59.726 ± 0.006 [2]		B2-B3 V [10]	14.9 [10]
SXP304	520 ± 12 [5]	-70.4 ± 6.2	B0-B2 III-V [12]	15.72 ± 0.01 [12]
SXP323	116.6 ± 0.6 [7]	-30.9 ± 1.1	B0-B0.5 V [12]	15.44 ± 0.04 [12]
SXP327	45.93 ± 0.01 [2]			16.3 [10]
SXP342				
SXP455	74.56 ± 0.05 [2]	-15.1 ± 2	B0.5-B2 IV-V [12]	15.49 ± 0.02 [12]
SXP504	270.1 ± 0.5 [2]	-52.9 ± 3.9	B1 III-V [12]	14.99 ± 0.01 [12]
SXP565	152.4 ± 0.3 [2]	-37.4 ± 2.9	B0-B2 IV-V [12]	15.97 ± 0.02 [12]
SXP645			B0-B0.5 IIIV [10]	14.6 [10]
SXP701	412 ± 5 [10]	-37.1 ± 3.5	O9.5 V [12]	15.87 ± 0.05 [12]
SXP726			B0.5-B3 III-V [10]	15.6 [10]
SXP756	393.6 ± 1.2 [2]	-27 ± 3.6	O9.5-B0.5 III-V [12]	14.98 ± 0.02 [12]
SXP893				16.3 [10]
SXP967	101.4 ± 0.2 [2]	-12.3 ± 5	B0-B0.5 III-V [10]	14.6 [10]
SXP1323	26.174 ± 0.002 [2]	-17.1 ± 1.5	B0 III-V [12]	14.65 ± 0.02 [12]

Table 2.2: P_{orb}, $EW\ H\alpha$, and the spectral type, luminosity class, and apparent V magnitude of the OBe star in each of the 42 BeXB listed in Table 2.1. References are as follows; [1] Schurch et al. (2008), [2] Bird et al. (2012), [3] Coe et al. (2005), [4] Townsend et al. (2011a), [5] Schmidtke et al. (2006), [6] Townsend et al. (2009), [7] Galache et al. (2008), [8] Laycock et al. (2005), [9] Townsend et al. (2013), [10] Rajoelimanana et al. (2011), [11] Townsend et al. (2011b), [12] McBride et al. (2008), [13] Coe et al. (2011).

BeXB	Eccentricity	Reference
SXP2.37	0.07 ± 0.02	Townsend et al. (2011a)
SXP6.85	0.26 ± 0.03	Townsend et al. (2011a)
SXP8.80	0.41 ± 0.04	Townsend et al. (2011a)
SXP11.5	0.28 ± 0.03	Townsend et al. (2011b)
SXP18.3	0.43 ± 0.03	Schurch (2009)
SXP74.7	0.4 ± 0.2	Townsend et al. (2011a)

Table 2.3: Known eccentricities for the BeXB listed in Tables 2.1 and 2.2.

class, and apparent V magnitude of the OBe star in each system are given in Table 2.2, known eccentricities are given in Table 2.3.

2.2.1 Accretion methods

The accretion method for each system is determined using equations (1.1)-(1.7). As discussed in Section 1.2, an accretion disc will form if the net angular momentum per unit mass of accreted material (J), is too large for it to accrete spherically. This occurs at R_{circ}, where

$$R_{circ} = \frac{J^2}{GM_{NS}}. \qquad \text{(1.2 revisited)}$$

A disc can only form outside the neutron star's magnetosphere, which is approximately at R_A (derived in Section 1.2), and so for disc accretion to occur $R_{circ} > R_A$,

$$\frac{J^2}{GM_{NS}} > \left(\frac{\mu^4}{2GM_{NS}\dot{M}^2}\right)^{1/7}. \qquad (2.2)$$

J is dependent on the relative velocity of accreted matter (V_{rel}), and so this inequality can be rearranged to find the maximum V_{rel} under-which disc accretion can occur (V_{Crel}). This can then be compared to the actual relative velocity for each system, determined from the orbital velocity (V_{orb}), the velocity of accreted material (V_w), and the angle at which they impact (θ_i). The orbital parameters for a typical BeXB can be seen in Figures 1.3 and 1.4.

In Klus et al. (2014), we derived J for accreted material in typical BeXB. This involves material accreting from the circumstellar disc of an OBe main sequence star on to the surface of a neutron star at periastron. We followed the derivation of Shapiro and Lightman (1976) (see also Wang (1981)) of the angular momentum of the accreting matter, but while Shapiro and Lightman (1976) determined J for matter accreting from a spherical wind, matter from the circumstellar disc is usually in prograde motion with the neutron star, meaning that they orbit in the same direction. Material in the circumstellar

disc also decreases in velocity and density with distance from the OBe star,

$$V_{rel} = V_{rel(0)} R_{cd}^{-0.5} \tag{2.3}$$

and

$$\rho = \rho_{(0)} R_{cd}^{-n_\rho}, \tag{2.4}$$

which means that there will be a net angular momentum change due to accretion. Waters et al. (1987) find that the density gradient (n_ρ) has a range of 2-3.5 for isolated OBe stars, the circumstellar disc of OBe stars in BeXB are generally denser, and so a value of 2.5 ± 0.5 is assumed.

When the neutron star enters the circumstellar disc, the star forms an accretion cylinder with a radius equal to the Bondi-Hoyle radius (R_B), given in equation (1.1). We consider a cross-section of the accretion cylinder, which defines the xy-plane (Davidson and Ostriker, 1973; Alpar et al., 1982). The angular momentum passing through this plane is

$$dl = (\rho \; dx \; dy \; V_{rel} \; dt) V_{rel} \; y = \rho y V_{rel}^2 \; dx \; dy \; dt, \tag{2.5}$$

where y is the radial distance from the cylinder axis, and ρ is the density of material at the edge of the circumstellar disc. The first-order density and velocity perturbation about the periastron separation q is

$$\rho(x, y) \cong \rho(q) + \left.\frac{d\rho}{dR_{cd}}\right|_q y = \rho(q) \left(1 - n_\rho \frac{y}{q}\right) \tag{2.6}$$

$$V_{rel}(x, y) \cong V_{rel}(q) + \left.\frac{dV_{rel}}{dR_{cd}}\right|_q y = V_{rel}(q) \left(1 - \frac{y}{2q}\right). \tag{2.7}$$

Here, the dV_{rel}/dR_{cd} term accounts for both the gradient in V_w and V_{orb}, where

$$q = a(1 - e) \tag{2.8}$$

and

$$a = \left[\frac{P_{orb}^2 G(M_{NS} + M_{OB})}{4\pi^2}\right]^{1/3}, \tag{2.9}$$

as shown in Figure 1.3.

Substituting back into the angular momentum equation,

$$\frac{dl}{dt} = \rho(q) y V_{rel}(q)^2 \; dx \; dy \left[1 - \left(n_\rho + \frac{1}{2}\right) \frac{y}{q}\right]. \tag{2.10}$$

J is then found by integrating dl/dt over the accretion cylinder and dividing by $\dot{M}$, where $\dot{M} = \pi R_B^2 \rho V_{rel}$, i.e.,

$$\begin{aligned} J &= \frac{\rho V_{rel}^2}{\pi R_B^2 \rho V_{rel}} \int y[1 - (n_\rho + 1/2)(y/q)] \; dx \; dy \\ &= -\frac{1}{4}(n_\rho + 1/2) V_{rel} \frac{R_B^2}{q}. \end{aligned} \tag{2.11}$$

In BeXB, the OBe star's circumstellar disc can be truncated, so that only approximately half the neutron star's magnetosphere is exposed to accreting material at a time (see Section 1.1.2.1 and Figures B.1-B.84). If this is the case, then

$$\begin{aligned} J_t &= \frac{V_{rel}}{\pi R_B^2} \int_\pi^{2\pi} \int_0^{R_B} [1 - (n_\rho + 1/2)(R_{cd} \sin\theta / q)] R_{cd}^2 \sin\theta dr d\theta \\ &= -V_{rel} R_B \left[\frac{2}{3\pi} + \frac{1}{8}(n_\rho + 1/2) \frac{R_B}{q} \right]. \end{aligned} \tag{2.12}$$

In order to cover all possibilities, and not presuppose a magnetic field, μ is assumed to be $10^{24} - 10^{33}$ G cm^{-3}. Assuming $R_{NS} = 10$ km, this corresponds to $B = 10^6 - 10^{15}$ G. Equation (2.2) is then rearranged to find the maximum V_{rel} under-which disc accretion can occur (V_{rel}).

V_{Crel} can then be compared to the actual V_{rel} for each system, which is determined using

$$V_{rel} = \sqrt{V_w^2 + V_{orb}^2 + 2 V_w V_{orb} \cos\theta_i}. \tag{2.13}$$

Here θ_i=180° indicates that the star and disc are in prograde motion (see Figure 1.3), and θ_i=-180° indicates that the star and disc are in retrograde motion. The neutron star spin is not taken into account and so more accurate results could be found using numerical simulations that are beyond the scope of this thesis.

For systems containing an OBe star with a circumstellar disc that has been truncated by the orbit of the neutron star, V_w is calculated by determining the the Keplerian velocity of the stellar wind at the edge of the circumstellar disc (R_{cd}),

$$V_w = \sqrt{\frac{GM_{OB}}{R_{cd}}}, \tag{2.14}$$

assuming that the circumstellar disc is in a circular orbit around the OBe star.

For systems containing an OBe star with a circumstellar disc that has not been truncated by the orbit of the neutron star, V_w is calculated by determining the Keplerian velocity of the stellar wind at periastron distance q,

$$V_w = \sqrt{\frac{GM_{OB}}{q}}. \tag{2.15}$$

R_{cd} is calculated using

$$\log\left(\sqrt{\frac{R_{OB}}{R_{cd}}}\right) = [-0.32 \times \log(-EW\ H\alpha)] - 0.2, \tag{2.16}$$

where R_{OB} refers to the spectroscopic radius of the OBe star (Hanuschik, 1989; Huang, 1972; Zamanov et al., 2001), and V_{orb} is calculated using

$$V_{orb} = \sqrt{\frac{G(M_{NS} + M_{OB})}{a}\frac{1+e}{1-e}}. \tag{2.17}$$

Many of these parameters are shown in Figure 1.3. Systems are assumed to be disc accreting if $V_{rel} < V_{Crel}$.

2.2.2 Accretion theories

The magnetic field of the neutron star in each system is determined using all of the accretion theories discussed in Sections 1.2.1 and 1.2.2. These will be summarised again here.

In the spin equilibrium model for wind accretion,

$$\tau_{up\ (wind)} = \tau_{down}, \tag{1.14 revisited}$$

and so, using equation 1.5,

$$B \cong 8.7 \times 10^{13}\ \mathrm{G}\ \left(\frac{4\eta}{3\kappa_t}\right)^{1/2} R_{NS6}^{-3} \left(\frac{M_{NS}}{M_\odot}\right)^{3/2} \dot{M}_{16}^{1/2} \left(\frac{V_{rel}}{100\ \mathrm{km\ s^{-1}}}\right)^{-2} \frac{P/100}{(P_{orb}/10\ \mathrm{d})^{1/2}}. \tag{1.16 revisited}$$

Whereas in the Shakura et al. (2012) spin equilibrium model for wind accretion,

$$B \cong 6 \times 10^{14}\ \mathrm{G}\ R_{NS6}^{-3} \dot{M}_{16}^{1/3} \left(\frac{V_{rel}}{100\ \mathrm{km\ s^{-1}}}\right)^{-11/3} \left(\frac{P/100}{P_{orb}/10\ \mathrm{d}}\right)^{11/12}. \tag{1.17 revisited}$$

In equations (1.16 revisited) and (1.17 revisited), V_{rel} is measured in km s^{-1}, P_{orb} is measured in d, and everything else is in cgs units. Equations (1.16 revisited) and (1.17 revisited) show that for neutron stars of a given M_{NS} and R_{NS}, B is proportional to P and L, and inversely proportional to V_{rel} and P_{orb}. B is most affected by V_{rel}, and is more affected by this factor in the Shakura et al. (2012) model than in the spin equilibrium model.

In the spin equilibrium model for disc accretion,

$$\tau_{up\ (disc)} = \tau_{down}, \tag{1.19 revisited}$$

and so

$$B \cong 1.9 \times 10^{13} \text{ G } \left(\frac{2\epsilon}{9\kappa_t^2}\right)^{7/24} R_{NS6}^{-3} \left(\frac{M_{NS}}{M_\odot}\right)^{5/6} \dot{M}_{16}^{1/2} \left(\frac{P}{100}\right)^{7/6}. \quad \text{(1.21 revisited)}$$

In the spin equilibrium radius model for disc accretion,

$$R_{co} = R_A, \quad \text{(1.22 revisited)}$$

and so

$$B \cong 1.5 \times 10^{13} \text{ G } R_{NS6}^{-3} \left(\frac{M_{NS}}{M_\odot}\right)^{5/6} \dot{M}_{16}^{1/2} \left(\frac{P}{100}\right)^{7/6}. \quad \text{(1.24 revisited)}$$

Equations (1.21 revisited) and (1.24 revisited) show that for a given M_{NS} and R_{NS}, B is proportional to P and L, and is most affected by P.

The Ghosh and Lamb (1979) and the Kluzniak and Rappaport (2007) models for disc accretion (discussed in Section 1.2.2) do not assume spin equilibrium. These models relate $\dot{P}$ to μ (and hence B; equation 1.5) via,

$$\tau_{tot} = \tau_{up\ (disc)} n(\omega_s), \quad \text{(1.30 revisited)}$$

where $n(\omega_s)$ (equation (1.31)) is referred to as $g(\omega_s)$ (equation (1.35)) in the Kluzniak and Rappaport (2007) model. In the Ghosh and Lamb (1979) model,

$$-\dot{P} = 5.0 \times 10^{-5} (\epsilon/0.5)^{1/2} \mu_{30}^{2/7} n(\omega_s) R_{NS6}^{6/7} \left(\frac{M_{NS}}{M_\odot}\right)^{-3/7} I_{45}^{-1} (P L_{37}^{3/7})^2 \text{ s yr}^{-1}, \quad \text{(1.34 revisited)}$$

and in the Kluzniak and Rappaport (2007) model,

$$-\dot{P} = 6.2 \times 10^{-5} (\epsilon/0.52)^{1/2} \mu_{30}^{2/7} g(\omega_s) R_{NS6}^{6/7} \left(\frac{M_{NS}}{M_\odot}\right)^{-3/7} I_{45}^{-1} (P L_{37}^{3/7})^2 \text{ s yr}^{-1}. \quad \text{(1.36 revisited)}$$

Equations (1.34 revisited) and (1.36 revisited) show that for a given M_{NS} and R_{NS}, B is is dependent only on $\dot{P}$ and $PL^{3/7}$. Results from these models can be found assuming the system is close to spin equilibrium by working out what value would give a $n(\omega_s)$ of 0, given P and L. Figures 1.9-1.12 show simulated results for neutron stars with different values of B, M_{NS}, R_{NS}, and ϵ determined using the Ghosh and Lamb (1979) and Kluzniak and Rappaport (2007) models.

2.3 Results

The long-term average L, P, and $\dot{P}$ were determined for neutron stars in 42 BeXB in the SMC. The results are given in Table 2.1, and plots of L and P as a function of MJD

are shown in Appendix B, with a line of best-fit indicating $\dot{P}$. A positive correlation is found between $\dot{P}$ and P, which follows a power-law with a gradient of $\sim 6/5$, as is shown in Figure 2.2. The Ghosh and Lamb model predicts a power-law of two for systems close to spin equilibrium, and the discrepancy between these two results is discussed below, in relation to Figure 2.13. Figure 2.2 also shows that there is an asymmetry between the number of systems that are spinning up on average (27/42) and the number of systems that are spinning down (15/42).

The Corbet (1984) diagram for the BeXB in this dataset can be seen in Figure 2.3. This is a plot of P_{orb} as a function of P where, in this case, L is also plotted. P_{orb} is roughly proportional to P, as the Corbet (1984) relation (discussed in Section 1.1.2) predicts for systems that are close to spin equilibrium. There is no obvious correlation between L (and hence $\dot{M}$; equation (1.8)) and either P_{orb} or P, however, the instrumental limitations of RXTE prevent the detection of luminosities below $\sim 10^{36}$ erg s^{-1} given the distance to the SMC.

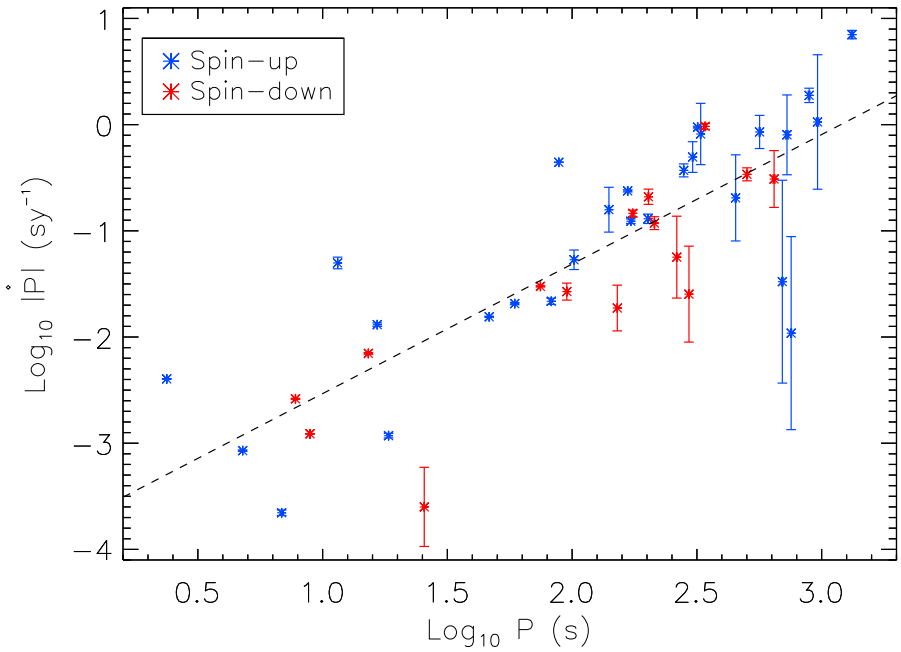

Figure 2.2: The long-term average $\dot{P}$ as a function of P, for neutron stars in the 42 BeXB listed in Table 2.1. 27 of these are spinning up on average ($\dot{P} < 0$; blue), and 15 are spinning down ($\dot{P} > 0$; red). A weighted $\dot{P}$ is found by fitting the time evolution of P, as shown in Figures B.1-B.84 (and discussed in Section 2.3). The dashed line indicates a correlation of $\dot{P} \propto P^{6/5}$. This is discussed further in Section 2.3, in relation to Figure 2.13.

Figure 2.4 shows the ratio of R_{cd} and R_{OB} (equation (2.16)) as a function of P_{orb}. The radius of the OBe star's circumstellar disc is proportional to P_{orb} in most cases. A possible exception to this is SXP4.78, which has a particularly large circumstellar disc, given its orbital period, as can be seen in Figure B.4.

BeXB	$M_{OB}/M_{\odot}$	$R_{OB}/R_{\odot}$	$R_{cd}/R_{\odot}$	$a/R_{\odot}$	$q/R_{\odot}$
SXP2.37	26 ± 7	12 ± 3	110 ± 28	89 ± 8	83 ± 7
SXP4.78	16 ± 2	8 ± 1	216 ± 20	90 ± 3	63 ± 18*
SXP6.85	22 ± 4	10 ± 2	60 ± 56	94 ± 6	69 ± 5
SXP7.78	16 ± 3	8 ± 2	110 ± 25	138 ± 9	96 ± 28*
SXP8.80	22 ± 4	10 ± 2	73 ± 14	112 ± 7	66 ± 6
SXP11.5	22 ± 4	10 ± 2	202 ± 135*	131 ± 8*	94 ± 7*
SXP15.3	25 ± 8	11 ± 3	226 ± 62	222 ± 21	155 ± 47*
SXP16.6	18 ± 4*	9 ± 2*	176 ± 121*	119 ± 9*	83 ± 25*
SXP18.3	11 ± 3	6 ± 1	115 ± 77*	66 ± 6*	38 ± 4*
SXP25.5	18 ± 4*	9 ± 2*	176 ± 121*	91 ± 7*	64 ± 19*
SXP46.6	20 ± 6	10 ± 3	173 ± 47	311 ± 28	218 ± 65*
SXP59.0	20 ± 0	9 ± 0	171 ± 7	288 ± 1	201 ± 58*
SXP74.7	8 ± 0	5 ± 0	76 ± 6	91 ± 0	54 ± 21
SXP82.4	16 ± 8	8 ± 3	164 ± 70	555 ± 90	388 ± 127*
SXP91.1	22 ± 6	10 ± 3	214 ± 57	239 ± 21	167 ± 50*
SXP95.2	18 ± 4*	9 ± 2*	176 ± 121*	487 ± 38*	341 ± 101*
SXP101	18 ± 4*	9 ± 2*	84 ± 45*	89 ± 7*	62 ± 18*
SXP140	14 ± 0	7 ± 0	207 ± 9	356 ± 6	249 ± 71*
SXP152	17 ± 8	8 ± 3	131 ± 50	454 ± 305*	318 ± 232*
SXP169	23 ± 5	11 ± 3	248 ± 69	204 ± 15	143 ± 42*
SXP172	18 ± 1	9 ± 0	121 ± 7	190 ± 2	133 ± 38*
SXP175	28 ± 0	14 ± 1	272 ± 175*	256 ± 0*	180 ± 51*
SXP202A	16 ± 2	8 ± 1	123 ± 25	188 ± 11	132 ± 38*
SXP202B	20 ± 8	10 ± 5	196 ± 155*	434 ± 54*	304 ± 95*
SXP214	19 ± 2	9 ± 1	173 ± 113*	468 ± 308*	328 ± 235*
SXP264	13 ± 1	7 ± 0	148 ± 9	138 ± 3	97 ± 28*
SXP280	20 ± 9	10 ± 4	276 ± 123	295 ± 41	206 ± 65*
SXP293	9 ± 2	5 ± 0	101 ± 66*	141 ± 7*	99 ± 29*
SXP304	20 ± 9	10 ± 4	384 ± 172	751 ± 105	526 ± 167*
SXP323	17 ± 1	8 ± 0	181 ± 8	264 ± 4	185 ± 53*
SXP327	18 ± 4*	9 ± 2*	176 ± 121*	146 ± 11*	102 ± 30*
SXP342	18 ± 4*	9 ± 2*	176 ± 121*	466 ± 308*	326 ± 235*
SXP455	17 ± 6	8 ± 3	118 ± 39	195 ± 20	137 ± 42*
SXP504	19 ± 5	9 ± 2	296 ± 75	483 ± 40	338 ± 101*
SXP565	17 ± 6	9 ± 3	226 ± 84	316 ± 35	221 ± 68*
SXP645	22 ± 6	11 ± 3	219 ± 156*	494 ± 327*	346 ± 249*
SXP701	19 ± 0	9 ± 0	220 ± 14	634 ± 5	444 ± 127*
SXP726	18 ± 10	9 ± 4	175 ± 140*	463 ± 315*	324 ± 239*
SXP756	24 ± 9	11 ± 3	231 ± 74	667 ± 73	467 ± 143*
SXP893	18 ± 4*	9 ± 2*	176 ± 121*	466 ± 308*	326 ± 235*
SXP967	22 ± 6	11 ± 3	139 ± 58	262 ± 23	184 ± 55*
SXP1323	23 ± 5	11 ± 3	176 ± 49	108 ± 8	75 ± 22*

Table 2.4: Orbital parameters for the BeXB listed in Table 2.2. These include M_{OB} and R_{OB} (determined from the spectral type and luminosity class), R_{cd} (equation (2.16)), a (equation (2.9)), and q (equation (2.8)). An asterisk denotes that this value is an estimate, as discussed in Section 2.3 and shown in Appendix B. Results that take M_{dyn} into account are given in Tables A.2 and A.3.

BeXB	Circ. disc status	V_{orb} (km s^{-1})	V_w (km s^{-1})	V_{rel} (prograde) (km s^{-1})	V_{Crel} (N-T) (km s^{-1})	V_{Crel} (T) (km s^{-1})
SXP2.37	N-T	259 ± 36	244 ± 35	15 ± 71	256 ± 29	867 ± 268
SXP4.78	N-T*	260 ± 44	219 ± 33*	41 ± 78*	247 ± 36	609 ± 187
SXP6.85	T	283 ± 27	261 ± 123	21 ± 150	252 ± 29	706 ± 216
SXP7.78	N-T*	211 ± 41	178 ± 32*	34 ± 73*	208 ± 31	554 ± 172
SXP8.80	N-T	307 ± 31	250 ± 26	56 ± 57	256 ± 29	698 ± 213
SXP11.5	N-T*	244 ± 24*	209 ± 21*	35 ± 45*	222 ± 25*	651 ± 199*
SXP15.3	N-T*	206 ± 46	176 ± 38*	30 ± 84*	183 ± 27	594 ± 185
SXP16.6	N-T*	243 ± 49*	205 ± 39*	38 ± 88*	212 ± 31*	514 ± 159*
SXP18.3	N-T*	298 ± 43*	235 ± 38*	63 ± 81*	294 ± 34*	632 ± 187*
SXP25.5	N-T*	278 ± 56*	235 ± 45*	43 ± 100*	237 ± 35*	553 ± 171*
SXP46.6	T*	156 ± 34	148 ± 29*	8 ± 63*	161 ± 24	573 ± 181
SXP59.0	T*	162 ± 26	150 ± 3*	13 ± 29*	169 ± 25	607 ± 191
SXP74.7	N-T	210 ± 44	163 ± 31	47 ± 75	266 ± 45	661 ± 206
SXP82.4	T*	106 ± 32	137 ± 46*	31 ± 78*	134 ± 21	582 ± 182
SXP91.1	N-T*	187 ± 40	159 ± 33*	28 ± 73*	182 ± 27	632 ± 197
SXP95.2	T*	120 ± 24*	141 ± 51*	21 ± 75*	141 ± 21*	594 ± 185*
SXP101	N-T*	280 ± 56*	237 ± 45*	43 ± 101*	248 ± 37*	613 ± 191*
SXP140	T*	125 ± 20	115 ± 2*	10 ± 23*	158 ± 23	620 ± 200
SXP152	T*	119 ± 51*	157 ± 47*	37 ± 98*	143 ± 38	586 ± 188
SXP169	N-T*	206 ± 41	175 ± 33*	31 ± 74*	192 ± 28	635 ± 199
SXP172	T*	191 ± 31	169 ± 6*	22 ± 37*	192 ± 28	593 ± 187
SXP175	N-T*	203 ± 33*	174 ± 25*	29 ± 58*	176 ± 26*	618 ± 195*
SXP202A	T*	180 ± 31	157 ± 18*	23 ± 49*	192 ± 28	594 ± 187
SXP202B	T*	133 ± 34*	141 ± 62*	7 ± 96*	142 ± 22*	548 ± 176*
SXP214	T*	123 ± 46*	144 ± 47*	20 ± 93*	140 ± 37*	569 ± 184*
SXP264	N-T*	194 ± 32	162 ± 24*	32 ± 56*	204 ± 30	526 ± 165
SXP280	N-T*	159 ± 43	135 ± 37*	24 ± 80*	163 ± 25	566 ± 181
SXP293	T*	163 ± 30*	132 ± 44*	31 ± 74*	206 ± 30*	553 ± 172*
SXP304	T*	100 ± 27	99 ± 31*	1 ± 58*	127 ± 19	665 ± 212
SXP323	T*	156 ± 26	133 ± 4*	23 ± 30*	172 ± 25	585 ± 184
SXP327	N-T*	219 ± 44*	185 ± 35*	34 ± 79*	196 ± 29*	495 ± 154*
SXP342	T*	123 ± 47*	141 ± 51*	18 ± 98*	146 ± 39*	637 ± 205*
SXP455	T*	180 ± 42	164 ± 39*	17 ± 81*	201 ± 30	696 ± 220
SXP504	T*	123 ± 26	112 ± 21*	12 ± 46*	139 ± 21	570 ± 180
SXP565	N-T*	143 ± 34	121 ± 28*	22 ± 62*	153 ± 23	508 ± 165
SXP645	T*	130 ± 51*	139 ± 53*	9 ± 104*	138 ± 37*	573 ± 186*
SXP701	T*	106 ± 17	127 ± 4*	21 ± 21*	126 ± 18	553 ± 175
SXP726	T*	122 ± 56*	140 ± 69*	18 ± 125*	148 ± 40*	665 ± 216*
SXP756	T*	117 ± 28	142 ± 34*	25 ± 61*	126 ± 19	581 ± 182
SXP893	T*	123 ± 47*	141 ± 51*	18 ± 98*	138 ± 36*	536 ± 173*
SXP967	T*	178 ± 38	174 ± 44*	4 ± 82*	184 ± 27	710 ± 226
SXP1323	N-T*	283 ± 57	241 ± 46*	42 ± 103*	246 ± 36	708 ± 220

Table 2.5: The status of the OBe star's circumstellar disc determined using orbital parameters listed in Table A.1, assuming $M_{OB} = M_{spec}$, as discussed in Section 2.3. Here T refers to a truncated circumstellar disc and $N-T$ to a non-truncated circumstellar disc. An asterisk indicates that the value is an estimate. V_{orb} (equation (2.17)), V_w (equation (2.15) assuming T, and equation (2.14) assuming $N-T$) and V_{rel} (equation (2.13)) are given, as is V_{Crel} (equations (1.2)-(1.7), where J is determined using equation (2.12) assuming T, and equation (2.11) assuming $N-T$). Disc accretion can only occur if $V_{rel} < V_{Crel}$. Results that take M_{dyn} into account are given in Tables A.4 and A.5.

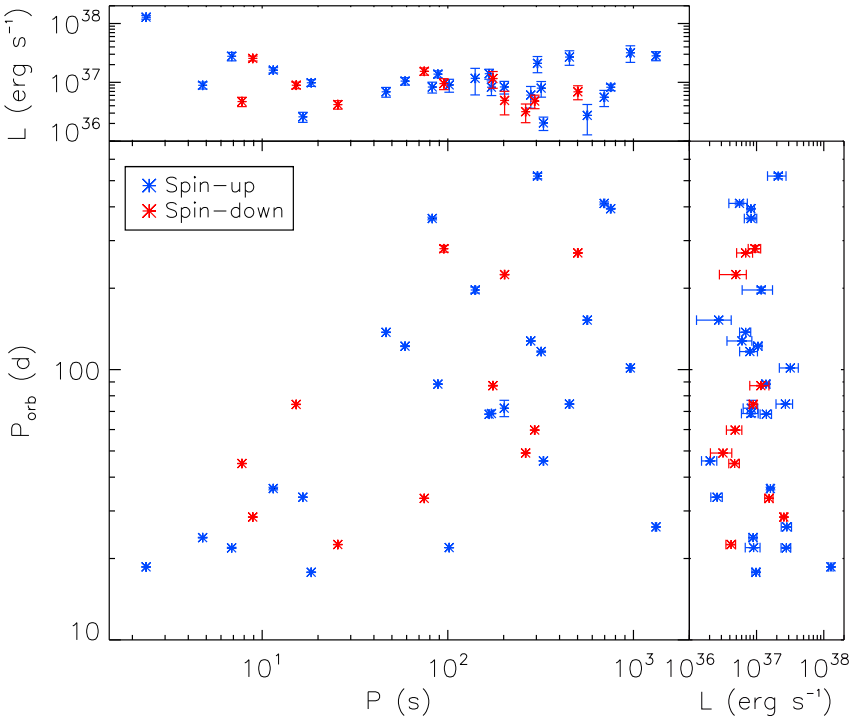

Figure 2.3: Corbet (1984) diagram (P_{orb} as a function of P) for neutron stars in 36 of the BeXB listed in Table 2.2 (discussed in Section 2.3), where L is also shown. 25 of these are spinning up on average ($\dot{P} < 0$; blue), and 11 are spinning down ($\dot{P} > 0$; red).

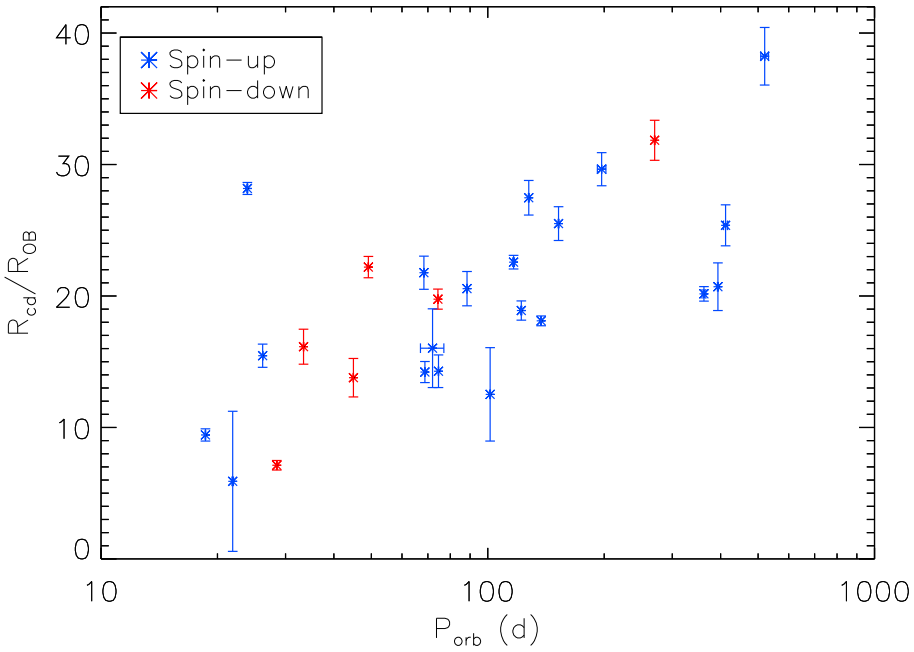

Figure 2.4: The ratio of R_{cd} and R_{OB} (equation (2.16)) as a function of P_{orb}, for 26 of the BeXB listed in Table 2.4 (discussed in Section 2.3). 20 of these are spinning up on average ($\dot{P} < 0$; blue), and 6 are spinning down ($\dot{P} > 0$; red).

The orbital parameters of each system are determined using a (equation (2.9)), q (equation (2.8)), R_{cd} (equation (2.16)), and R_{OB}, as shown in Figure 1.3. R_{cd} depends on $EW\ H\alpha$, which is known for 28 systems, where R_{cd} could not be calculated, the median value of 176 $\pm$ 121 $R_{\odot}$ was assumed, with the errors covering the range of the dataset. a depends on P_{orb}, which is known for 36 systems, where P_{orb} was not known, the median value of 262 $\pm$ 258 d was used. a also depends on M_{NS}, which was assumed to be 1.4 $M_{\odot}$, and M_{OB}. q depends on a and e, where e is known for 6 systems (see Table 2.3) and otherwise assumed to be 0.3 $\pm$ 0.2. M_{OB} and R_{OB} are determined from the spectral type and luminosity class of the OBe star, which is known for 35 systems, otherwise the average values of $M_{OB}/M_{\odot}$=18.36 $\pm$ 4.42, and $R_{OB}/R_{\odot}$=8.95 $\pm$ 2.08, were assumed. These results are given in Table 2.4. As discussed in Section 2.2, the spectroscopic mass of OBe stars in X-ray binaries may be larger than the actual mass (which can be derived in some systems using dynamical methods (Coe et al., 2015a,b)), where M_{dyn} is $\sim$ 20% lower than M_{spec}, and so I consider the effects of both masses. A full set of results, assuming both $M_{OB} = M_{spec}$ and $M_{OB} = M_{dyn}$, are given in Tables A.2 and A.3.

While values of $P_{orb} = 262 \pm 258$ d and $R_{cd} = 176 \pm 121\ R_{\odot}$ are used in calculations when P_{orb} or $EW\ H\alpha$ are not known, in order to cover a full range of possible results, the most probable values were calculated in order to determine whether or not each of these systems accretes from a truncated or non-truncated circumstellar disc. These were calculated by fitting the results of P_{orb} and P, and R_{cd} and P_{orb} (using MPFITEXPR[2]). It was found that $P_{orb} \propto P^{5/14}$, and $P_{orb} \propto R_{cd}^{7/100}$. These values were then used, along with all other values taken from Tables A.2 and A.3, in order to to create diagrams of each system. These values are given in Table A.1 and diagrams are shown in Figures B.1-B.84, where the estimated values are highlighted.

Figures B.1-B.84 show that about half of all systems (23/42 if $M_{OB} = M_{spec}$, and 19/42 if $M_{OB} = M_{dyn}$) are expected to contain OBe stars with truncated circumstellar discs, where this is defined as having orbital parameters that place it outside of the OBe star's circumstellar disc at periastron. Of the 26 systems where P_{orb}, $EW\ H\alpha$, and the spectral type and luminosity class of the OBe star were known, 14 systems contain OBe stars with truncated circumstellar discs, and 12 systems contain OBe stars with non-truncated circumstellar discs. The status of the circumstellar disc in each of these systems, assuming $M_{OB} = M_{spec}$, is is given in Table 2.5, results assuming $M_{OB} = M_{dyn}$ are given in Table A.1.

Table 2.5 also lists V_{orb} (equation (2.17)), V_w (equation (2.15) for systems containing an OBe star with a truncated circumstellar disc, and equation (2.14) for systems containing an OBe star with a non-truncated circumstellar disc), V_{rel} (equation (2.13); equal to $|V_{orb} - V_w|$ if the system is in a prograde orbit, and $|V_{orb} + V_w|$ if the system is in a retrograde orbit), and V_{Crel} (equations (1.2)-(1.7), where J is determined using equation

[2] www.physics.wisc.edu/~craigm/idl/down/mpfitexpr.pro

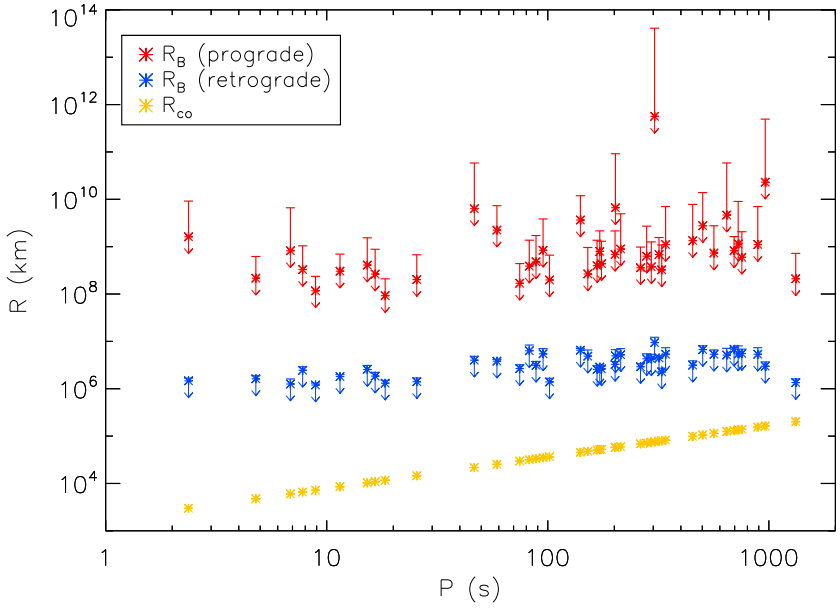

Figure 2.5: R_B for prograde (θ_i=180°; equation (1.15); red) and retrograde (θ_i=-180°; equation (1.15); blue) systems, both assuming $M_{OB} = M_{spec}$, and R_{co} (equation (1.13); yellow), as a function of P, for 26 of the BeXB in this dataset (discussed in Section 2.3). When a system is in spin equilibrium, $R_{co} \cong R_A$ (equation (1.7)), and so an accretion disc can form between R_B and R_{co}.

(2.12) assuming a truncated circumstellar disc, and equation (2.11) assuming a non-truncated circumstellar disc). These are derived from parameters given in Table 2.4, assuming $M_{OB} = M_{spec}$. A full set of results, assuming both $M_{OB} = M_{spec}$ and $M_{OB} = M_{dyn}$, are given in Tables A.4 and A.5. Disc accretion can only occur if $V_{rel} < V_{Crel}$.

Figure 2.5 shows R_B (equation (1.15)), assuming prograde and retrograde orbits and $M_{OB} = M_{spec}$, as a function of P. R_B is the radius at which matter begins accreting onto the neutron star's magnetosphere. R_{co} (equation (1.13)) is also shown. This is the radius at which matter co-rotates with the neutron star and its magnetosphere. If a system is close to spin equilibrium, then $R_{co} \cong R_A$, where R_A (equation (1.7)) is approximately equal to the radius of the neutron star's magnetosphere, and so an accretion disc can form between R_B and R_A. R_{co} is proportional to P, and so R_A is proportional to P for systems that are close to spin equilibrium. R_B, on the other hand, is not directly related to P, and remains fairly constant. This implies that if these systems are close to spin equilibrium, then the accretion disc may be larger for systems with shorter spin periods. The disc may also be larger for systems in prograde rather than retrograde orbits.

Figure 2.6 shows V_w as a function of P, assuming $M_{OB} = M_{spec}$. V_{orb} and V_{Crel}, for prograde systems with truncated and non-truncated discs, are also shown. The V_{Crel} for systems with truncated discs is ∼2-5 times larger than in the non-truncated case. It

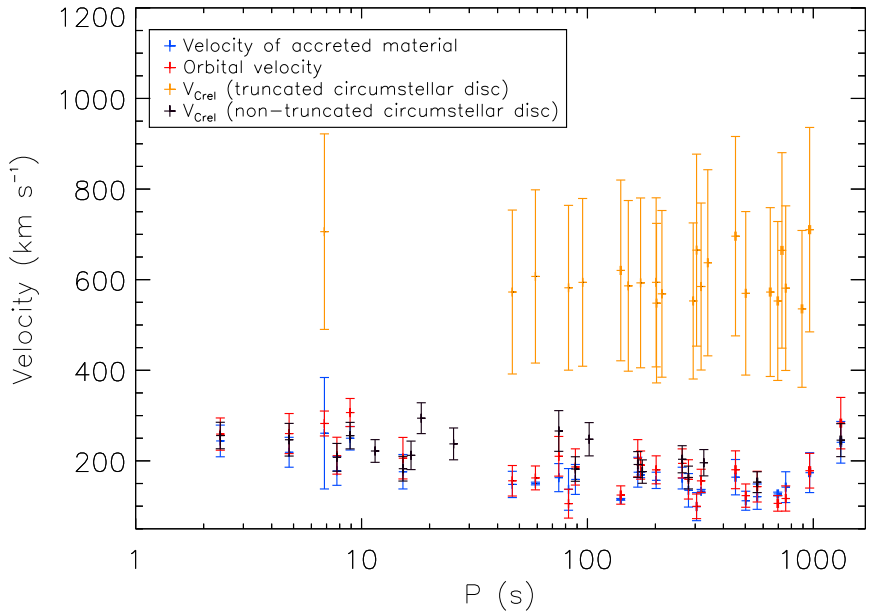

Figure 2.6: V_w (equation (2.14); blue), V_{orb} (equation (2.17); red), and V_{Crel}, for systems where the OBe star has a circumstellar disc that is (equation (2.12); orange), and is not (equation (2.11); black), truncated by the orbit of the neutron star, assuming $M_{OB} = M_{spec}$, as a function of P, for 26 of the BeXB listed in Table 2.5 (discussed in Section 2.3). The status of the OBe star's circumstellar disc is determined from orbital parameters, as given in Table A.1 and shown in Figures B.1-B.84.

is easier to form a disc in the truncated case because of the asymmetry in the accretion of angular momentum.

Figure 2.7 shows the ratio of V_{rel} and V_{Crel} as a function of P for all systems, assuming prograde orbits, for both $M_{OB} = M_{spec}$, and $M_{OB} = M_{dyn}$. Figure 2.7 shows that all of these systems contain neutron stars that are most-likely accreting via an accretion disc. Figure 2.8 shows that wind accretion is also possible in all systems where the OBe star's circumstellar disc is not truncated by the orbit of the neutron star and the neutron star is in a retrograde orbit, however the majority of neutron stars in BeXB are thought to be in prograde orbits (Brandt and Podsiadlowski, 1995).

Figures 2.7 and 2.8 show that all of the BeXB in this dataset most likely contain neutron stars that are disc-accreting. The long-term average $\dot{P}$ for the neutron star in each system is known, and so the Ghosh and Lamb (1979) (equation (2.13)) and Kluzniak and Rappaport (2007) (equation (2.13)) models are the most appropriate models for determining the neutron star's magnetic field.

Figures 2.9 and 2.10 show results for the systems in this dataset over-plotted onto the simulated results shown in Figures 1.9 and 1.10 (these are plots of $\dot{P}$ as a function of $PL^{3/7}$ for different values of B). Five systems - SXP2.37 (SMC X-2), SXP4.78 (which

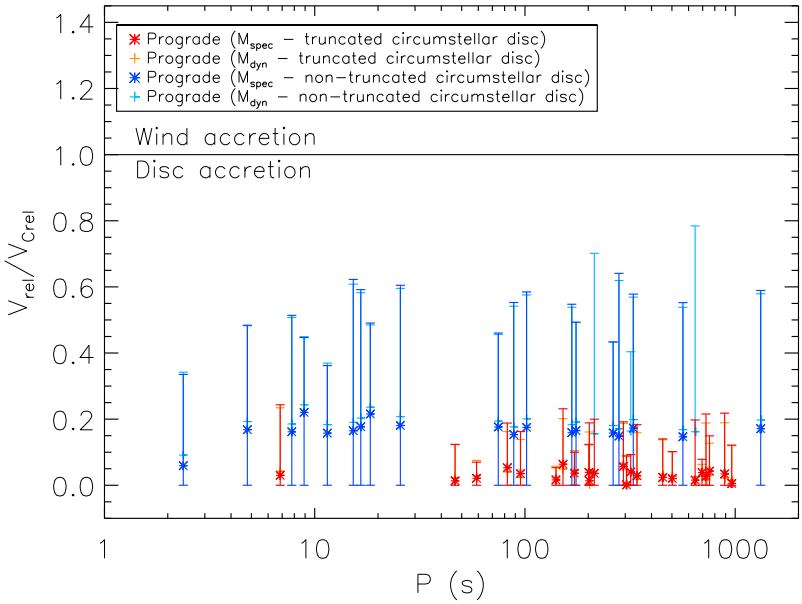

Figure 2.7: The ratio of V_{rel} (equation (2.13)) and V_{Crel} as a function of P, assuming a prograde orbit, for the BeXB listed in Table A.5. Results are shown for systems where the OBe star has a circumstellar disc that is (equation (2.12); red), and is not (equation (2.11); dark blue), truncated by the orbit of the neutron star, assuming $M_{OB} = M_{spec}$, and that is (orange), and is not (light blue), truncated by the orbit of the neutron star, assuming $M_{OB} = M_{dyn}$. The status of the OBe star's circumstellar disc is determined from orbital parameters given in Table A.1 and shown in Figures B.1-B.84. Disc accretion occurs when V_{rel}/V_{Crel} <1, and wind accretion when V_{rel}/V_{Crel} >1.

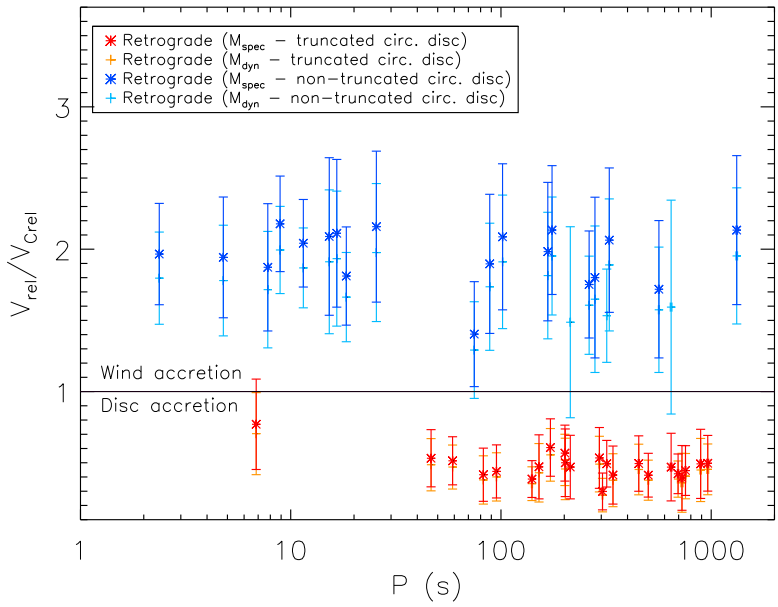

Figure 2.8: As for Figure 2.7, except results are given assuming a retrograde rather than prograde orbit.

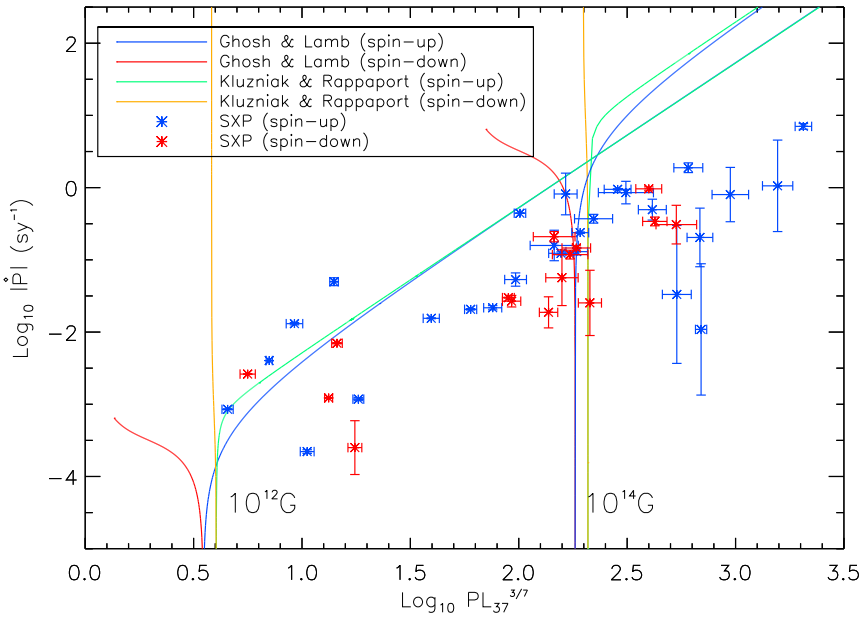

Figure 2.9: $\dot{P}$ as a function of $PL^{3/7}$; results for neutron stars in the 42 BeXB listed in Table 2.1 (discussed in Section 2.3) over-plotted onto Figure 1.9. 27 of these are spinning up on average ($\dot{P} < 0$; blue stars), and 15 are spinning down ($\dot{P} > 0$; red stars).

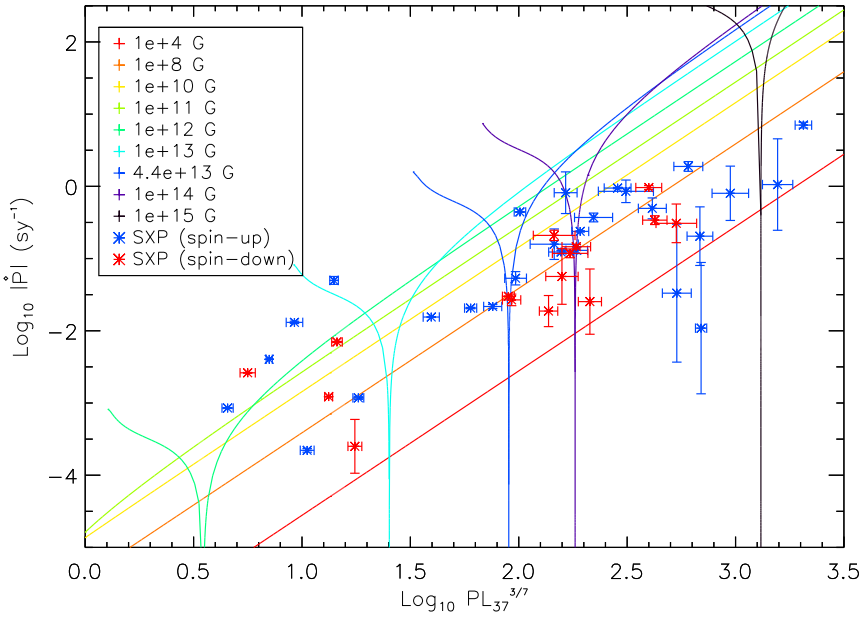

Figure 2.10: As for Figure 2.9, except results are over-plotted onto Figure 1.10 rather than Figure 1.9.

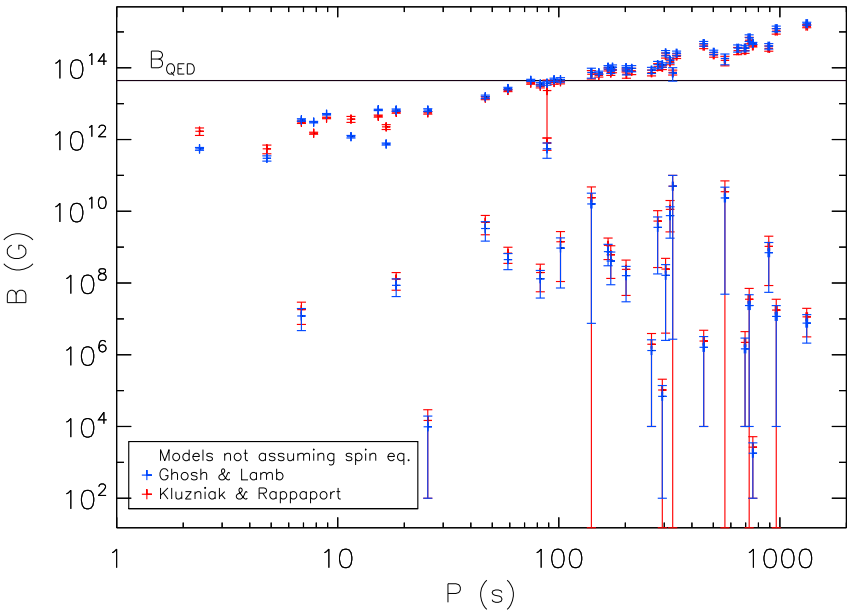

Figure 2.11: B as a function of P for the 42 BeXB listed in Table 2.6 (discussed in Section 2.3), where B is determined using the Ghosh and Lamb (1979) (equation (1.34); blue) and Kluzniak and Rappaport (2007) (equation (1.36); red) non-spin equilibrium models. The fact that there are two possible results for some systems is discussed in Sections 1.2.2 and 2.3.

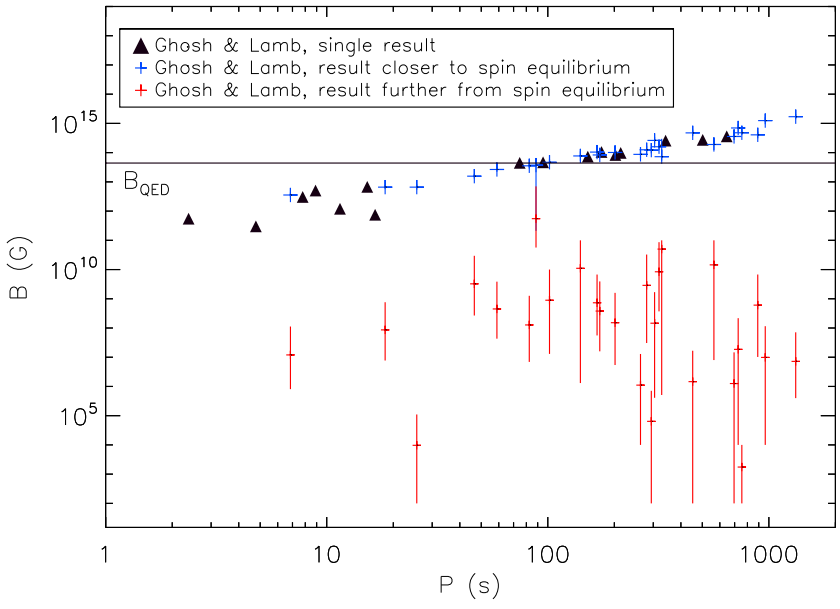

Figure 2.12: As for Figure 2.11, except only showing results for the Ghosh and Lamb (1979) model. Systems with only one possible result are highlighted (black triangles), given two possible results, one will be closer to spin equilibrium (blue), and one will further from spin equilibrium (red). Results are shown for M_{NS}=1.4 $M_{\odot}$, where error bars represent the highest and lowest possible results if M_{NS}=1 $M_{\odot}$ and M_{NS}=2 $M_{\odot}$ respectively.

accretes from a particularly large circumstellar disc, as discussed above), SXP7.78 (SMC X-3), SXP11.5, and SXP16.6 - are above all possible spin equilibrium lines for the Ghosh and Lamb (1979) and Kluzniak and Rappaport (2007) models. This means that they are not close to spin equilibrium. SXP2.37, SXP4.78, SXP11.5, and SXP16.6 are not close to spin equilibrium and are spinning up on average, and SXP7.78 is not close to spin equilibrium and is spinning down on average. All of these systems are thought to accrete from a non-truncated circumstellar disc, via an accretion disc.

Figure 2.10 shows that all other systems that are spinning up on average have two possible results; they fall on the non-spin equilibrium, spin-up lines corresponding to relatively low ($\sim 10^3 - 10^{10}$ G) magnetic fields, and the spin equilibrium lines corresponding to relatively high ($\sim 10^{11} - 10^{15}$ G) magnetic fields (as discussed in Section 1.2.2). This applies to 26 systems. 11 systems are spinning down on average, and are below all possible spin-down lines. This means that they must be close to spin equilibrium. These are SXP8.80, SXP15.3, SXP74.7, SXP95.2, SXP152, SXP175, SXP202B, SXP214, SXP342, SXP504, and SXP645.

Results for the surface magnetic field determined using the Ghosh and Lamb (1979) and Kluzniak and Rappaport (2007) models are shown in Figure 2.11. The Kluzniak and Rappaport (2007) model has a particularly large lower error bar on the spin equilibrium results for SXP91.1, it is so large that it intersects with the non-spin equilibrium result. SXP91.1 is the only system with two possible results where the non-spin equilibrium result is similar in strength to the magnetic field of neutron stars that we know are not close to spin equilibrium (SXP2.37, SXP4.78, SXP7.78, SXP11.5, and SXP16.6; $\sim 10^{11}$ G). It may be more likely, therefore, that the lower results for SXP91.1 are correct, and it is also not close to spin equilibrium.

Figure 2.12 shows results for the Ghosh and Lamb (1979) model for M_{NS}=1.4 $M_{\odot}$, where the error bars indicate results for M_{NS}=1 $M_{\odot}$ - 2 $M_{\odot}$. This confirms that the magnetic field does not have a strong dependence on M_{NS}, as is expected given Figure 1.11.

For the other 25 systems with two possible results, the spin equilibrium results are assumed to be correct for a number of reasons. Firstly, it was previously noted that a correlation of $\dot{P} \propto P^{6/5}$ is found in our results, whereas the Ghosh and Lamb (1979) model predicts a correlation of $\dot{P} \propto P^2$ for systems that are close to spin equilibrium. The discrepancy between these two results can be resolved if the non-spin equilibrium results are removed, giving a weighted correlation of $\dot{P} \propto P^{12/7}$. If two further points are removed (SXP8.80 and SXP15.3; the two systems with the lowest P that are spinning down), then a weighted correlation of $\dot{P} \propto P^2$ is found, as shown in in Figure 2.13.

Secondly, 12 neutron stars in Galactic BeXB have had their magnetic fields measured directly using CRSF (see Table 2.7). These were found to have magnetic fields of $\sim 10^{12} - 10^{13}$ G (see Figure 2.17). While these are lower than some of the spin equilibrium results

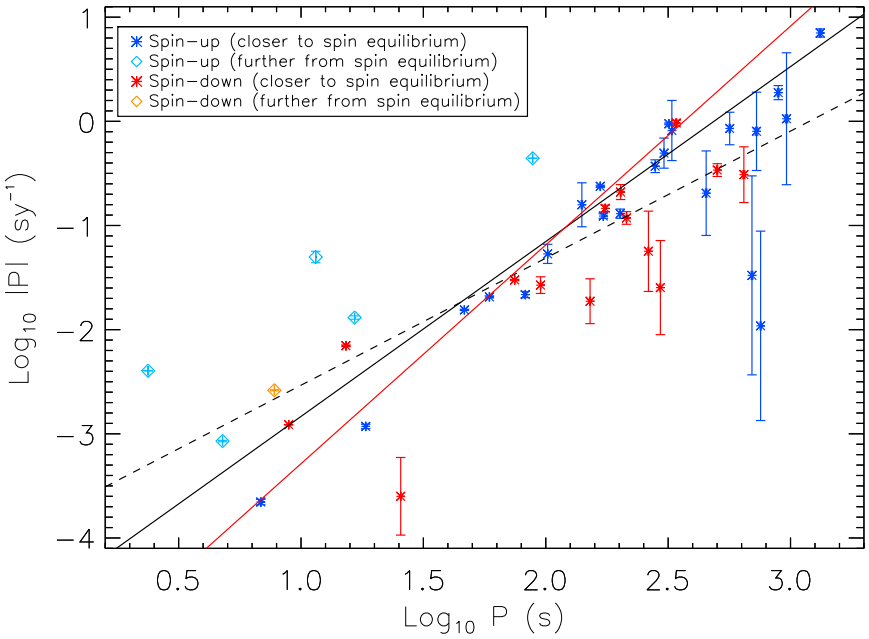

Figure 2.13: As for Figure 2.2, except that results are highlighted for systems not thought to be close to spin equilibrium, both spinning up (light blue diamonds) and spinning down (orange diamond). The Ghosh and Lamb (1979) model predicts a correlation of $\dot{P} \propto P^2$ for systems that are close to spin equilibrium. The dashed black line indicates a correlation, between all results, of $\dot{P} \propto P^{6/5}$. When only the spin equilibrium results are considered, a correlation of $\dot{P} \propto P^{12/7}$ is found (black line). If SXP8.80 and SXP15.3 are also removed from the dataset (these are the two systems with the lowest P that are spinning down), then a correlation of $\dot{P} \propto P^2$ is found (red line).

(which will be discussed further below), they are much closer to the spin equilibrium results ($10^{11} - 10^{15}$ G) than the non-spin equilibrium results ($10^{3} - 10^{10}$ G).

Thirdly, Figure 2.9 shows that at least 11 systems are almost certainly close to spin equilibrium, and at least 5 are almost certainly not, 6 if SXP91.1 is included (as discussed above). All 6 are still predicted to have magnetic fields much closer to the spin equilibrium results than the non-spin equilibrium results ($B > 10^{11}$ G). This can be seen in Figures 2.14 and 2.15, which show results assuming that the spin equilibrium results are correct for systems with two possibilities (with the exception of SXP91.1), and results assuming $\dot{P} = 0$ in all cases, using the Ghosh and Lamb (1979) and Kluzniak and Rappaport (2007) models respectively. This allows us to see how close the neutron star in each system is to spin equilibrium (assuming the close-to-spin-equilibrium results are correct when two results are possible, with the exception of SXP91.1).

Finally, many of these systems follow the Corbet (1984) relation, which is expected if they are close to spin equilibrium. The Corbet (1984) relation shows that for neutron stars in BeXB, P is proportional to P_{orb}. This is because systems with longer orbital

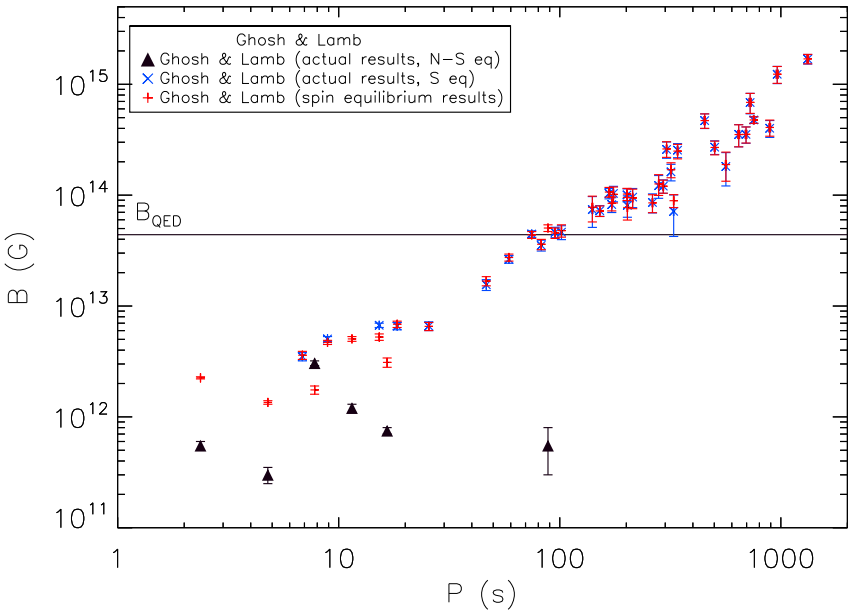

Figure 2.14: B as a function of P for neutron stars in the 42 BeXB listed in Table 2.6. The most probable results determined using the Ghosh and Lamb (1979) (equation (1.34)) model are shown (as discussed in Section 2.3). 36 neutron stars in this dataset are assumed to be close to spin equilibrium (blue), and 6 are not (black). Results found using the Ghosh and Lamb (1979) model assuming that the system is in spin equilibrium, and hence $\dot{P} = 0$, are also shown (red). The largest disparity between these results is in SXP91.1. This suggests that it is the furthest from spin equilibrium.

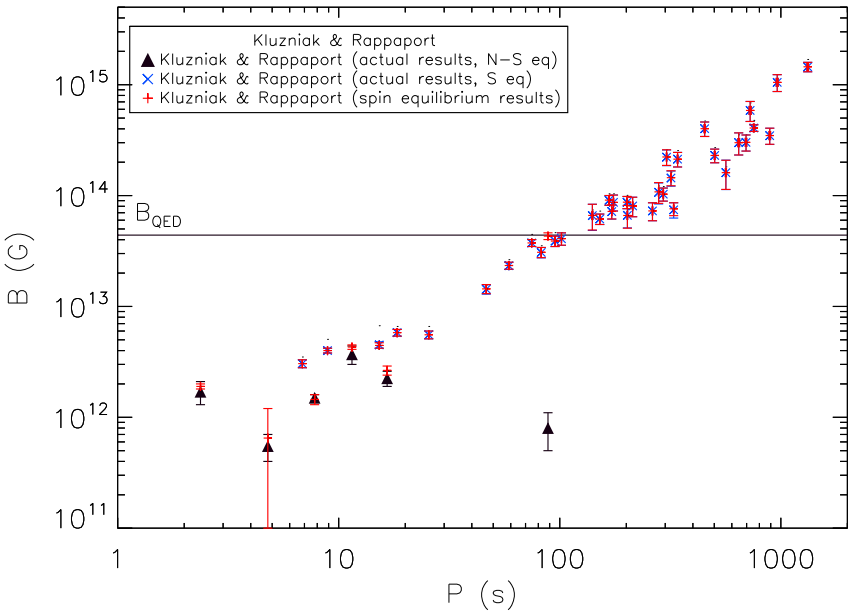

Figure 2.15: As for Figure 2.14, except results are determined using the Kluzniak and Rappaport (2007) rather than Ghosh and Lamb (1979) model.

periods accrete less often, and spend longer amounts of time spinning down between accretion events, which means that they tend to have longer spin equilibrium periods.

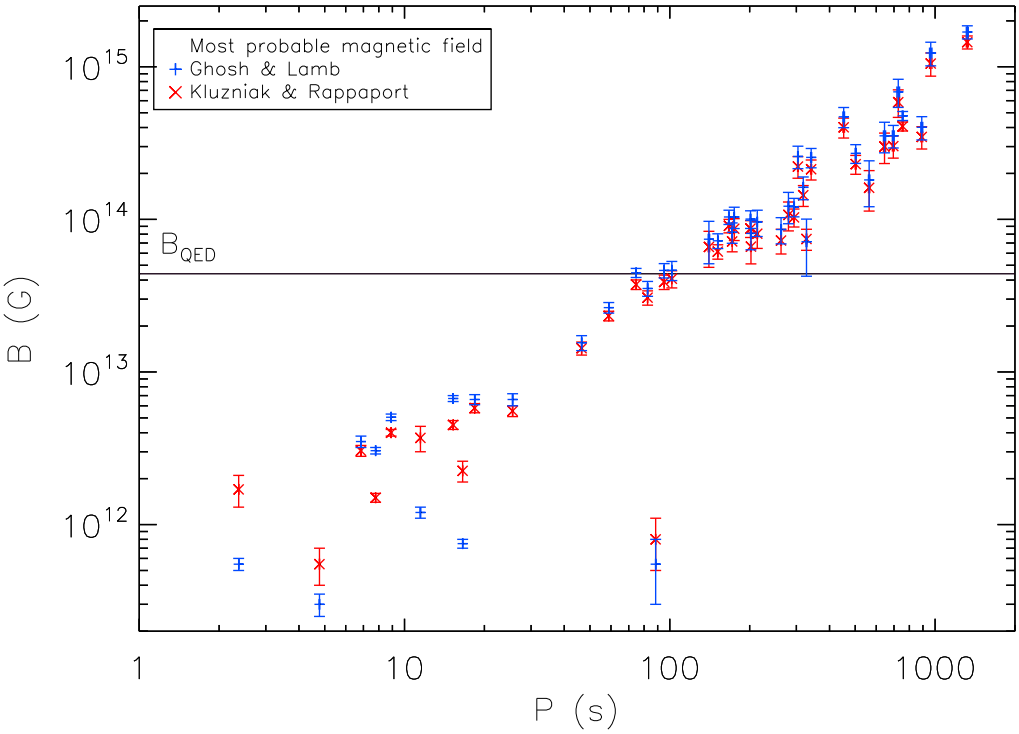

Figure 2.16: B as a function of P for neutron stars in the 42 BeXB listed in Table 2.6. The most probable results are shown (as discussed in Section 2.3), determined using the Ghosh and Lamb (1979) (equation (1.34); blue) and Kluzniak and Rappaport (2007) (equation (1.36); red) models.

Figure 2.16 shows the most probable B found using the Ghosh and Lamb (1979) and Kluzniak and Rappaport (2007) models (as described above), as a function of P. This assumes that all systems are close to spin equilibrium, with the exception of SXP2.37, SXP4.78, SXP7.78, SXP11.5, SXP16.6, and SXP91.1. Table 2.6 summarises the results for each system, giving the accretion method, spin equilibrium status, the status of the OBe star's circumstellar disc, and the most probable B given this information.

Figure 2.16 shows that both models predict $B > B_{QED}$ (where B_{QED}=4.4×10^{13} G; equation 1.41) for all systems with $P \gtrsim 100$ s. Two thirds (28/42) of the systems in this dataset contain neutron stars with $B > B_{QED}$ according to the Ghosh and Lamb (1979) model, and 60% (25/42) contain neutron stars with $B > B_{QED}$ according to the Kluzniak and Rappaport (2007) model.

Figure 2.17 shows the most probable B as a function of P, alongside results for almost all known neutron stars, including magnetars, and neutron stars in Galactic BeXB that have had B determined from CRSF. If these results are correct, then this plot, first

BeXB	Acc. method	Spin equilibrium status	Circ. disc status	Ghosh & Lamb B (G)	Kluzniak & Rappaport B (G)
SXP2.37	Disc	N-S eq, u	N-T	$(5.5 \pm 0.5) \times 10^{11}$	$(1.7 \pm 0.4) \times 10^{12}$
SXP4.78	Disc	N-S eq, u	N-T*	$(3.0 \pm 0.5) \times 10^{11}$	$(5.5 \pm 1.5) \times 10^{11}$
SXP6.85	Disc	S eq*	T	$(3.5 \pm 0.3) \times 10^{12}$	$(3.1 \pm 0.3) \times 10^{12}$
SXP7.78	Disc	N-S eq, d	N-T*	$(3.1 \pm 0.2) \times 10^{12}$	$(1.5 \pm 0.1) \times 10^{12}$
SXP8.80	Disc	S eq	N-T	$(5.1 \pm 0.3) \times 10^{12}$	$(4.0 \pm 0.2) \times 10^{12}$
SXP11.5	Disc	N-S eq, u	N-T*	$(1.2 \pm 0.1) \times 10^{12}$	$(3.7 \pm 0.7) \times 10^{12}$
SXP15.3	Disc	S eq	N-T*	$(6.7 \pm 0.3) \times 10^{12}$	$(4.5 \pm 0.3) \times 10^{12}$
SXP16.6	Disc	N-S eq, u	N-T*	$(7.5 \pm 0.5) \times 10^{11}$	$(2.3 \pm 0.4) \times 10^{12}$
SXP18.3	Disc	S eq*	N-T*	$(6.6 \pm 0.5) \times 10^{12}$	$(5.8 \pm 0.4) \times 10^{12}$
SXP25.5	Disc	S eq*	N-T*	$(6.6 \pm 0.6) \times 10^{12}$	$(5.6 \pm 0.5) \times 10^{12}$
SXP46.6	Disc	S eq*	T*	$(1.6 \pm 0.2) \times 10^{13}$	$(1.4 \pm 0.1) \times 10^{13}$
SXP59.0	Disc	S eq*	T*	$(2.6 \pm 0.2) \times 10^{13}$	$(2.3 \pm 0.2) \times 10^{13}$
SXP74.7	Disc	S eq	N-T	$(4.5 \pm 0.3) \times 10^{13}$	$(3.7 \pm 0.3) \times 10^{13}$
SXP82.4	Disc	S eq*	T*	$(3.5 \pm 0.4) \times 10^{13}$	$(3.1 \pm 0.3) \times 10^{13}$
SXP91.1	Disc	N-S eq*, u	N-T*	$(5.5 \pm 2.5) \times 10^{11}$	$(8.0 \pm 3.0) \times 10^{11}$
SXP95.2	Disc	S eq	T*	$(4.6 \pm 0.5) \times 10^{13}$	$(3.9 \pm 0.4) \times 10^{13}$
SXP101	Disc	S eq*	N-T*	$(4.6 \pm 0.7) \times 10^{13}$	$(4.1 \pm 0.5) \times 10^{13}$
SXP140	Disc	S eq*	T*	$(7.4 \pm 2.3) \times 10^{13}$	$(6.6 \pm 1.8) \times 10^{13}$
SXP152	Disc	S eq	T*	$(7.2 \pm 0.8) \times 10^{13}$	$(6.1 \pm 0.7) \times 10^{13}$
SXP169	Disc	S eq*	N-T*	$(1.0 \pm 0.1) \times 10^{14}$	$(9.1 \pm 0.9) \times 10^{13}$
SXP172	Disc	S eq*	T*	$(8.2 \pm 1.3) \times 10^{13}$	$(7.2 \pm 1.0) \times 10^{13}$
SXP175	Disc	S eq	N-T*	$(1.0 \pm 0.2) \times 10^{14}$	$(8.7 \pm 1.4) \times 10^{13}$
SXP202A	Disc	S eq*	T*	$(1.0 \pm 0.1) \times 10^{14}$	$(8.7 \pm 1.1) \times 10^{13}$
SXP202B	Disc	S eq	T*	$(8.1 \pm 1.8) \times 10^{13}$	$(6.6 \pm 1.5) \times 10^{13}$
SXP214	Disc	S eq	T (N-T)*	$(9.6 \pm 1.9) \times 10^{13}$	$(8.1 \pm 1.6) \times 10^{13}$
SXP264	Disc	S eq*	N-T*	$(8.6 \pm 1.7) \times 10^{13}$	$(7.3 \pm 1.3) \times 10^{13}$
SXP280	Disc	S eq*	N-T*	$(1.2 \pm 0.3) \times 10^{14}$	$(1.1 \pm 0.2) \times 10^{14}$
SXP293	Disc	S eq*	T*	$(1.2 \pm 0.2) \times 10^{14}$	$(1.0 \pm 0.1) \times 10^{14}$
SXP304	Disc	S eq*	T*	$(2.6 \pm 0.4) \times 10^{14}$	$(2.2 \pm 0.4) \times 10^{14}$
SXP323	Disc	S eq*	T (N-T)*	$(1.6 \pm 0.3) \times 10^{14}$	$(1.4 \pm 0.2) \times 10^{14}$
SXP327	Disc	S eq*	N-T*	$(7.1 \pm 2.9) \times 10^{13}$	$(7.4 \pm 1.2) \times 10^{13}$
SXP342	Disc	S eq	T*	$(2.5 \pm 0.4) \times 10^{14}$	$(2.1 \pm 0.3) \times 10^{14}$
SXP455	Disc	S eq*	T*	$(4.7 \pm 0.7) \times 10^{14}$	$(4.0 \pm 0.6) \times 10^{14}$
SXP504	Disc	S eq	T*	$(2.7 \pm 0.4) \times 10^{14}$	$(2.3 \pm 0.3) \times 10^{14}$
SXP565	Disc	S eq*	N-T*	$(1.8 \pm 0.6) \times 10^{14}$	$(1.6 \pm 0.5) \times 10^{14}$
SXP645	Disc	S eq	T (N-T)*	$(3.5 \pm 0.8) \times 10^{14}$	$(3.0 \pm 0.7) \times 10^{14}$
SXP701	Disc	S eq*	T*	$(3.5 \pm 0.6) \times 10^{14}$	$(3.0 \pm 0.5) \times 10^{14}$
SXP726	Disc	S eq*	T*	$(6.8 \pm 1.4) \times 10^{14}$	$(5.9 \pm 1.2) \times 10^{14}$
SXP756	Disc	S eq*	T*	$(4.8 \pm 0.3) \times 10^{14}$	$(4.1 \pm 0.3) \times 10^{14}$
SXP893	Disc	S eq*	T*	$(4.0 \pm 0.7) \times 10^{14}$	$(3.5 \pm 0.6) \times 10^{14}$
SXP967	Disc	S eq*	T*	$(1.2 \pm 0.2) \times 10^{15}$	$(1.1 \pm 0.2) \times 10^{15}$
SXP1323	Disc	S eq*	N-T*	$(1.7 \pm 0.2) \times 10^{15}$	$(1.4 \pm 0.1) \times 10^{15}$

Table 2.6: Accretion method, spin equilibrium status, the status of the OBe star's circumstellar disc (results assuming $M_{OB} = M_{spec}$, where results assuming $M_{OB} = M_{dyn}$ are in parenthesis), and the corresponding magnetic fields determined from the Ghosh and Lamb (1979) and Kluzniak and Rappaport (2007) models. Here, S *eq* refers to systems that are close to spin equilibrium, and $N - S$ *eq* to systems that are not, where u refers to spin-up, and d to spin-down. Other nomenclature is the same as in Table 2.5, where an asterisk denotes that the value is an estimate, as discussed in Section 2.3 and shown in Appendix B.

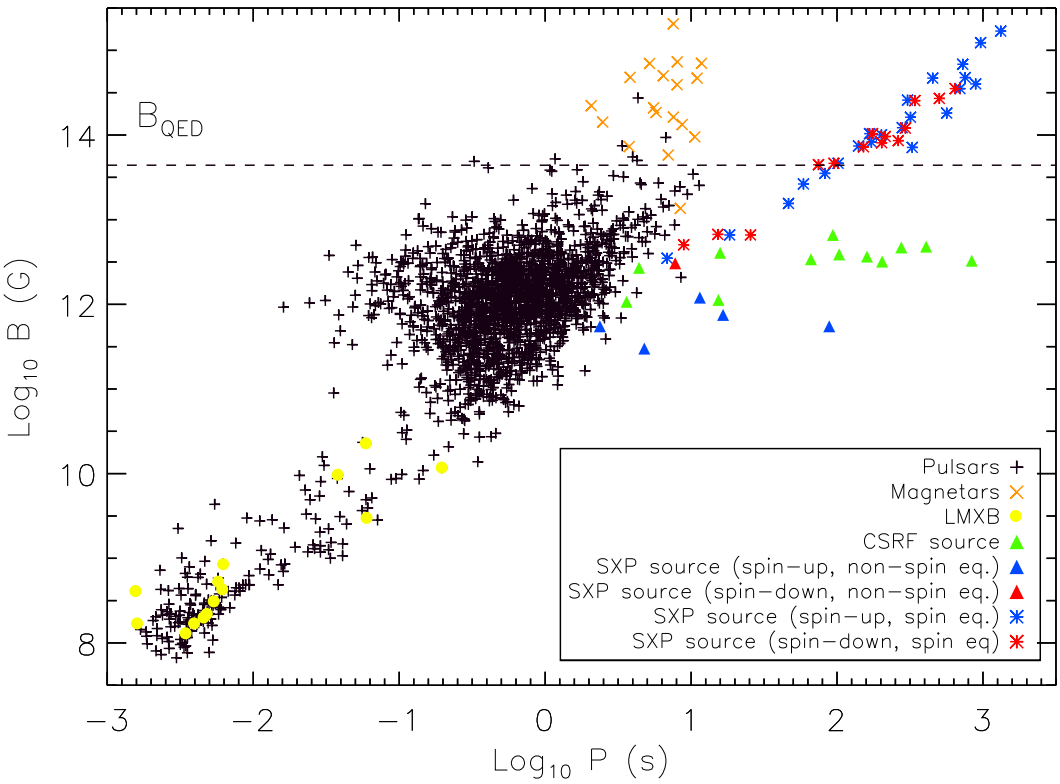

Figure 2.17: The most probable B (as discussed in Section 2.3) for neutron stars in the 42 BeXB listed in Table 2.6 determined using the Ghosh and Lamb (1979) (equation (1.34)) model. Neutron stars in 27 of these systems are spinning up on average ($\dot{P} < 0$; blue), and 15 are spinning down ($\dot{P} > 0$; red). 36 are close to spin equilibrium (stars), and 6 are not (triangles). Neutron stars in Galactic BeXB, where B has been measured using CRSF, are also shown (green triangles; for references see Table 2.7), as are neutron stars in LMXB (yellow circles; Camilo et al. (1994)), magnetars (orange 'x's; Manchester et al. (2005)), and isolated radio pulsars (black crosses; Manchester et al. (2005)).

published in Ho et al. (2014), shows that all neutron stars in accreting X-ray binaries follow the same relationship between P and B if they are close to spin equilibrium (Ho et al., 2014). This is assuming that the CRSF sources are not close to spin equilibrium, which is discussed further in Section 2.4.

Figure 2.18 shows results from the spin equilibrium disc accretion models (discussed in Section 1.2.2), and results using the Ghosh and Lamb (1979) and Kluzniak and Rappaport (2007) models with $\dot{P} = 0$. The spin equilibrium disc accretion models give slightly higher results than the Ghosh and Lamb (1979) and Kluzniak and Rappaport (2007) models, as discussed in Section 1.2.2.

Wind accretion is possible in some systems if they are in retrograde orbits and are accreting from a non-truncated circumstellar disc, and so results from the spin equilibrium

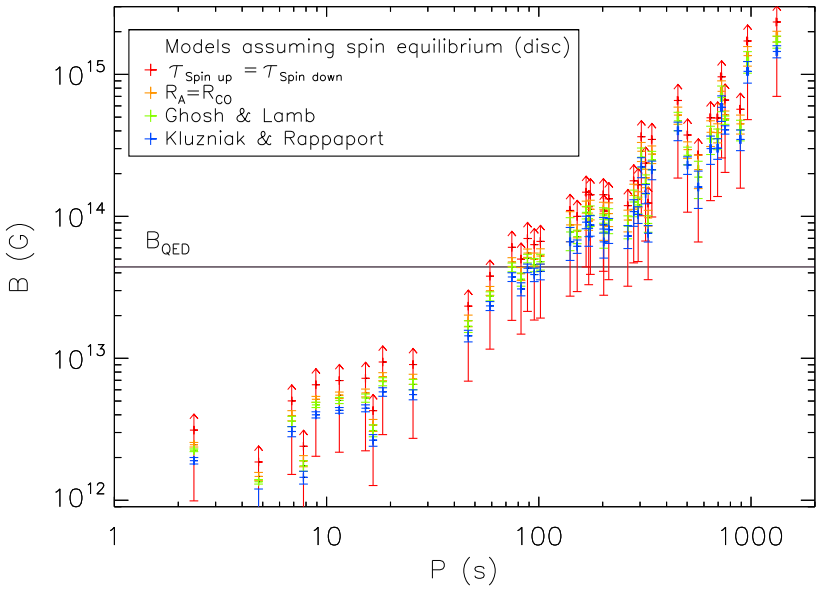

Figure 2.18: B as a function of P, where B is determined using the spin equilibrium disc accretion models, discussed in Section 1.2.2. These include the spin equilibrium ($\tau_{up\ (disc)} = \tau_{down}$; orange), and the spin equilibrium radius ($R_{co} = R_A$; red) models for disc accretion. Results from the Ghosh and Lamb (1979) (equation (1.34); green), and Kluzniak and Rappaport (2007) (equation (1.36): blue) models, assuming $\dot{P} = 0$, are also shown.

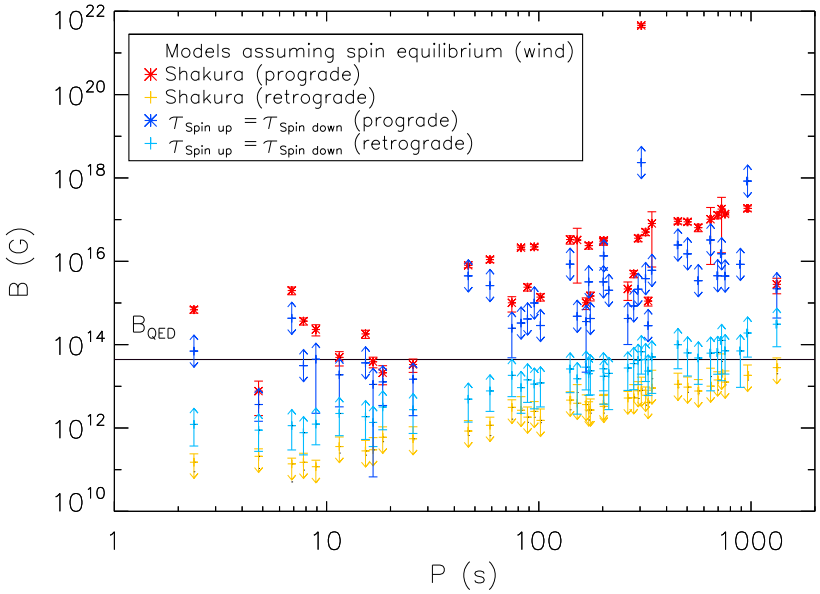

Figure 2.19: B as a function of P, where B is determined using the spin equilibrium wind accretion models discussed in Section 1.2.1, assuming $M_{OB} = M_{spec}$. These include the spin equilibrium model ($\tau_{up\ (wind)} = \tau_{down}$) for prograde ($\theta_i$=180°; dark blue) and retrograde ($\theta_i = -180°$; light blue) systems, and the Shakura et al. (2012) model (equation (1.17)) for prograde (θ_i=180°; red) and retrograde ($\theta_i = -180°$; yellow) systems.

wind accretion models, assuming both prograde and retrograde orbits and $M_{OB} = M_{spec}$, are shown in Figure 2.19. The Shakura et al. (2012) model has a stronger dependence on V_{rel} than the spin equilibrium model for wind accretion, and so shows a greater difference between prograde and retrograde systems. Wind accretion is not possible in most prograde systems, whether or not the disc is truncated. If it were possible, then the magnetic fields for neutron stars in most systems would be predicted to be $> B_{QED}$. The system with the highest predicted magnetic field, assuming a prograde orbit, is SXP304, which also has the longest orbital period and the shortest orbital velocity, as shown in Figure B.58.

The magnetic field for systems in retrograde orbits are $\sim 10^{11} - 10^{14}$ G using the Shakura et al. (2012) model and $10^{12} - 10^{14}$ G using the spin equilibrium model. These results are closer to the results of CRSF sources, but it is very unlikely that the majority of BeXB in the SMC are in retrograde orbits (Brandt and Podsiadlowski, 1995). It is not possible for prograde systems containing OBe stars with truncated circumstellar discs to be wind-accreting. In order for wind accretion to be possible in prograde, truncated, systems that the Ghosh and Lamb (1979) model predicts have $> B_{QED}$, V_w would have to increase from $\sim$150 km s^{-1} to $\sim$ 800 km s^{-1}. Wind accretion would also be possible if the orbital velocity (V_{orb}) increased from $\sim$ 50 km s^{-1} to $\sim$ 900 km s^{-1}, assuming P_{orb} is correct, then this is only possible if $e > 0.98$. Wind accretion is, therefore, extremely unlikely in all systems.

2.4 Discussion and conclusions

In Sections 2.1-2.3, I showed that neutron stars in 42 BeXB in the SMC are most likely disc-accreting. About half are accreting from a circumstellar disc that is truncated by the orbit of the neutron star (23/42 assuming $M_{OB} = M_{spec}$, and 19/42 assuming $M_{OB} = M_{dyn}$). 36 systems are close to spin equilibrium, and 6 are not; these are SXP2.37 (SMC X-2), SXP4.78, SXP7.78 (SMC X-3), SXP11.5, SXP16.6, and SXP91.1. SXP7.78 is the only member of this group that is spinning down on average. $\sim 2/3$ systems, and all systems with $P > 100$ s, are predicted to have $B > B_{QED}$ (where B_{QED}=4.4×10^{13} G; equation 1.41). Similarly high estimates for the magnetic fields of neutron stars in X-ray binaries have been made before (as discussed in Section 1.2.2). These systems were thought to be unusual, but results from this chapter suggest that systems with $B > B_{QED}$ may be common.

The main objection to these results is that they do not match the magnetic fields of neutron stars directly measured with CRSF, where a similar difference in field determination using these two methods has previously been noted for SGXB GX 301-2 (Doroshenko et al., 2010a). Twelve Galactic BeXB contain neutron stars that have had B measured

using CRSF (see Table 2.7), and all have magnetic fields between $10^{12} - 10^{13}$ G (see Figure 2.17). There are a number of possibilities to explain this disparity.

Firstly, it may be the case that accretion theories are simply wrong, overestimating the magnetic field of systems with spin periods $\gtrsim 100$ s. This seems unlikely, however; if this were the case then we may need to rethink most of accretion physics. Secondly, our understanding of CRSF may be wrong. Although this seems less likely than accretion theories being wrong as the method (described in Section 1.3.1) is based on fewer theoretical assumptions. Thirdly, it is possible that both results are correct, where the result determined from accretion theory is the magnetic field at the neutron star's surface, and the CRSF result originates from above the surface, from the top of the accretion column. Finally, it is possible that both results are correct if the CRSF sources with $P > 100$ s are not close to spin equilibrium. The last two possibilities are investigated below, although the long-term average L, P, and $\dot{P}$ are not known for most CRSF sources, and so the results are approximate at best.

BeXB	B_{cyc} (10^{12} G)	P (s)	$\dot{P}$ (s yr^{-1})	L (10^{37} erg s^{-1})	Spin eq. status
4U 0115+634	1.07 [1]	3.61 [1]			U
V 0332+53	2.70 [2]	4.40 [2]			U
Swift J1626.6-5156	1.13 [3]	15.40 [3]	0.034 [3]	0.0098 [4]	N-S eq, d
XTE J1946+274	4.06 [5]	15.80 [5]			U
Cep X-4	3.41 [6]	66.25 [6]			U
GRO J1008-57	6.60 [7]	93.63 [7]	2 [7]	0.22 [8]	S eq, d
A0535+26	3.89 [9]	103.4 [9]	0.037 [9]	0.0068 [10]	S eq, d
MXB 0656-072	3.67 [11]	160.4 [11]	0.66 [11]	-3.7 [11]	S eq, u
RX J0440.9+4431	3.20 [12]	203.8 [12]	0.71 [12]	0.20 [12]	S eq, d
GX 304-1	4.70 [13]	275.5 [13]			U
1A1118-616	4.80 [14]	407.7 [14]	2.90 [15]	-14.5 [14]	N-S eq, u
X Per	3.28 [16]	837.0 [16]	0.0042 [16]	0.11 [16]	S eq, d

Table 2.7: Galactic BeXB that have had B directly measured via CRSF (as discussed in Sections 1.3.1 and 2.4), and P, L, and $\dot{P}$ where known. The spin equilibrium status is also given. This is determined from Figure 2.21, where U means the statues is unknown, and other nomenclature is the same as in Table 2.6. Some of these results may be incorrect since the values used for P, L, and $\dot{P}$ are not long-term averages. References are as follows; [1] Heindl et al. (1999), [2] Pottschmidt et al. (2005), [3] DeCesar et al. (2013), [4] Baykal et al. (2010), [5] Heindl et al. (2001), [6] Mihara et al. (1991), [7] Yamamoto et al. (2014), [8] Shrader et al. (1991), [9] Terada et al. (2006), [10] Kendziorra et al. (1994), [11] McBride et al. (2006), [12] Tsygankov et al. (2012), [13] Yamamoto et al. (2011), [14] Doroshenko et al. (2010b), [15] Reig and Nespoli (2013), [16] Coburn et al. (2001).

Figures 2.20 and 2.21 show results for the CRSF sources over-plotted onto Figures 1.9 and 1.10. Figures 1.9 and 1.10 show $\dot{P}$ as a function of $PL^{3/7}$ with simulated results over-plotted for varying magnetic fields determined using the Ghosh and Lamb (1979)

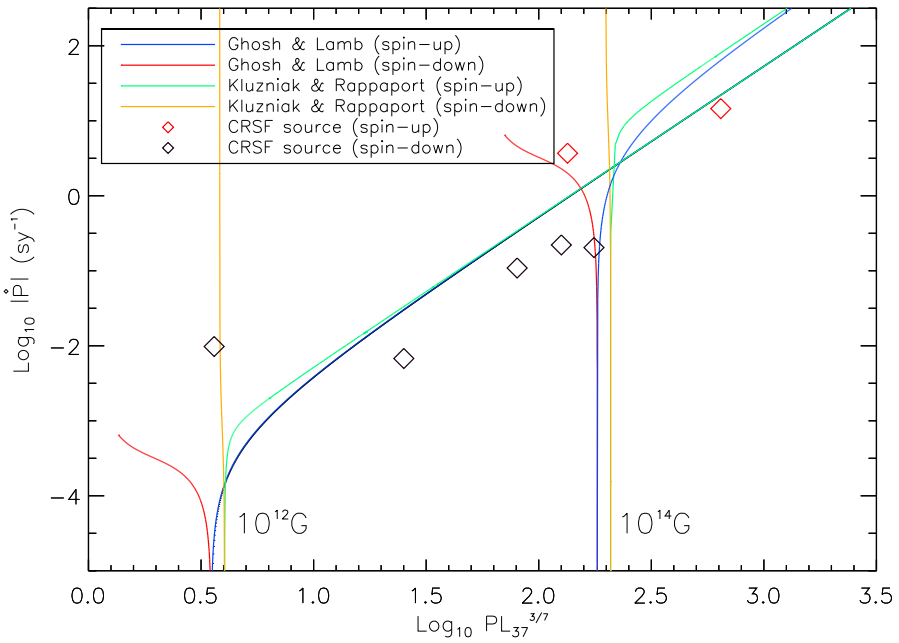

Figure 2.20: $\dot{P}$ as a function of $PL^{3/7}$; results for CRSF sources (given in Table 2.7 and discussed in Section 2.4), over-plotted onto Figure 1.9. 2 CRSF sources are spinning up on average ($\dot{P} < 0$; red diamonds), and 5 are spinning down ($\dot{P} > 0$; black diamonds).

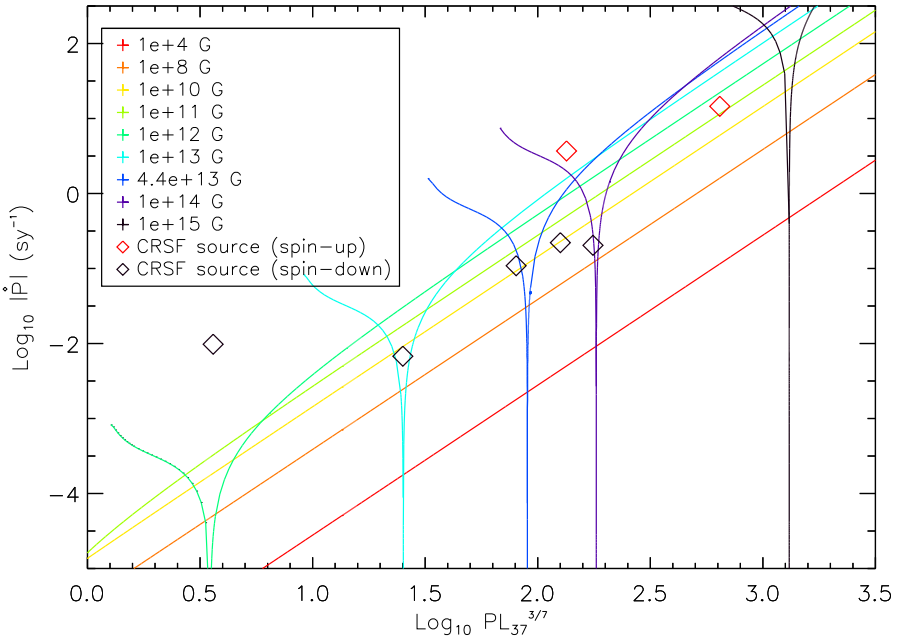

Figure 2.21: As for Figure 2.20, except results are over-plotted onto Figure 1.10 rather than Figure 1.9.

BeXB	Spin eq. status	B_{cyc} (10^{12} G)	$B_{G\&L}$ (10^{12} G)	Height needed if $B_{G\&L} = B_s$ (km)	Height predicted if $B_{G\&L} = B_s$ (km)
4U 0115+634	U	1.07 [1]	1.00	<0	1.48
V 0332+53	U	2.70 [2]	1.30	<0	1.27
Swift J1626.6-5156	N-S eq, d	1.13 [3]	3.10	4.01	8.68
XTE J1946+274	U	4.06 [5]	5.80	1.26	0.54
Cep X-4	U	3.41 [6]	30.79	10.83	0.21
GRO J1008-57	S eq, d	6.60 [7]	65.20	11.91	0.08
A0535+26	S eq, d	3.89 [9]	10.00	4.06	4.00
MXB 0656-072	S eq, u	3.67 [11]	70.20	6.57	0.40
RX J0440.9+4431	S eq, d	3.20 [12]	96.20	21.38	0.14
GX 304-1	U	4.70 [13]	162.30	22.56	0.08
1A1118-616	N-S eq, u	4.80 [14]	0.22	<0	0.02
X Per	S eq, d	3.28 [16]	38.50	13.41	8.72

Table 2.8: CRSF sources, spin equilibrium status, and B_{cyc} from Table 2.7. The fourth column shows B determined using the Ghosh and Lamb (1979) ($B_{G\&L}$; equation (1.34)) model, given the spin equilibrium status. If the status is unknown, it is assumed that the system is close to spin equilibrium, with a $\dot{P}$ of 0. If L is not known, a value of 10^{37} erg s^{-1} is assumed. If $B_{G\&L}$ is equal to the surface magnetic field (B_s), and B_{cyc} originates from above this, in an accretion column, then the height of the column can be determined (using equation (1.5), assuming $R_{NS} = 10$ km), and is given in the fifth column. The height of the accretion column can also be determined from L and B following Becker et al. (2012) (equations (2.18)-(2.20)), as discussed in Section 2.4. This height is given in the last column, assuming $B_s = B_{G\&L}$. Results may be incorrect since the values used for P, L, and $\dot{P}$ are either not known, or are not long-term averages. References for B_{cyc} are given in Table 2.7.

and Kluzniak and Rappaport (2007) models. Figures 2.20 and 2.21 show that if the values of L, P, and $\dot{P}$ are representative of their long-term behaviour, then one system is certainly not close to spin equilibrium. This is Swift J1626.6-5156, which is spinning down on average. There is one system that may or may not be close to spin equilibrium, this is 1A1118-616, which is spinning up on average. 1A1118-616 will be classified as not being close to spin equilibrium for the same reasons applied to SXP91.1 in Section 2.3. Figure 2.21 shows that the rest of the systems are expected to be close to spin equilibrium. These include four systems that are spinning down on average and one system that is spinning up. The results are given in Table 2.7. The magnetic field of each CRSF source is then determined using the Ghosh and Lamb (1979) model, given these results. Where $\dot{P}$ and L were not known, it was assumed that $\dot{P} = 0$, and $L = 10^{37}$ erg s^{-1}. Once the expected magnetic field from the Ghosh and Lamb (1979) model is known, the height that the CRSF must originate from in order for that to be the correct surface field can be determined (given equation (1.5), and assuming R_{NS}=10 km). This height is given in column five of Table 2.8. The height of the accretion column can also be determined from L and B using the Becker et al. (2012) model.

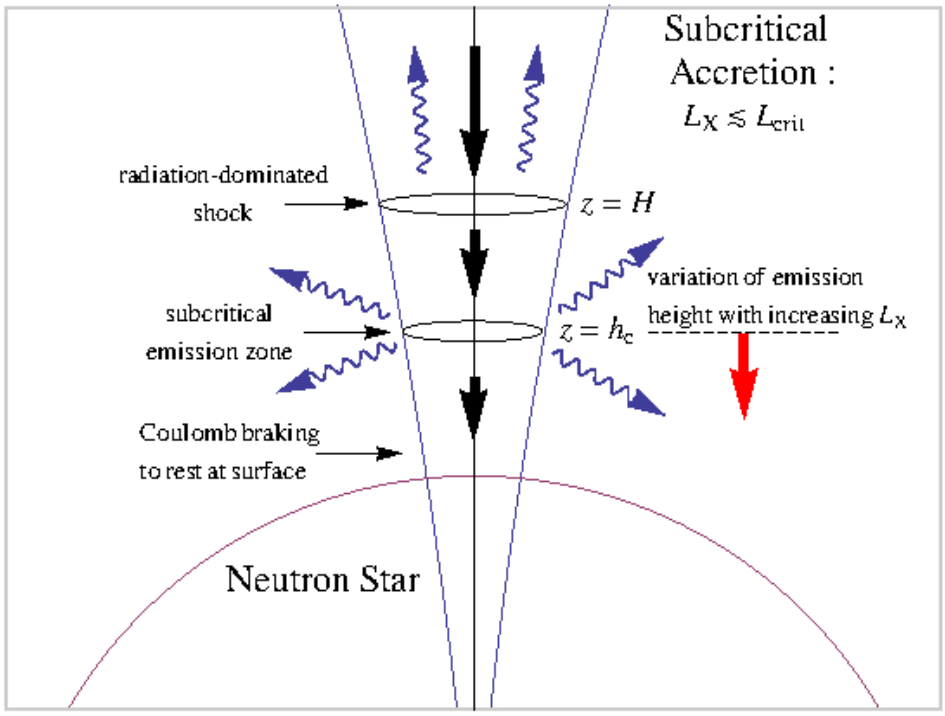

Figure 2.22: Diagram of an accretion column in the subcritical state, following the Becker et al. (2012) model (discussed in Section 2.4). Image credit: Becker et al. (2012).

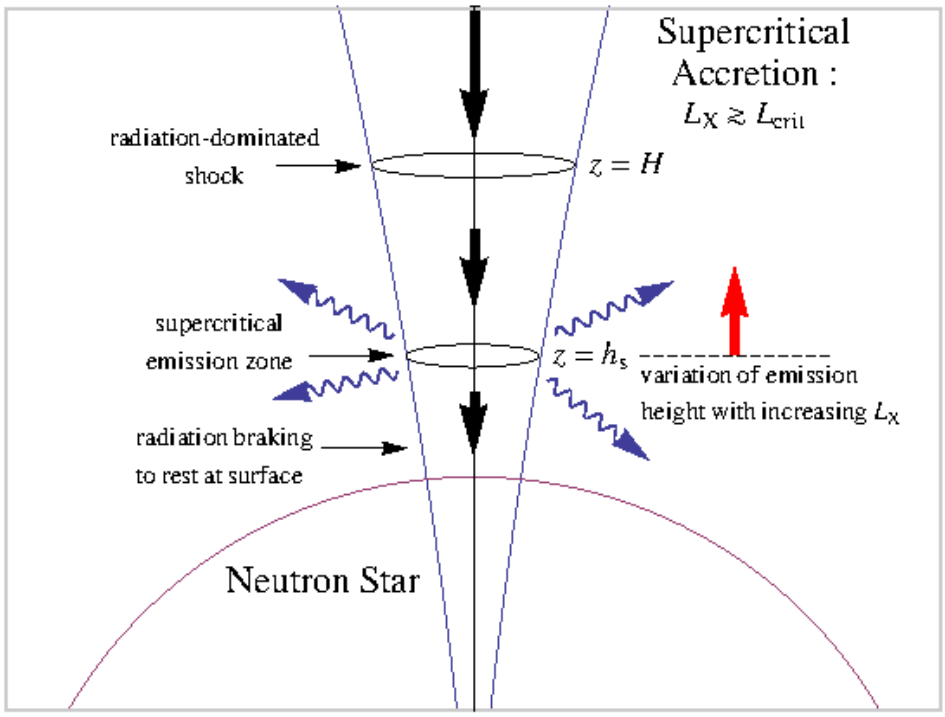

Figure 2.23: Diagram of an accretion column in the supercritical state, following the Becker et al. (2012) model (discussed in Section 2.4). Image credit: Becker et al. (2012).

Within the Becker et al. (2012) model, the height of the accretion column depends on whether or not the pencil beam is fully suppressed (as discussed in Section 1.4.2). The pencil beam is observable, and the system is referred to as subcritical, if $L < L_{crit}$. The pencil beam is suppressed, and the system is referred to as supercritical, if $L > L_{crit}$. For M_{NS}=1.4 $M_{\odot}$ and R_{NS}=10 km,

$$L_{crit} = 1.49 \times 10^{37} \text{ erg s}^{-1} \left(\frac{\Lambda}{0.1}\right)^{-7/5} w^{-28/15} \left(\frac{B}{10^{12} \text{ G}}\right)^{16/15}. \quad (2.18)$$

Here, Λ is a numerical coefficient that depends on the symmetry of accretion, where $\Lambda = 1$ for spherical wind accretion, and $\Lambda < 1$ for disc accretion. Becker et al. (2012) assume a value of 0.1. w is a numerical coefficient that depends on the shape of the spectrum inside the accretion column, and is assumed to be equal to 1 (Becker et al., 2012). Diagrams of subcritical and supercritical systems are shown in Figures 2.22 and 2.23 respectively.

In subcritical systems, where the pencil beam is still visible, the height of the accretion column (h_c) is found via

$$h_c = 1.48 \times 10^{5} \text{ cm} \left(\frac{\Lambda}{0.1}\right)^{-1} \left(\frac{\tau}{20}\right) \left(\frac{B}{10^{12} \text{ G}}\right)^{-4/7} \left(\frac{L}{10^{37} \text{ erg s}^{-1}}\right)^{-5/7} \quad (2.19)$$

for M_{NS}=1.4 $M_{\odot}$ and R_{NS}=10 km, where τ is the Thomson optical depth required to stop the flow of accreted material via Coulomb interactions, and is assumed to be equal to 20. Here, the height of the accretion column is inversely proportional to B and L.

In supercritical systems, where the pencil beam is fully suppressed and the fan beam is dominant, the height of the accretion column (h_s) is found via

$$h_s = 2.28 \times 10^{3} \text{ cm} \left(\frac{\xi_h}{0.01}\right) \left(\frac{L}{10^{37} \text{ erg s}^{-1}}\right) \quad (2.20)$$

for M_{NS}=1.4 $M_{\odot}$ and R_{NS}=10 km, where ξ_h is a numerical coefficient that depends on the flow velocity of accreted material, and is assumed to be equal to $10^{-2.5}$. Here, the height of the accretion column is proportional to L and unaffected by B.

Results from the Becker et al. (2012) model, assuming that the B determined using the Ghosh and Lamb (1979) model is the surface field (and R_{NS}=10 km), are given in Table 2.8. If this is the surface field, then the Becker et al. (2012) model predicts that most CRSF sources have accretion columns < 2 km, and most are < 1 km. One system (A0535+26) is predicted to have a ~ 4 km accretion column, and two (Swift J1626.6-5156 and X Per) are predicted to have accretion columns of ~ 8 km. Given that a neutron star has a radius of ~ 10 km, this suggests that these results are incorrect, and that the L, P, and $\dot{P}$ used for these systems are not representative of the long-term averages. Excluding these systems, the only other systems where the expected and predicted heights are compatible are those that are not assumed to be close to spin

BeXB	B (10^{12} G)	Height of accretion column (m)	Predicted B_{cyc} (10^{12} G)	Predicted E_{cyc} (keV)
SXP2.37	0.55 ± 0.05	92.1 ± 6.8	0.54 ± 0.05	4.7 ± 0.4
SXP4.78	0.30 ± 0.05	6.4 ± 0.9	0.30 ± 0.05	2.7 ± 0.4
SXP6.85	3.50 ± 0.30	349 ± 44	3.16 ± 0.27	28.0 ± 2.4
SXP7.78	3.05 ± 0.15	1339 ± 176	2.09 ± 0.14	18.5 ± 1.3
SXP8.80	5.05 ± 0.25	301 ± 22	4.62 ± 0.23	40.9 ± 2.0
SXP11.5	1.20 ± 0.10	949 ± 83	0.91 ± 0.08	8.1 ± 0.7
SXP15.3	6.70 ± 0.30	541 ± 51	5.72 ± 0.27	50.7 ± 2.4
SXP16.6	0.75 ± 0.05	4581 ± 659	0.24 ± 0.04	2.1 ± 0.3
SXP18.3	6.60 ± 0.50	510 ± 52	5.69 ± 0.44	50.4 ± 3.9
SXP25.5	6.60 ± 0.60	937 ± 120	5.04 ± 0.49	44.7 ± 4.3
SXP46.6	15.6 ± 1.8	403 ± 60	13.8 ± 1.6	122 ± 14
SXP59.0	26.4 ± 2.1	220 ± 25	24.7 ± 2.0	219 ± 18
SXP74.7	44.7 ± 3.1	124 ± 13	43.0 ± 2.9	381 ± 26
SXP82.4	35.3 ± 4.0	220 ± 36	33.0 ± 3.7	293 ± 33
SXP91.1	0.55 ± 0.25	9.9 ± 1.4	0.55 ± 0.25	4.9 ± 2.2
SXP95.2	46.3 ± 5.0	171 ± 28	44.0 ± 4.8	390 ± 42
SXP101	46.4 ± 6.7	178 ± 35	44.0 ± 6.3	390 ± 56
SXP140	74.2 ± 23.0	113 ± 43	71.7 ± 22.2	635 ± 197
SXP152	72.4 ± 8.0	150 ± 24	69.2 ± 7.7	613 ± 68
SXP169	104 ± 11	82.0 ± 12.4	101 ± 11	897 ± 96
SXP172	82.3 ± 12.6	137 ± 30	79.0 ± 12.1	700 ± 107
SXP175	104 ± 17	93.8 ± 22.8	101 ± 16	893 ± 142
SXP202A	101 ± 13	121 ± 23	96.9 ± 12.8	859 ± 114
SXP202B	80.9 ± 17.7	200 ± 66	76.2 ± 16.7	676 ± 148
SXP214	96.0 ± 18.8	151 ± 44	91.8 ± 18.0	813 ± 160
SXP264	85.9 ± 16.8	264 ± 72	79.4 ± 15.6	703 ± 138
SXP280	122 ± 28	136 ± 43	117 ± 27	1038 ± 242
SXP293	121 ± 17	162 ± 32	115 ± 16	1018 ± 141
SXP304	258 ± 43	36.4 ± 8.7	256 ± 43	2264 ± 380
SXP323	162 ± 28	95.1 ± 22.2	158 ± 27	1396 ± 238
SXP327	71.4 ± 29.0	401 ± 118	63.4 ± 25.9	562 ± 229
SXP342	255 ± 37	47.5 ± 10.4	251 ± 36	2224 ± 323
SXP455	470 ± 71	21.7 ± 4.7	467 ± 71	4137 ± 625
SXP504	271 ± 38	78.7 ± 16.3	264 ± 37	2343 ± 329
SXP565	181 ± 60	191 ± 81	171 ± 57	1519 ± 507
SXP645	353 ± 80	68.7 ± 22.0	346 ± 78	3064 ± 695
SXP701	353 ± 60	78.6 ± 18.7	345 ± 58	3057 ± 516
SXP726	685 ± 143	22.2 ± 6.5	680 ± 142	6028 ± 1262
SXP756	477 ± 32	50.1 ± 4.8	470 ± 32	4162 ± 283
SXP893	401 ± 70	90.0 ± 21.5	391 ± 68	3461 ± 602
SXP967	1231 ± 217	11.1 ± 2.7	1227 ± 217	10875 ± 1920
SXP1323	1689 ± 167	10.1 ± 1.4	1684 ± 167	14924 ± 1477

Table 2.9: Most probable B for neutron stars in the 42 BeXB discussed in this chapter. Results are determined using the Ghosh and Lamb (1979) model, as given in Table 2.6. The height of the accretion column is also given, determined from L and B, following Becker et al. (2012) (equations (2.18)-(2.20); as discussed in Section 2.4). The corresponding predicted B_{cyc} and E_{cyc}, for electrons, from this radius (equations (1.5) and (1.39)) are also given, assuming $n = 1$, R_{NS}=10 km, and $M_{NS} = 1.4$ M$_\odot$.

equilibrium (1A1118-616), and systems with spin periods < 15 s (4U 0115+634 and V 0332+53). This leaves six systems where the two results are not compatible. In these cases, the spin equilibrium assumption is most likely flawed. This means that the values of L, P, and $\dot{P}$ that were used are not representative of the source's long-term behaviour.

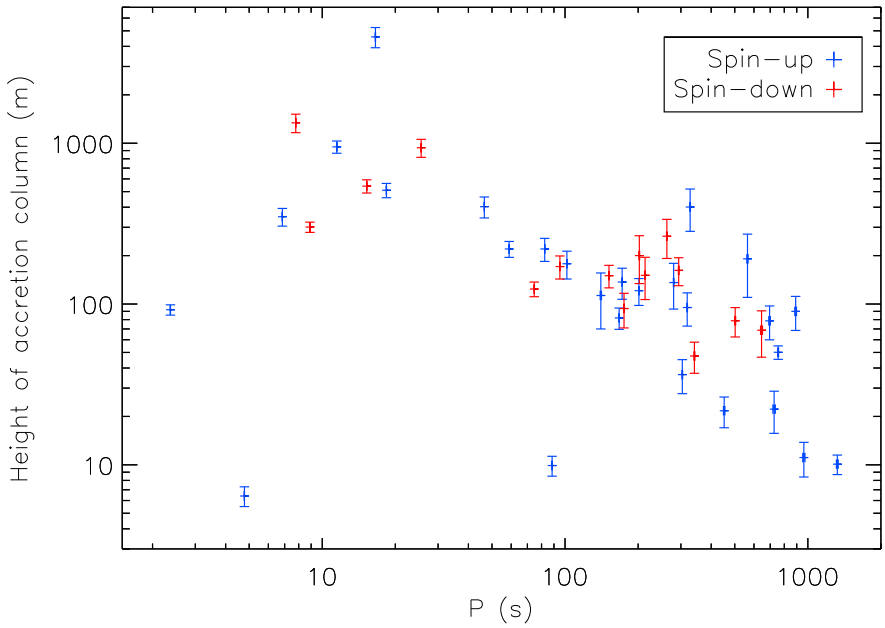

Figure 2.24: The height of the accretion column for neutron stars in the 42 BeXB listed in Table 2.9, determined using the Becker et al. (2012) model (equations (2.18)-(2.20)), as a function of spin period (as discussed in Section 2.4). 27 of these systems are spinning up on average ($\dot{P} < 0$; blue), and 15 are spinning down ($\dot{P} > 0$; red).

The most likely explanation as to why the magnetic fields of neutron stars in SXP diverge from those in BeXB that have been measured using CRSF, is that the CRSF sources are not close to spin equilibrium, whereas most SXP sources are. This is combined with an instrumental bias, which prevents CRSF, from electrons, from being detected in systems containing neutron stars with $B \gtrsim 10^{13}$ G (as discussed in Section 1.3.1). All of the SXP sources that are not close to spin equilibrium are predicted to have magnetic fields similar to those of CRSF sources. This can be seen in Figures 2.17 and 4.34, where Figure 4.34 includes the non-spin equilibrium, persistent LMC source LXP187, which is discussed in Chapter 4.

Further evidence of this could be obtained by monitoring the long-term average L, P, and $\dot{P}$ of CRSF sources, so that a proper comparison with the Ghosh and Lamb (1979) model can be made. Conversely, the SXP sources could be targeted for observation. The energy of the predicted CRSF for each SXP source is given in Table 2.9 and Figures

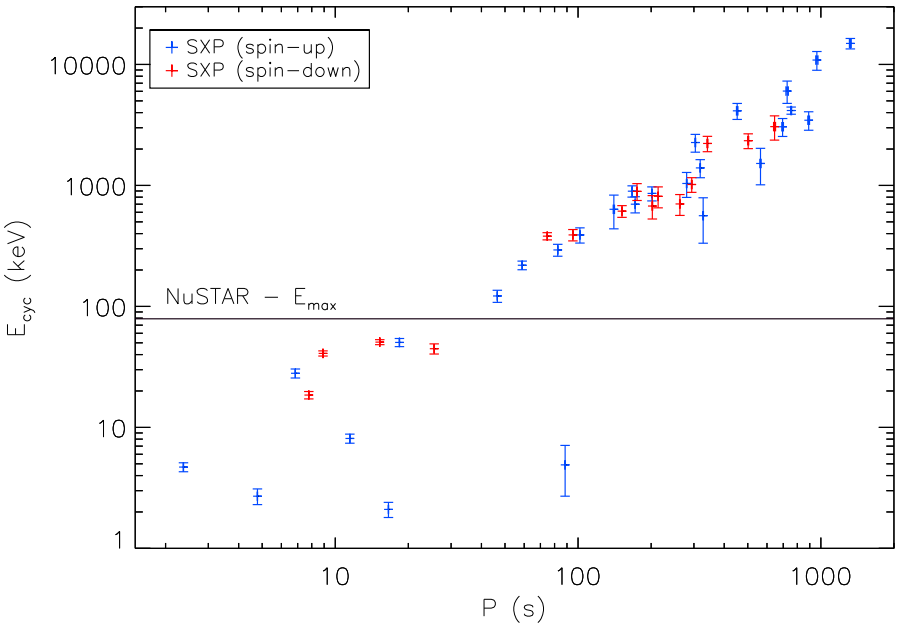

Figure 2.25: As for Figure 2.24, except E_{cyc}, from electrons, is shown rather than the height of the accretion column. The black line indicates the maximum energy range of NASA's NuStar (Nuclear Spectroscopic Telescope Array Mission), and shows that most sources would not be expected to have detectable CRSF.

2.24 and 2.25. The height of the accretion column in each SXP is determined using the Becker et al. (2012) model. The magnetic field at this height is determined (using equation (1.5), assuming $R_{NS} = 10$ km), and the energy of the predicted CRSF is then calculated using equation (1.39), assuming $n = 1$ and M_{NS}=1.4 $M_{\odot}$.

Figure 2.24 shows that most SXP are expected to contain accretion columns of < 1 km. Most systems are subcritical, and so are still predicted to have a visible pencil beam. In subcritical systems, the height of the accretion column is inversely proportional to B and L. The Ghosh and Lamb (1979) model predicts that B is proportional to P for systems that are close to spin equilibrium, and so the height of the accretion column is inversely proportional to P in most cases. Three systems are supercritical, with a suppressed pencil beam, and so the heights of their accretion columns only depend on L; these are SXP2.37, SXP4.78, and SXP91.1, all of which are not close to spin equilibrium, are spinning up on average, and are accreting from non-truncated circumstellar discs. Figure 2.25 shows the predicted E_{cyc}, from electrons, for all of the SXP sources. The black line indicates the maximum energy range of NASA's NuStar (Nuclear Spectroscopic Telescope Array Mission). This shows that most sources would not be expected to have detectable CRSF. Evidence of $B > B_{QED}$ could also be obtained if any of these systems undergo a magnetar-like gamma-ray outburst (as described in Section 1.1).

If $\sim 2/3$ SXP sources do have $B > B_{QED}$, then this may suggest that there are many more isolated neutron stars with $B > B_{QED}$. If isolated neutron stars have $B > B_{QED}$, then their magnetic fields can usually only be measured when they undergo a magnetar-like outburst. The SXP sources have not been observed to undergo these outbursts, and this suggests that perhaps these outbursts are not common for neutron stars with $B > B_{QED}$, and there is a hidden population of isolated neutron stars with $B > B_{QED}$ that cannot be observed. It may also mean that magnetic field decay occurs more slowly than previously thought (Pons et al., 2009). These conclusions are discussed further in Chapters 3 and 4.

Chapter 3

The pulse-profiles of neutron stars in BeXB in the SMC

3.1 Introduction

In Chapter 2, I showed that 42 transient BeXB in the SMC are most likely disc-accreting. About half of all systems (23/42 if $M_{OB} = M_{spec}$, and 19/42 if $M_{OB} = M_{dyn}$) are accreting from a circumstellar disc that is truncated by the orbit of the neutron star. 36 systems are close to spin equilibrium, and 6 systems are not; these are SXP2.37 (SMC X-2), SXP4.78, SXP7.78 (SMC X-3), SXP11.5, SXP16.6, and SXP91.1. SXP7.78 is the only member of this group that is spinning down on average. The magnetic field of the neutron star in each system was calculated based on this information, and $\sim 2/3$ were shown to have $B > B_{QED}$.

In this chapter, pulse-profiles are created for every observation of all of these systems. They are then modelled in order to determine i, θ, and M_{NS}/R_{NS} (as discussed in Section 1.4.1) using the Beloborodov (2002) approximation, and visually inspected for the features discussed in Section 1.4. If the magnetic fields given in Chapter 2 are correct, then we might expect to see different structures in the pulse-profiles of systems with relatively long and short spin periods, and hence relatively high and low magnetic fields.

Data used in this chapter was originally extracted by S. Laycock, L.J. Galache, and L.J. Townsend.

An outline of this chapter is as follows: observations are discussed in Section 3.2, with the Beloborodov (2002) approximation described in Section 3.2.1. Results are presented in Section 3.3, firstly results from the Beloborodov (2002) approximation in Section 3.3.1, and secondly results regarding other features within the pulse-profiles, in Section 3.3.2. Conclusions are given in Section 3.4.

3.2 Observations

The observations in this chapter come from the study of the SMC carried out using RXTE over the period 1997-2012. These are discussed in Section 2.2. As stated in Section 2.2, the SMC was observed once or twice a week, for durations of ∼10,000 s. The quality of any single observation depends upon the significance of the detected period combined with the collimator response to the source, and so any period detections with a significance $< 99\%$, or a collimator response < 0.2 are removed, as are any datasets with < 5 detections. This leaves results for 42 BeXB, with between 5 and 88 detections per source (see Table 2.1), and over 1000 detections in total. The average count-rate (CR), measured in counts PCU^{-1} s^{-1}, is converted to luminosity using equation (2.1).

Each observation records CR every 10 ms. These data were binned into 1 s intervals, with the error taken as the square-root of the total number of counts in each bin. Pulse-profiles were then created, folded on the spin period specific to the observation (as shown in Appendix B), and plotted normalised to the average count-rate, with 30 bins per phase. The background level is uncertain because RXTE's PCAs had no spatial resolution or imaging capability, and so it is not known if other systems were in outburst during the observation. This means that the true pulse-fraction is not known. The pulse-profiles cannot be phase locked between observations, and so the phase-shift is also unknown. These pulse-profiles were then modelled using the Beloborodov (2002) approximation, and visually inspected, to look for the features discussed in Section 1.4.

3.2.1 The Beloborodov approximation

The Beloborodov (2002) approximation determines how the pulse-profile should look, depending on how many magnetic poles are visible at any one time (as discussed in Section 1.4.1, see also King and Shaviv (1984) with regard to white dwarfs). It is applicable to compact objects emitting from two point-like antipodal hot-spots that can be approximated as blackbodies. Beloborodov (2002) shows that the bending angle (β) of a photon in a spherically symmetric gravitational field can be approximated as,

$$\beta = \psi - \alpha, \tag{3.1}$$

where the exact angle is given by an elliptic integral (Pechenick et al., 1983). Here α is the angle at which the photon is emitted, from point E with respect to the compact object, and ψ is the angle between the observer's line of sight and the current position of the photon. These parameters are shown in Figure 3.1. Beloborodov (2002) describes the photon's trajectory, in polar co-ordinates (r, ψ), as approximately

$$\cos(\alpha) = \cos(\psi)\left(1 - \frac{r_g}{R_{NS}}\right) + \frac{r_g}{R_{NS}}. \tag{3.2}$$

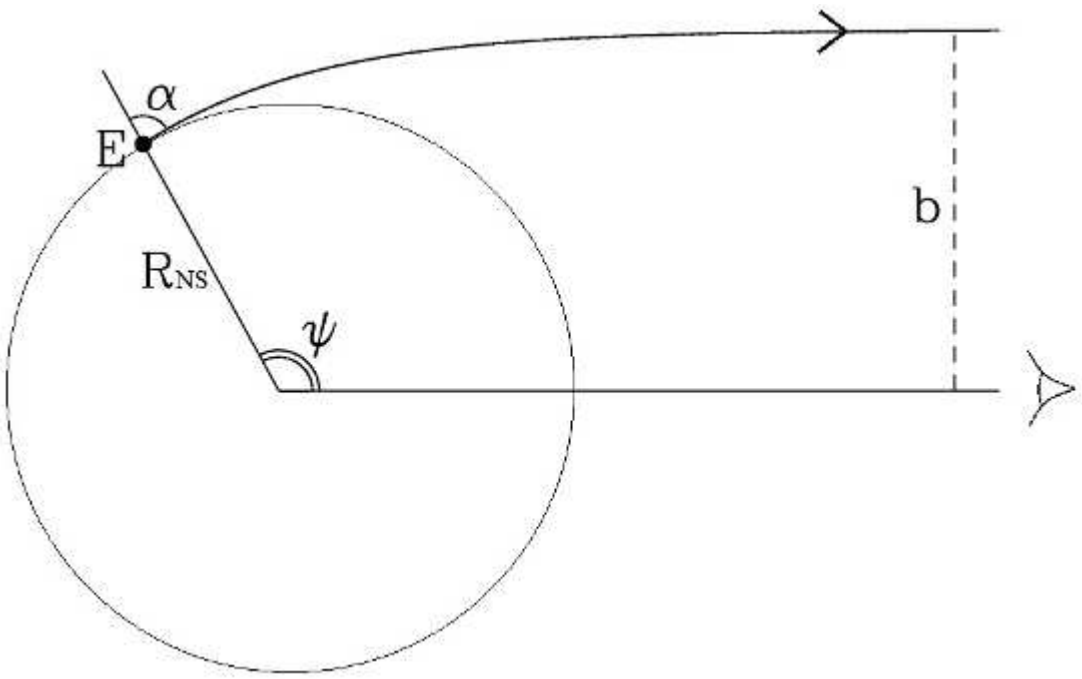

Figure 3.1: Diagram showing the trajectory a photon, travelling from emission point E, in a strong gravitational field (as discussed in Section 3.2.1), where b is the impact parameter. Image credit: modified from Beloborodov (2002).

This method is accurate, to about 1% of the exact value, for systems with $R_{NS} \geq 2r_g$, and $\beta < 90°$. Here r_g is the object's Schwarzschild radius,

$$r_g = \frac{2GM_{NS}}{c^2}. \tag{3.3}$$

Assuming R_{NS}=10 km, this model is accurate for neutron stars with M_{NS} <1.7 $M_\odot$. Assuming M_{NS}=1.4 $M_\odot$, then this model is accurate for neutron stars with R_{NS} > 8.3 km.

Beloborodov (2002) assumes that the flux (dF) from a surface element (dS) is

$$dF = \left(1 - \frac{r_g}{R_{NS}}\right)^2 I_0(\alpha)\cos(\alpha)\frac{dS}{D^2}, \tag{3.4}$$

where $I_0(\alpha)$ is the local intensity of radiation and D is the distance to the observer.

For a neutron star with two antipodal poles, the flux from each pole can be assumed to only differ in terms of $\cos(\alpha)$, and so Beloborodov (2002) shows that,

$$\frac{F_P}{F_1} = \cos(\alpha)_P, \tag{3.5}$$

and

$$\frac{F_S}{F_1} = \cos(\alpha)_S, \tag{3.6}$$

where F_P is the flux emitted from the primary pole (the pole closest to the observer), F_S is the flux emitted from the secondary pole (the pole furthest from the observer).

$$F_1 = \left(1 - \frac{r_g}{R_{NS}}\right)^2 I_0(\alpha)\frac{dS}{D^2}, \tag{3.7}$$

and does not contribute to the pulsed flux.

This gives a total flux, F_{obs} of,

$$F_{obs} = \frac{F_P}{F_1} + \frac{F_S}{F_1}. \tag{3.8}$$

$$\cos(\alpha)_P = \cos(\psi)\left(1 - \frac{r_g}{R_{NS}}\right) + \frac{r_g}{R_{NS}}, \tag{3.9}$$

and

$$\cos(\alpha)_S = -\cos(\psi)\left(1 - \frac{r_g}{R_{NS}}\right) + \frac{r_g}{R_{NS}}. \tag{3.10}$$

ψ varies between $i+\theta$ and $i-\theta$ as the neutron star rotates, where i is the angle between the neutron star's rotational axis and the observer's line-of-sight, and θ is the angle between the neutron star's magnetic axis and its spin axis, as shown in Figure 3.2. Specifically,

$$\cos(\psi) = \sin(\theta)\sin(i)\cos(2\pi\Omega) + \cos(\theta)\cos(i), \tag{3.11}$$

where Ω is the phase, and i and θ are degenerate. $F_P = 0$, and only the secondary pole is visible, when $-\cos(\psi) > r_g/(R_{NS} - r_g)$. $F_S = 0$, and only the primary pole is visible, when $\cos(\psi) > r_g/(R_{NS} - r_g)$.

F_{obs}/F_1 can be plotted as a function of phase for various values of θ, i, and M_{NS}/R_{NS} using Equations (3.2)-(3.11). These values determine how many poles contribute to the total flux, and this affects the shape of the pulse-profiles as shown in Figure 3.3. Figure 3.3 shows that pulse-profiles can be split into four approximate shapes, designated classes I-IV.

The angles that produce each class depend on M_{NS} and R_{NS} via

$$\cos(\xi) = \frac{R_{NS}}{r_g} - 1 = \frac{c^2}{2G}\left(\frac{M_{NS}}{R_{NS}}\right)^{-1} - 1, \tag{3.12}$$

as shown in Figure 3.4. Figure 3.4 shows how the boundaries change for systems containing neutron stars with $z+1$ values of 1.2, 1.3, and 1.4, where z is the gravitational red-shift, and is related to M_{NS}/R_{NS} via

$$1 + z = \left(1 - \frac{r_g}{R_{NS}}\right)^{-0.5} = \left(1 - \frac{2G}{c^2}\frac{M_{NS}}{R_{NS}}\right)^{-0.5}. \tag{3.13}$$

For relatively low values of θ and i (as shown in the blue sections of the plots in Figure 3.4, which represent class I systems), the primary pole is visible all of the time and the

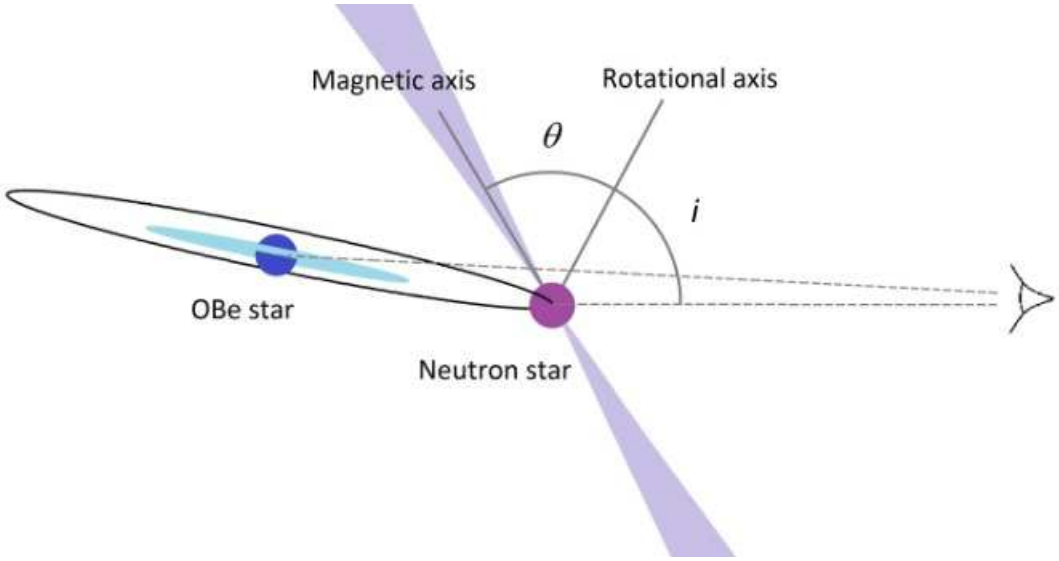

Figure 3.2: Diagram showing angles i and θ, where i is the angle between the neutron star's rotational axis and the observer's line-of-sight, and θ is the angle between the neutron star's rotational axis and magnetic axis. These angles determine how many magnetic poles are visible at any one time (as discussed in Section 3.2.1, image not to scale).

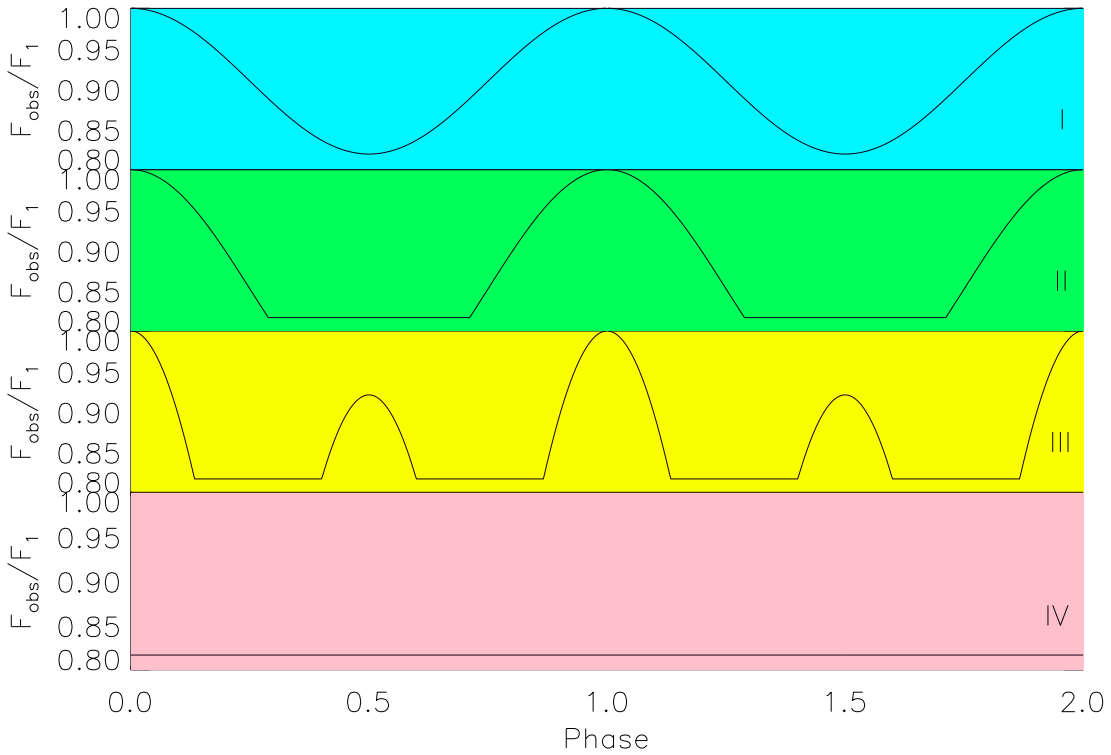

Figure 3.3: Pulse-profiles predicted by the Beloborodov (2002) approximation for class I-IV neutron stars, where classes are defined by how many magnetic poles are visible at once (as discussed in Section 3.2.1). These correspond to specific areas on plots of i as a function of θ, as shown in Figure 3.4.

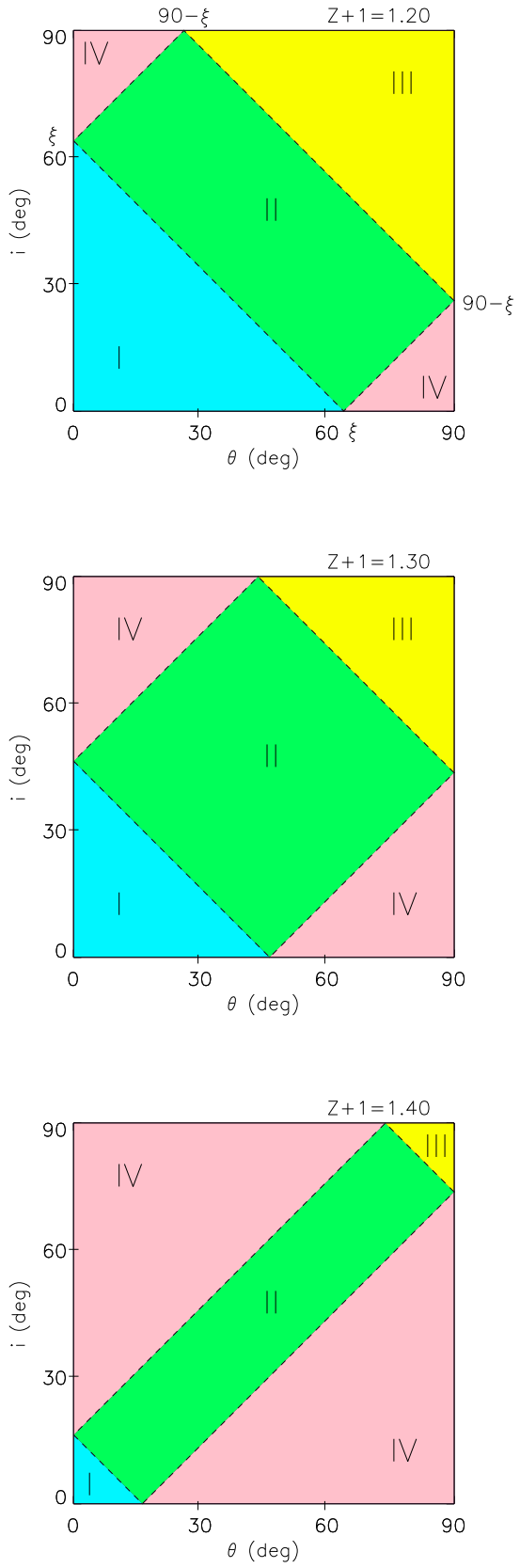

Figure 3.4: Plots of i as a function of θ for different values of $z+1$ (equation (3.13)) using the Beloborodov (2002) approximation (as discussed in Section 3.2.1). The boundary between classes is related to M_{NS}/R_{NS} via equation (3.12). The three plots are for $z+1$ =1.20 (top), $z+1$ =1.30 (middle), and $z+1$ =1.40 (bottom).

secondary pole is never visible. This leads to a sinusoidal pulse-profile (as shown in the blue section of Figure 3.3). If the values of θ and i are slightly higher (as shown in the green sections of the plots in Figure 3.4, which represent class II systems), the secondary pole becomes visible when the primary pole is at its lowest flux. This fills in the trough of the sine wave, making it flat (as shown in the green section of Figure 3.3). If the values of θ and i are higher still (as shown in the yellow sections of Figure 3.4, which represent class III systems), then the first pole sometimes becomes invisible, so that the flat section can now be filled (as shown in the yellow section of Figure 3.3). If either θ is relatively high and i is relatively low, or vice versa (as shown in the pink sections of the plots in Figure 3.4, which represent class IV systems), then both poles are always visible, and so a flat profile is produced (as shown in the pink section of Figure 3.3).

This model is applied to over 1000 pulse-profiles, composed from the dataset discussed in Chapter 2, in order to determine the most probable values of θ, i, and M_{NS}/R_{NS} for each system. θ and i were varied from $0° - 90°$, in intervals of $1°$, and values of $1 + z$ were varied from $1.15 - 1.41$, in intervals of 0.01. The phase-shift is also varied, where the maximum point on the model is moved to the maximum count-rate on the pulse-profile, the phase-shift is then varied, in intervals of 0.01, across one complete phase. Not knowing the true pulse-fraction, the model is normalised to the data by assuming that the maximum and minimum points on the model correspond to the maximum and minimum counts on the pulse-profile. The reduced χ^2 (χ^2_r) is then calculated between the observed results and the results predicted from the model.

3.3 Results

3.3.1 The Beloborodov approximation

Pulse-profiles were modelled for every observation of every system in the dataset discussed in Chapter 2. This is over 1000 pulse-profiles. Figure 3.5 shows χ^2_r as a function of P for all of the observations discussed in Section 3.2. Figure 3.5 shows that most pulse-profiles are not well-fit using the Beloborodov (2002) approximation, and the fit often varies within systems, as does the predicted class of the system. 76.4% of results correspond to class I systems, 20.8% to class II systems, and 2.9% to class III systems. Only 15 pulse-profiles can be fit with a χ^2_r <1.1. These include pulse-profiles for 12 different systems. When combined with a visual inspection, the four best-fit profiles are for SXP2.37, SXP8.80, SXP16.6, and SXP169. These are shown in Figures 3.6-3.9, with results given in Table 3.1.

Three out of four of the best-fit profiles come from neutron stars with $P < 100$ s, and three out of the four are predicted to be class I systems. This means that they have only one visible pole, which is visible all of the time, leading to sinusoidal pulse-profiles.

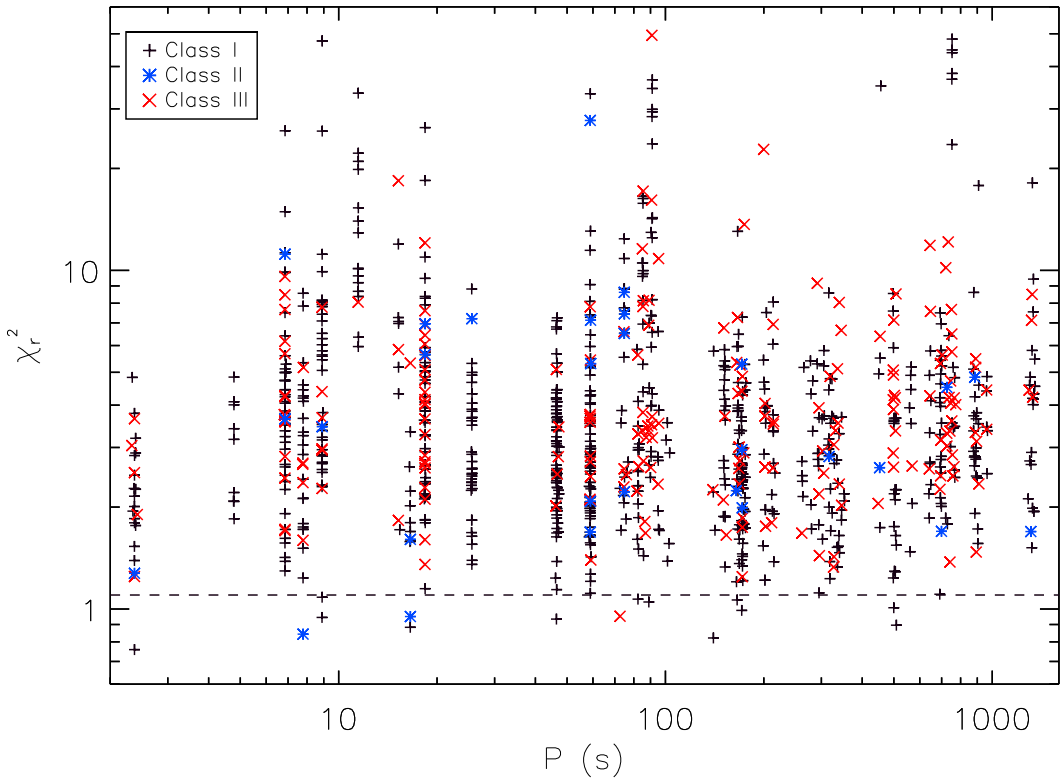

Figure 3.5: χ_r^2 as a function of P for all of the observations discussed in Section 3.2 when fit using the Beloborodov (2002) approximation. These are predicted to be class I (black), class II (blue), and class III (red) systems (as discussed in Section 3.2.1). The dashed line indicates a χ_r^2 of 1.1.

BeXB	MJD (-50000)	Period (s)	Luminosity (10^{37} erg s^{-1})	χ_r^2	Class
SXP2.37	1573.2969	2.37209 ± 0.00002	23 ± 2	0.76	I
SXP8.80	2961.4805	8.893 ± 0.001	0.3 ± 0.1	0.94	I
SXP16.6	1801.4453	16.576 ± 0.001	0.27 ± 0.04	0.95	II
SXP169	4704.0312	165.7 ± 0.1	0.9 ± 0.3	1.06	I

Table 3.1: Results for the four observations best-fit by the Beloborodov (2002) approximation (as discussed in Section 3.3.1). χ_r^2 contour plots for these systems are shown in Figures 3.6-3.9.

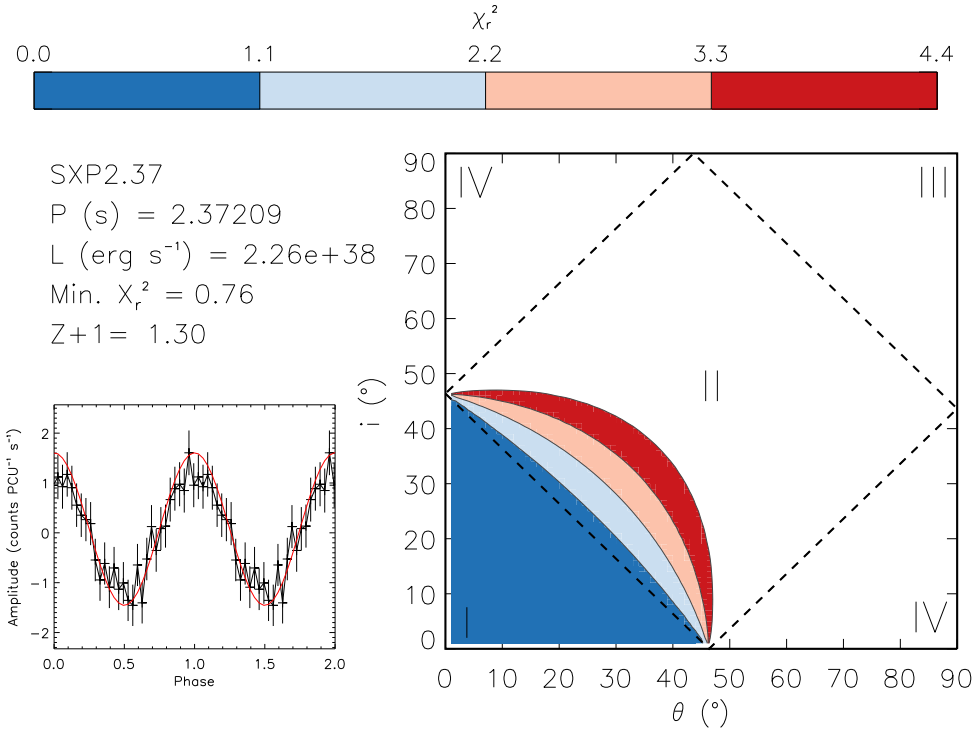

Figure 3.6: χ^2_r contour plot for SXP2.37 at $L = 2.26 \times 10^{38}$ erg s^{-1} (right). This shows χ^2_r between the pulse-profile (left; black) and the Beloborodov (2002) approximation, as discussed in Section 3.3.1. The best-fit values of i and θ are in the dark blue area of the contour plot, and the best-fit model is plotted (left; red).

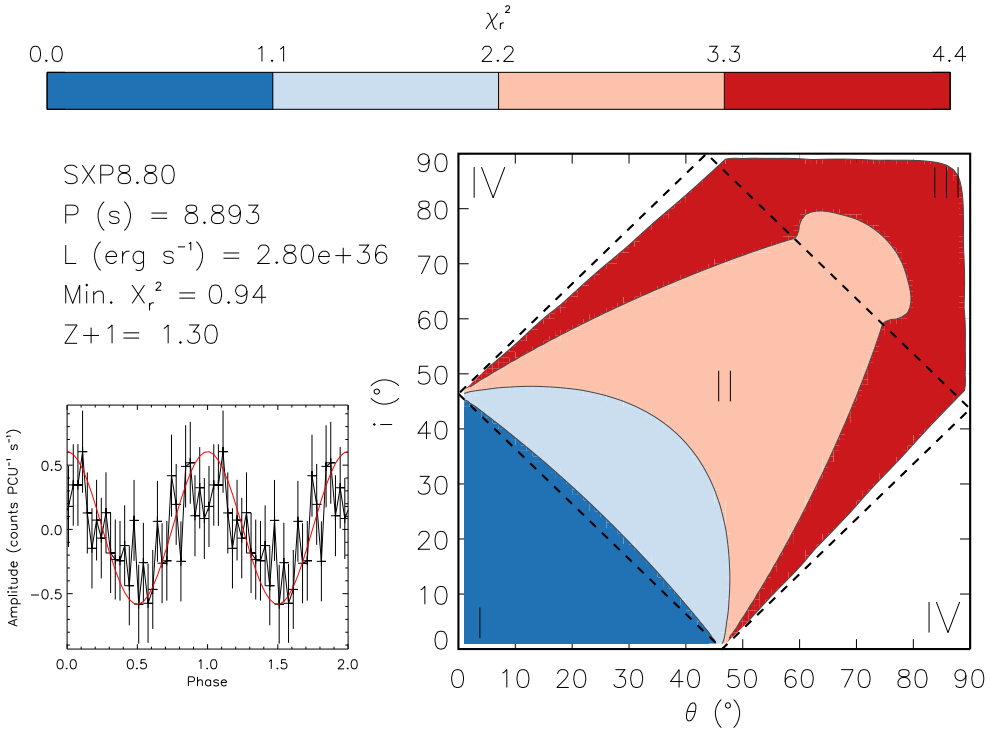

Figure 3.7: As for Figure 3.6 but for SXP8.80 at $L = 2.80 \times 10^{36}$ erg s^{-1}.

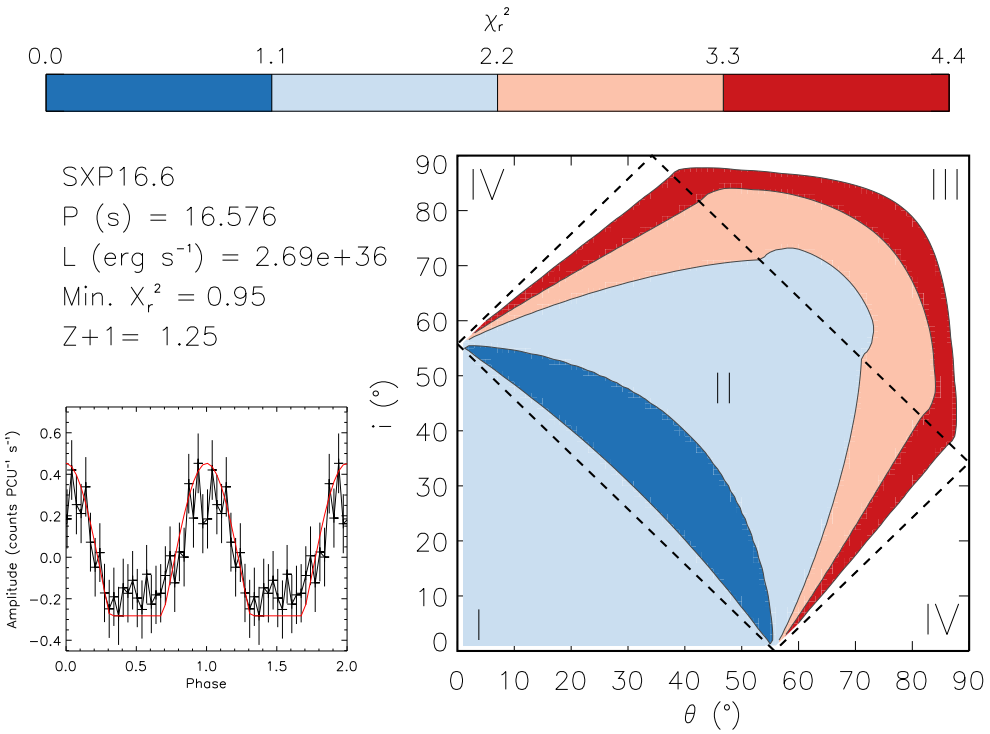

Figure 3.8: As for Figure 3.6 but for SXP16.6 at $L = 2.69 \times 10^{36}$ erg s^{-1}.

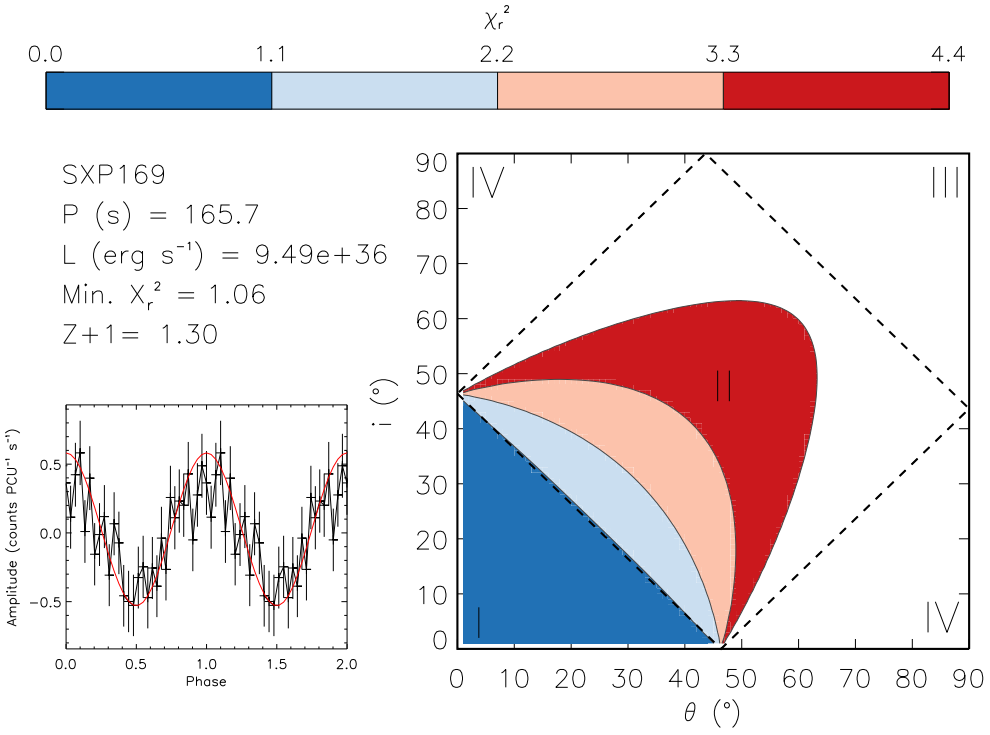

Figure 3.9: As for as Figure 3.6 but for SXP169 at $L = 9.49 \times 10^{36}$ erg s^{-1}.

SXP16.6 is predicted to be a class II system. This means that its primary pole is always visible and a secondary pole is sometimes visible.

The fact that the majority of systems are predicted to be class I may be a coincidence. It may also be due to an instrumental bias, class IV systems will not be classified as pulsating, for example, and so may not be discovered. Wang and Welter (1981) found similar results and suggested that this may be because θ - the angle between the neutron star's rotational axis and magnetic axis - is not random, there may be a bias that makes θ tend towards zero in X-ray binaries.

The four best-fit profiles were predicted to have $1 + z$ values of ~ 1.3, which means that if they have a radius of 10 km, then they have a mass of 1.4 $M_{\odot}$. There are large errors on this parameter, however, with similarly well-fit results over the full range of values.

3.3.2 Double-peaked structure & other interesting features

All of the pulse-profiles in this dataset are shown in Appendix C. These are colour-coded, where the colours represent luminosity bands and are explained in Figure C.1. Many of the systems in this dataset produce pulse-profiles that exhibit a slight asymmetry (as described in Section 1.4.3), with some showing a gradual rise and sharp fall, and some showing the opposite behaviour. These vary across, and sometimes within, individual systems, with no obvious correlation between the type of asymmetry and either P or L.

Many systems produce pulse-profiles with one or more dips (as described in Section 1.4.4). Dips are thought to be caused by an additional absorption component that obscures the radiation (Galloway et al., 2001). As with asymmetry, dips vary across, and sometimes within, individual systems.

There are also a high number of systems with pulse-profiles containing both single and double-peaked structure at different luminosities. As described in Section 1.4.2, double-peaked structure is defined as structure containing a secondary peak, about half a phase apart from the main peak, that has an amplitude over half the amplitude of the main peak. A secondary peak about half a phase apart from the main peak, and less than half the amplitude, will be referred to as the 'emergence of double-peaked structure'. This is similar in appearance to pulse-profiles produced by class III systems, described in Section 3.3.1. Pulse-profiles showing the emergence of double-peaked structure can be distinguished from class III systems, however, because we would expect class III systems to always produce pulse-profiles that display this shape, since the parameters entered into the Beloborodov (2002) approximation (M_{NS}, R_{NS}, i, and θ) are not expected to change over the observation period. It is also sometimes difficult to distinguish double-peaked structure from dips, where the structure appears as a dip in the main peak, but is so deep that it is hard to distinguish from double-peaked structure (see Figure 3.15). This is particularly true if there are no pulse-profiles showing the emergence of the peak.

As described in Section 1.4.2, double-peaked structure is thought to result from the transition from a pencil beam to a fan beam (the geometry relating to this is shown in Figure 1.13). At relatively low L, the pencil beam dominates the pulse-profile, with a single pole producing an approximately sinusoidal peak. As L increases, an accretion column forms, and a fan beam appears, resulting in a secondary peak appearing in the pulse-profile, about half a phase apart from the first. As L increases further, the fan beam may dominate, causing the secondary peak to become larger than the first. The first peak may even disappear completely, as radiation is no longer emitted parallel to the magnetic field lines. Double-peaked structure may also result from systems with more than two magnetic poles (as described in Section 1.4.5).

Figures 3.10 and 3.11 show L as a function of P for all pulse-profiles, highlighting those that show double-peaked structure, and distinguishing between double-peaked structure that does, and does not, contain a dip. Figure 3.10 shows that SXP46.6 is the only system with pulse-profiles that exhibit double-peaked structure both with and without dips. With the exception of SXP175, systems with $P < 46.6$ s always have a dip in their pulse-profiles when they exhibit double-peaked structure, and systems with $P > 46.6$ s never have a dip in their pulse-profiles when they exhibit double-peaked structure. The L at which double-peaked structure appears tends to decrease with P for systems with $P < 46.6$ s. Double-peaked structure appears across a range of luminosities for systems with $P > 46.6$ s. SXP11.5 produces the most pulse-profiles with double-peaked structure, with seven. This system was shown not to be close to spin equilibrium in Chapter 2.

Figure 3.11 is the same as Figure 3.10, but also shows any other pulse-profiles that exhibit dips. Figure 3.11 shows that dips appear across roughly the same luminosity range ($\sim 6\times10^{36}-10^{38}$ erg s^{-1}) at all spin periods. For systems with $P < 46.6$ s, the dips tends to appear at luminosities lower than the L at which they exhibit double-peaked structure. The dip then remains when the double-peaked structure appears. Systems with $P > 46.6$ s are more likely to exhibit double-peaked structure without a dip, with the dip appearing at higher luminosities.

As stated above, SXP46.6 is the only system that exhibits double-peaked structure both with and without a dip. The double-peaked structure without a dip appears at $\sim 1.6\times10^{36}$ erg s^{-1}, and the double-peaked structure with a dip appears at $\sim 4.8\times10^{37}$ erg s^{-1}, with many single-peaked pulse-profiles appearing at luminosities in between. This is a range of $\sim 4.6\times10^{37}$ erg s^{-1}, three times larger than the range between double-peaked profiles in SXP11.5, and over twenty times larger than the range between double-peaked pulse-profiles for any other system. This suggests that the double-peaked profiles seen at relatively high and relatively low L in SXP46.6 (and perhaps in other systems) might have different causes. If the system has more than two magnetic poles, for example, then double-peaked structure may occur if the flow of accreted material moves to a different pole, thereby changing trajectory (Parmar et al., 1989).

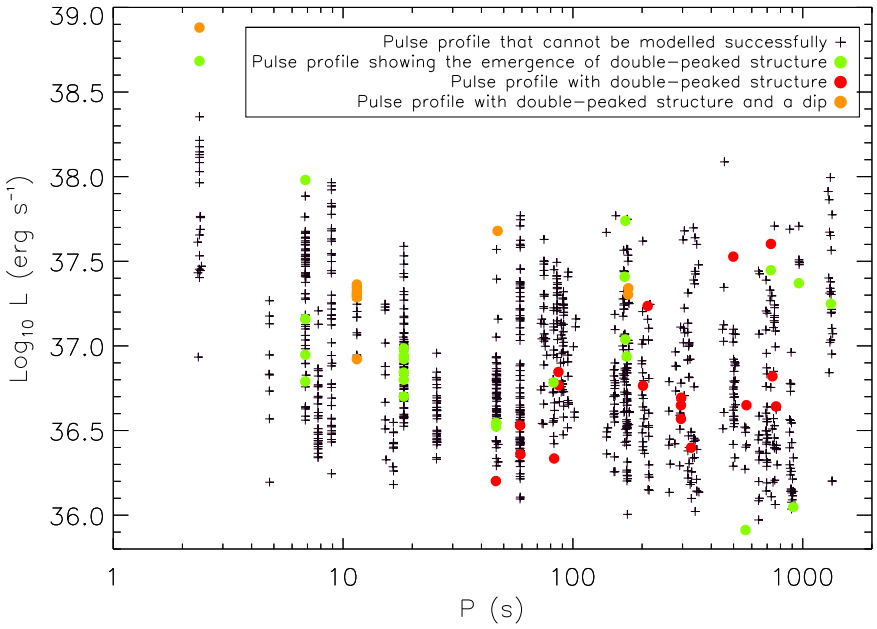

Figure 3.10: L as a function of P for all detections. Pulse-profiles showing the emergence of double-peaked structure (as defined in Section 3.3.2) are highlighted (green), as are pulse-profiles showing double-peaked structure both with (orange) and without (red) dips (as described in Section 1.4.4).

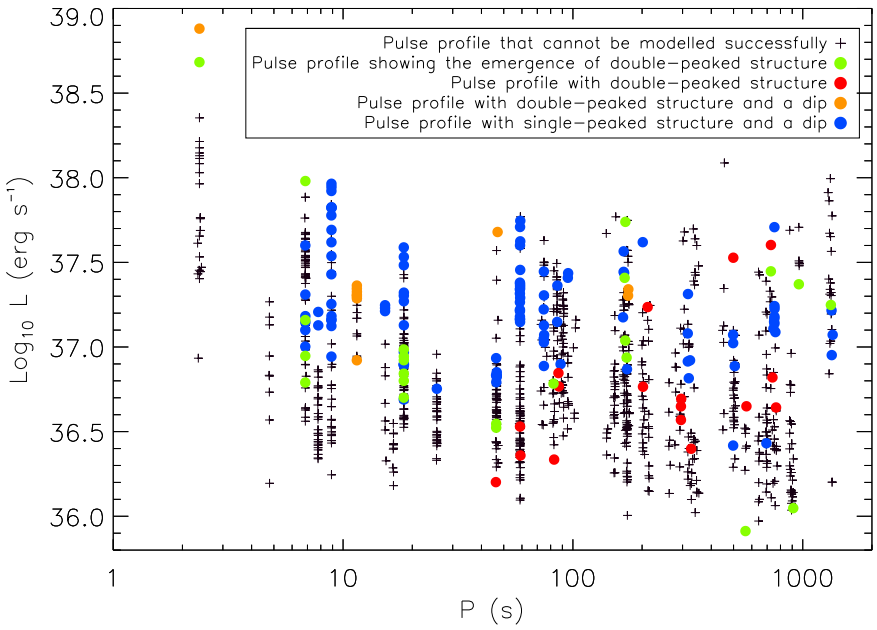

Figure 3.11: As for Figure 3.10 but also showing single-peaked structure with dips (as described in Section 1.4.4; blue).

If double-peaked structure is generally caused by the transition from pencil to fan beam emission, then Figure 3.10 shows that this occurs over a wide range of L, where systems with relatively long spin periods tend to transition at lower mass-accretion rates than systems with relatively short spin periods. These results are highly inconclusive, however, because of the subjective nature of classification. It is difficult to know if double-peaked structure is evident, or if the appearance of double-peaked structure is caused by dips. This is particularly true for SXP8.80, as discussed in Section 3.3.2.2. Figures 3.14-3.19 show pulse-profiles that exhibit single and double-peaked structure at varying L for SXP2.37, SXP8.80, SXP59.0, and SXP91.1.

3.3.2.1 SXP2.37

SXP2.37 (also known as SMC X-2) was discovered in 1977, with a L of $\sim 10^{38}$ erg s^{-1} (Clark et al., 1978), and remained in a Type II outburst (as defined in Section 1.1.2.1) for about a month (Clark et al., 1979). SXP2.37 underwent another Type II outburst in 2000 (Corbet et al., 2001). This can be seen in Figure 3.12, which shows P and L as a function of MJD for SXP2.37 over 11 yr, starting on the 30th January 2000. The luminosity peaks at $\sim 7.6 \times 10^{38}$ erg s^{-1} on the 18th February (MJD 51592.2266). This is the highest L of all the observations, for all 42 sources in this dataset, and exceeds the Eddington luminosity ($L_{Edd} \cong 1.26 \times 10^{38} M_{NS}/M_{\odot}$ erg s^{-1}, as discussed in Section 1.2). This outburst was followed by a period of spin-down that lasted ~ 3 months. For the next ~ 10 yr, this system has been spinning up. In Chapter 2, I showed that SXP2.37 is one of six systems that are not close to spin equilibrium. The OBe star in SXP2.37 has a non-truncated circumstellar disc, as is shown in Figure 3.13.

All of the pulse-profiles for SXP2.37 are shown in Figure C.2. Figure 3.14 shows the change in pulse-profiles throughout the 2000 outburst. At a L of $\sim 2.3 \times 10^{38}$ erg s^{-1}, SXP2.37 is well-fit by the Beloborodov (2002) approximation as a class I system (with a χ^2_r of 0.76; as shown in Figure 3.6). The pulse-profiles of SXP2.37 remain roughly single-peaked at L below this. As L increases to $\sim 4.8 \times 10^{38}$ erg s^{-1}, however, double-peaked structure begins to emerge. The secondary peak becomes more dominant, resulting in double-peaked structure, at the maximum L of $\sim 7.6 \times 10^{38}$ erg s^{-1}. There is no clear dip present until this L, when a peak rises between the main and secondary peak on one side.

If this behaviour can be interpreted in terms of changing geometry, then during Type I outbursts, SXP2.37 emits a pencil beam. During Type II outbursts, an accretion column can form and it transitions into a fan beam. During Type II outbursts it may also exhibit a dip, possibly due to inhomogeneous material in the accretion disc. This is inconsistent with findings in Chapter 2, which show that SXP2.37 is one of three systems (including SXP4.78 and SXP91.1) predicted to be in a supercritical state (following Becker et al. (2012), as discussed in Section 2.4). This means that the pencil beam is suppressed.

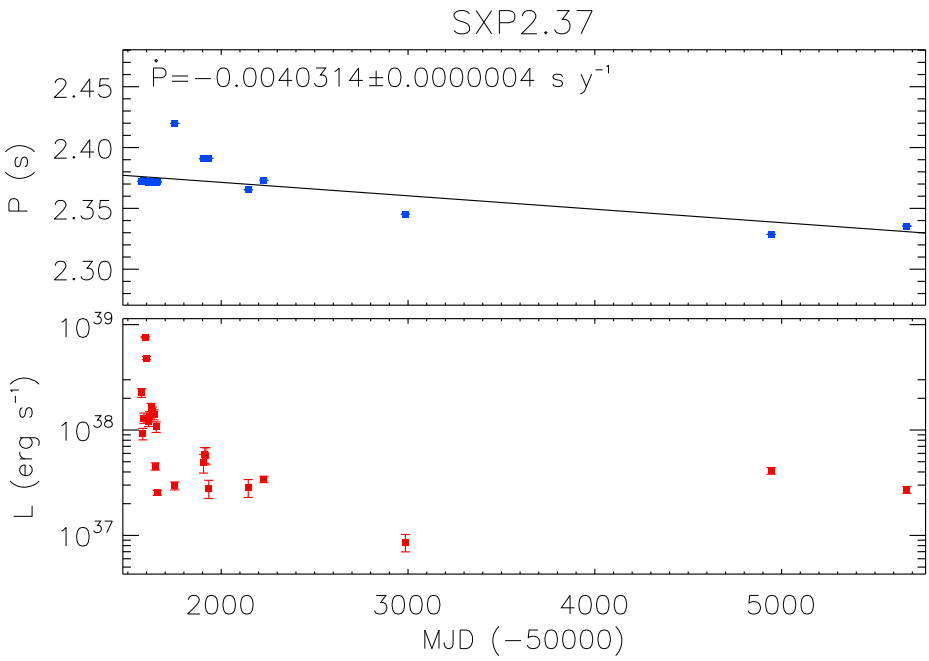

Figure 3.12: P (upper panel; blue) and L (lower panel; red) as a function of MJD for SXP2.37. The black line in the upper panel shows the best-fit $\dot{P}$ (also shown in Figure B.1).

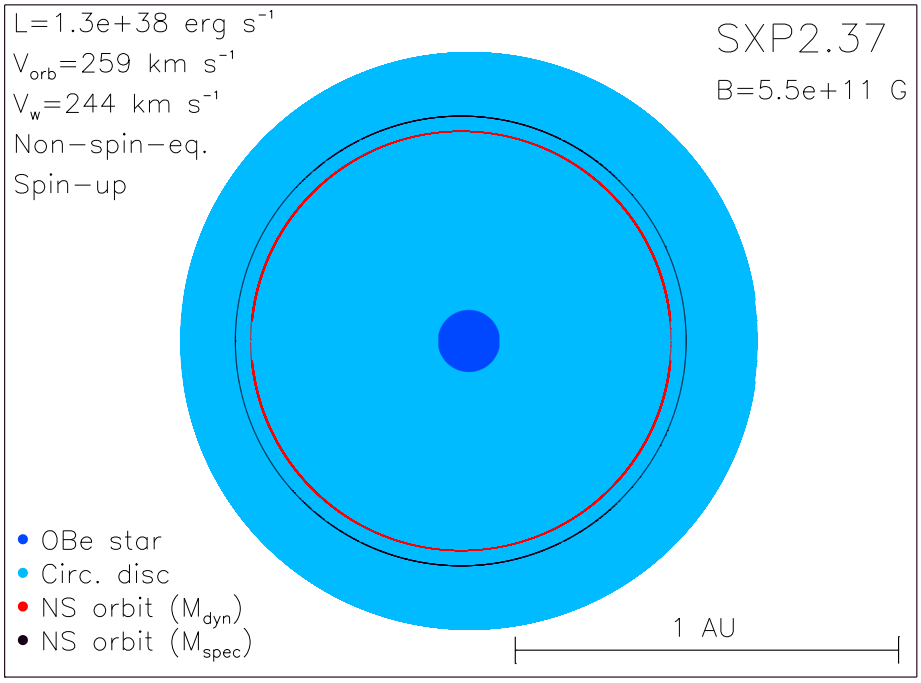

Figure 3.13: Diagram of SXP2.37, using orbital parameters discussed in Section 2.3 (also given in Table A.1 and shown in Figure B.2).

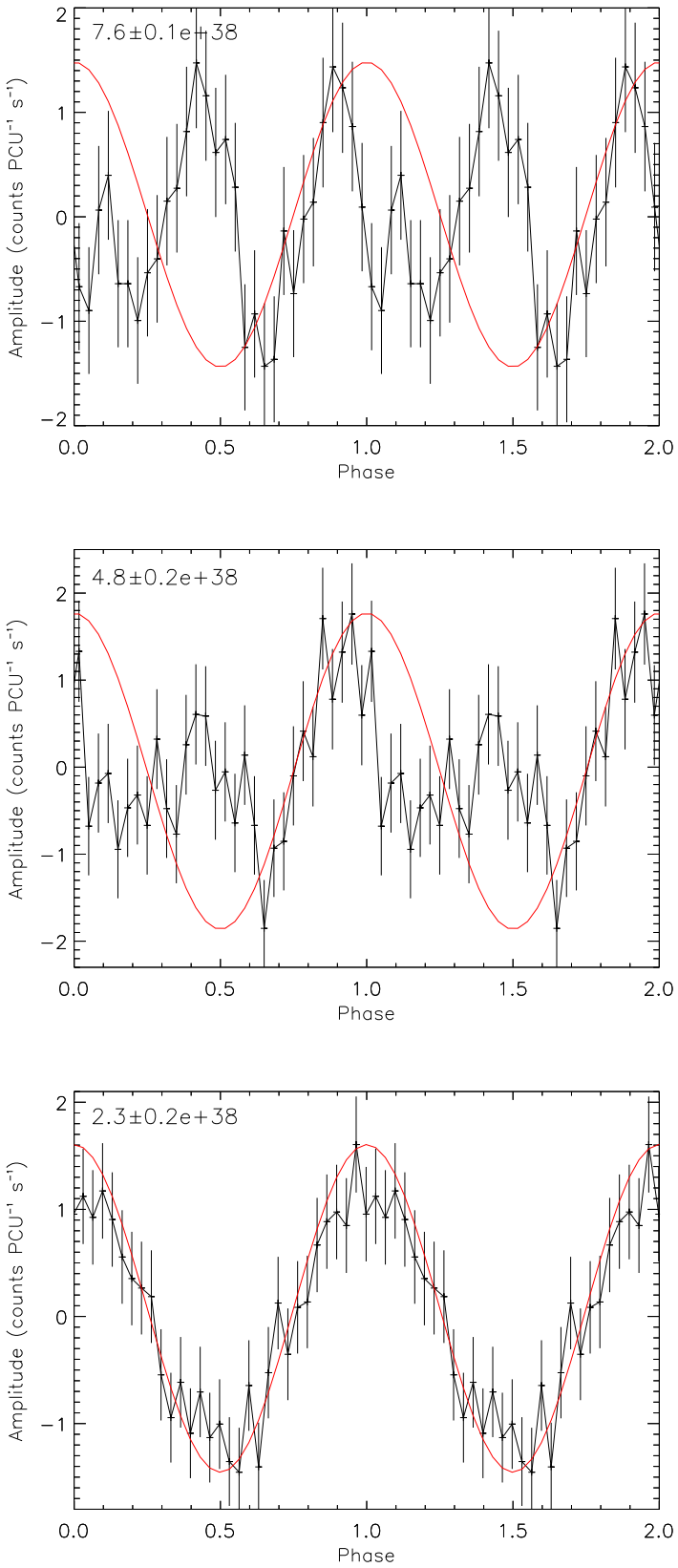

Figure 3.14: Pulse-profiles for SXP2.37, depicted in order of decreasing L from top to bottom (black). Results from the Beloborodov (2002) approximation (discussed in Section 3.3.1) that best-fit the bottom pulse-profile are over-plotted (red). The luminosity during the observation is given in the top left-hand corner in erg s^{-1}.

Using equation (2.18), and assuming the results for the magnetic field given in Table 2.9 are correct, the pencil beam in SXP2.37 should be suppressed above 8×10^{36} erg s^{-1}. All pulse-profiles for SXP2.37 are above 8×10^{36} erg s^{-1}, and so the pencil beam should be suppressed in all pulse-profiles, and the transition between pencil and fan beam patterns should not be seen. This suggests that perhaps the double-peaked structure in this system has a different cause, such as multiple magnetic poles, as discussed in relation to SXP46.6 in Section 3.3.2.

3.3.2.2 SXP8.80

In Chapter 2, SXP8.80 was shown to be close to spin equilibrium. The pulse-profiles of SXP8.80 are shown in Figures C.6 and 3.15. SXP8.80 is not well-fit by the Beloborodov (2002) approximation. In SXP8.80, pulse-profiles develop small dips at $L \cong 1.3 \times 10^{37}$ erg s^{-1}, increasing until $\sim 2.7 \times 10^{37}$ erg s^{-1}, when they remain somewhat stable. Double-peaked structure appears at $\sim 9.2 \times 10^{37}$ erg s^{-1}. It is difficult to know if this is caused by the transition between pencil and fan beam patterns, or if it is caused by an increase in size of the dip. While in this case, the presence of the dip in the other pulse-profiles for this system indicates that it is more likely that the double-peaked structure is caused by an increase in size of the dip, it would be very difficult to tell if this pulse-profile were considered in isolation.

3.3.2.3 SXP59.0

In Chapter 2, SXP59.0 was shown to be close to spin equilibrium. The pulse-profiles of SXP59.0 are shown in Figures C.13 and 3.16. Unlike with SXP2.37 and SXP8.80, the pulse-profiles of SXP59.0 exhibit double-peaked structure at relatively low L, at $\sim 2.3 \times 10^{36}$ erg s^{-1} and $\sim 3.4 \times 10^{36}$ erg s^{-1}. At a L of $\sim 6.3 \times 10^{36}$ erg s^{-1}, SXP59.0 is well-fit by the Beloborodov (2002) approximation as a class II system (with a χ^2_r of 0.93). The pulse-profiles of SXP59.0 begin to exhibit a dip at $\sim 1.4 \times 10^{37}$ erg s^{-1}.

3.3.2.4 SXP91.1

Figure 3.17 shows P and L as a function of MJD for SXP91.1 over 13 yr, starting in 1997. In Chapter 2, SXP91.1 was shown not to be close to spin equilibrium. The OBe star in the system has a non-truncated circumstellar disc, as is shown in Figure 3.18. The pulse-profiles of SXP91.1 are shown in Figures C.16 and 3.19. SXP91.1 is not well-fit by the Beloborodov (2002) approximation. SXP91.1 shows double-peaked structure between $\sim 5.8 \times 10^{36}$ erg s^{-1} and $\sim 7.0 \times 10^{36}$ erg s^{-1}. The secondary peak begins to disappear at $\sim 8.0 \times 10^{36}$ erg s^{-1}, and between $\sim 1.0 \times 10^{37}$ erg s^{-1} and $\sim 3.1 \times 10^{37}$ erg s^{-1} the pulse-profiles show single-peaked structure that is non-sinusoidal. This is

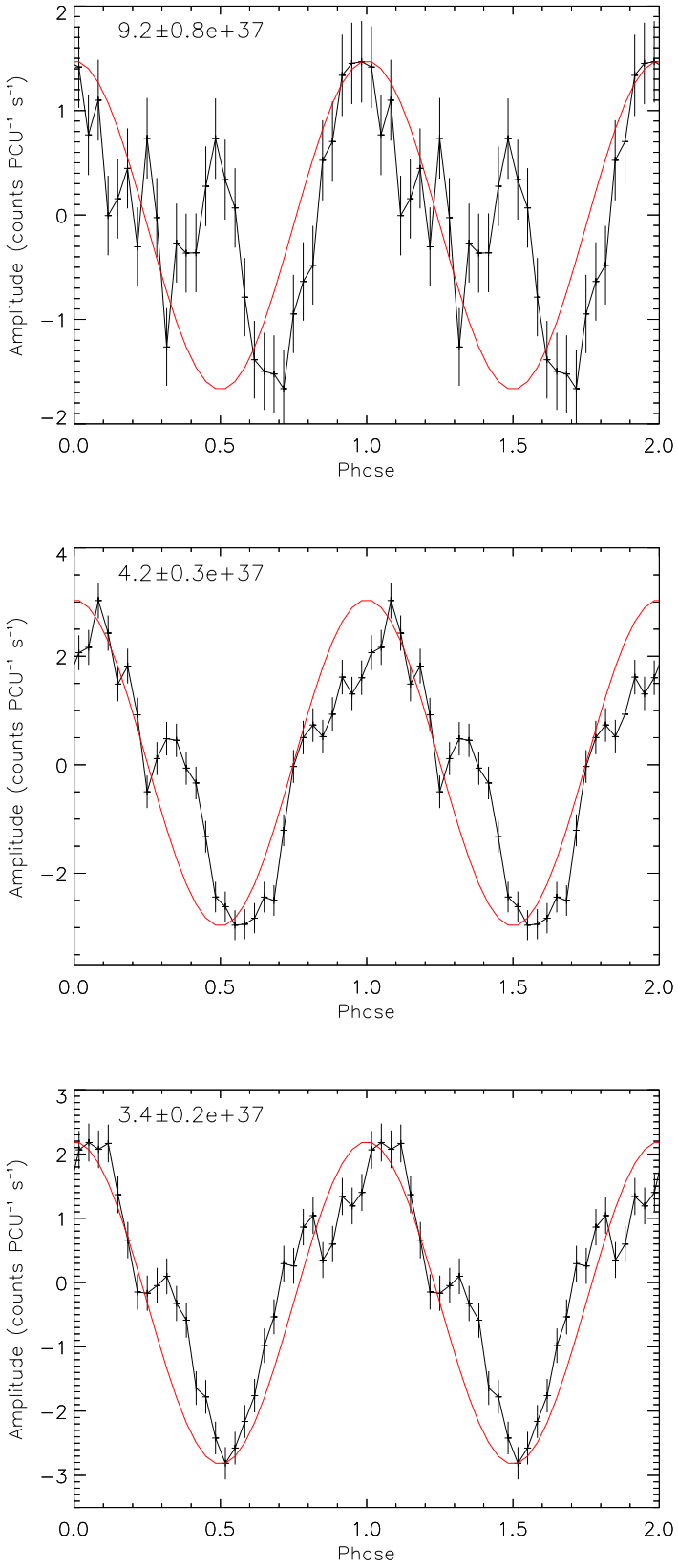

Figure 3.15: As for Figure 3.14 but for SXP8.80.

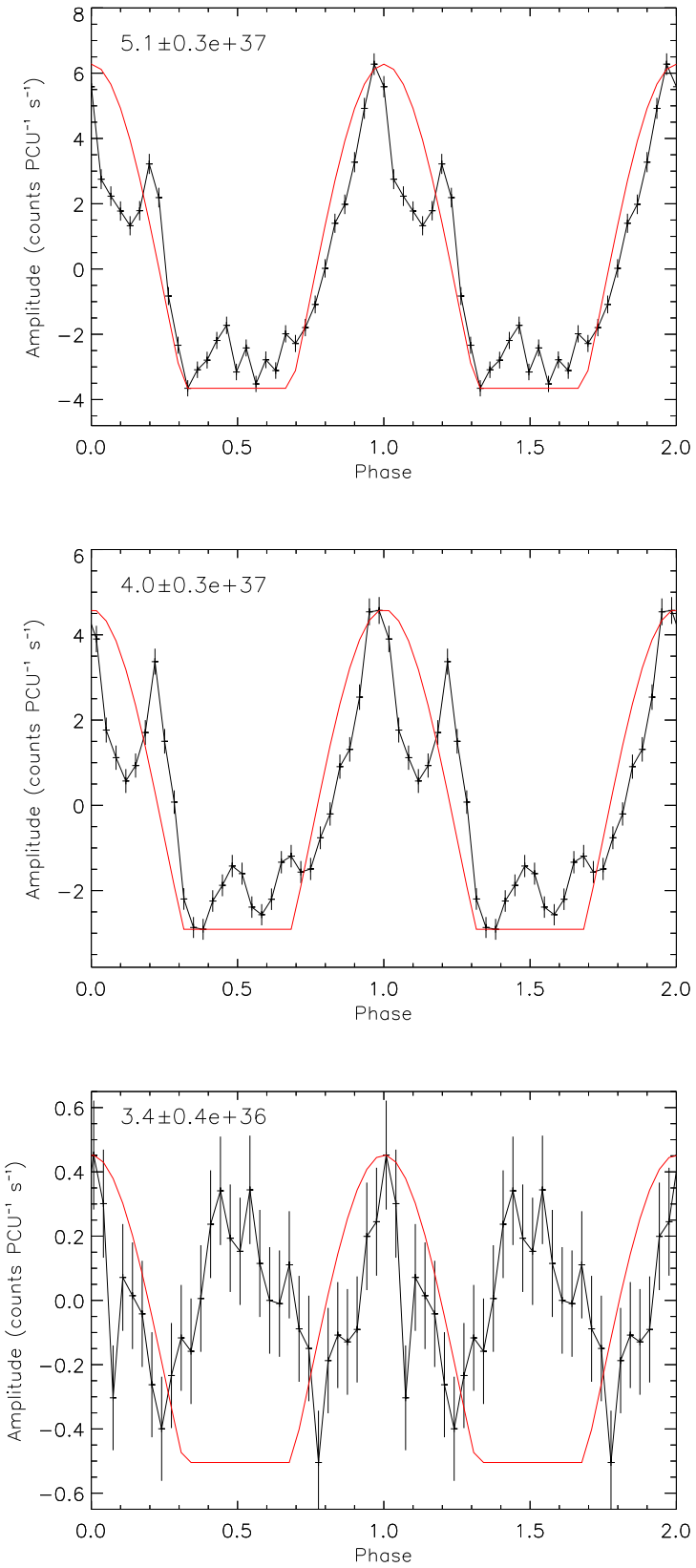

Figure 3.16: As for Figure 3.14, except results from the Beloborodov (2002) approximation that best-fit the top, rather than bottom, pulse-profile are over-plotted, and pulse-profiles are for SXP59.0.

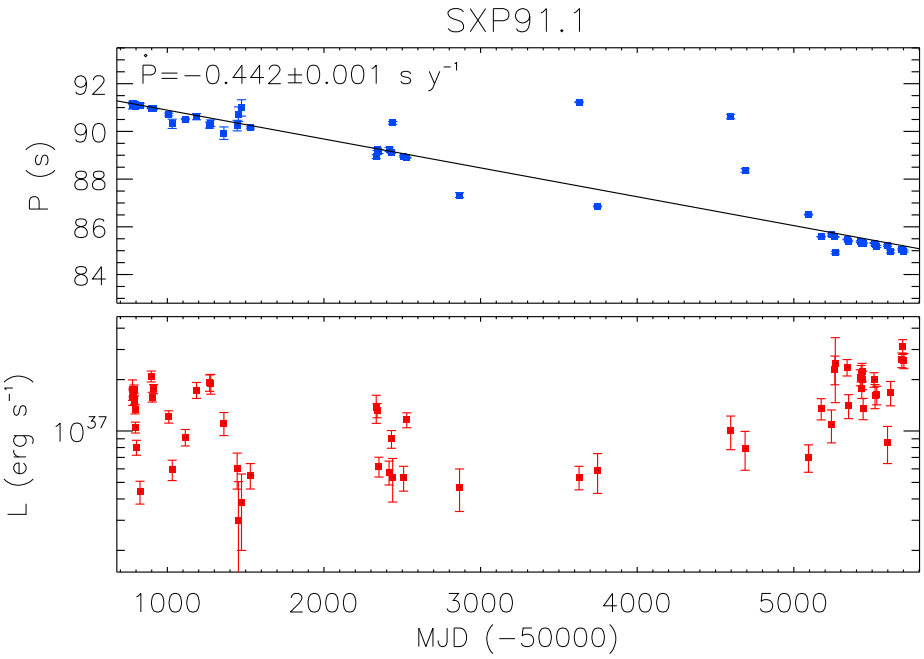

Figure 3.17: P (upper panel; blue) and L (lower panel; red) as a function of MJD for SXP91.1. The black line in the upper panel shows the best-fit $\dot{P}$ (also shown in Figure B.29).

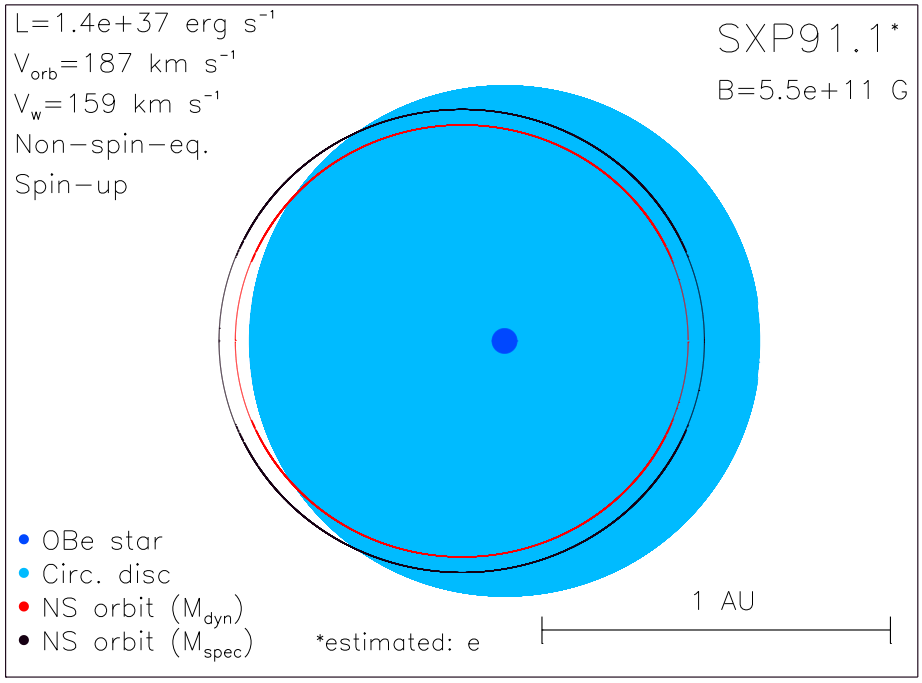

Figure 3.18: Diagram of SXP91.1, using orbital parameters discussed in Section 2.3 (also given in Table A.1 and shown in Figure B.30).

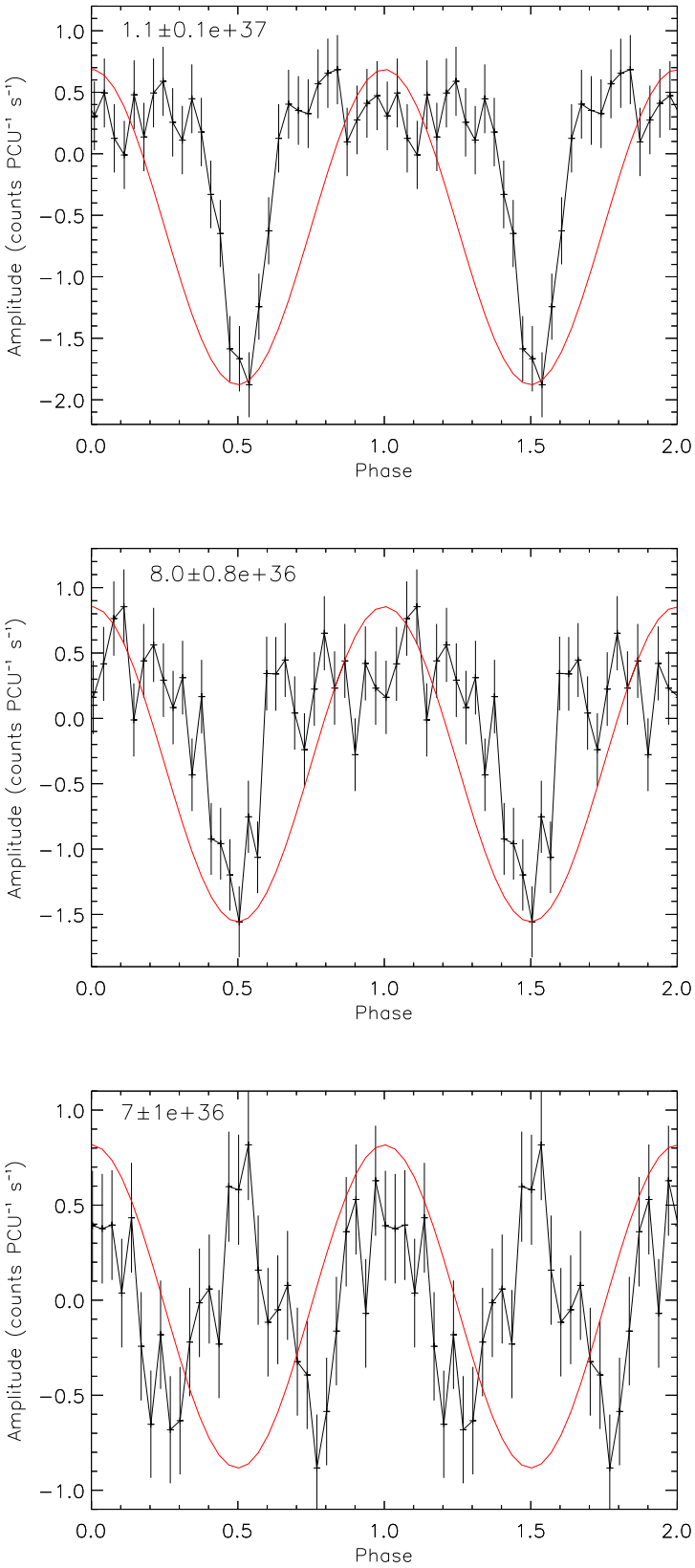

Figure 3.19: As for Figure 3.16 but for SXP91.1.

consistent with findings in Chapter 2 that predict SXP91.1 is in a supercritical state, which means that the pencil beam is suppressed. Using equation (2.18), and assuming the results for the magnetic field given in Table 2.9 are correct, the pencil beam in SXP91.1 should be suppressed above 8×10^{36} erg s^{-1}.

The single trough in the pulse-profile of SXP91.1 is much sharper than the troughs of the pulse-profiles of other systems, with a full-width half maximum of less than a quarter of a phase. Almost none of the pulse-profiles of SXP91.1 contain dips, including the pulse-profiles exhibiting double-peaked structure. The structure of the pulse-profiles may be related to the fact that SXP91.1 has the longest spin period of all the neutron stars in this dataset that are not close to spin equilibrium. Wang and Welter (1981) show that fan beams can produce sharp features, as the fan beam rotates behind the horizon of the neutron star. The sharp features may also be caused by matter outside of the neutron star's magnetosphere absorbing the light, so that it is only seen when viewed directly.

3.4 Discussion and conclusions

In Sections 3.1-3.3, I created over 1000 pulse-profiles for BeXB in the SMC. I modelled these using the Beloborodov (2002) approximation, and found that only 15 could be well-fit (with a χ^2_r <1.1). These include pulse-profiles for 12 different systems. The Beloborodov (2002) approximation does not seem well-suited to these pulse-profiles. This is probably because they cannot be assumed to simply be emitting from two point-like hotspots. By visually inspecting the pulse-profiles, it is evident that they vary not just from system to system, but from observation to observation. They display a range of structure containing all the complexities discussed in Section 1.4.

In Section 3.3, I showed that systems with relatively long spin periods tend to transition from a pencil beam to a fan beam at lower luminosities than systems with relatively short spin periods. These results are far from conclusive, however, because of the subjective nature of classification; it is sometimes difficult to distinguish between double-peaked structure and dips, which produce the same shape in the pulse-profile.

Future work in this area involves modelling the pulse-profiles with models that take into account the effects of fan beam radiation, asymmetric poles, and multiple poles. This is currently being undertaken by S. Laycock and R. Cappallo et al. at the University of Massachusetts.

Chapter 4

LXP187: a persistent BeXB in the LMC

4.1 Introduction

LXP187 is a newly discovered BeXB located in the LMC. It was first discovered by Beardmore et al. (2009) within Swift/Burst Alert Telescope (Swift/BAT) observations (where it is referred to as Swift J0451.5-6949), with a 14-195 keV flux of $(2.8 \pm 0.3) \times 10^{-11}$ erg cm^{-2} s^{-1}, and fit with a power-law of photon index 2.5 ± 0.4. Swift/BAT data show LXP187 to be a persistent X-ray source.

Beardmore et al. (2009) report the X-ray source position to be at an RA, Dec (J2000) of 04:51:06.8 and -69:48:03.2 respectively, with an uncertainty of 3.5″, using data from Swift/X-ray Telescope (Swift/XRT) (where it is referred to as Swift J045106.8-694803) taken on 23rd October 2008 and 14th November 2008. This is consistent with the location of a V=14.70 blue star, known as LMC 9775 (Massey, 2002). Beardmore et al. (2009) use the XRT data to determine an X-ray flux of $(1.68 \pm 0.11) \times 10^{-11}$ erg cm^{-2} s^{-1} (0.3-10 keV), fit with a power-law of photon index $0.96 \pm ^{0.06}_{0.04}$ and a column density of $(1.9 \pm 0.3) \times 10^{21}$ cm^{-2}. They also determine a possible neutron star spin period of ∼187 s, and report strong secondary peaks in the Lomb-Scargle periodogram, occurring at 181 s and 193 s. These may be side-bands due to Swift's 95 min orbital period. Beardmore et al. (2009) also report an orbital period of 21.64 ± 0.02 d, which they found in blue band optical data taken with the MAssive Compact Halo Objects' (MACHO's) 1.27 m telescope (where it is referred to by MACHO ID 44.1741.17). Grebenev et al. (2013) created energy spectra of LXP187 over 3-200 keV using data from the INTErnational Gamma-Ray Astrophysics Laboratory/Imager on-Board the INTEGRAL Satellite (INTEGRAL/IBIS). They showed that the high-energy cut-off in the spectrum is at 16.0 ± 5.0 keV, and calculated a photon index of 0.5 ± 0.5.

In Klus et al. (2013), we analysed optical spectra of LXP187, taken with the 1.9 m Radcliffe telescope at SAAO on the 12th December 2009 and 26th September 2011, and the NTT, in La Silla, Chile on the 8th and 10th December 2011. We used these data to classify the optical companion to the neutron star in LXP187 as a B0-B1 III-V star (see Figure 4.1) and determined the *EW* $H\alpha$ (see Figure 4.2), which is directly related to the size of the OBe star's circumstellar disc (equation (2.16)). The *EW* $H\alpha$ was found to be -29 ± 2 Å in 2009, and -33 ± 1 Å and -34.5 ± 0.6 Å for the SAAO and ESO spectra taken in 2011. This consistency is uncommon, and almost certainly related to the persistent activity Beardmore et al. (2009) saw in the Swift/BAT data.

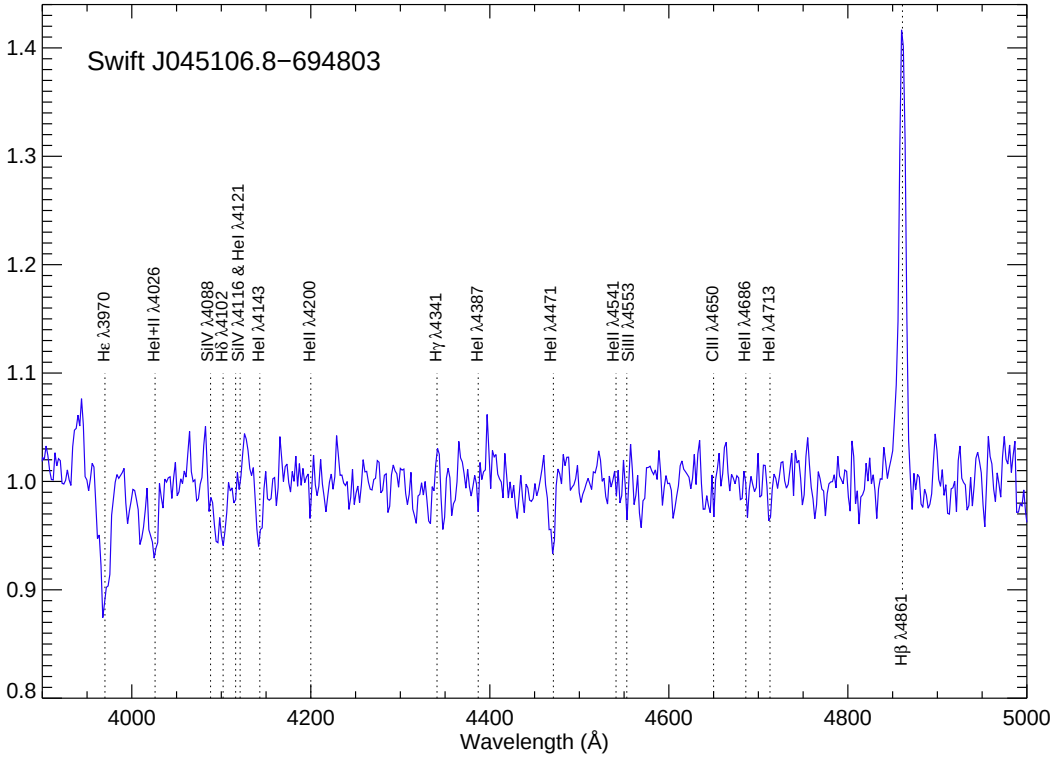

Figure 4.1: Spectrum of the OBe star in LXP187 in the blue band (wavelength range $\lambda\lambda 3900-5000$Å), taken with the NTT on 8th December 2011 (as discussed in Section 4.1). The spectrum has been normalised to remove the continuum, and redshift corrected by ~ 280 km s^{-1}. Atomic transitions relevant to spectral classification have been marked, and the OBe star has been classified as a B0-B1 III-V star.

Bartlett et al. (2013) used data from a ∼7 ks X-ray Multi-Mirror Mission - Newton/European Photon Imaging Camera (XMM-Newton/EPIC) target of opportunity (ToO) observation, taken on 17th July 2012, in order to confirm the position of LXP187, which they found to be at an RA, Dec (J2000) of 04:51:06.7 and -69:48:04.2 respectively, with a 1σ uncertainty of $1''$. This is shown in Figure 4.3. Bartlett et al. (2013) also used these data to determine the neutron star spin period (discussed further in Section 4.3.1.3), and analyse the 0.2-10 keV spectra (see Figure 4.4).

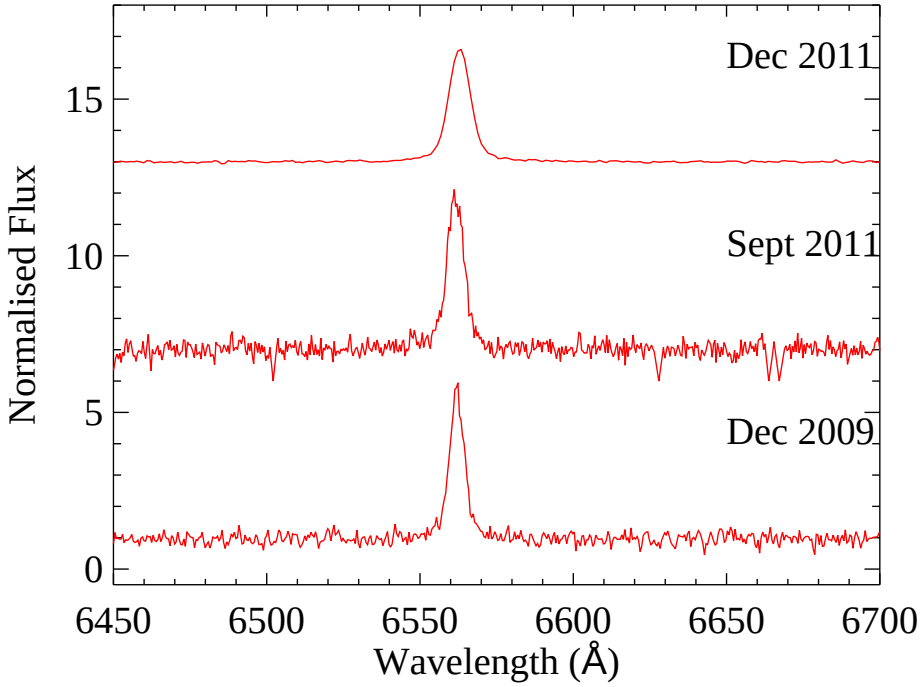

Figure 4.2: Spectra of the OBe star in LXP187 in the red band (wavelength range $\lambda\lambda 6400-6700$Å), taken with the NTT in December 2011 (top panel), and the Radcliffe telescope in December 2009 (bottom panel) and September 2011 (middle panel) (as discussed in Section 4.1). Spectra have been normalised to remove the continuum and shifted by $\sim$ 280 km s^{-1}. The $H\alpha$ emission lines indicate the presence of a circumstellar disc (as discussed in Section 1.1.2.1). The line has a similar equivalent-width in all cases, indicating that the disc has not changed size in $\sim$ 2 yr (equation (2.16)).

Bartlett et al. (2013) use these data to show that LXP187 has other qualities in common with the class of persistent BeXB discussed in Section 1.1.2.1. This class contains at least 6 BeXB that emit persistent, low luminosity ($\sim 10^{34}$ erg s^{-1}) radiation, and have spin periods $\gtrsim$ 150 s. They have a hot thermal excess within their spectra (with blackbody temperatures kT_{BB} >1 keV) that correspond to small emitting regions (<1 km^2). These are attributed to the neutron star's magnetic polar caps (as discussed in Section 1.3). The radius of the caps tend to be inversely proportional to spin period (Bartlett et al., 2013), and hence to the magnetic field of disc-accreting systems that are close to spin equilibrium. LXP187 has the highest luminosity of all members of this class. It also has the shortest spin period. Bartlett et al. (2013) show that LXP187 has a hot thermal excess, corresponding to a blackbody component with a temperature of $kT_{BB} = 1.8 \pm ^{0.2}_{0.3}$ keV, and a radius of 0.5 $\pm$ 0.2 km. The unabsorbed flux from the blackbody component accounts for $\sim$40% of the total X-ray emission. This value varies as the neutron star rotates, and decreases with increasing energy. This is consistent with the idea that the pulsations are coming from the geometry associated with a pencil beam (discussed

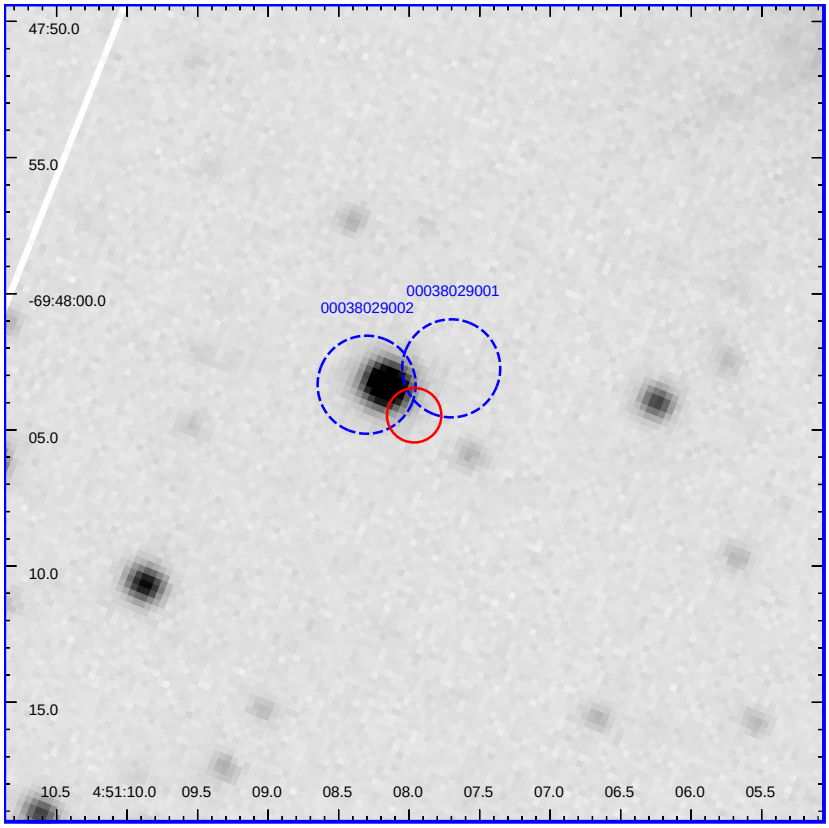

Figure 4.3: The location of LXP187 (as discussed in Section 4.1). V-band image taken with EFOSC2 on the NTT, with 1σ error circles from Swift/XRT (blue) and XMM-Newton/EPIC (red). Swift/XRT data were taken on 23rd October 2008 (right, labelled 00038029001) and 11th November 2008 (left, labelled 00038029002). Image credit: Bartlett et al. (2013).

further in Section 1.3).

Bartlett et al. (2013) modelled the XMM-Newton pulse-profile using the Beloborodov (2002) approximation (discussed in Section 3.2.1). They assumed a $z+1$ value of 1.24, and found i and θ to be 53° and 70° (although these numbers are degenerate), with a χ^2_r of 0.54 (as shown in Figure 4.5). This suggests LXP187 is a class III system, with two poles that are both only sometimes visible.

In Sections 4.2-4.3, I determine the average L, P, and $\dot{P}$ for LXP187 over ~ 3.5 yr, and apply the same methods used in Chapter 2 to show that LXP187 most likely contains a neutron star that is accreting via an accretion disc, from a non-truncated circumstellar disc. It is not close to spin equilibrium and is spinning up on average. LXP187 has a longer spin period than all of the non-spin equilibrium SXP discussed in Chapters 2 and 3. If the results of Chapter 2 are correct - that CRSF sources have lower magnetic fields than the SXP sources because the CRSF sources are not close to spin equilibrium, whereas most SXP sources are - then we would expect the neutron star in LXP187 to have a similar magnetic field to the CRSF sources. The magnetic field of the neutron

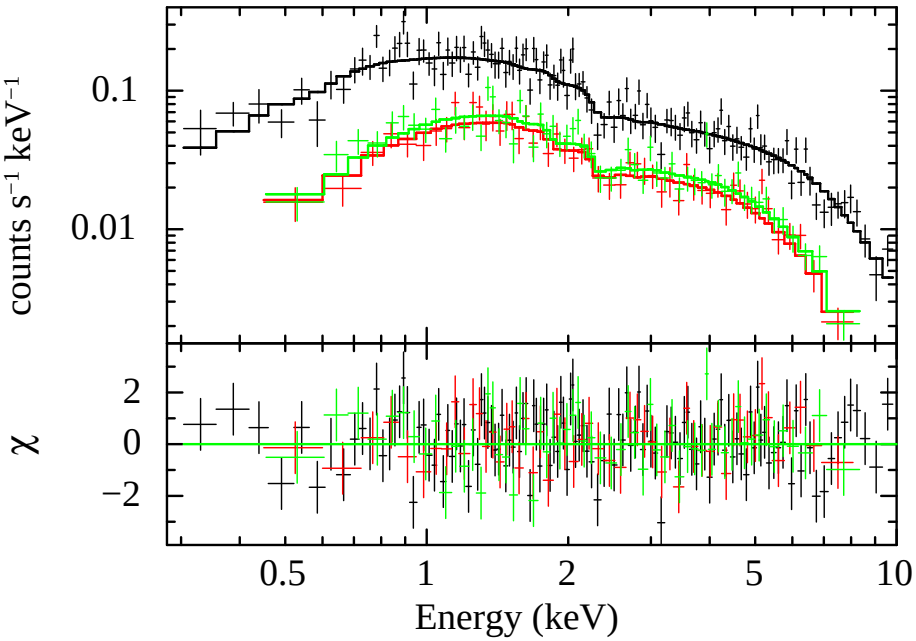

Figure 4.4: The 0.2-10.0 keV EPIC-pn (black), EPIC-MOS1 (red), and EPIC-MOS2 (green) spectra of LXP187, showing a blackbody component (as discussed in Section 4.1). The top panel shows the background subtracted spectrum with best fit power-law plus blackbody model, and the bottom panel shows residuals. The spectrum is composed using data from XMM-Newton/EPIC. Image credit: Bartlett et al. (2013).

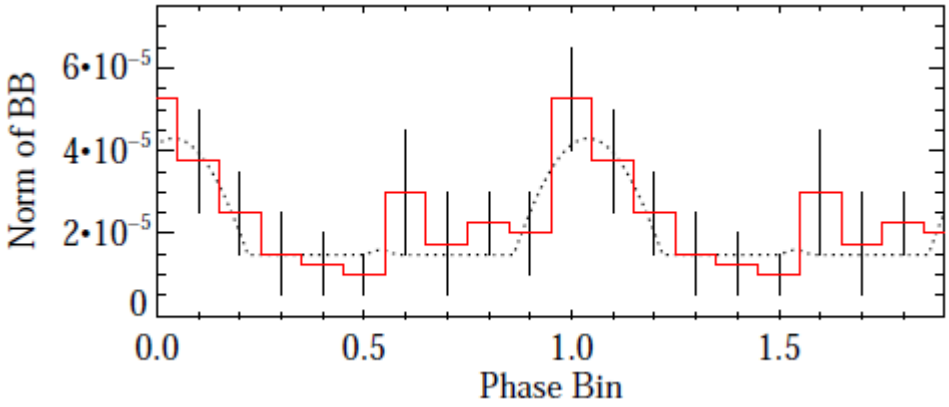

Figure 4.5: Pulse-profile of LXP187, composed using data from XMM-Newton/EPIC (red line), with results from the Beloborodov (2002) approximation (black dots) (as discussed in Sections 4.1 and 3.2.1). The phase-shift is arbitrary. Image credit: Bartlett et al. (2013).

star in LXP187 is determined using the same methods as in Chapter 2, and is found to be $\sim 1.4 \times 10^{13}$ G, consistent with the conclusions of Chapter 2.

Work from this chapter has previously been published as Klus et al. (2013), where the spectra of LXP187 were originally analysed by E.S. Bartlett, who produced Figures 4.1 and 4.2, and classified the OBe star as a B0-B1 III-V star.

An outline of this chapter is as follows: observations are discussed in Section 4.2, with X-ray observations in Section 4.2.1, optical observations in Section 4.2.2, and observations regarding the magnetic field in Section 4.2.3. Results are given in Section 4.3, starting with results from X-ray observations in Section 4.3.1, including a brief discussion of the spin period and luminosity given in Bartlett et al. (2013), followed by the results of optical observations in Section 4.3.2, and finally results regarding the magnetic field in Section 4.3.3. Conclusions are given in Section 4.4, including a discussion of how the results for LXP187 relate to SXP and CRSF sources.

4.2 Observations

4.2.1 X-ray Observations

4.2.1.1 Swift/XRT

Swift/XRT is a CCD imaging spectrometer, operating over 0.2-10 keV in photon counting mode. Archival data were downloaded from NASA's High Energy Astrophysics Science Archive Research Center (HEASARC)[1], as summarised in Table 4.1.

Images were extracted using the *ftool*[2] *xselect*. Source and background spectra were then extracted from regions of 34″ radii. The spectra were binned to 50 counts per bin. The ancillary response files (ARF) were calculated with *xrtmkarf*, and a redistribution matrix file (RMF) was taken from HEASARC's calibration database (CALDB). The position of the source was confirmed using *ftool xrtcentroid*.

The total count-rate and error of each dataset, as well as the intrinsic hydrogen column density (N_H) and photon index, were calculated using *ftool xspec*. The spectra were described by an absorbed power-law with a fixed Galactic foreground column density of 8.4×10^{20} cm^{-2} (Dickey and Lockman, 1990) and abundances set in accordance with Wilms et al. (2000). Intrinsic absorption and the abundances of elements heavier than helium, were set to 0.4 (Borkowski et al., 2006). X-ray spectra were then compiled in *xspec* over 0.2-10 keV, and in four energy-bands, with approximately equal count-rates of 0.5-1.5, 1.5-3, 3-4.5, and 4.5-8 keV. The 0.2-10 keV flux of each dataset was also

[1] http://heasarc.gsfc.nasa.gov/
[2] http://heasarc.nasa.gov/ftools/

Instrument	Start Date	Exposure/ End Date	Energy-band	Average P (s)	Average L (10^{37} erg s^{-1})
Swift/XRT	23.10.2008	6.56 ks	0.2 - 10 keV	186.6 ± 0.3	
Swift/XRT	11.11.2008	6.40 ks	0.2 - 10 keV	(180.8 ± 0.3)	0.67 ± 0.04
RXTE	28.10.2011	9.005 ks	3 - 10 keV		
RXTE	28.10.2011	0.849 ks	3 - 10 keV	169.8 ± 0.3	
XMM-Newton	17.07.2012	7 ks	0.2 - 10 keV	168.5 ± 0.2	0.098 ± 0.009
Swift/BAT	16.12.2004	31.05.2010	14 - 195 keV		
INTEGRAL	02.01.2003	21.12.2010	15 keV- 10 MeV		
OGLE	14.09.2001	15.05.2012	I		
MACHO	03.11.1992	14.12.1999	R		
MACHO	03.11.1992	29.12.1999	B		

Table 4.1: Summary of datasets used in Chapter 4, where values of P and L are derived by combining all datasets of a given instrument, results in parenthesis are also considered (as discussed in Section 4.2.1.1). Results from XMM-Newton are taken from Bartlett et al. (2013) (as discussed in Section 4.2).

determined using *xspec*. The luminosity was then calculated using a distance of 50.6 ± 1.6 kpc to the LMC (Bonanos et al., 2011).

The light-curves of each dataset were extracted in *xselect*. The two datasets were combined and a Lomb-Scargle normalised periodogram was produced using time-series analysis package *Period*[3], with a frequency interval of 1×10^{-5} Hz. Pulse-profiles were also produced for the combined dataset over 0.2-10 keV, and over the four energy-bands mentioned above. The 0.2-10 keV pulse-profile, binned to 30 bins per phase, was then modelled using the Beloborodov (2002) approximation (discussed in Section 3.2.1).

4.2.1.2 RXTE/PCA

Archival data from RXTE/PCA were taken from HEASARC. These were recorded in two datasets, both on the 28th October 2011, over 3-10 keV, as summarised in Table 4.1. Cleaned light-curves were produced for each dataset and combined. A Lomb-Scargle normalised periodogram and pulse-profile was then created using *Period*, with a frequency interval of 1×10^{-5} Hz. The pulse-profile, binned to 30 bins per phase, was then modelled using the Beloborodov (2002) approximation (discussed in Section 3.2.1).

4.2.1.3 Swift/BAT

The Swift/BAT data were taken with the Hard X-ray Transient Monitor from 16th December 2004 to the 31st May 2010, over 14-195 keV, as summarised in Table 4.1. A 58 month light-curve was downloaded from NASA's Swift/BAT 58-Month Hard X-ray

[3]http://www.starlink.rl.ac.uk/docs/sun167.htx/sun167.html

Survey[4]. This contained an average of ∼15 observations per day split into 9 energy-bands. Plots of count-rate as a function of time were produced for energy ranges of 14-50, 50-75, 75-150, and 150-195 keV, as well as for the full 14-195 keV range, with one bin per month.

4.2.1.4 INTEGRAL/IBIS

The INTEGRAL/IBIS data were taken from 2nd January 2003 to the 21st December 2010, over 15 keV - 10 MeV, as summarised in Table 4.1. A plot of count-rate as a function of time was produced with 30 bins.

4.2.2 Optical observations

4.2.2.1 OGLE III/IV

Optical Gravitational Lensing Experiment (OGLE) III/IV data were taken from 14th September 2001 to 16th May 2012 in the I-band, as summarised in Table 4.1. A plot of count-rate as a function of time was produced, and a Lomb-Scargle normalised periodogram and pulse-profile was then created using *Period*, with a frequency interval of 1×10^{-5} Hz.

4.2.2.2 MACHO

Archival data were taken from the MACHO project's 1.27 m telescope, located at the Mount Stromlo Observatory in Australia. This covered the period from 1st November 1992 to the 29th December 1999, and contains instrumental magnitudes using red (R) and blue (B) filters, as summarised in Table 4.1. The data were filtered to remove results flagged as erroneous. The four points remaining in the R-band dataset that were over 2.4σ from the mean were also removed. Lomb-Scargle normalised periodograms and pulse-profiles were then created using *Period* for both the R and B-band datasets, using frequency intervals of 1×10^{-5} Hz.

4.2.3 Accretion methods and magnetic fields

The long-term average L and P are derived using data taken from Swift/XRT, RXTE/PCA, and XMM-Newton/EPIC, where the XMM-Newton/EPIC data are taken from Bartlett et al. (2013). The same method is then followed as in Chapter 2. A weighted $\dot{P}$ is found by fitting the time evolution of P using MPFITEXPR[5]. The mass

[4] http://swift.gsfc.nasa.gov/docs/swift/results/bs58mon/
[5] www.physics.wisc.edu/∼craigm/idl/down/mpfitexpr.pro

and radius of the OBe star are determined from its spectral type and luminosity class, as given in Klus et al. (2013), and M_{dyn} is assumed to be 80% of M_{spec} (as discussed in Section 2.3). The radius of the OBe star's circumstellar disc is determined from its *EW* $H\alpha$ (equation (2.16)), where the *EW* $H\alpha$ is also taken from Klus et al. (2013). It is assumed that $e = 0.3 \pm 0.2$, $M_{NS} = 1.4\ M_{\odot}$, and R_{NS}=10 km, unless otherwise stated. Equations (1.1)-(1.7), and (2.11)-(2.12), are used to determine whether or not LXP187 is disc-accreting. Equations (1.34) and (1.36) are then used to determine its magnetic field.

4.3 Results

4.3.1 X-ray Results

4.3.1.1 Swift/XRT

Figure 4.3 shows the positions calculated for the Swift/XRT datasets on 23rd October and 11th November 2008. The first dataset has an RA, Dec (J2000) of 04:51:06.4 and -69:48:02.5, and the second has an RA, Dec (J2000) of 04:51:07.0 and -69:48:03.1, both have a 2σ error radius of $3.6''$. The photon index is determined to be 0.7 ± 0.1, and the average luminosity is $(6.7 \pm 0.4) \times 10^{36}$ erg s^{-1}. Figure 4.7 shows the Lomb-Scargle normalised periodogram for the combined datasets. This shows the 186.6 ± 0.3 s spin period and the two side-peaks mentioned by Beardmore et al. (2009), where the peak at 180.8 s is slightly higher than the 186.6 s peak. These results are given in Table 4.1.

The side-peaks in the periodograms are due to gaps in the observations. This was confirmed firstly by fitting sine waves, with periods of 186.6 s and 180.8 s, to the data, which gave rise to similar peaks, as can be seen in Figures 4.8 and 4.9. Secondly, by splitting the datasets into shorter datasets composed of continuous observations, and adding the individual periodograms, as can be seen in Figure 4.6.

It is not clear why the 180.8 s peak is higher than the 186.6 s peak, and neither Figure 4.8 nor 4.9 are prefect reconstructions of Figure 4.7, and so I will consider both results when determining the system's magnetic field in Section 4.3.3.

Pulse-profiles, folded at 186.6 s and 180.8 s, are shown in Figures 4.10 and 4.11. Neither is well-fit by the Beloborodov (2002) approximation (discussed in Section 3.2.1). Assuming $P = 186.6$ s, the pulse-profile is best-fit as a class I system, on the border of class II, with a χ^2_r of 1.8, as shown in Figure 4.12. Assuming $P = 180.8$ s, the pulse-profile is best-fit as a class I system, but has a χ^2_r of 3.2. These results are not consistent with those found by Bartlett et al. (2013) (see Figure 4.5), who suggest that LXP187 is a class III system.

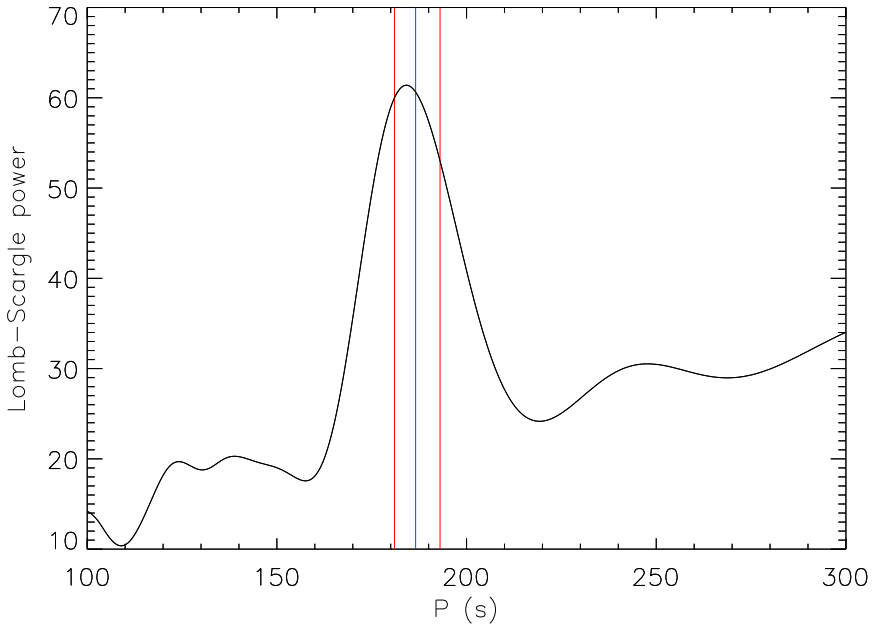

Figure 4.6: Lomb-Scargle normalised periodogram for LXP187, from the combined Swift/XRT datasets over 0.2-10 keV (as discussed in Section 4.3.1.1). To remove spikes due to gaps in the data, the datasets were split into 13 shorter datasets composed of continuous observations. The individual periodograms were then added together. The 186.6 ± 0.3 s period is highlighted (blue line), as are the two side-peaks, of 181 s and 193 s mentioned by Beardmore et al. (2009) (red lines).

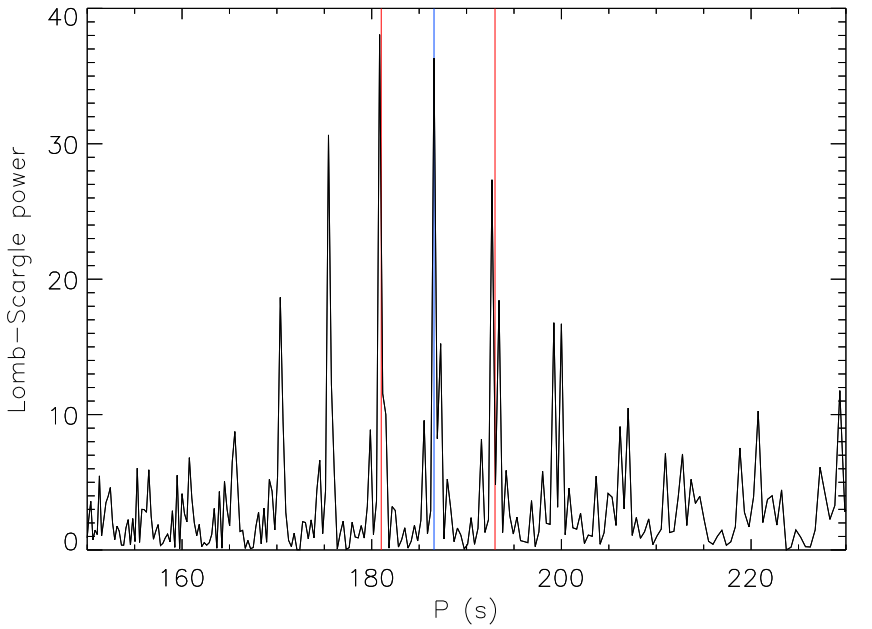

Figure 4.7: As for Figure 4.6 but using a combined dataset with non-continuous observations.

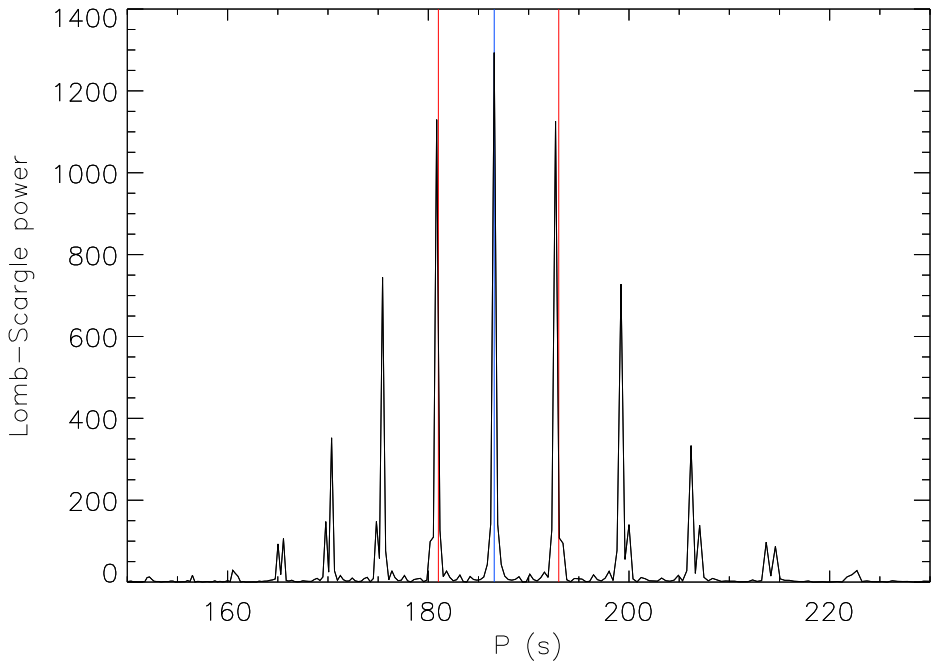

Figure 4.8: Lomb-Scargle normalised periodogram; the results of a simulated Swift/XRT dataset composed of a sine wave with a period of 186.6 ± 0.3 s, as discussed in Section 4.3.1.1.

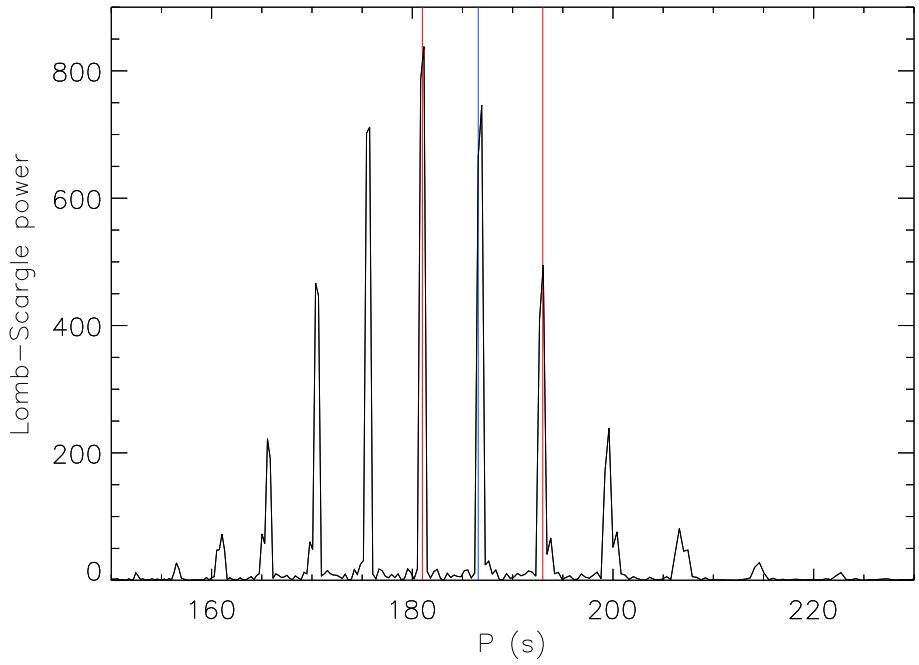

Figure 4.9: As for Figure 4.8, except the period of the simulated results is 180.8 ± 0.3 s rather than 186.6 ± 0.3 s.

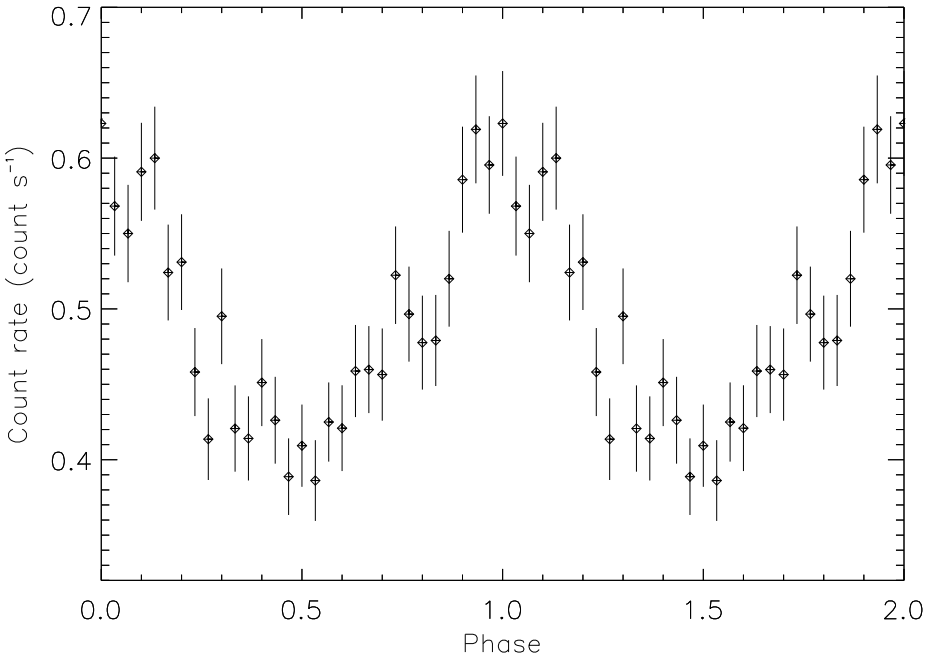

Figure 4.10: Pulse-profile for LXP187 from the combined Swift/XRT datasets, folded at 186.6 s, over 0.2-10 keV (as discussed in Section 4.3.1.1). The phase-shift is arbitrary.

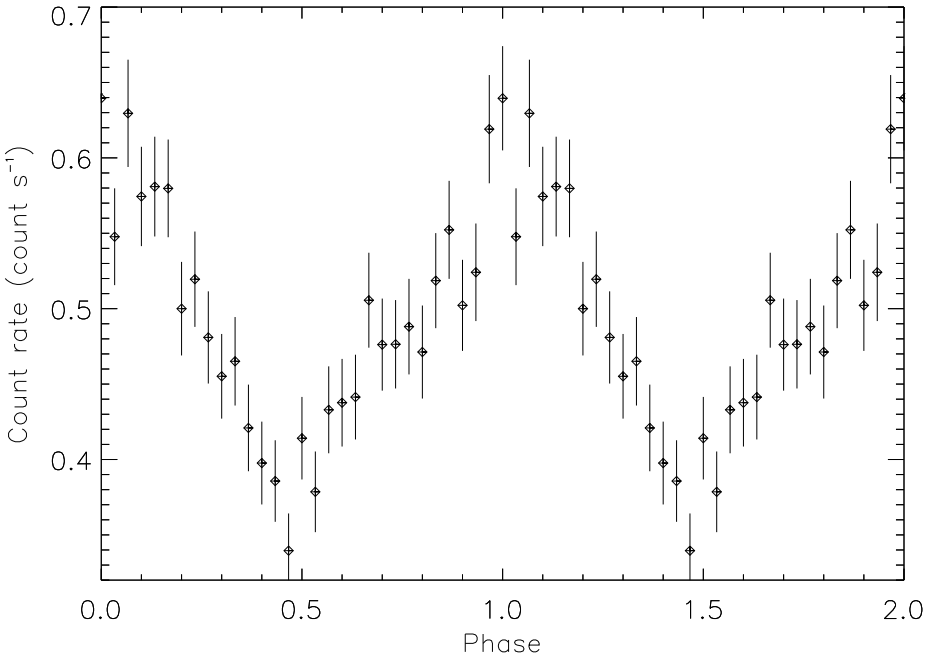

Figure 4.11: As for Figure 4.10, except folded at 180.8 s rather than 186.6 s.

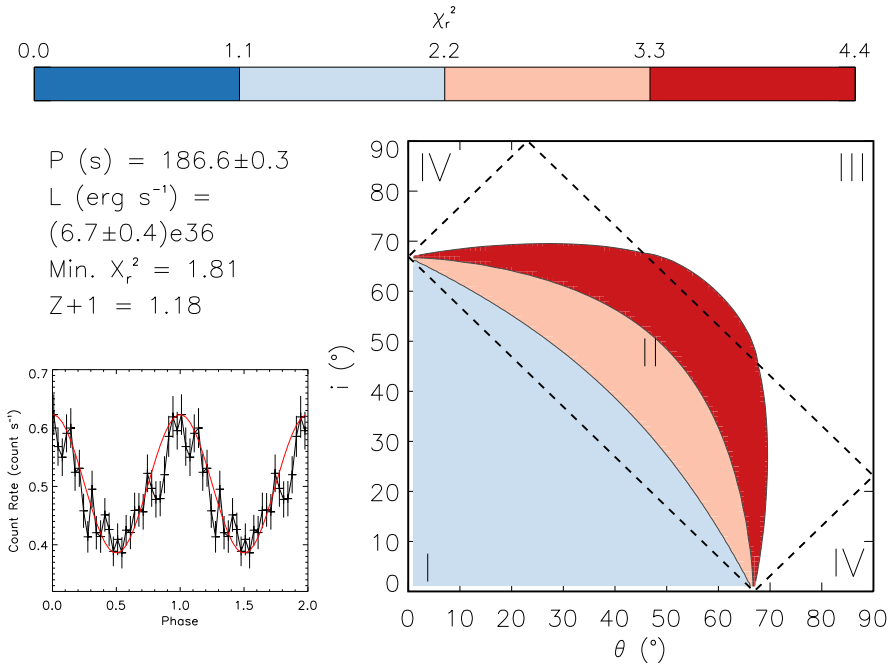

Figure 4.12: χ^2_r contour plot for LXP187 from the combined Swift/XRT datasets, assuming $P = 186.6$ s (as discussed in Section 4.3.1.1). This shows the χ^2_r between the pulse-profile (left; black; also shown in Figure 4.10) and the Beloborodov (2002) approximation (discussed in Section 3.2.1). The best-fit values of i and θ are in the blue area of the contour plot, and the best-fit model is plotted (left; red).

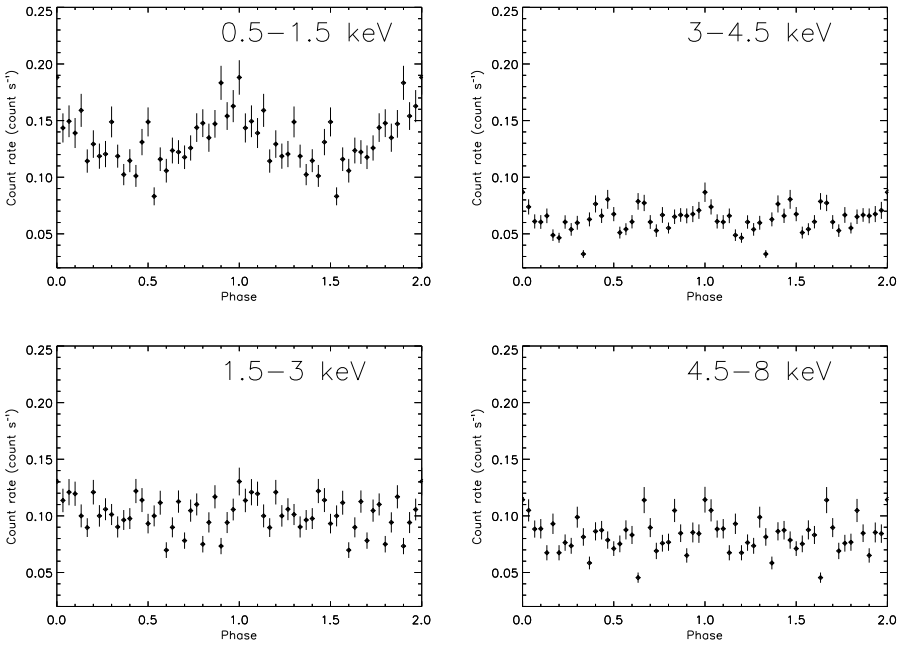

Figure 4.13: Pulse-profiles for LXP187, folded at 186.6 s, from the combined Swift/XRT datasets over 0.5-1.5, 1.5-3, 3-4.5, and 4.5-8 keV (as discussed in Section 4.3.1.1). Energy increases from top to bottom, left to right. The phase-shift is arbitrary.

Pulse-profiles were also made for the combined datasets, folded at 186.6 s, in four energy-bands with approximately equal count-rates; these are 0.5-1.5, 1.5-3, 3-4.5, and 4.5-8 keV, as shown in Figure 4.13. The pulse-fraction appears to decrease with increasing energy. This is consistent with observations by Bartlett et al. (2013), although the large error bars make this inconclusive.

4.3.1.2 RXTE/PCA

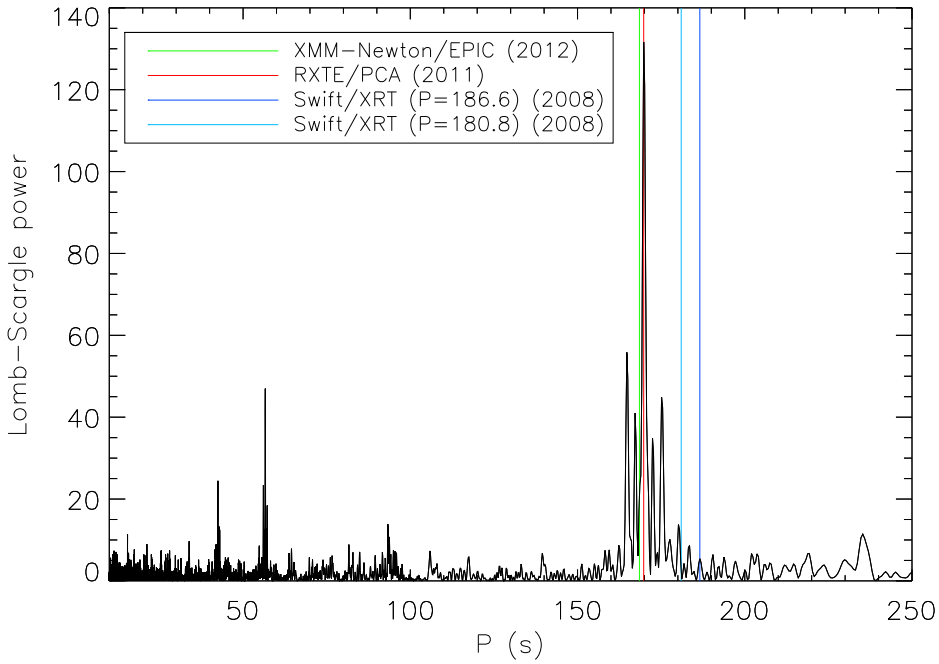

Figure 4.14: Lomb-Scargle normalised periodogram for LXP187, from the combined RXTE datasets over 3-10 keV, as discussed in Section 4.3.1.2. The spin period is highlighted (red), as is the spin period found from the Swift/XRT data, taken three years previously, assuming $P = 186.6$ s (dark blue) and $P = 180.8$ s (light blue), and the spin period found by Bartlett et al. (2013) using data from XMM-Newton/EPIC taken in 2012 (green). Harmonics can be seen at 1/3 and 1/4 of the pulse period (at 56.6 s and 42.45 s).

Lomb-Scargle normalised periodograms, created from the RXTE data, are shown in Figures 4.14 and 4.15. These give a period of 169.8 ± 0.3 s, as shown in Table 4.1. As with the Swift/XRT data, the side-peaks are due to gaps in the observations. This was confirmed by fitting a sine wave with the same period to the data, as can be seen in Figure 4.16. The harmonics, at exactly 1/3 and 1/4 of the pulse period (at 56.6 s and 42.45 s) indicate that the pulse-profile should be non-sinusoidal. The pulse-profile is shown in Figure 4.17, where results from the Beloborodov (2002) approximation are over-plotted in red. The pulse-profile shows a large dip in the peak, and so is not well-fit, with a best-fit χ^2_r of 96.

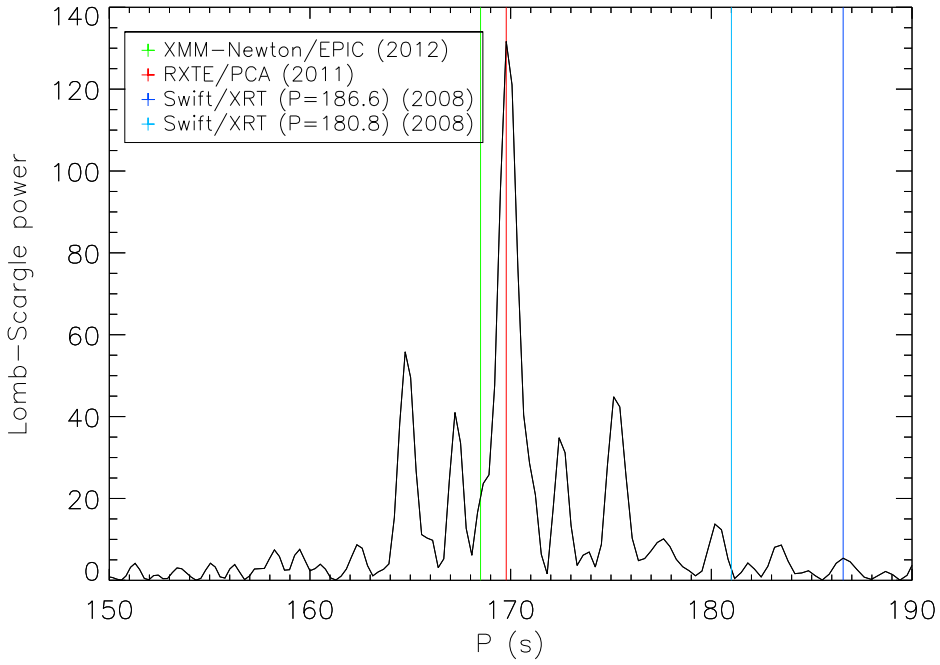

Figure 4.15: As for Figure 4.14 but showing a smaller range of P.

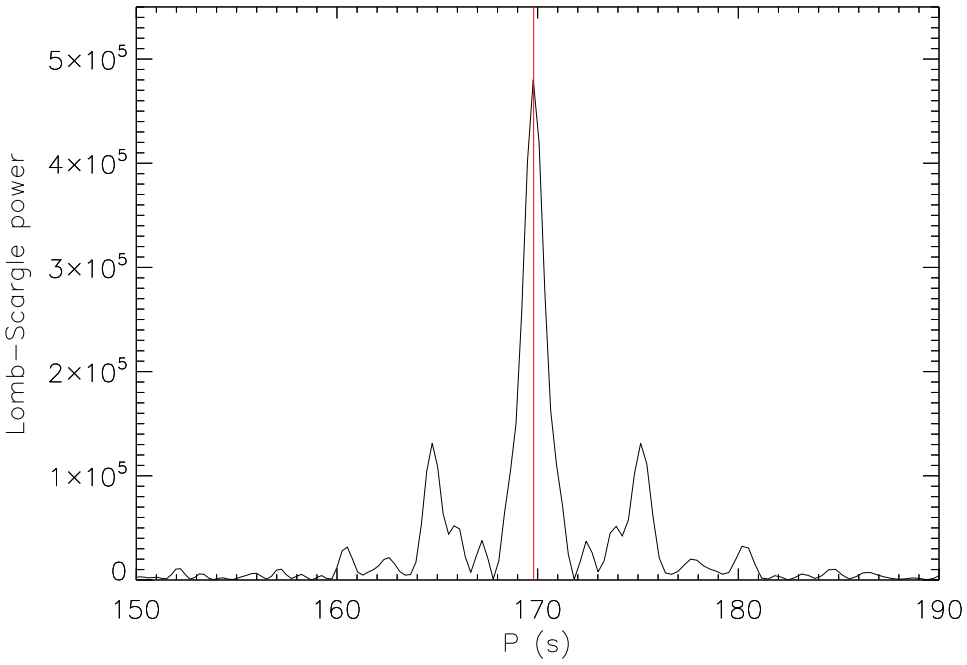

Figure 4.16: Lomb-Scargle normalised periodogram; the results of a simulated RXTE dataset composed of a sine wave, as discussed in Section 4.3.1.2.

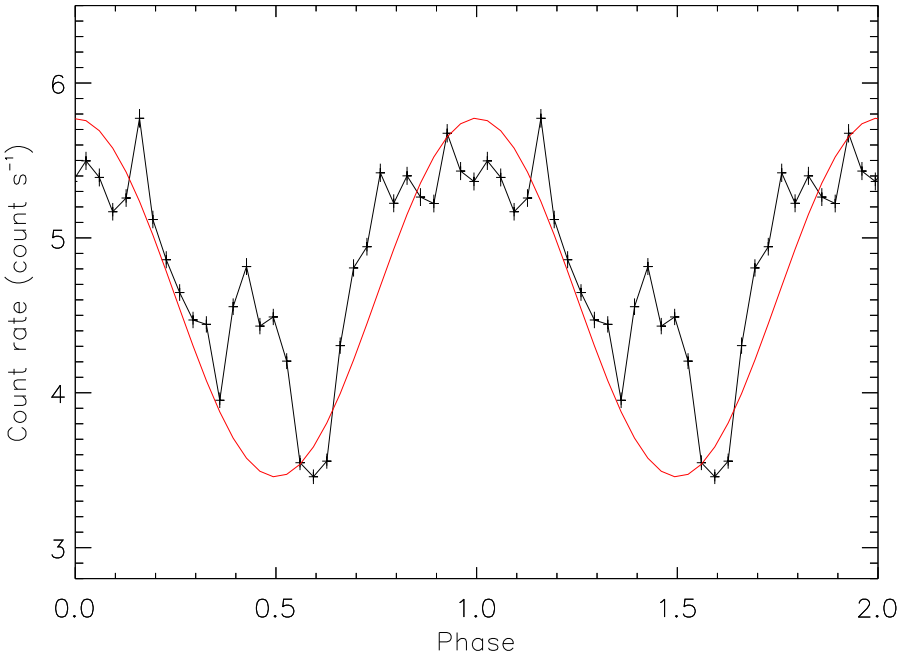

Figure 4.17: Pulse-profile for LXP187, from the combined RXTE datasets over 3-10 keV (as discussed in Section 4.3.1.2). The best-fit results from the Beloborodov (2002) approximation (discussed in Section 3.2.1) are over-plotted (red). The phase-shift is arbitrary.

Both the Swift/XRT and RXTE pulse-profiles produce results from the Beloborodov (2002) approximation that are inconsistent with those found by Bartlett et al. (2013). The Swift/XRT profile is best fit (with a χ^2_r of 1.8) as a class I system, on the border of class II. The pulse-profile taken with the RXTE data cannot be fit. The XMM-Newton/EPIC data, on the other hand, is very well-fit (with a χ^2_r of 0.54), as a class III system. Although the results from Bartlett et al. (2013) are better fit, it is unclear which, if any, of these fits are correct. This is because the pulse-profiles of a single system can vary enormously (as discussed in Chapter 3).

4.3.1.3 XMM-Newton/EPIC

LXP187 was observed by XMM-Newton/EPIC on 17th July 2012 (Bartlett et al., 2013). Bartlett et al. (2013) confirmed the position of LXP187 to be at an RA, Dec (J2000) of 04:51:06.7 and -69:48:04.2 respectively, with a 1σ uncertainty of $1''$. This is shown in Figure 4.3. The luminosity was found to be $(9.8 \pm 0.9)\times10^{34}$ ergs s^{-1}, and the spin period 168.5 $\pm$ 0.2 s, as shown in Table 4.1. This is either 12.5 or 18.1 s less than the spin period calculated from Swift/XRT data in 2008 (depending on whether the period from the Swift/XRT data is assumed to be 180.8 s or 186.6 s), as is shown in Figure 4.14.

4.3.1.4 Swift/BAT

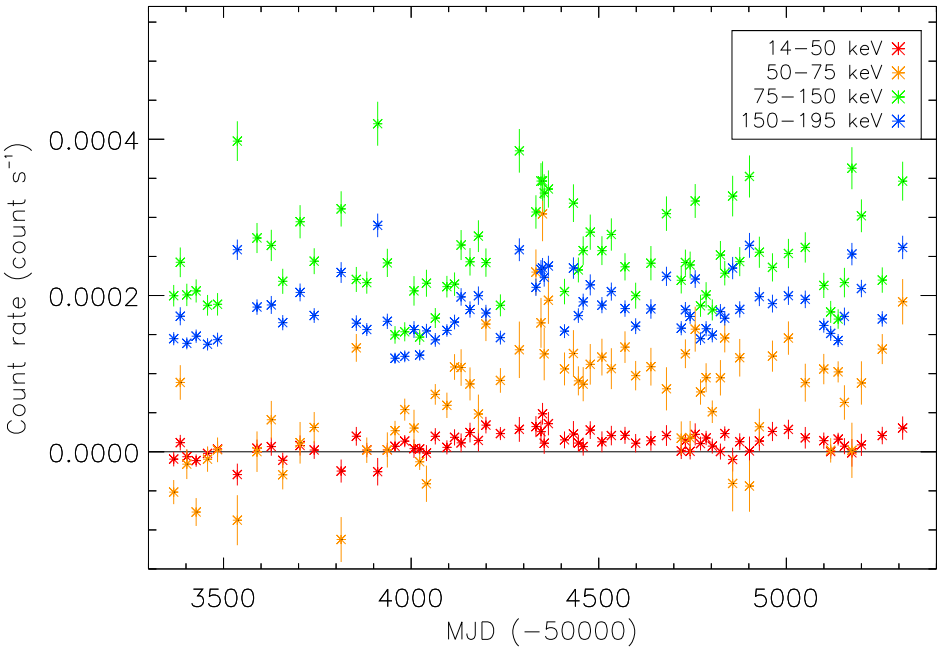

Figure 4.18: Long-term light-curve for LXP187, from Swift/BAT data, over a range of energy-bands with approximately equal count-rates; these are 14-50 keV (red), 50-75 keV (orange), 75-150 keV (green), and 150-195 keV (blue) (as discussed in Section 4.3.1.4). The black line indicates 0 counts.

Figure 4.18 shows the long-term light-curve for LXP187 in energy-bands of 14-50, 50-75, 75-150, and 150-195 keV. The count-rate in the 14-50, 75-150, and 150-195 keV bands remain fairly constant. The count-rate in the 50-75 keV range, however, begins to increase at ∼MJD 54000, peaking at ∼ MJD 54350.

The middle panel of Figure 4.19 shows the long-term light-curve of LXP187 over the total energy range of 14-195 keV. This shows that LXP187 has been a persistent X-ray source for at least 5 years. The persistent X-ray activity is almost certainly related to the consistency in the EW $H\alpha$, and hence the size of the OBe star's circumstellar disc.

4.3.1.5 INTEGRAL/IBIS

The light-curve compiled from the INTEGRAL/IBIS data is shown in the top panel of Figure 4.19. It shows a slight increase in count-rate over time.

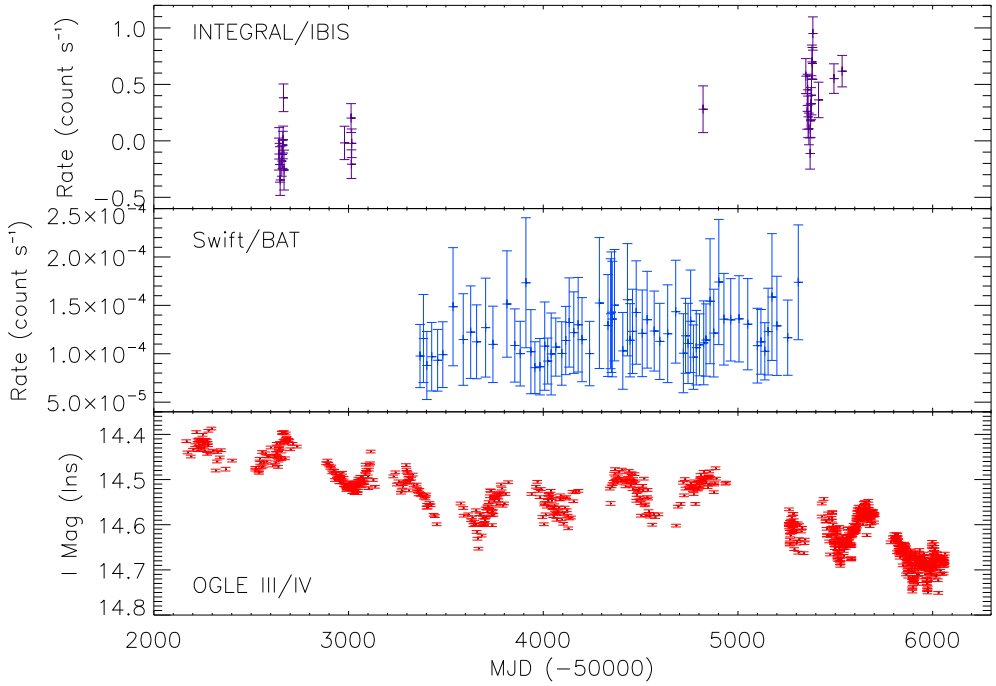

Figure 4.19: Long-term light-curves for LXP187 from INTEGRAL/IBIS (15 keV - 10 MeV; top), Swift/BAT (14-195 keV; middle), and OGLE III and IV (I-band; bottom) (as discussed in Section 4.3.1.4).

4.3.2 Optical results

4.3.2.1 OGLE III/IV

The light-curve compiled from the OGLE III and IV I-band data is shown in the bottom panel of Figure 4.19. It shows a decrease in brightness over time. The Lomb-Scargle normalised periodogram is shown in Figure 4.20. It shows a peak at 440.5 d. Other peaks are present, indicating that other time-scale changes are occurring, and that the 440.5 d period is unlikely to be directly related to the orbital period. These long-term changes may be due to fluctuations in the stellar wind, or precessional motion of the circumstellar disc. There is no evidence of the 21.631 d period found in the MACHO data (as discussed in Section 4.3.2.2). However, if the better-sampled OGLE IV data are merged with the MACHO data (normalised to the approximate starting magnitude of the OGLE III data), then the strength of the 21.631 d peak in the Lomb-Scargle power spectrum increases slightly. The pulse-profile, folded on the 440.5 d modulation, is shown in Figure 4.21.

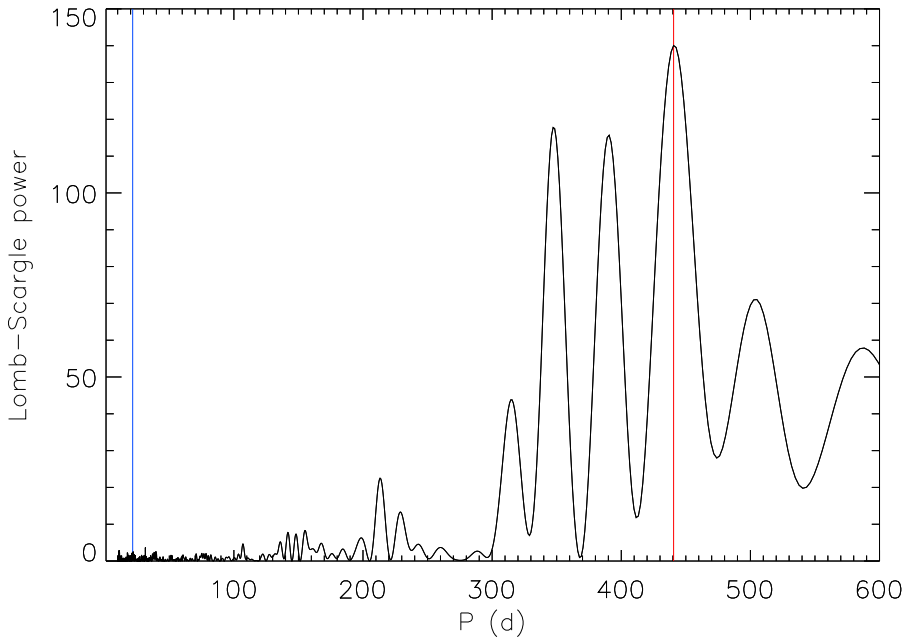

Figure 4.20: Lomb-Scargle normalised periodogram for LXP187, using data from OGLE III/IV (as discussed in Section 4.3.2.1). The 440.5 d peak is highlighted (red), as is the 21.631 d period found in the MACHO data (blue).

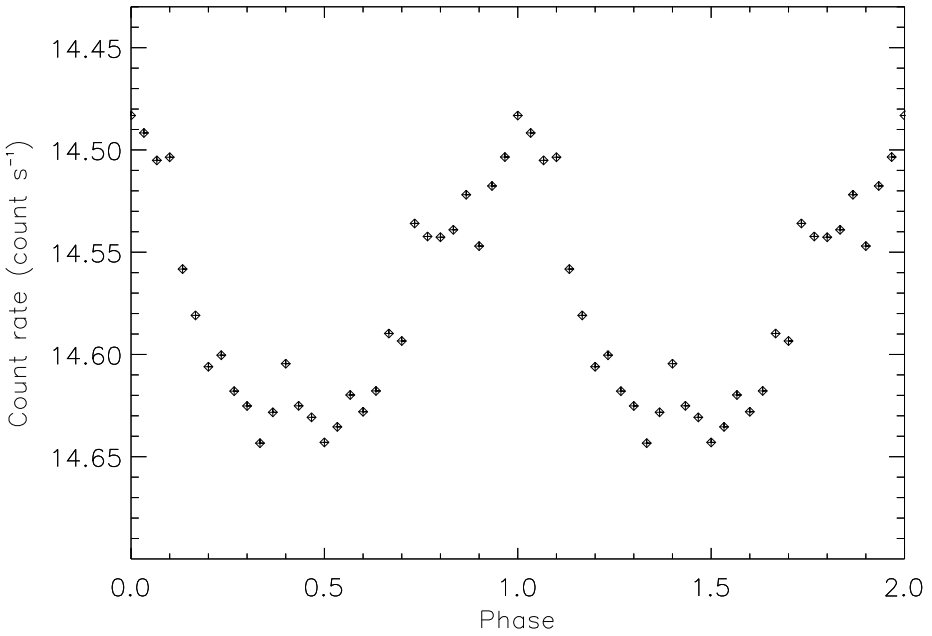

Figure 4.21: Pulse-profile for LXP187, using data from OGLE III/IV, folded on the 440.5 d long-term modulation (as discussed in Section 4.3.2.1). The phase-shift is arbitrary.

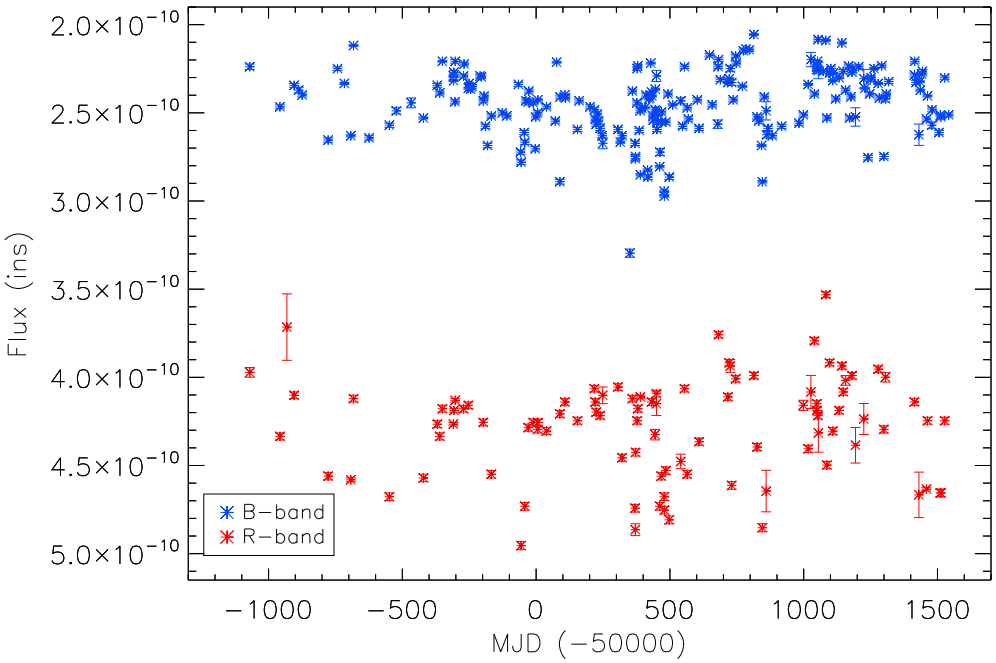

Figure 4.22: Light-curves for LXP187 in the B (blue) and R (red) energy-bands, using data from MACHO (as discussed in Section 4.3.2.2).

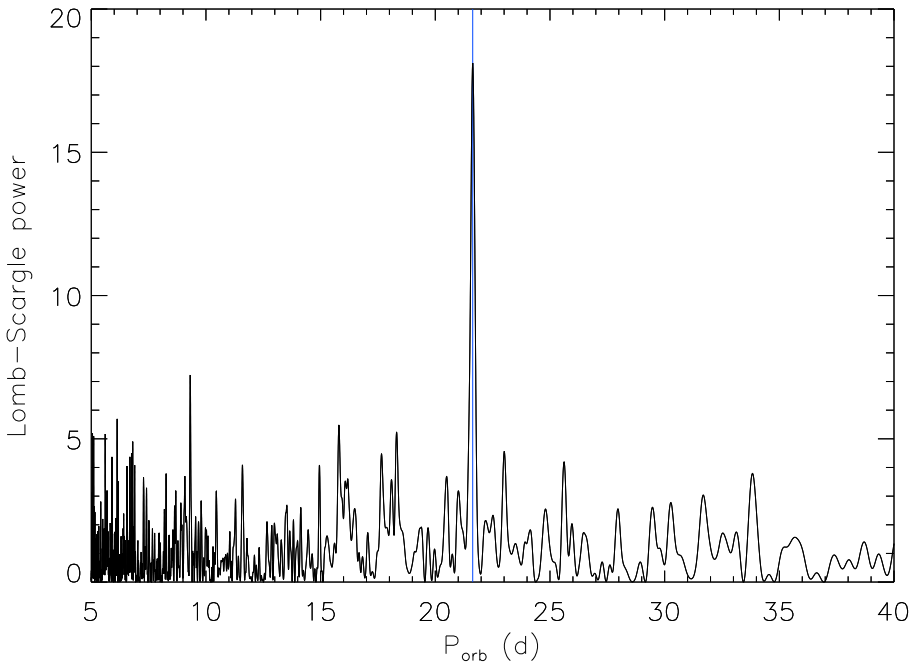

Figure 4.23: Lomb-Scargle normalised periodogram for LXP187, from the B-band MACHO dataset. A possible orbital period of 21.631 d is highlighted (blue) (as discussed in Section 4.3.2.2).

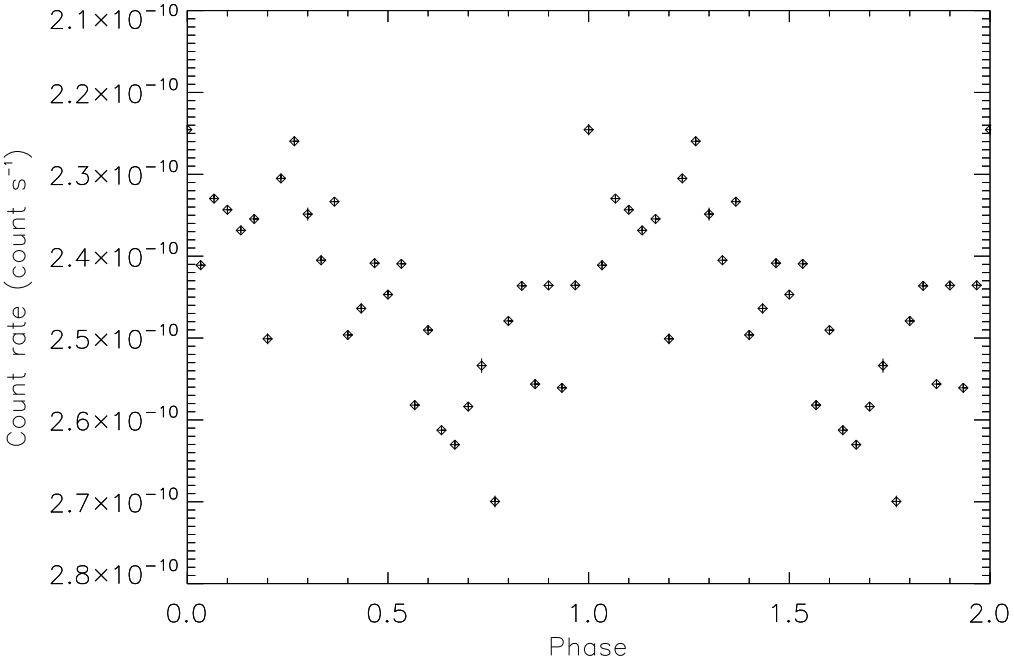

Figure 4.24: Pulse-profile for LXP187, from the B-band MACHO dataset (as discussed in Section 4.3.2.2). The phase-shift is arbitrary.

4.3.2.2 MACHO

Figure 4.22 shows that the flux of the optical companion to LXP187 appears to have remained fairly consistent in the B and R-bands over 7 years (from 1992-1999). The B-band data show a possible orbital period of 21.631 ± 0.005 d as shown in Figure 4.23, although any underlying non-radial pulsations from the OBe star may affect the results (Bird et al., 2012). Non-radial pulsations occur when some parts of the stellar surface move inwards, while other parts move outwards. The pulse-profile of the B-band data is shown in Figure 4.24.

The ∼ 21.6 s orbital period is not evident in the R-band data. This is most likely because the R-band data has less than half the data points of the B-band dataset. This is confirmed by randomly removing half of the B-band data points and creating a new Lomb-Scargle normalised periodogram, which also failed to show any evidence of an orbital period.

4.3.3 Accretion methods and magnetic fields

Figure 4.25 shows the spin periods (top) and luminosities (bottom) calculated using data from Swift/XRT, RXTE/PCA, and XMM-Newton/EPIC, as a function of time. The long-term average L is found to be $(3.82 \pm 0.22)\times10^{36}$ erg s^{-1}, and, assuming the

Swift/XRT data has $P = 186.6$ s, then the long-term average P is 174.95 ± 0.28 s, and the line of best-fit between the changing spin periods indicates a $\dot{P}$ of -4.92 ± 0.11 s yr^{-1}. If the Swift/XRT data has $P = 180.8$ s (as discussed in Section 4.3.1.1), then the long-term average P is 173.04 ± 0.27 s, and the line of best-fit between the changing spin periods indicates a $\dot{P}$ of -3.36 ± 0.10 s yr^{-1}. These results are given in Tables 4.1 and 4.2.

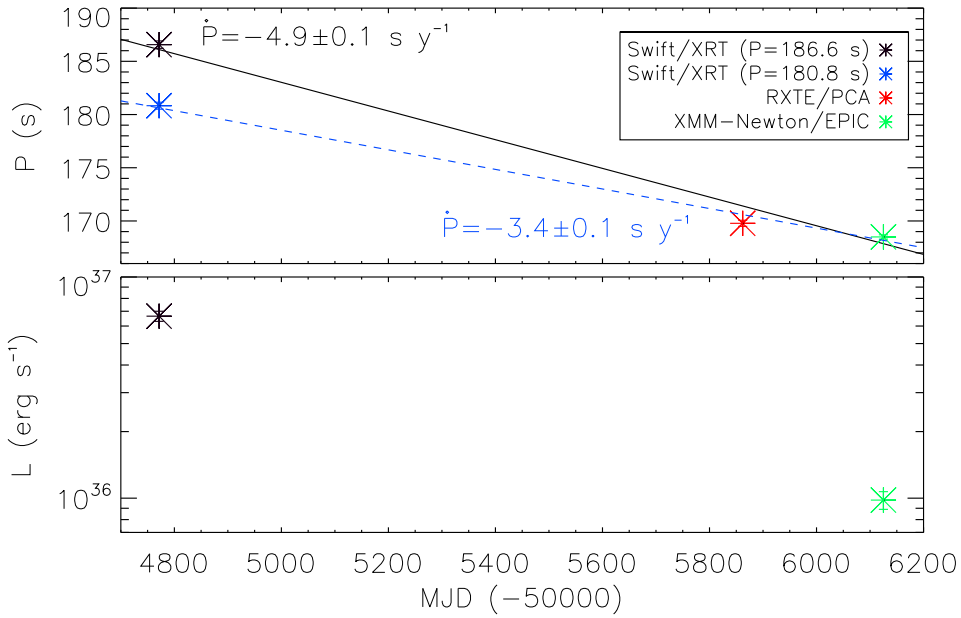

Figure 4.25: P (top), and L (bottom), as a function of MJD for LXP187, using data from Swift/XRT assuming P=186.6 s (black), and P=180.8 s (blue), and data from RXTE/PCA (red), and XMM-Newton/EPIC (green) (as discussed in Section 4.3.3). The black line in the upper panel shows the best-fit $\dot{P}$ assuming the Swift/XRT data has P=186.6 s, and the blue dashed line shows the best-fit $\dot{P}$ assuming the Swift/XRT data has P=180.8 s. The XMM-Newton results are taken from Bartlett et al. (2013).

Orbital parameters are determined assuming that the orbital period taken from the B-band MACHO data is correct, these are given in Table 4.2, and Tables A.1-A.3. Figures 4.26 and 4.27 show that the OBe star in LXP187 has a relatively large, non-truncated circumstellar disc. This makes it similar to SXP4.78, which is also not close to spin equilibrium and spinning up on average.

V_w is determined to be 257 ± 49 km s^{-1}, and V_{orb} to be 302 ± 61 km s^{-1}. This gives a V_{rel} of 45 ± 109 km s^{-1}, for prograde systems, and a V_{Crel} of 233 ± 34 km s^{-1}, assuming the circumstellar disc is non-truncated. These results are given in Table 4.1 and Tables A.4 and A.5, and are shown in Figures 4.28 and 4.29. $V_{rel} < V_{Crel}$, and so the neutron star should be accreting via an accretion disc.

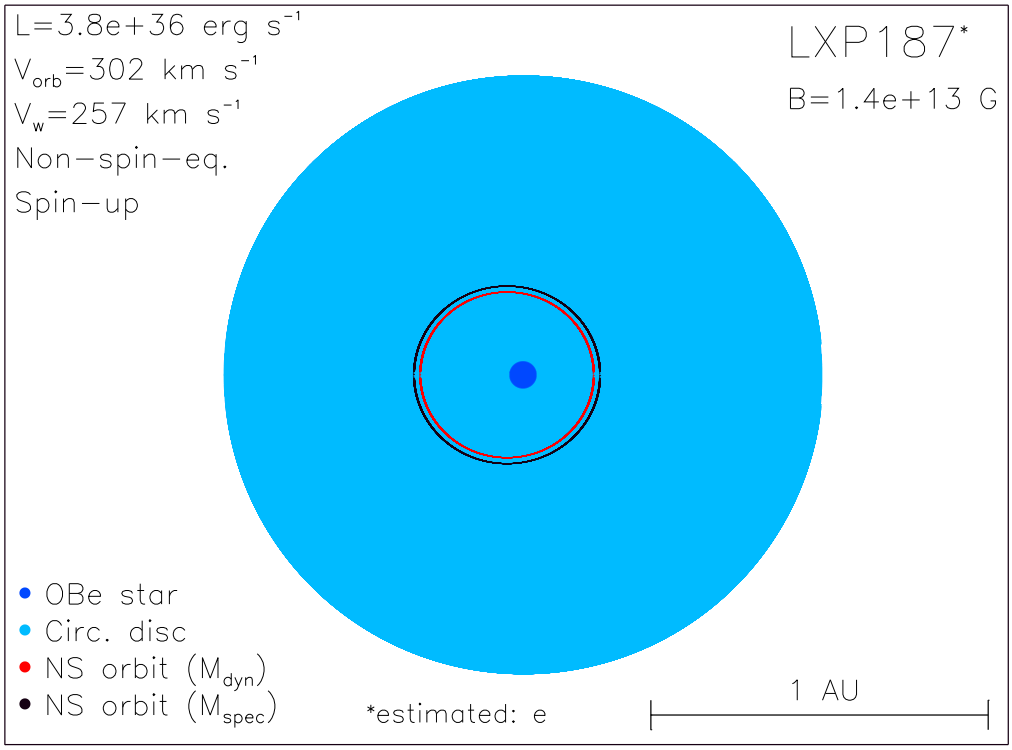

Figure 4.26: Diagram of LXP187 using orbital parameters given in Table 4.2 (and discussed in Section 4.2.3). The spin equilibrium status is determined from Figure 4.25. B corresponds to the magnetic field determined using the Ghosh and Lamb (1979) (equation (1.34)) model (as discussed in Section 4.3.3).

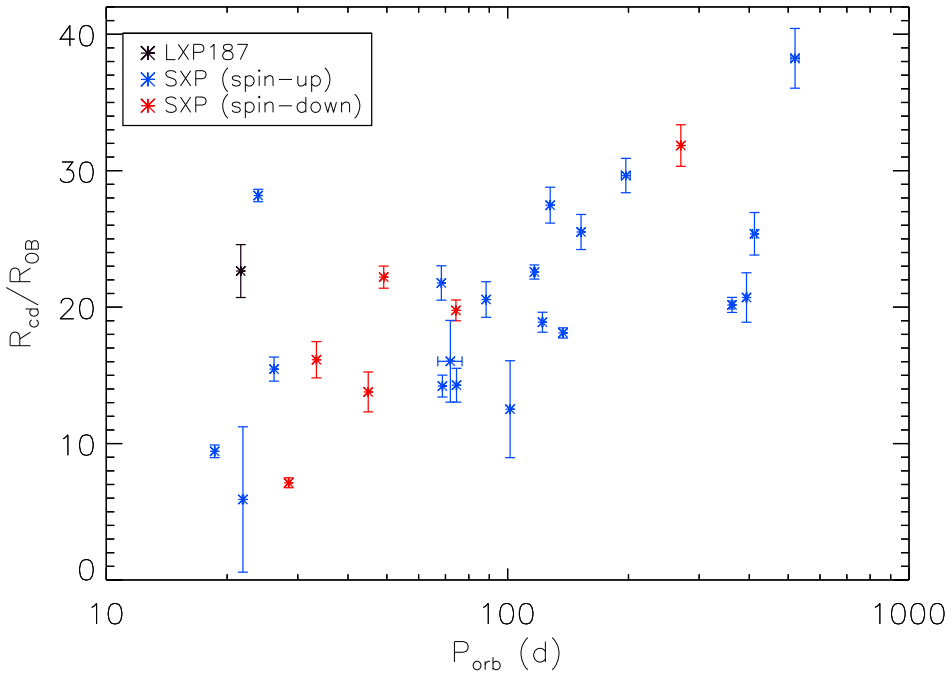

Figure 4.27: The ratio of R_{cd} and R_{OB} (equation (2.16)) as a function of P_{orb}; result for LXP187 (black) over-plotted onto Figure 2.4. LXP187 appears in a similar location to SXP4.78 (as discussed in Section 4.3.3).

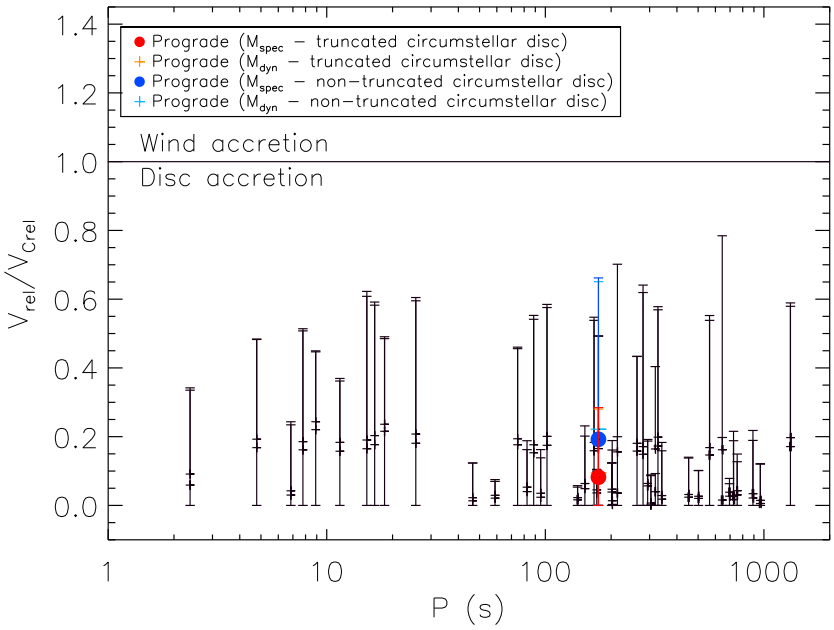

Figure 4.28: The ratio of V_{rel} (equation (2.13)) and V_{Crel}; results for LXP187 over-plotted onto Figure 2.7 (as discussed in Section 4.3.3). V_{Crel} is determined assuming a prograde orbit, and assuming that the OBe star has a circumstellar disc that is (equation (2.12); red) and is not (equation (2.11); blue) truncated by the orbit of the neutron star. LXP187 is expected to contain an OBe star with a non-truncated circumstellar disc, as shown in Figure 4.26. Results for the SXP dataset discussed in Chapters 2 and 3 are shown in black.

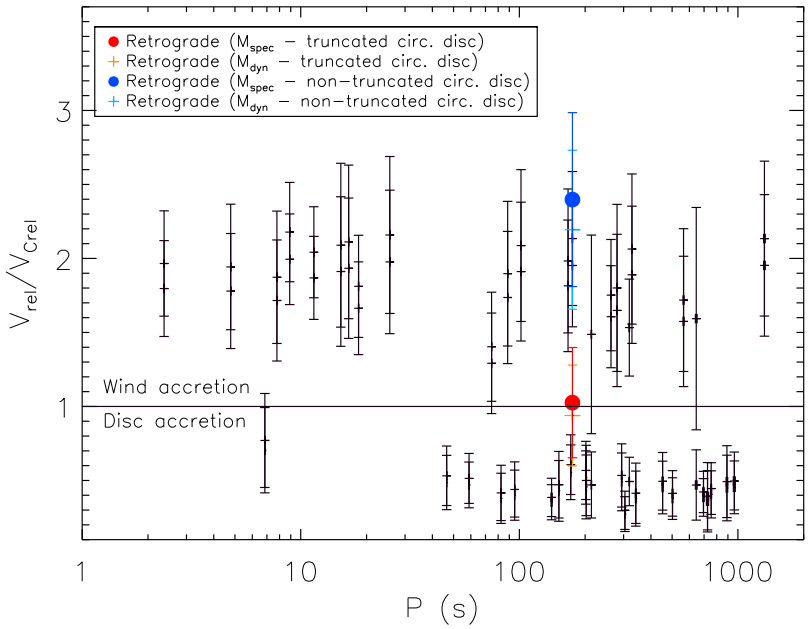

Figure 4.29: As for Figure 4.28 but assuming retrograde, rather than prograde, orbits.

LXP187 is most likely disc-accreting, and cannot be assumed to be close to spin equilibrium, and so the Ghosh and Lamb (1979) and Kluzniak and Rappaport (2007) models are the most appropriate models for determining the magnetic field. These models (discussed in Section 1.2.2) show that the magnetic field of a neutron star in a BeXB, with a given mass and radius, can be determined from $\dot{P}$ and $PL^{3/7}$.

Plots of $\dot{P}$ as a function of $PL^{3/7}$, showing simulated results from the Ghosh and Lamb (1979) and Kluzniak and Rappaport (2007) models for different values of B, are shown in Figures 4.30 and 4.31. Results for LXP187 are over-plotted, as are results for the SXP discussed in Chapters 2 and 3. The results for LXP187 assume M_{NS} =1.4 $M_{\odot}$, but the error bars, which are contained within the symbol, correspond to results using a range of masses between 1 $M_{\odot}$ and 2 $M_{\odot}$. Figure 4.31 shows that LXP187 cannot be well-fit by the simulated spin equilibrium lines for the Ghosh and Lamb (1979) or Kluzniak and Rappaport (2007) models, and this does not change whether it is assumed that the Swift/XRT data has $P = 186.6$ s or $P = 180.8$ s. This means that like $\sim 40\%$ of the SXP discussed in Chapter 2, LXP187 has only one possible result for each model, and like five of those systems (SXP2.37, SXP4.78, SXP11.5, SXP16.6, and SXP91.1), it is not close to spin equilibrium and is spinning up on average.

If it is assumed that the Swift/XRT dataset has $P = 186.6$ s, then the Ghosh and Lamb (1979) model predicts that LXP187 has a surface magnetic field of $(1.41 \pm 0.04)\times10^{13}$ G, and the Kluzniak and Rappaport (2007) model predicts that it has a surface magnetic field of $(5.37 \pm 1.25)\times10^{13}$ G. If it is assumed that the Swift/XRT dataset has $P = 180.8$ s, then the Ghosh and Lamb (1979) model predicts $B = (1.39 \pm 0.04) \times 10^{13}$ G, and the Kluzniak and Rappaport (2007) model predicts $B = (3.96 \pm 0.12) \times 10^{13}$ G. These results are given in Table 4.2, and shown in Figure 4.32. LXP187 would be predicted to have a higher magnetic field if it were closer to spin equilibrium, given the same values of P and L, and assuming it is disc-accreting. The result from equating R_A and R_{co}, for example, is B=$(6.4 \pm 0.2)\times10^{13}$ G. The Shakura et al. (2012) wind accretion model, however, predicts a magnetic field of $(2.9 \pm 2.1)\times10^{12}$ G, assuming the neutron star is in spin equilibrium, wind-accreting, and in a retrograde orbit.

LXP187 is predicted to be subcritical using the Becker et al. (2012) model discussed in Section 2.4. This means that, like most of the SXP discussed in Chapters 2 and 3, the pencil beam in LXP187 is not completely suppressed. The height of the accretion column is therefore inversely proportional to B and L, and is predicted to be $\sim$650 m using equation (2.19), assuming R_{NS} = 10 km, and that results from the Ghosh and Lamb (1979) model give the surface magnetic field. This means that the magnetic field at the top of the accretion column, where CRSF may be present, is $(1.16 \pm 0.04)\times10^{13}$ G, corresponding to an energy of 135 keV (using equation (1.39), assuming CRSF are from electrons, $n = 1$, and M_{NS}=1.4 $M_{\odot}$). These results are given in Table 4.2. Figure 4.33 shows the predicted E_{cyc} for LXP187 and the SXP discussed in Chapters 2 and 3, like many SXP, LXP187 would not be expected to have detectable CRSF.

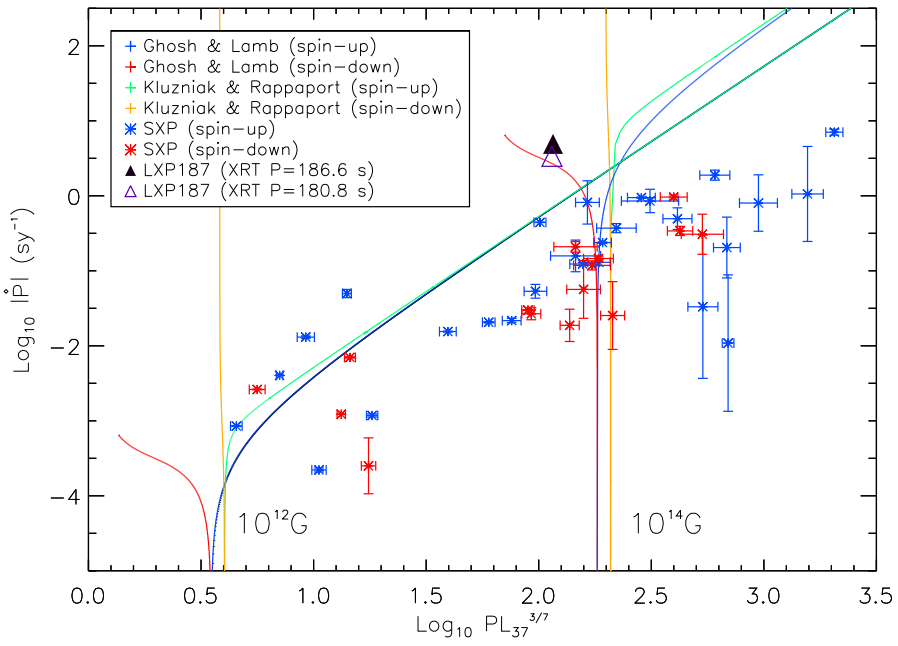

Figure 4.30: $\dot{P}$ as a function of $PL^{3/7}$; results for LXP187 assuming that the spin period from the Swift/XRT data is 186.6 s (black, filled triangle), and 180.8 s (purple triangle), over-plotted onto Figure 2.9. Error bars correspond to results using a range of masses between 1 $M_{\odot}$ and 2 $M_{\odot}$ and are within the size of the symbols (as discussed in Section 4.3.3).

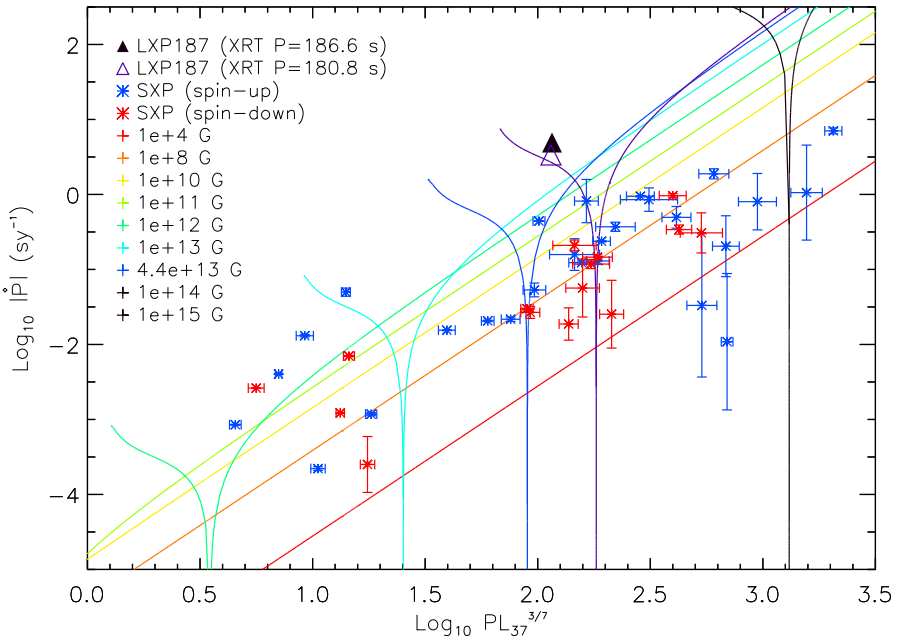

Figure 4.31: As for Figure 4.30, except results over-plotted onto Figure 2.10 rather than Figure 4.30.

Spectral type & luminosity class	B0-B1 III-V
V	14.70 ± 0.02
P_{orb} (d)	21.6310 ± 0.0047
Long-term average EW $H\alpha$ (Å)	-31.1 ± 4.1
Long-term average P (s)	174.95 ± 0.28 [173.04 ± 0.27]
Long-term average L (10^{37} erg s^{-1})	0.382 ± 0.022
Long-term average $\dot{P}$ (s yr^{-1})	-4.92 ± 0.11 [-3.36 ± 0.10]
$M_{OB}/M_{\odot}$	23.0 ± 5.5 (18.4 ± 4.4)
$R_{OB}/R_{\odot}$	11.4 ± 3.1 (10.6 ± 2.9)
$R_{cd}/R_{\odot}$	258 ± 73
$a/R_{\odot}$	95 ± 7 (88 ± 6)
$q/R_{\odot}$	66 ± 20 (62 ± 18)
V_{orb} (km s^{-1})	302 ± 61 (282 ± 56)
V_w (km s^{-1})	257 ± 49 (230 ± 44)
V_{rel} (km s^{-1}) (prograde)	45 ± 109 (52 ± 100)
V_{Crel} (km s^{-1}) (non-truncated)	233 ± 34
V_{Crel} (km s^{-1}) (truncated)	545 ± 167
B (10^{12} G) Ghosh and Lamb (1979) (disc)	14.1 ± 0.4 [13.9 ± 0.4]
B (10^{12} G) Kluzniak and Rappaport (2007) (disc)	53.7 ± 12.5 [39.6 ± 1.2]
Height of accretion column (m)	651 ± 30
Predicted B_{cyc} (10^{12} G)	11.63 ± 0.38
Predicted E_{cyc} (keV)	134.5 ± 4.5

Table 4.2: A summary of results for LXP187. The apparent V magnitude is taken from Massey (2002), and the spectral type, luminosity class, and long-term average EW $H\alpha$ are taken from Klus et al. (2013) (as discussed in Section 4.1). P_{orb} is determined using data from MACHO (discussed in Section 4.3.2.2). P is determined using data from Swift/XRT, RXTE/PCA, and XMM-Newton/EPIC (Bartlett et al., 2013) (as discussed in Section 4.3.3). L is determined using data from Swift/XRT and XMM-Newton/EPIC. A weighted $\dot{P}$ is found by fitting the time evolution of P (as shown in Figure 4.25, and discussed in Section 4.3.3). $M_{OB}/M_{\odot}$ and $R_{OB}/R_{\odot}$ are determined from the spectral type and luminosity class, where results in curved brackets assume M_{dyn} (as discussed in Section 2.3). R_{cd} (equation (2.16)), a (equation (2.9)), q (equation (2.8)), V_{orb} (equation (2.17)), V_w (equation (2.15)), V_{rel} (equation (2.13)), and V_{Crel} (equations (2.2)-(2.9)) are also given (as discussed in Section 4.3.3). B is determined using the Ghosh and Lamb (1979) (equation (1.34)), and Kluzniak and Rappaport (2007) (equation (1.36)) models (as discussed in Section 4.3.3). The height of the accretion column is determined from L and B (determined using the Ghosh and Lamb (1979) model) following Becker et al. (2012) (equations (2.18)-(2.20); discussed in Section 4.3.3). The corresponding predicted B_{cyc} and E_{cyc}, from electrons, from this radius (equations (1.5) and (1.39)) is given assuming $n = 1$. Results assume $P = 186.6$ s for the Swift/XRT data, where results in square brackets assume $P = 180.8$ s (as discussed in Section 4.3.1.1).

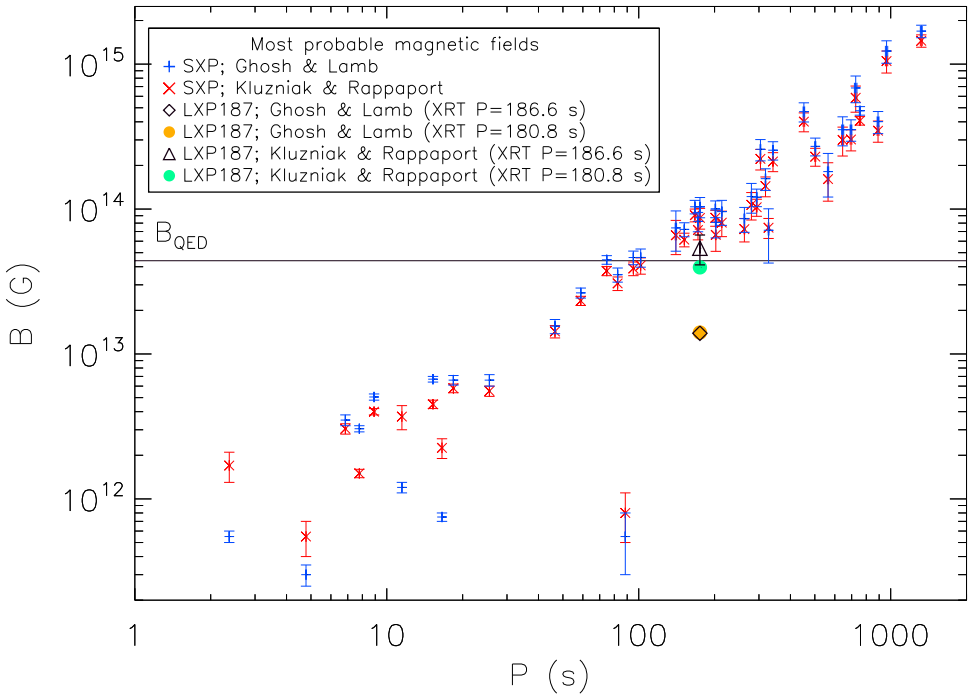

Figure 4.32: B as a function of P; results for LXP187 over-plotted onto Figure 2.16, where B is determined using the Ghosh and Lamb (1979) model assuming the spin period from the Swift/XRT dataset is 186.6 s (equation (1.34); black diamond) and 180.8 s (yellow circle), and the Kluzniak and Rappaport (2007) model assuming the spin period from the Swift/XRT dataset is 186.6 s (equation (1.36); black triangle) and 180.8 s (green circle).

4.4 Discussion and conclusions

Beardmore et al. (2009) show that LXP187 is part of a persistent BeXB in the LMC containing a neutron star with a ∼187 s spin period, and a V=14.70 OBe star. They suggest an orbital period of ∼21.6 d. In Klus et al. (2013) we showed that the optical component of this BeXB is a B0-B1 III-V star, with a circumstellar disc that has remained relatively constant in size over ∼ 2 yr, corresponding to an average EW $H\alpha$ of ∼-31 Å. Bartlett et al. (2013) show that LXP187 has a hot thermal excess, corresponding to a blackbody component with a radius of 0.5 ± 0.2 km. This is almost certainly the neutron star's magnetic polar cap.

In Sections 4.1-4.3, I show that the spin period, luminosity, and pulse-profiles of LXP187 change over time. The pulse-profile taken from the Swift/XRT data, corresponding to a luminosity of $(6.7 \pm 0.4) \times 10^{36}$ erg s^{-1} and a spin period of 186.6 ± 0.3 s, is shown in Figures 4.10 and 4.12. It is reasonably well-fit by the Beloborodov (2002) approximation as a class I system on the border of class II. A class I system has one pole that is always visible, and a class II system also has a second pole that is sometimes visible when the

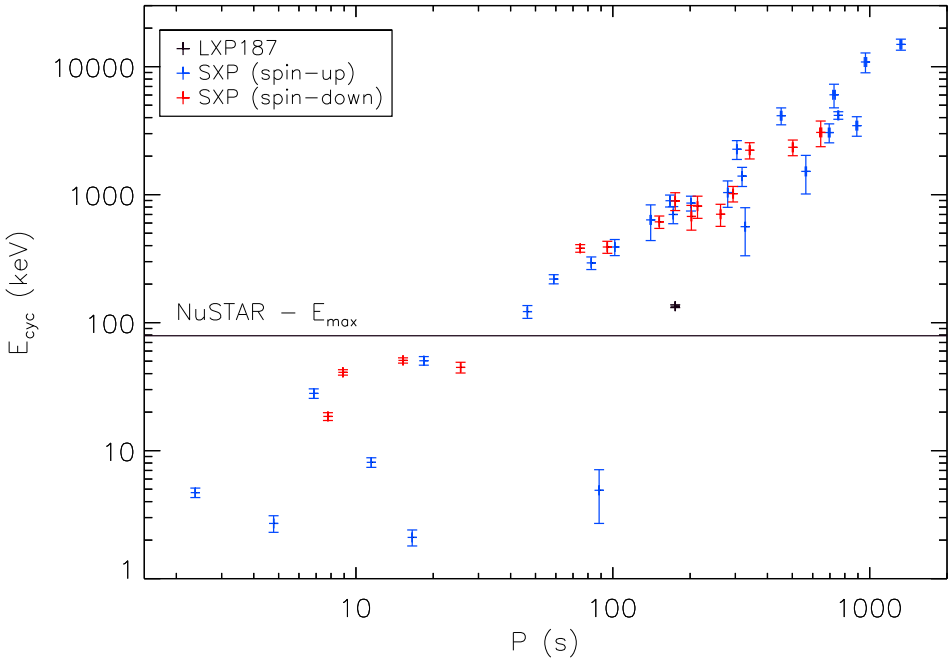

Figure 4.33: Predicted E_{cyc}, from electrons, as a function of P; result for LXP187 (black) determined using the Becker et al. (2012) model (equations (2.18)-(2.20), and equation (1.39), using B determined from the Ghosh and Lamb (1979) model), over-plotted onto Figure 2.25 (as discussed in Section 2.4). The black line indicates the maximum energy range of NASA's NuStar (Nuclear Spectroscopic Telescope Array Mission), and shows that, like many SXP, LXP187 would not be expected to have detectable CRSF (as discussed in Section 4.3.3).

first pole is at its dimmest (as discussed in Section 3.2.1). A dip appears in the bottom of the pulse-profile as the neutron star spins up to 169.8 ± 0.3 s. This is shown in Figure 4.17, using data from RXTE. As the spin period decreases to 168.5 ± 0.2 s, and the luminosity decreases to $(9.8 \pm 0.9)\times10^{34}$ ergs s^{-1}, the dip changes position so that the system is well-fit by the Beloborodov (2002) approximation as a class III system (Bartlett et al., 2013). This is shown in Figure 4.5, using data from XMM-Newton.

In Section 4.3, I show that LXP187 is most likely accreting via an accretion disc, from a non-truncated circumstellar disc. It is not close to spin equilibrium, and is spinning up on average. This is most likely due to its persistent accretion, which is almost certainly related to the fact that the OBe star's circumstellar disc has remained at a constant size over $\sim$ 2 yr. This means that the magnetic field is best described by the Ghosh and Lamb (1979) and Kluzniak and Rappaport (2007) models, which predict magnetic fields of $(1.41 \pm 0.04) \times 10^{13}$ G and $(5.37 \pm 1.25) \times 10^{13}$ G respectively (assuming $M_{OB} = M_{spec}$). The height of the accretion column is predicted to be ∼650 m, corresponding to an energy of $\sim$ 135 keV, too high to be detected by most X-ray telescopes.

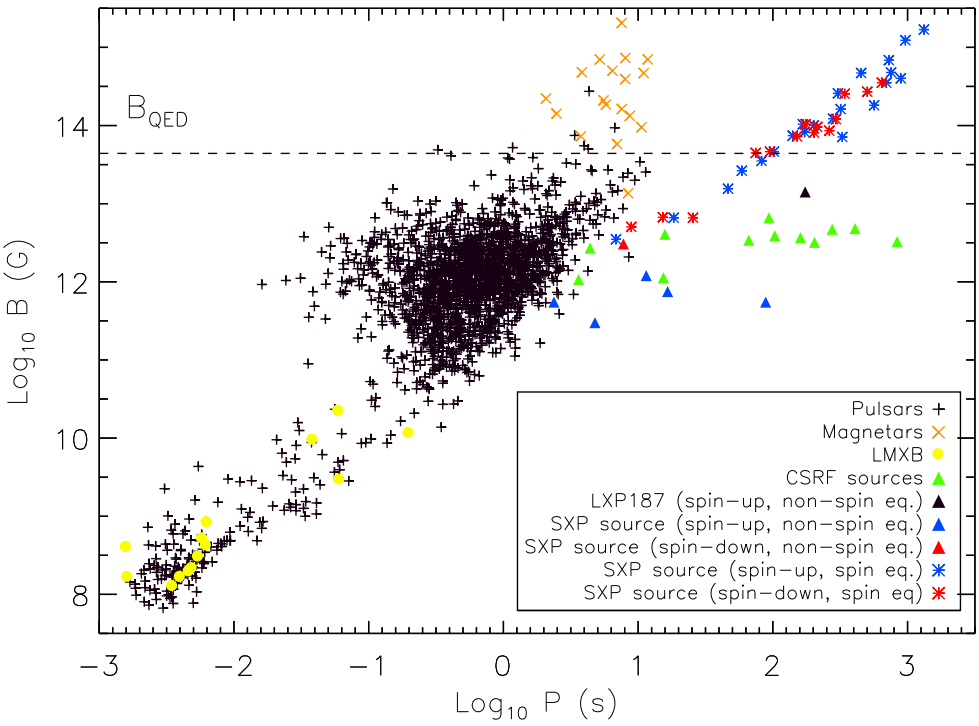

Figure 4.34: B as a function of P; result for LXP187 (black triangle), determined using the Ghosh and Lamb (1979) (equation (1.34)) model, over-plotted onto Figure 2.17 (as discussed in Section 4.4).

In Chapter 2, I concluded that the magnetic fields of most SXP are higher than those of CRSF sources because CRSF sources are not close to spin equilibrium, whereas most SXP are. Results from LXP187 support these conclusions. Figure 4.34 shows results for LXP187 over-plotted onto Figure 2.17. This shows B as a function of P for most known neutron stars, where LXP187, which is not close to spin equilibrium, has a similar magnetic field to the CRSF sources.

Chapter 5

Conclusions and future work

5.1 Conclusions

In Chapter 2, I showed that 42 BeXB in the SMC contain neutron stars that are disc-accreting. Approximately half are expected to be accreting from a circumstellar disc that is truncated by the orbit of the neutron star, and ∼85% are expected to be close to spin equilibrium; the exceptions being SXP2.37 (SMC X-2), SXP4.78, SXP7.78 (SMC X-3), SXP11.5, SXP16.6, and SXP91.1, where all are spinning up on average except for SXP7.78, which is spinning down. I determined the most likely surface magnetic field for the neutron star in each system, given its spin equilibrium status, using the Ghosh and Lamb (1979) and Kluzniak and Rappaport (2007) models. I found that $\sim 2/3$ systems, including all systems with $P \gtrsim 100$ s, are predicted to contain neutron stars with $B > B_{QED}$ (where B_{QED}=4.4×10^{13} G). This means that all neutron stars in binary systems that are close to spin equilibrium follow the same relationship between P and B, as is shown in Figure 4.34.

The neutron stars in BeXB can also have their surface magnetic fields measured directly, via CRSF. Galactic BeXB that have had their magnetic fields measured in this way are predicted to have magnetic fields of $\sim 10^{12} - 10^{13}$ G. It is difficult to measure magnetic fields $> 10^{13}$ G using CRSF from electrons. This is because $E_{cyc} \propto B$, and CRSF are no longer within the observable energy-bands of most X-ray telescopes above $\gtrsim 10^{13}$ G, as shown in Figure 4.33.

I suggest that most of the neutron stars in the BeXB in this dataset are predicted to have higher magnetic fields than CRSF sources because the CRSF sources are not close to spin equilibrium, whereas most of the BeXB in this dataset are. I predict that if the CRSF sources were close to spin equilibrium, then they would require much stronger magnetic fields, and CRSF would not be visible in the X-ray spectrum.

If $\sim 2/3$ neutron stars in BeXB have $B > B_{QED}$, and only one BeXB, LSI+61°303, is known to have undergone magnetar-like outbursts (Torres et al., 2012; Papitto et al., 2012), then this suggests that this behaviour may be rare for neutron stars with $B > B_{QED}$. This behaviour may be related to age (Thompson et al., 2002). It may also be related to spin period, since BeXB with magnetar-strength magnetic fields have spin periods $\gtrsim 100$ s and do not tend to undergo these outbursts, whereas magnetars, which have spin periods of $\sim 2 - 10$ s, do. This means that $\sim 2/3$ isolated neutron stars may have $B > B_{QED}$, but remain unobserved. The fact that $\sim 2/3$ neutron stars in the BeXB in this dataset have $B > B_{QED}$ may also mean that magnetic field decay occurs more slowly than previously thought (Pons et al., 2009).

In Chapter 3, I created pulse-profiles for every observation used in Chapter 2, I then visually inspected them, and modelled them using the Beloborodov (2002) approximation. I found that the pulse-profiles contained a variety of features, including asymmetry, dips, and double-peaked structure, which vary both within and across individual systems. Most pulse-profiles were not well-fit by the Beloborodov (2002) approximation. Assuming that double-peaked structure indicates a transition from a pencil beam to a fan beam, systems containing neutron stars with relatively longer spin periods seem to transition to a fan beam at lower luminosities than systems containing neutron stars with relatively shorter spin periods, as shown in Figure 3.10. These results are inconclusive, however, because of the subjective nature of classification; it is sometimes difficult to distinguish between double-peaked structure and dips, which produce the same shape in pulse-profiles.

In Chapter 4, I apply the same methods used in Chapter 2 to LXP187, a persistent BeXB located in the LMC. I show that it is most likely accreting via a disc, that it is not close to spin equilibrium, and that it is spinning up on average. LXP187 has a longer spin period than any of the SXP discussed in Chapters 2 and 3 that are not close to spin equilibrium (the next longest being SXP91.1). This allows us to compare its magnetic field to those of CRSF sources, which I suggest cannot be close to spin equilibrium. I show that LXP187 is predicted to have a similar magnetic field to the CRSF sources. This is consistent with the conclusions of Chapter 2 - that the magnetic field of most SXP are higher than those of CRSF sources because CRSF sources are not close to spin equilibrium, whereas most SXP are. The magnetic field of LXP187 is slightly too high for CRSF to be observed using most X-ray telescopes (as shown in Figure 4.33), adding credence to the idea that most BeXB have magnetic fields that are not observable via CRSF.

5.2 Future work

In Section 5.1, I suggested that $\sim 2/3$ neutron stars may have $B > B_{QED}$, and that the magnetic field of most SXP are higher than those of CRSF sources because CRSF sources are not close to spin equilibrium, whereas most SXP are.

Evidence of magnetic fields $> B_{QED}$ could be obtained if any of these systems undergo a magnetar-like gamma-ray outburst. However, the fact that only one BeXB, LSI+61°303, is known to have undergone magnetar-like outbursts suggests that this behaviour is rare (Torres et al., 2012; Papitto et al., 2012).

Evidence that the CRSF sources are not close to spin equilibrium could be obtained by determining their long-term average L, P, and $\dot{P}$. This would allow us to determine their magnetic fields using the Ghosh and Lamb (1979) and Kluzniak and Rappaport (2007) models, to see if they match the values determined by CRSF.

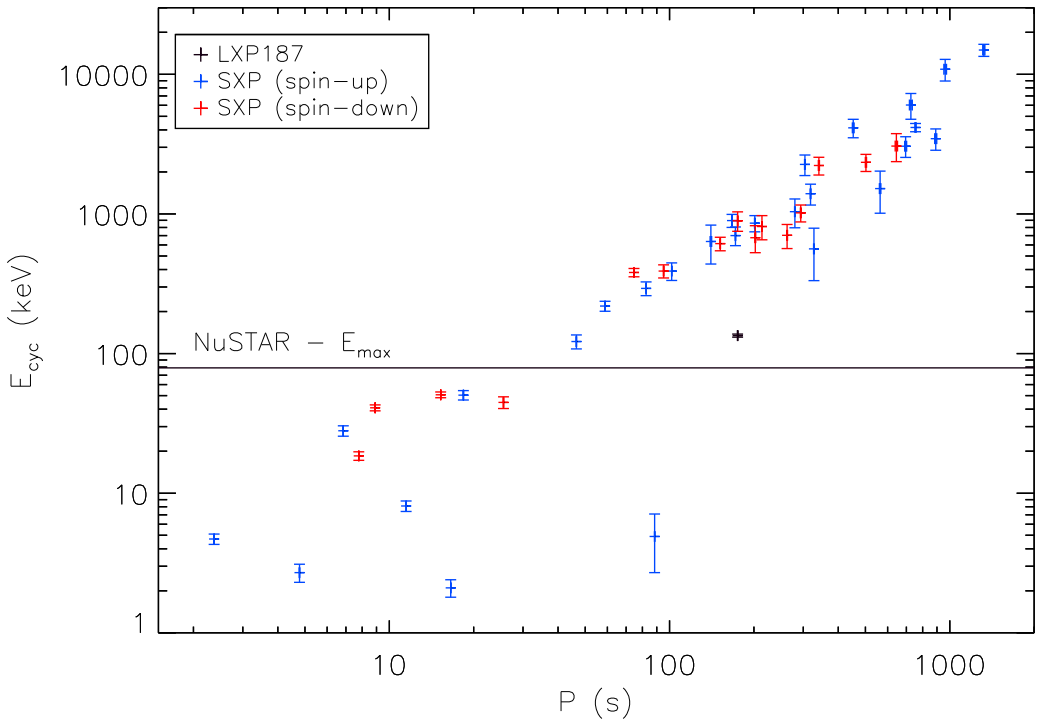

Figure 4.33 revisited: Predicted E_{cyc}, from electrons, as a function of P; results for LXP187 (black), and SXP sources that are spinning up ($\dot{P} < 0$; blue) and down ($\dot{P} > 0$; red) on average. The black line indicates the maximum energy range of NASA's NuStar (Nuclear Spectroscopic Telescope Array Mission) (as discussed in Section 4.3.3).

Conversely, the SXP sources, and LXP187, could be monitored for CRSF. Predictions for the energy of these features, assuming results from the Ghosh and Lamb (1979) model are correct, are given in Tables 2.9 and 4.2 and shown in Figure 4.33. Most

sources are not predicted to produce CRSF, from electrons, that are observable with X-ray telescopes, although CRSF from protons are possible. Only 11 systems are predicted to have $E_{cyc} < 100$ keV, these are the 10 systems with the shortest spin periods, and SXP91.1. Six of these are predicted to not be close to spin equilibrium.

Evidence from Chapter 3 suggests that the pulse-profiles of systems with relatively short spin periods (and hence relatively low magnetic fields, assuming results from Chapters 2 and 3 are correct) tend to exhibit double-peaked structure at higher luminosities than systems with relatively long spin periods. Dips are also evident in the double-peaked structure of systems with relatively short spin periods, and do not tend to be evident in the double-peaked structure of systems with relatively long spin periods. This may mean that systems with relatively short spin periods transition from a pencil beam to a fan beam at relatively higher luminosities. It is also possible that the double-peaked structure in some observations are due to the neutron star having multiple magnetic poles. These results are far from conclusive, however, because it is difficult to distinguish between double-peaked structure and dips, which produce the same shape in the pulse-profile.

The problems could be resolved with more complex modelling, including modelling that takes into account the effects of fan beam radiation, asymmetric poles, and multiple poles. Future work in this area is currently being undertaken by S. Laycock and R. Cappallo et al. at the University of Massachusetts.

Appendix A

Tables of orbital parameters

Tables A.1-A.5 give the orbital parameters for the BeXB discussed in this work, including the SXP discussed in Chapters 2 and 3, and LXP187, which is discussed in Chapter 4. Table A.1 lists the orbital parameters used to determine the status of the OBe star's circumstellar disc, and to create diagrams of each system, shown in Appendix B and Figure 4.26. When values of M_{OB} and R_{OB} were not known, average values of $M_{OB}/M_{\odot}$=18.36 ± 4.42 and $R_{OB}/R_{\odot}$=8.95 ± 2.08 were used. When values of P_{orb} and R_{cd} were not known, the most probable values were used to create diagrams, and to determine the status of the OBe star's circumstellar disc (with values determined from $P_{orb} \propto P^{5/14}$ and $P_{orb} \propto R_{cd}^{7/100}$, as discussed in Section 2.3). In all other calculations, a full range of values were used for P_{orb} and R_{cd} (P_{orb} = 262 ± 258 d and R_{cd} = 176 ± 121 $R_{\odot}$), as given in Tables A.2 and A.3. The derived velocities are given in Tables A.4-A.5. Results in Tables A.1-A.5 assume M_{OB}=M_{spec}, where results calculated using M_{dyn} are in parenthesis.

BeXB	P_{orb} (d)	$\frac{M_{OB}}{M_\odot}$	$\frac{R_{OB}}{R_\odot}$	$\frac{R_{cd}}{R_\odot}$	$\frac{a}{R_\odot}$	e	$\frac{q}{R_\odot}$	Circ. disc status
SXP2.37	18.62	26 (21)	12 (11)	110	89 (83)	0.07	83 (77)	N-T
SXP4.78	23.90	16 (13)	8 (7)	216	90 (84)	0.30*	63 (59)*	N-T*
SXP6.85	21.90	22 (17)	10 (10)	60	94 (87)	0.26	69 (65)	T
SXP7.78	44.93	16 (13)	8 (7)	110	138 (129)	0.30*	96 (90)*	N-T*
SXP8.80	28.47	22 (17)	10 (10)	73	112 (104)	0.41	66 (61)	N-T
SXP11.5	36.30	22 (17)	10 (10)	128*	131 (122)	0.28	94 (88)	N-T*
SXP15.3	74.32	25 (20)	11 (11)	227	222 (207)	0.30*	155 (145)*	N-T*
SXP16.6	33.72	18 (15)*	9 (8)*	108*	119 (111)*	0.30*	83 (78)*	N-T*
SXP18.3	17.79	11 (9)	6 (5)	50*	66 (62)	0.43	38 (35)	N-T*
SXP25.5	22.53	18 (15)*	9 (8)*	88*	91 (85)*	0.30*	64 (59)*	N-T*
SXP46.6	137.40	20 (16)	10 (9)	173	311 (290)	0.30*	218 (203)*	T*
SXP59.0	122.10	20 (16)	9 (8)	171	288 (268)	0.30*	201 (188)*	T*
SXP74.7	33.39	8 (6)	5 (4)	76	91 (85)	0.40	54 (51)	N-T
SXP82.4	362.20	16 (13)	8 (8)	164	555 (518)	0.30*	388 (363)*	T*
SXP91.1	88.37	22 (18)	10 (10)	214	239 (223)	0.30*	167 (156)*	N-T*
SXP95.2	280.00	18 (15)*	9 (8)*	212*	487 (455)*	0.30*	341 (318)*	T*
SXP101	21.95	18 (15)*	9 (8)*	87*	89 (83)*	0.30*	62 (58)*	N-T*
SXP140	197.00	14 (11)	7 (6)	207	356 (333)	0.30*	249 (233)*	T*
SXP152	81.93*	17 (14)	8 (8)	131	209 (195)*	0.30*	146 (137)*	T*
SXP169	68.37	23 (18)	11 (11)	249	204 (190)	0.30*	143 (133)*	N-T*
SXP172	68.78	18 (15)	9 (8)	121	190 (178)	0.30*	133 (124)*	T*
SXP175	87.20	28 (23)	14 (13)	239*	256 (239)	0.30*	180 (167)*	N-T*
SXP202A	71.98	16 (13)	8 (7)	123	188 (176)	0.30*	132 (123)*	T*
SXP202B	224.60	20 (16)	10 (9)	224*	434 (405)	0.30*	304 (284)*	T*
SXP214	92.57*	19 (15)	9 (8)	155*	234 (219)*	0.30*	164 (153)*	T (N-T)*
SXP264	49.12	13 (11)	7 (6)	148	138 (130)	0.30*	97 (91)*	N-T*
SXP280	127.62	20 (16)	10 (9)	276	295 (275)	0.30*	206 (192)*	N-T*
SXP293	59.73	9 (7)	5 (5)	78*	141 (133)	0.30*	99 (93)*	T*
SXP304	520.00	20 (16)	10 (9)	384	751 (701)	0.30*	526 (491)*	T*
SXP323	116.60	17 (13)	8 (7)	181	264 (246)	0.30*	185 (172)*	T (N-T)*
SXP327	45.93	18 (15)*	9 (8)*	123*	146 (136)*	0.30*	102 (95)*	N-T*
SXP342	109.35*	18 (15)*	9 (8)*	166*	260 (243)*	0.30*	182 (170)*	T*
SXP455	74.56	17 (13)	8 (8)	118	195 (182)	0.30*	137 (128)*	T*
SXP504	270.10	19 (15)	9 (9)	296	483 (451)	0.30*	338 (316)*	T*
SXP565	152.40	17 (14)	9 (8)	226	316 (296)	0.30*	221 (207)*	N-T*
SXP645	137.19*	22 (18)	11 (10)	220*	321 (299)*	0.30*	225 (209)*	T (N-T)*
SXP701	412.00	19 (15)	9 (8)	221	634 (592)	0.30*	444 (414)*	T*
SXP726	143.15*	18 (14)	9 (8)	178*	309 (289)*	0.30*	216 (202)*	T*
SXP756	393.60	24 (19)	11 (10)	231	667 (622)	0.30*	467 (436)*	T*
SXP893	153.95*	18 (15)*	9 (8)*	183*	327 (305)*	0.30*	229 (214)*	T*
SXP967	101.40	22 (18)	11 (10)	139	262 (245)	0.30*	184 (171)*	T*
SXP1323	26.17	23 (18)	11 (11)	177	108 (100)	0.30*	75 (70)*	N-T*
LXP187	21.63	23 (18)	11 (11)	259	95 (88)	0.30*	66 (62)*	N-T

Table A.1: Orbital parameters used to create diagrams for each system (shown in Appendix B and Figure 4.26) and used to determine status of the OBe star's circumstellar disc. Here T refers to a truncated circumstellar disc, and $N-T$ to non-truncated. An asterisk denotes that the value is an estimate, as discussed in Appendix A. Results assume M_{OB}=M_{spec}, where results calculated using M_{dyn} are in parenthesis.

BeXB	P_{orb} (d)	$-EWH\alpha$ (Å)	$\frac{M_{OB}}{M_\odot}$	$\frac{R_{OB}}{R_\odot}$
SXP2.37	18.62±0.02	-7.9±0.6	26±7 (21±6)	12±3 (11±3)
SXP4.78	23.9±0.1	-43.7±1.1	16±2 (13±1)	8±1 (7±1)
SXP6.85	21.9±0.1	-3.8±3.7	22±4 (17±3)	10±2 (10±2)
SXP7.78	44.93±0.01	-14.3±2.3	16±3 (13±3)	8±2 (7±2)
SXP8.80	28.47±0.04	-5.1±0.4	22±4 (17±3)	10±2 (10±2)
SXP11.5	36.3±0.4	-25±20*	22±4 (17±3)	10±2 (10±2)
SXP15.3	74.32±0.03	-25.1±1.5	25±8 (20±6)	11±3 (11±3)
SXP16.6	33.7±0.1	-25±20*	18±4 (15±4)*	9±2 (8±2)*
SXP18.3	17.79±0.03	-25±20*	11±3 (9±3)	6±1 (5±1)
SXP25.5	22.53±0.01	-25±20*	18±4 (15±4)*	9±2 (8±2)*
SXP46.6	137.4±0.2	-21.9±0.7	20±6 (16±5)	10±3 (9±2)
SXP59.0	122.1±0.4	-23.4±1.4	20±0 (16±0)	9±0 (8±0)
SXP74.7	33.39±0.01	-18.3±2.3	8±0 (6±0)	5±0 (4±0)
SXP82.4	362.2±4.1	-25.9±1.1	16±8 (13±7)	8±3 (8±3)
SXP91.1	88.37±0.03	-26.7±2.6	22±6 (18±5)	10±3 (10±2)
SXP95.2	280.0±8.0	-25±20*	18±4 (15±4)*	9±2 (8±2)*
SXP101	21.949±0.003	-7.8±5	18±4 (15±4)*	9±2 (8±2)*
SXP140	197.0±5.0	-47.3±3.1	14±0 (11±0)	7±0 (6±0)
SXP152	262.0±258.0*	-17.3±1.7	17±8 (14±6)	8±3 (8±3)
SXP169	68.4±0.1	-29.2±2.6	23±5 (18±4)	11±3 (11±3)
SXP172	68.8±0.1	-15±1.3	18±1 (15±1)	9±0 (8±0)
SXP175	87.2±0.2	-25±20*	28±0 (23±0)	14±1 (13±1)
SXP202A	72.0±5.0	-18.1±5	16±2 (13±1)	8±1 (7±1)
SXP202B	224.6±0.3	-25±20*	20±8 (16±6)	10±5 (9±4)
SXP214	262.0±258.0*	-25±20*	19±2 (15±2)	9±1 (8±1)
SXP264	49.12±0.03	-30.1±1.7	13±1 (11±1)	7±0 (6±0)
SXP280	127.6±0.3	-42±3.1	20±9 (16±7)	10±4 (9±4)
SXP293	59.73±0.01	-25±20*	9±2 (7±1)	5±0 (5±0)
SXP304	520.0±12.0	-70.4±6.2	20±9 (16±7)	10±4 (9±4)
SXP323	116.6±0.6	-30.9±1.1	17±1 (13±1)	8±0 (7±0)
SXP327	45.93±0.01	-25±20*	18±4 (15±4)*	9±2 (8±2)*
SXP342	262.0±258.0*	-25±20*	18±4 (15±4)*	9±2 (8±2)*
SXP455	74.6±0.1	-15.1±2	17±6 (13±4)	8±3 (8±2)
SXP504	270.1±0.5	-52.9±3.9	19±5 (15±4)	9±2 (9±2)
SXP565	152.4±0.3	-37.4±2.9	17±6 (14±5)	9±3 (8±3)
SXP645	262.0±258.0*	-25±20*	22±6 (18±5)	11±3 (10±3)
SXP701	412.0±5.0	-37.1±3.5	19±0 (15±0)	9±0 (8±0)
SXP726	262.0±258.0*	-25±20*	18±10 (14±8)	9±4 (8±4)
SXP756	393.6±1.2	-27±3.6	24±9 (19±7)	11±3 (10±3)
SXP893	262.0±258.0*	-25±20*	18±4 (15±4)*	9±2 (8±2)*
SXP967	101.4±0.2	-12.3±5	22±6 (18±5)	11±3 (10±3)
SXP1323	26.174±0.002	-17.1±1.5	23±5 (18±4)	11±3 (11±3)
LXP187	21.631±0.005	-31.05±4.05	23±5 (18±4)	11±3 (11±3)

Table A.2: Orbital parameters for each system, where references for P_{orb} and $-EWH\alpha$ are given in Table 2.2. An asterisk denotes that the value is an estimate, as discussed in Appendix A. Results assume M_{OB}=M_{spec}, where results calculated using M_{dyn} are in parenthesis.

BeXB	$\frac{R_{cd}}{R_\odot}$	$\frac{a}{R_\odot}$	e	$\frac{q}{R_\odot}$
SXP2.37	110±28	89±8 (83±7)	0.07±0.02	83±7 (77±7)
SXP4.78	216±20	90±3 (84±3)	0.3±0.2*	63±18 (59±17)*
SXP6.85	60±56	94±6 (87±5)	0.26±0.03	69±5 (65±5)
SXP7.78	110±25	138±9 (129±8)	0.3±0.2*	96±28 (90±26)*
SXP8.80	73±14	112±7 (104±6)	0.41±0.04	66±6 (61±6)
SXP11.5	202±135*	131±8 (122±7)	0.28±0.03	94±7 (88±6)
SXP15.3	226±62	222±21 (207±20)	0.3±0.2*	155±47 (145±44)*
SXP16.6	176±121*	119±9 (111±8)*	0.3±0.2*	83±25 (78±23)*
SXP18.3	115±77*	66±6 (62±5)	0.43±0.03	38±4 (35±4)
SXP25.5	176±121*	91±7 (85±6)*	0.3±0.2*	64±19 (59±17)*
SXP46.6	173±47	311±28 (290±26)	0.3±0.2*	218±65 (203±61)*
SXP59.0	171±7	288±1 (268±1)	0.3±0.2*	201±58 (188±54)*
SXP74.7	76±6	91±0 (85±0)	0.40±0.23	54±21 (51±20)
SXP82.4	164±70	555±90 (518±82)	0.3±0.2*	388±127 (363±119)*
SXP91.1	214±57	239±21 (223±19)	0.3±0.2*	167±50 (156±47)*
SXP95.2	176±121*	487±38 (455±34)*	0.3±0.2*	341±101 (318±94)*
SXP101	84±45*	89±7 (83±6)*	0.3±0.2*	62±18 (58±17)*
SXP140	207±9	356±6 (333±6)	0.3±0.2*	249±71 (233±67)*
SXP152	131±50	209±305 (195±284)*	0.3±0.2*	146±232 (137±216)*
SXP169	248±69	204±15 (190±14)	0.3±0.2*	143±42 (133±39)*
SXP172	121±7	190±2 (178±2)	0.3±0.2*	133±38 (124±36)*
SXP175	272±175*	256±0 (239±0)	0.3±0.2*	180±51 (167±48)*
SXP202A	123±25	188±11 (176±10)	0.3±0.2*	132±38 (123±36)*
SXP202B	196±155*	434±54 (405±49)	0.3±0.2*	304±95 (284±88)*
SXP214	173±113*	234±308 (219±287)*	0.3±0.2*	164±235 (153±219)*
SXP264	148±9	138±3 (130±2)	0.3±0.2*	97±28 (91±26)*
SXP280	276±123	295±41 (275±37)	0.3±0.2*	206±65 (192±61)*
SXP293	101±66*	141±7 (133±7)	0.3±0.2*	99±29 (93±27)*
SXP304	384±172	751±105 (701±96)	0.3±0.2*	526±167 (491±156)*
SXP323	181±8	264±4 (246±4)	0.3±0.2*	185±53 (172±49)*
SXP327	176±121*	146±11 (136±10)*	0.3±0.2*	102±30 (95±28)*
SXP342	176±121*	260±308 (243±287)*	0.3±0.2*	182±235 (170±219)*
SXP455	118±39	195±20 (182±19)	0.3±0.2*	137±42 (128±39)*
SXP504	296±75	483±40 (451±37)	0.3±0.2*	338±101 (316±94)*
SXP565	226±84	316±35 (296±32)	0.3±0.2*	221±68 (207±63)*
SXP645	219±156*	321±327 (299±305)*	0.3±0.2*	225±249 (209±233)*
SXP701	220±14	634±5 (592±5)	0.3±0.2*	444±127 (414±118)*
SXP726	175±140*	309±315 (289±294)*	0.3±0.2*	216±239 (202±223)*
SXP756	231±74	667±73 (622±68)	0.3±0.2*	467±143 (436±133)*
SXP893	176±121*	327±308 (305±287)*	0.3±0.2*	229±235 (214±219)*
SXP967	139±58	262±23 (245±21)	0.3±0.2*	184±55 (171±51)*
SXP1323	176±49	108±8 (100±7)	0.3±0.2*	75±22 (70±21)*
LXP187	258±73	95±7 (88±6)	0.3±0.2*	66±20 (62±18)*

Table A.3: Orbital parameters for each system, where references for e are given in Table 2.3. An asterisk denotes that the value is an estimate, as discussed in Appendix A. Results assume M_{OB}=M_{spec}, where results calculated using M_{dyn} are in parenthesis.

BeXB	V_{orb} (km s^{-1})	V_w (km s^{-1})
SXP2.37	259±36 (242±33)	244±35 (218±31)
SXP4.78	260±44 (243±41)	219±33 (196±30)*
SXP6.85	283±27 (264±25)	261±123 (234±110)
SXP7.78	211±41 (198±38)	178±32 (159±29)*
SXP8.80	307±31 (286±29)	250±26 (224±24)
SXP11.5	244±24 (228±22)*	209±21 (187±19)*
SXP15.3	206±46 (192±42)	176±38 (157±34)*
SXP16.6	243±49 (227±45)*	205±39 (184±35)*
SXP18.3	298±43 (279±39)*	235±38 (210±34)*
SXP25.5	278±56 (259±52)*	235±45 (210±40)*
SXP46.6	156±34 (146±31)	148±29 (133±26)*
SXP59.0	162±26 (152±25)	150±3 (134±3)*
SXP74.7	210±44 (198±41)	163±31 (146±28)
SXP82.4	106±32 (99±29)	137±46 (122±41)*
SXP91.1	187±40 (174±37)	159±33 (142±29)*
SXP95.2	120±24 (112±22)*	141±51 (126±46)*
SXP101	280±56 (262±52)*	237±45 (212±40)*
SXP140	125±20 (117±19)	115±2 (102±2)*
SXP152	119±51 (112±47)*	157±47 (140±42)*
SXP169	206±41 (192±38)	175±33 (157±30)*
SXP172	191±31 (178±29)	169±6 (151±5)*
SXP175	203±33 (189±31)*	174±25 (155±22)*
SXP202A	180±31 (168±29)	157±18 (140±16)*
SXP202B	133±34 (124±31)*	141±62 (126±56)*
SXP214	123±46 (115±43)*	144±47 (93±34)*
SXP264	194±32 (182±30)	162±24 (145±21)*
SXP280	159±43 (149±40)	135±37 (121±33)*
SXP293	163±30 (153±28)*	132±44 (118±40)*
SXP304	100±27 (93±25)	99±31 (88±28)*
SXP323	156±26 (146±24)	133±4 (117±17)*
SXP327	219±44 (205±41)*	185±35 (166±32)*
SXP342	123±47 (114±44)*	141±51 (126±46)*
SXP455	180±42 (169±39)	164±39 (146±35)*
SXP504	123±26 (115±24)	112±21 (100±18)*
SXP565	143±34 (134±31)	121±28 (108±25)*
SXP645	130±51 (121±47)*	139±53 (99±38)*
SXP701	106±17 (99±16)	127±4 (114±4)*
SXP726	122±56 (114±52)*	140±69 (125±62)*
SXP756	117±28 (109±26)	142±34 (127±30)*
SXP893	123±47 (114±44)*	141±51 (126±46)*
SXP967	178±38 (166±35)	174±44 (156±39)*
SXP1323	283±57 (264±53)	241±46 (216±41)*
LXP187	302±61 (282±56)*	257±49 (230±44)*

Table A.4: V_{orb} and V_w for each system. An asterisk denotes that the value is an estimate, as discussed in Appendix A. Results assume M_{OB}=M_{spec}, where results calculated using M_{dyn} are in parenthesis.

BeXB	V_{rel} (prograde) (km s^{-1})	V_{rel} (retrograde) (km s^{-1})	V_{Crel} (non-truncated) (km s^{-1})	V_{Crel} (truncated) (km s^{-1})
SXP2.37	15±71 (23±64)	503±71 (460±64)	256±29	867±268
SXP4.78	41±78 (48±71)*	479±78 (439±71)*	247±36	609±187
SXP6.85	21±150 (30±135)	544±150 (497±135)	252±29	706±216
SXP7.78	34±73 (39±67)*	389±73 (357±67)*	208±31	554±172
SXP8.80	56±57 (62±52)	557±57 (510±52)	256±29	698±213
SXP11.5	35±45 (41±41)*	453±45 (414±41)*	222±25*	651±199*
SXP15.3	30±84 (35±76)*	382±84 (349±76)*	183±27	594±185
SXP16.6	38±88 (43±80)*	448±88 (410±80)*	212±31*	514±159*
SXP18.3	63±81 (69±73)*	533±81 (489±73)*	294±34*	632±187*
SXP25.5	43±100 (49±92)*	513±100 (469±92)*	237±35*	553±171*
SXP46.6	8±63 (13±58)*	304±63 (278±58)*	161±24	573±181
SXP59.0	13±29 (18±27)*	312±29 (285±27)*	169±25	607±191
SXP74.7	47±75 (52±69)	373±75 (343±69)	266±45	661±206
SXP82.4	31±78 (23±71)*	242±78 (221±71)*	134±21	582±182
SXP91.1	28±73 (32±66)*	345±73 (316±66)*	182±27	632±197
SXP95.2	21±75 (14±68)*	261±75 (238±68)*	141±21*	594±185*
SXP101	43±101 (50±93)*	517±101 (474±93)*	248±37*	613±191*
SXP140	10±23 (14±21)*	239±23 (219±21)*	158±23	620±200
SXP152	37±98 (29±89)*	276±98 (252±89)*	143±38	586±188
SXP169	31±74 (35±68)*	381±74 (348±68)*	192±28	635±199
SXP172	22±37 (27±34)*	360±37 (329±34)*	192±28	593±187
SXP175	29±58 (34±53)*	376±58 (344±53)*	176±26*	618±195*
SXP202A	23±49 (28±45)*	337±49 (309±45)*	192±28	594±187
SXP202B	7±96 (2±87)*	274±96 (250±87)*	142±22*	548±176*
SXP214	20±93 (22±76)*	267±93 (208±76)*	140±37*	569±184*
SXP264	32±56 (37±51)*	357±56 (327±51)*	204±30	526±165
SXP280	24±80 (28±73)*	294±80 (269±73)*	163±25	566±181
SXP293	31±74 (35±67)*	295±74 (271±67)*	206±30*	553±172*
SXP304	1±58 (5±53)*	198±58 (181±53)*	127±19	665±212
SXP323	23±30 (28±41)*	288±30 (263±41)*	172±25	585±184
SXP327	34±79 (39±72)*	404±79 (370±72)*	196±29*	495±154*
SXP342	18±98 (12±90)*	264±98 (241±90)*	146±39*	637±205*
SXP455	17±81 (22±73)*	344±81 (315±73)*	201±30	696±220
SXP504	12±46 (15±42)*	235±46 (215±42)*	139±21	570±180
SXP565	22±62 (26±57)*	264±62 (242±57)*	153±23	508±165
SXP645	9±104 (22±86)*	269±104 (220±86)*	138±37*	573±186*
SXP701	21±21 (15±20)*	234±21 (213±20)*	126±18	553±175
SXP726	18±125 (11±114)*	262±125 (239±114)*	148±40*	665±216*
SXP756	25±61 (18±56)*	259±61 (236±56)*	126±19	581±182
SXP893	18±98 (12±90)*	264±98 (241±90)*	138±36*	536±173*
SXP967	4±82 (10±75)*	353±82 (322±75)*	184±27	710±226
SXP1323	42±103 (48±94)*	524±103 (480±94)*	246±36	708±220
LXP187	45±109 (52±100)*	559±109 (511±100)*	233±34*	545±167*

Table A.5: V_{rel} for each system, assuming prograde and retrograde orbits, and V_{Crel} assuming accretion is occurring from both a non-truncated, and truncated circumstellar disc. Disc accretion is only possible if $V_{rel} < V_{Crel}$. An asterisk denotes that the value is an estimate, as discussed in Appendix A. Results assume M_{OB}=M_{spec}, where results calculated using M_{dyn} are in parenthesis.

Appendix B

Plots of P and L as a function of MJD, and diagrams of BeXB

The odd numbered figures within Figures B.1-B.84 show plots of P (upper panel; blue) and L (lower panel; red) as functions of MJD, for neutron stars in the 42 BeXB in the dataset discussed in Chapters 2 and 3. The black line in the upper panel shows the weighted line of best fit used to determine the long-term average $\dot{P}$. This is calculated using MPFITEXPR[1] (see Section 2.2).

The even numbered figures within Figures B.1-B.84 show diagrams of the aforementioned BeXB (as discussed in Appendix A). These diagrams are to scale, composed using values of a (equation (2.9)), q (equation (2.8)), R_{cd} (equation (2.16)), and R_{OB}, all of which are given in Table A.1. L, V_{orb} (equation (2.17)), V_w (equations (2.14) and (2.15)), the spin equilibrium status, and B, determined using the Ghosh and Lamb (1979) model (equation (1.34)), are also given. These are determined using the methods described in Section 2.2. All images are to the same scale.

[1] www.physics.wisc.edu/∼craigm/idl/down/mpfitexpr.pro

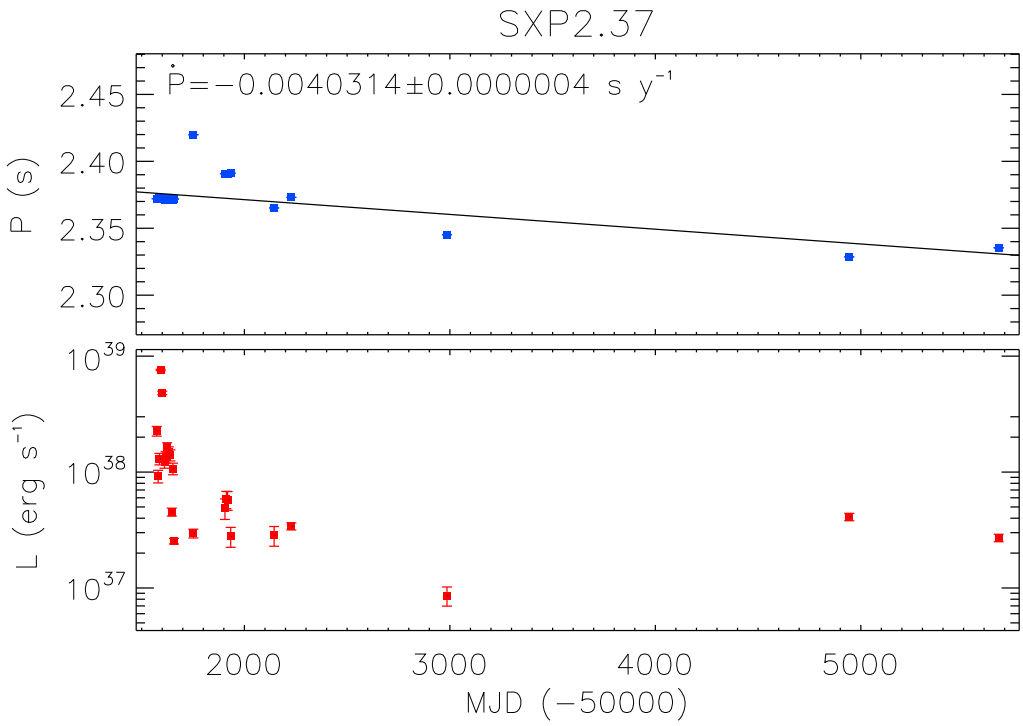

Figure B.1: P (upper panel; blue) and L (lower panel; red) as a function of MJD for SXP2.37. The black line in the upper panel shows the best-fit $\dot{P}$.

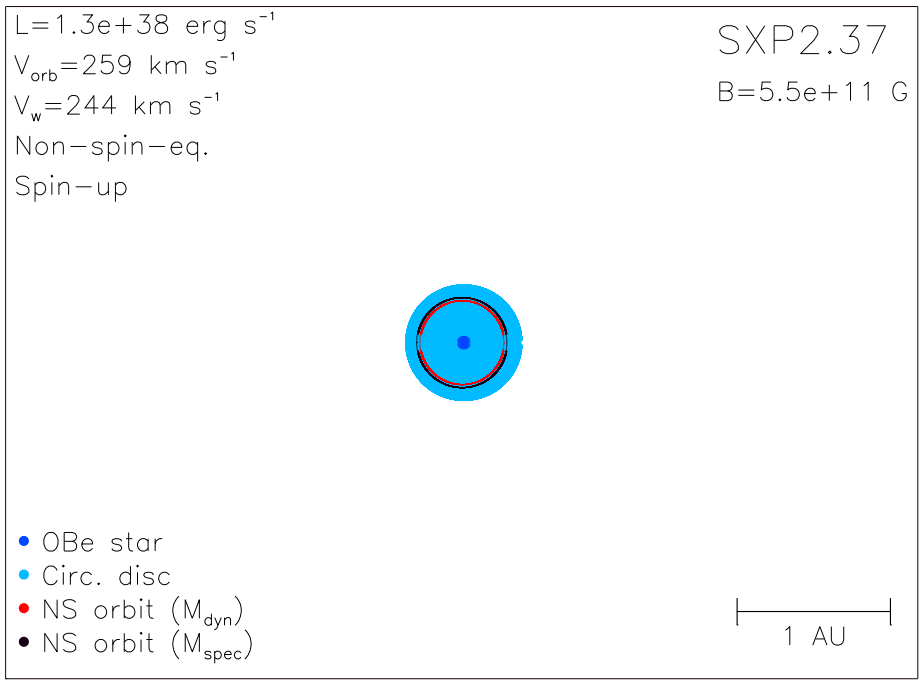

Figure B.2: Diagram of SXP2.37, using orbital parameters given in Table A.1 and discussed in Section 2.3.

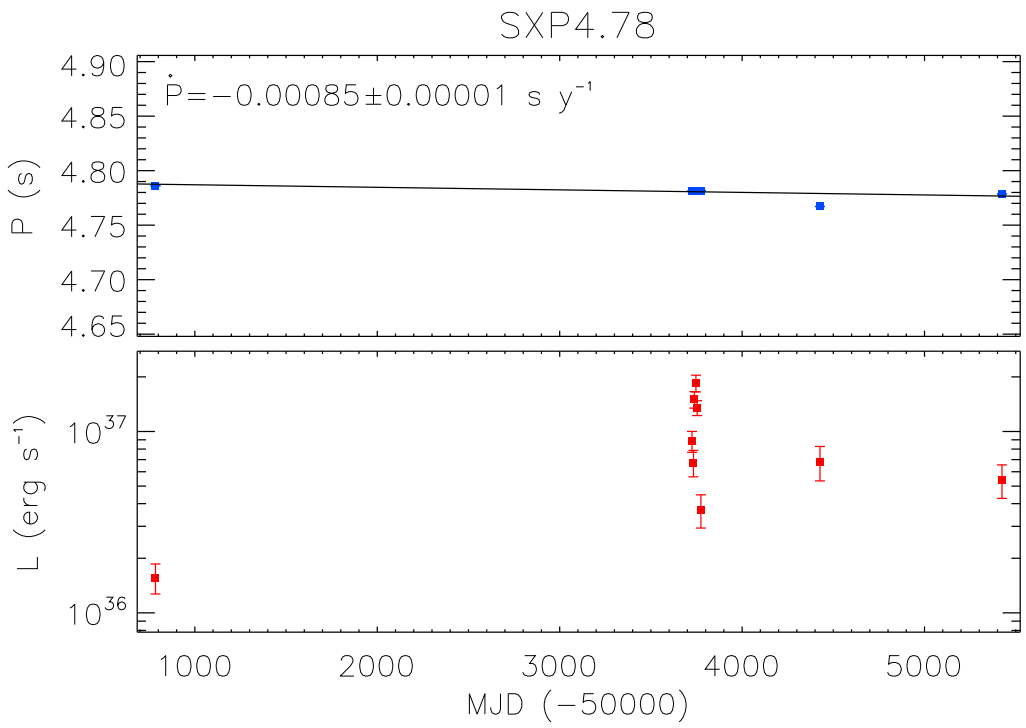

Figure B.3: P (upper panel; blue) and L (lower panel; red) as a function of MJD for SXP4.78. The black line in the upper panel shows the best-fit $\dot{P}$.

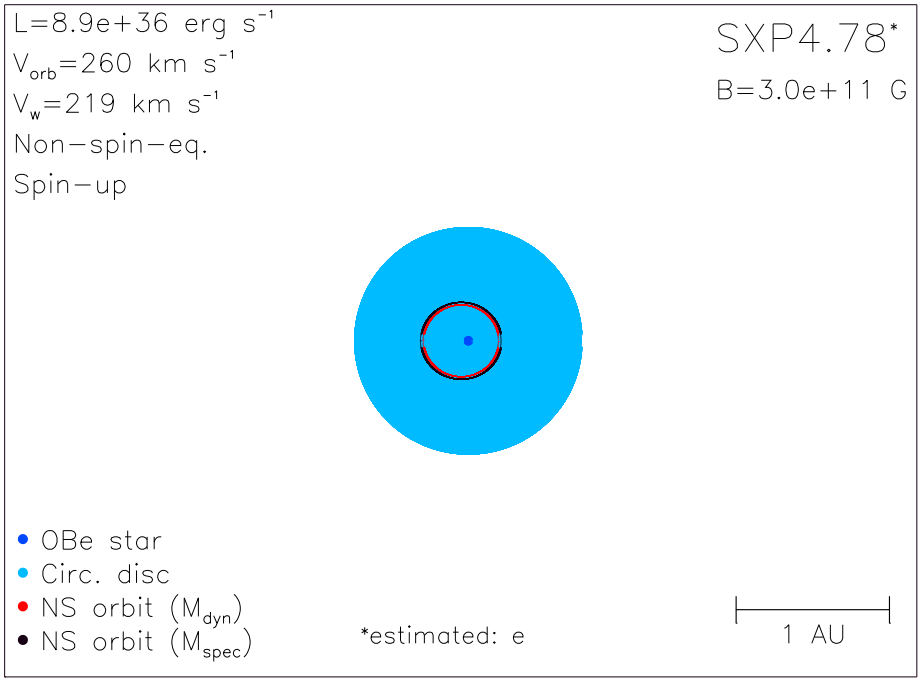

Figure B.4: Diagram of SXP4.78, using orbital parameters given in Table A.1 and discussed in Section 2.3.

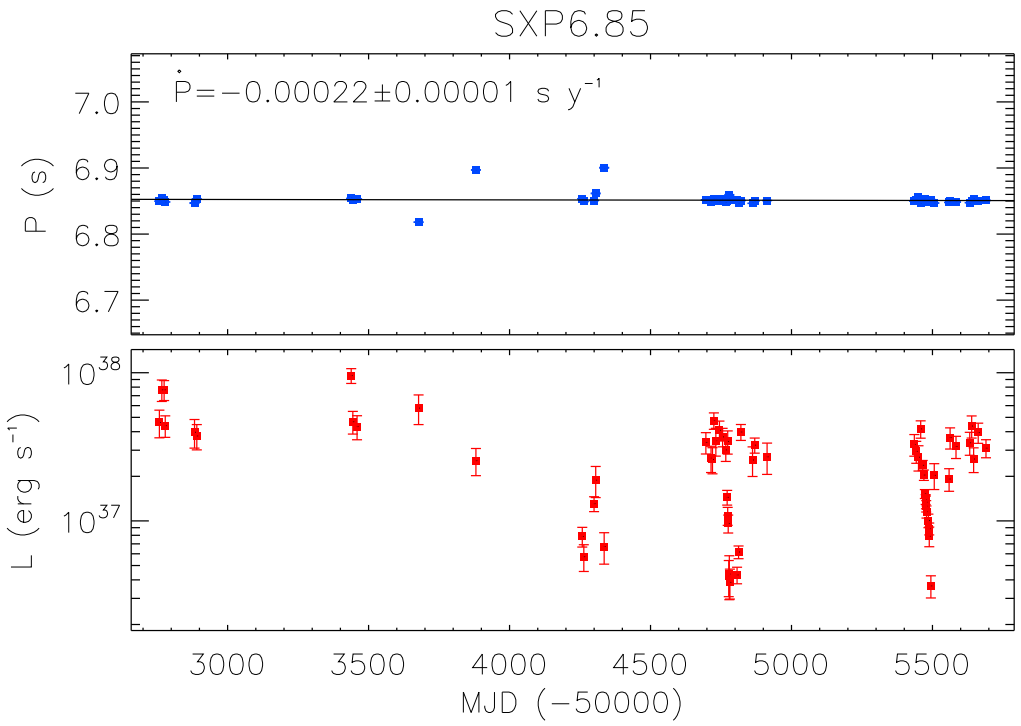

Figure B.5: P (upper panel; blue) and L (lower panel; red) as a function of MJD for SXP6.85. The black line in the upper panel shows the best-fit $\dot{P}$.

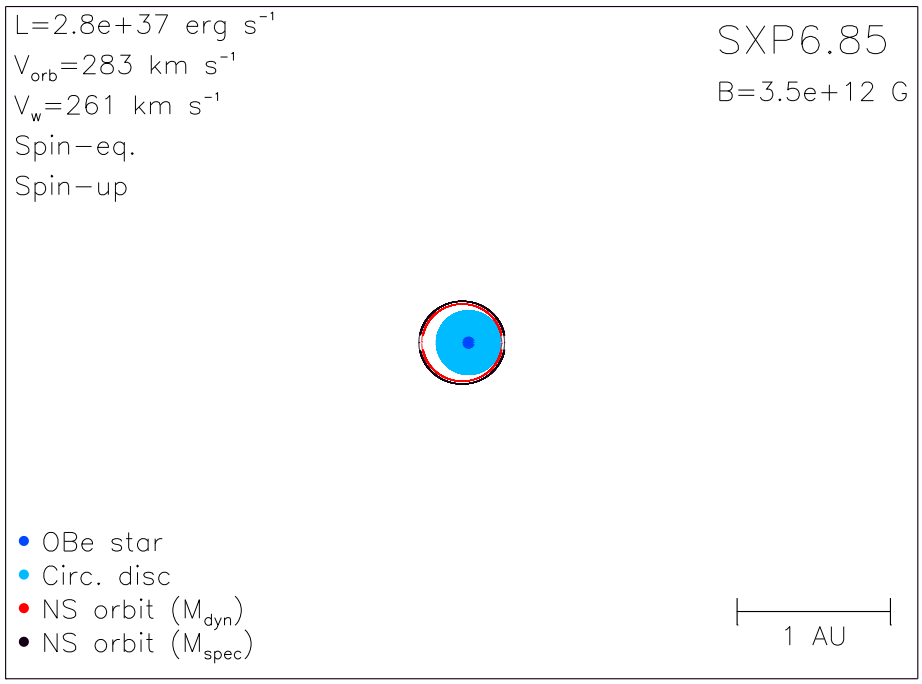

Figure B.6: Diagram of SXP6.85, using orbital parameters given in Table A.1 and discussed in Section 2.3.

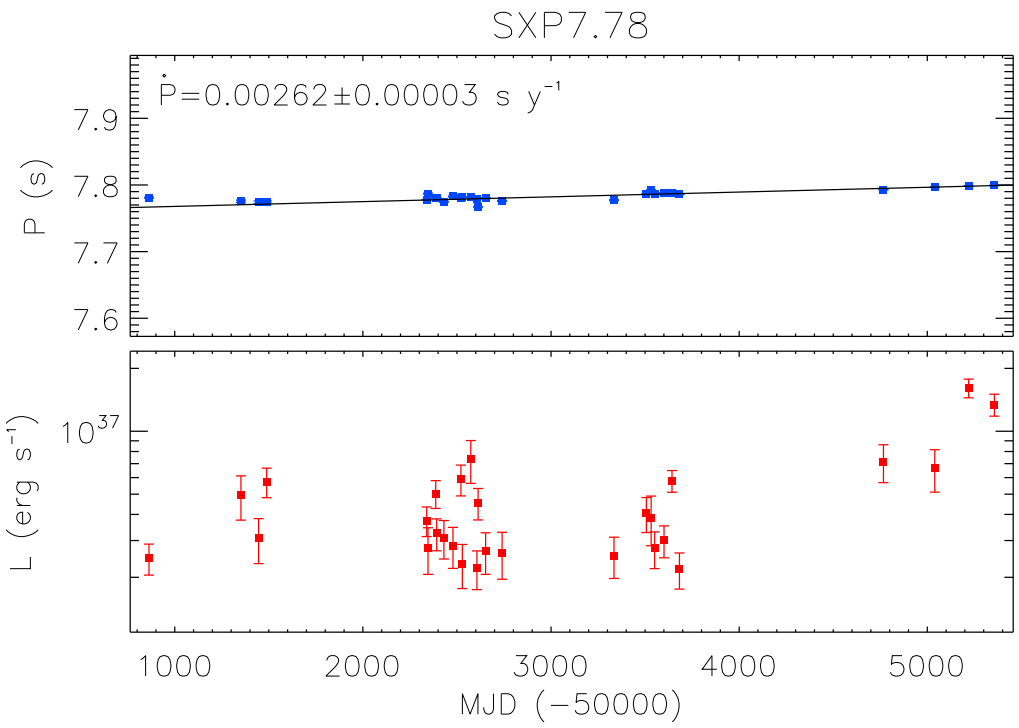

Figure B.7: P (upper panel; blue) and L (lower panel; red) as a function of MJD for SXP7.78. The black line in the upper panel shows the best-fit $\dot{P}$.

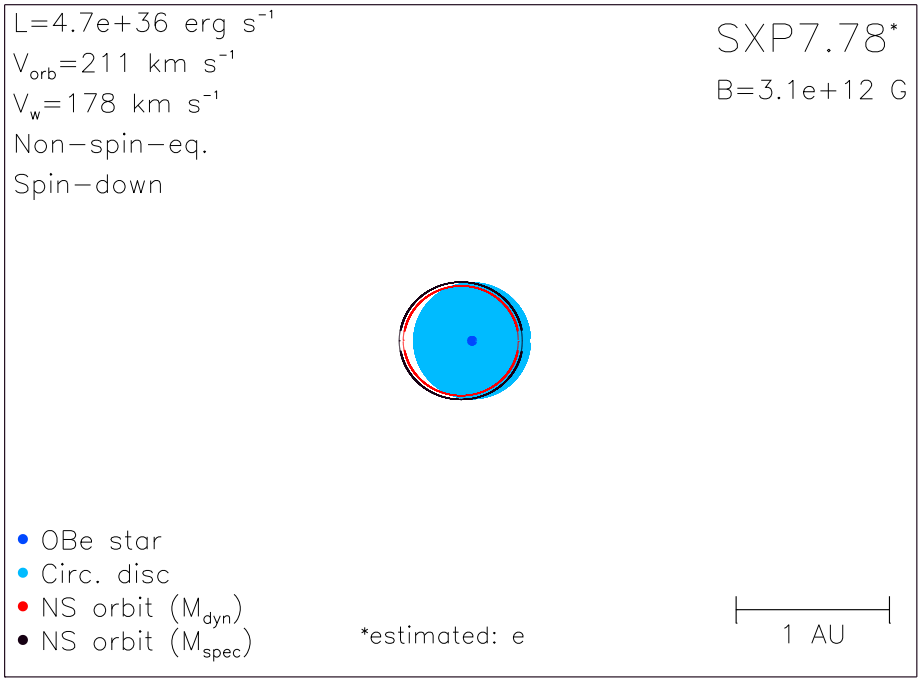

Figure B.8: Diagram of SXP7.78, using orbital parameters given in Table A.1 and discussed in Section 2.3.

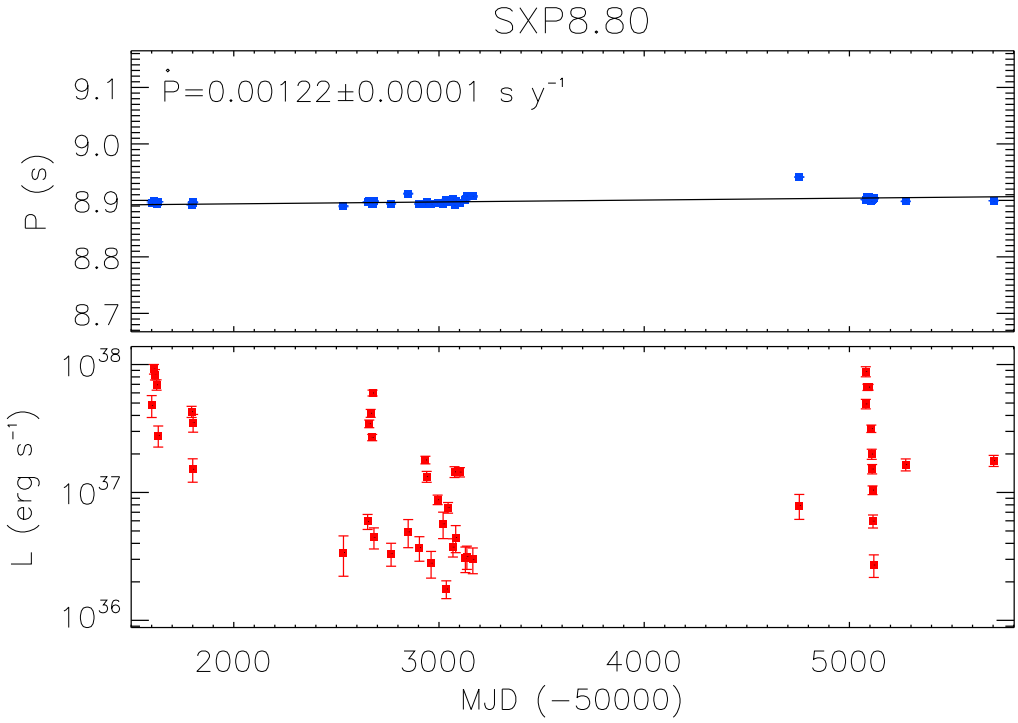

Figure B.9: P (upper panel; blue) and L (lower panel; red) as a function of MJD for SXP8.80. The black line in the upper panel shows the best-fit $\dot{P}$.

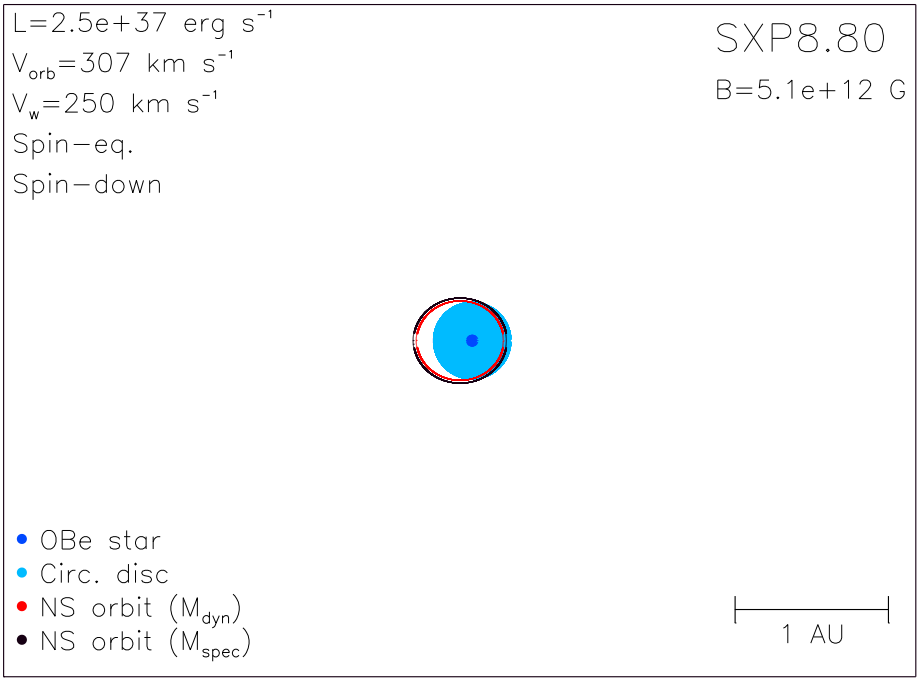

Figure B.10: Diagram of SXP8.80, using orbital parameters given in Table A.1 and discussed in Section 2.3.

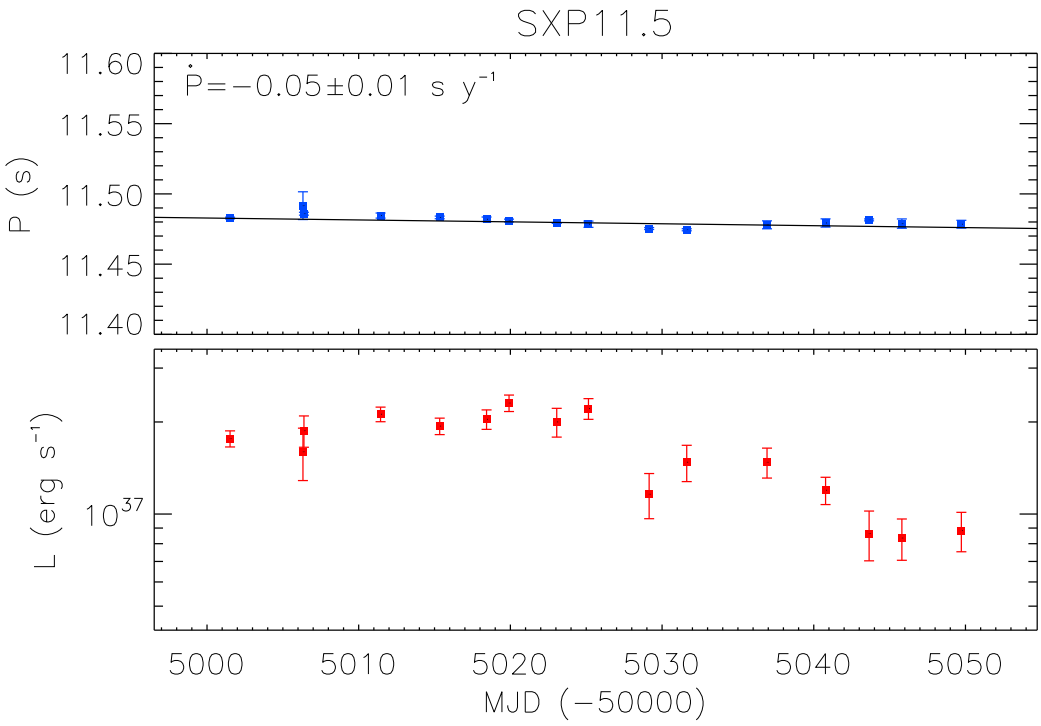

Figure B.11: P (upper panel; blue) and L (lower panel; red) as a function of MJD for SXP11.5. The black line in the upper panel shows the best-fit $\dot{P}$.

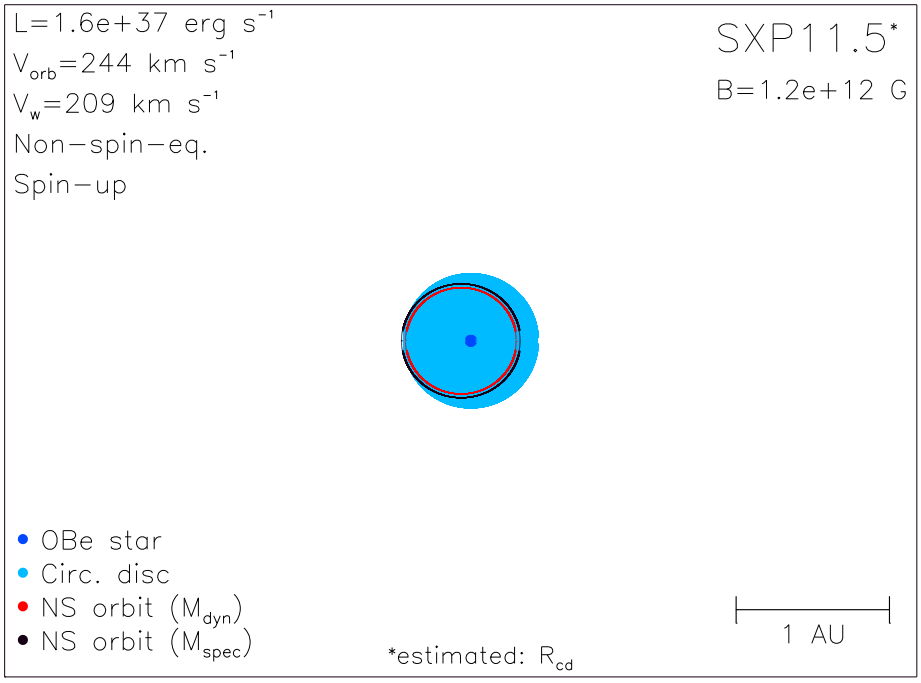

Figure B.12: Diagram of SXP11.5, using orbital parameters given in Table A.1 and discussed in Section 2.3.

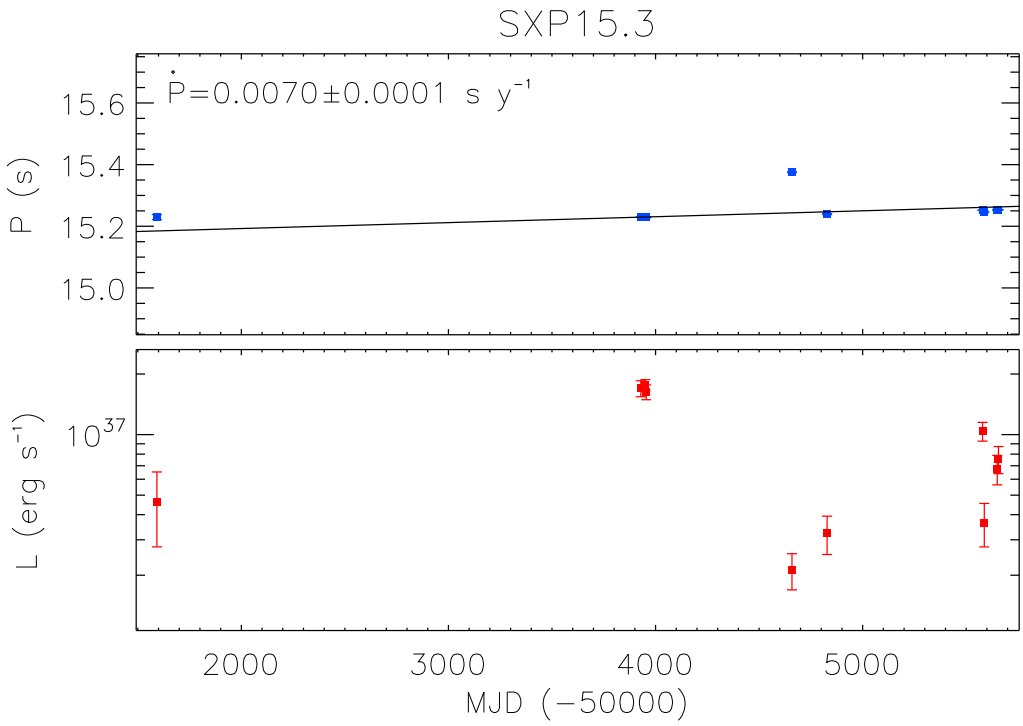

Figure B.13: P (upper panel; blue) and L (lower panel; red) as a function of MJD for SXP15.3. The black line in the upper panel shows the best-fit $\dot{P}$.

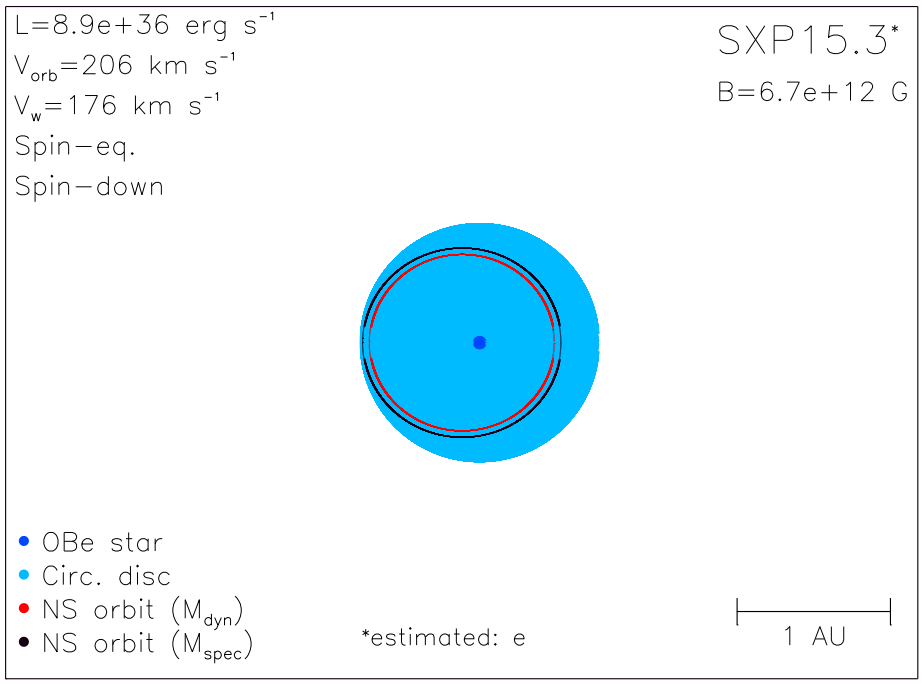

Figure B.14: Diagram of SXP15.3, using orbital parameters given in Table A.1 and discussed in Section 2.3.

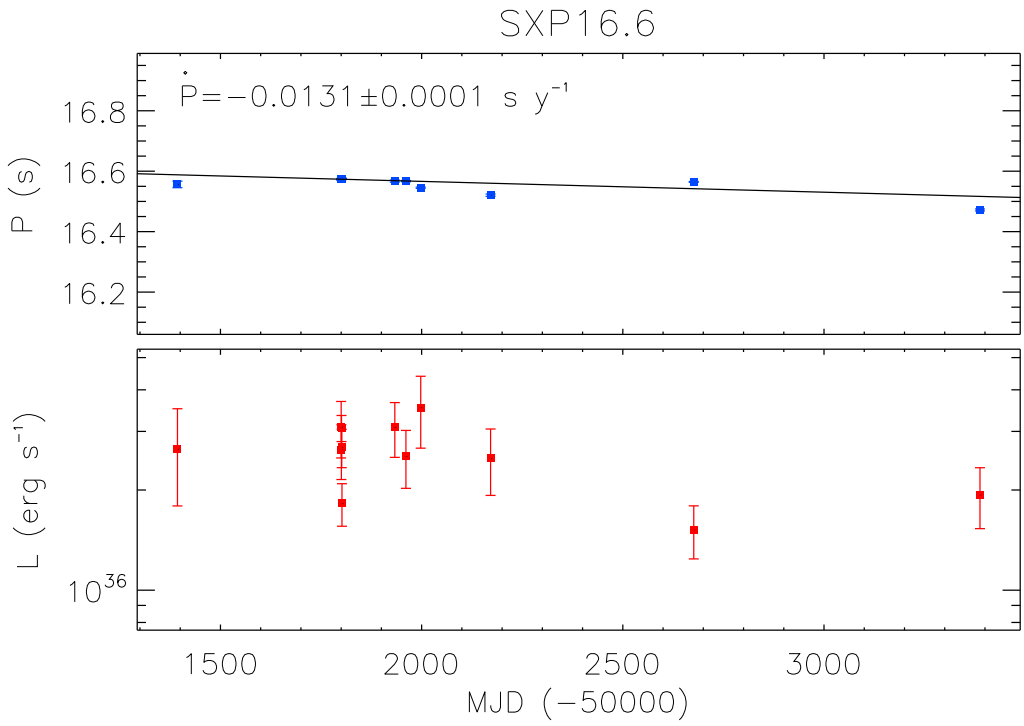

Figure B.15: P (upper panel; blue) and L (lower panel; red) as a function of MJD for SXP16.6. The black line in the upper panel shows the best-fit $\dot{P}$.

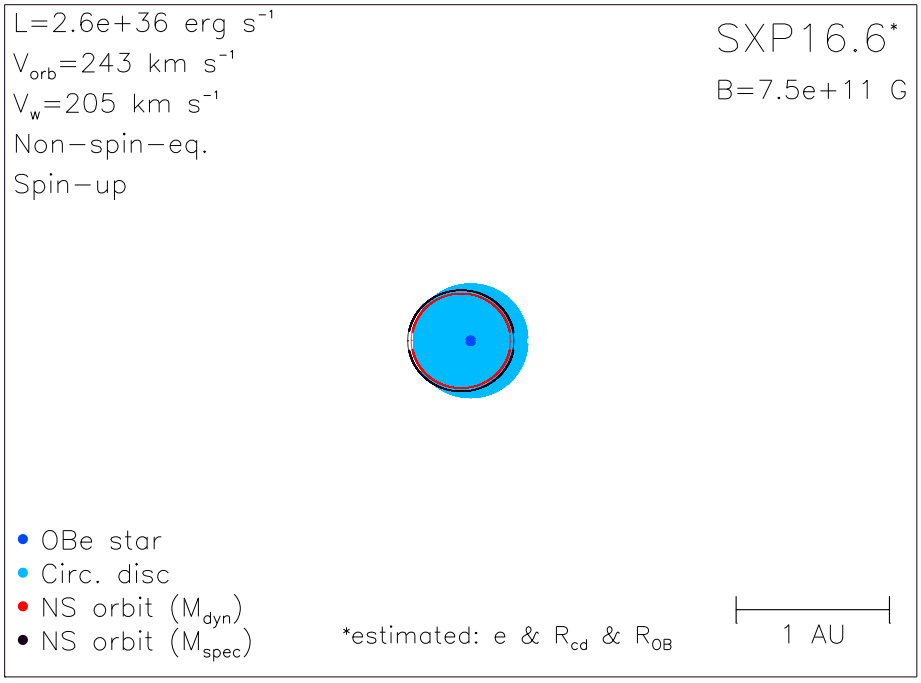

Figure B.16: Diagram of SXP16.6, using orbital parameters given in Table A.1 and discussed in Section 2.3.

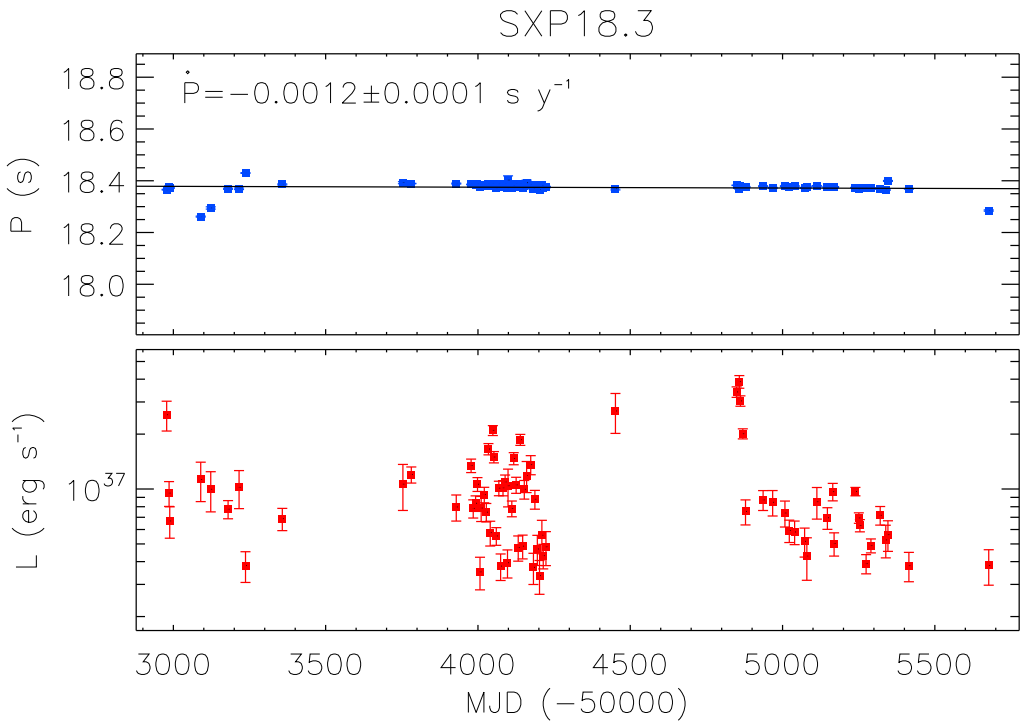

Figure B.17: P (upper panel; blue) and L (lower panel; red) as a function of MJD for SXP18.3. The black line in the upper panel shows the best-fit $\dot{P}$.

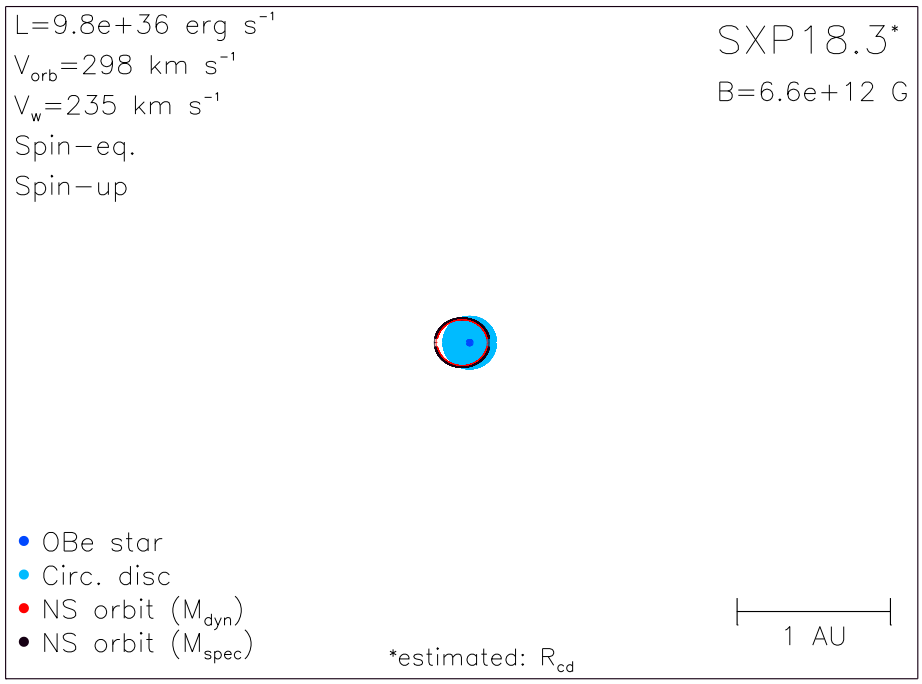

Figure B.18: Diagram of SXP18.3, using orbital parameters given in Table A.1 and discussed in Section 2.3.

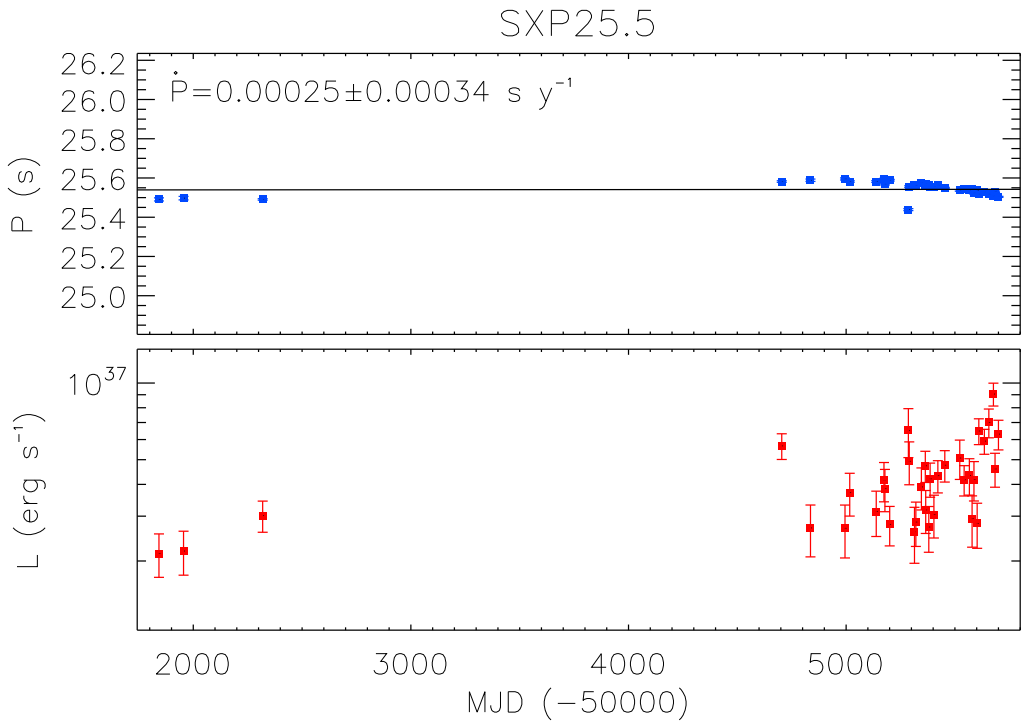

Figure B.19: P (upper panel; blue) and L (lower panel; red) as a function of MJD for SXP25.5. The black line in the upper panel shows the best-fit $\dot{P}$.

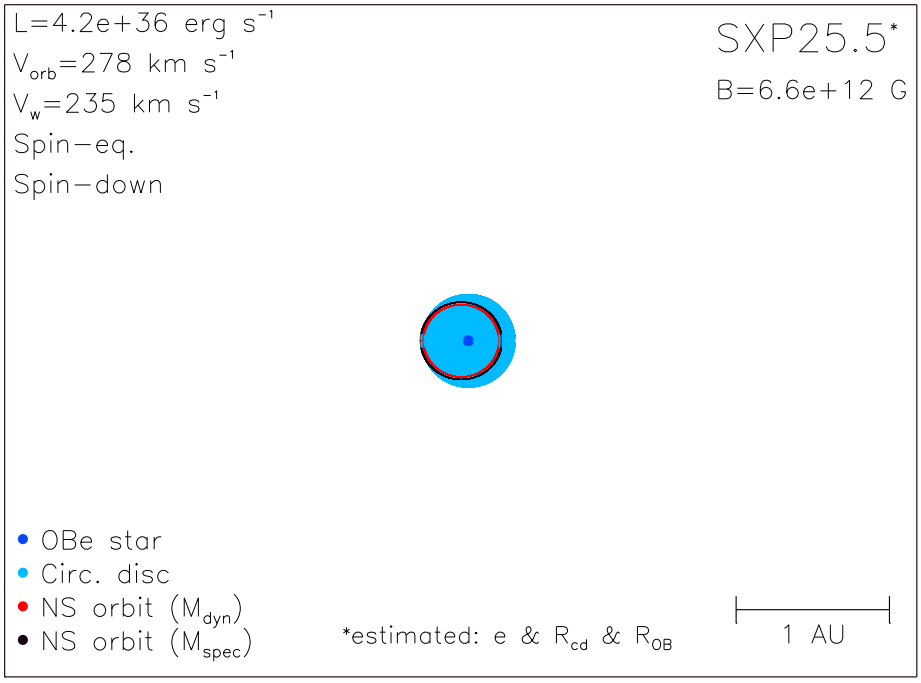

Figure B.20: Diagram of SXP25.5, using orbital parameters given in Table A.1 and discussed in Section 2.3.

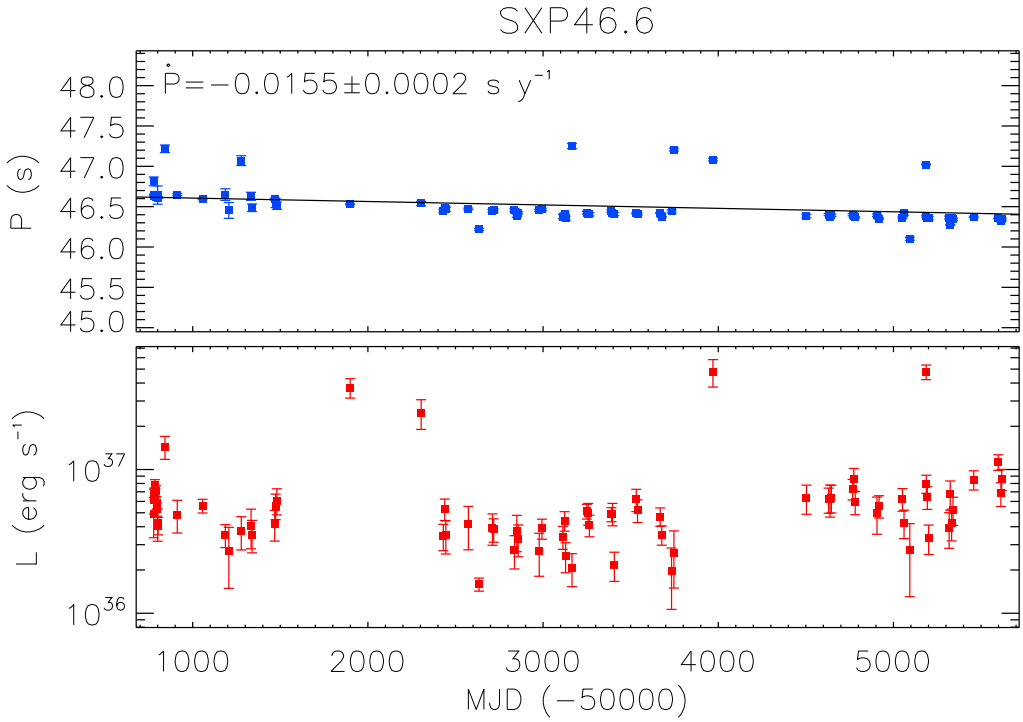

Figure B.21: P (upper panel; blue) and L (lower panel; red) as a function of MJD for SXP46.6. The black line in the upper panel shows the best-fit $\dot{P}$.

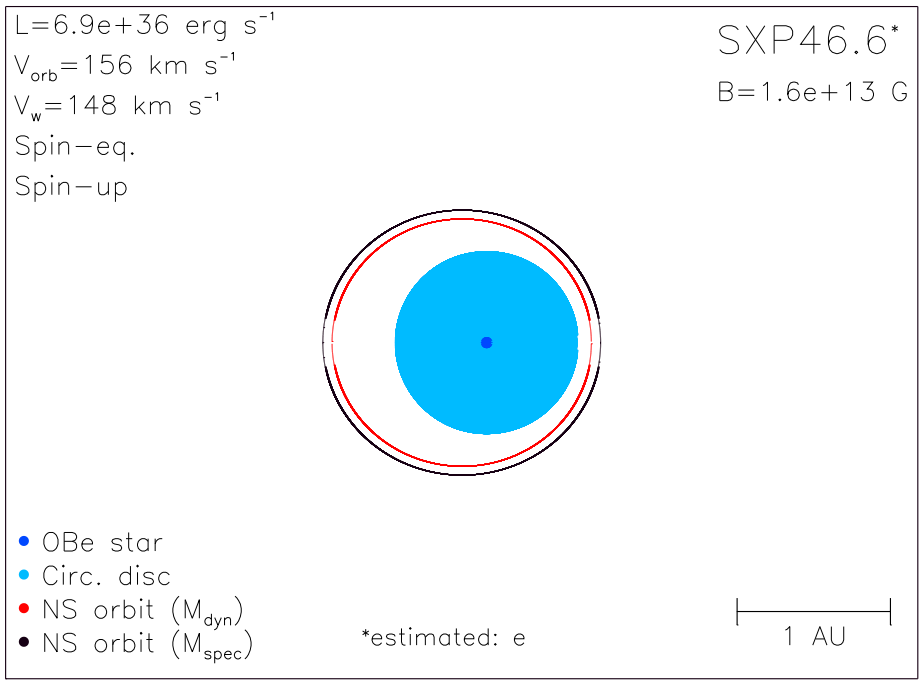

Figure B.22: Diagram of SXP46.6, using orbital parameters given in Table A.1 and discussed in Section 2.3.

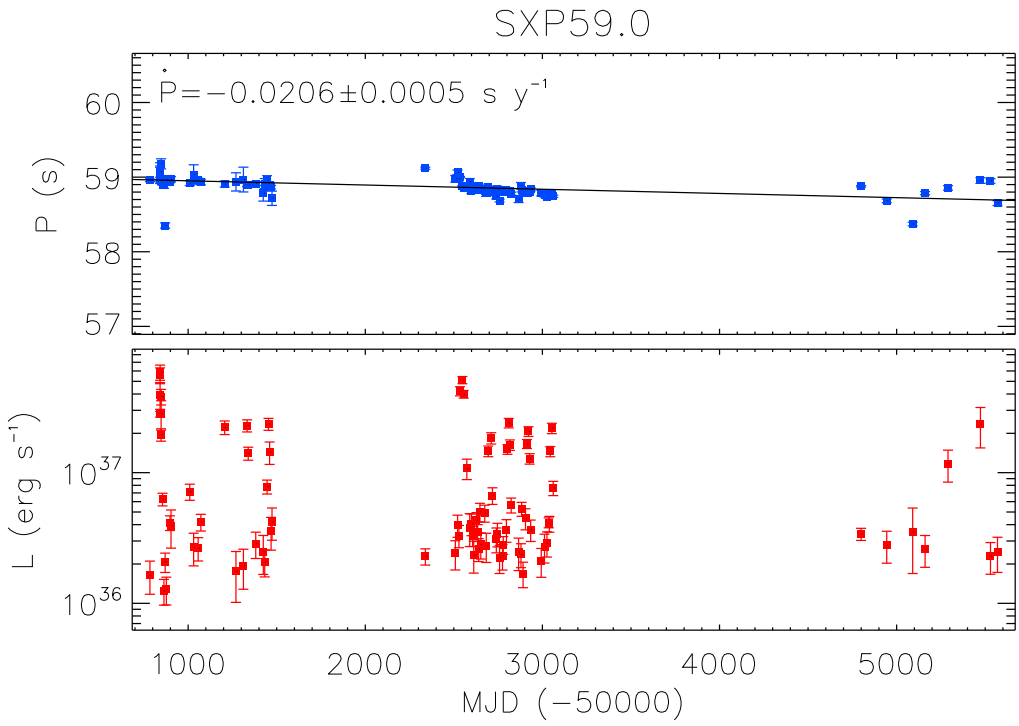

Figure B.23: P (upper panel; blue) and L (lower panel; red) as a function of MJD for SXP59.0. The black line in the upper panel shows the best-fit $\dot{P}$.

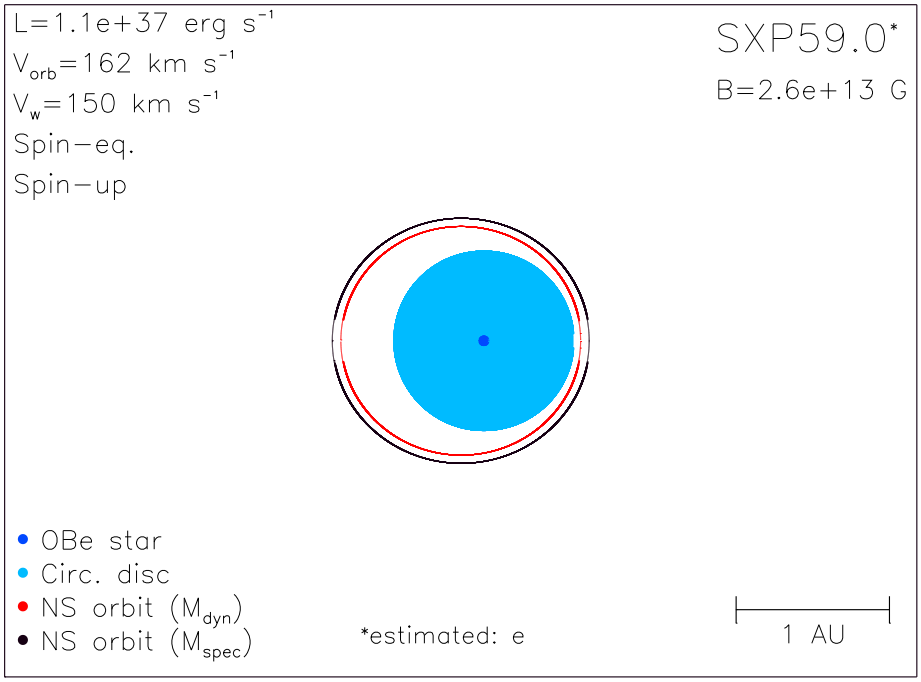

Figure B.24: Diagram of SXP59.0, using orbital parameters given in Table A.1 and discussed in Section 2.3.

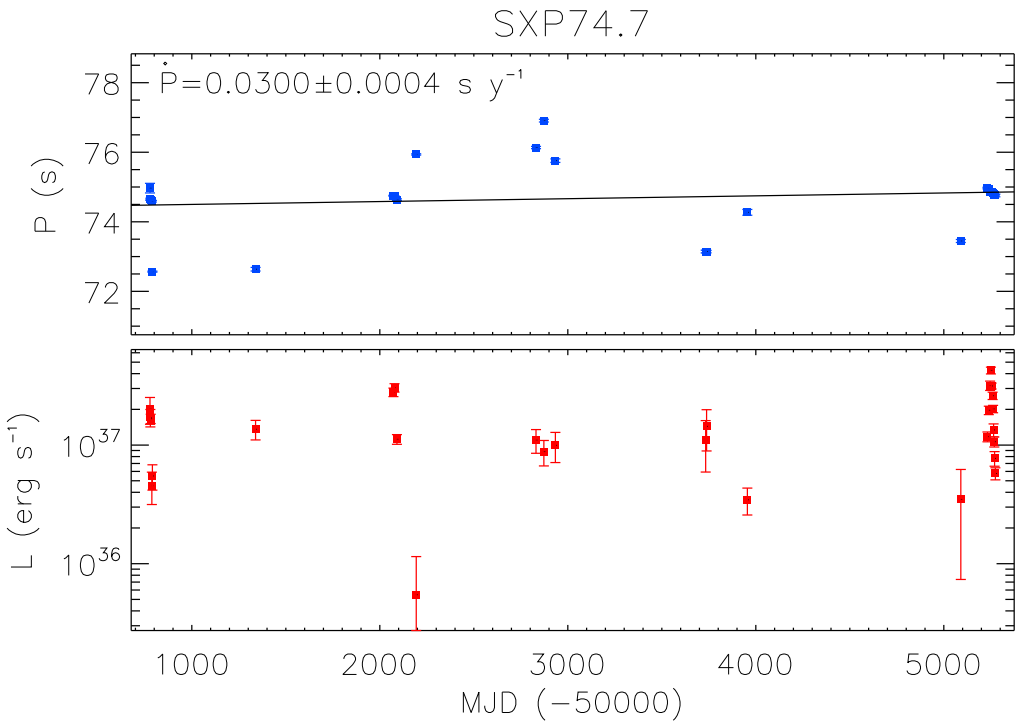

Figure B.25: P (upper panel; blue) and L (lower panel; red) as a function of MJD for SXP74.7. The black line in the upper panel shows the best-fit $\dot{P}$.

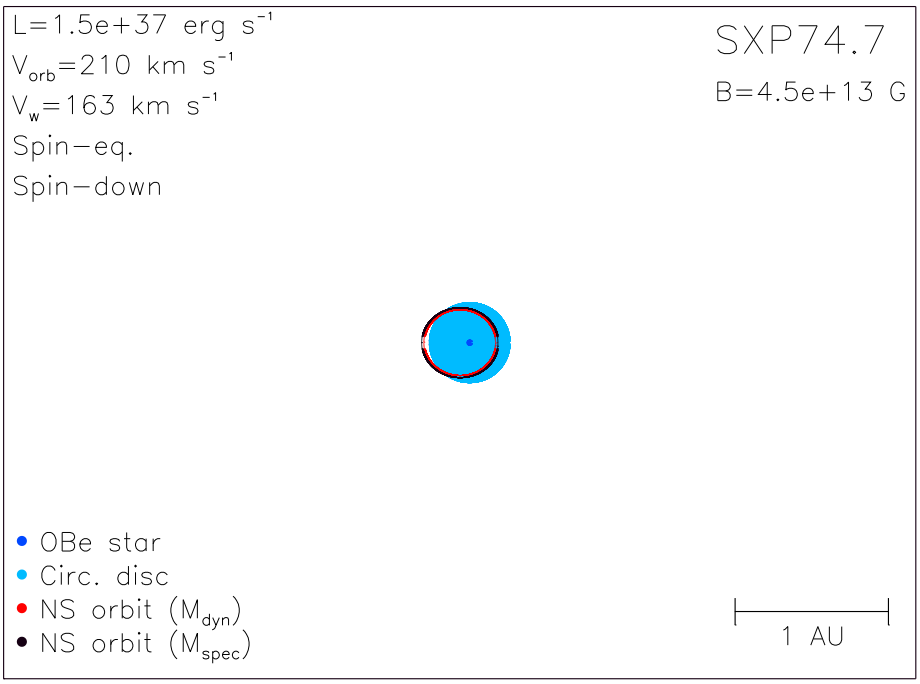

Figure B.26: Diagram of SXP74.7, using orbital parameters given in Table A.1 and discussed in Section 2.3.

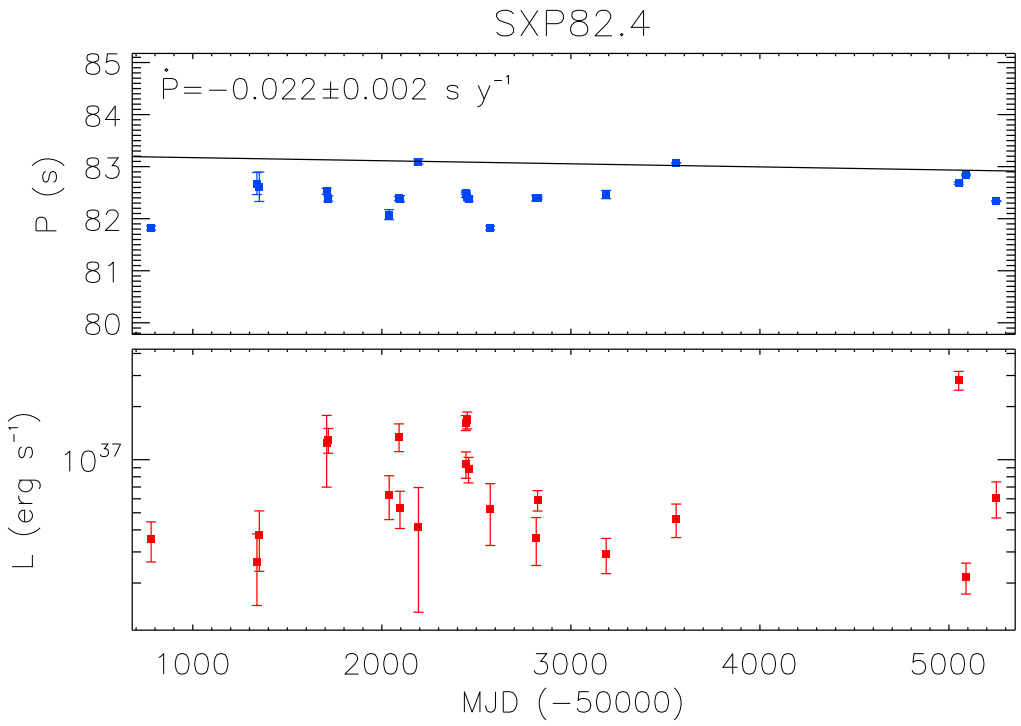

Figure B.27: P (upper panel; blue) and L (lower panel; red) as a function of MJD for SXP82.4. The black line in the upper panel shows the best-fit $\dot{P}$.

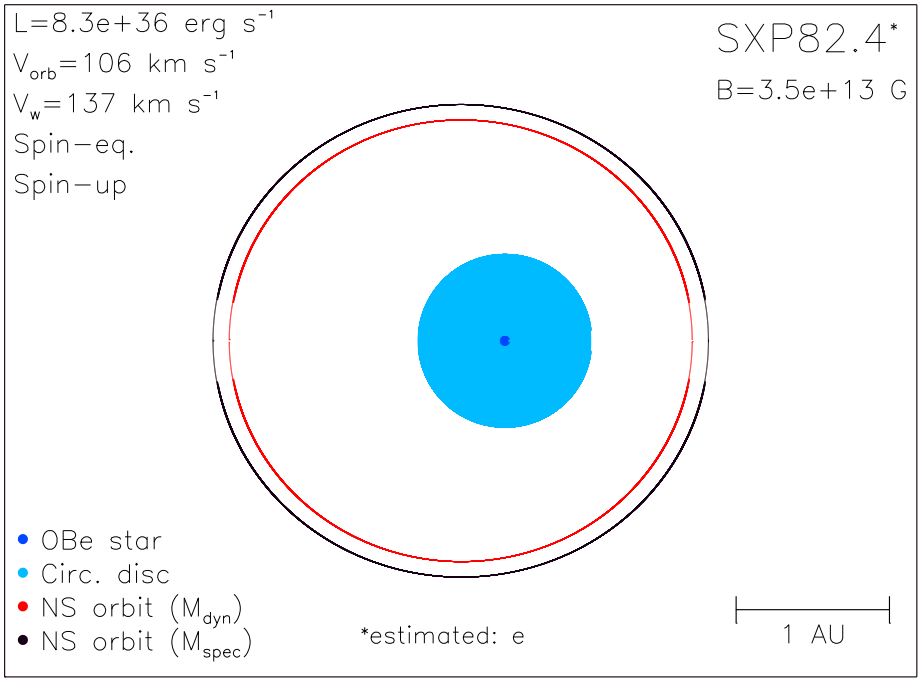

Figure B.28: Diagram of SXP82.4, using orbital parameters given in Table A.1 and discussed in Section 2.3.

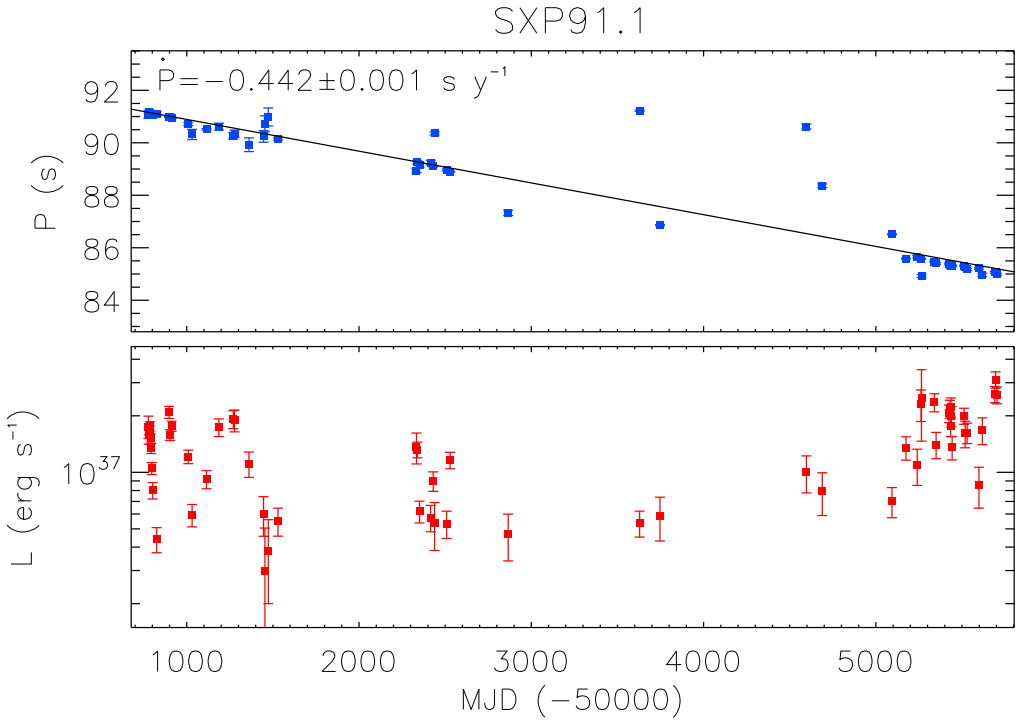

Figure B.29: P (upper panel; blue) and L (lower panel; red) as a function of MJD for SXP91.1. The black line in the upper panel shows the best-fit $\dot{P}$.

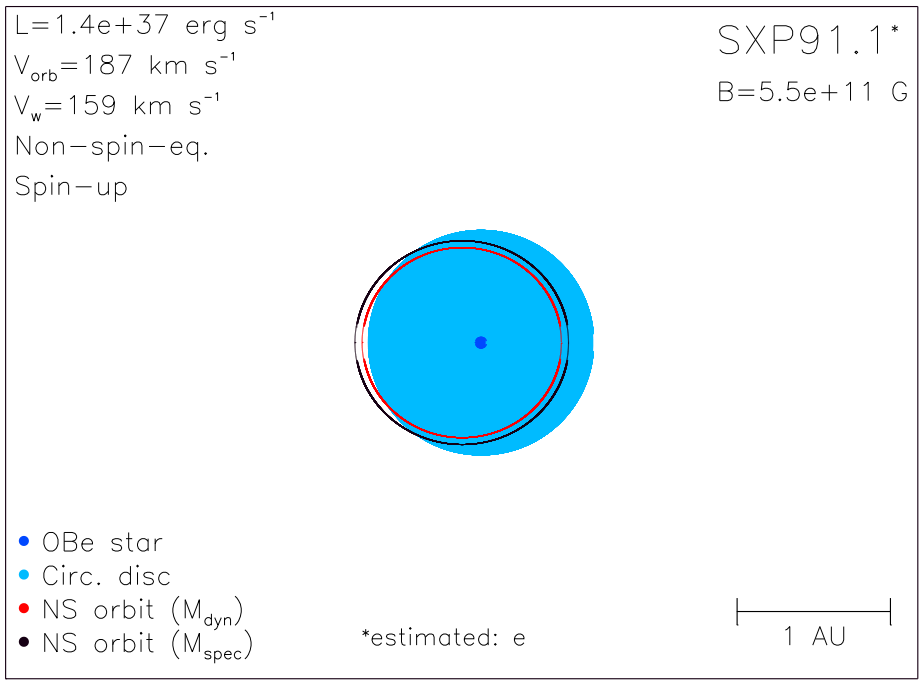

Figure B.30: Diagram of SXP91.1, using orbital parameters given in Table A.1 and discussed in Section 2.3.

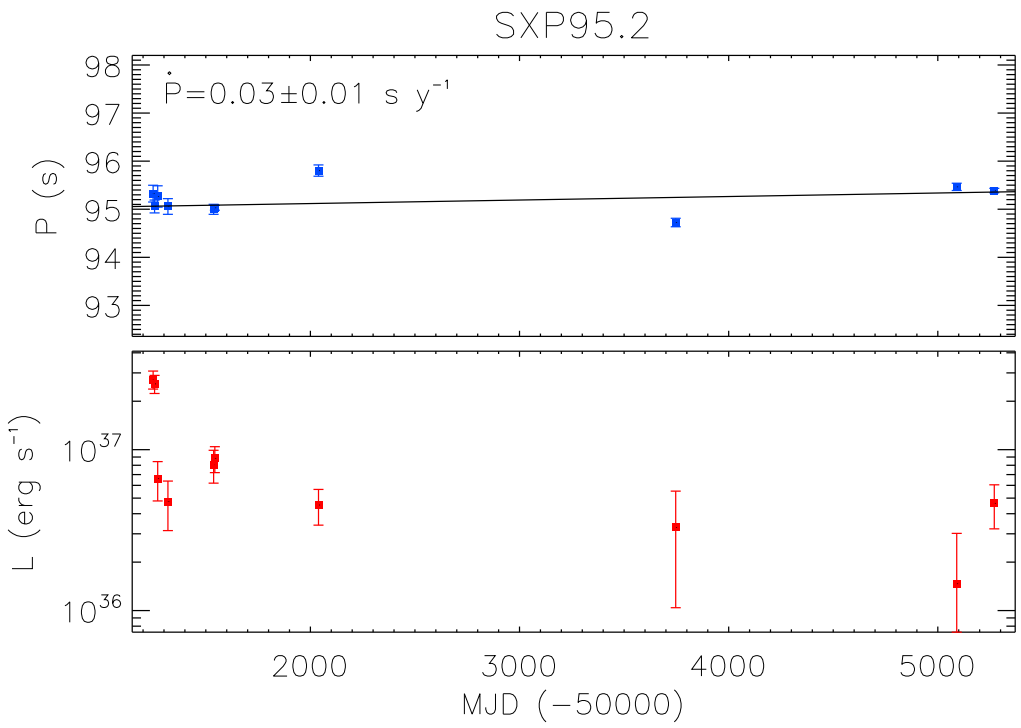

Figure B.31: P (upper panel; blue) and L (lower panel; red) as a function of MJD for SXP95.2. The black line in the upper panel shows the best-fit $\dot{P}$.

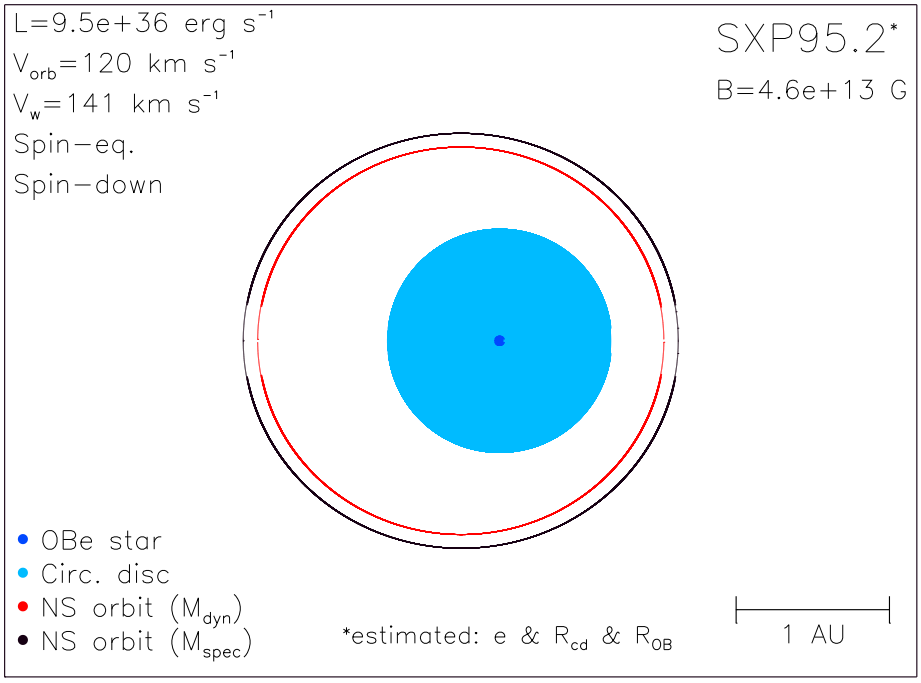

Figure B.32: Diagram of SXP95.2, using orbital parameters given in Table A.1 and discussed in Section 2.3.

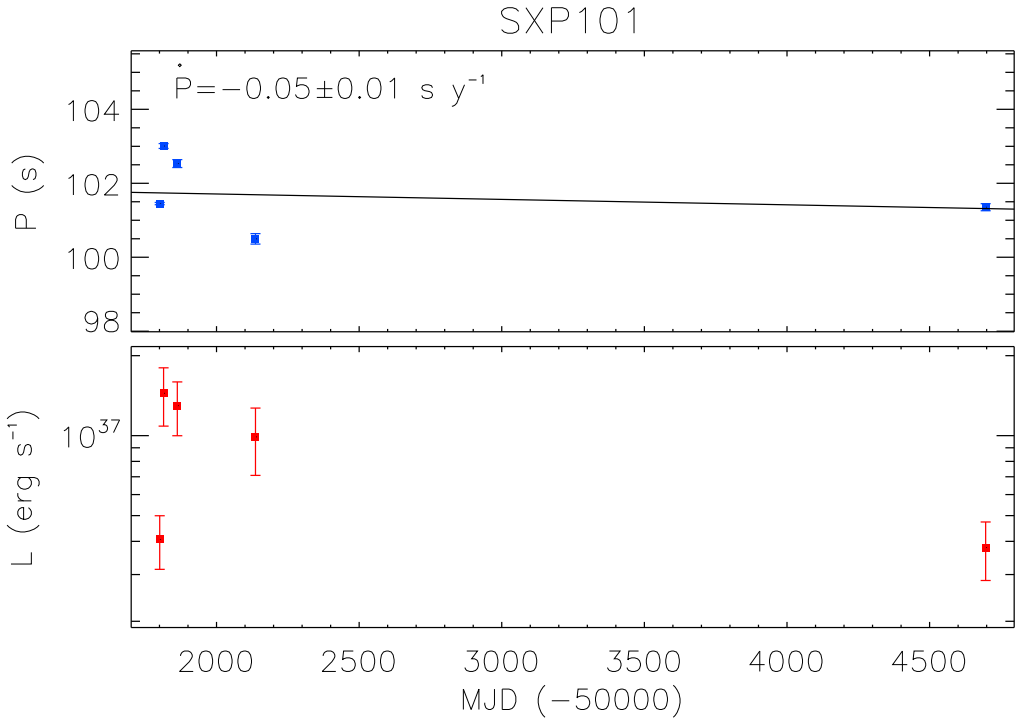

Figure B.33: P (upper panel; blue) and L (lower panel; red) as a function of MJD for SXP101. The black line in the upper panel shows the best-fit $\dot{P}$.

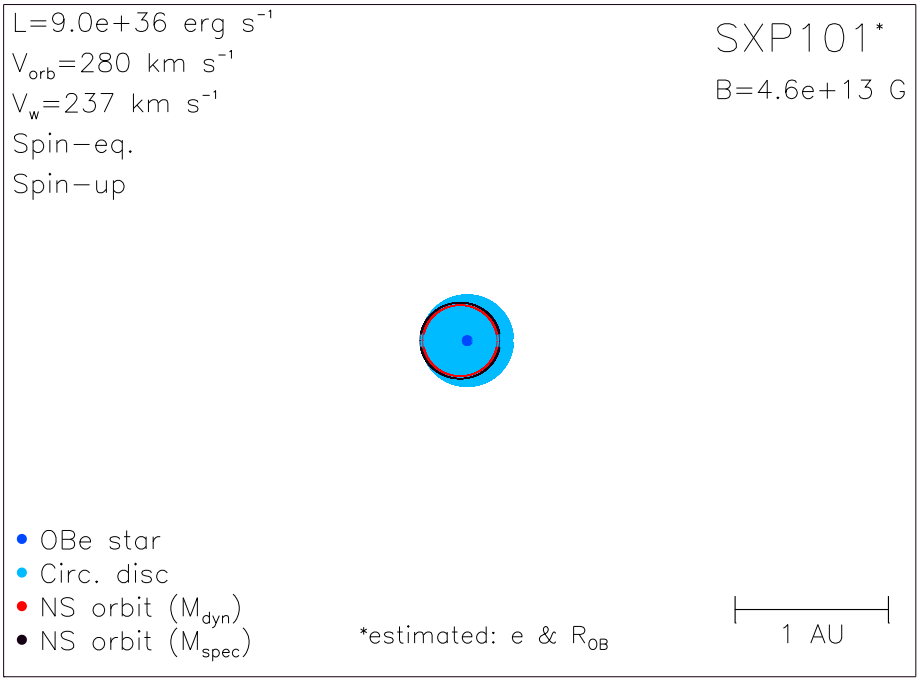

Figure B.34: Diagram of SXP101, using orbital parameters given in Table A.1 and discussed in Section 2.3.

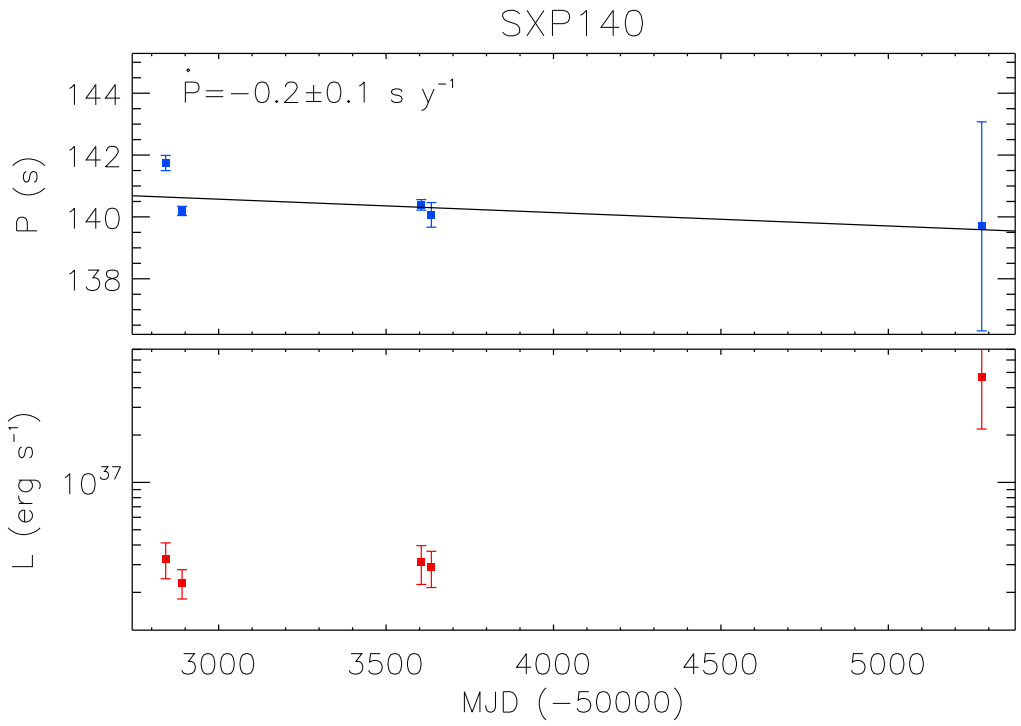

Figure B.35: P (upper panel; blue) and L (lower panel; red) as a function of MJD for SXP140. The black line in the upper panel shows the best-fit $\dot{P}$.

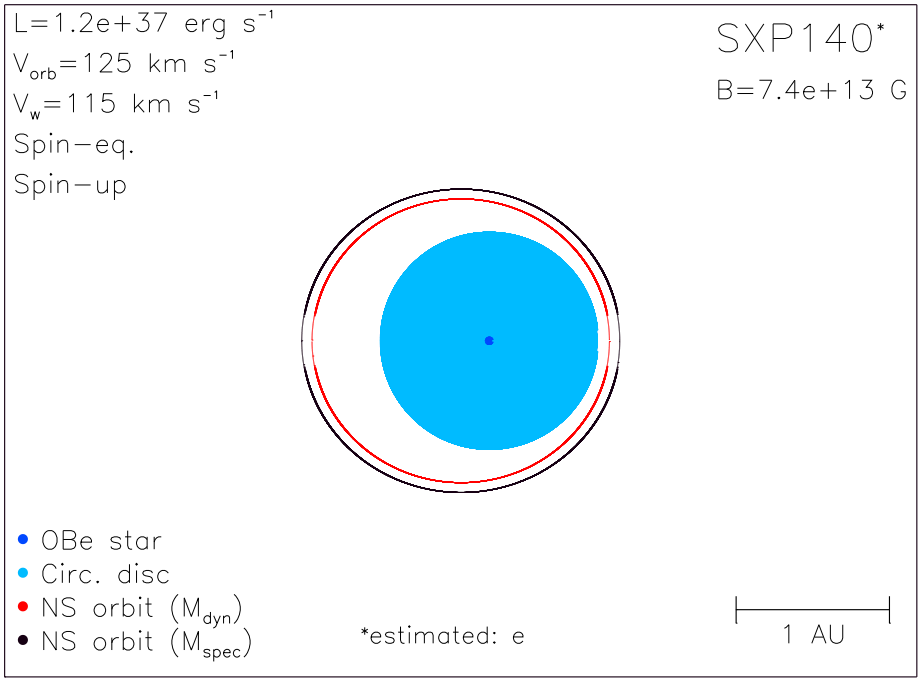

Figure B.36: Diagram of SXP140, using orbital parameters given in Table A.1 and discussed in Section 2.3.

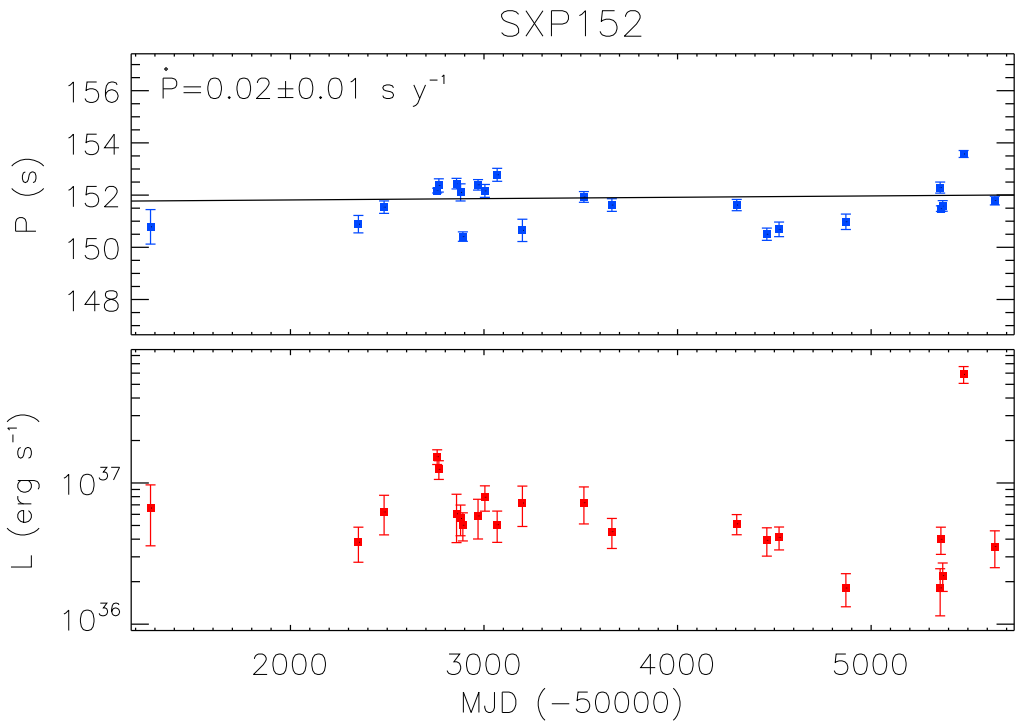

Figure B.37: P (upper panel; blue) and L (lower panel; red) as a function of MJD for SXP152. The black line in the upper panel shows the best-fit $\dot{P}$.

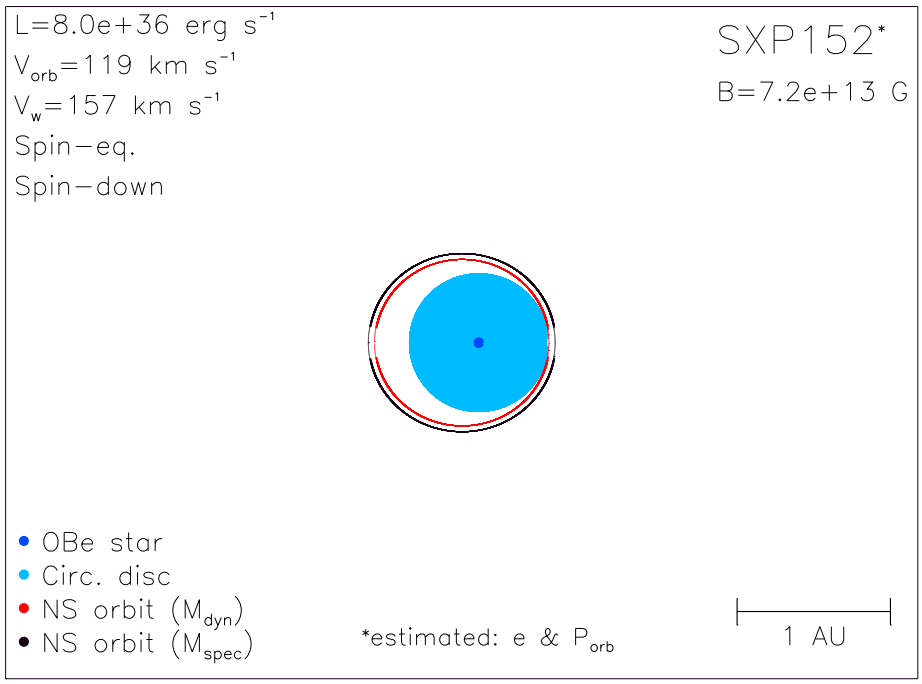

Figure B.38: Diagram of SXP152, using orbital parameters given in Table A.1 and discussed in Section 2.3.

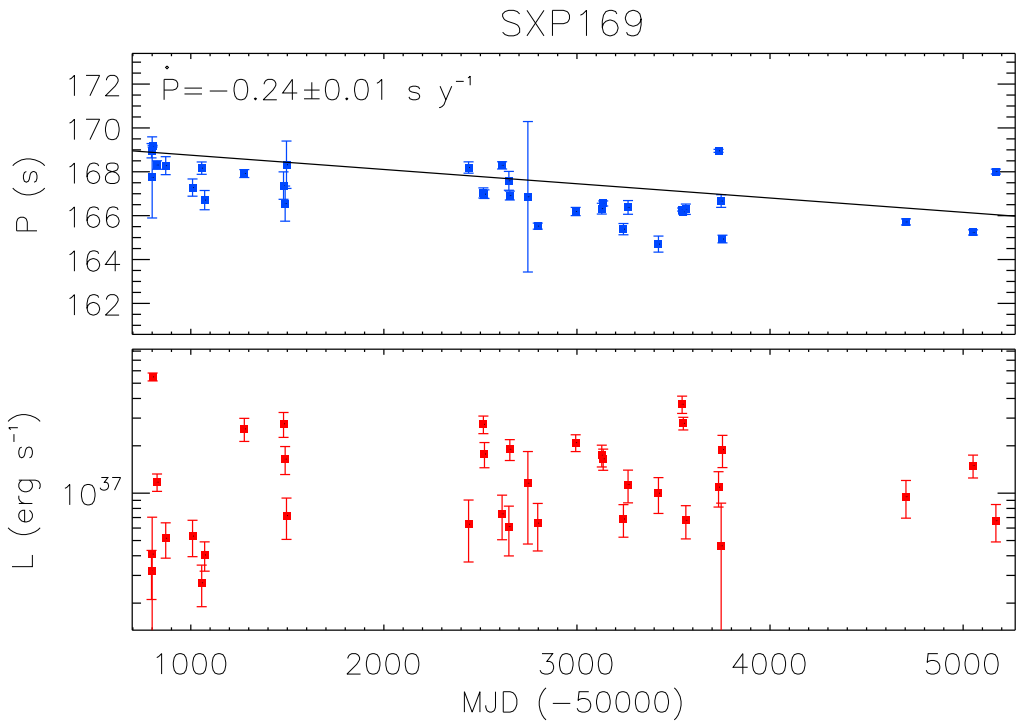

Figure B.39: P (upper panel; blue) and L (lower panel; red) as a function of MJD for SXP169. The black line in the upper panel shows the best-fit $\dot{P}$.

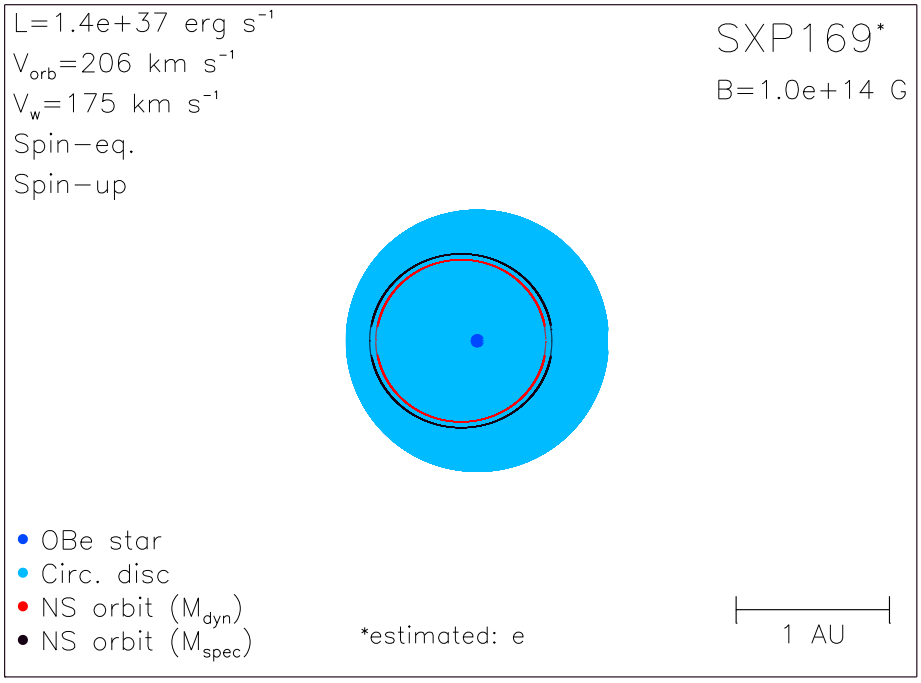

Figure B.40: Diagram of SXP169, using orbital parameters given in Table A.1 and discussed in Section 2.3.

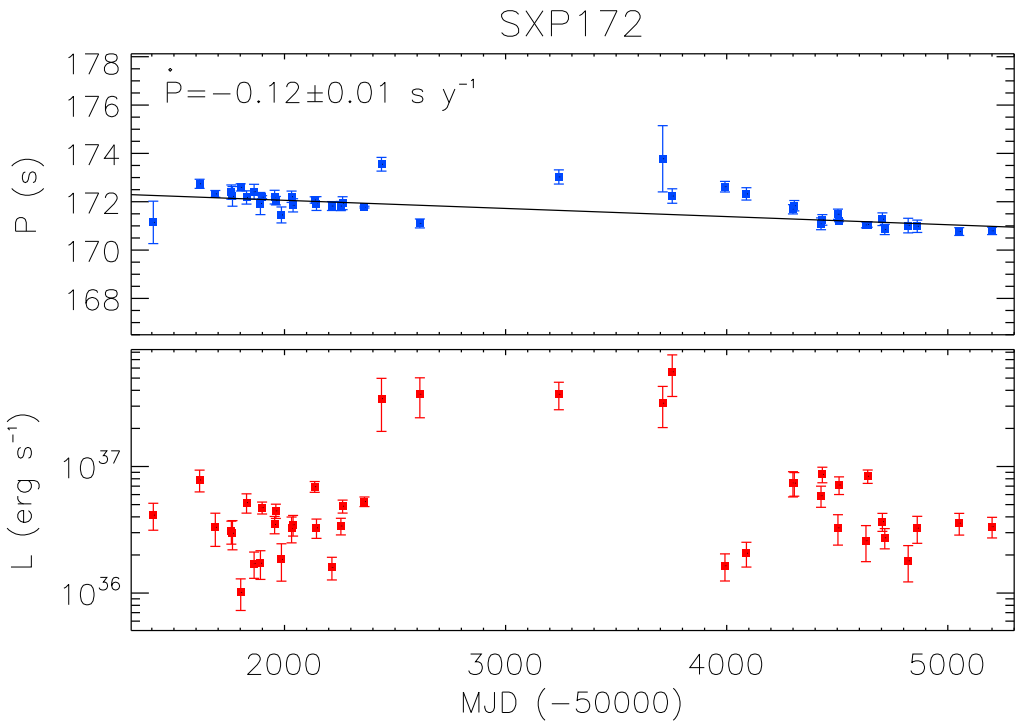

Figure B.41: P (upper panel; blue) and L (lower panel; red) as a function of MJD for SXP172. The black line in the upper panel shows the best-fit $\dot{P}$.

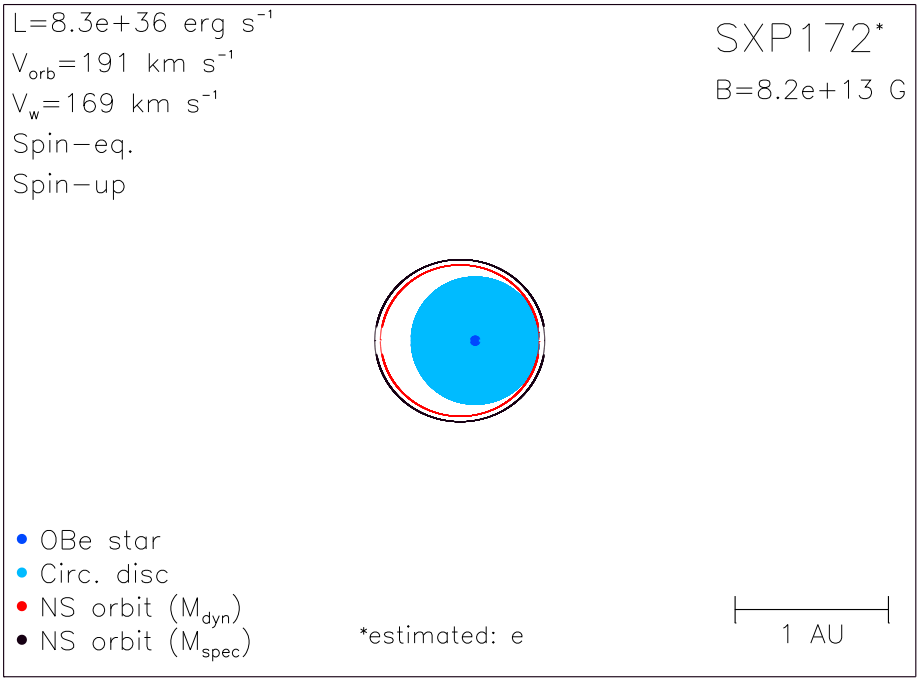

Figure B.42: Diagram of SXP172, using orbital parameters given in Table A.1 and discussed in Section 2.3.

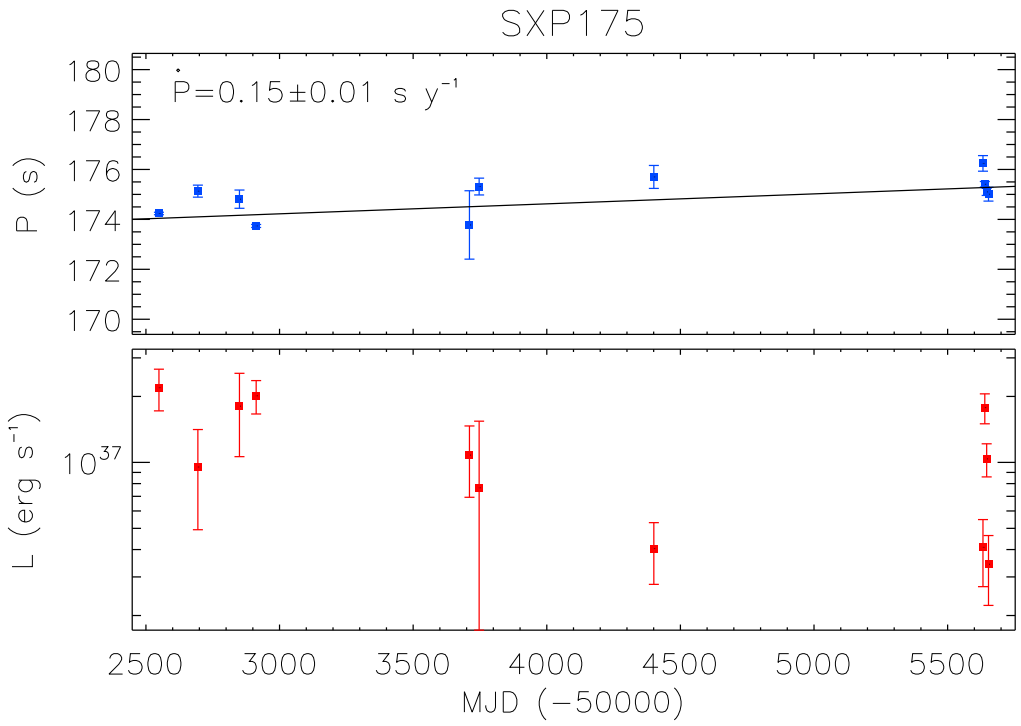

Figure B.43: P (upper panel; blue) and L (lower panel; red) as a function of MJD for SXP175. The black line in the upper panel shows the best-fit $\dot{P}$.

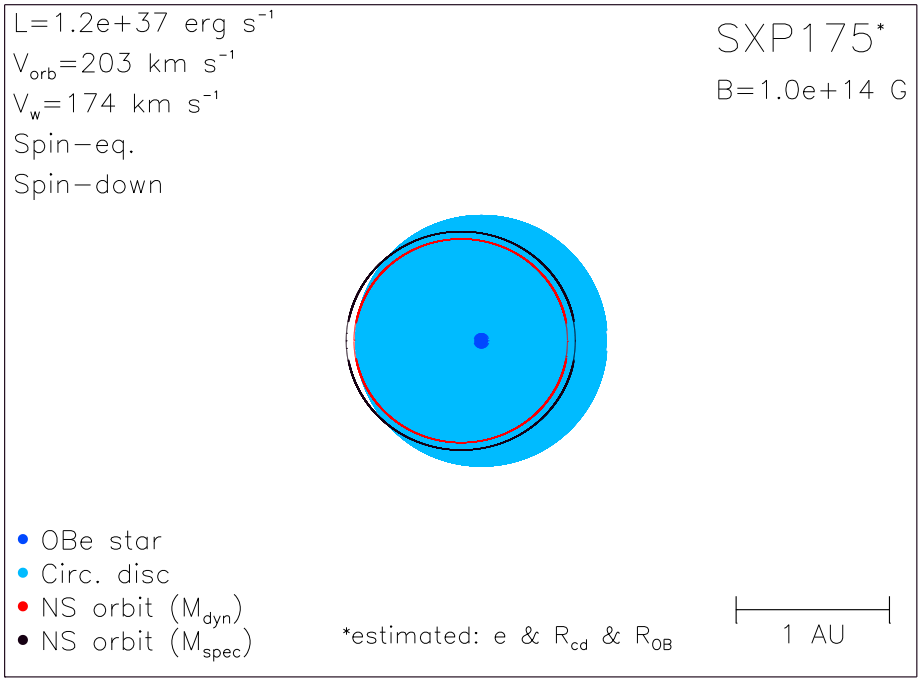

Figure B.44: Diagram of SXP175, using orbital parameters given in Table A.1 and discussed in Section 2.3.

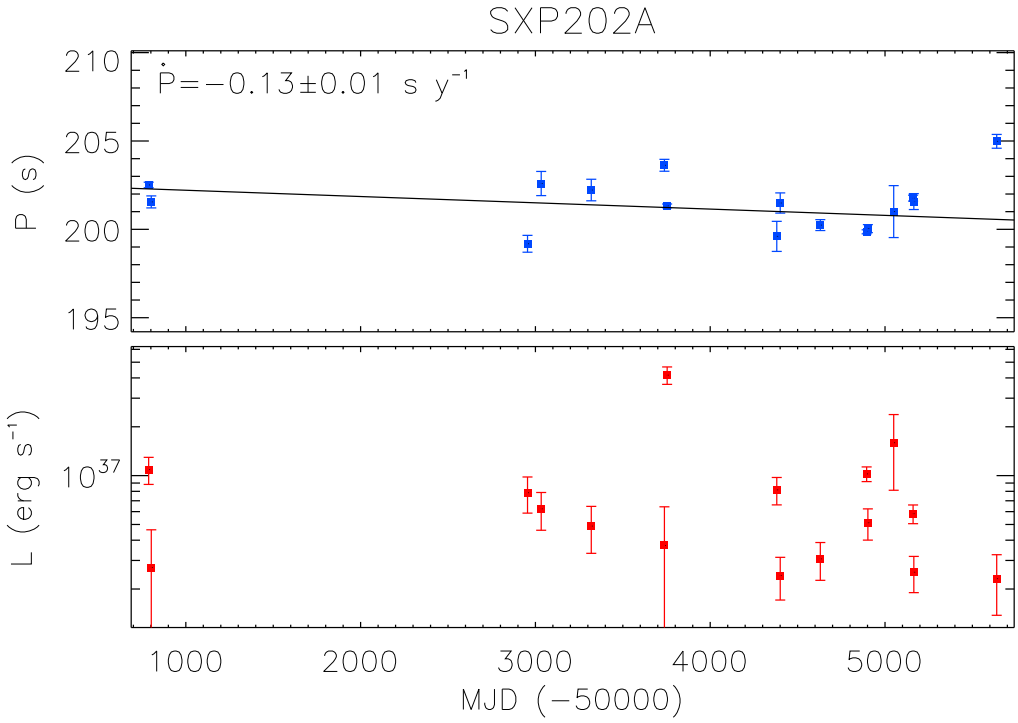

Figure B.45: P (upper panel; blue) and L (lower panel; red) as a function of MJD for SXP202A. The black line in the upper panel shows the best-fit $\dot{P}$.

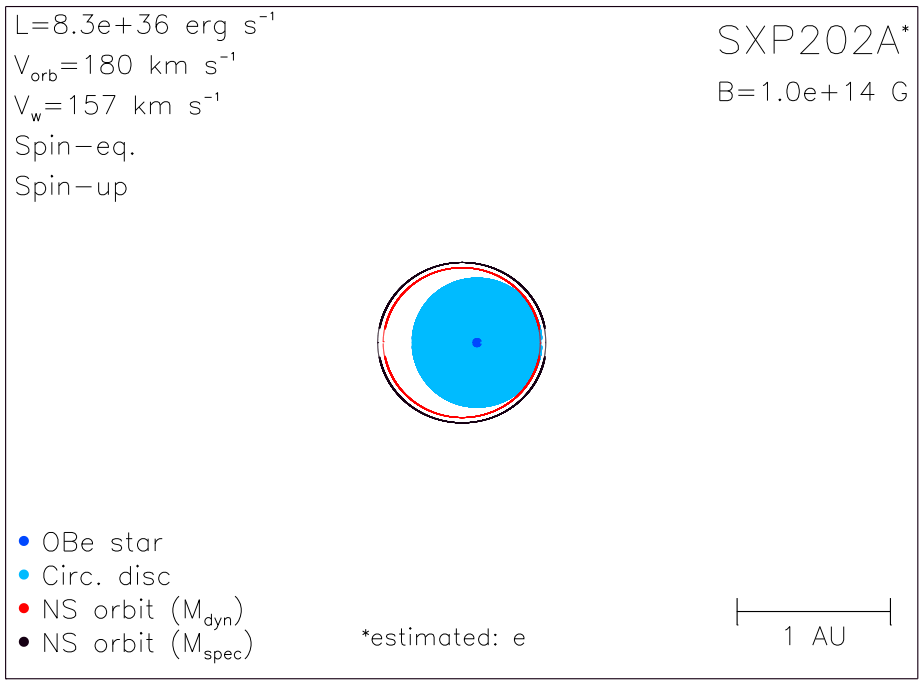

Figure B.46: Diagram of SXP202A, using orbital parameters given in Table A.1 and discussed in Section 2.3.

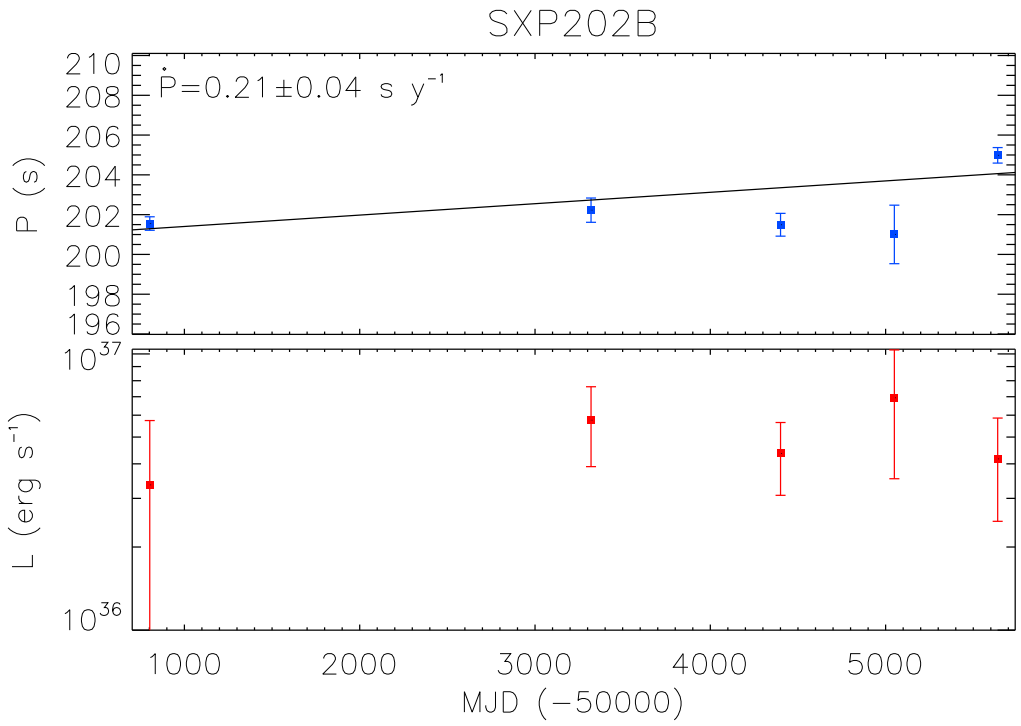

Figure B.47: P (upper panel; blue) and L (lower panel; red) as a function of MJD for SXP202B. The black line in the upper panel shows the best-fit $\dot{P}$.

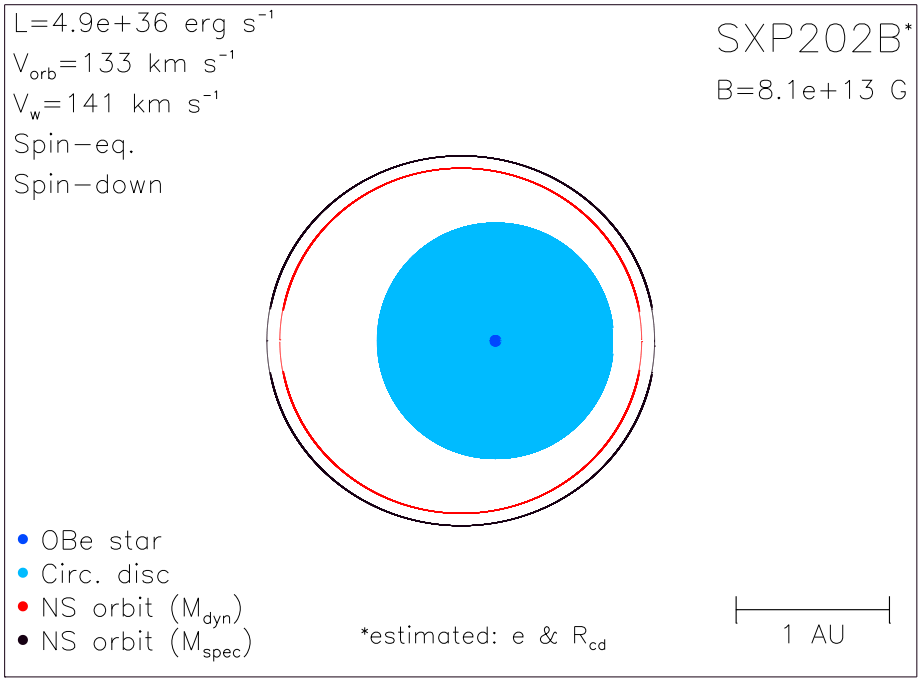

Figure B.48: Diagram of SXP202B, using orbital parameters given in Table A.1 and discussed in Section 2.3.

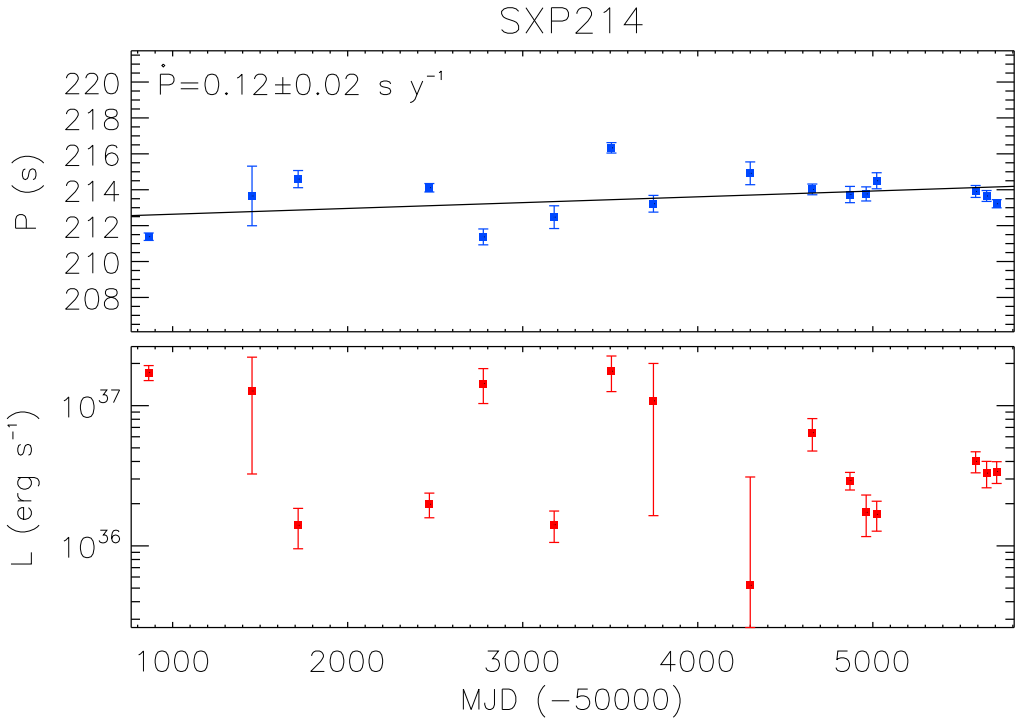

Figure B.49: P (upper panel; blue) and L (lower panel; red) as a function of MJD for SXP214. The black line in the upper panel shows the best-fit $\dot{P}$.

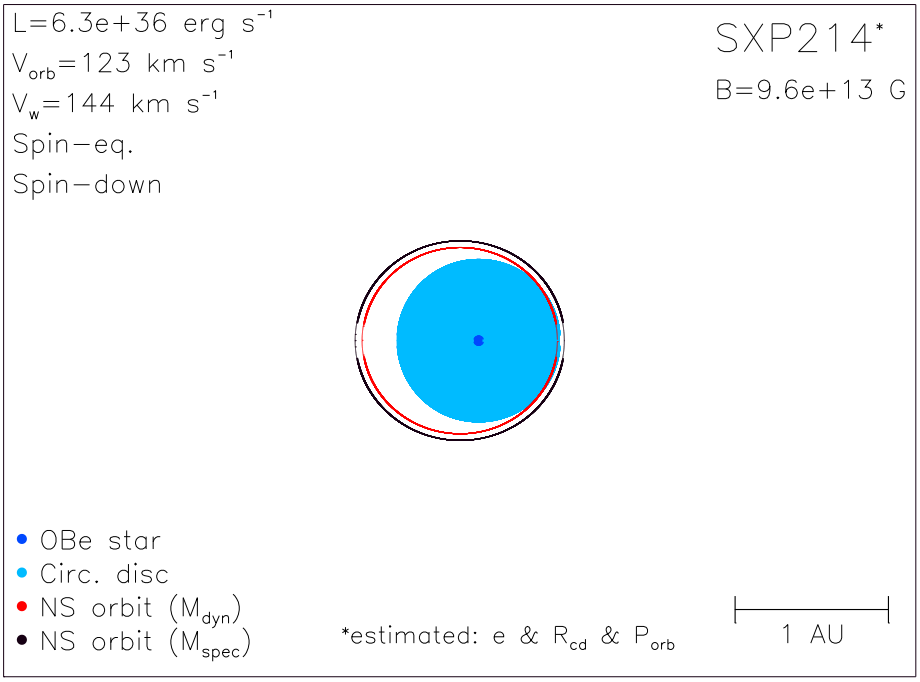

Figure B.50: Diagram of SXP214, using orbital parameters given in Table A.1 and discussed in Section 2.3.

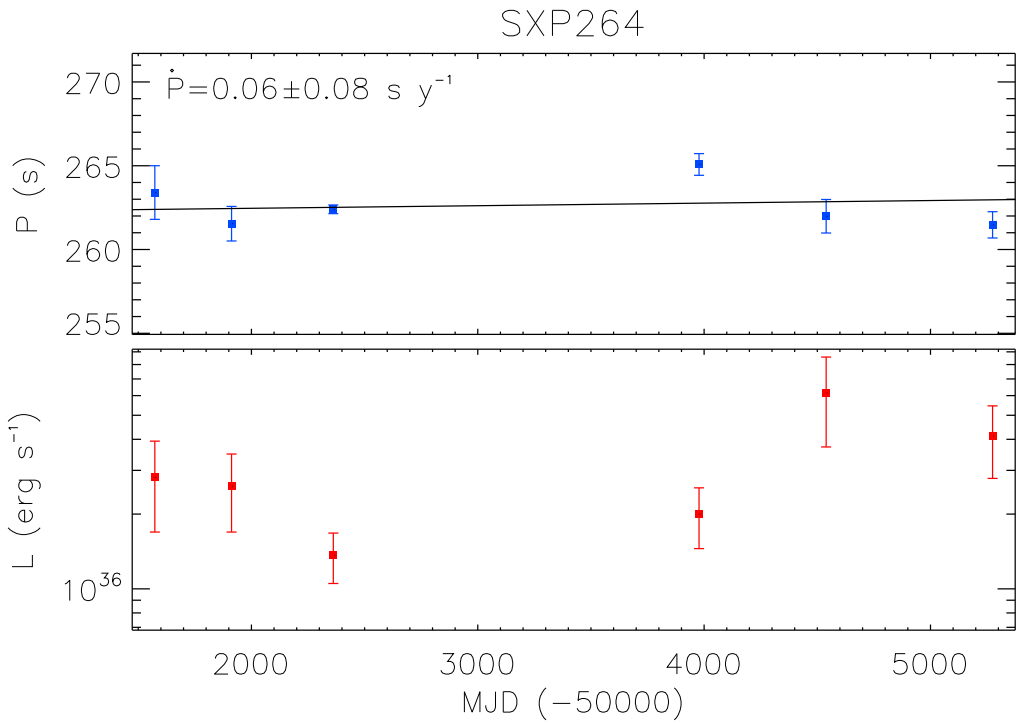

Figure B.51: P (upper panel; blue) and L (lower panel; red) as a function of MJD for SXP264. The black line in the upper panel shows the best-fit $\dot{P}$.

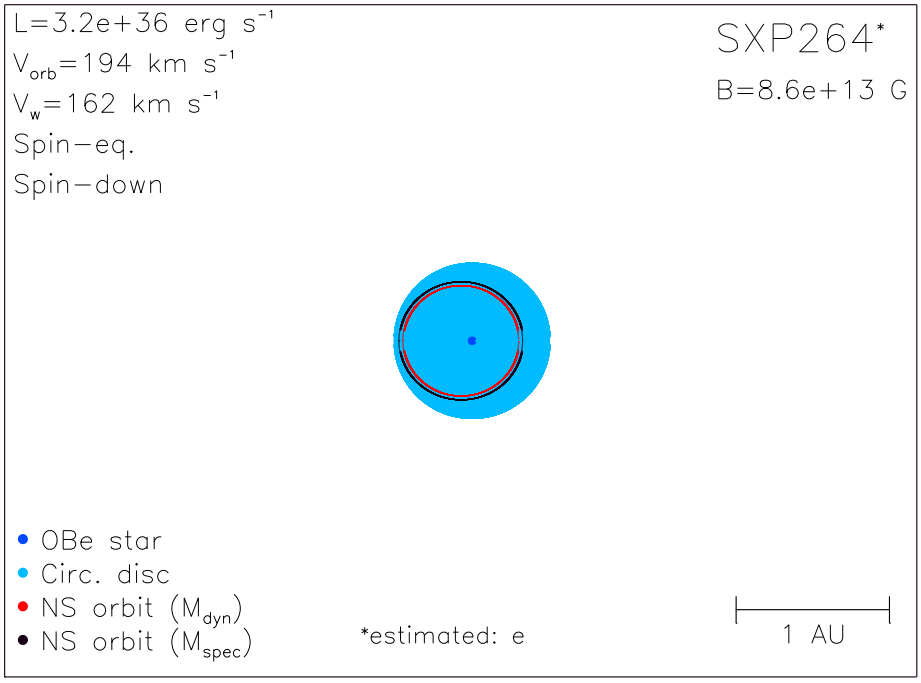

Figure B.52: Diagram of SXP264, using orbital parameters given in Table A.1 and discussed in Section 2.3.

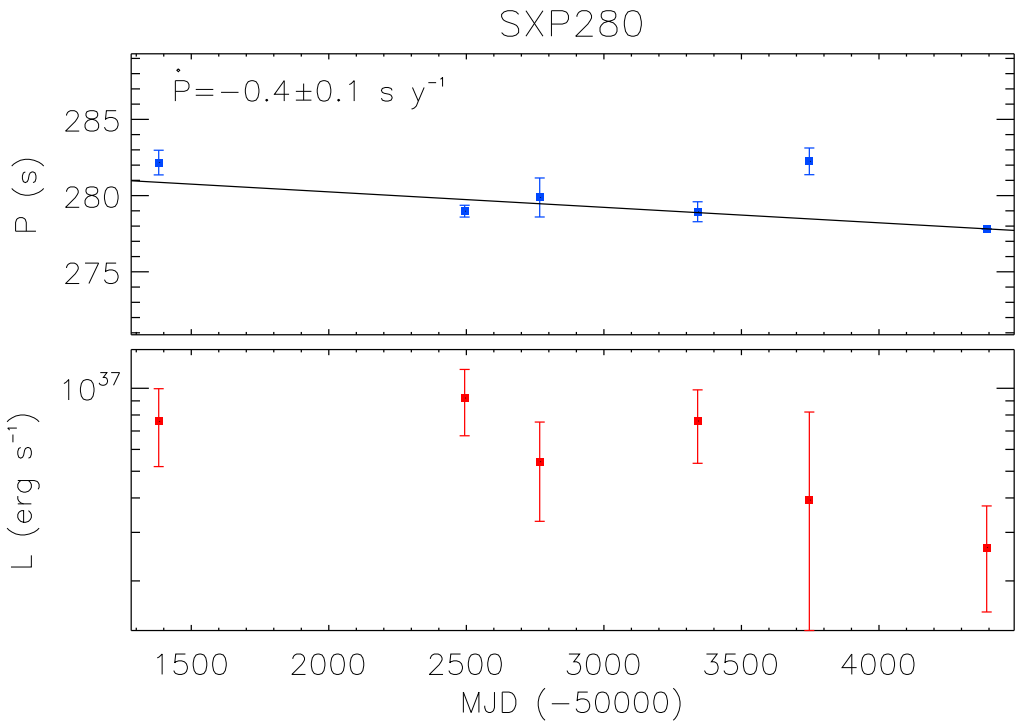

Figure B.53: P (upper panel; blue) and L (lower panel; red) as a function of MJD for SXP280. The black line in the upper panel shows the best-fit $\dot{P}$.

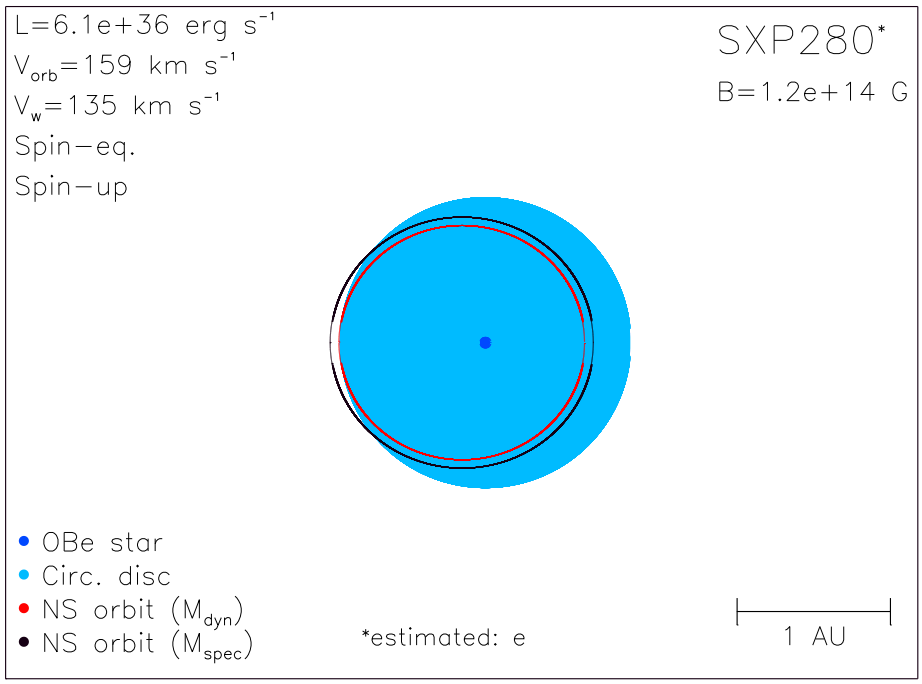

Figure B.54: Diagram of SXP280, using orbital parameters given in Table A.1 and discussed in Section 2.3.

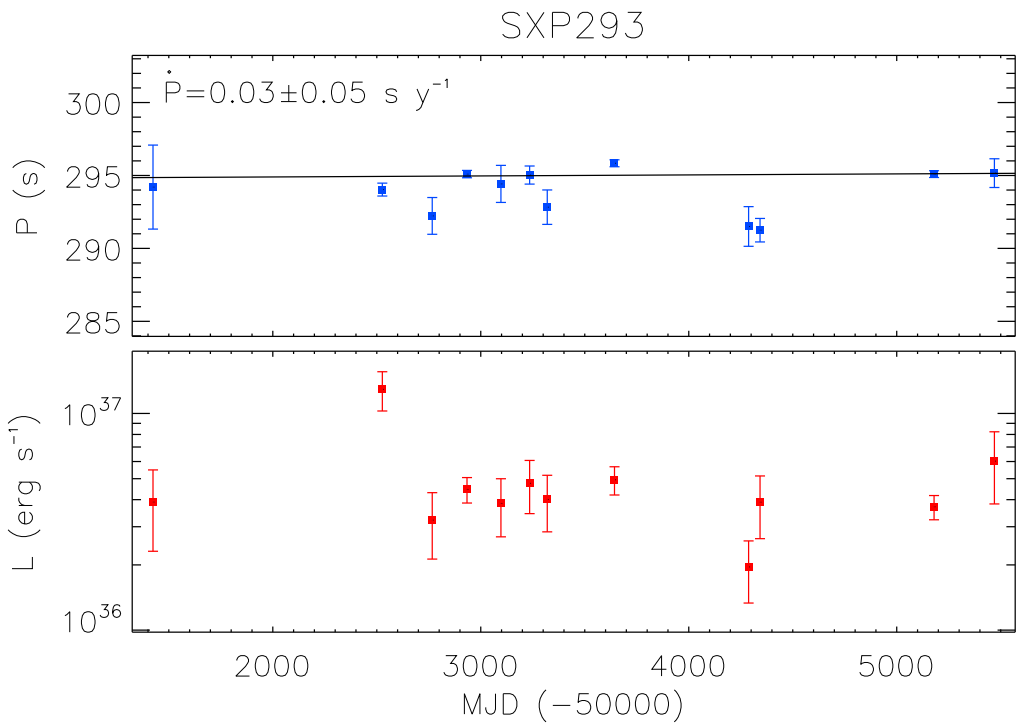

Figure B.55: P (upper panel; blue) and L (lower panel; red) as a function of MJD for SXP293. The black line in the upper panel shows the best-fit $\dot{P}$.

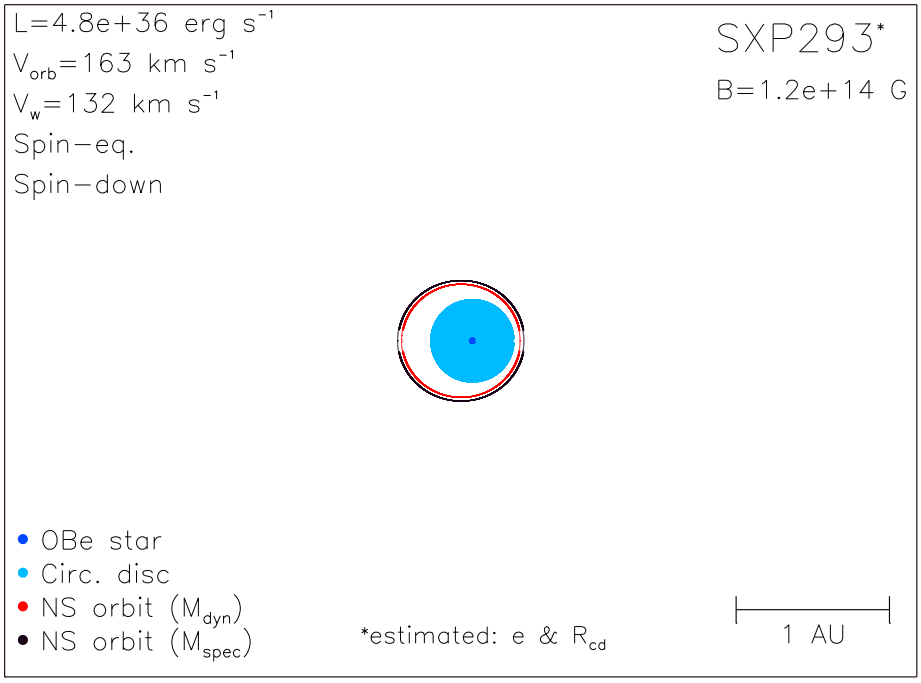

Figure B.56: Diagram of SXP293, using orbital parameters given in Table A.1 and discussed in Section 2.3.

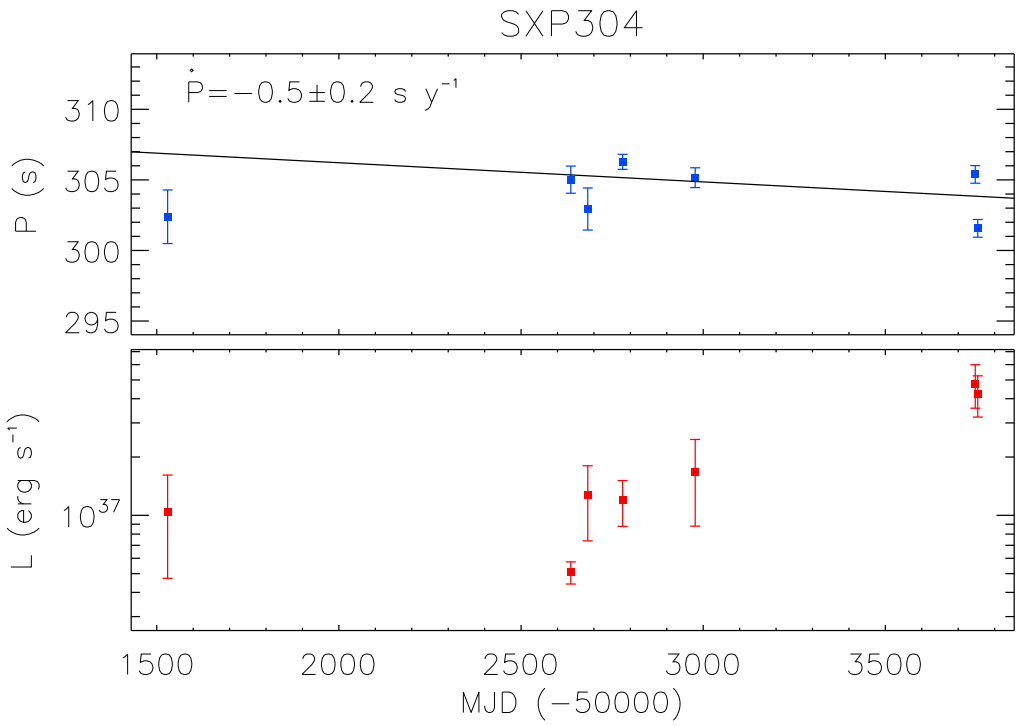

Figure B.57: P (upper panel; blue) and L (lower panel; red) as a function of MJD for SXP304. The black line in the upper panel shows the best-fit $\dot{P}$.

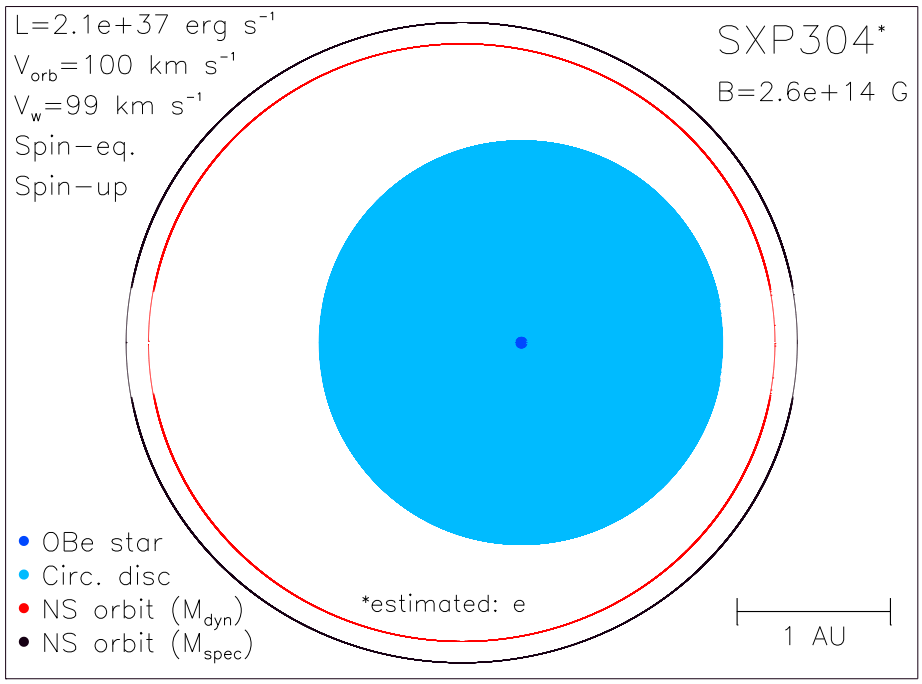

Figure B.58: Diagram of SXP304, using orbital parameters given in Table A.1 and discussed in Section 2.3.

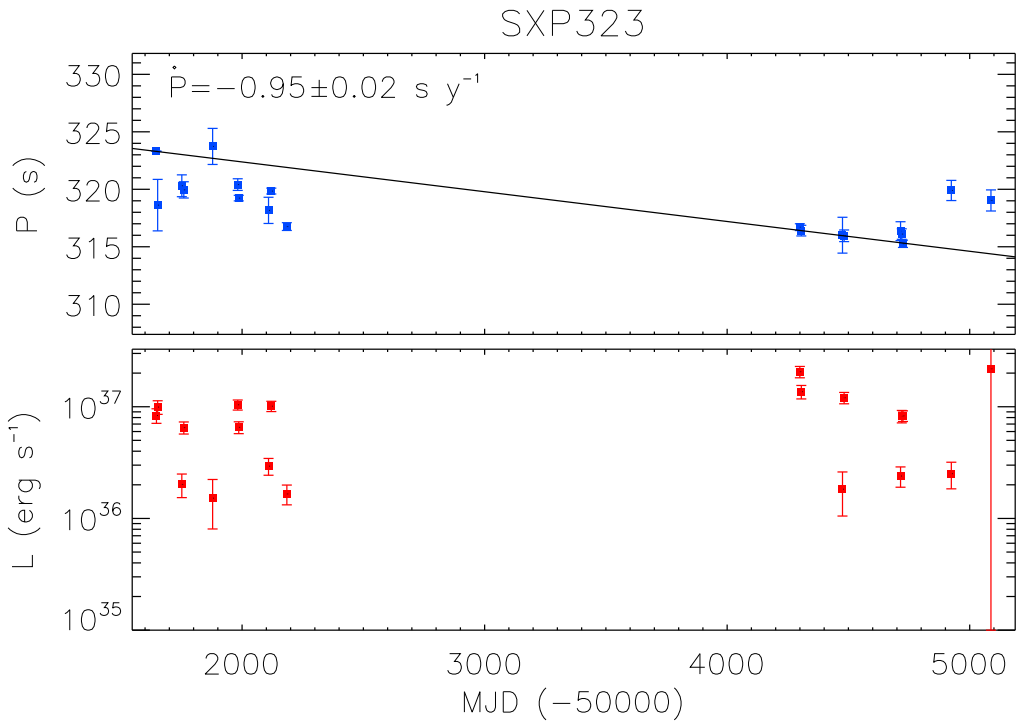

Figure B.59: P (upper panel; blue) and L (lower panel; red) as a function of MJD for SXP323. The black line in the upper panel shows the best-fit $\dot{P}$.

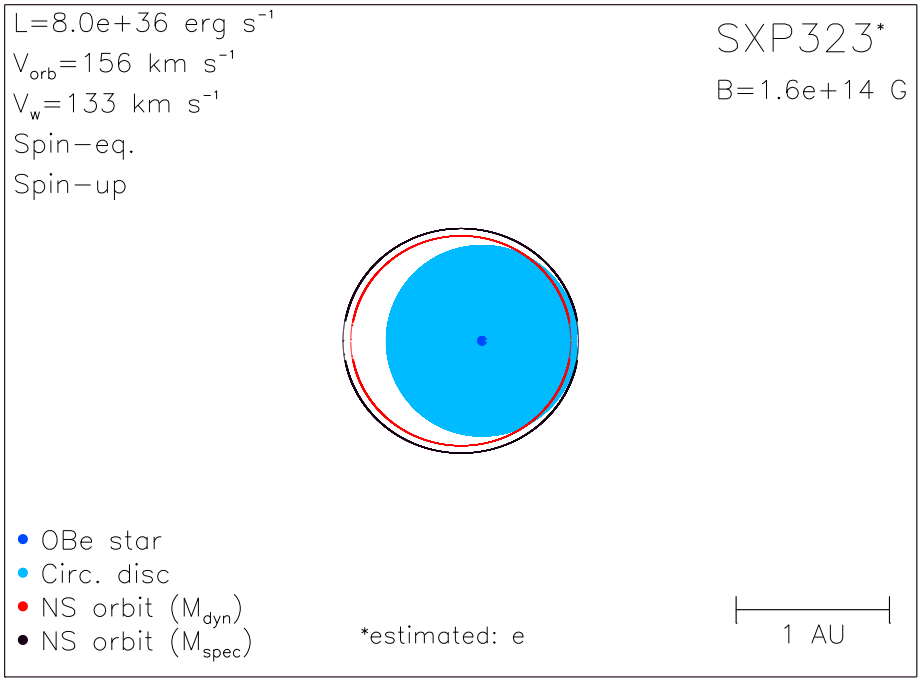

Figure B.60: Diagram of SXP323, using orbital parameters given in Table A.1 and discussed in Section 2.3.

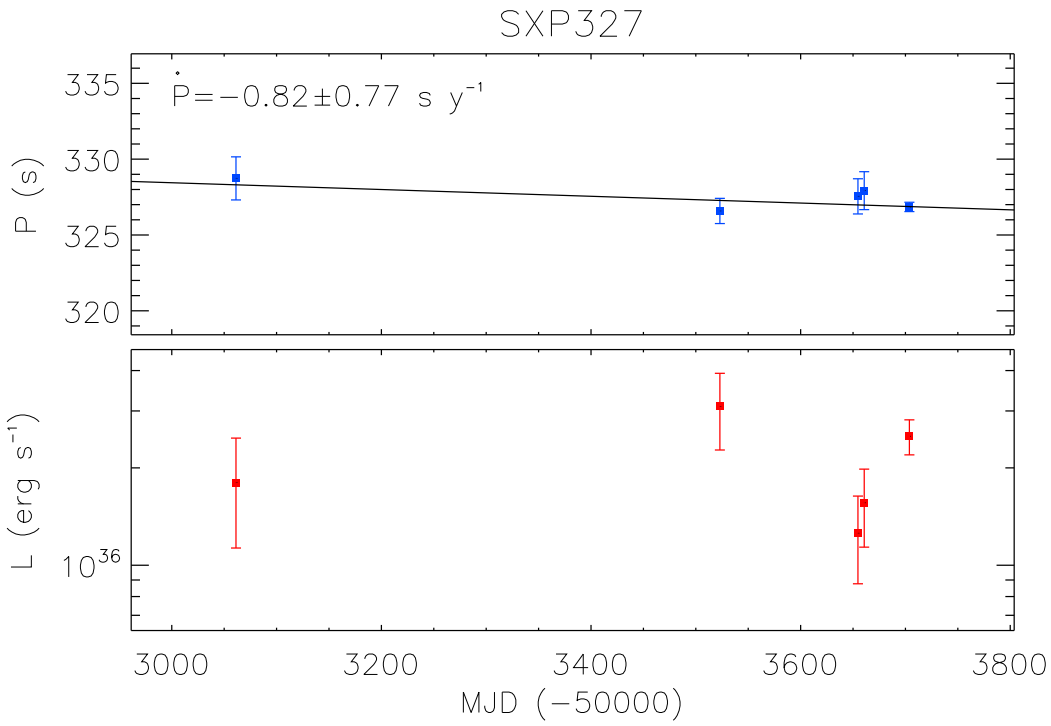

Figure B.61: P (upper panel; blue) and L (lower panel; red) as a function of MJD for SXP327. The black line in the upper panel shows the best-fit $\dot{P}$.

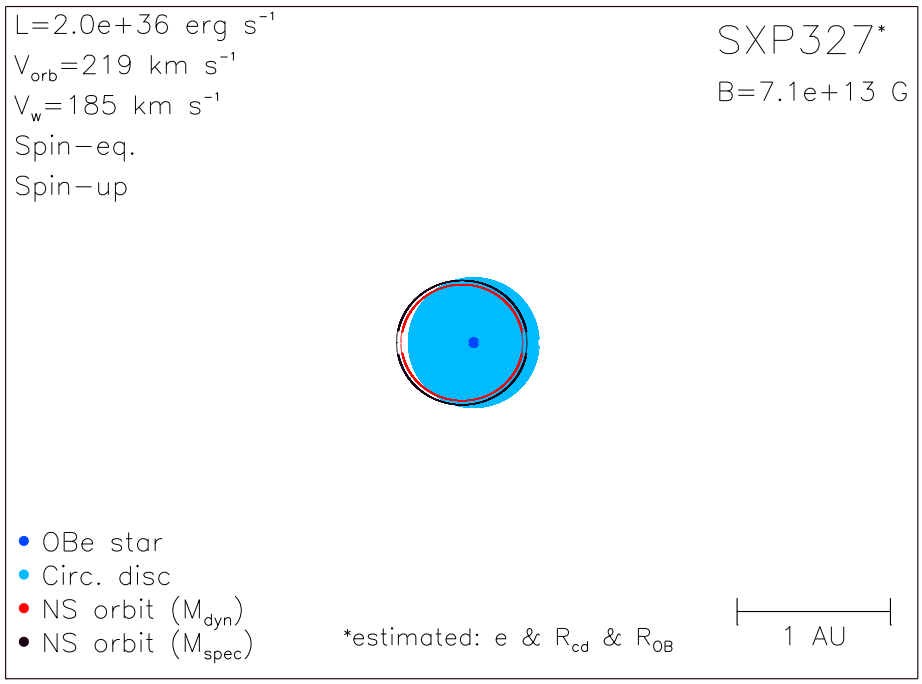

Figure B.62: Diagram of SXP327, using orbital parameters given in Table A.1 and discussed in Section 2.3.

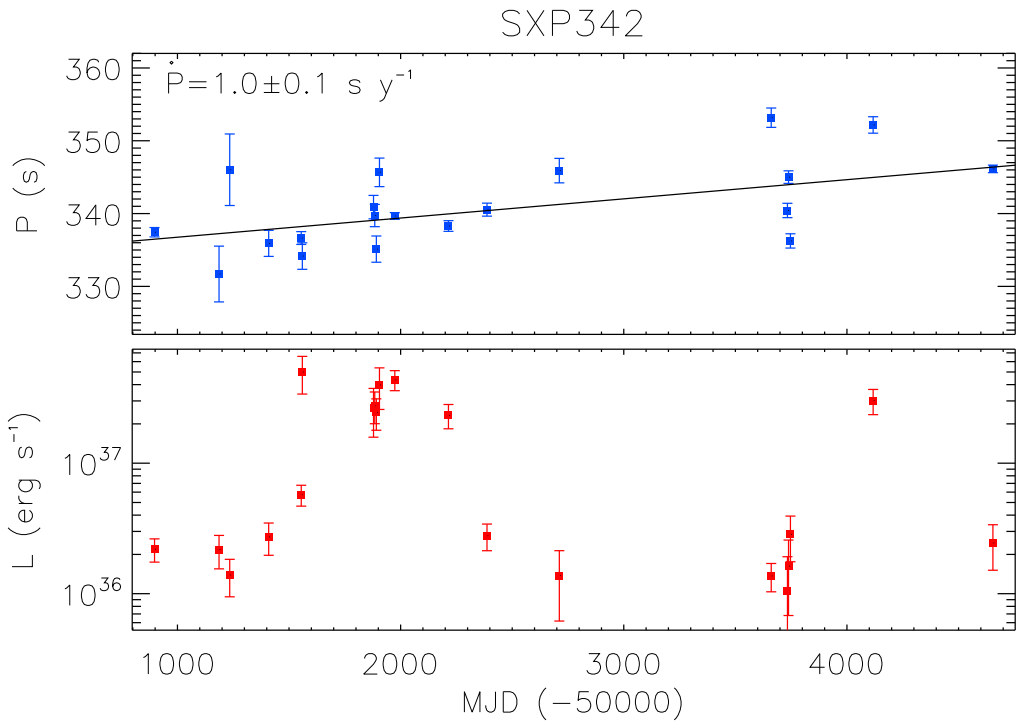

Figure B.63: P (upper panel; blue) and L (lower panel; red) as a function of MJD for SXP342. The black line in the upper panel shows the best-fit $\dot{P}$.

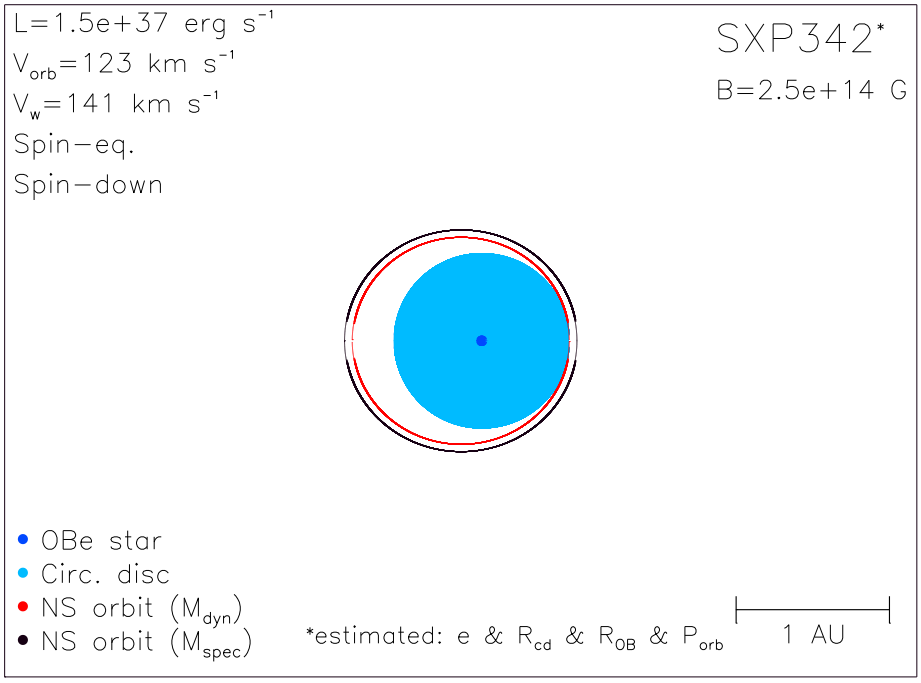

Figure B.64: Diagram of SXP342, using orbital parameters given in Table A.1 and discussed in Section 2.3.

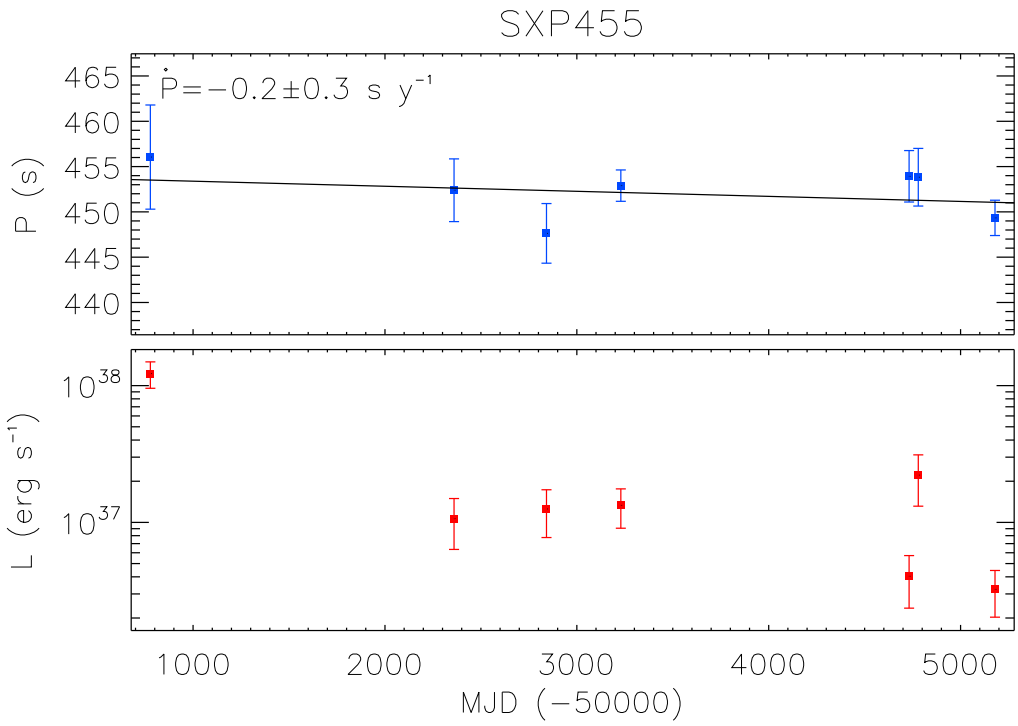

Figure B.65: P (upper panel; blue) and L (lower panel; red) as a function of MJD for SXP455. The black line in the upper panel shows the best-fit $\dot{P}$.

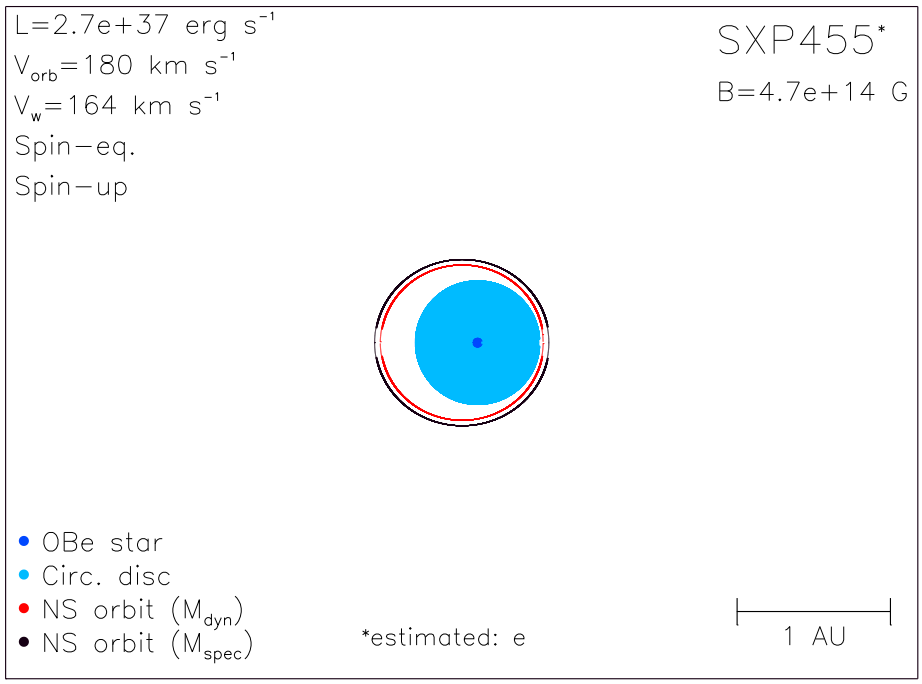

Figure B.66: Diagram of SXP455, using orbital parameters given in Table A.1 and discussed in Section 2.3.

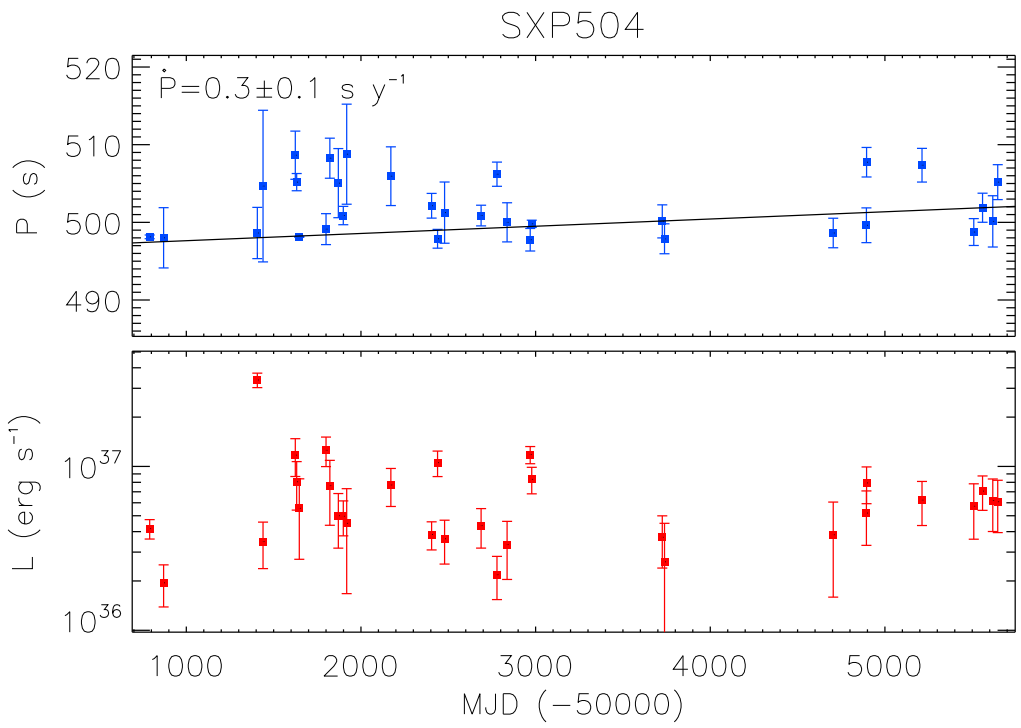

Figure B.67: P (upper panel; blue) and L (lower panel; red) as a function of MJD for SXP504. The black line in the upper panel shows the best-fit $\dot{P}$.

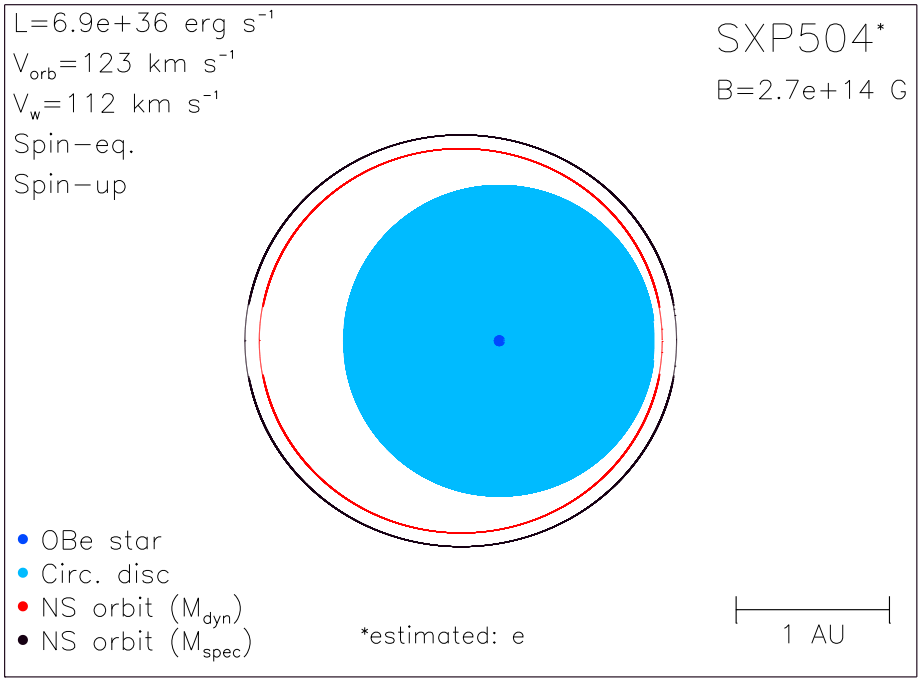

Figure B.68: Diagram of SXP504, using orbital parameters given in Table A.1 and discussed in Section 2.3.

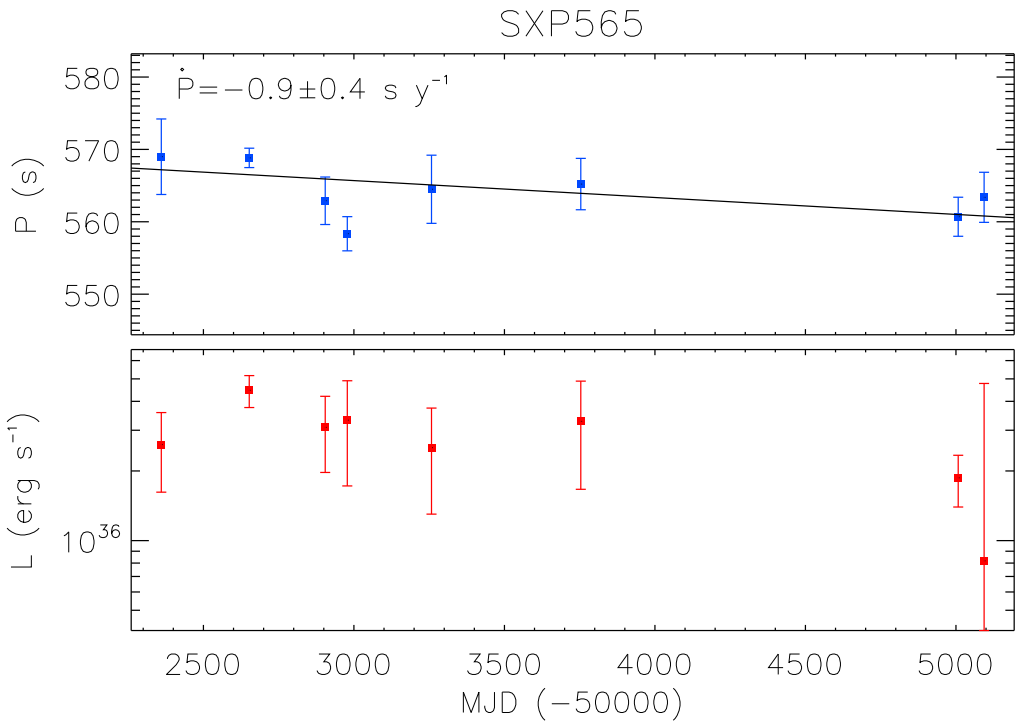

Figure B.69: P (upper panel; blue) and L (lower panel; red) as a function of MJD for SXP565. The black line in the upper panel shows the best-fit $\dot{P}$.

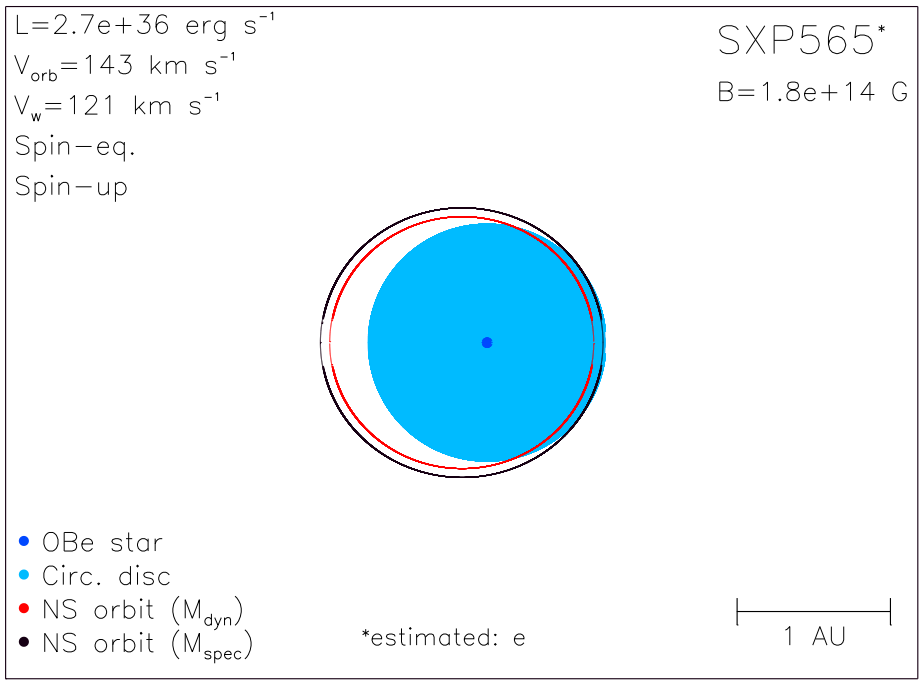

Figure B.70: Diagram of SXP565, using orbital parameters given in Table A.1 and discussed in Section 2.3.

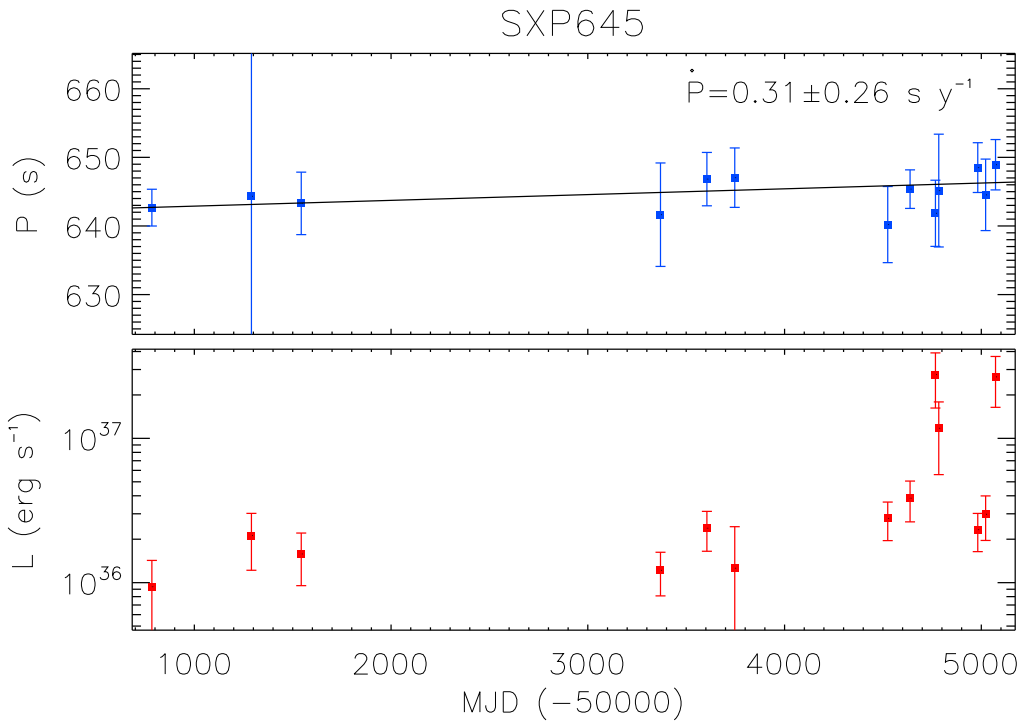

Figure B.71: P (upper panel; blue) and L (lower panel; red) as a function of MJD for SXP645. The black line in the upper panel shows the best-fit $\dot{P}$.

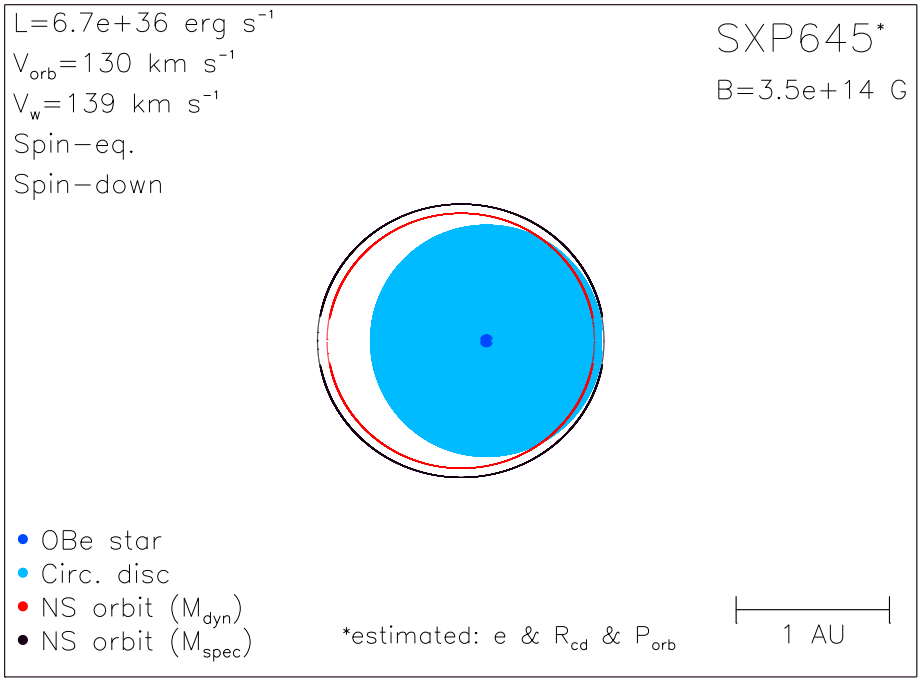

Figure B.72: Diagram of SXP645, using orbital parameters given in Table A.1 and discussed in Section 2.3.

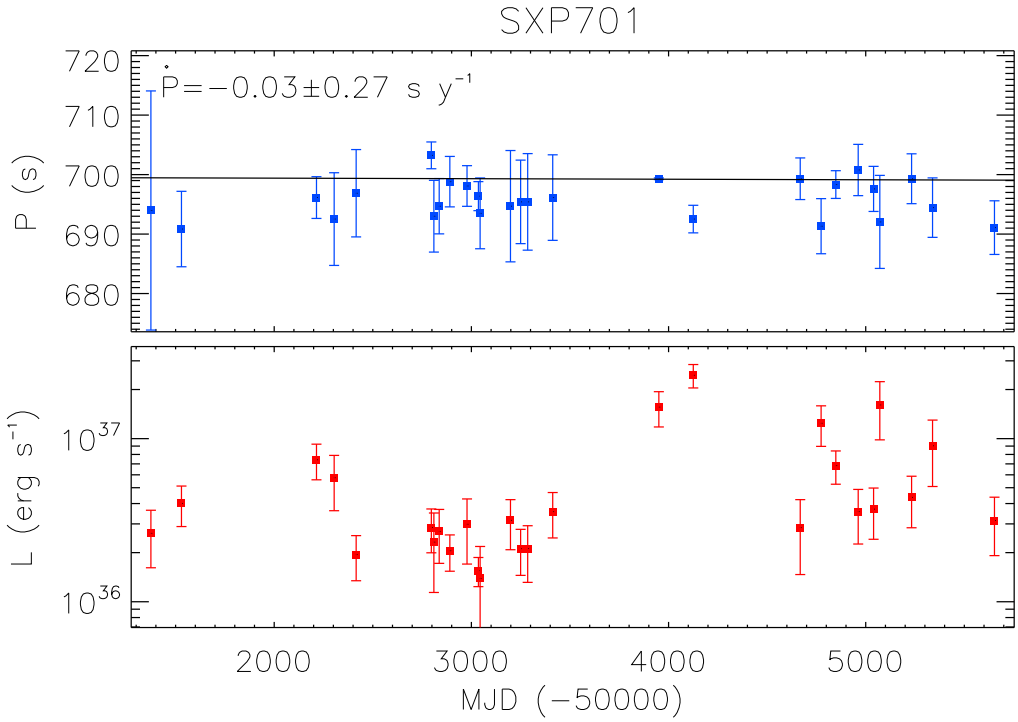

Figure B.73: P (upper panel; blue) and L (lower panel; red) as a function of MJD for SXP701. The black line in the upper panel shows the best-fit $\dot{P}$.

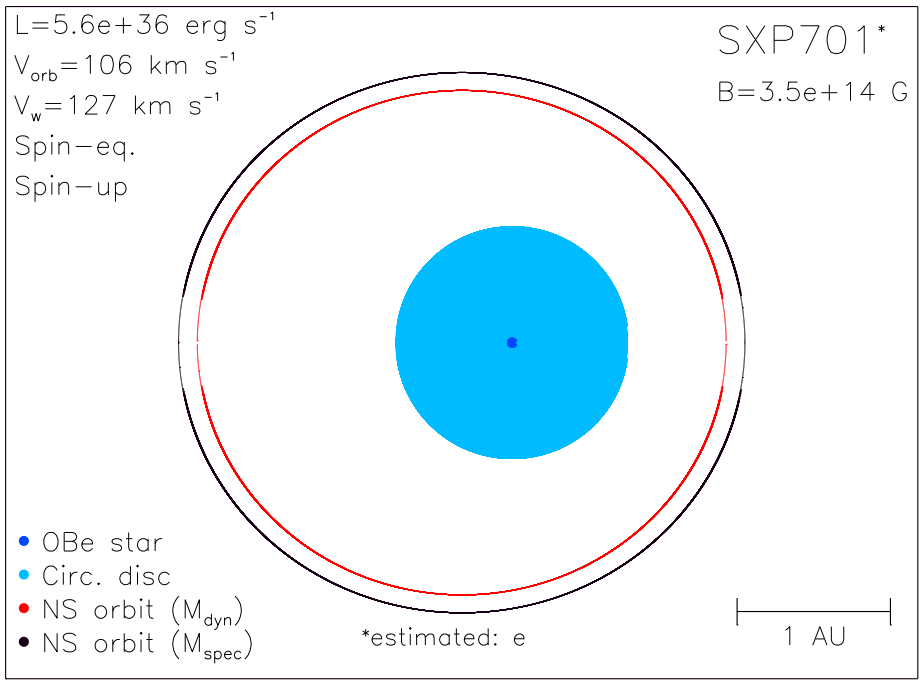

Figure B.74: Diagram of SXP701, using orbital parameters given in Table A.1 and discussed in Section 2.3.

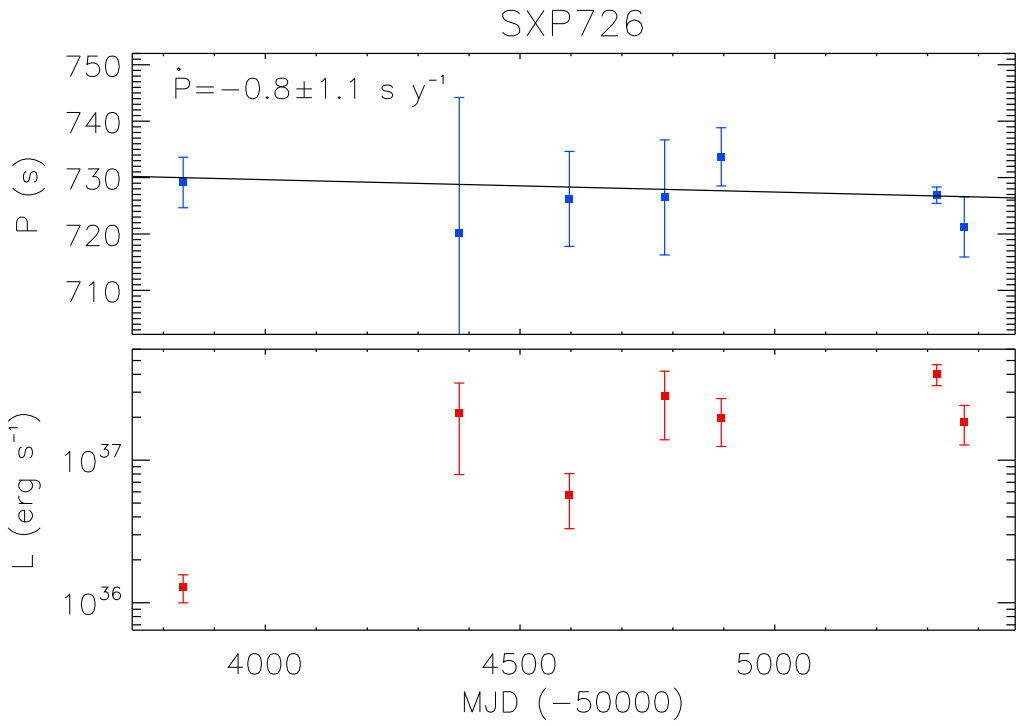

Figure B.75: P (upper panel; blue) and L (lower panel; red) as a function of MJD for SXP726. The black line in the upper panel shows the best-fit $\dot{P}$.

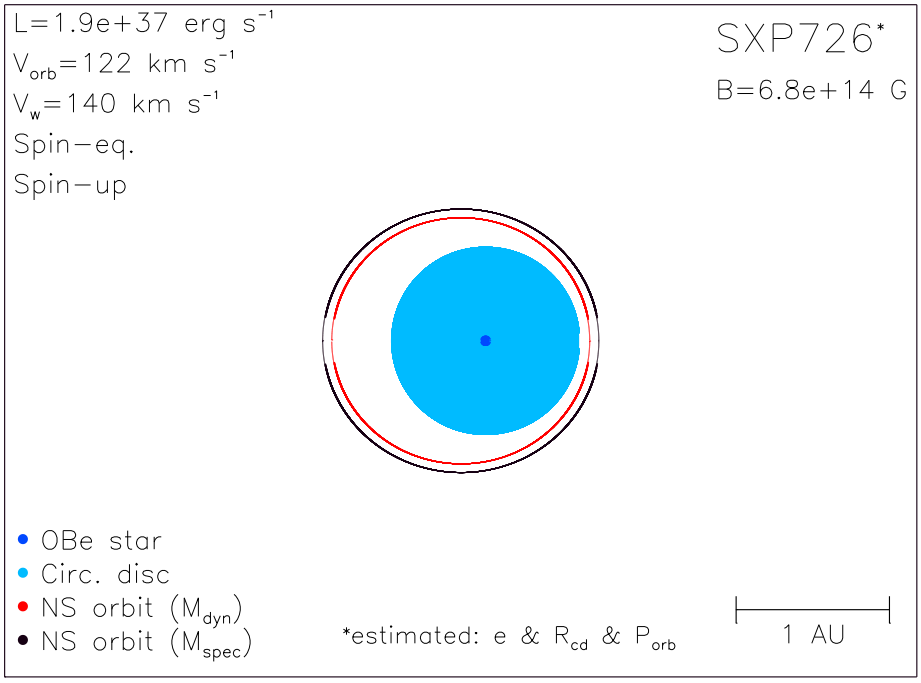

Figure B.76: Diagram of SXP726, using orbital parameters given in Table A.1 and discussed in Section 2.3.

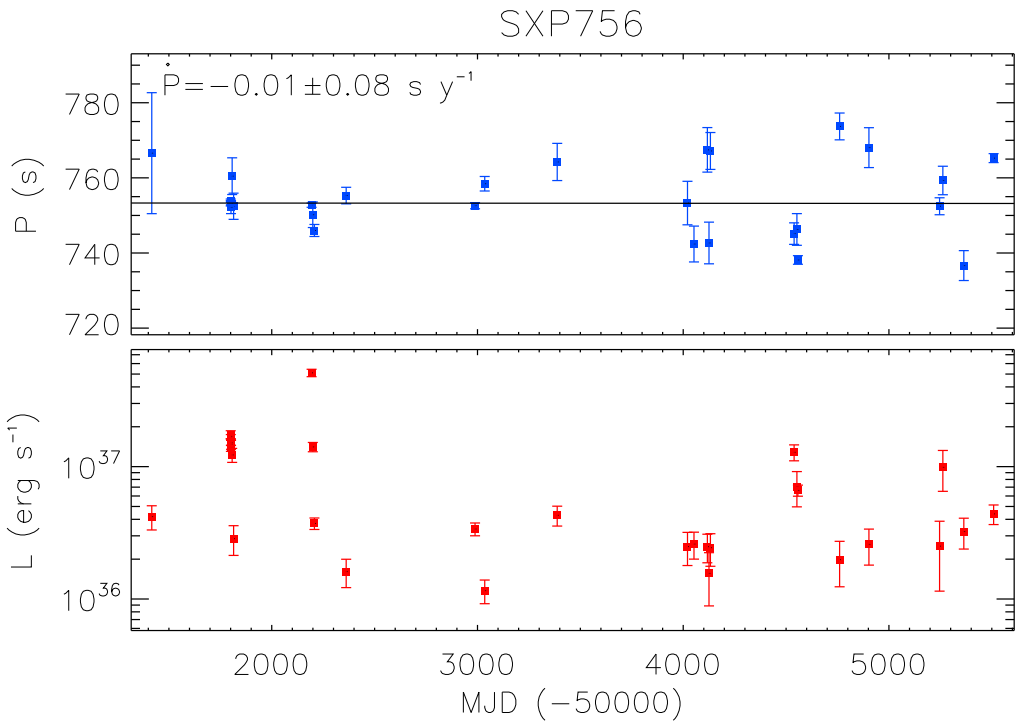

Figure B.77: P (upper panel; blue) and L (lower panel; red) as a function of MJD for SXP756. The black line in the upper panel shows the best-fit $\dot{P}$.

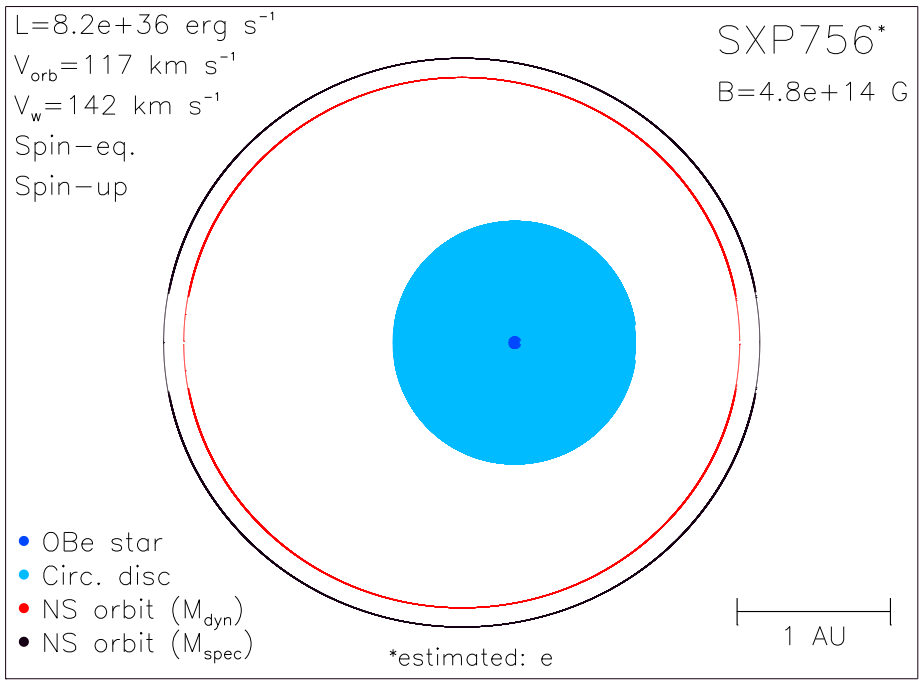

Figure B.78: Diagram of SXP756, using orbital parameters given in Table A.1 and discussed in Section 2.3.

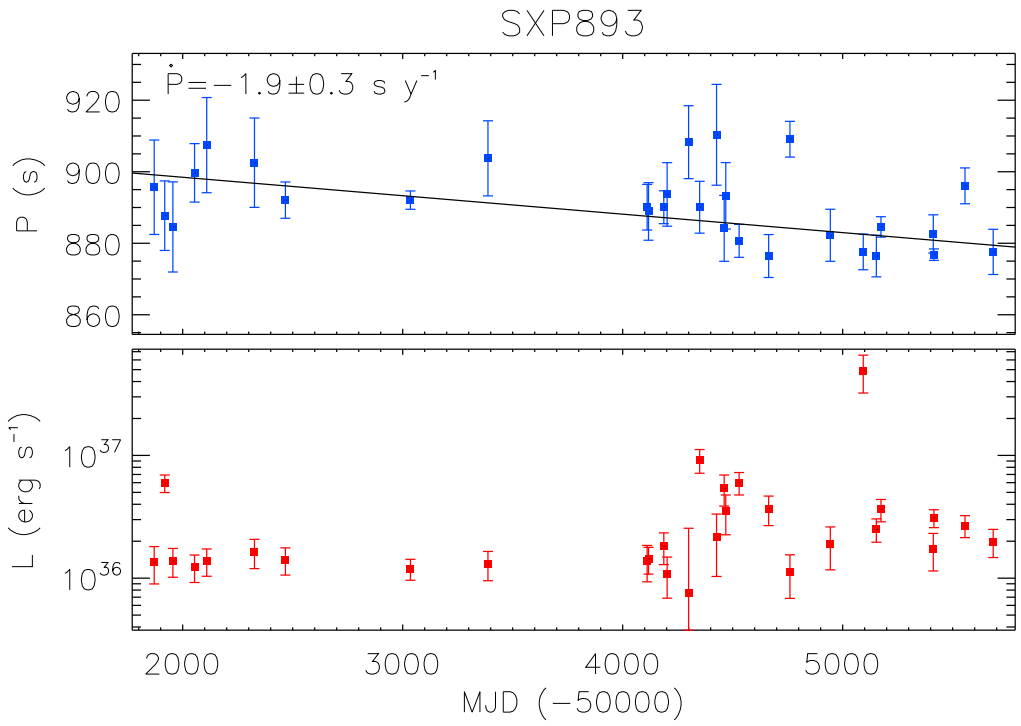

Figure B.79: P (upper panel; blue) and L (lower panel; red) as a function of MJD for SXP893. The black line in the upper panel shows the best-fit $\dot{P}$.

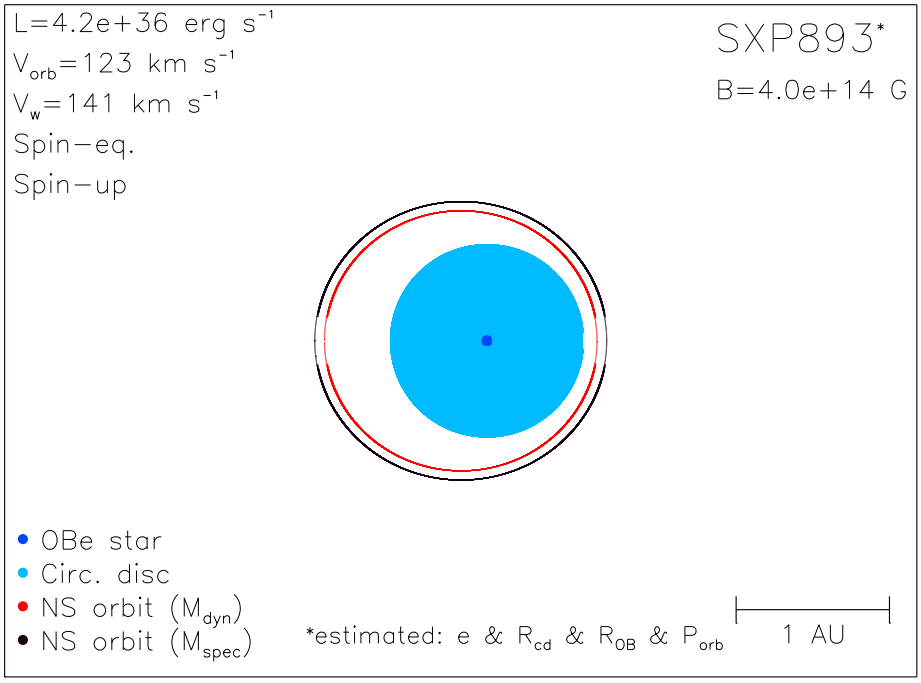

Figure B.80: Diagram of SXP893, using orbital parameters given in Table A.1 and discussed in Section 2.3.

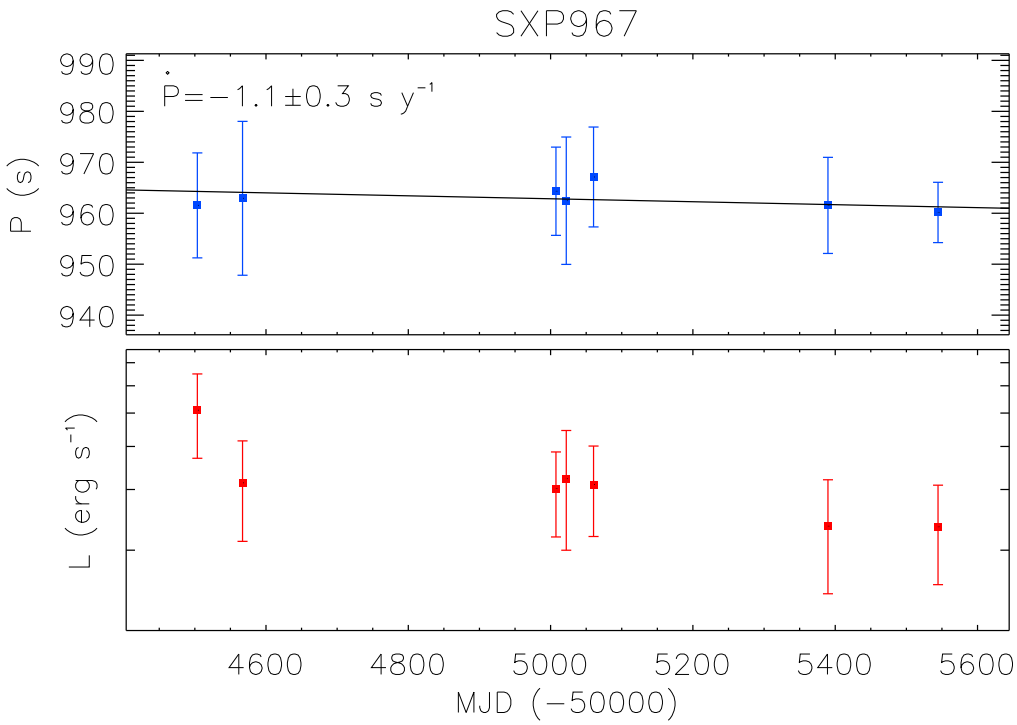

Figure B.81: P (upper panel; blue) and L (lower panel; red) as a function of MJD for SXP967. The black line in the upper panel shows the best-fit $\dot{P}$.

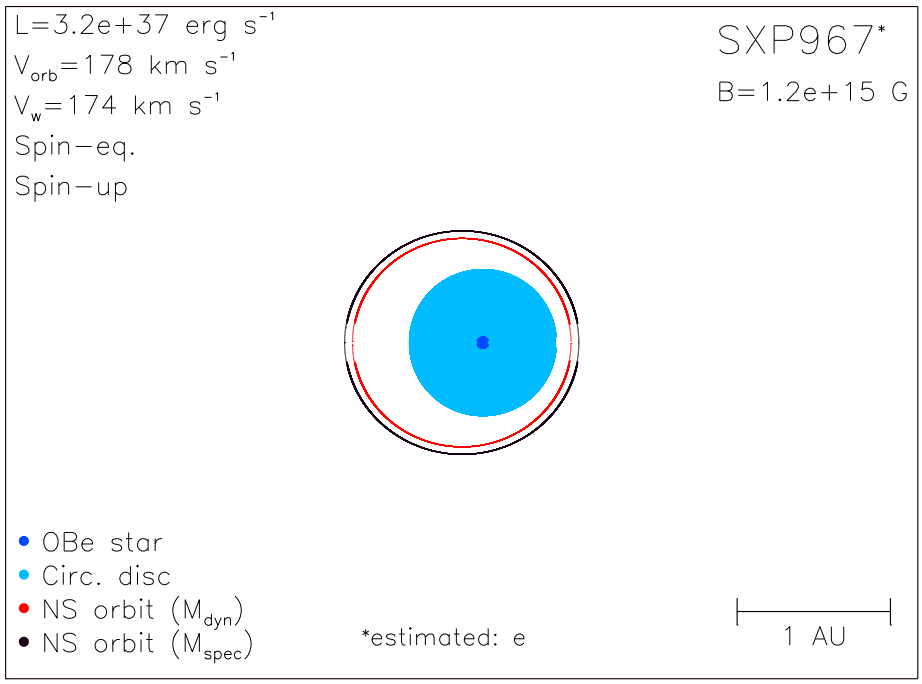

Figure B.82: Diagram of SXP967, using orbital parameters given in Table A.1 and discussed in Section 2.3.

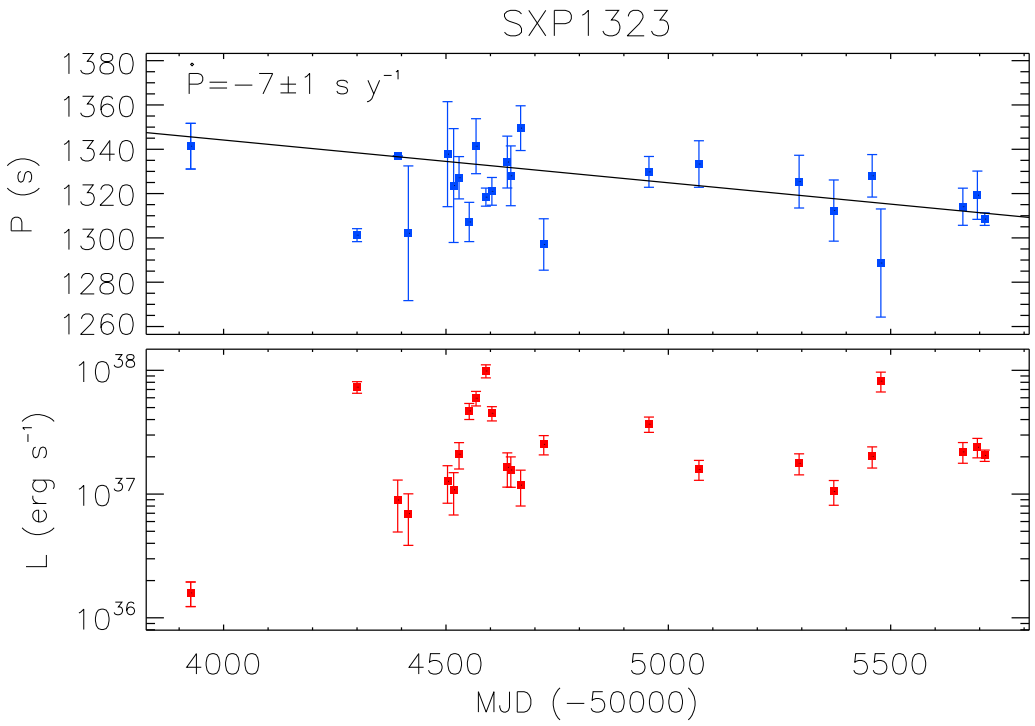

Figure B.83: P (upper panel; blue) and L (lower panel; red) as a function of MJD for SXP1323. The black line in the upper panel shows the best-fit $\dot{P}$.

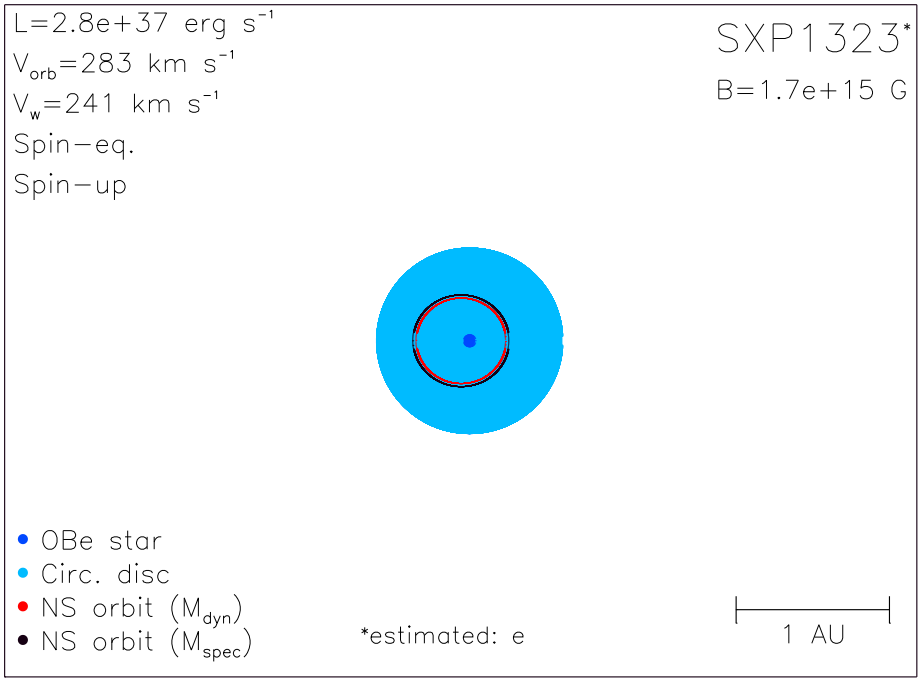

Figure B.84: Diagram of SXP1323, using orbital parameters given in Table A.1 and discussed in Section 2.3.

Appendix C

All pulse-profiles

Figures C.2-C.43 show pulse-profiles for neutron stars in the 42 BeXB discussed in Chapters 2 and 3. These are normalised to the average count-rate, and the phase-shift is arbitrary (as discussed in Section 3.3). Pulse-profiles are coloured according to their luminosity, where the colour-coding is explained in Figure C.1. Pulse-profiles that show double-peaked structure (as defined in Section 3.3.2) are highlighted with diagonal lines in the corners of the plot.

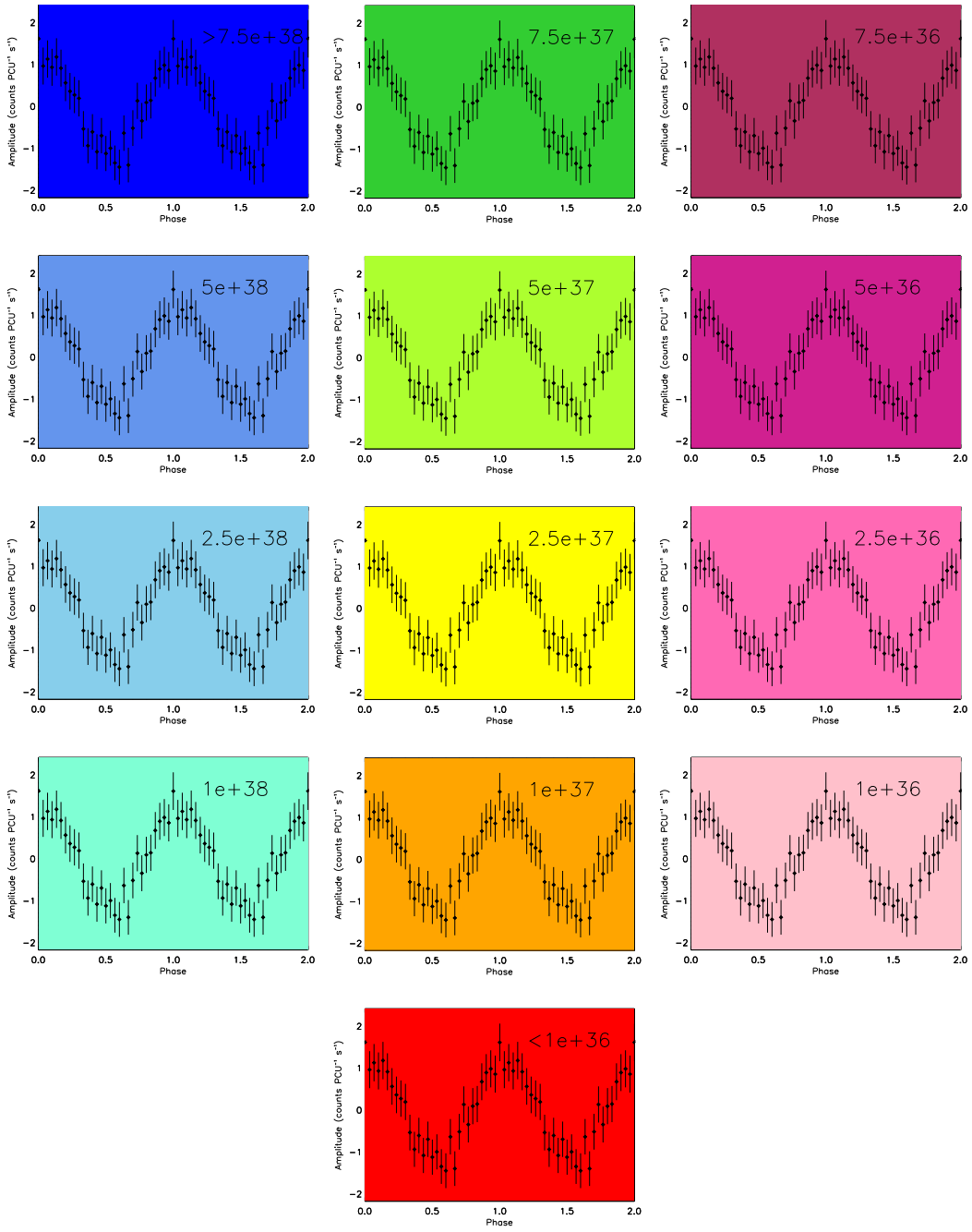

Figure C.1: Figures C.2-C.43 show all of the pulse-profiles for SXP in the dataset discussed in Chapters 2 and 3, in order of decreasing L from top to bottom, left to right. The plots are colour-coded according to L, where pulse-profiles relating to detections in multiples of 10^{38} erg s^{-1} are depicted in shades of blue, detections in multiples of 10^{37} erg s^{-1} are depicted in shades of green, yellow, and orange, detections in multiples of 10^{36} erg s^{-1} are depicted in shades of pink, and detections below 10^{36} erg s^{-1} are depicted in red. This figure shows the colour associated with each energy-band, where the lowest L in each energy-band is listed in the top right of each plot, except in the case of the red plot; all plots with $L < 10^{36}$ erg s^{-1} are depicted in red.

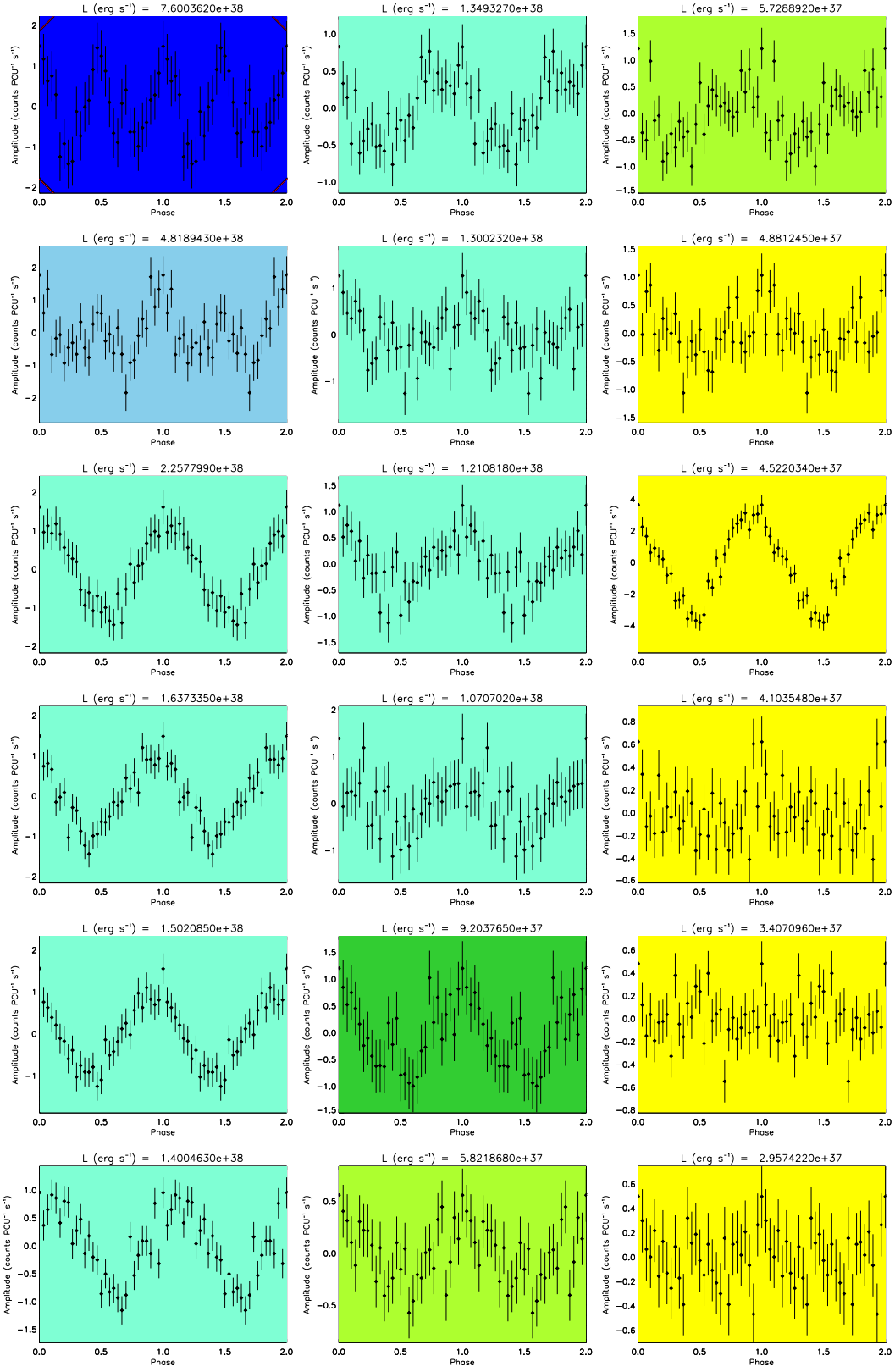
L (erg s⁻¹) = 7.6003620e+38
L (erg s⁻¹) = 1.3493270e+38
L (erg s⁻¹) = 5.7288920e+37
L (erg s⁻¹) = 4.8189430e+38
L (erg s⁻¹) = 1.3002320e+38
L (erg s⁻¹) = 4.8812450e+37
L (erg s⁻¹) = 2.2577990e+38
L (erg s⁻¹) = 1.2108180e+38
L (erg s⁻¹) = 4.5220340e+37
L (erg s⁻¹) = 1.6373350e+38
L (erg s⁻¹) = 1.0707020e+38
L (erg s⁻¹) = 4.1035480e+37
L (erg s⁻¹) = 1.5020850e+38
L (erg s⁻¹) = 9.2037650e+37
L (erg s⁻¹) = 3.4070960e+37
L (erg s⁻¹) = 1.4004630e+38
L (erg s⁻¹) = 5.8218680e+37
L (erg s⁻¹) = 2.9574220e+37
Amplitude (counts PCU⁻¹ s⁻¹)
Phase

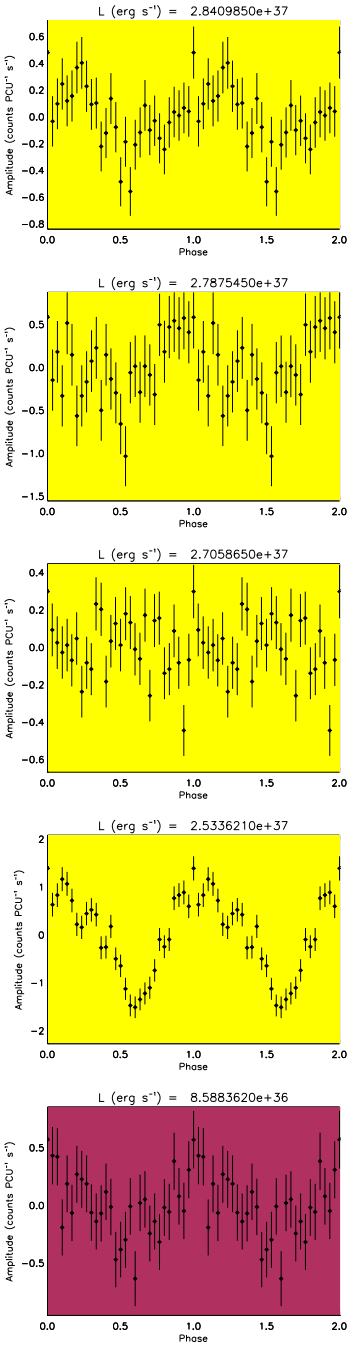

Figure C.2: Pulse-profiles for SXP2.37, in order of decreasing L (from top to bottom, left to right). The colour-coding is explained in Figure C.1.

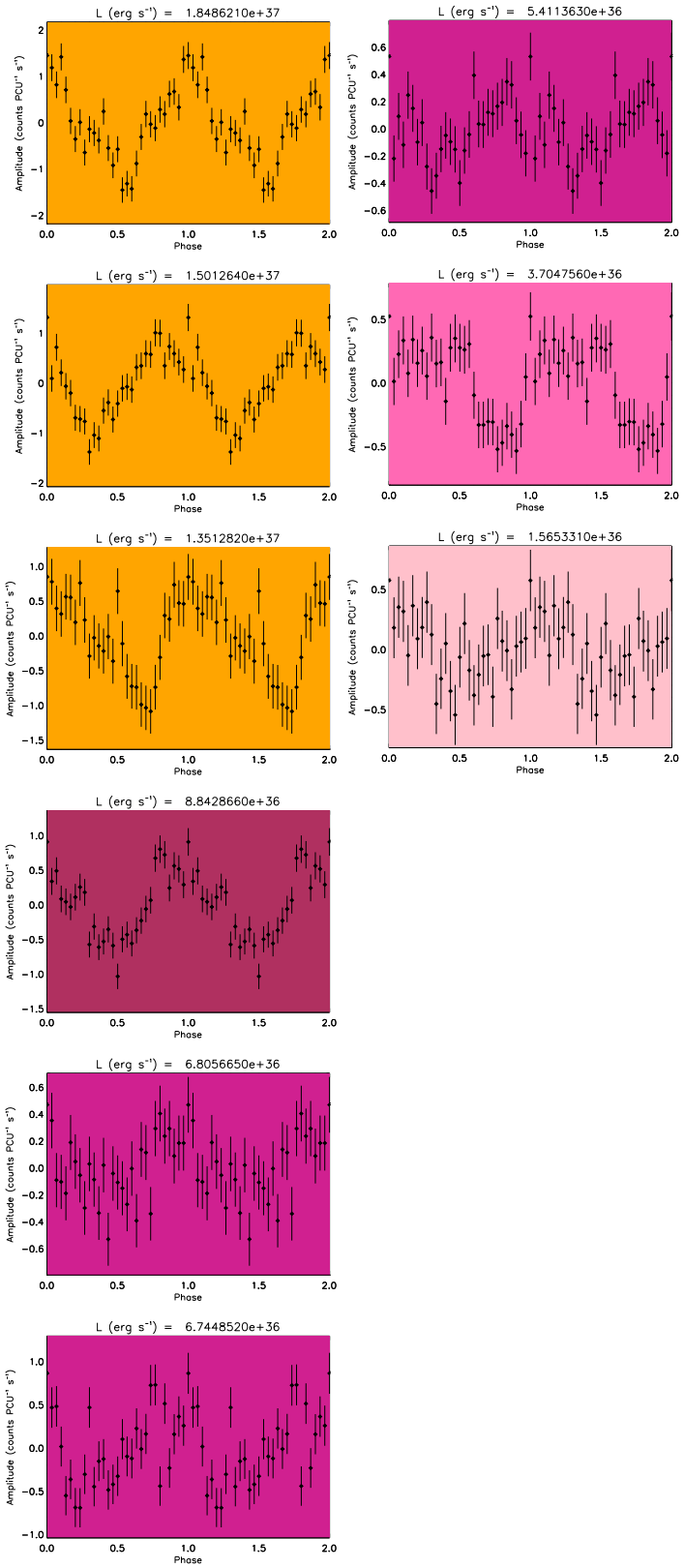

Figure C.3: Pulse-profiles for SXP4.78, in order of decreasing L (from top to bottom, left to right). The colour-coding is explained in Figure C.1.

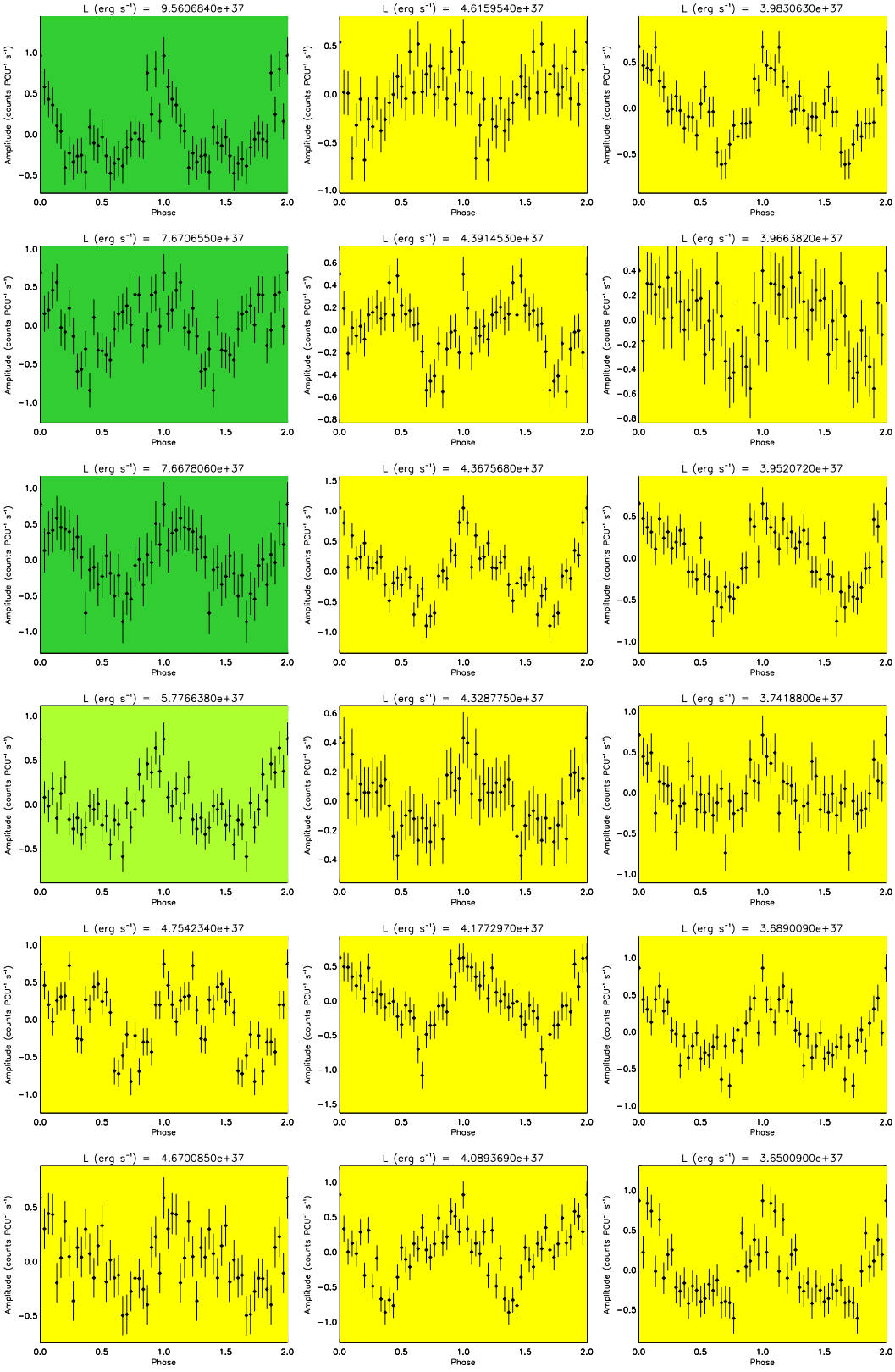
L (erg s⁻¹) = 9.5606840e+37
L (erg s⁻¹) = 4.6159540e+37
L (erg s⁻¹) = 3.9830630e+37
L (erg s⁻¹) = 7.6706550e+37
L (erg s⁻¹) = 4.3914530e+37
L (erg s⁻¹) = 3.9663820e+37
L (erg s⁻¹) = 7.6678060e+37
L (erg s⁻¹) = 4.3675680e+37
L (erg s⁻¹) = 3.9520720e+37
L (erg s⁻¹) = 5.7766380e+37
L (erg s⁻¹) = 4.3287750e+37
L (erg s⁻¹) = 3.7418800e+37
L (erg s⁻¹) = 4.7542340e+37
L (erg s⁻¹) = 4.1772970e+37
L (erg s⁻¹) = 3.6890090e+37
L (erg s⁻¹) = 4.6700850e+37
L (erg s⁻¹) = 4.0893690e+37
L (erg s⁻¹) = 3.6500900e+37
Amplitude (counts PCU⁻¹ s⁻¹)
Phase

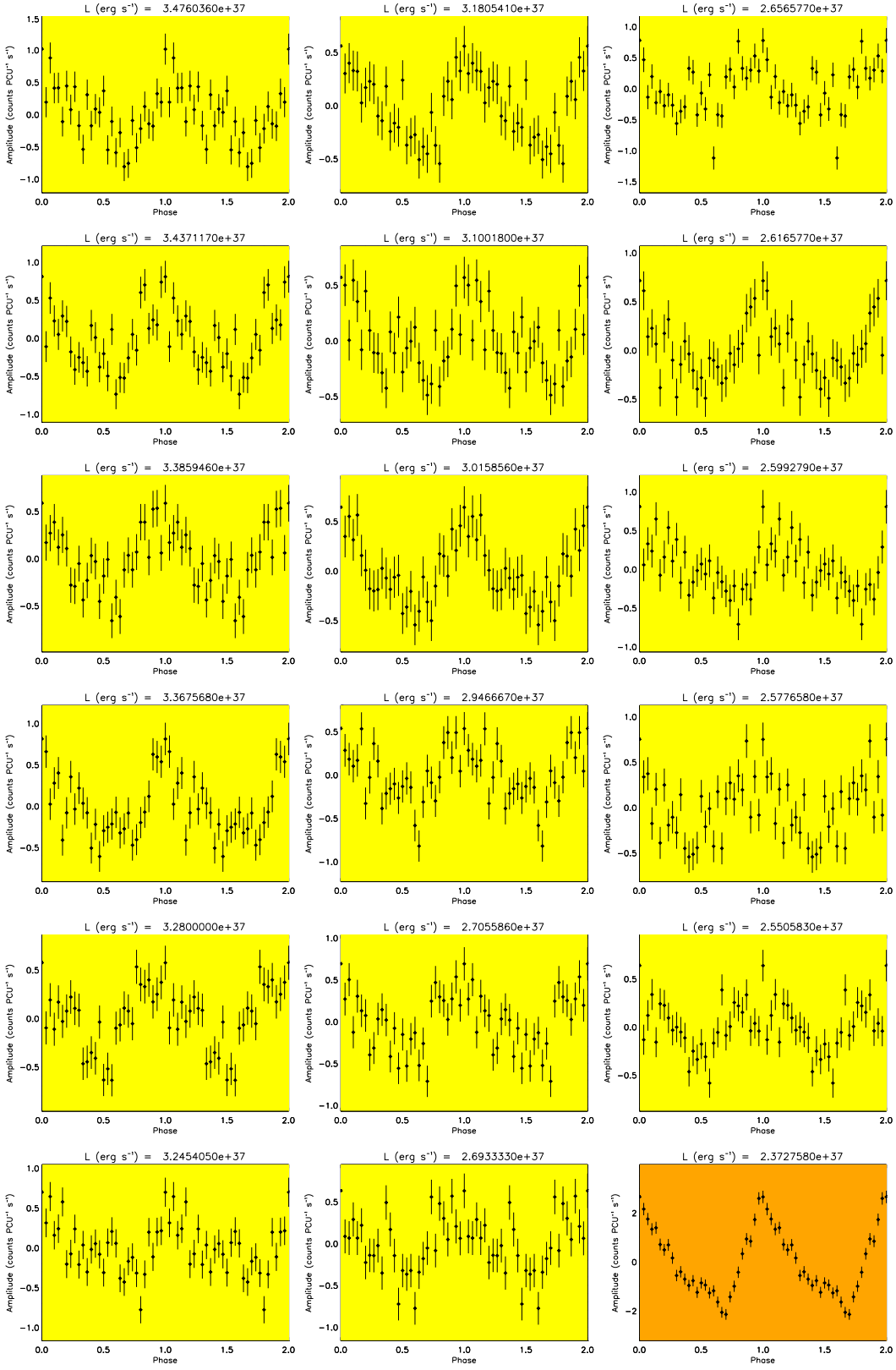
L (erg s⁻¹) = 3.4760360e+37
L (erg s⁻¹) = 3.1805410e+37
L (erg s⁻¹) = 2.6565770e+37
L (erg s⁻¹) = 3.4371170e+37
L (erg s⁻¹) = 3.1001800e+37
L (erg s⁻¹) = 2.6165770e+37
L (erg s⁻¹) = 3.3859460e+37
L (erg s⁻¹) = 3.0158560e+37
L (erg s⁻¹) = 2.5992790e+37
L (erg s⁻¹) = 3.3675680e+37
L (erg s⁻¹) = 2.9466670e+37
L (erg s⁻¹) = 2.5776580e+37
L (erg s⁻¹) = 3.2800000e+37
L (erg s⁻¹) = 2.7055860e+37
L (erg s⁻¹) = 2.5505830e+37
L (erg s⁻¹) = 3.2454050e+37
L (erg s⁻¹) = 2.6933330e+37
L (erg s⁻¹) = 2.3727580e+37
Amplitude (counts PCU⁻¹ s⁻¹)
Phase

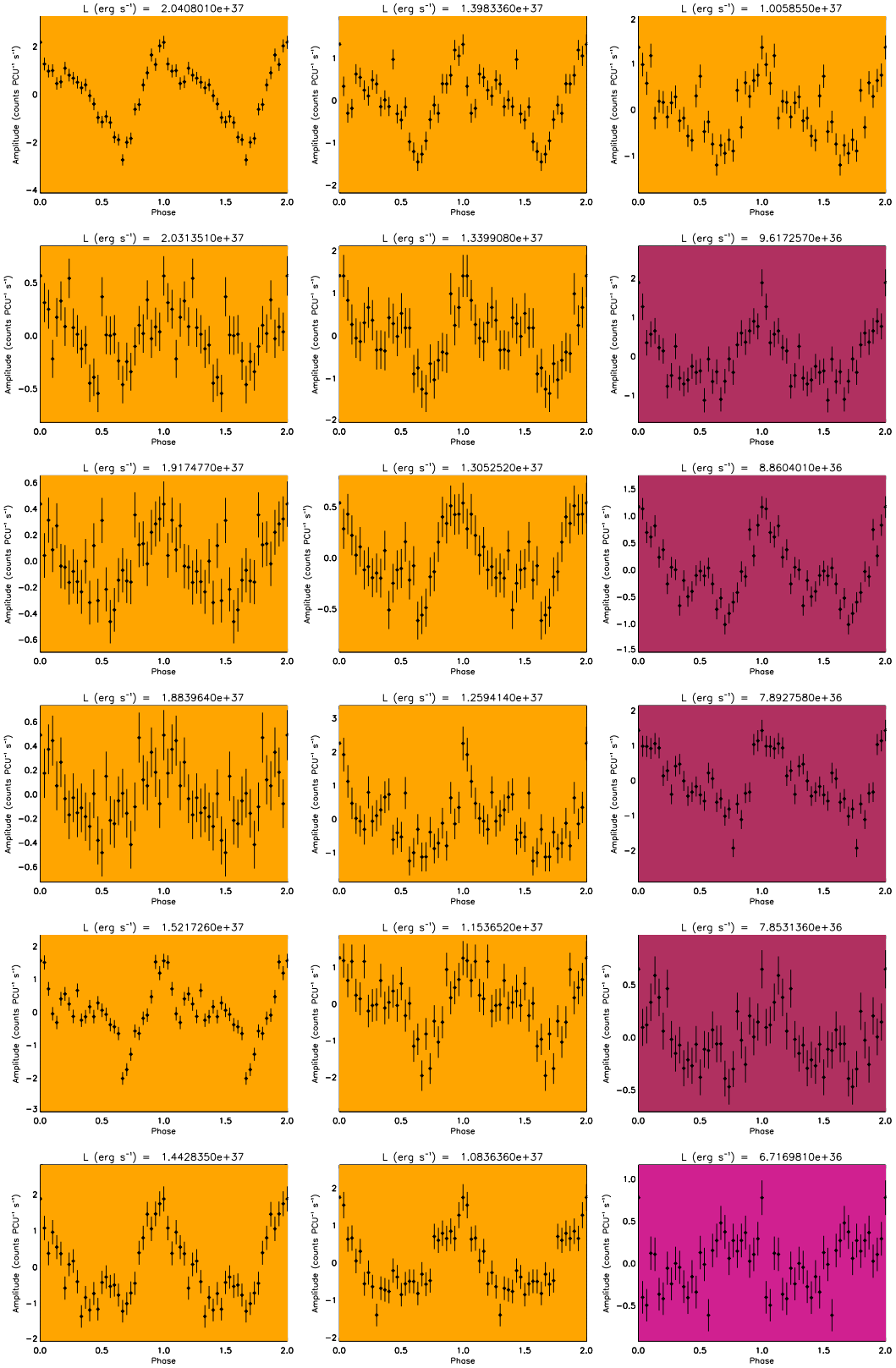
L (erg s⁻¹) = 2.0408010e+37
L (erg s⁻¹) = 1.3983360e+37
L (erg s⁻¹) = 1.0058550e+37
L (erg s⁻¹) = 2.0313510e+37
L (erg s⁻¹) = 1.3399080e+37
L (erg s⁻¹) = 9.6172570e+36
L (erg s⁻¹) = 1.9174770e+37
L (erg s⁻¹) = 1.3052520e+37
L (erg s⁻¹) = 8.8604010e+36
L (erg s⁻¹) = 1.8839640e+37
L (erg s⁻¹) = 1.2594140e+37
L (erg s⁻¹) = 7.8927580e+36
L (erg s⁻¹) = 1.5217260e+37
L (erg s⁻¹) = 1.1536520e+37
L (erg s⁻¹) = 7.8531360e+36
L (erg s⁻¹) = 1.4428350e+37
L (erg s⁻¹) = 1.0836360e+37
L (erg s⁻¹) = 6.7169810e+36
Amplitude (counts PCU⁻¹ s⁻¹)
Phase

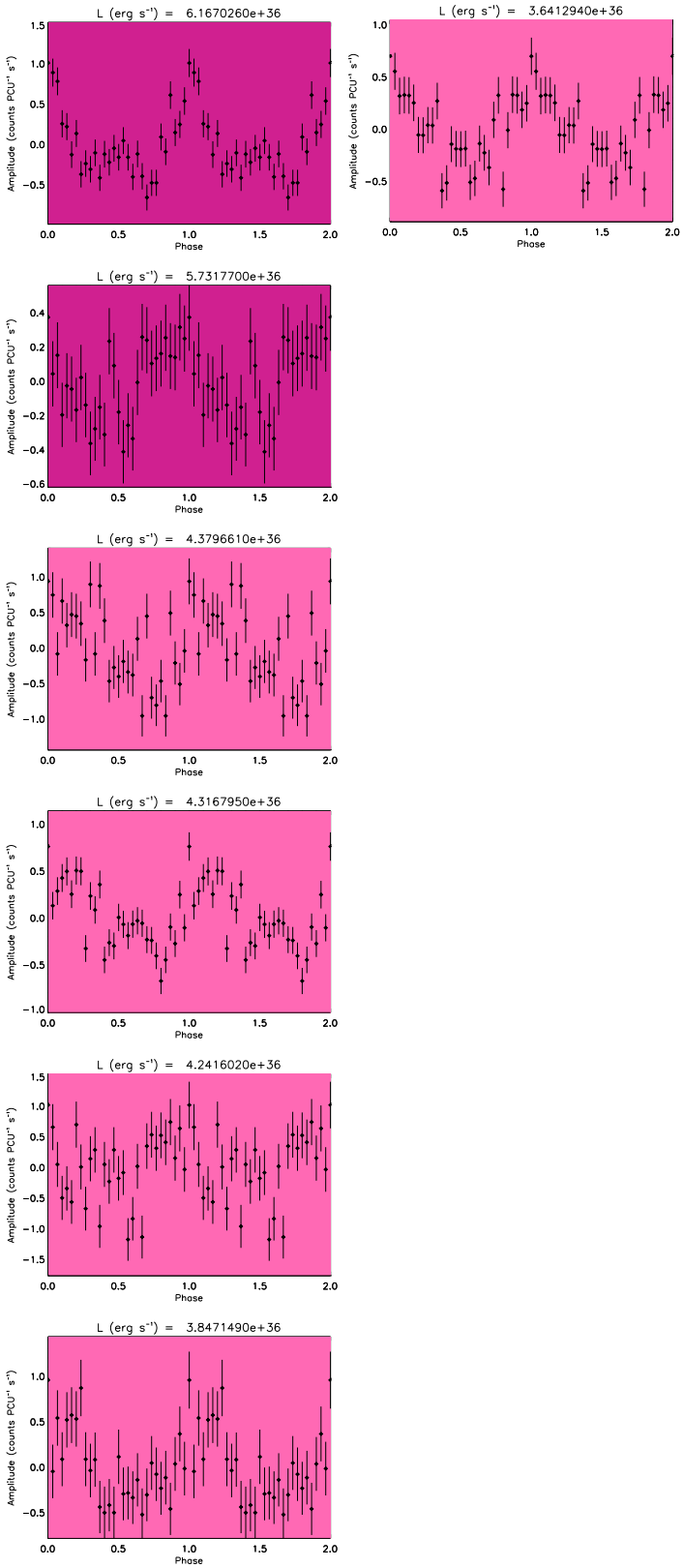

Figure C.4: Pulse-profiles for SXP6.85, in order of decreasing L (from top to bottom, left to right). The colour-coding is explained in Figure C.1.

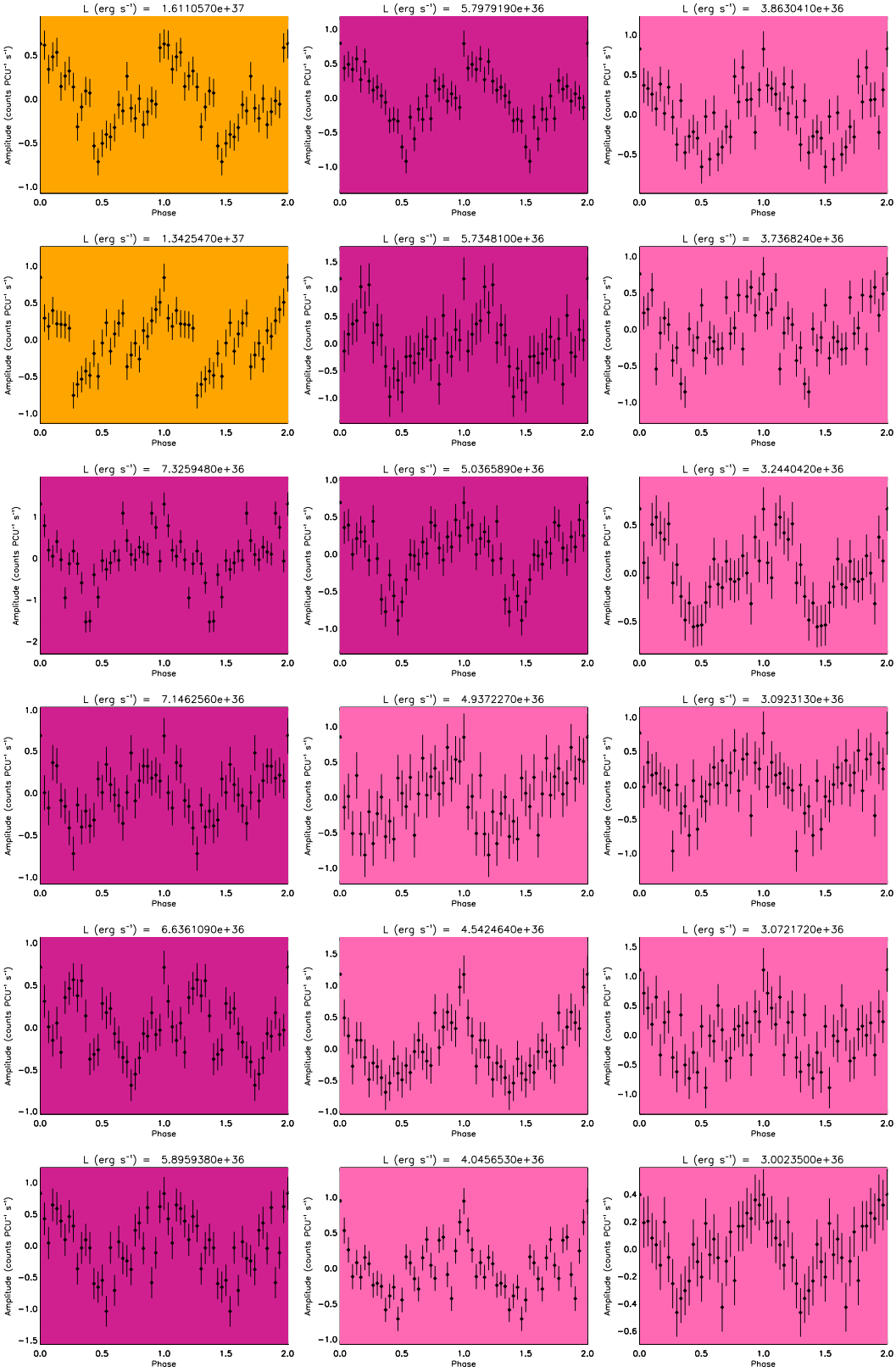
L (erg s⁻¹) = 1.6110570e+37
L (erg s⁻¹) = 5.7979190e+36
L (erg s⁻¹) = 3.8630410e+36
L (erg s⁻¹) = 1.3425470e+37
L (erg s⁻¹) = 5.7348100e+36
L (erg s⁻¹) = 3.7368240e+36
L (erg s⁻¹) = 7.3259480e+36
L (erg s⁻¹) = 5.0365890e+36
L (erg s⁻¹) = 3.2440420e+36
L (erg s⁻¹) = 7.1462560e+36
L (erg s⁻¹) = 4.9372270e+36
L (erg s⁻¹) = 3.0923130e+36
L (erg s⁻¹) = 6.6361090e+36
L (erg s⁻¹) = 4.5424640e+36
L (erg s⁻¹) = 3.0721720e+36
L (erg s⁻¹) = 5.8959380e+36
L (erg s⁻¹) = 4.0456530e+36
L (erg s⁻¹) = 3.0023500e+36
Amplitude (counts PCU⁻¹ s⁻¹)
Phase

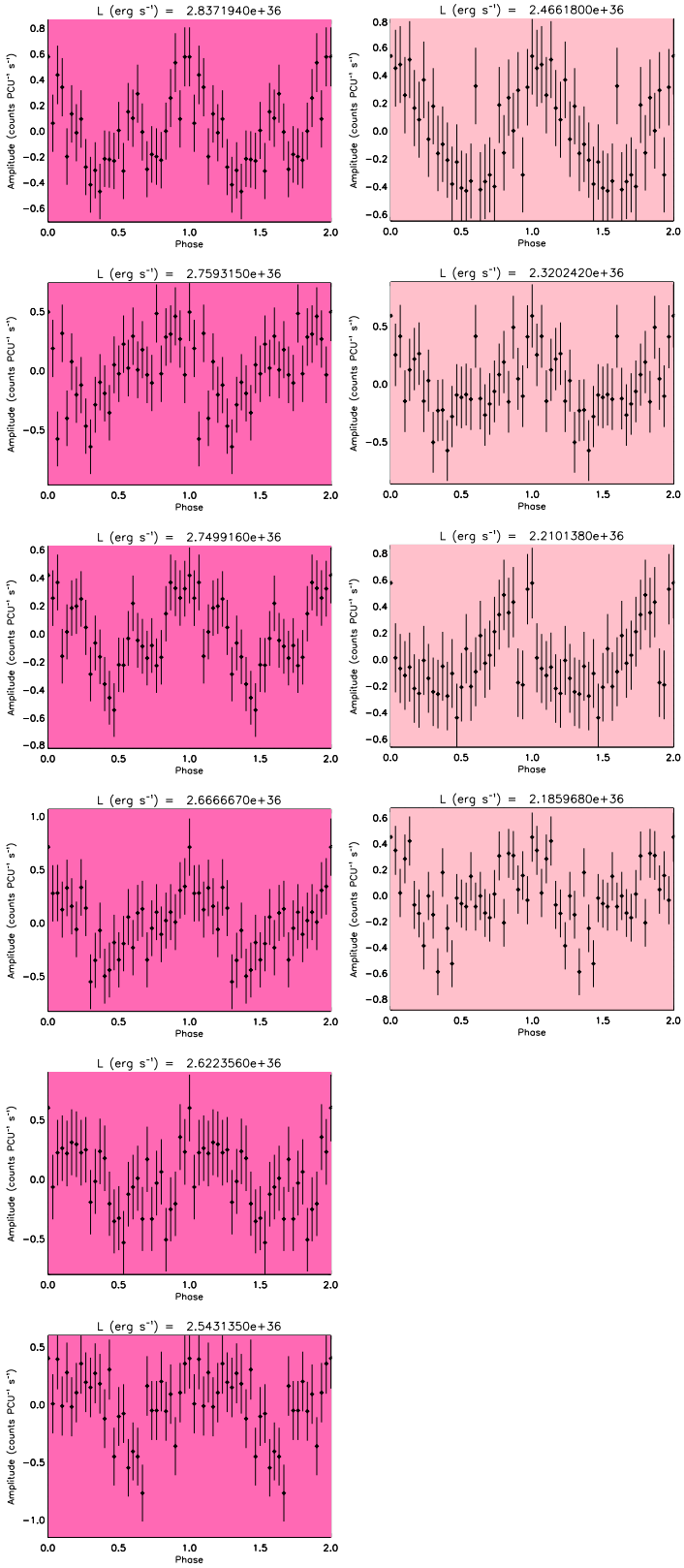

Figure C.5: Pulse-profiles for SXP7.78, in order of decreasing L (from top to bottom, left to right). The colour-coding is explained in Figure C.1.

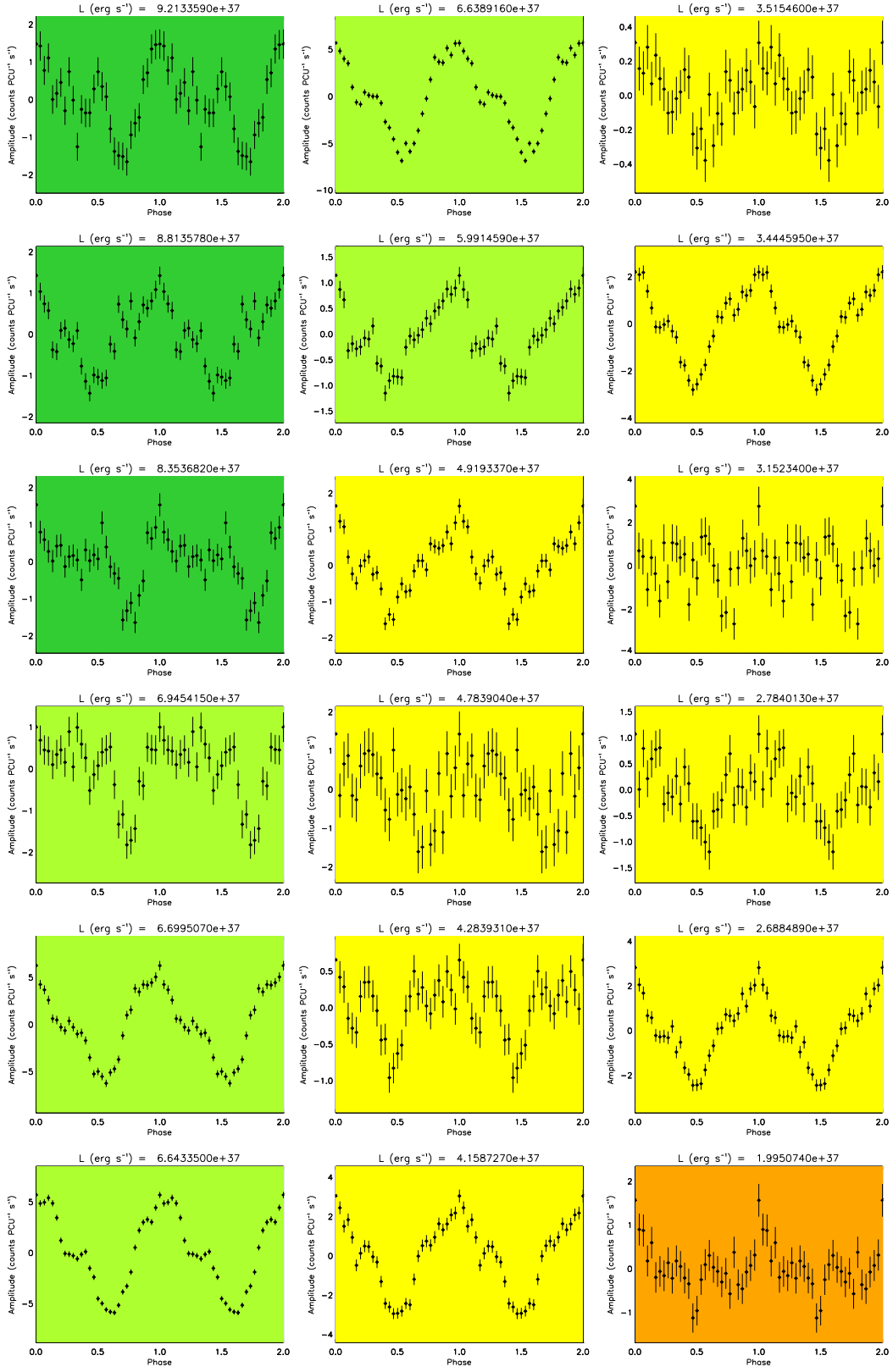
L (erg s⁻¹) = 9.2133590e+37
L (erg s⁻¹) = 6.6389160e+37
L (erg s⁻¹) = 3.5154600e+37
L (erg s⁻¹) = 8.8135780e+37
L (erg s⁻¹) = 5.9914590e+37
L (erg s⁻¹) = 3.4445950e+37
L (erg s⁻¹) = 8.3536820e+37
L (erg s⁻¹) = 4.9193370e+37
L (erg s⁻¹) = 3.1523400e+37
L (erg s⁻¹) = 6.9454150e+37
L (erg s⁻¹) = 4.7839040e+37
L (erg s⁻¹) = 2.7840130e+37
L (erg s⁻¹) = 6.6995070e+37
L (erg s⁻¹) = 4.2839310e+37
L (erg s⁻¹) = 2.6884890e+37
L (erg s⁻¹) = 6.6433500e+37
L (erg s⁻¹) = 4.1587270e+37
L (erg s⁻¹) = 1.9950740e+37
Amplitude (counts PCU⁻¹ s⁻¹)
Phase

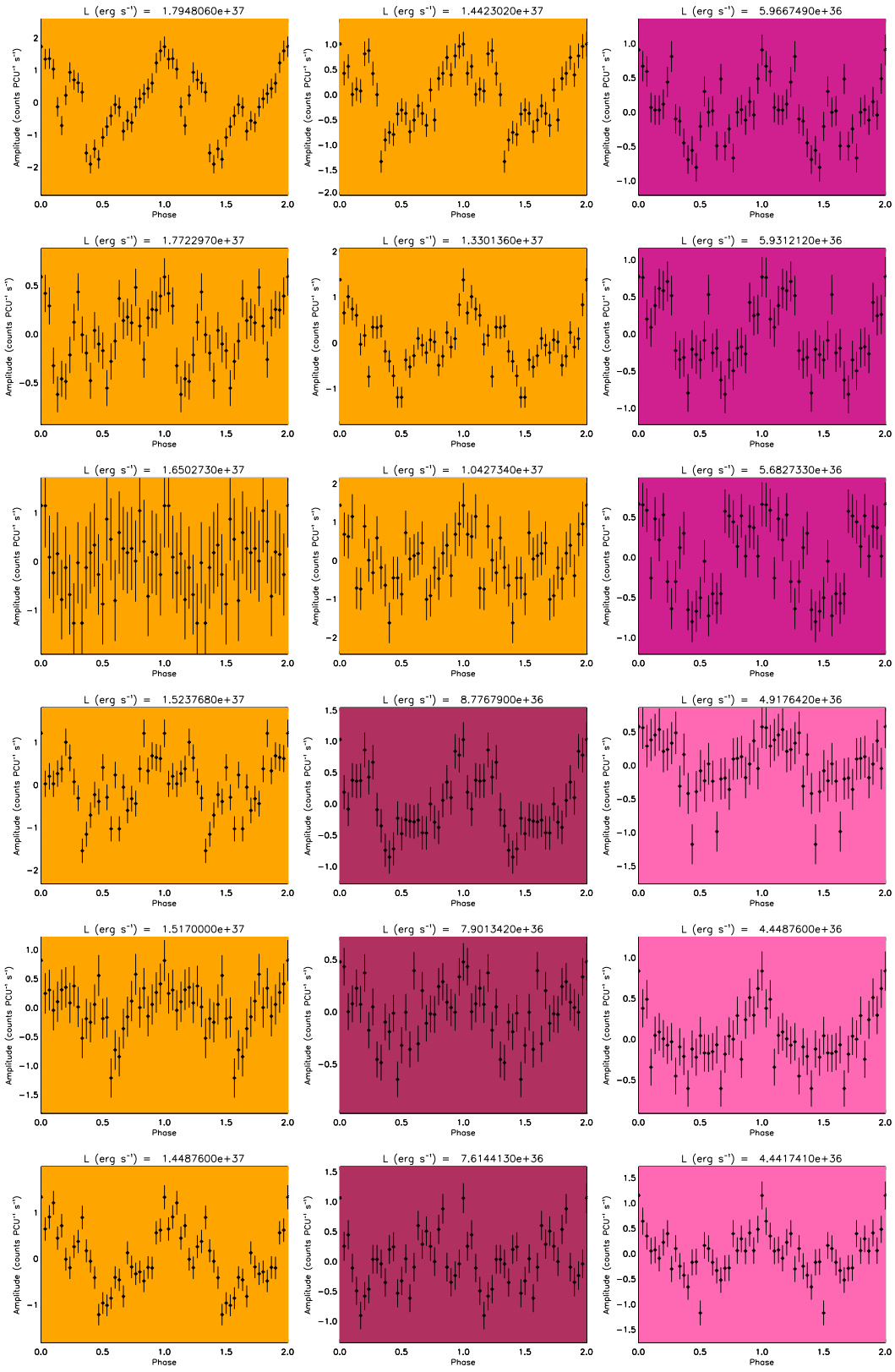
L (erg s⁻¹) = 1.7948060e+37
L (erg s⁻¹) = 1.4423020e+37
L (erg s⁻¹) = 5.9667490e+36
L (erg s⁻¹) = 1.7722970e+37
L (erg s⁻¹) = 1.3301360e+37
L (erg s⁻¹) = 5.9312120e+36
L (erg s⁻¹) = 1.6502730e+37
L (erg s⁻¹) = 1.0427340e+37
L (erg s⁻¹) = 5.6827330e+36
L (erg s⁻¹) = 1.5237680e+37
L (erg s⁻¹) = 8.7767900e+36
L (erg s⁻¹) = 4.9176420e+36
L (erg s⁻¹) = 1.5170000e+37
L (erg s⁻¹) = 7.9013420e+36
L (erg s⁻¹) = 4.4487600e+36
L (erg s⁻¹) = 1.4487600e+37
L (erg s⁻¹) = 7.6144130e+36
L (erg s⁻¹) = 4.4417410e+36
Amplitude (counts PCU⁻¹ s⁻¹)
Phase

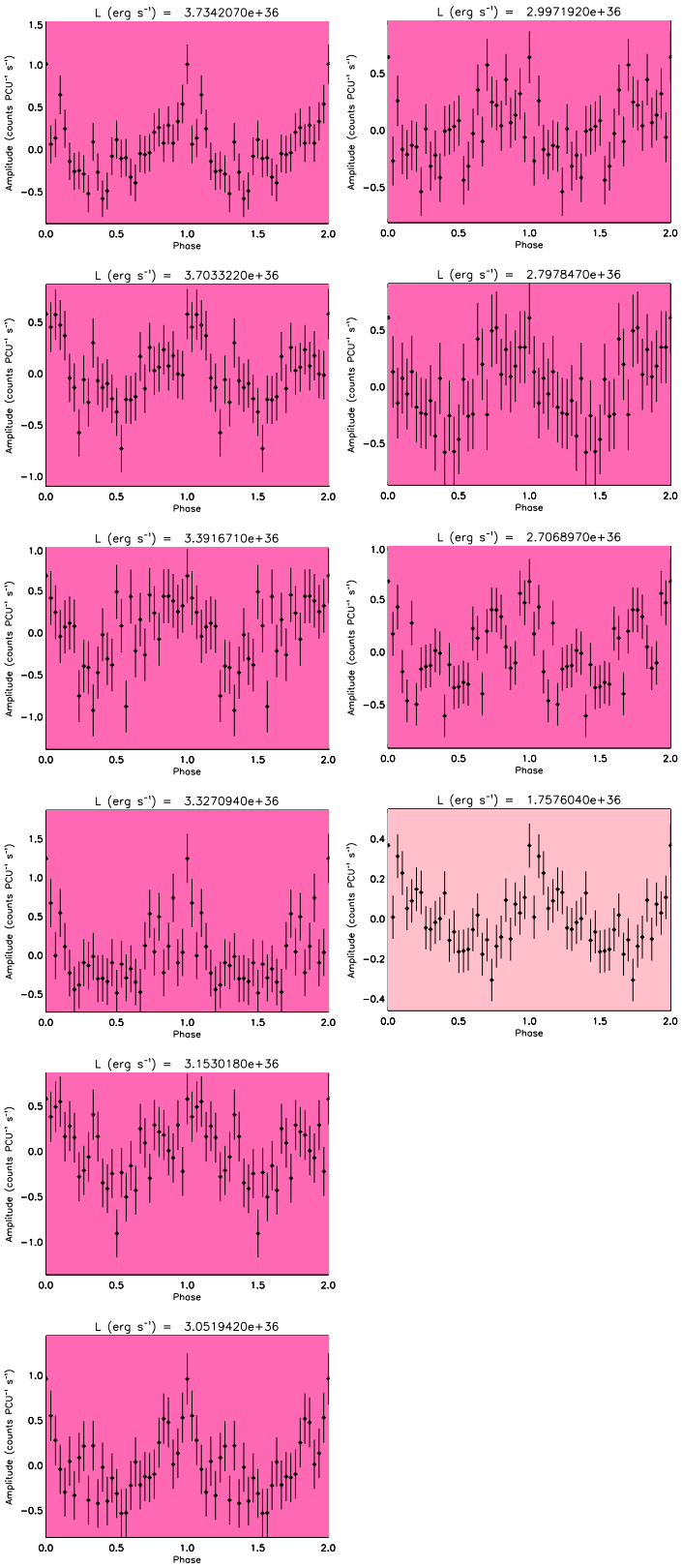

Figure C.6: Pulse-profiles for SXP8.80, in order of decreasing L (from top to bottom, left to right). The colour-coding is explained in Figure C.1.

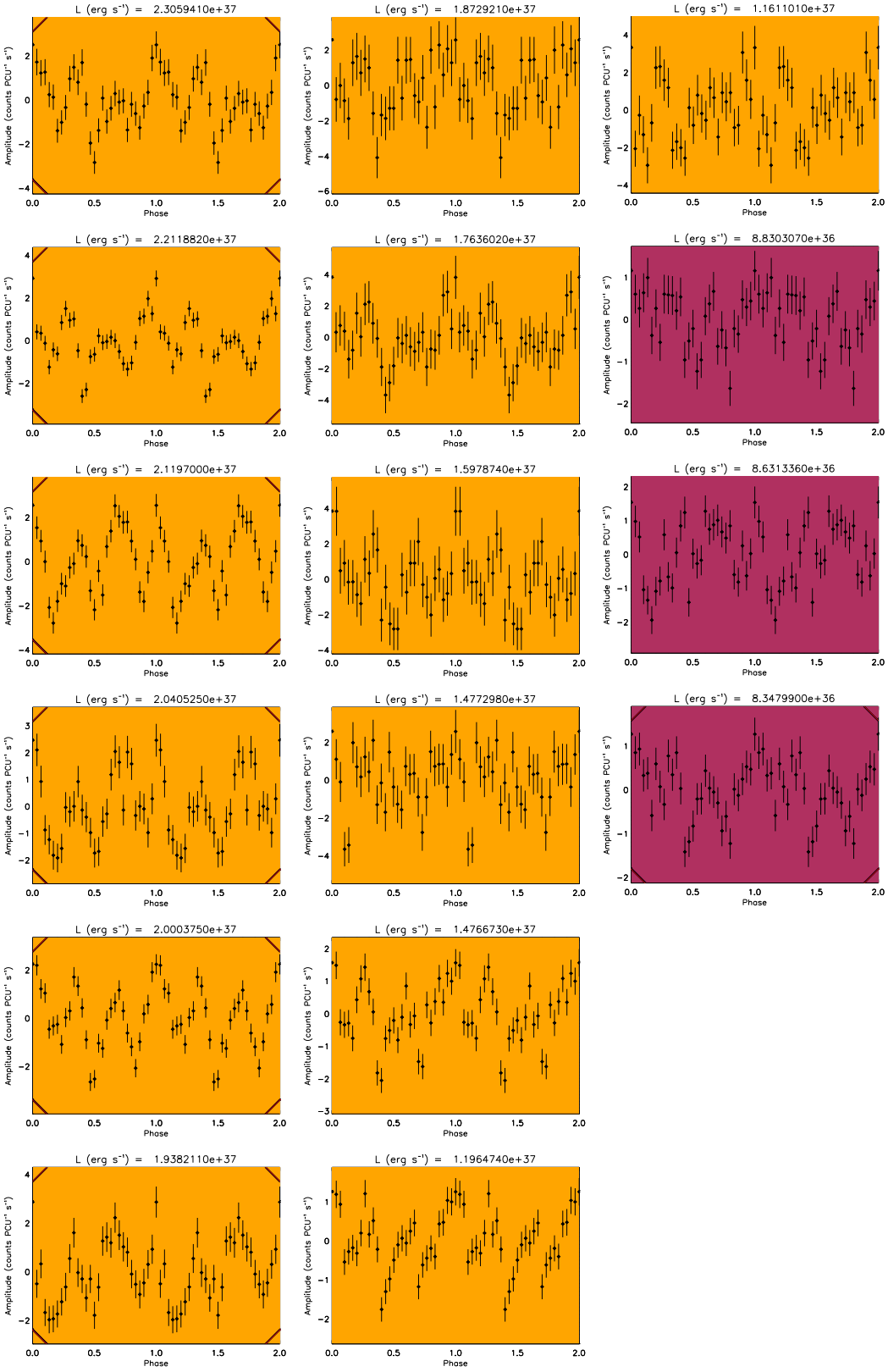

Figure C.7: Pulse-profiles for SXP11.5, in order of decreasing L (from top to bottom, left to right). The colour-coding is explained in Figure C.1.

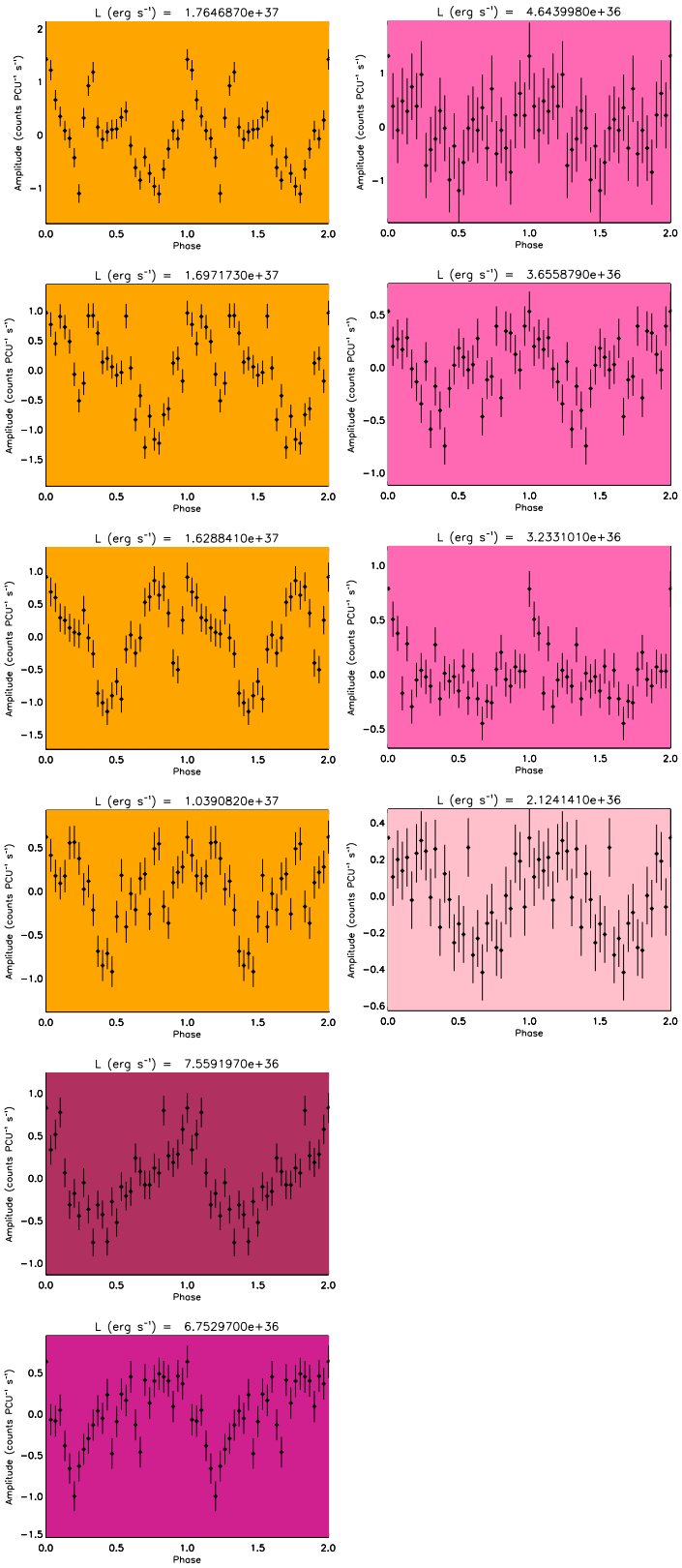

Figure C.8: Pulse-profiles for SXP15.3, in order of decreasing L (from top to bottom, left to right). The colour-coding is explained in Figure C.1.

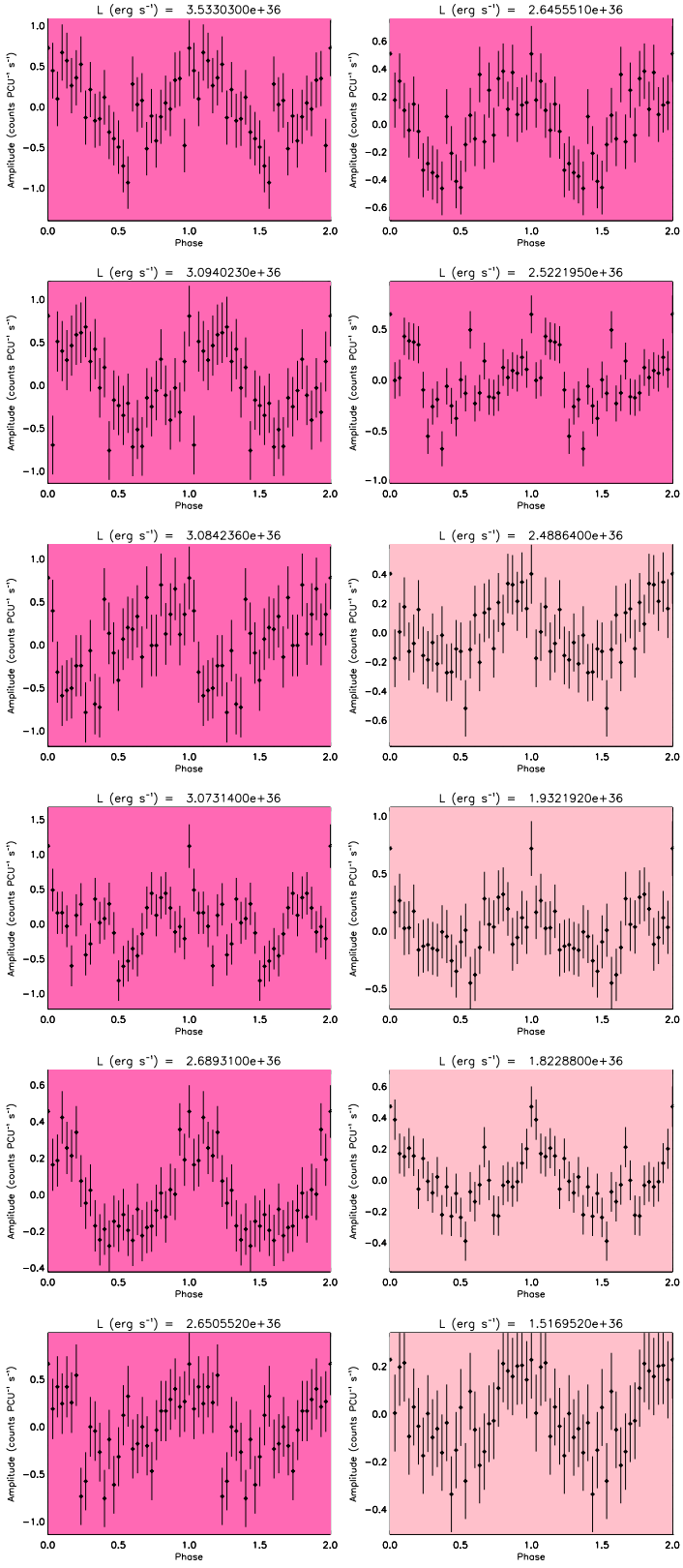

Figure C.9: Pulse-profiles for SXP16.6, in order of decreasing L (from top to bottom, left to right). The colour-coding is explained in Figure C.1.

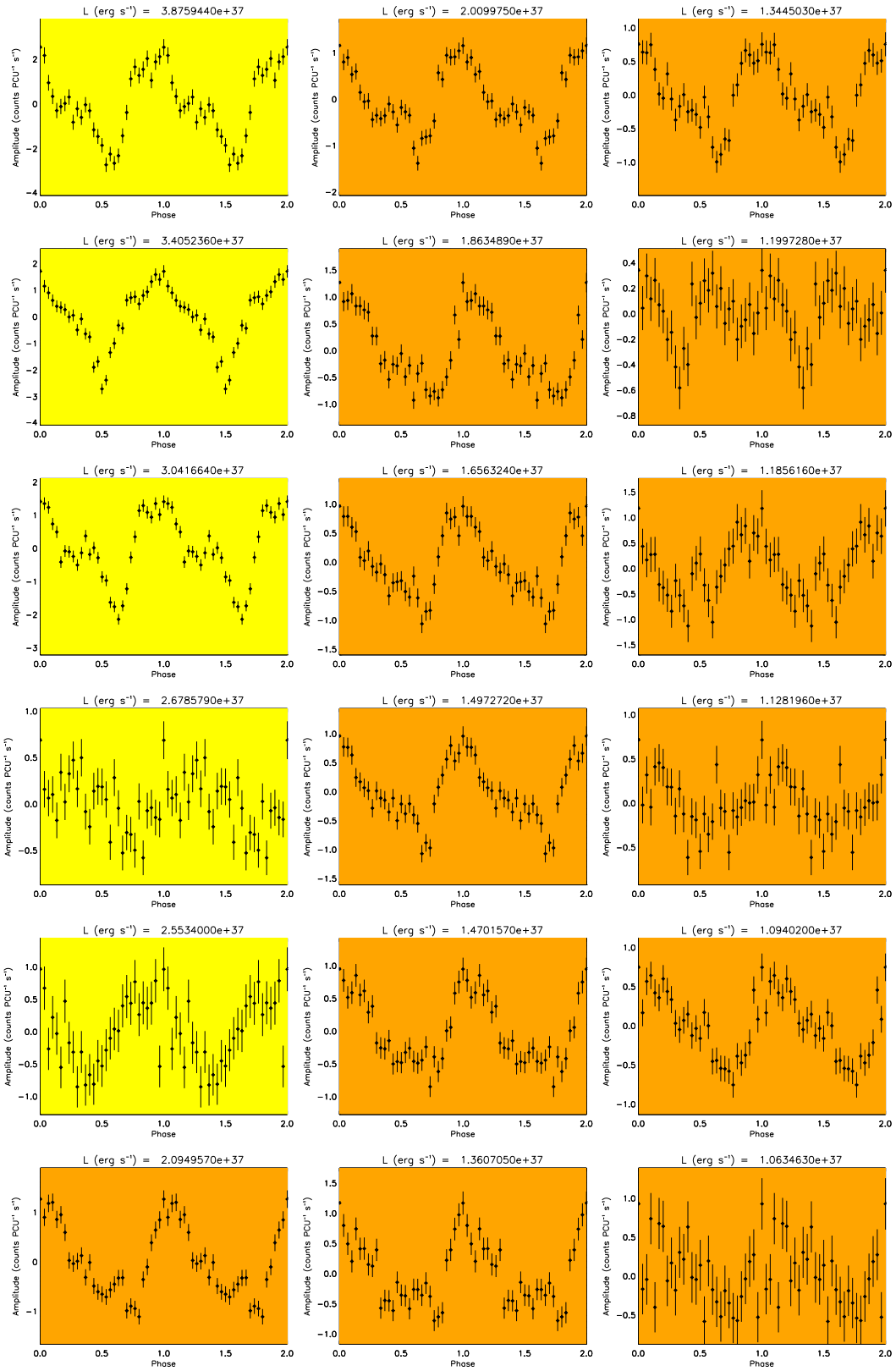
L (erg s⁻¹) = 3.8759440e+37
L (erg s⁻¹) = 2.0099750e+37
L (erg s⁻¹) = 1.3445030e+37
L (erg s⁻¹) = 3.4052360e+37
L (erg s⁻¹) = 1.8634890e+37
L (erg s⁻¹) = 1.1997280e+37
L (erg s⁻¹) = 3.0416640e+37
L (erg s⁻¹) = 1.6563240e+37
L (erg s⁻¹) = 1.1856160e+37
L (erg s⁻¹) = 2.6785790e+37
L (erg s⁻¹) = 1.4972720e+37
L (erg s⁻¹) = 1.1281960e+37
L (erg s⁻¹) = 2.5534000e+37
L (erg s⁻¹) = 1.4701570e+37
L (erg s⁻¹) = 1.0940200e+37
L (erg s⁻¹) = 2.0949570e+37
L (erg s⁻¹) = 1.3607050e+37
L (erg s⁻¹) = 1.0634630e+37
Amplitude (counts PCU⁻¹ s⁻¹)
Phase

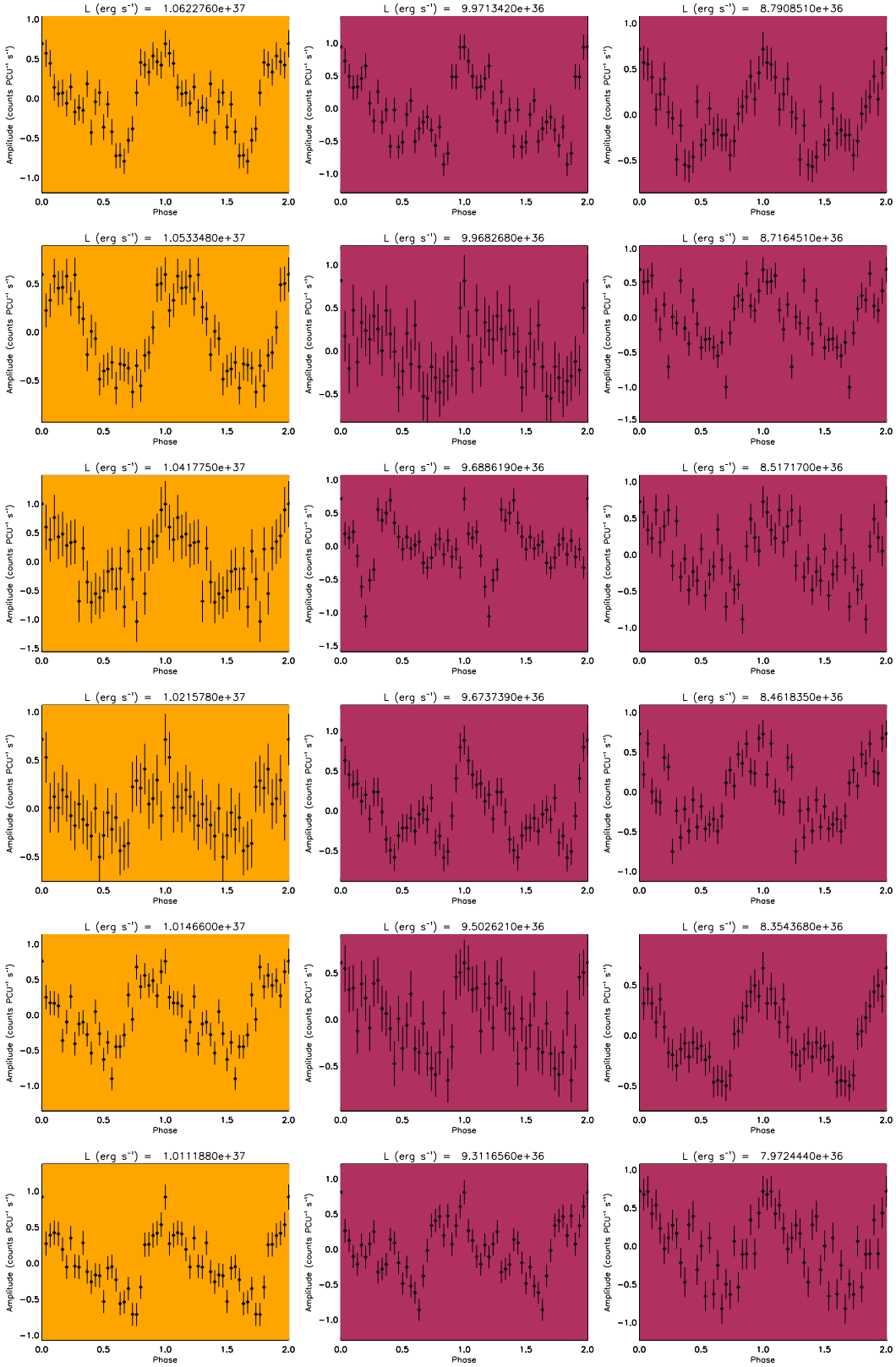
L (erg s⁻¹) = 1.0622760e+37
L (erg s⁻¹) = 9.9713420e+36
L (erg s⁻¹) = 8.7908510e+36
L (erg s⁻¹) = 1.0533480e+37
L (erg s⁻¹) = 9.9682680e+36
L (erg s⁻¹) = 8.7164510e+36
L (erg s⁻¹) = 1.0417750e+37
L (erg s⁻¹) = 9.6886190e+36
L (erg s⁻¹) = 8.5171700e+36
L (erg s⁻¹) = 1.0215780e+37
L (erg s⁻¹) = 9.6737390e+36
L (erg s⁻¹) = 8.4618350e+36
L (erg s⁻¹) = 1.0146600e+37
L (erg s⁻¹) = 9.5026210e+36
L (erg s⁻¹) = 8.3543680e+36
L (erg s⁻¹) = 1.0111880e+37
L (erg s⁻¹) = 9.3116560e+36
L (erg s⁻¹) = 7.9724440e+36
Amplitude (counts PCU⁻¹ s⁻¹)
Phase

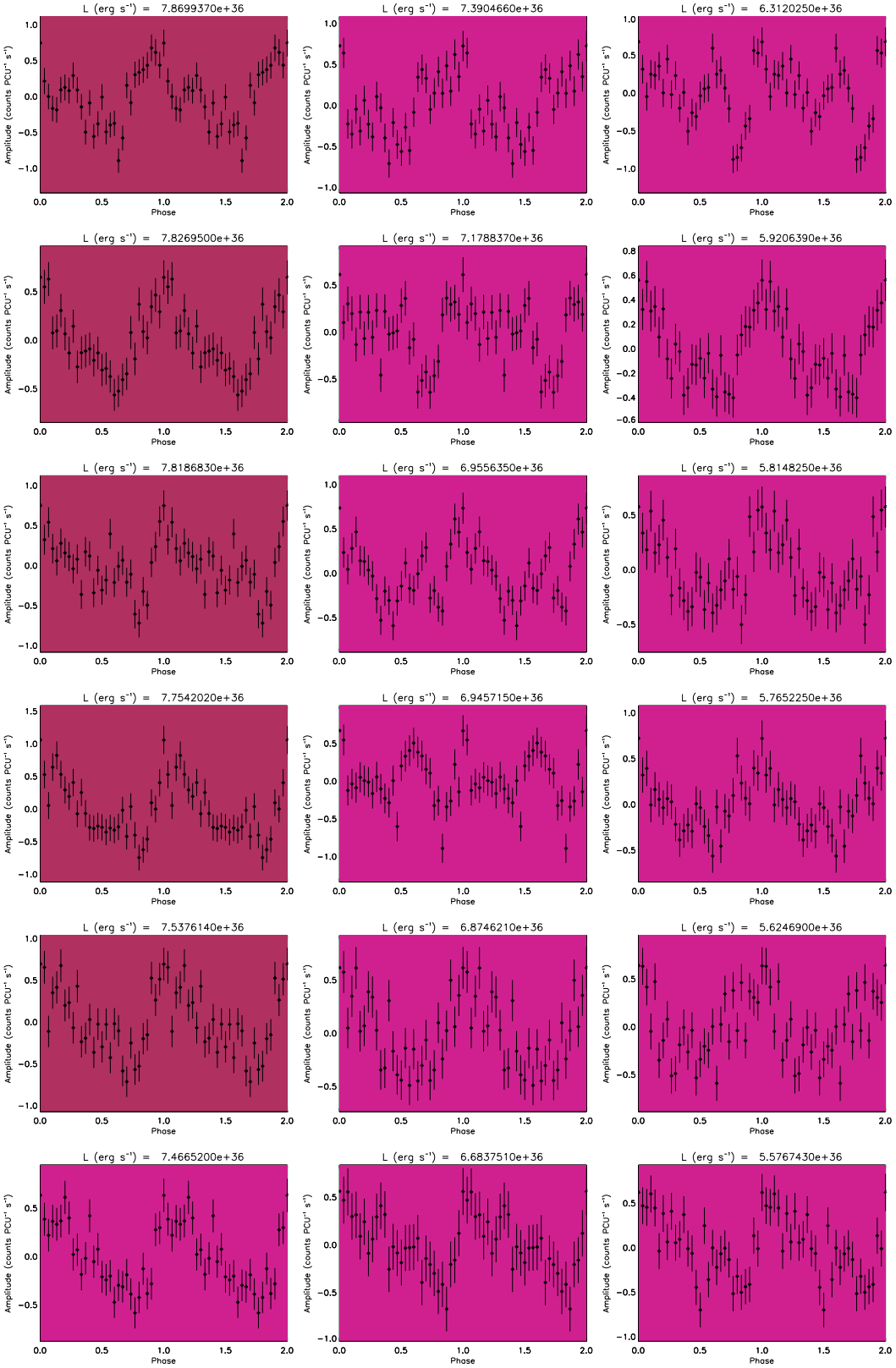
L (erg s⁻¹) = 7.8699370e+36
L (erg s⁻¹) = 7.3904660e+36
L (erg s⁻¹) = 6.3120250e+36
L (erg s⁻¹) = 7.8269500e+36
L (erg s⁻¹) = 7.1788370e+36
L (erg s⁻¹) = 5.9206390e+36
L (erg s⁻¹) = 7.8186830e+36
L (erg s⁻¹) = 6.9556350e+36
L (erg s⁻¹) = 5.8148250e+36
L (erg s⁻¹) = 7.7542020e+36
L (erg s⁻¹) = 6.9457150e+36
L (erg s⁻¹) = 5.7652250e+36
L (erg s⁻¹) = 7.5376140e+36
L (erg s⁻¹) = 6.8746210e+36
L (erg s⁻¹) = 5.6246900e+36
L (erg s⁻¹) = 7.4665200e+36
L (erg s⁻¹) = 6.6837510e+36
L (erg s⁻¹) = 5.5767430e+36
Amplitude (counts PCU⁻¹ s⁻¹)
Phase

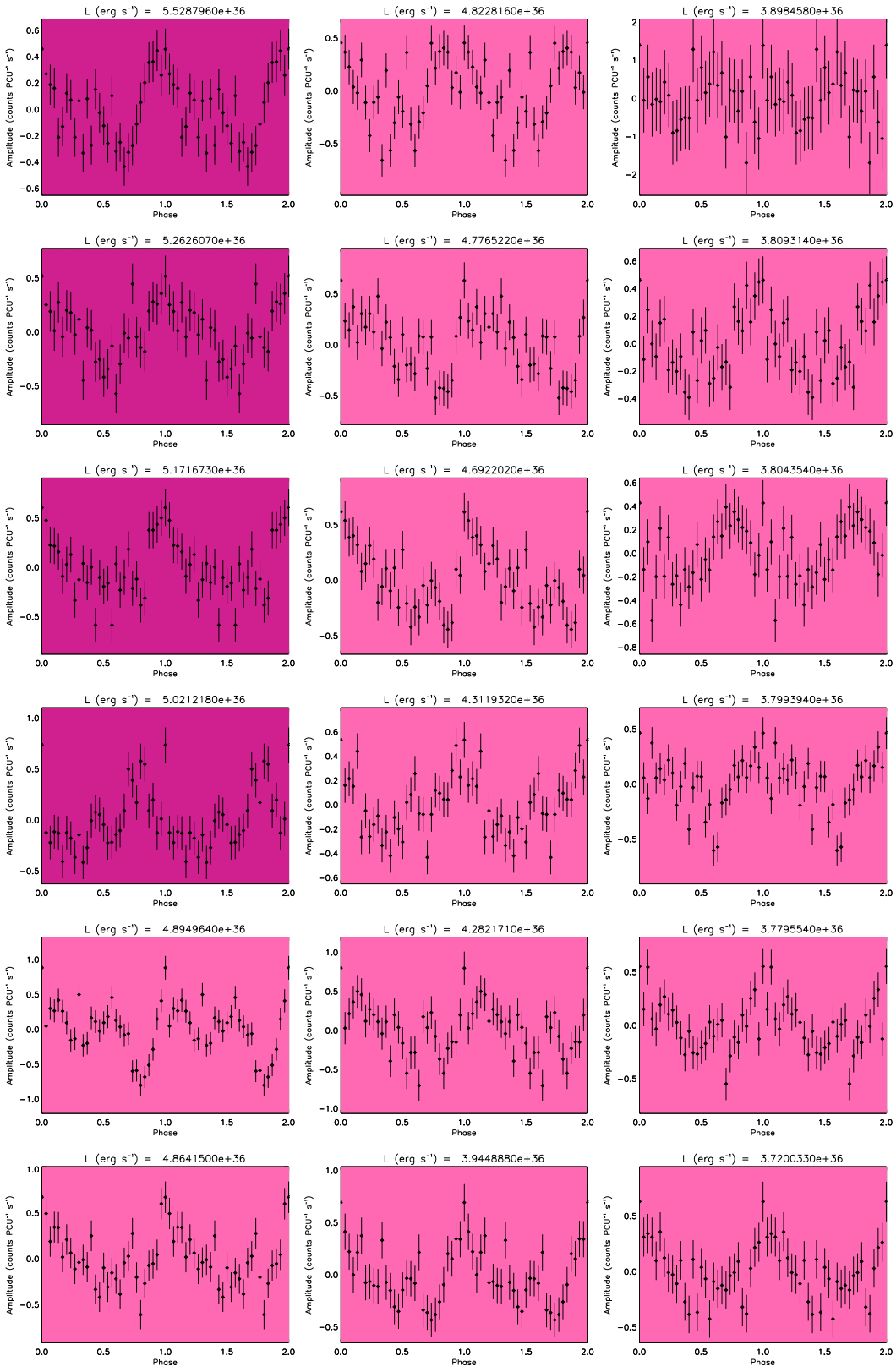
L (erg s⁻¹) = 5.5287960e+36
L (erg s⁻¹) = 4.8228160e+36
L (erg s⁻¹) = 3.8984580e+36
L (erg s⁻¹) = 5.2626070e+36
L (erg s⁻¹) = 4.7765220e+36
L (erg s⁻¹) = 3.8093140e+36
L (erg s⁻¹) = 5.1716730e+36
L (erg s⁻¹) = 4.6922020e+36
L (erg s⁻¹) = 3.8043540e+36
L (erg s⁻¹) = 5.0212180e+36
L (erg s⁻¹) = 4.3119320e+36
L (erg s⁻¹) = 3.7993940e+36
L (erg s⁻¹) = 4.8949640e+36
L (erg s⁻¹) = 4.2821710e+36
L (erg s⁻¹) = 3.7795540e+36
L (erg s⁻¹) = 4.8641500e+36
L (erg s⁻¹) = 3.9448880e+36
L (erg s⁻¹) = 3.7200330e+36
Amplitude (counts PCU⁻¹ s⁻¹)
Phase

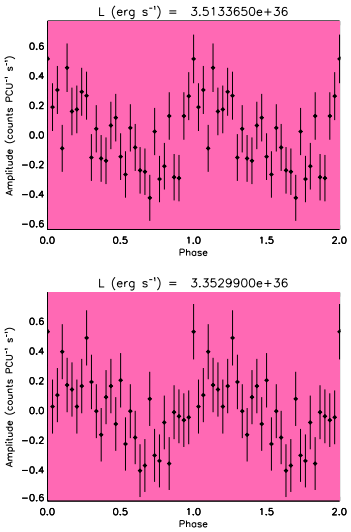

Figure C.10: Pulse-profiles for SXP18.3, in order of decreasing L (from top to bottom, left to right). The colour-coding is explained in Figure C.1.

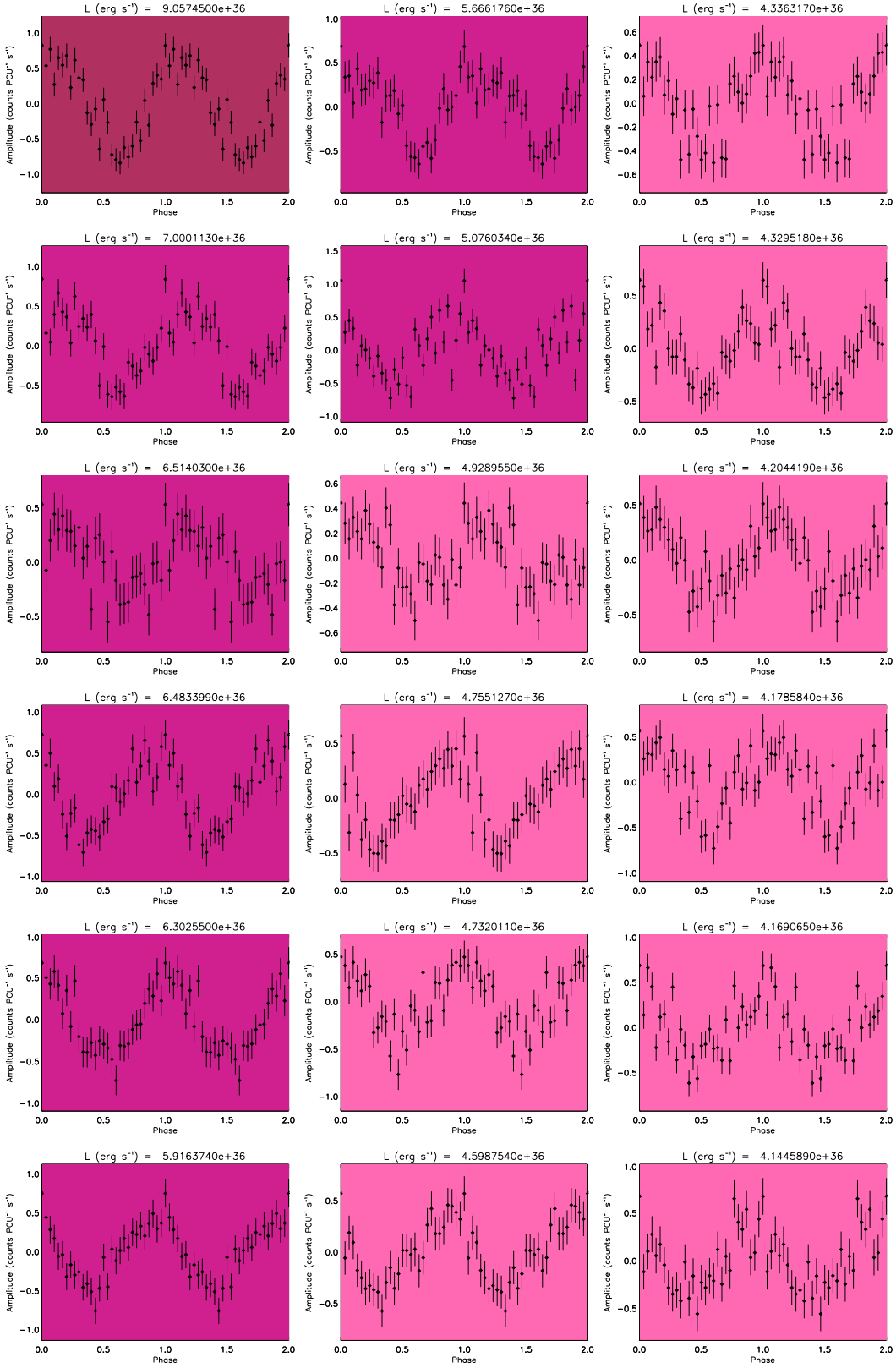
L (erg s⁻¹) = 9.0574500e+36
L (erg s⁻¹) = 5.6661760e+36
L (erg s⁻¹) = 4.3363170e+36
L (erg s⁻¹) = 7.0001130e+36
L (erg s⁻¹) = 5.0760340e+36
L (erg s⁻¹) = 4.3295180e+36
L (erg s⁻¹) = 6.5140300e+36
L (erg s⁻¹) = 4.9289550e+36
L (erg s⁻¹) = 4.2044190e+36
L (erg s⁻¹) = 6.4833990e+36
L (erg s⁻¹) = 4.7551270e+36
L (erg s⁻¹) = 4.1785840e+36
L (erg s⁻¹) = 6.3025500e+36
L (erg s⁻¹) = 4.7320110e+36
L (erg s⁻¹) = 4.1690650e+36
L (erg s⁻¹) = 5.9163740e+36
L (erg s⁻¹) = 4.5987540e+36
L (erg s⁻¹) = 4.1445890e+36
Amplitude (counts PCU⁻¹ s⁻¹)
Phase

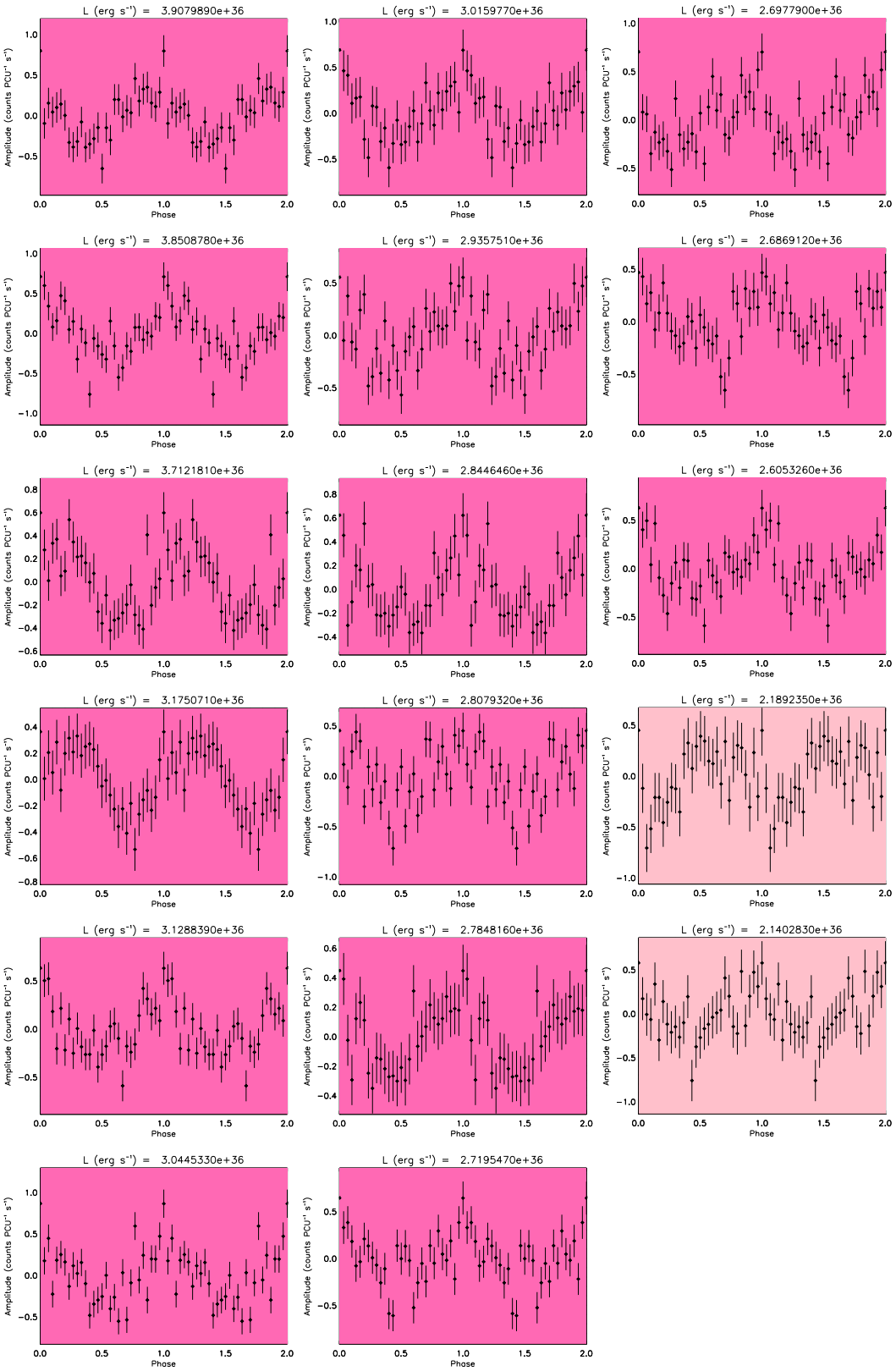

Figure C.11: Pulse-profiles for SXP25.5, in order of decreasing L (from top to bottom, left to right). The colour-coding is explained in Figure C.1.

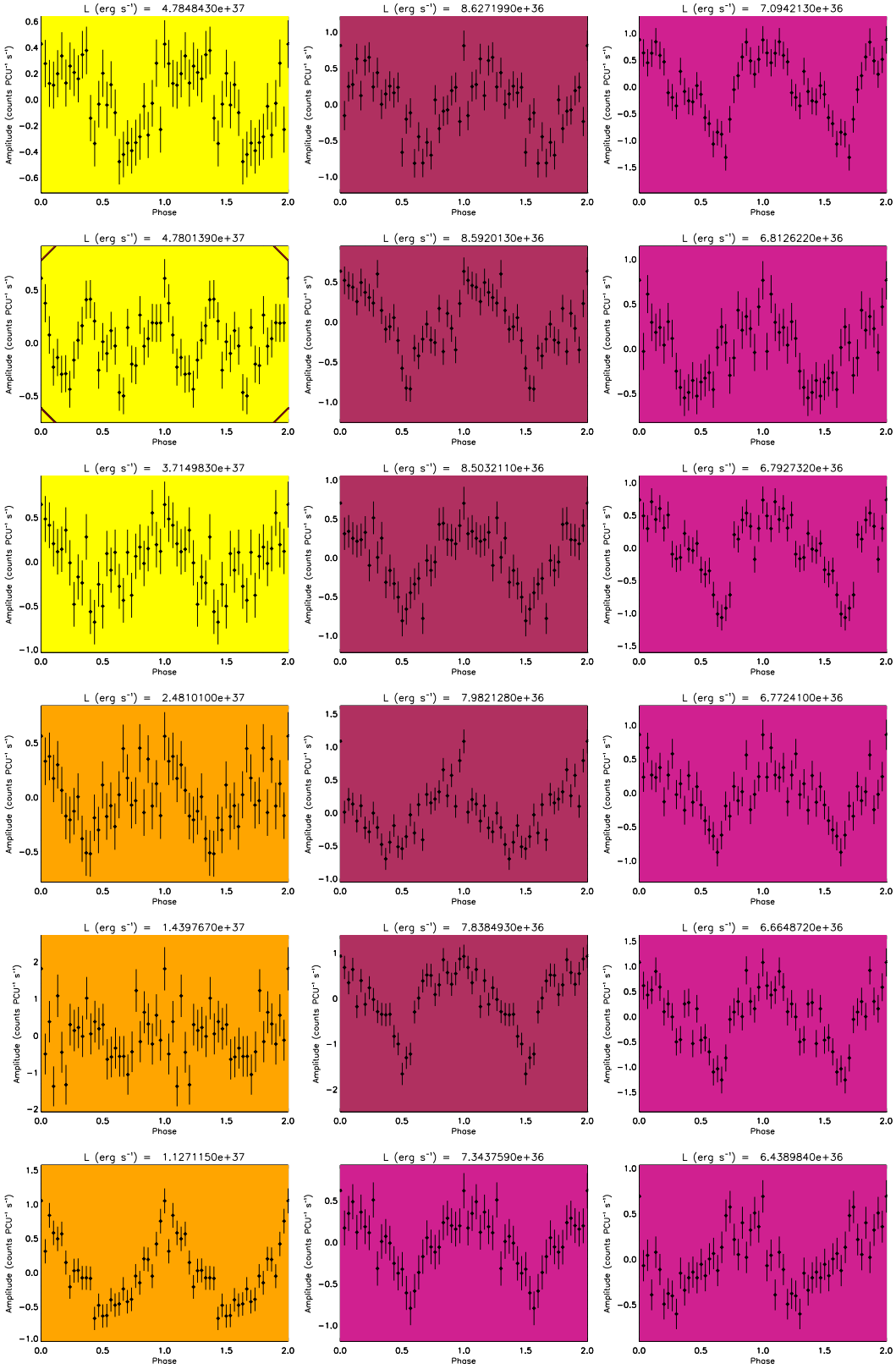
L (erg s⁻¹) = 4.7848430e+37
L (erg s⁻¹) = 8.6271990e+36
L (erg s⁻¹) = 7.0942130e+36
L (erg s⁻¹) = 4.7801390e+37
L (erg s⁻¹) = 8.5920130e+36
L (erg s⁻¹) = 6.8126220e+36
L (erg s⁻¹) = 3.7149830e+37
L (erg s⁻¹) = 8.5032110e+36
L (erg s⁻¹) = 6.7927320e+36
L (erg s⁻¹) = 2.4810100e+37
L (erg s⁻¹) = 7.9821280e+36
L (erg s⁻¹) = 6.7724100e+36
L (erg s⁻¹) = 1.4397670e+37
L (erg s⁻¹) = 7.8384930e+36
L (erg s⁻¹) = 6.6648720e+36
L (erg s⁻¹) = 1.1271150e+37
L (erg s⁻¹) = 7.3437590e+36
L (erg s⁻¹) = 6.4389840e+36
Amplitude (counts PCU⁻¹ s⁻¹)
Phase

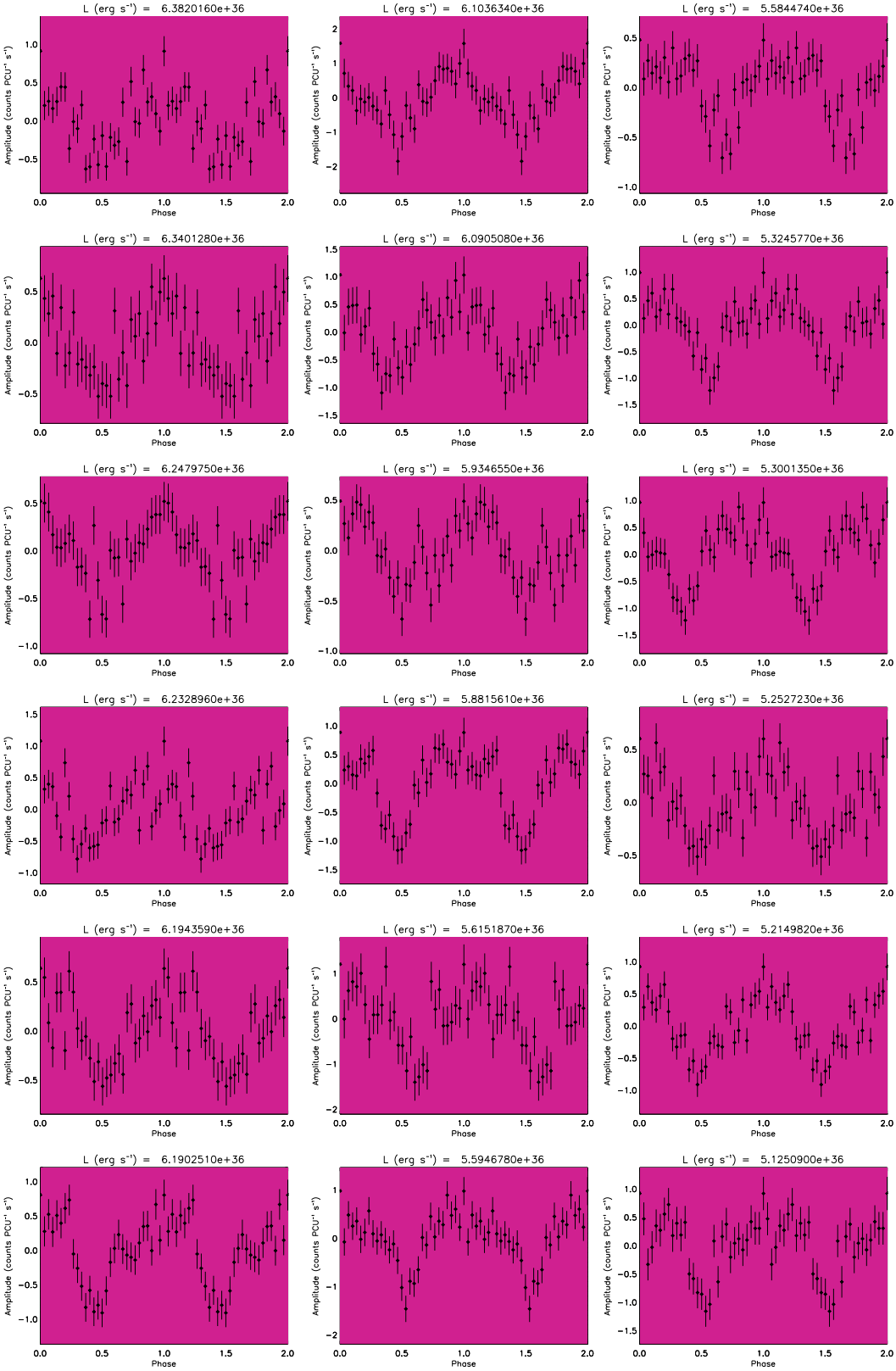
L (erg s⁻¹) = 6.3820160e+36
L (erg s⁻¹) = 6.1036340e+36
L (erg s⁻¹) = 5.5844740e+36
L (erg s⁻¹) = 6.3401280e+36
L (erg s⁻¹) = 6.0905080e+36
L (erg s⁻¹) = 5.3245770e+36
L (erg s⁻¹) = 6.2479750e+36
L (erg s⁻¹) = 5.9346550e+36
L (erg s⁻¹) = 5.3001350e+36
L (erg s⁻¹) = 6.2328960e+36
L (erg s⁻¹) = 5.8815610e+36
L (erg s⁻¹) = 5.2527230e+36
L (erg s⁻¹) = 6.1943590e+36
L (erg s⁻¹) = 5.6151870e+36
L (erg s⁻¹) = 5.2149820e+36
L (erg s⁻¹) = 6.1902510e+36
L (erg s⁻¹) = 5.5946780e+36
L (erg s⁻¹) = 5.1250900e+36
Amplitude (counts PCU⁻¹ s⁻¹)
Phase

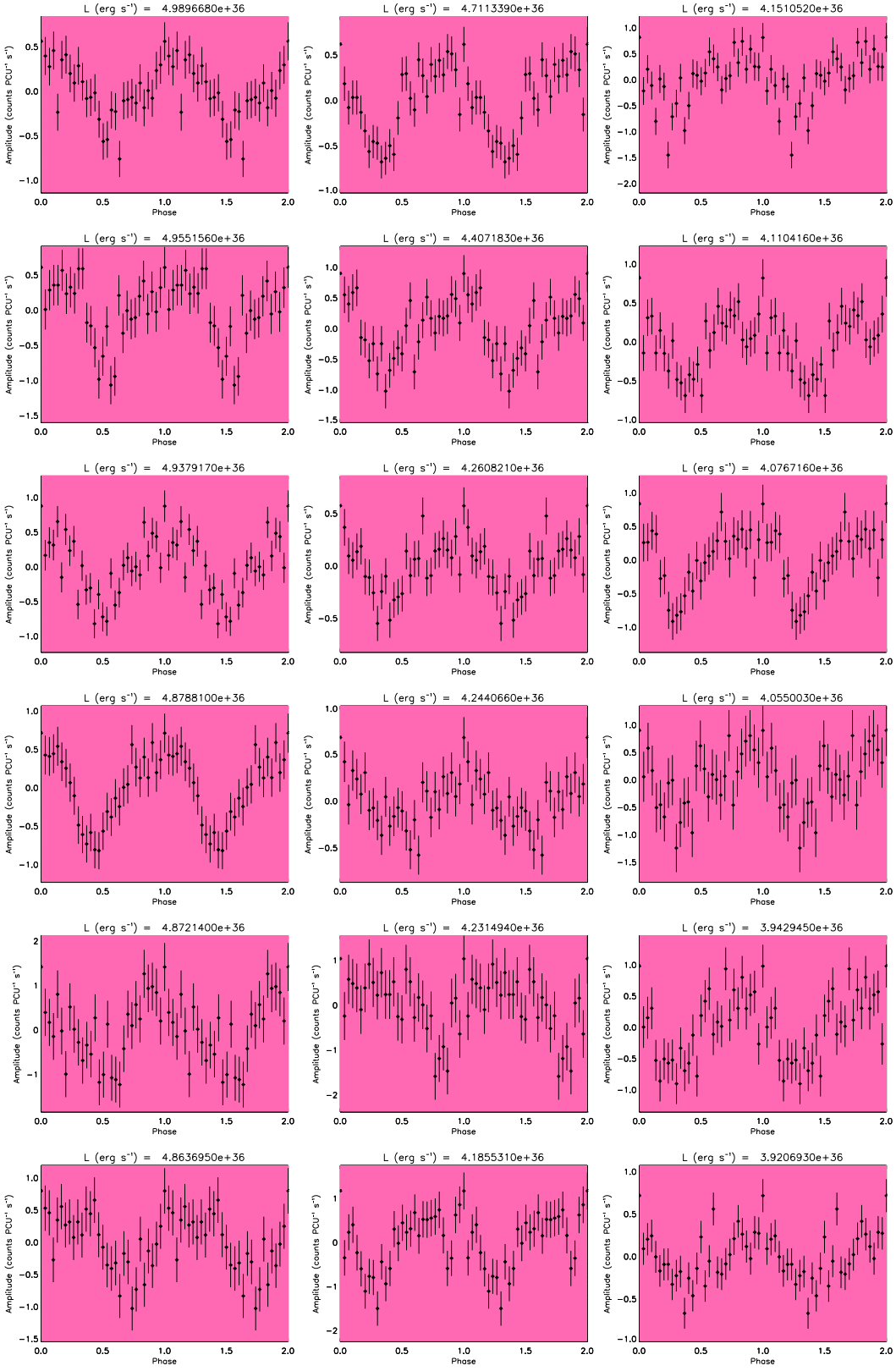
L (erg s⁻¹) = 4.9896680e+36
L (erg s⁻¹) = 4.7113390e+36
L (erg s⁻¹) = 4.1510520e+36
L (erg s⁻¹) = 4.9551560e+36
L (erg s⁻¹) = 4.4071830e+36
L (erg s⁻¹) = 4.1104160e+36
L (erg s⁻¹) = 4.9379170e+36
L (erg s⁻¹) = 4.2608210e+36
L (erg s⁻¹) = 4.0767160e+36
L (erg s⁻¹) = 4.8788100e+36
L (erg s⁻¹) = 4.2440660e+36
L (erg s⁻¹) = 4.0550030e+36
L (erg s⁻¹) = 4.8721400e+36
L (erg s⁻¹) = 4.2314940e+36
L (erg s⁻¹) = 3.9429450e+36
L (erg s⁻¹) = 4.8636950e+36
L (erg s⁻¹) = 4.1855310e+36
L (erg s⁻¹) = 3.9206930e+36
Amplitude (counts PCU⁻¹ s⁻¹)
Phase

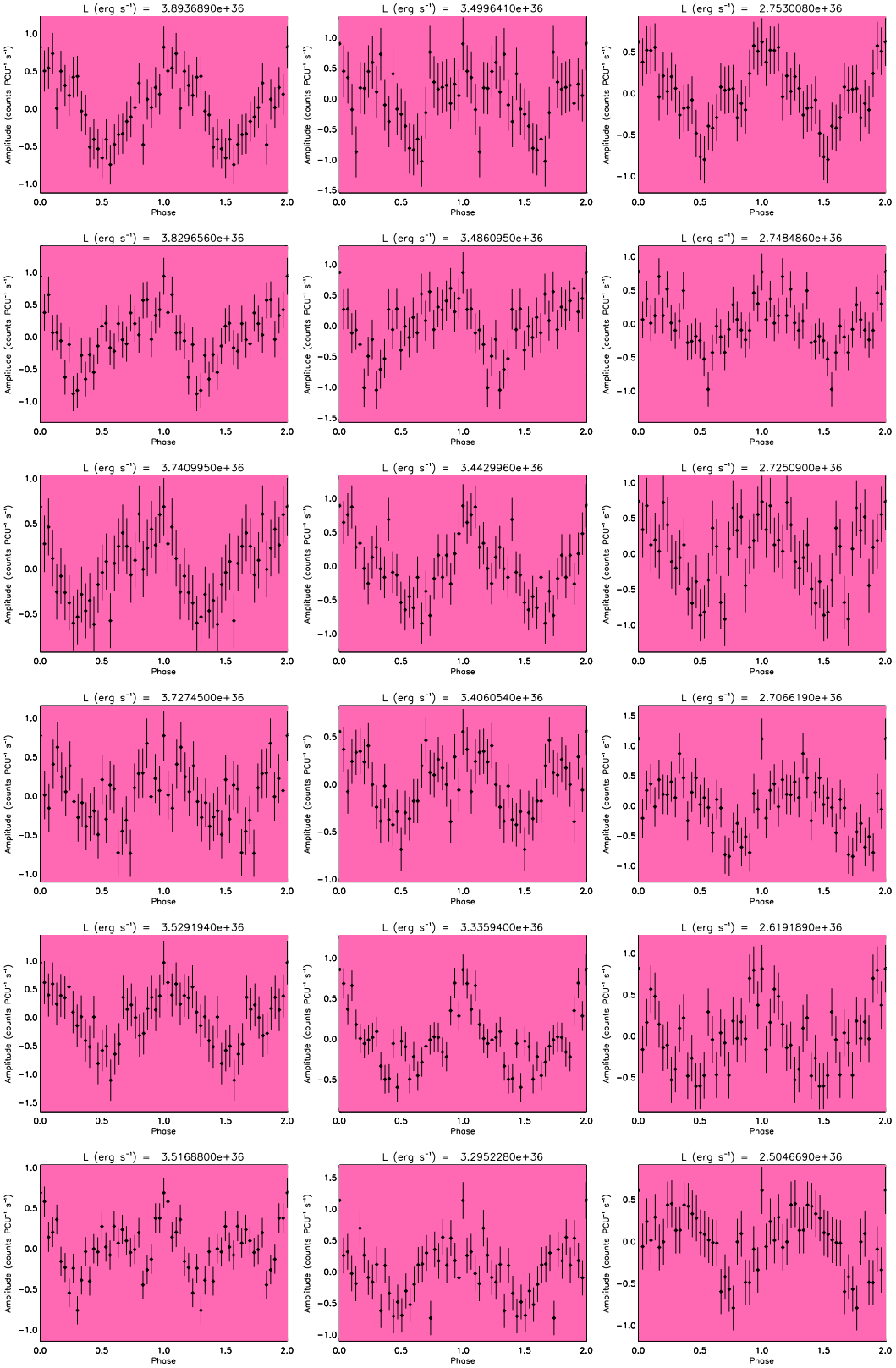
L (erg s⁻¹) = 3.8936890e+36
L (erg s⁻¹) = 3.4996410e+36
L (erg s⁻¹) = 2.7530080e+36
L (erg s⁻¹) = 3.8296560e+36
L (erg s⁻¹) = 3.4860950e+36
L (erg s⁻¹) = 2.7484860e+36
L (erg s⁻¹) = 3.7409950e+36
L (erg s⁻¹) = 3.4429960e+36
L (erg s⁻¹) = 2.7250900e+36
L (erg s⁻¹) = 3.7274500e+36
L (erg s⁻¹) = 3.4060540e+36
L (erg s⁻¹) = 2.7066190e+36
L (erg s⁻¹) = 3.5291940e+36
L (erg s⁻¹) = 3.3359400e+36
L (erg s⁻¹) = 2.6191890e+36
L (erg s⁻¹) = 3.5168800e+36
L (erg s⁻¹) = 3.2952280e+36
L (erg s⁻¹) = 2.5046690e+36
Amplitude (counts PCU⁻¹ s⁻¹)
Phase

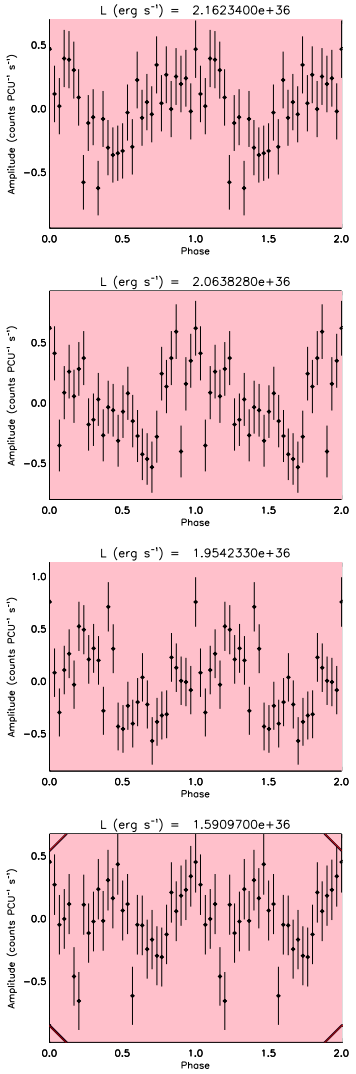

Figure C.12: Pulse-profiles for SXP46.6, in order of decreasing L (from top to bottom, left to right). The colour-coding is explained in Figure C.1.

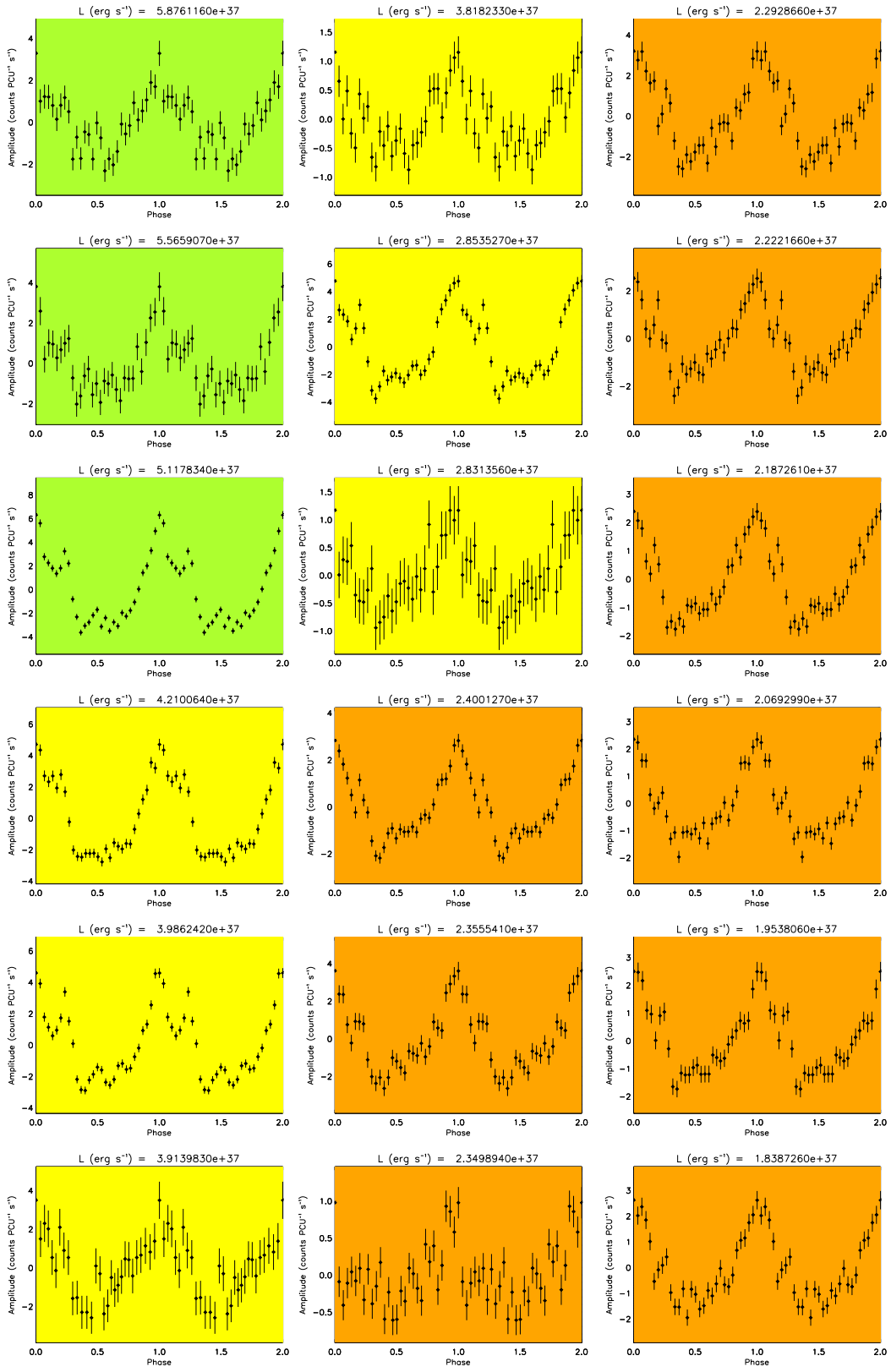
L (erg s⁻¹) = 5.8761160e+37
L (erg s⁻¹) = 3.8182330e+37
L (erg s⁻¹) = 2.2928660e+37
L (erg s⁻¹) = 5.5659070e+37
L (erg s⁻¹) = 2.8535270e+37
L (erg s⁻¹) = 2.2221660e+37
L (erg s⁻¹) = 5.1178340e+37
L (erg s⁻¹) = 2.8313560e+37
L (erg s⁻¹) = 2.1872610e+37
L (erg s⁻¹) = 4.2100640e+37
L (erg s⁻¹) = 2.4001270e+37
L (erg s⁻¹) = 2.0692990e+37
L (erg s⁻¹) = 3.9862420e+37
L (erg s⁻¹) = 2.3555410e+37
L (erg s⁻¹) = 1.9538060e+37
L (erg s⁻¹) = 3.9139830e+37
L (erg s⁻¹) = 2.3498940e+37
L (erg s⁻¹) = 1.8387260e+37
Amplitude (counts PCU⁻¹ s⁻¹)
Phase

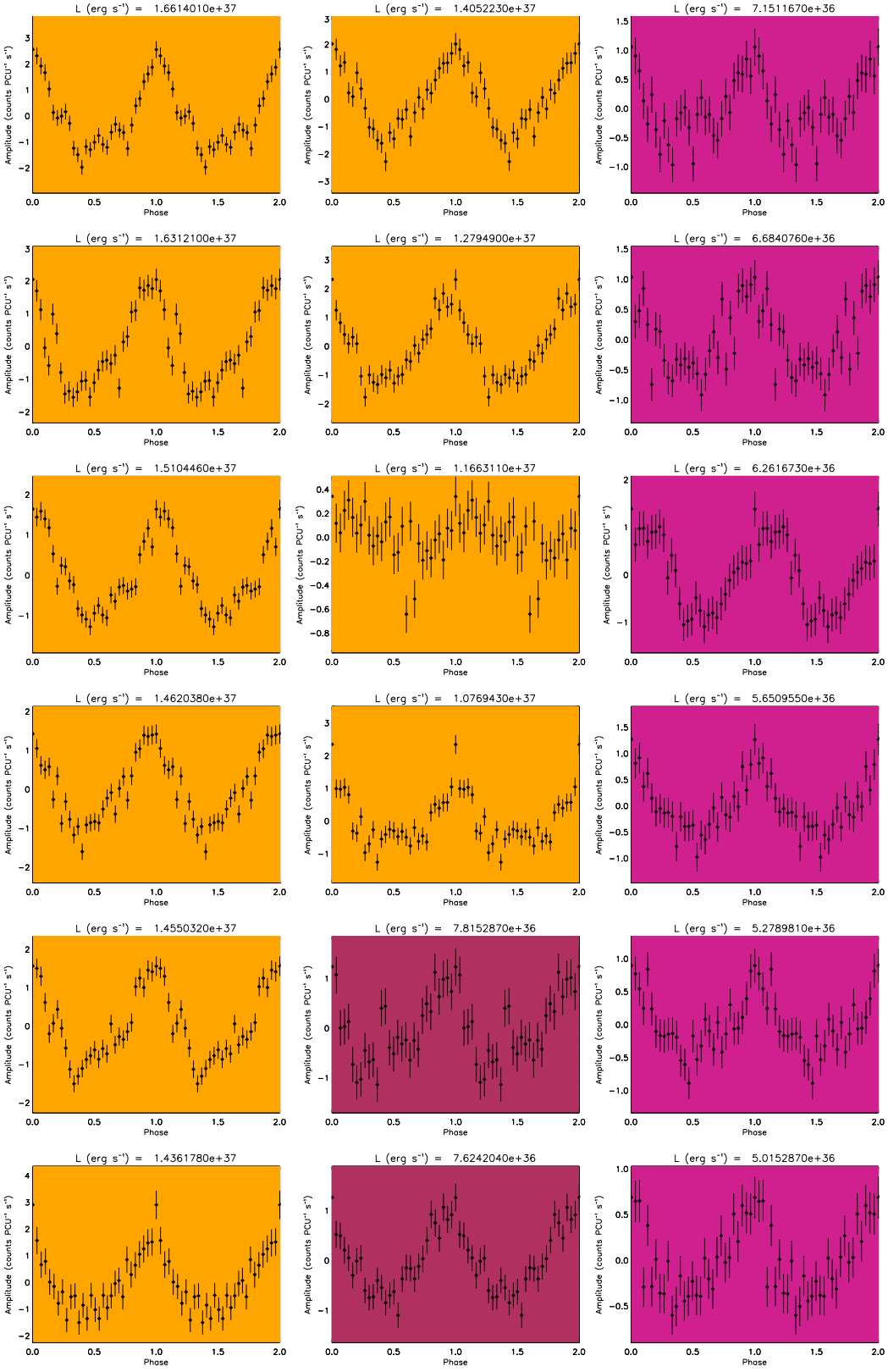
L (erg s⁻¹) = 1.6614010e+37
L (erg s⁻¹) = 1.4052230e+37
L (erg s⁻¹) = 7.1511670e+36
L (erg s⁻¹) = 1.6312100e+37
L (erg s⁻¹) = 1.2794900e+37
L (erg s⁻¹) = 6.6840760e+36
L (erg s⁻¹) = 1.5104460e+37
L (erg s⁻¹) = 1.1663110e+37
L (erg s⁻¹) = 6.2616730e+36
L (erg s⁻¹) = 1.4620380e+37
L (erg s⁻¹) = 1.0769430e+37
L (erg s⁻¹) = 5.6509550e+36
L (erg s⁻¹) = 1.4550320e+37
L (erg s⁻¹) = 7.8152870e+36
L (erg s⁻¹) = 5.2789810e+36
L (erg s⁻¹) = 1.4361780e+37
L (erg s⁻¹) = 7.6242040e+36
L (erg s⁻¹) = 5.0152870e+36
Amplitude (counts PCU⁻¹ s⁻¹)
Phase

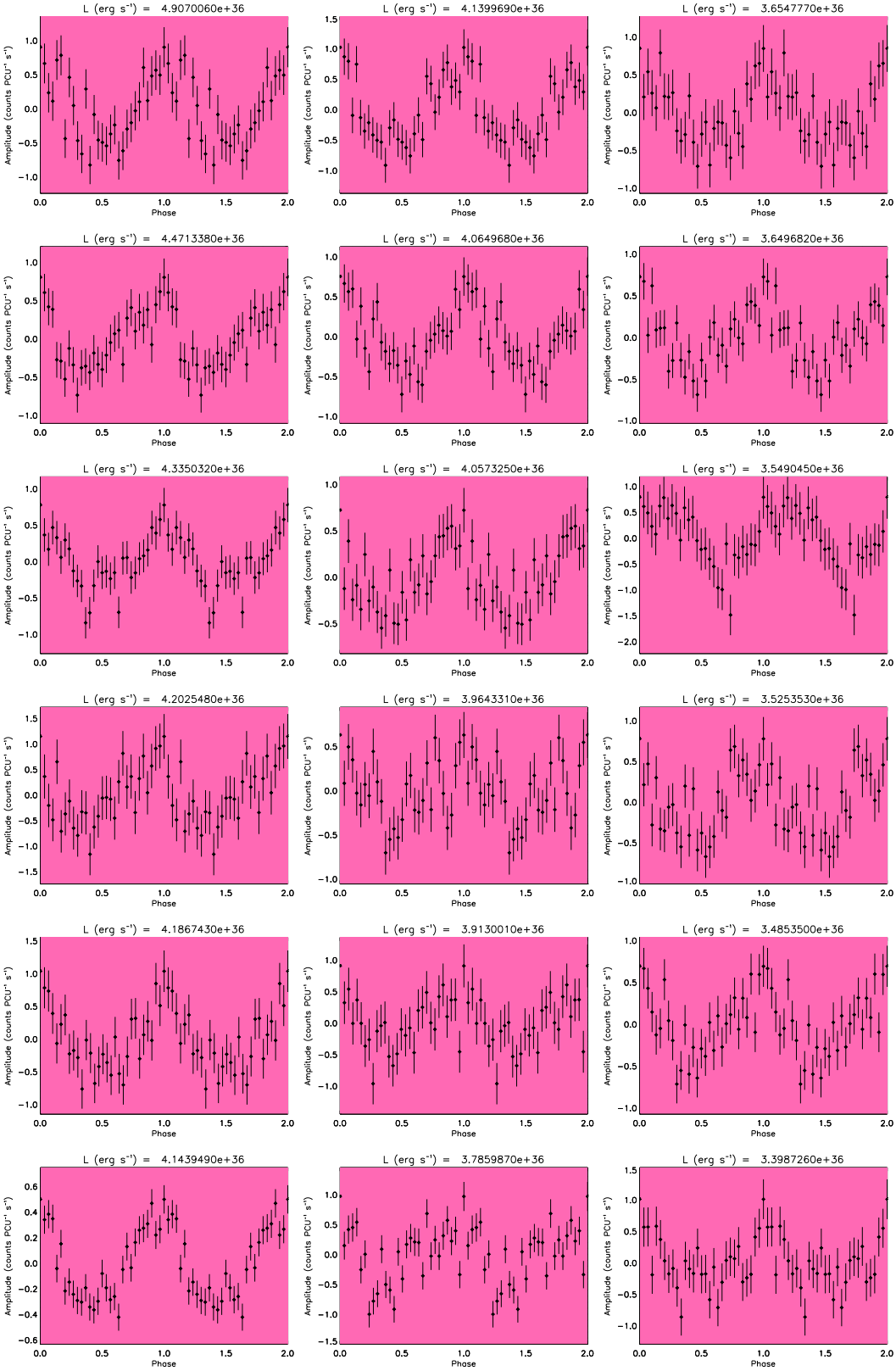
L (erg s⁻¹) = 4.9070060e+36
L (erg s⁻¹) = 4.1399690e+36
L (erg s⁻¹) = 3.6547770e+36
L (erg s⁻¹) = 4.4713380e+36
L (erg s⁻¹) = 4.0649680e+36
L (erg s⁻¹) = 3.6496820e+36
L (erg s⁻¹) = 4.3350320e+36
L (erg s⁻¹) = 4.0573250e+36
L (erg s⁻¹) = 3.5490450e+36
L (erg s⁻¹) = 4.2025480e+36
L (erg s⁻¹) = 3.9643310e+36
L (erg s⁻¹) = 3.5253530e+36
L (erg s⁻¹) = 4.1867430e+36
L (erg s⁻¹) = 3.9130010e+36
L (erg s⁻¹) = 3.4853500e+36
L (erg s⁻¹) = 4.1439490e+36
L (erg s⁻¹) = 3.7859870e+36
L (erg s⁻¹) = 3.3987260e+36
Amplitude (counts PCU⁻¹ s⁻¹)
Phase

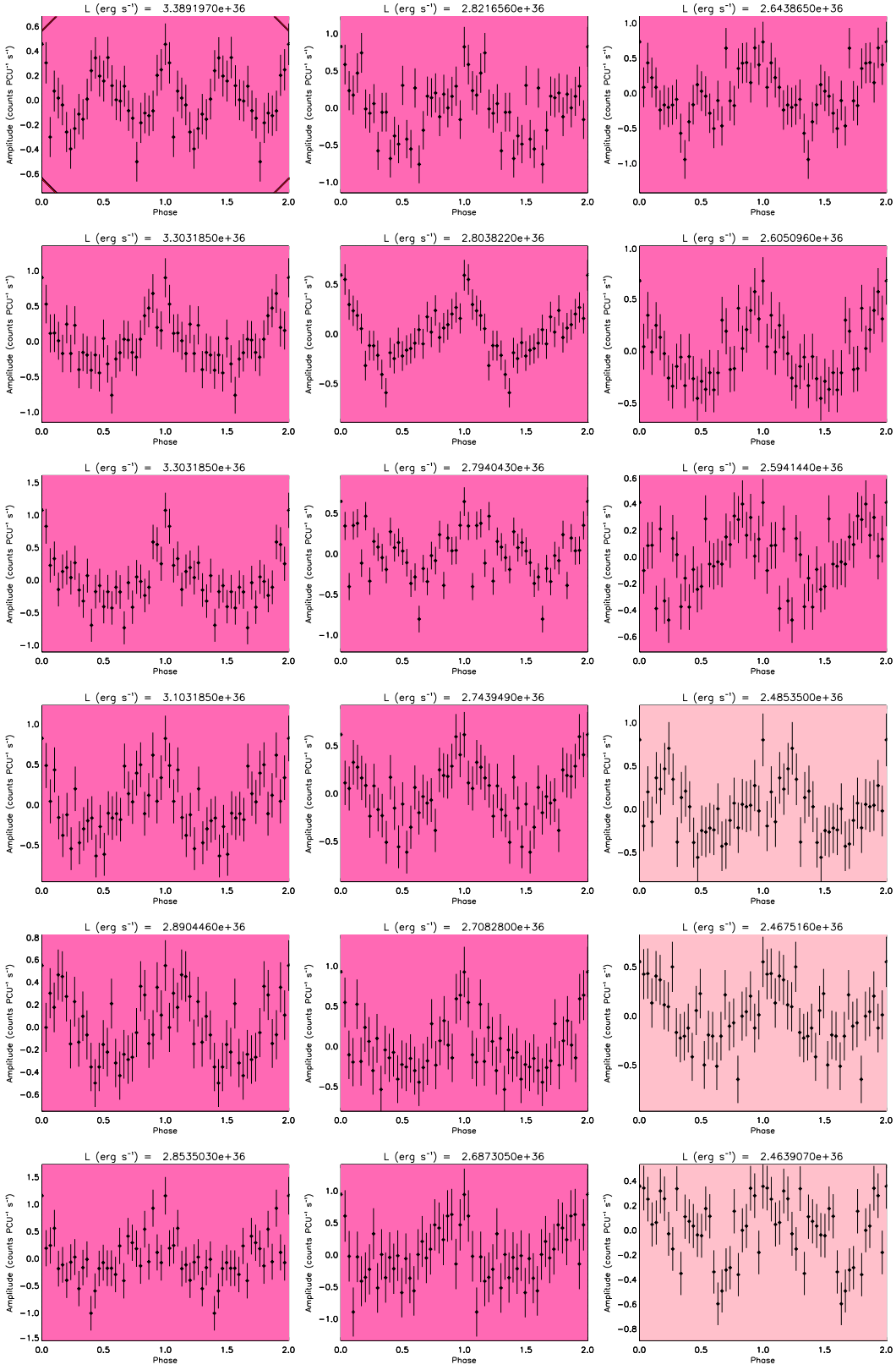
L (erg s⁻¹) = 3.3891970e+36
L (erg s⁻¹) = 2.8216560e+36
L (erg s⁻¹) = 2.6438650e+36
L (erg s⁻¹) = 3.3031850e+36
L (erg s⁻¹) = 2.8038220e+36
L (erg s⁻¹) = 2.6050960e+36
L (erg s⁻¹) = 3.3031850e+36
L (erg s⁻¹) = 2.7940430e+36
L (erg s⁻¹) = 2.5941440e+36
L (erg s⁻¹) = 3.1031850e+36
L (erg s⁻¹) = 2.7439490e+36
L (erg s⁻¹) = 2.4853500e+36
L (erg s⁻¹) = 2.8904460e+36
L (erg s⁻¹) = 2.7082800e+36
L (erg s⁻¹) = 2.4675160e+36
L (erg s⁻¹) = 2.8535030e+36
L (erg s⁻¹) = 2.6873050e+36
L (erg s⁻¹) = 2.4639070e+36
Amplitude (counts PCU⁻¹ s⁻¹)
Phase

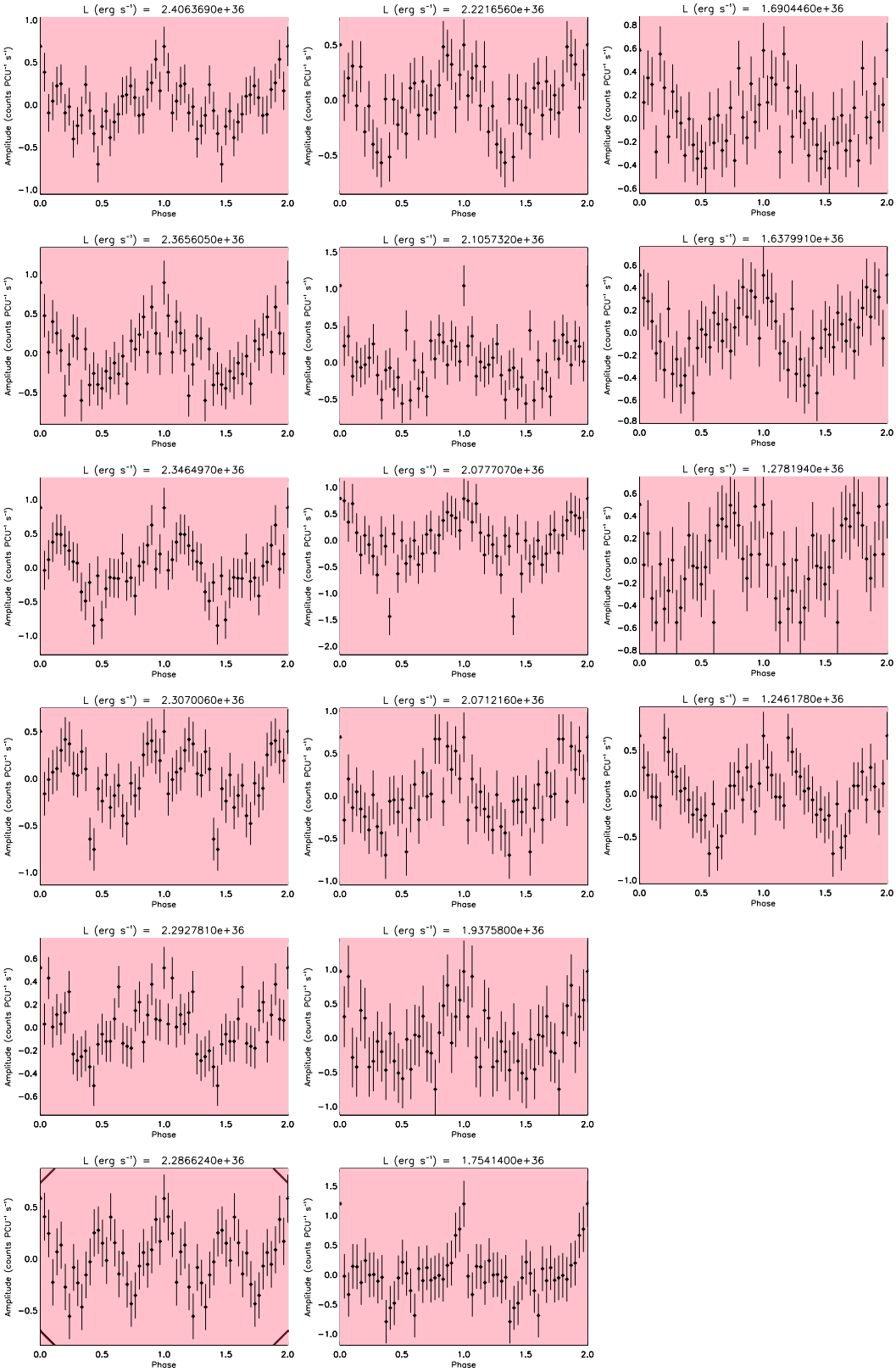

Figure C.13: Pulse-profiles for SXP59.0, in order of decreasing L (from top to bottom, left to right). The colour-coding is explained in Figure C.1.

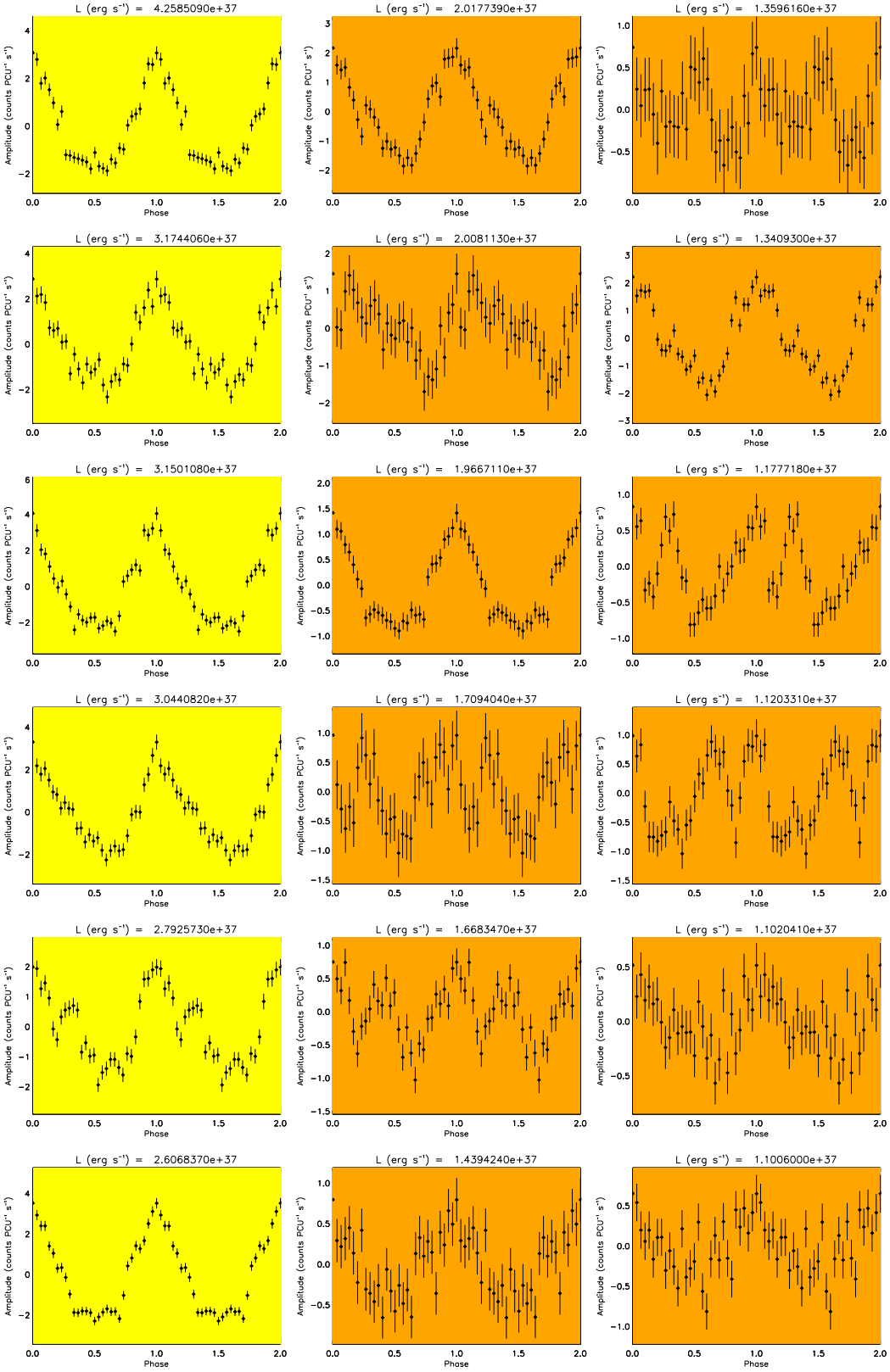
L (erg s⁻¹) = 4.2585090e+37
L (erg s⁻¹) = 2.0177390e+37
L (erg s⁻¹) = 1.3596160e+37
L (erg s⁻¹) = 3.1744060e+37
L (erg s⁻¹) = 2.0081130e+37
L (erg s⁻¹) = 1.3409300e+37
L (erg s⁻¹) = 3.1501080e+37
L (erg s⁻¹) = 1.9667110e+37
L (erg s⁻¹) = 1.1777180e+37
L (erg s⁻¹) = 3.0440820e+37
L (erg s⁻¹) = 1.7094040e+37
L (erg s⁻¹) = 1.1203310e+37
L (erg s⁻¹) = 2.7925730e+37
L (erg s⁻¹) = 1.6683470e+37
L (erg s⁻¹) = 1.1020410e+37
L (erg s⁻¹) = 2.6068370e+37
L (erg s⁻¹) = 1.4394240e+37
L (erg s⁻¹) = 1.1006000e+37
Amplitude (counts PCU⁻¹ s⁻¹)
Phase

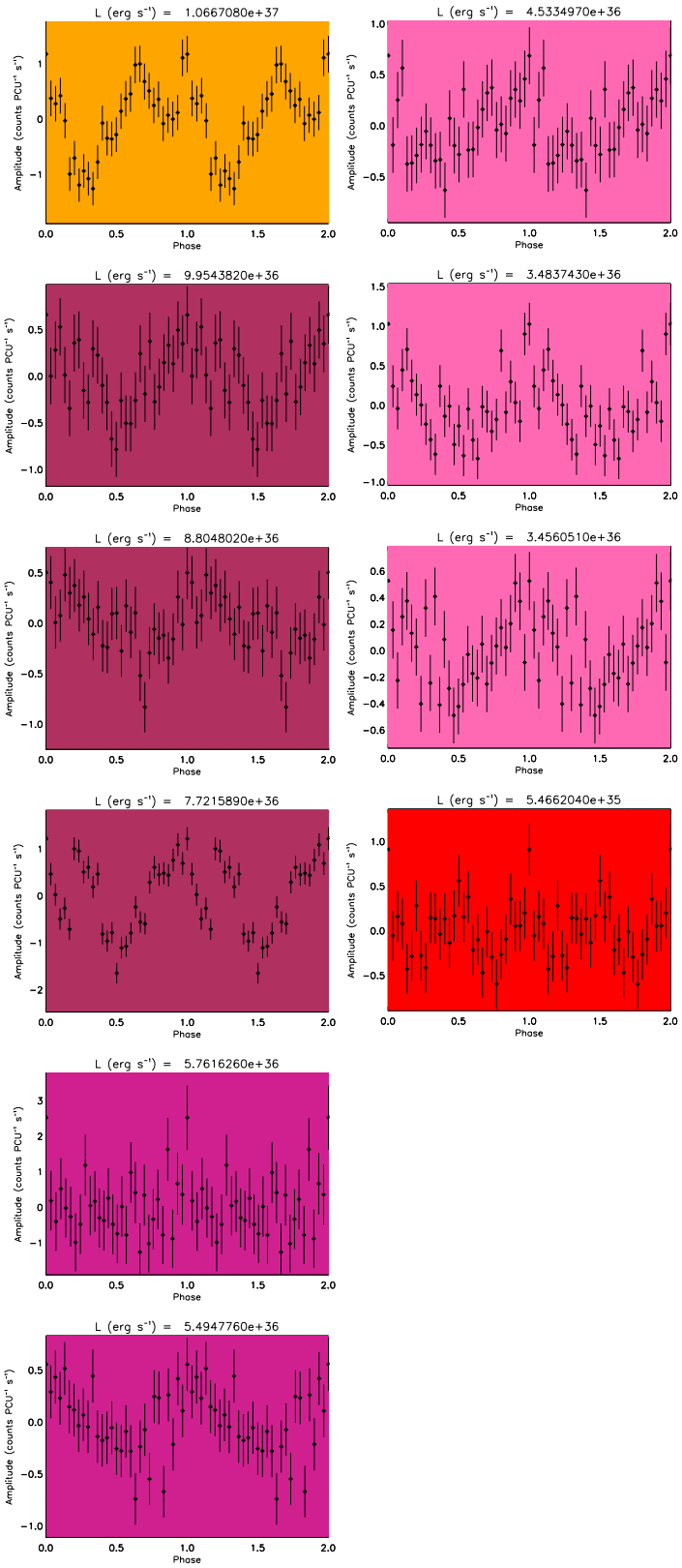

Figure C.14: Pulse-profiles for SXP74.7, in order of decreasing L (from top to bottom, left to right). The colour-coding is explained in Figure C.1.

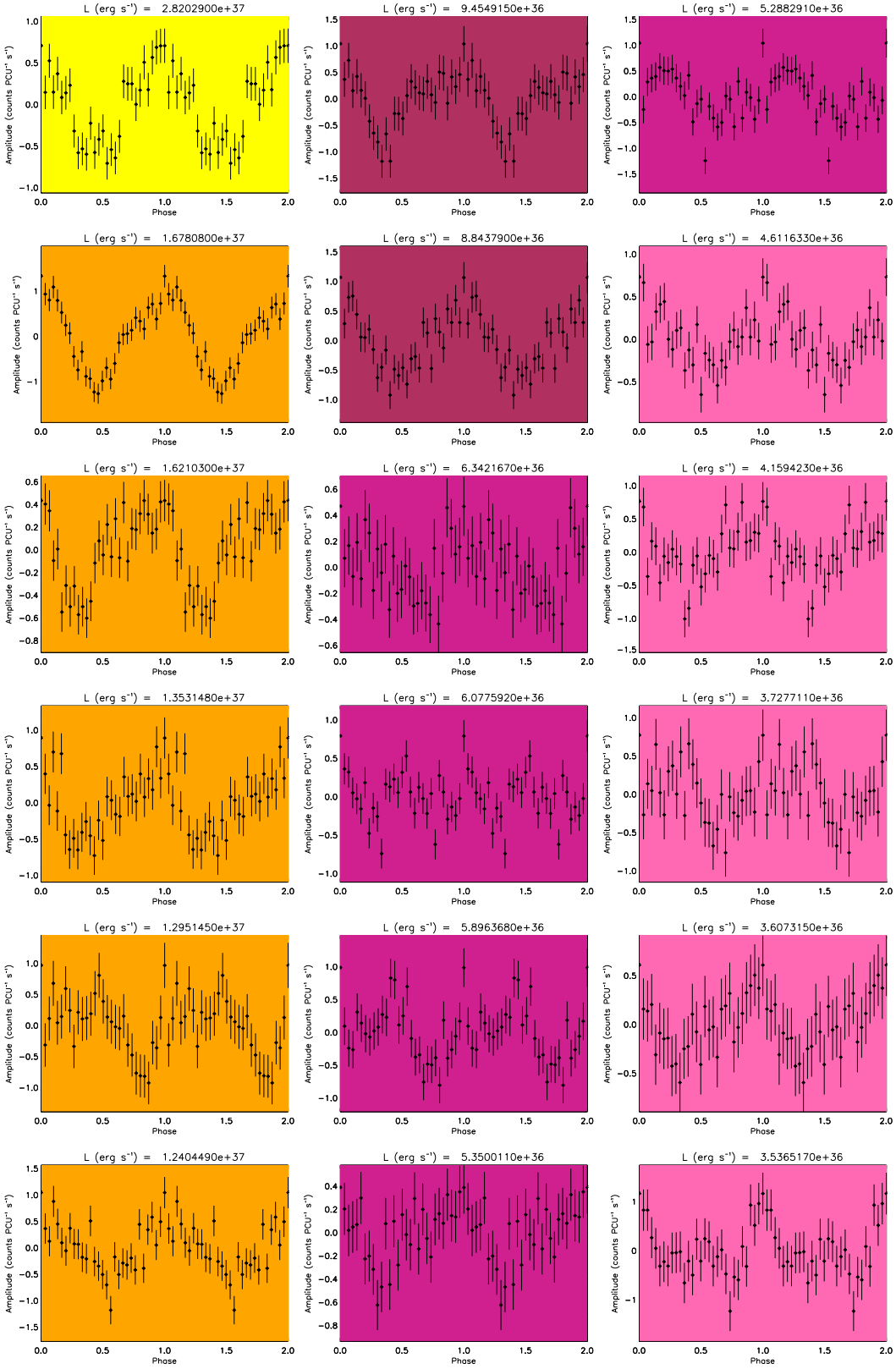
L (erg s⁻¹) = 2.8202900e+37
L (erg s⁻¹) = 9.4549150e+36
L (erg s⁻¹) = 5.2882910e+36
L (erg s⁻¹) = 1.6780800e+37
L (erg s⁻¹) = 8.8437900e+36
L (erg s⁻¹) = 4.6116330e+36
L (erg s⁻¹) = 1.6210300e+37
L (erg s⁻¹) = 6.3421670e+36
L (erg s⁻¹) = 4.1594230e+36
L (erg s⁻¹) = 1.3531480e+37
L (erg s⁻¹) = 6.0775920e+36
L (erg s⁻¹) = 3.7277110e+36
L (erg s⁻¹) = 1.2951450e+37
L (erg s⁻¹) = 5.8963680e+36
L (erg s⁻¹) = 3.6073150e+36
L (erg s⁻¹) = 1.2404490e+37
L (erg s⁻¹) = 5.3500110e+36
L (erg s⁻¹) = 3.5365170e+36
Amplitude (counts PCU⁻¹ s⁻¹)
Phase

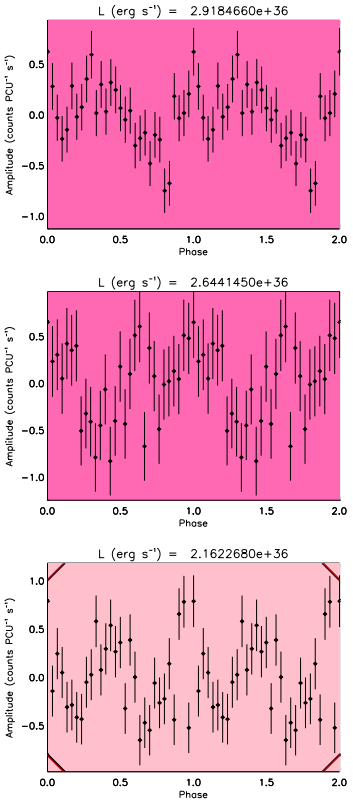

Figure C.15: Pulse-profiles for SXP82.4, in order of decreasing L (from top to bottom, left to right). The colour-coding is explained in Figure C.1.

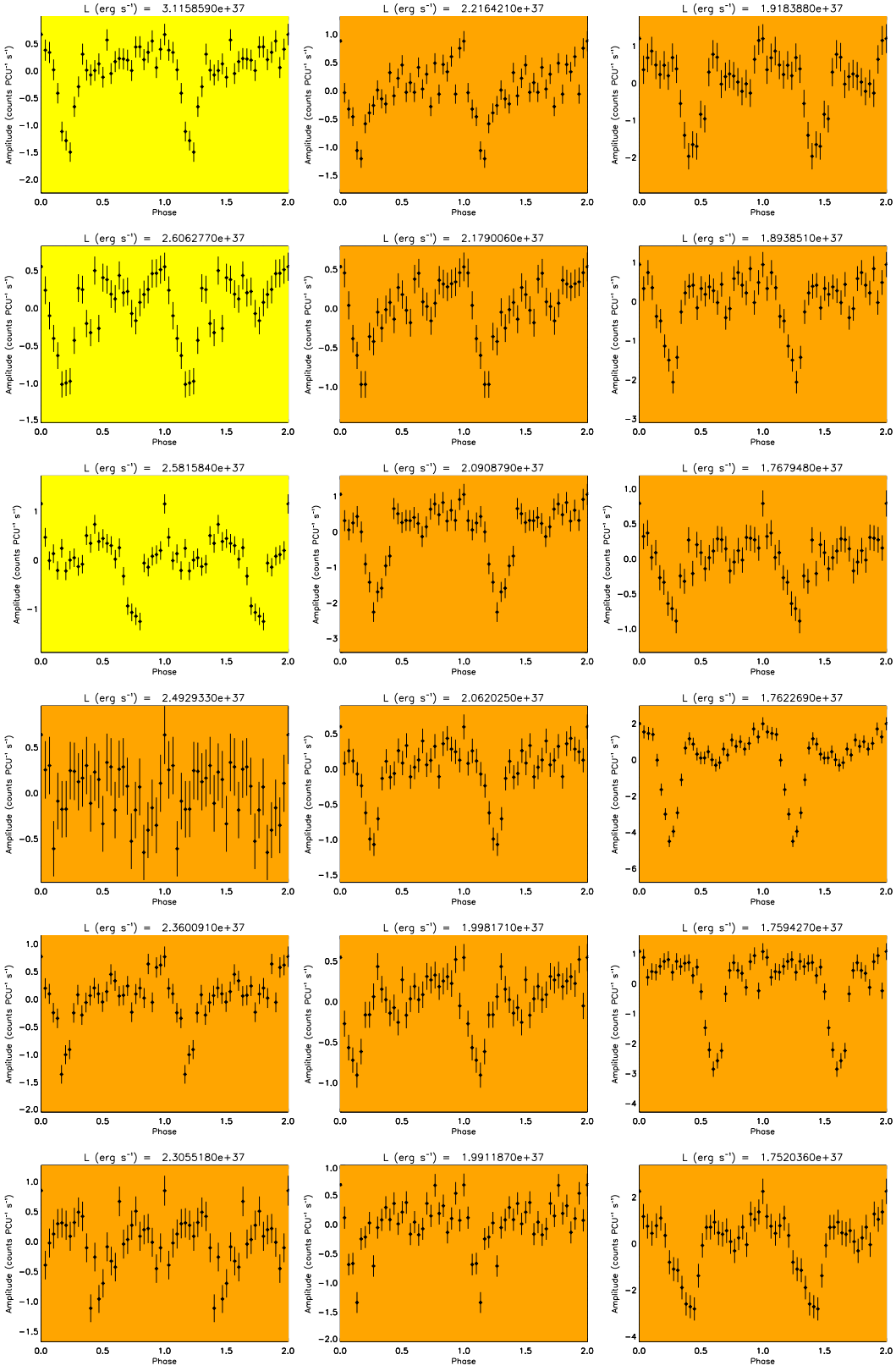
L (erg s⁻¹) = 3.1158590e+37
L (erg s⁻¹) = 2.2164210e+37
L (erg s⁻¹) = 1.9183880e+37
L (erg s⁻¹) = 2.6062770e+37
L (erg s⁻¹) = 2.1790060e+37
L (erg s⁻¹) = 1.8938510e+37
L (erg s⁻¹) = 2.5815840e+37
L (erg s⁻¹) = 2.0908790e+37
L (erg s⁻¹) = 1.7679480e+37
L (erg s⁻¹) = 2.4929330e+37
L (erg s⁻¹) = 2.0620250e+37
L (erg s⁻¹) = 1.7622690e+37
L (erg s⁻¹) = 2.3600910e+37
L (erg s⁻¹) = 1.9981710e+37
L (erg s⁻¹) = 1.7594270e+37
L (erg s⁻¹) = 2.3055180e+37
L (erg s⁻¹) = 1.9911870e+37
L (erg s⁻¹) = 1.7520360e+37
Amplitude (counts PCU⁻¹ s⁻¹)
Phase

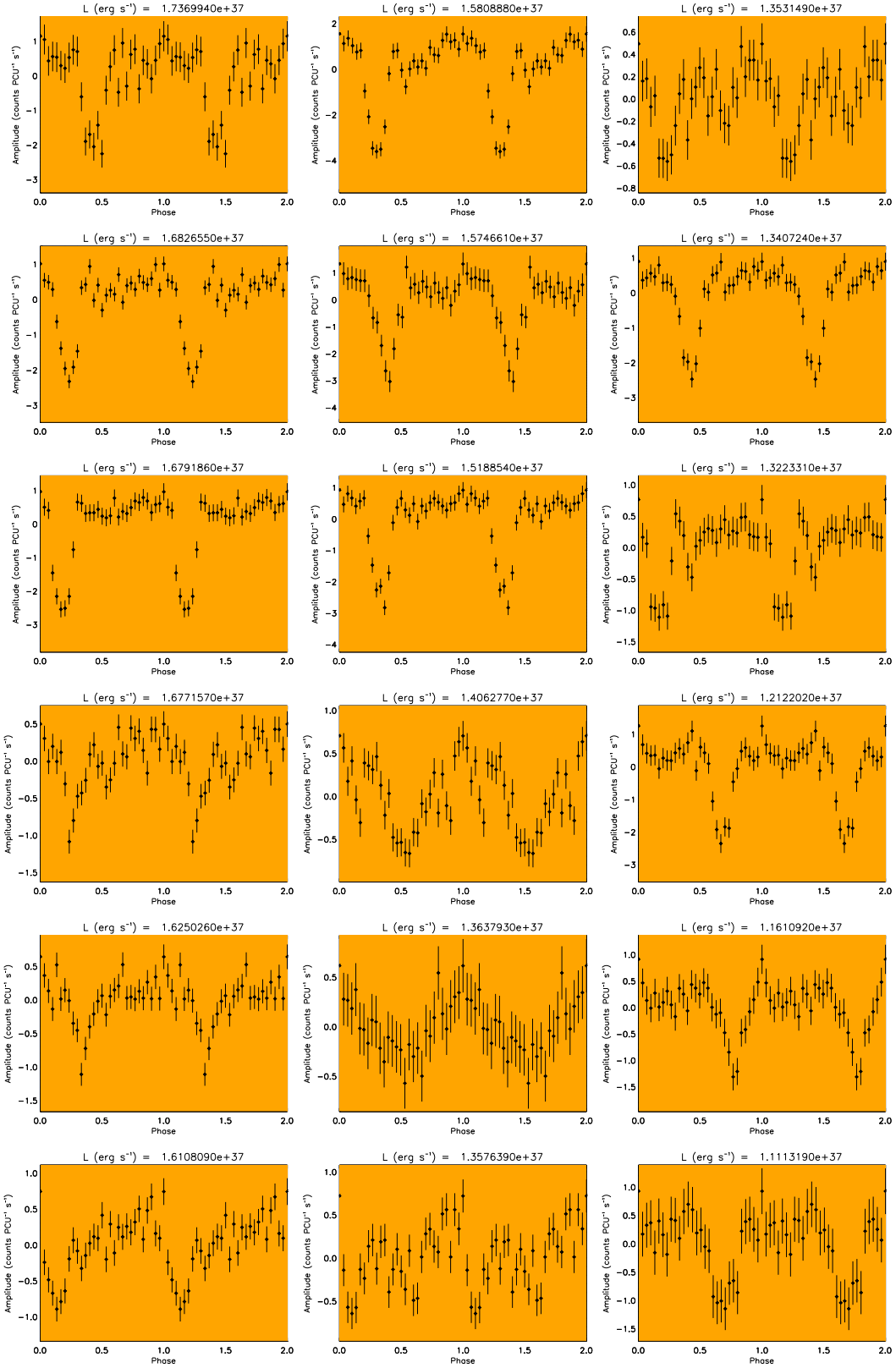
L (erg s⁻¹) = 1.7369940e+37
L (erg s⁻¹) = 1.5808880e+37
L (erg s⁻¹) = 1.3531490e+37
L (erg s⁻¹) = 1.6826550e+37
L (erg s⁻¹) = 1.5746610e+37
L (erg s⁻¹) = 1.3407240e+37
L (erg s⁻¹) = 1.6791860e+37
L (erg s⁻¹) = 1.5188540e+37
L (erg s⁻¹) = 1.3223310e+37
L (erg s⁻¹) = 1.6771570e+37
L (erg s⁻¹) = 1.4062770e+37
L (erg s⁻¹) = 1.2122020e+37
L (erg s⁻¹) = 1.6250260e+37
L (erg s⁻¹) = 1.3637930e+37
L (erg s⁻¹) = 1.1610920e+37
L (erg s⁻¹) = 1.6108090e+37
L (erg s⁻¹) = 1.3576390e+37
L (erg s⁻¹) = 1.1113190e+37
Amplitude (counts PCU⁻¹ s⁻¹)
Phase

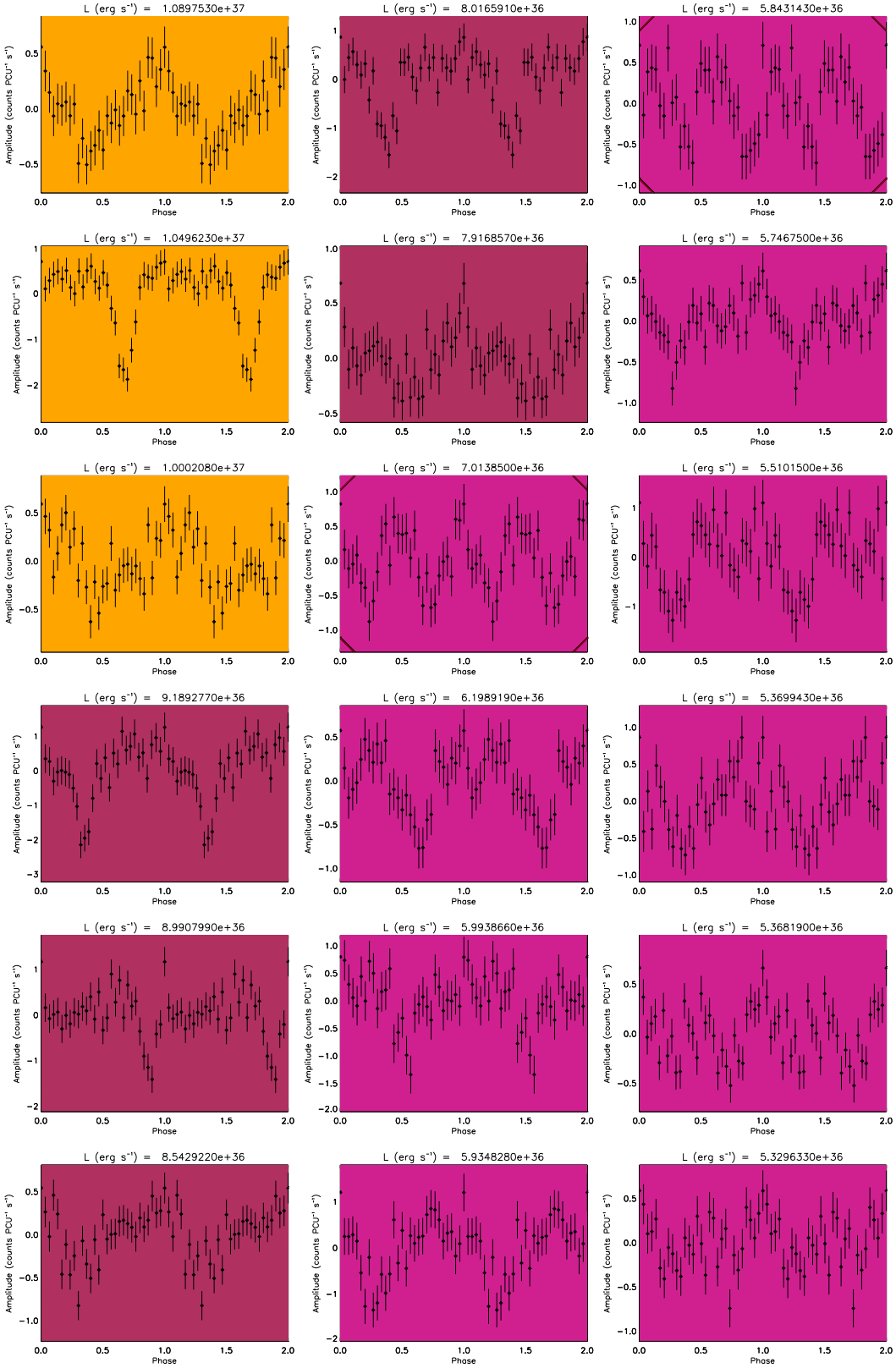
L (erg s⁻¹) = 1.0897530e+37
L (erg s⁻¹) = 8.0165910e+36
L (erg s⁻¹) = 5.8431430e+36
L (erg s⁻¹) = 1.0496230e+37
L (erg s⁻¹) = 7.9168570e+36
L (erg s⁻¹) = 5.7467500e+36
L (erg s⁻¹) = 1.0002080e+37
L (erg s⁻¹) = 7.0138500e+36
L (erg s⁻¹) = 5.5101500e+36
L (erg s⁻¹) = 9.1892770e+36
L (erg s⁻¹) = 6.1989190e+36
L (erg s⁻¹) = 5.3699430e+36
L (erg s⁻¹) = 8.9907990e+36
L (erg s⁻¹) = 5.9938660e+36
L (erg s⁻¹) = 5.3681900e+36
L (erg s⁻¹) = 8.5429220e+36
L (erg s⁻¹) = 5.9348280e+36
L (erg s⁻¹) = 5.3296330e+36
Amplitude (counts PCU⁻¹ s⁻¹)
Phase

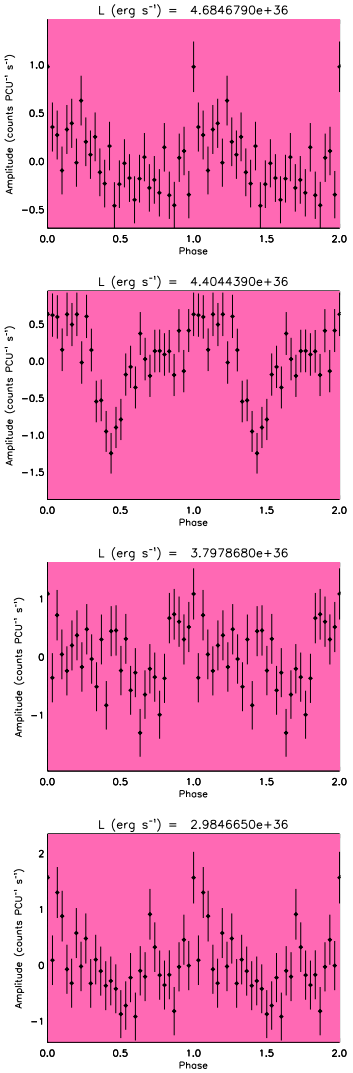

Figure C.16: Pulse-profiles for SXP91.1, in order of decreasing L (from top to bottom, left to right). The colour-coding is explained in Figure C.1.

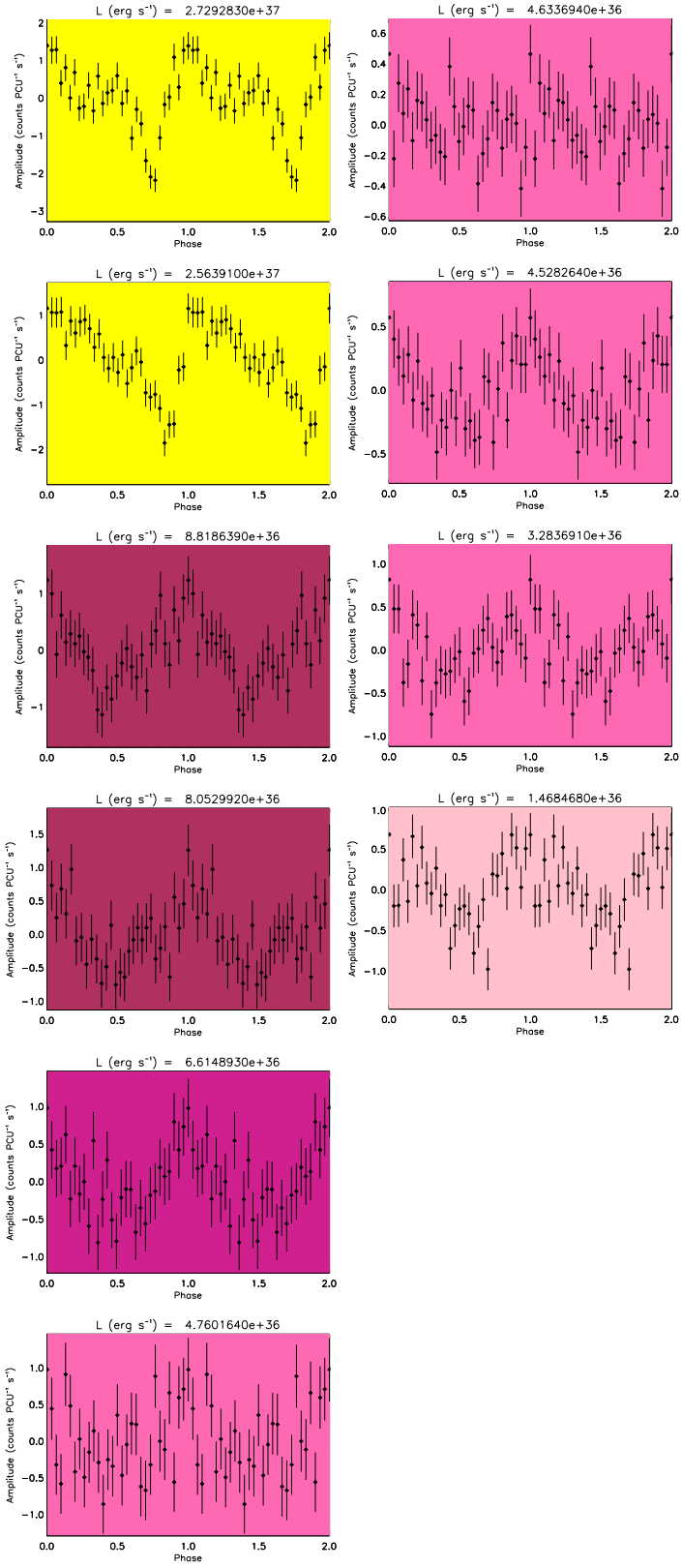

Figure C.17: Pulse-profiles for SXP95.2, in order of decreasing L (from top to bottom, left to right). The colour-coding is explained in Figure C.1.

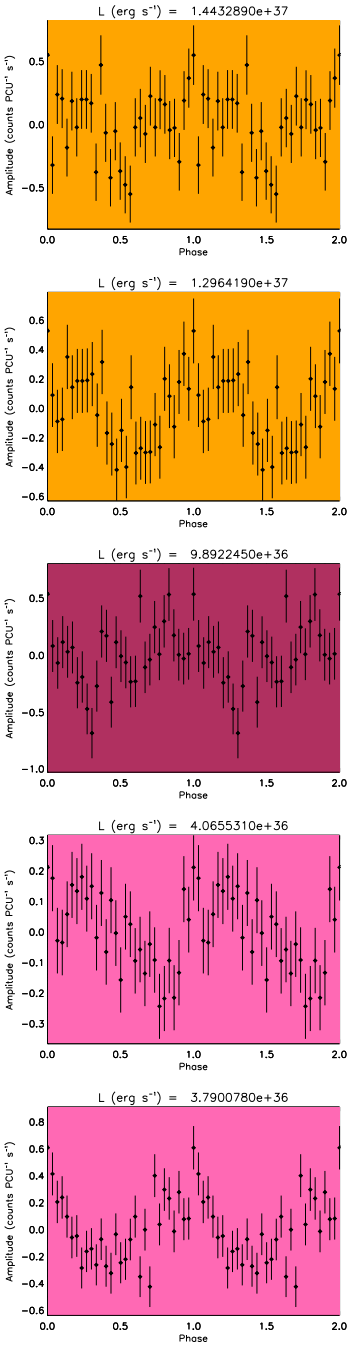

Figure C.18: Pulse-profiles for SXP101, in order of decreasing L (from top to bottom, left to right). The colour-coding is explained in Figure C.1.

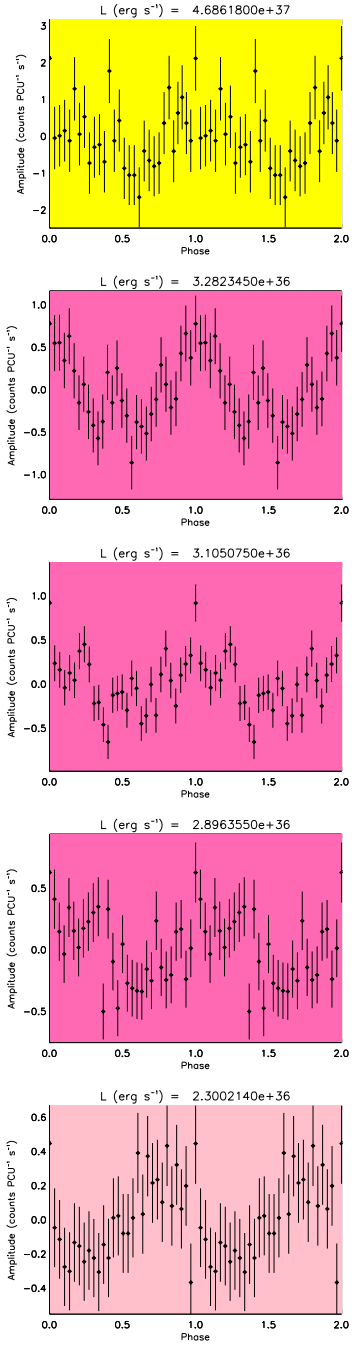

Figure C.19: Pulse-profiles for SXP140, in order of decreasing L (from top to bottom, left to right). The colour-coding is explained in Figure C.1.

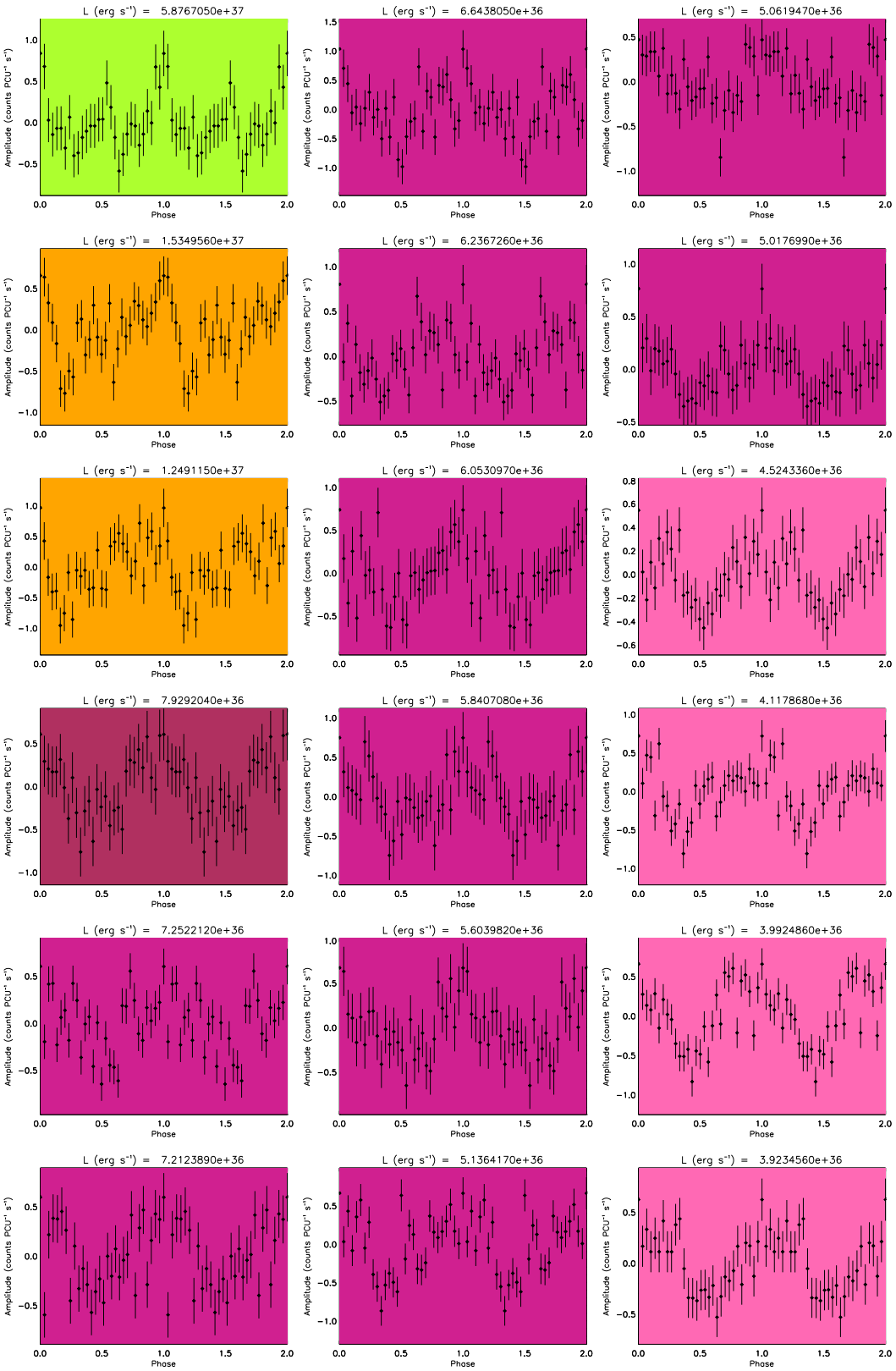
L (erg s⁻¹) = 5.8767050e+37
L (erg s⁻¹) = 6.6438050e+36
L (erg s⁻¹) = 5.0619470e+36
L (erg s⁻¹) = 1.5349560e+37
L (erg s⁻¹) = 6.2367260e+36
L (erg s⁻¹) = 5.0176990e+36
L (erg s⁻¹) = 1.2491150e+37
L (erg s⁻¹) = 6.0530970e+36
L (erg s⁻¹) = 4.5243360e+36
L (erg s⁻¹) = 7.9292040e+36
L (erg s⁻¹) = 5.8407080e+36
L (erg s⁻¹) = 4.1178680e+36
L (erg s⁻¹) = 7.2522120e+36
L (erg s⁻¹) = 5.6039820e+36
L (erg s⁻¹) = 3.9924860e+36
L (erg s⁻¹) = 7.2123890e+36
L (erg s⁻¹) = 5.1364170e+36
L (erg s⁻¹) = 3.9234560e+36
Amplitude (counts PCU⁻¹ s⁻¹)
Phase

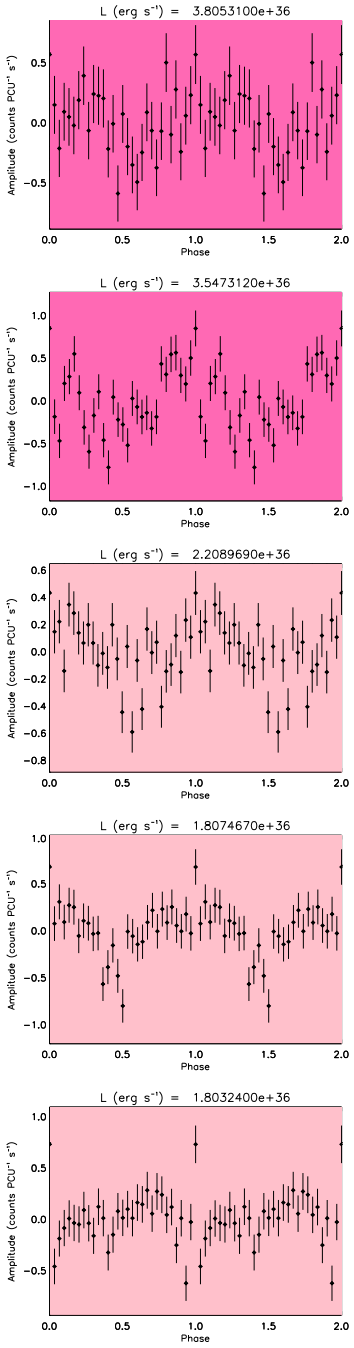

Figure C.20: Pulse-profiles for SXP152, in order of decreasing L (from top to bottom, left to right). The colour-coding is explained in Figure C.1.

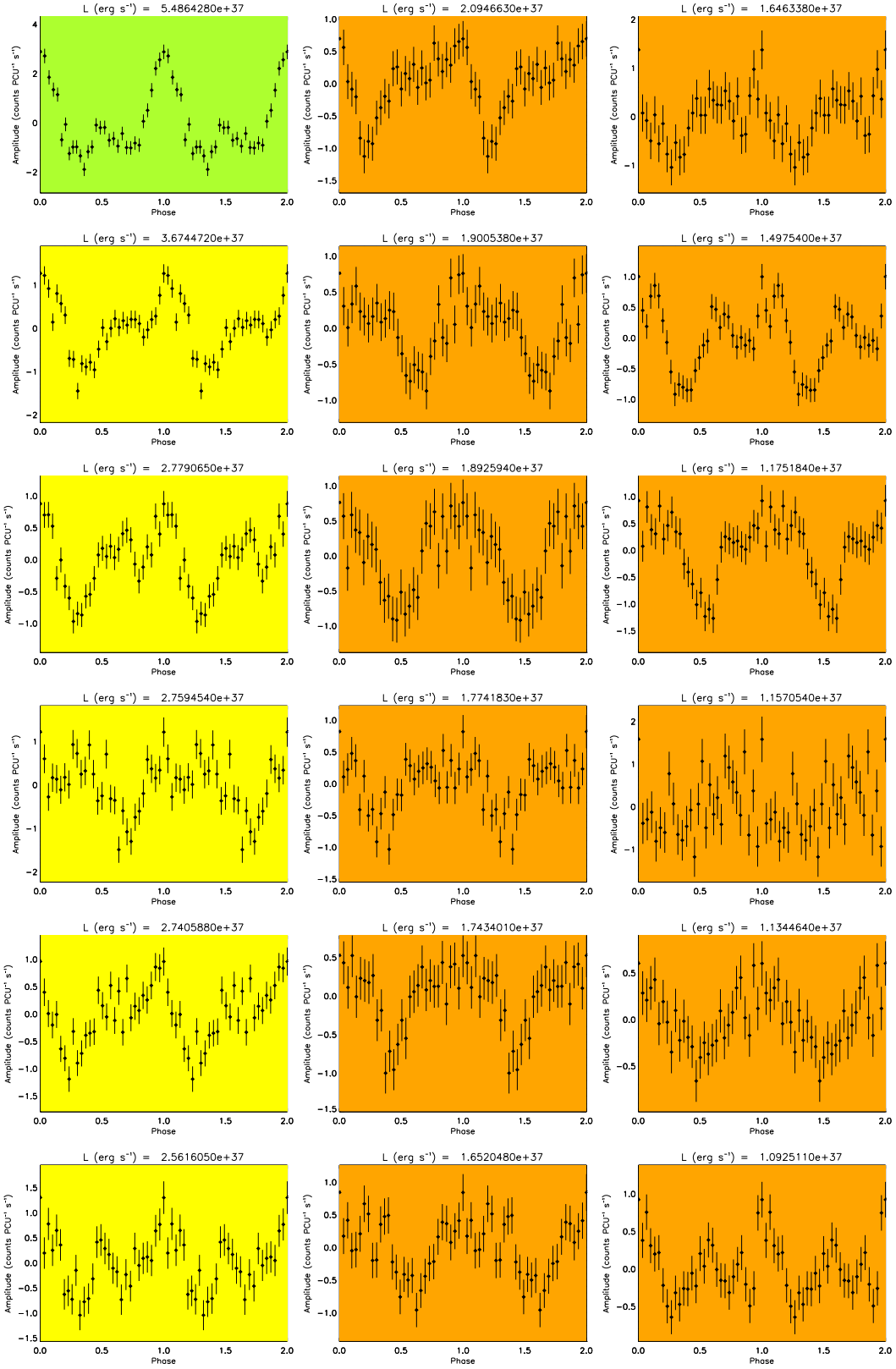
L (erg s⁻¹) = 5.4864280e+37
L (erg s⁻¹) = 2.0946630e+37
L (erg s⁻¹) = 1.6463380e+37
L (erg s⁻¹) = 3.6744720e+37
L (erg s⁻¹) = 1.9005380e+37
L (erg s⁻¹) = 1.4975400e+37
L (erg s⁻¹) = 2.7790650e+37
L (erg s⁻¹) = 1.8925940e+37
L (erg s⁻¹) = 1.1751840e+37
L (erg s⁻¹) = 2.7594540e+37
L (erg s⁻¹) = 1.7741830e+37
L (erg s⁻¹) = 1.1570540e+37
L (erg s⁻¹) = 2.7405880e+37
L (erg s⁻¹) = 1.7434010e+37
L (erg s⁻¹) = 1.1344640e+37
L (erg s⁻¹) = 2.5616050e+37
L (erg s⁻¹) = 1.6520480e+37
L (erg s⁻¹) = 1.0925110e+37
Amplitude (counts PCU⁻¹ s⁻¹)
Phase

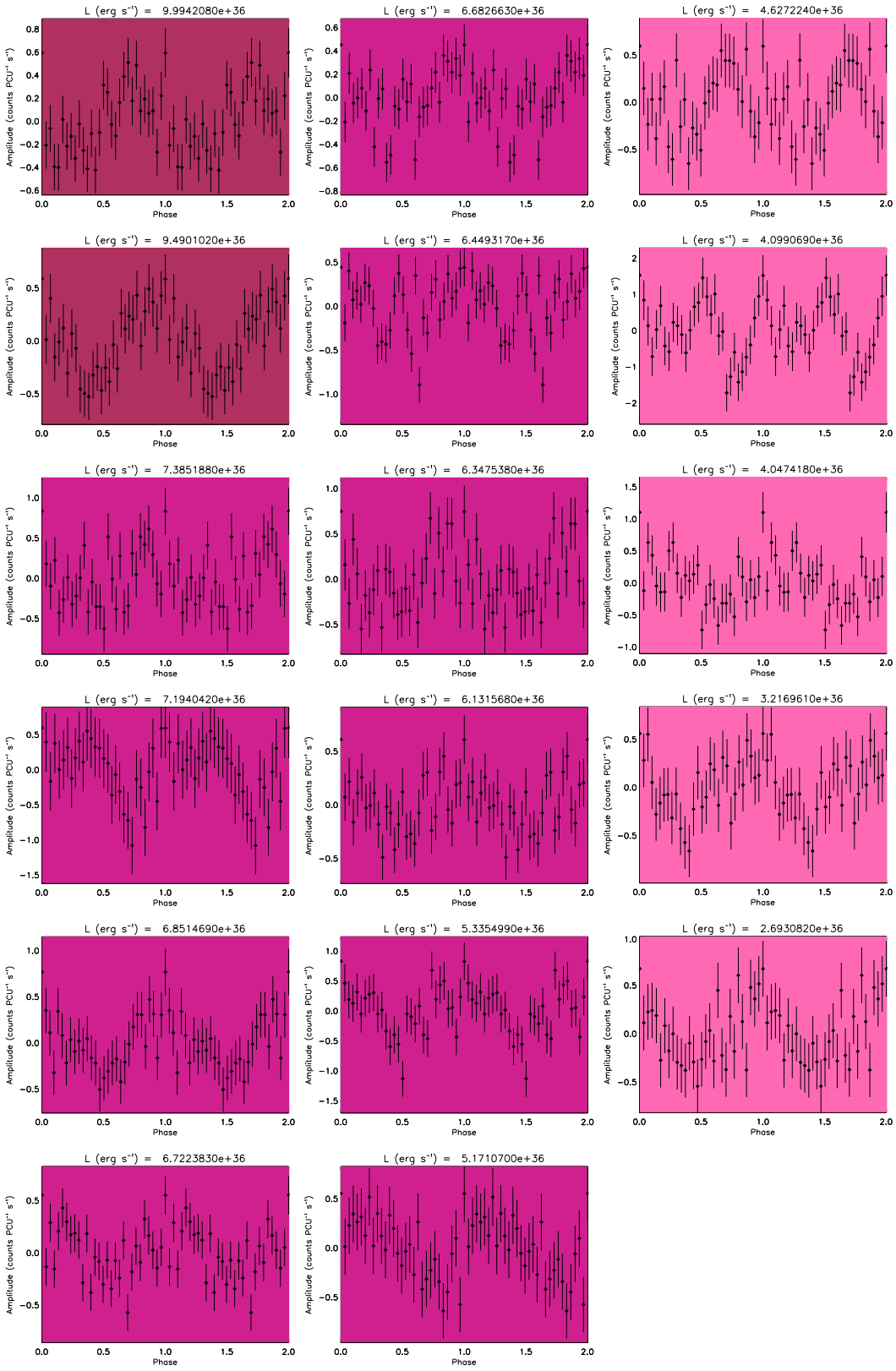

Figure C.21: Pulse-profiles for SXP169, in order of decreasing L (from top to bottom, left to right). The colour-coding is explained in Figure C.1.

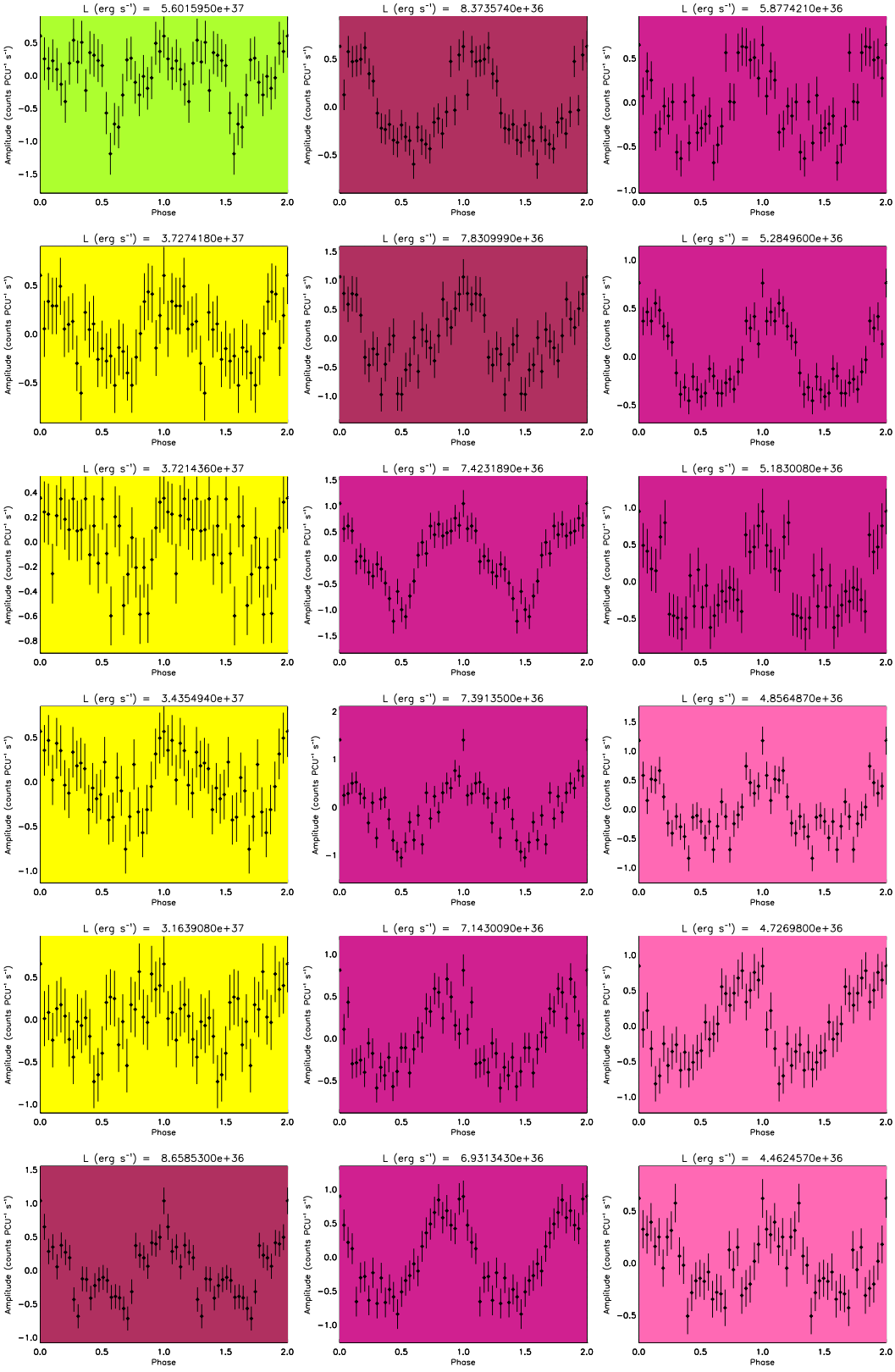
L (erg s⁻¹) = 5.6015950e+37
L (erg s⁻¹) = 8.3735740e+36
L (erg s⁻¹) = 5.8774210e+36
L (erg s⁻¹) = 3.7274180e+37
L (erg s⁻¹) = 7.8309990e+36
L (erg s⁻¹) = 5.2849600e+36
L (erg s⁻¹) = 3.7214360e+37
L (erg s⁻¹) = 7.4231890e+36
L (erg s⁻¹) = 5.1830080e+36
L (erg s⁻¹) = 3.4354940e+37
L (erg s⁻¹) = 7.3913500e+36
L (erg s⁻¹) = 4.8564870e+36
L (erg s⁻¹) = 3.1639080e+37
L (erg s⁻¹) = 7.1430090e+36
L (erg s⁻¹) = 4.7269800e+36
L (erg s⁻¹) = 8.6585300e+36
L (erg s⁻¹) = 6.9313430e+36
L (erg s⁻¹) = 4.4624570e+36
Amplitude (counts PCU⁻¹ s⁻¹)
Phase

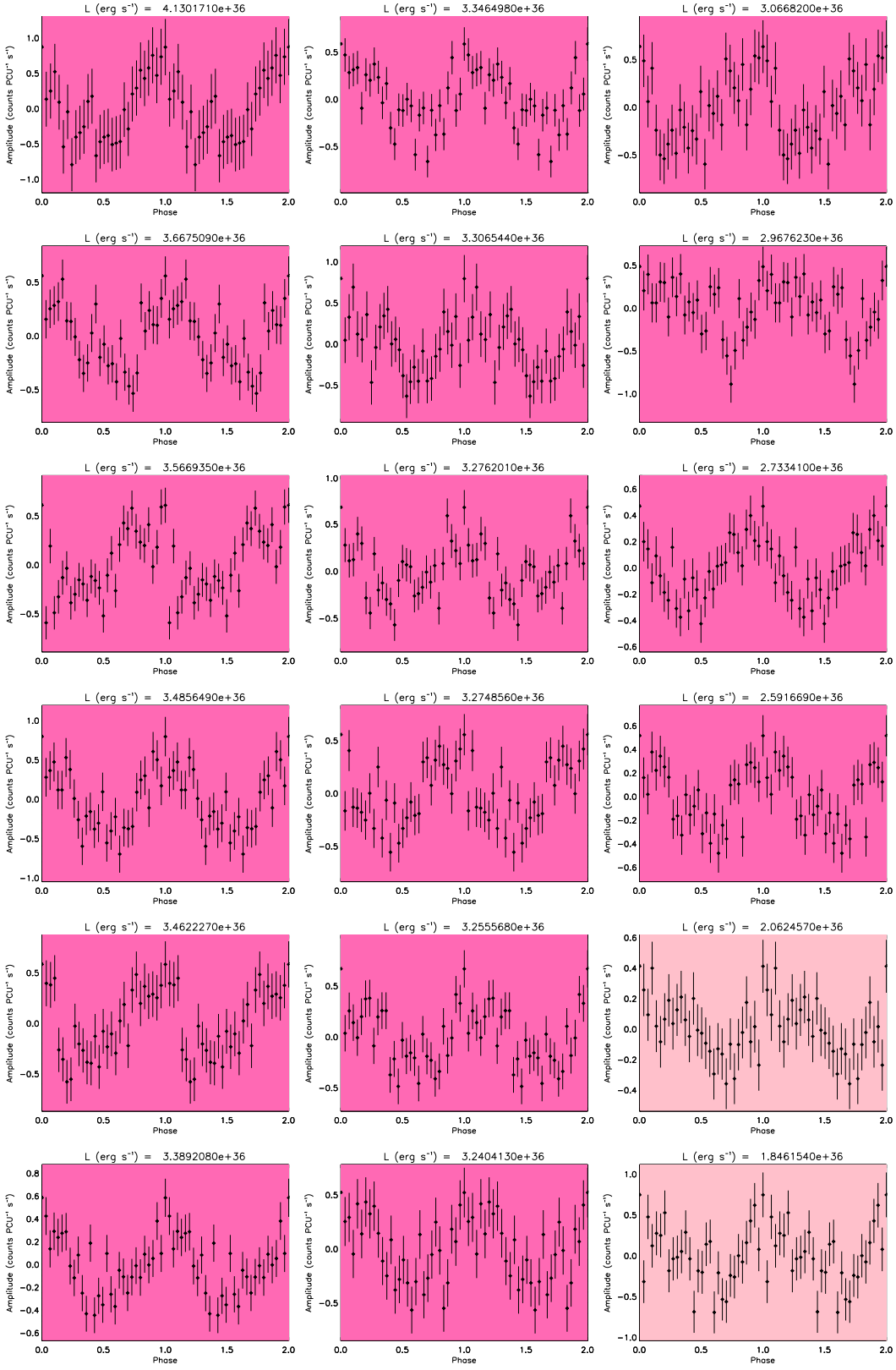
L (erg s⁻¹) = 4.1301710e+36
L (erg s⁻¹) = 3.3464980e+36
L (erg s⁻¹) = 3.0668200e+36
L (erg s⁻¹) = 3.6675090e+36
L (erg s⁻¹) = 3.3065440e+36
L (erg s⁻¹) = 2.9676230e+36
L (erg s⁻¹) = 3.5669350e+36
L (erg s⁻¹) = 3.2762010e+36
L (erg s⁻¹) = 2.7334100e+36
L (erg s⁻¹) = 3.4856490e+36
L (erg s⁻¹) = 3.2748560e+36
L (erg s⁻¹) = 2.5916690e+36
L (erg s⁻¹) = 3.4622270e+36
L (erg s⁻¹) = 3.2555680e+36
L (erg s⁻¹) = 2.0624570e+36
L (erg s⁻¹) = 3.3892080e+36
L (erg s⁻¹) = 3.2404130e+36
L (erg s⁻¹) = 1.8461540e+36
Amplitude (counts PCU⁻¹ s⁻¹)
Phase

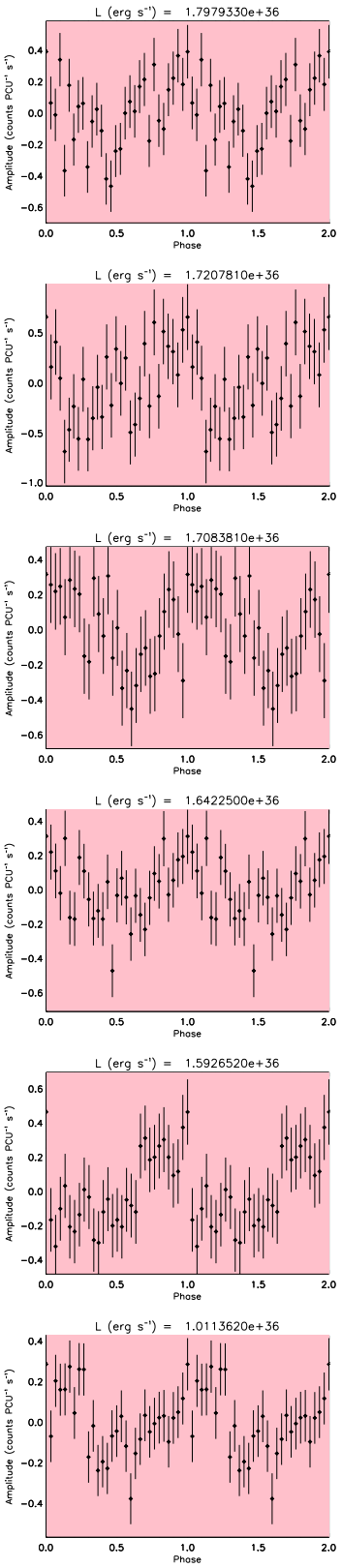

Figure C.22: Pulse-profiles for SXP172, in order of decreasing L (from top to bottom, left to right). The colour-coding is explained in Figure C.1.

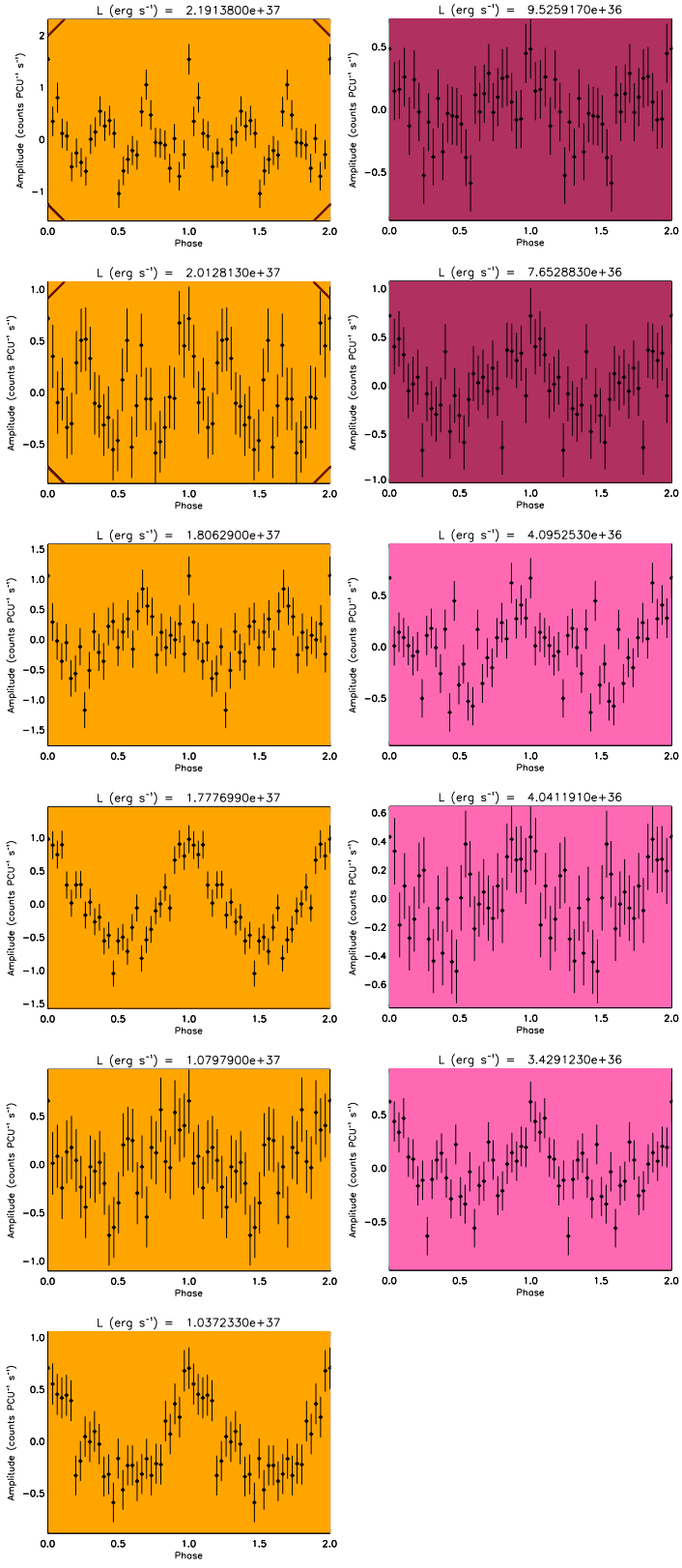

Figure C.23: Pulse-profiles for SXP175, in order of decreasing L (from top to bottom, left to right). The colour-coding is explained in Figure C.1.

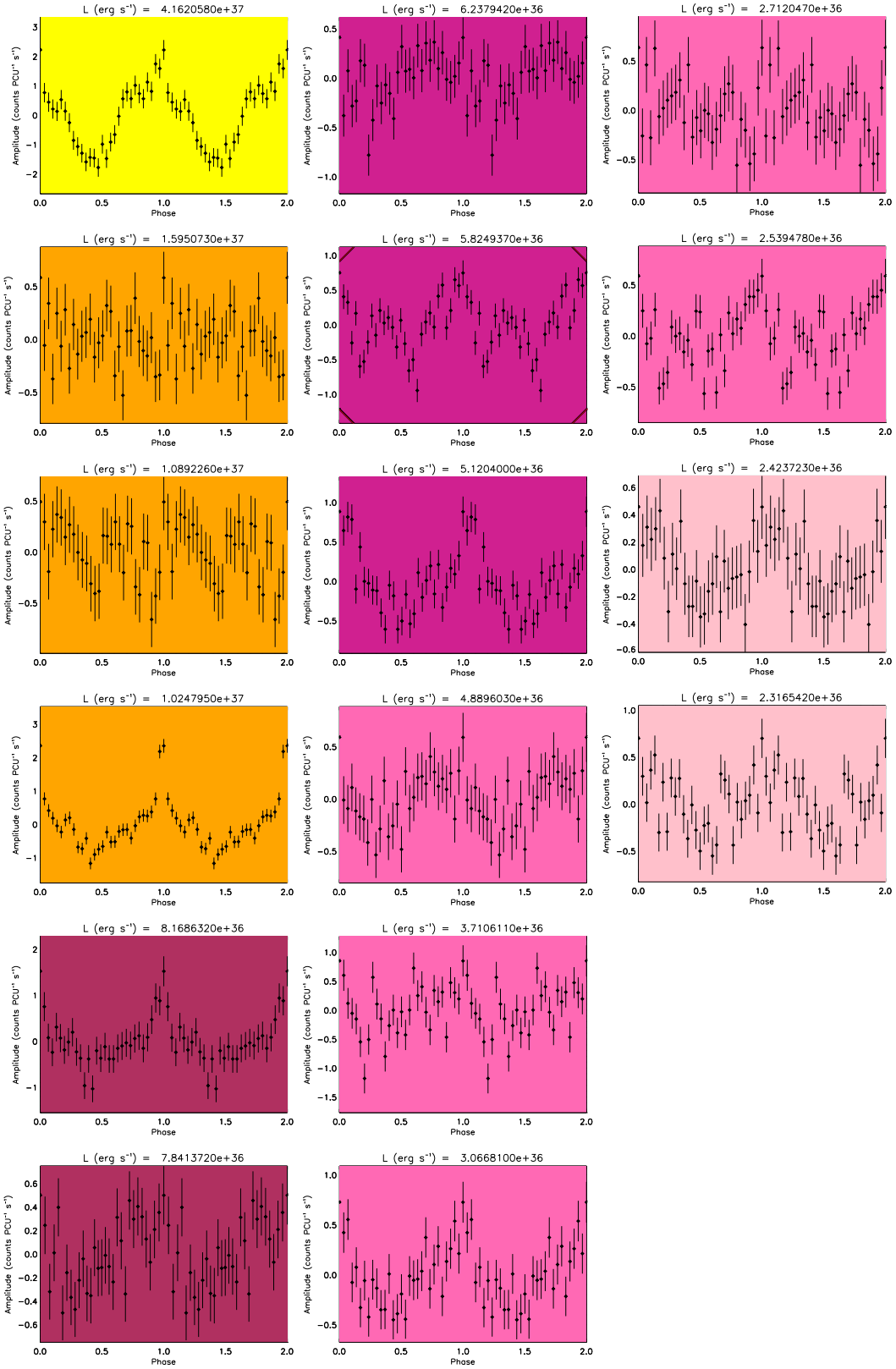

Figure C.24: Pulse-profiles for SXP202A, in order of decreasing L (from top to bottom, left to right). The colour-coding is explained in Figure C.1.

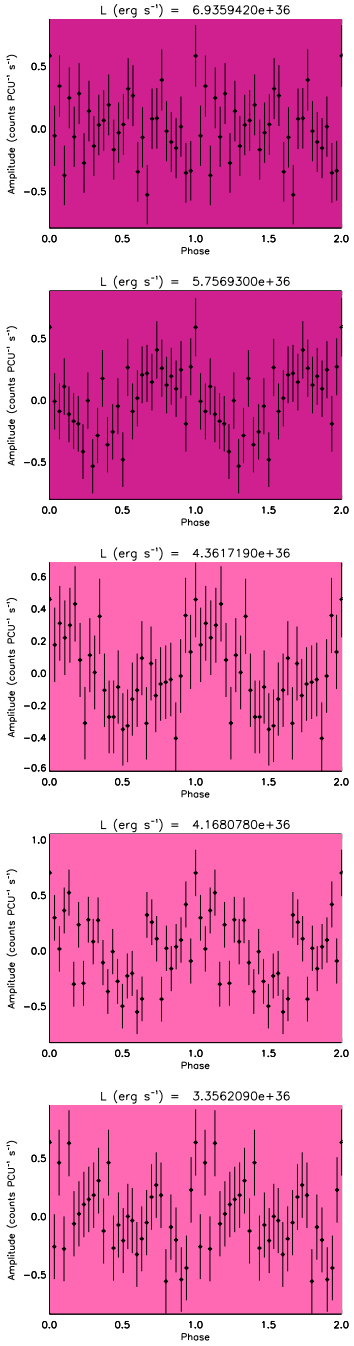

Figure C.25: Pulse-profiles for SXP202B, in order of decreasing L (from top to bottom, left to right). The colour-coding is explained in Figure C.1.

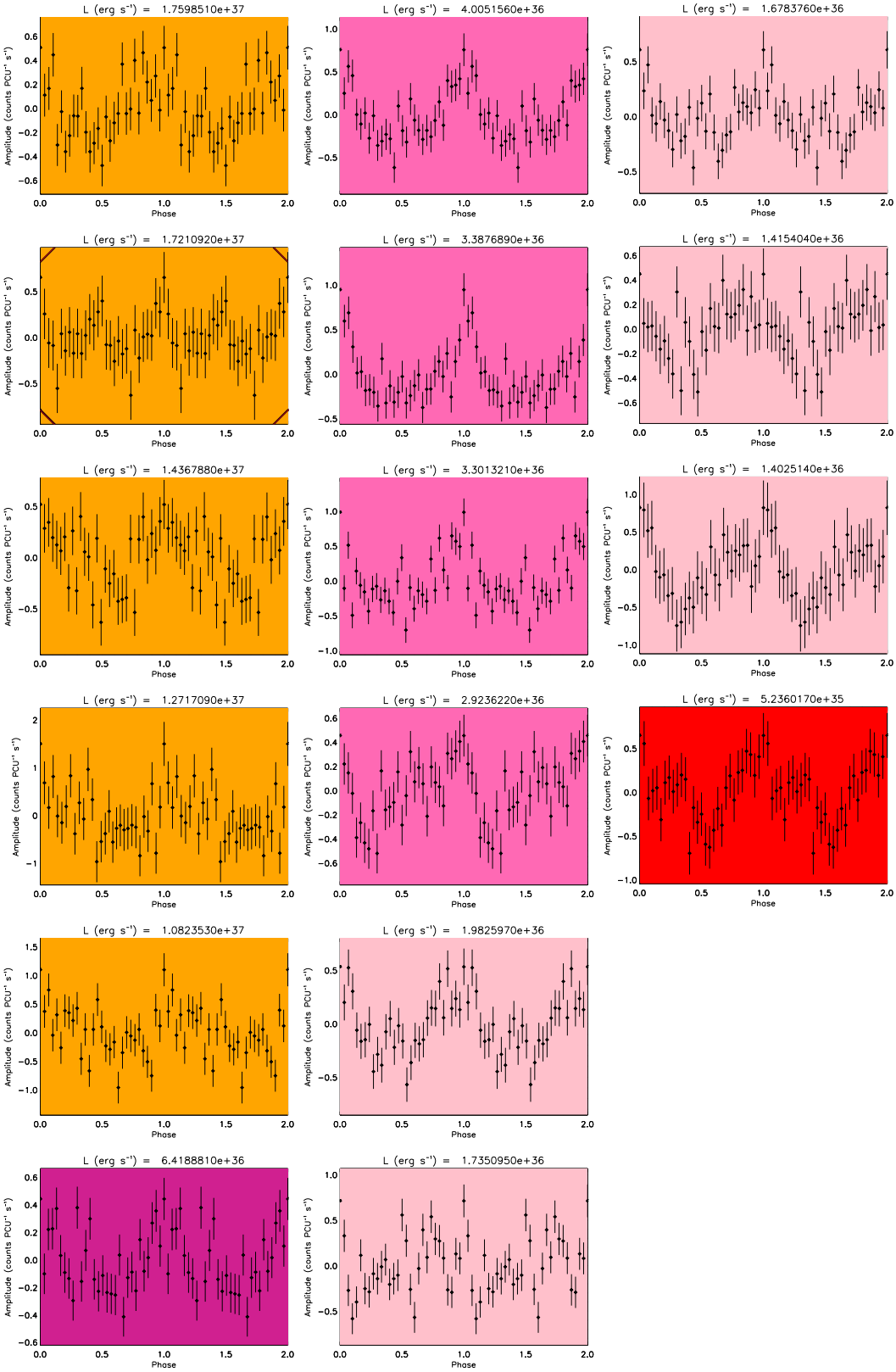

Figure C.26: Pulse-profiles for SXP214, in order of decreasing L (from top to bottom, left to right). The colour-coding is explained in Figure C.1.

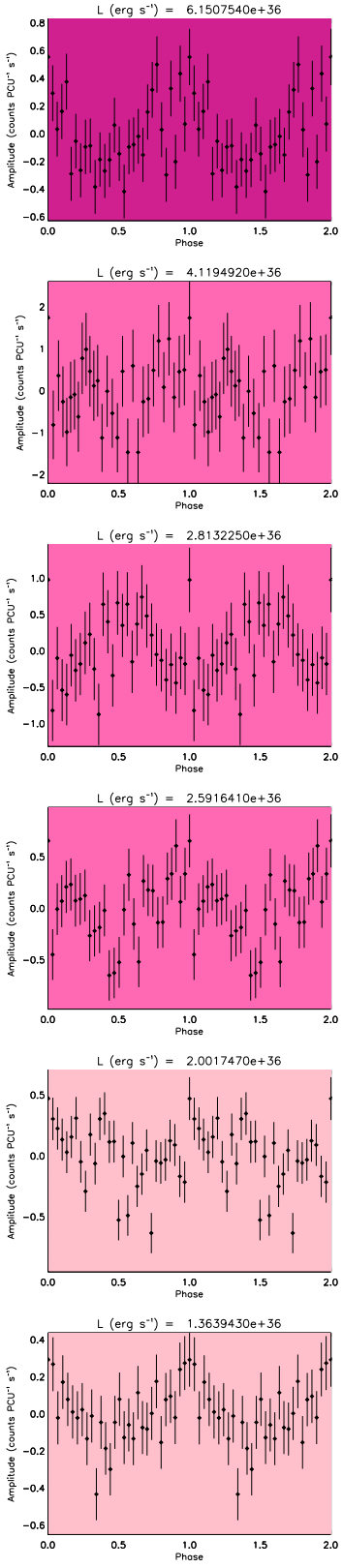

Figure C.27: Pulse-profiles for SXP264, in order of decreasing L (from top to bottom, left to right). The colour-coding is explained in Figure C.1.

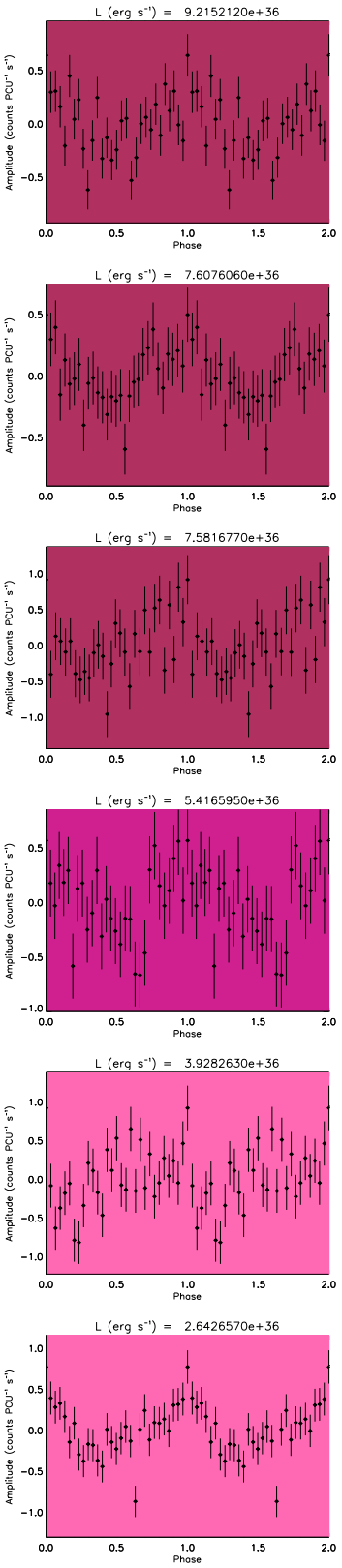

Figure C.28: Pulse-profiles for SXP280, in order of decreasing L (from top to bottom, left to right). The colour-coding is explained in Figure C.1.

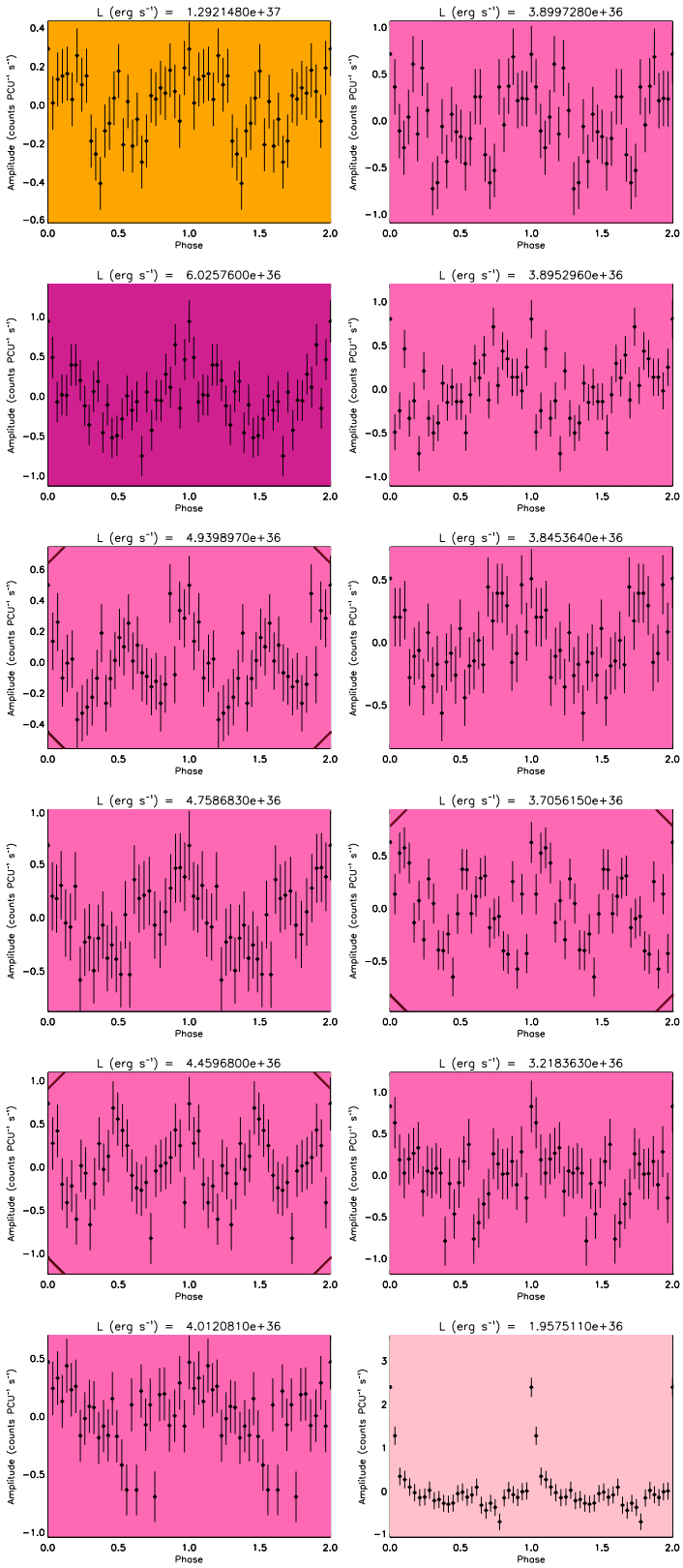

Figure C.29: Pulse-profiles for SXP293, in order of decreasing L (from top to bottom, left to right). The colour-coding is explained in Figure C.1.

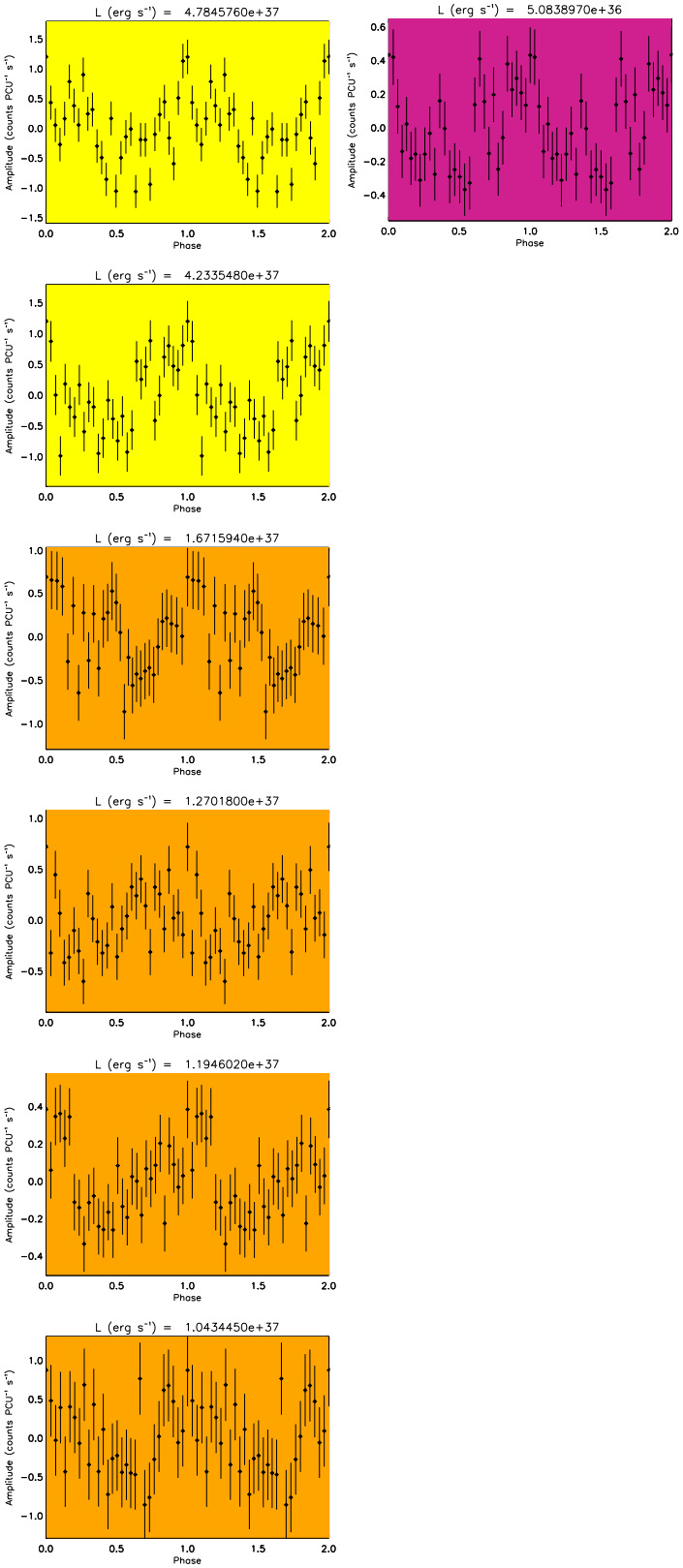

Figure C.30: Pulse-profiles for SXP304, in order of decreasing L (from top to bottom, left to right). The colour-coding is explained in Figure C.1.

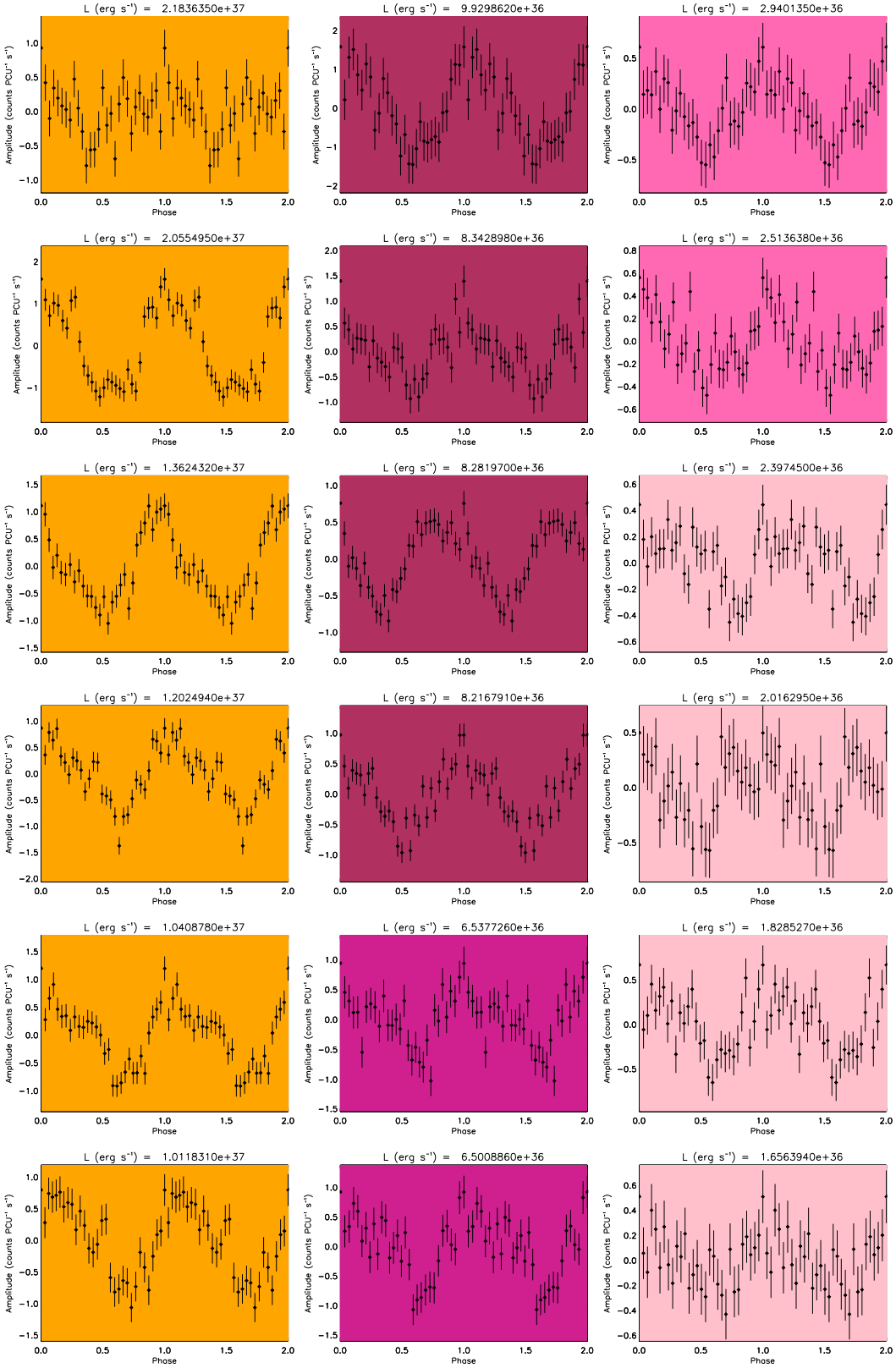
L (erg s⁻¹) = 2.1836350e+37
L (erg s⁻¹) = 9.9298620e+36
L (erg s⁻¹) = 2.9401350e+36
L (erg s⁻¹) = 2.0554950e+37
L (erg s⁻¹) = 8.3428980e+36
L (erg s⁻¹) = 2.5136380e+36
L (erg s⁻¹) = 1.3624320e+37
L (erg s⁻¹) = 8.2819700e+36
L (erg s⁻¹) = 2.3974500e+36
L (erg s⁻¹) = 1.2024940e+37
L (erg s⁻¹) = 8.2167910e+36
L (erg s⁻¹) = 2.0162950e+36
L (erg s⁻¹) = 1.0408780e+37
L (erg s⁻¹) = 6.5377260e+36
L (erg s⁻¹) = 1.8285270e+36
L (erg s⁻¹) = 1.0118310e+37
L (erg s⁻¹) = 6.5008860e+36
L (erg s⁻¹) = 1.6563940e+36
Amplitude (counts PCU⁻¹ s⁻¹)
Phase

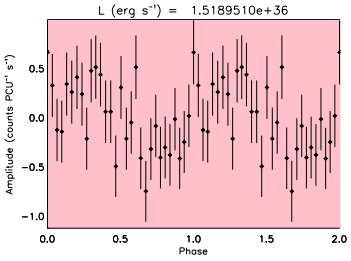

Figure C.31: Pulse-profiles for SXP323, in order of decreasing L (from top to bottom, left to right). The colour-coding is explained in Figure C.1.

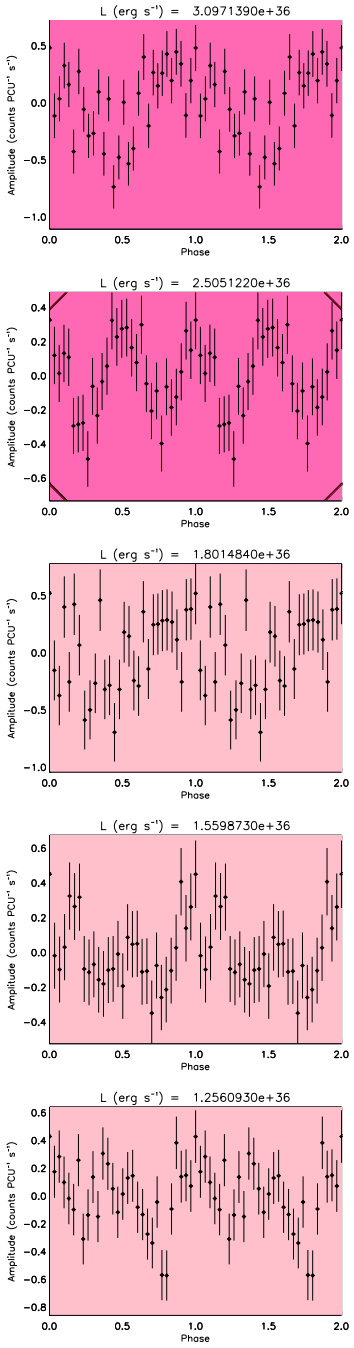

Figure C.32: Pulse-profiles for SXP327, in order of decreasing L (from top to bottom, left to right). The colour-coding is explained in Figure C.1.

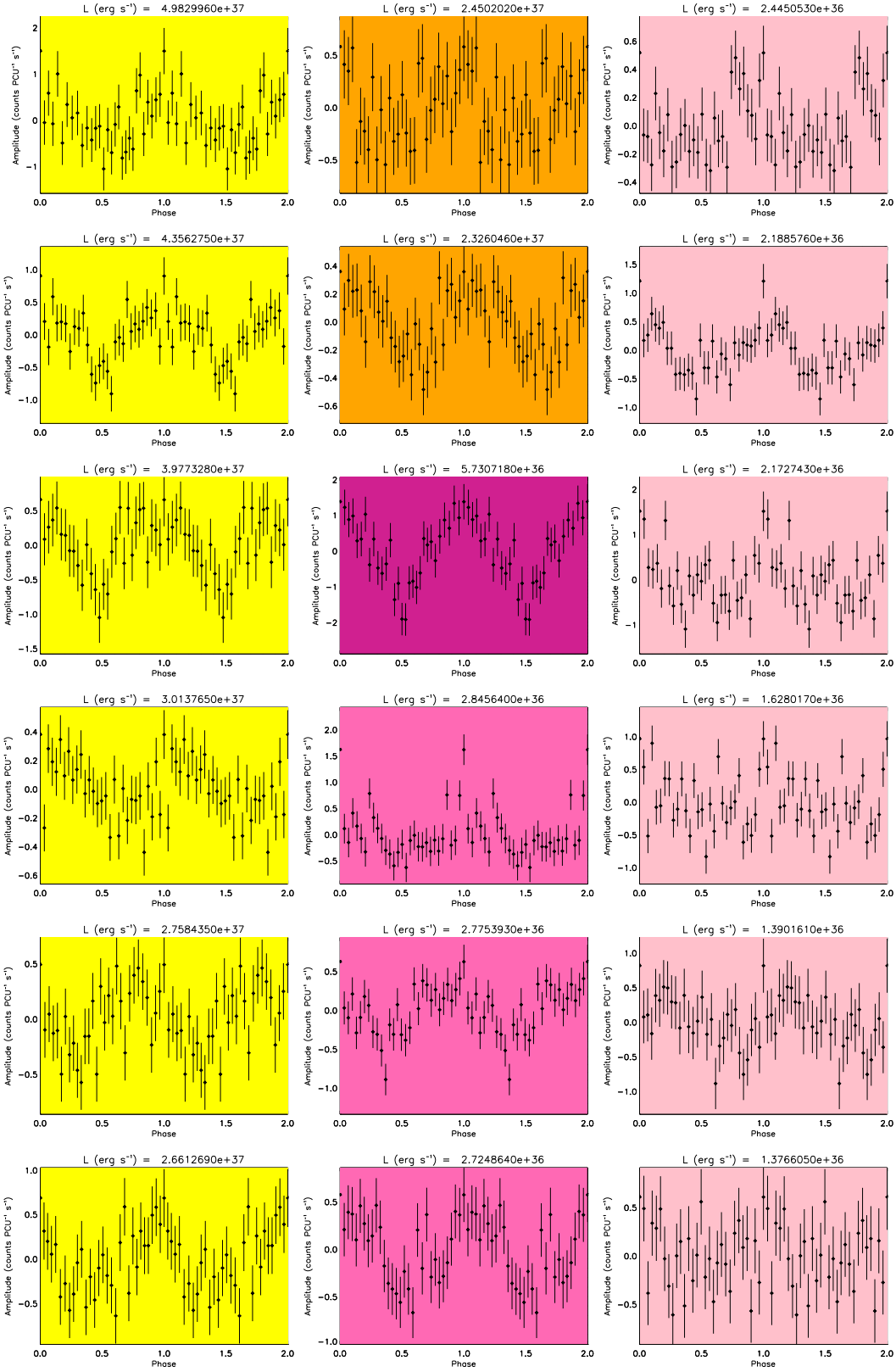
L (erg s⁻¹) = 4.9829960e+37
L (erg s⁻¹) = 2.4502020e+37
L (erg s⁻¹) = 2.4450530e+36
L (erg s⁻¹) = 4.3562750e+37
L (erg s⁻¹) = 2.3260460e+37
L (erg s⁻¹) = 2.1885760e+36
L (erg s⁻¹) = 3.9773280e+37
L (erg s⁻¹) = 5.7307180e+36
L (erg s⁻¹) = 2.1727430e+36
L (erg s⁻¹) = 3.0137650e+37
L (erg s⁻¹) = 2.8456400e+36
L (erg s⁻¹) = 1.6280170e+36
L (erg s⁻¹) = 2.7584350e+37
L (erg s⁻¹) = 2.7753930e+36
L (erg s⁻¹) = 1.3901610e+36
L (erg s⁻¹) = 2.6612690e+37
L (erg s⁻¹) = 2.7248640e+36
L (erg s⁻¹) = 1.3766050e+36
Amplitude (counts PCU⁻¹ s⁻¹)
Phase

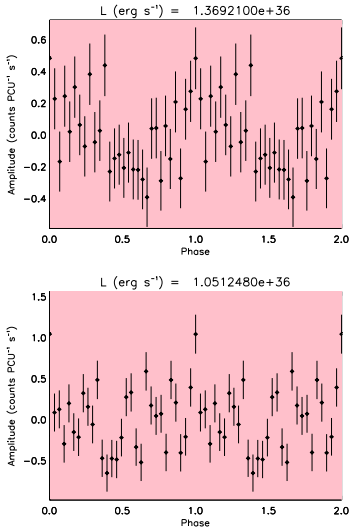

Figure C.33: Pulse-profiles for SXP342, in order of decreasing L (from top to bottom, left to right). The colour-coding is explained in Figure C.1.

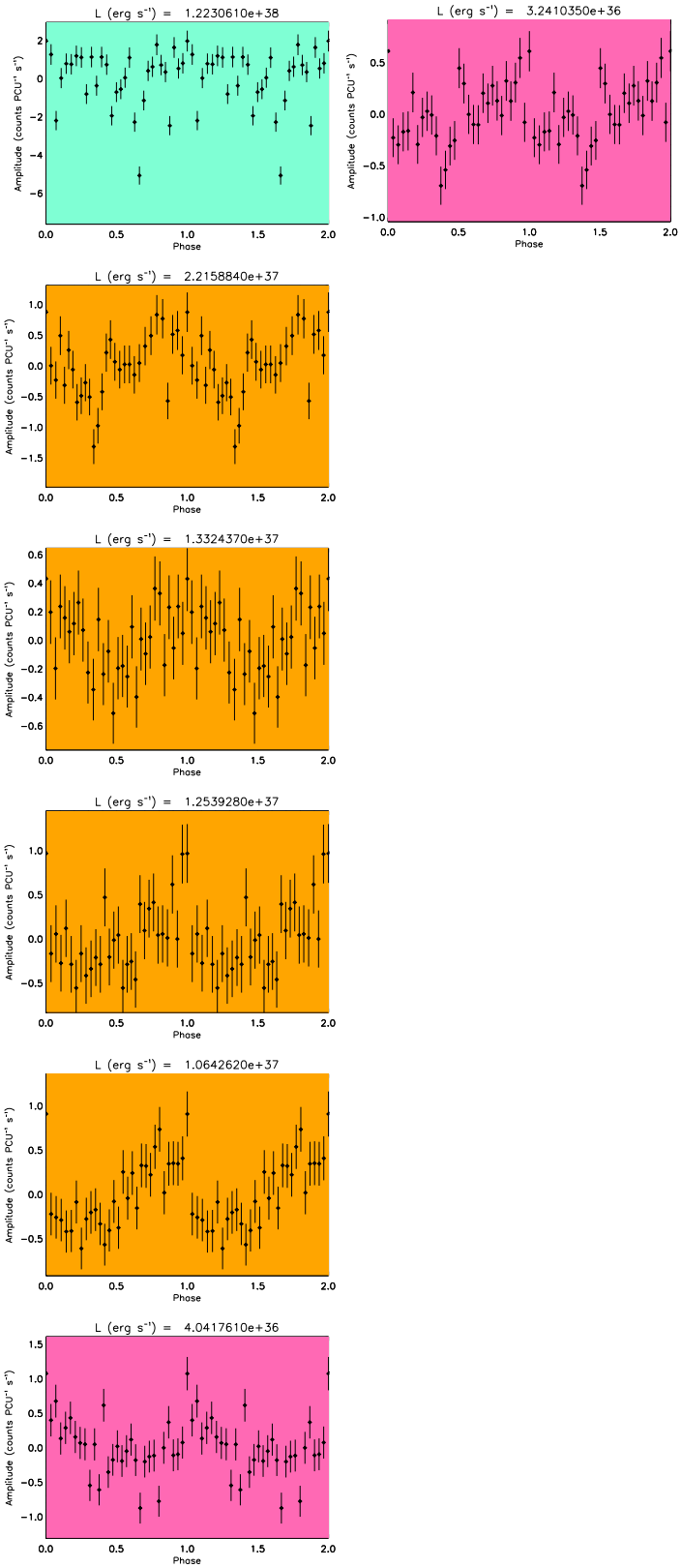

Figure C.34: Pulse-profiles for SXP455, in order of decreasing L (from top to bottom, left to right). The colour-coding is explained in Figure C.1.

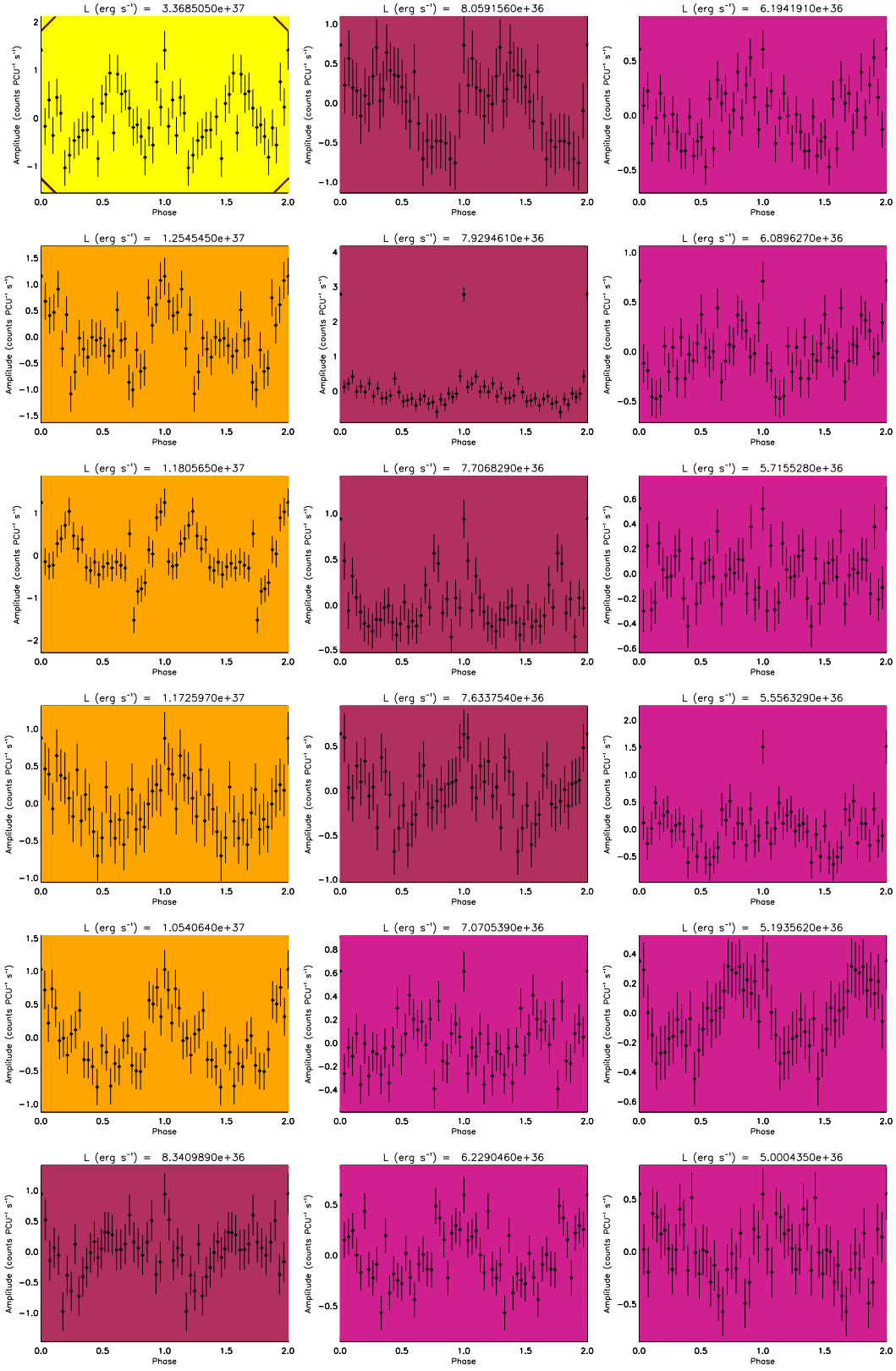
L (erg s⁻¹) = 3.3685050e+37
L (erg s⁻¹) = 8.0591560e+36
L (erg s⁻¹) = 6.1941910e+36
L (erg s⁻¹) = 1.2545450e+37
L (erg s⁻¹) = 7.9294610e+36
L (erg s⁻¹) = 6.0896270e+36
L (erg s⁻¹) = 1.1805650e+37
L (erg s⁻¹) = 7.7068290e+36
L (erg s⁻¹) = 5.7155280e+36
L (erg s⁻¹) = 1.1725970e+37
L (erg s⁻¹) = 7.6337540e+36
L (erg s⁻¹) = 5.5563290e+36
L (erg s⁻¹) = 1.0540640e+37
L (erg s⁻¹) = 7.0705390e+36
L (erg s⁻¹) = 5.1935620e+36
L (erg s⁻¹) = 8.3409890e+36
L (erg s⁻¹) = 6.2290460e+36
L (erg s⁻¹) = 5.0004350e+36
Amplitude (counts PCU⁻¹ s⁻¹)
Phase

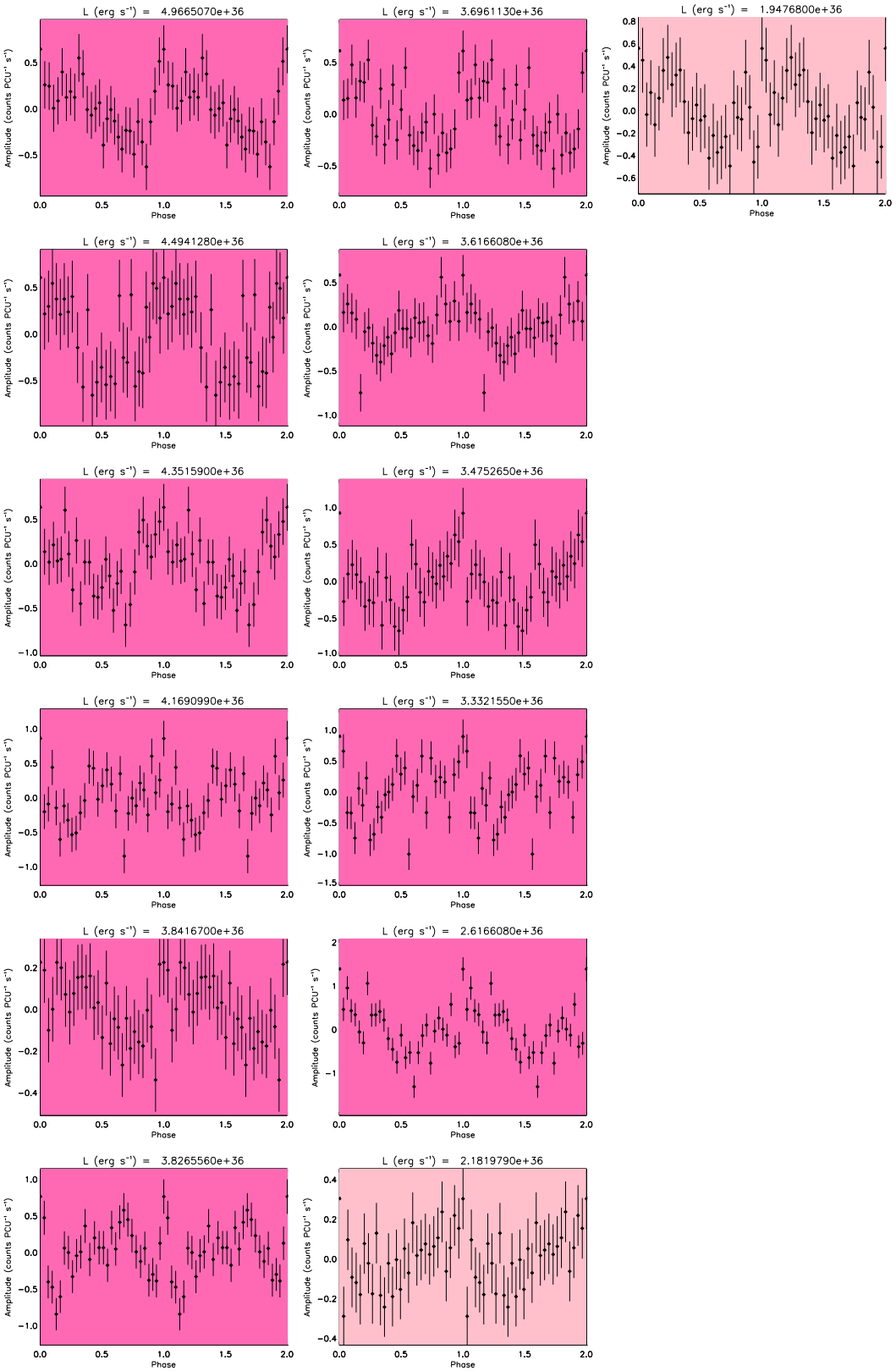

Figure C.35: Pulse-profiles for SXP504, in order of decreasing L (from top to bottom, left to right). The colour-coding is explained in Figure C.1.

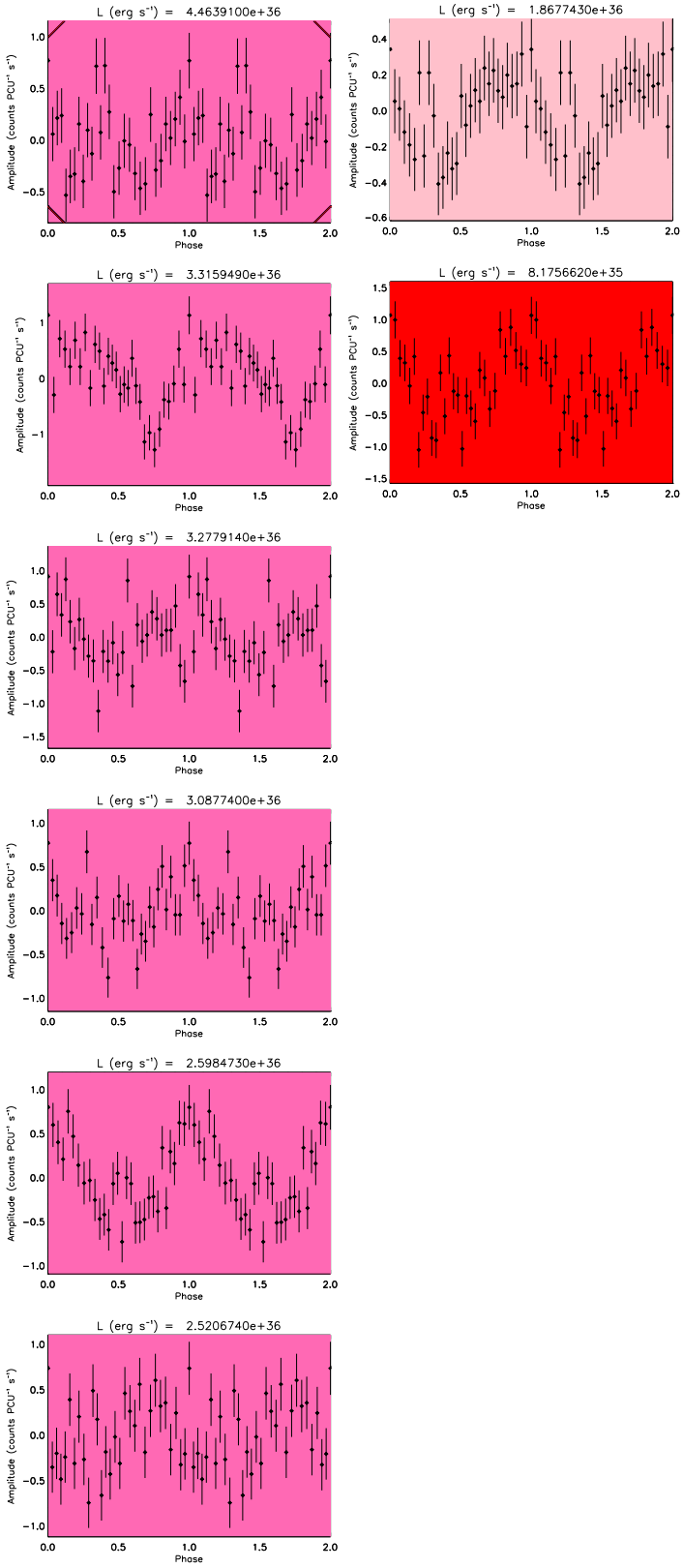

Figure C.36: Pulse-profiles for SXP565, in order of decreasing L (from top to bottom, left to right). The colour-coding is explained in Figure C.1.

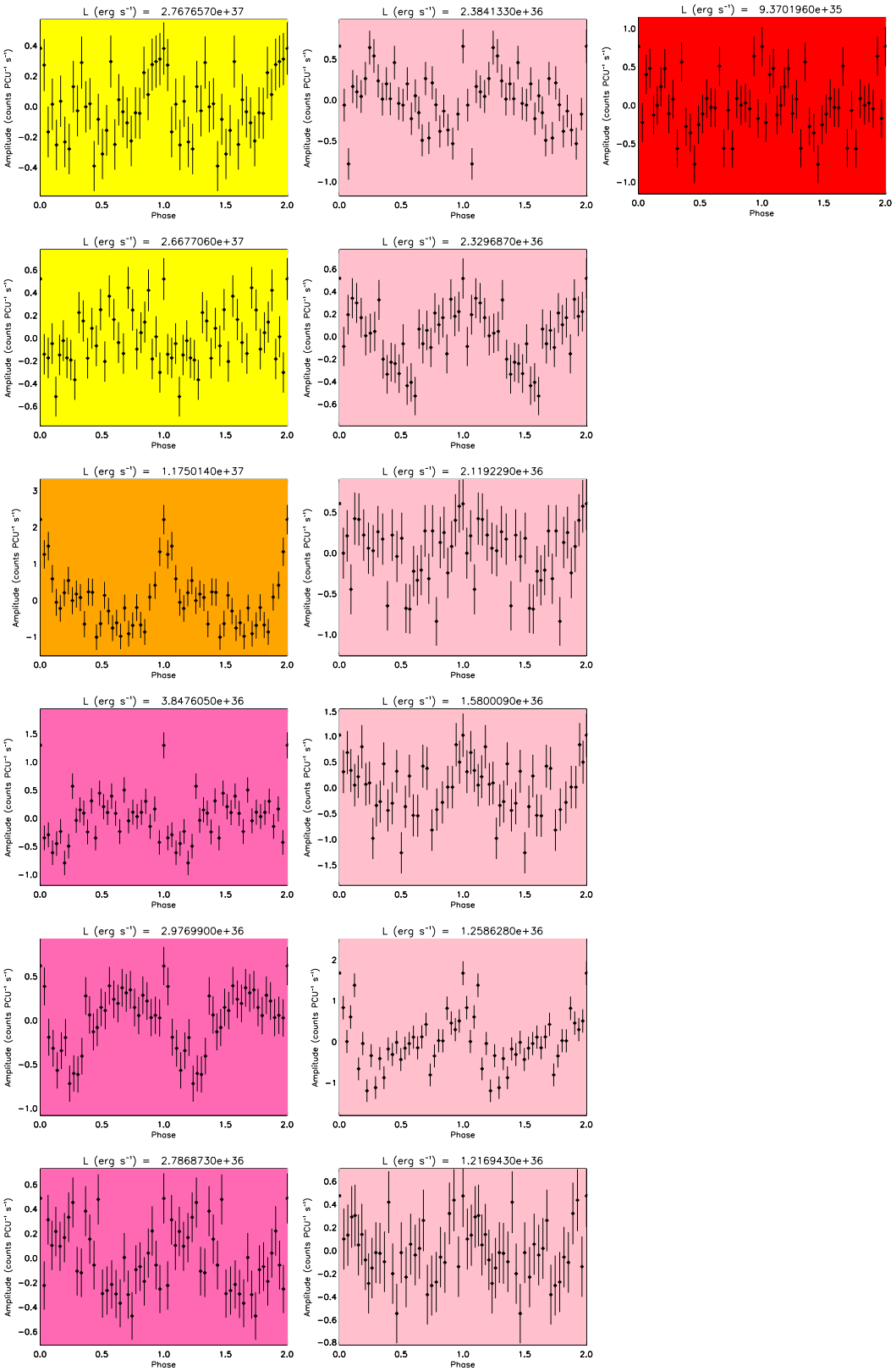

Figure C.37: Pulse-profiles for SXP645, in order of decreasing L (from top to bottom, left to right). The colour-coding is explained in Figure C.1.

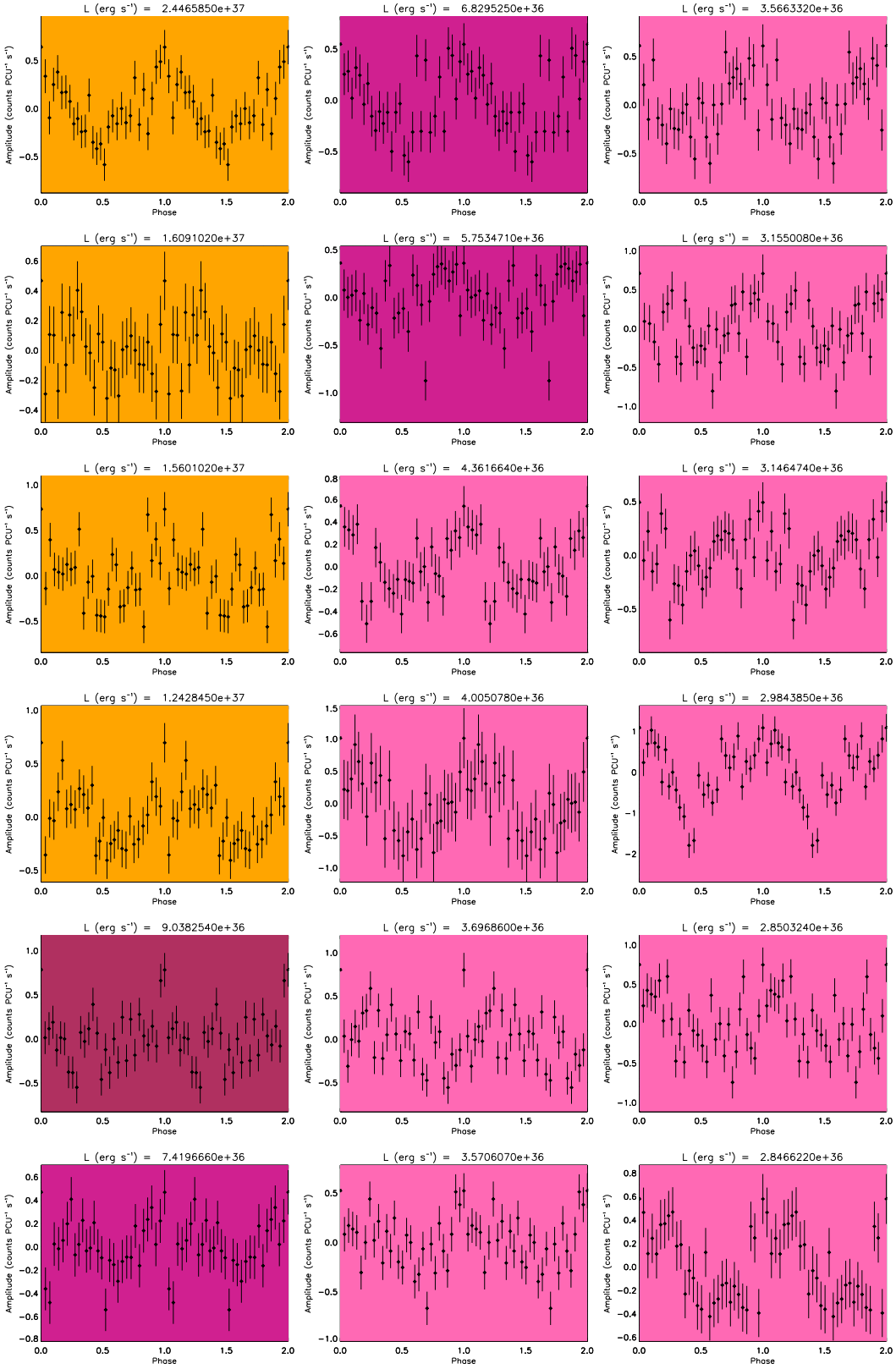
L (erg s⁻¹) = 2.4465850e+37
L (erg s⁻¹) = 6.8295250e+36
L (erg s⁻¹) = 3.5663320e+36
L (erg s⁻¹) = 1.6091020e+37
L (erg s⁻¹) = 5.7534710e+36
L (erg s⁻¹) = 3.1550080e+36
L (erg s⁻¹) = 1.5601020e+37
L (erg s⁻¹) = 4.3616640e+36
L (erg s⁻¹) = 3.1464740e+36
L (erg s⁻¹) = 1.2428450e+37
L (erg s⁻¹) = 4.0050780e+36
L (erg s⁻¹) = 2.9843850e+36
L (erg s⁻¹) = 9.0382540e+36
L (erg s⁻¹) = 3.6968600e+36
L (erg s⁻¹) = 2.8503240e+36
L (erg s⁻¹) = 7.4196660e+36
L (erg s⁻¹) = 3.5706070e+36
L (erg s⁻¹) = 2.8466220e+36
Amplitude (counts PCU⁻¹ s⁻¹)
Phase

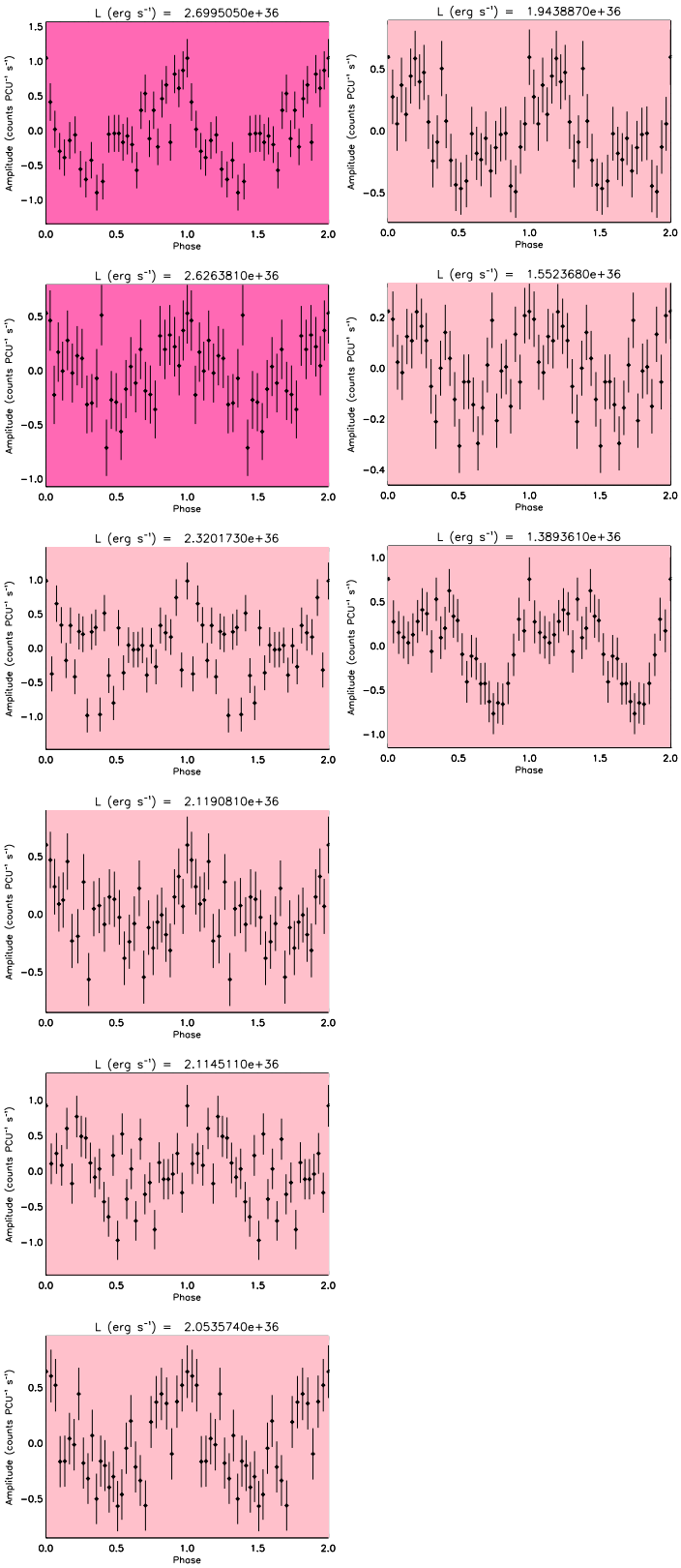

Figure C.38: Pulse-profiles for SXP701, in order of decreasing L (from top to bottom, left to right). The colour-coding is explained in Figure C.1.

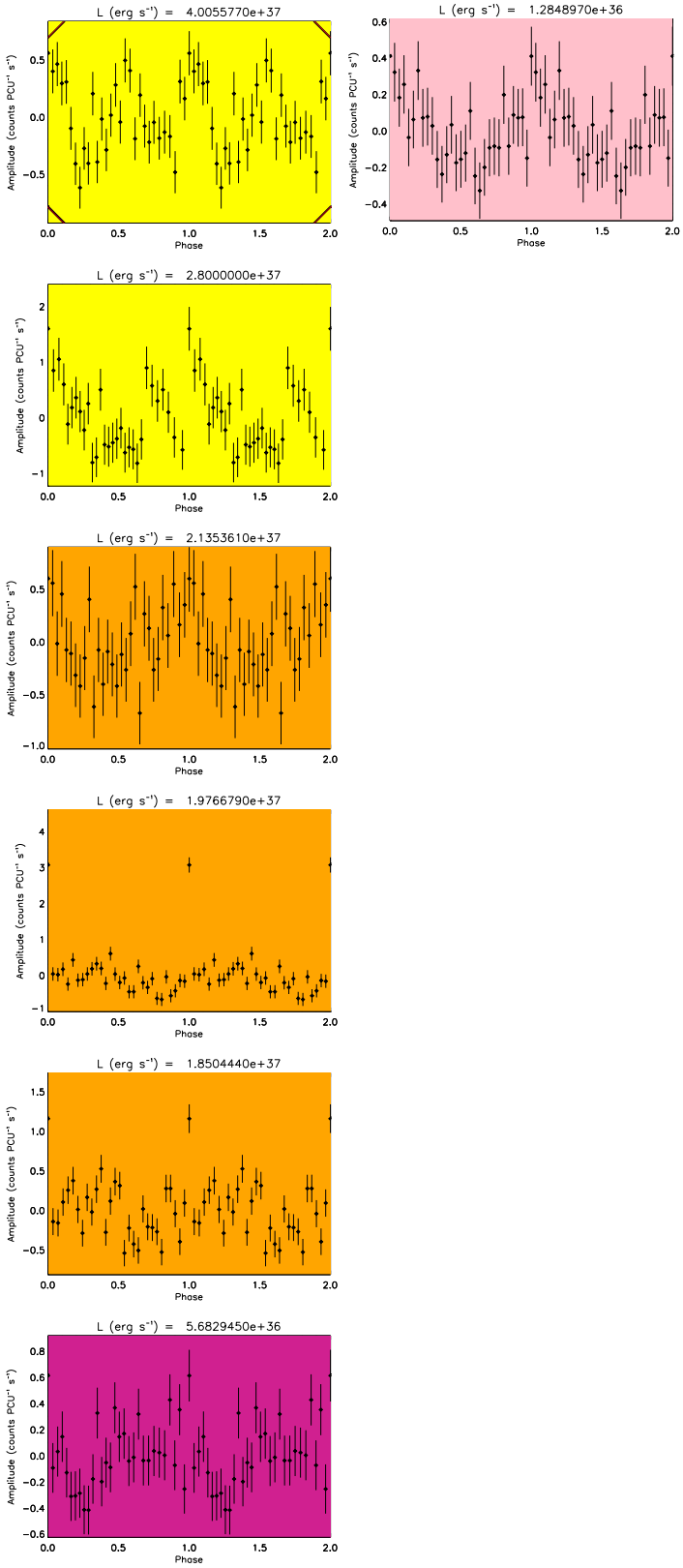

Figure C.39: Pulse-profiles for SXP726, in order of decreasing L (from top to bottom, left to right). The colour-coding is explained in Figure C.1.

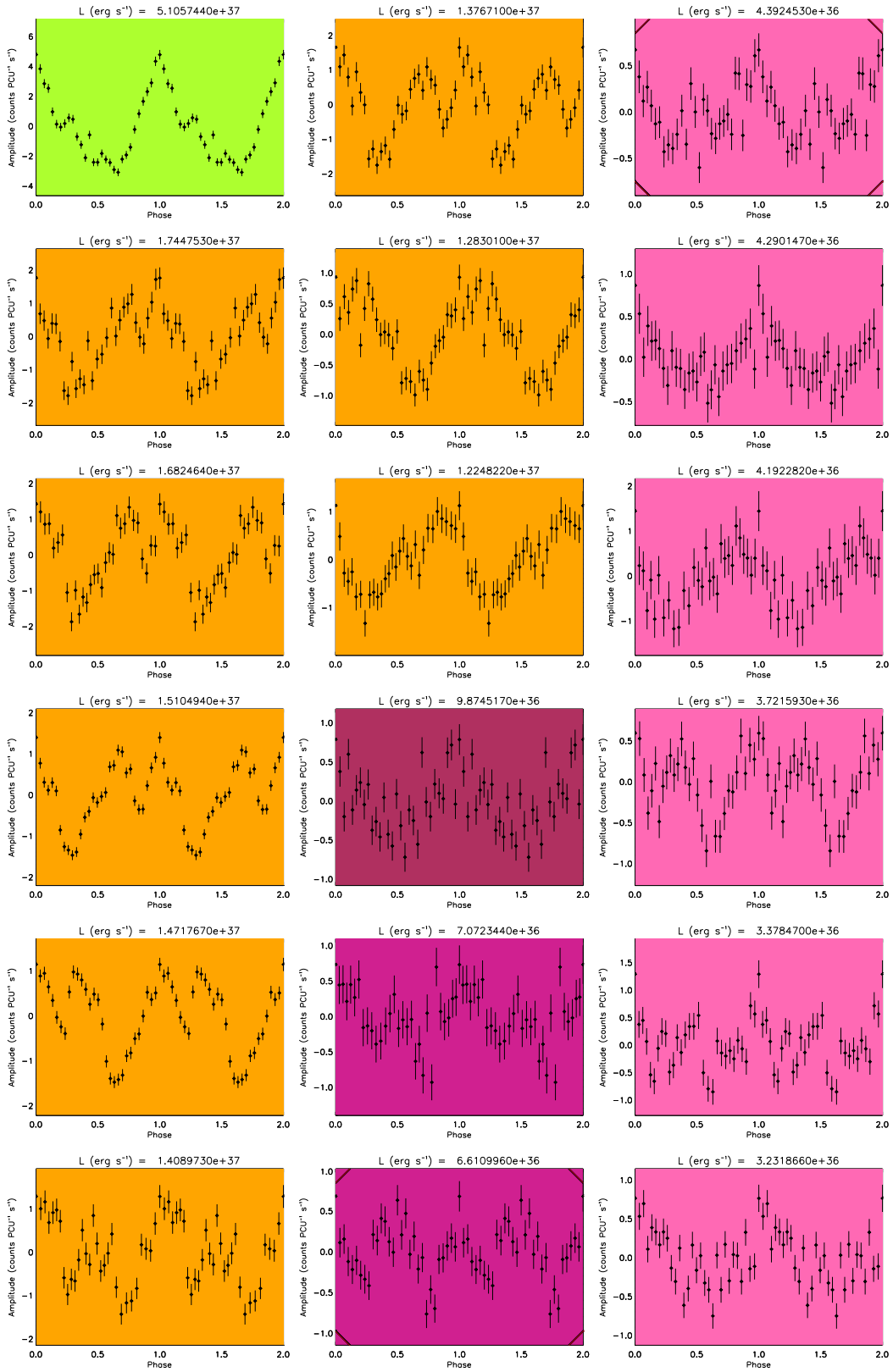
L (erg s⁻¹) = 5.1057440e+37
L (erg s⁻¹) = 1.3767100e+37
L (erg s⁻¹) = 4.3924530e+36
L (erg s⁻¹) = 1.7447530e+37
L (erg s⁻¹) = 1.2830100e+37
L (erg s⁻¹) = 4.2901470e+36
L (erg s⁻¹) = 1.6824640e+37
L (erg s⁻¹) = 1.2248220e+37
L (erg s⁻¹) = 4.1922820e+36
L (erg s⁻¹) = 1.5104940e+37
L (erg s⁻¹) = 9.8745170e+36
L (erg s⁻¹) = 3.7215930e+36
L (erg s⁻¹) = 1.4717670e+37
L (erg s⁻¹) = 7.0723440e+36
L (erg s⁻¹) = 3.3784700e+36
L (erg s⁻¹) = 1.4089730e+37
L (erg s⁻¹) = 6.6109960e+36
L (erg s⁻¹) = 3.2318660e+36
Amplitude (counts PCU⁻¹ s⁻¹)
Phase

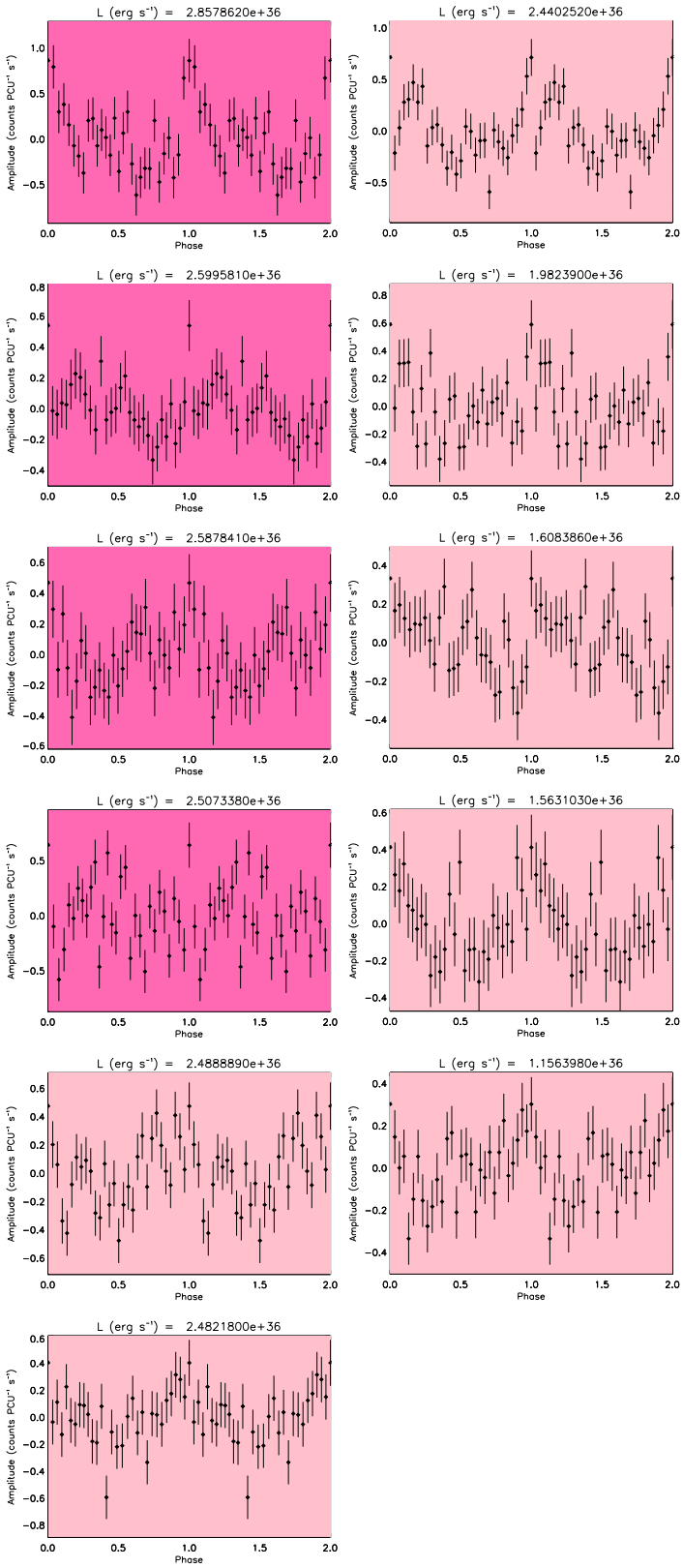

Figure C.40: Pulse-profiles for SXP756, in order of decreasing L (from top to bottom, left to right). The colour-coding is explained in Figure C.1.

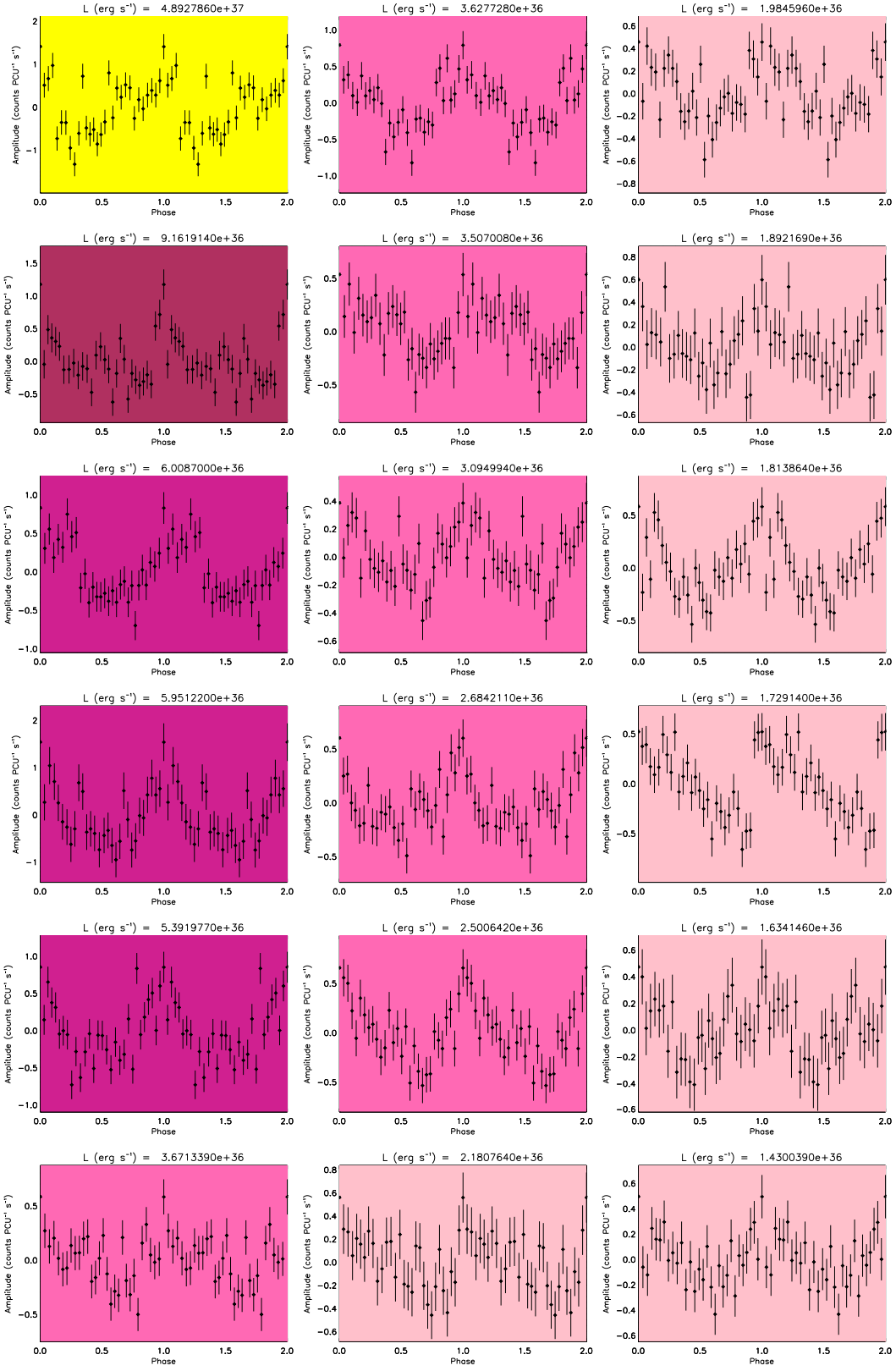
L (erg s⁻¹) = 4.8927860e+37
L (erg s⁻¹) = 3.6277280e+36
L (erg s⁻¹) = 1.9845960e+36
L (erg s⁻¹) = 9.1619140e+36
L (erg s⁻¹) = 3.5070080e+36
L (erg s⁻¹) = 1.8921690e+36
L (erg s⁻¹) = 6.0087000e+36
L (erg s⁻¹) = 3.0949940e+36
L (erg s⁻¹) = 1.8138640e+36
L (erg s⁻¹) = 5.9512200e+36
L (erg s⁻¹) = 2.6842110e+36
L (erg s⁻¹) = 1.7291400e+36
L (erg s⁻¹) = 5.3919770e+36
L (erg s⁻¹) = 2.5006420e+36
L (erg s⁻¹) = 1.6341460e+36
L (erg s⁻¹) = 3.6713390e+36
L (erg s⁻¹) = 2.1807640e+36
L (erg s⁻¹) = 1.4300390e+36
Amplitude (counts PCU⁻¹ s⁻¹)
Phase

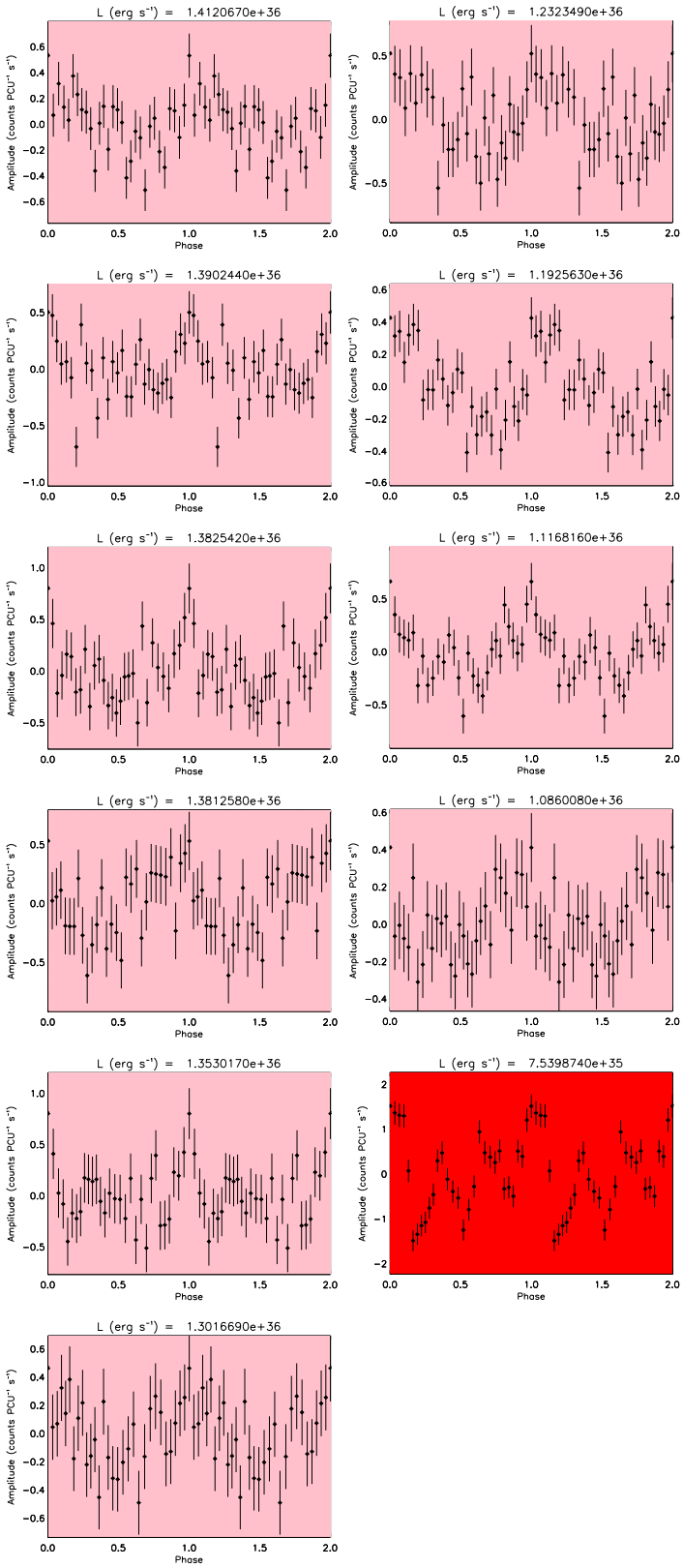

Figure C.41: Pulse-profiles for SXP893, in order of decreasing L (from top to bottom, left to right). The colour-coding is explained in Figure C.1.

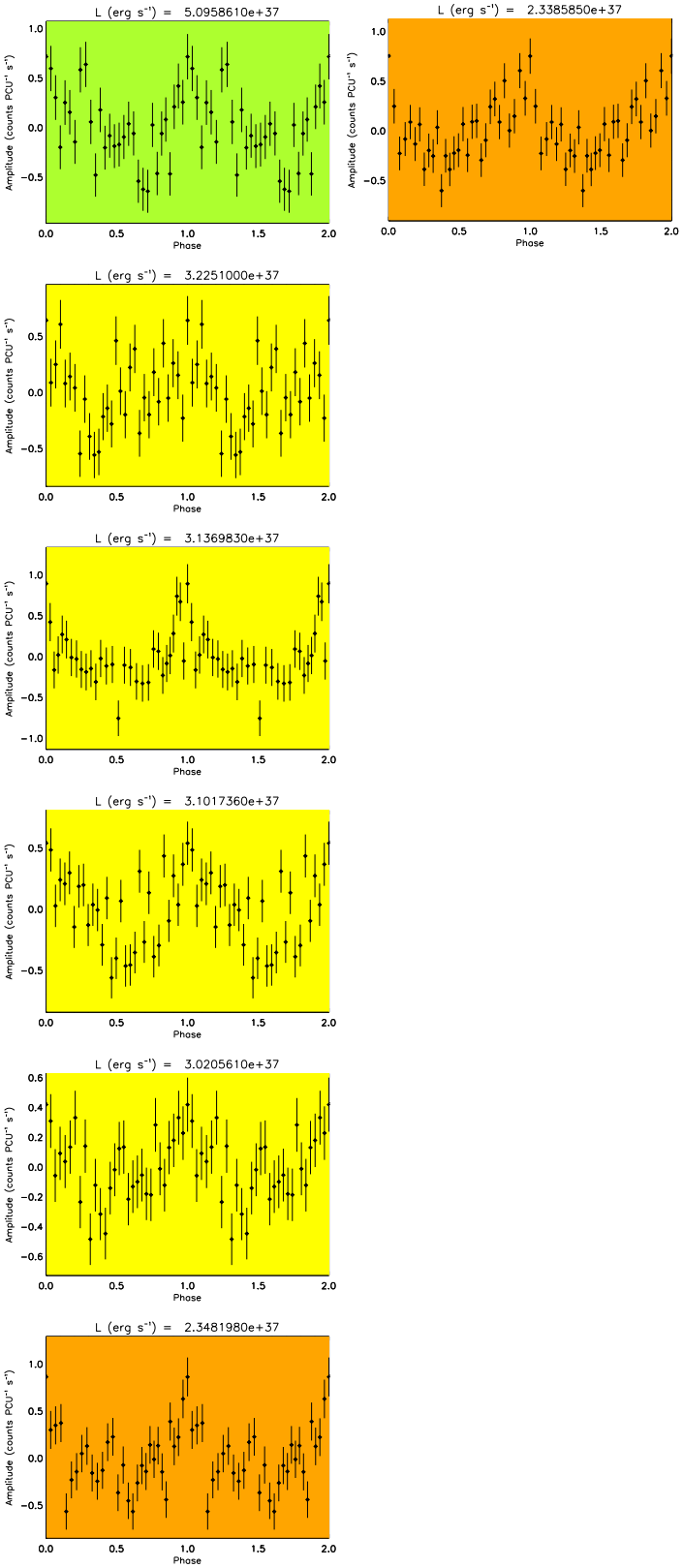

Figure C.42: Pulse-profiles for SXP967, in order of decreasing L (from top to bottom, left to right). The colour-coding is explained in Figure C.1.

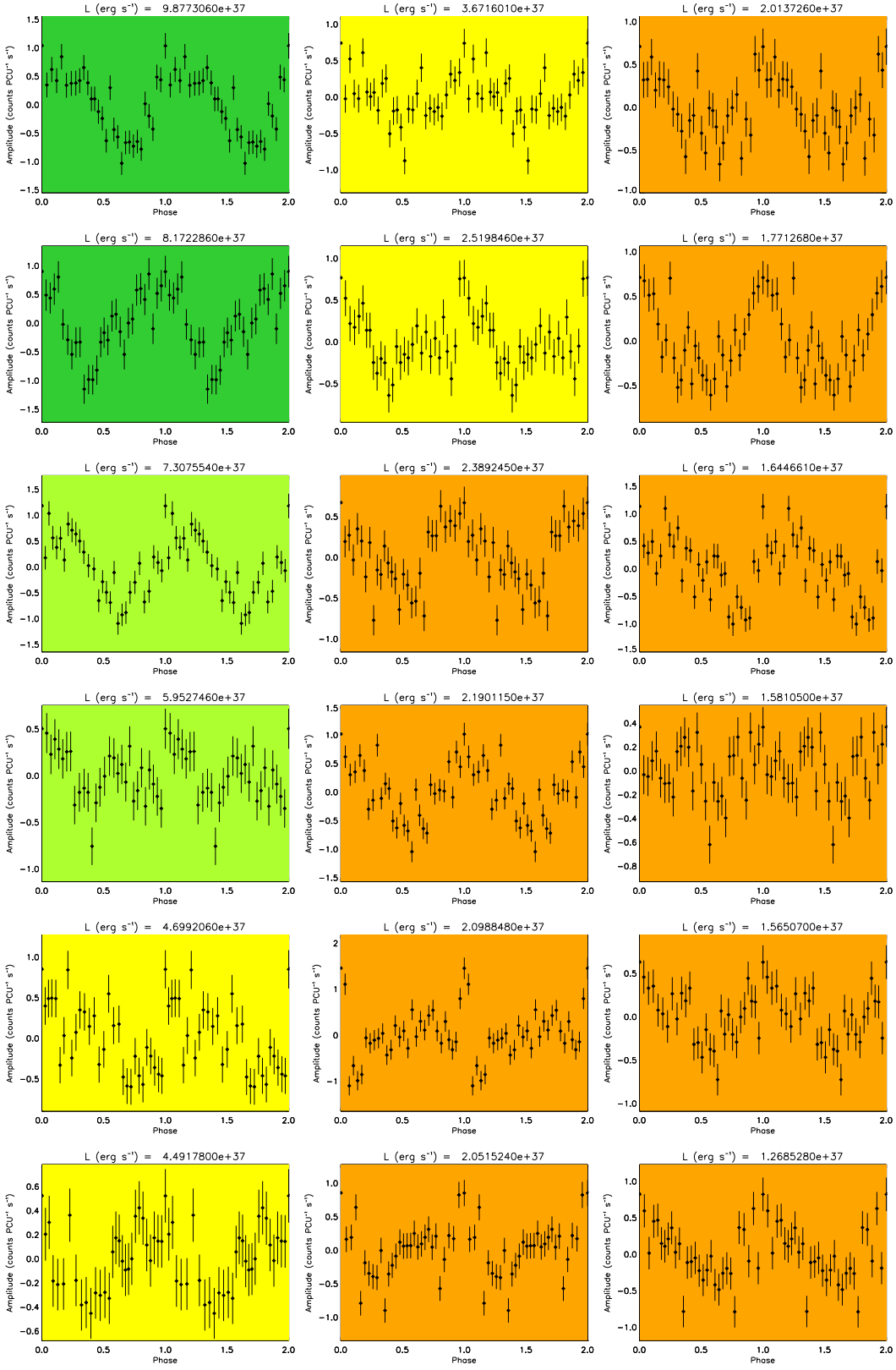
L (erg s⁻¹) = 9.8773060e+37
L (erg s⁻¹) = 3.6716010e+37
L (erg s⁻¹) = 2.0137260e+37
L (erg s⁻¹) = 8.1722860e+37
L (erg s⁻¹) = 2.5198460e+37
L (erg s⁻¹) = 1.7712680e+37
L (erg s⁻¹) = 7.3075540e+37
L (erg s⁻¹) = 2.3892450e+37
L (erg s⁻¹) = 1.6446610e+37
L (erg s⁻¹) = 5.9527460e+37
L (erg s⁻¹) = 2.1901150e+37
L (erg s⁻¹) = 1.5810500e+37
L (erg s⁻¹) = 4.6992060e+37
L (erg s⁻¹) = 2.0988480e+37
L (erg s⁻¹) = 1.5650700e+37
L (erg s⁻¹) = 4.4917800e+37
L (erg s⁻¹) = 2.0515240e+37
L (erg s⁻¹) = 1.2685280e+37
Amplitude (counts PCU⁻¹ s⁻¹)
Phase

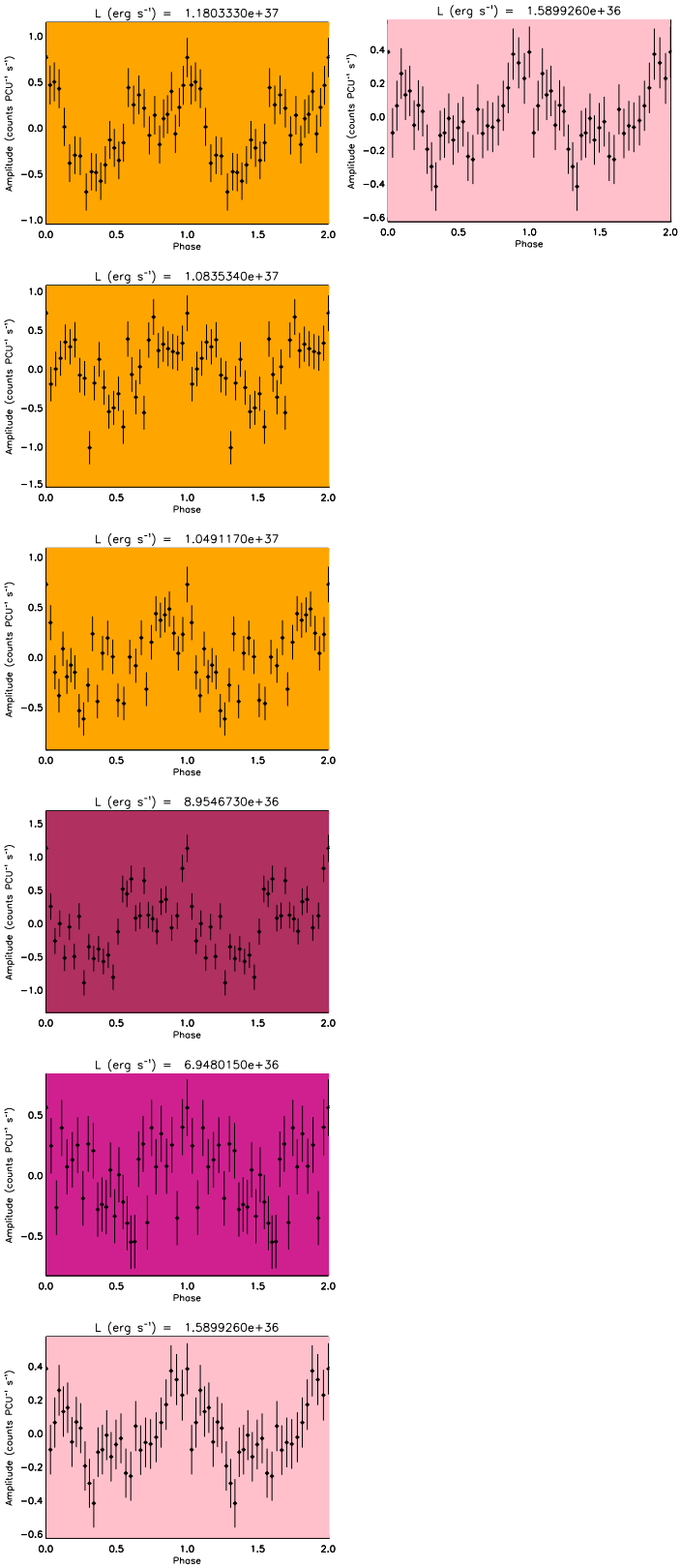

Figure C.43: Pulse-profiles for SXP1323, in order of decreasing L (from top to bottom, left to right). The colour-coding is explained in Figure C.1.

References

Alpar, M. A., Cheng, A. F., Ruderman, M. A., and Shaham, J. (1982). *Nature*, 300:728.

Antoniou, V., Zezas, A., Hatzidimitriou, D., and Kalogera, V. (2010). *ApJ*, 716:L140.

Bartlett, E. S., Coe, M. J., and Ho, W. C. G. (2013). *MNRAS*, 436:2054.

Basko, M. M. and Sunyaev, R. A. (1975). *A&A*, 42:311.

Baykal, A., Göğüş, E., İnam, S. Ç., and Belloni, T. (2010). *ApJ*, 711:1306.

Beardmore, A. P., Coe, M. J., Markwadt, C., Osborne, J. P., Baumgartner, W. H., Tueller, J., and Gehrels, N. (2009). ATel, #1901.

Becker, P. A., Klochkov, D., Schonherr, G., Nishimura, O., Ferrigno, C., Caballero, I., Kretschmar, P., Wolff, M. T., Wilms, J., and Staubert, R. (2012). *A&A*, 544:A123.

Becker, P. A. and Wolff, M. T. (2007). *ApJ*, 654:435.

Belczynski, K. and Ziolkowski, J. (2009). *ApJ*, 707:870.

Beloborodov, A. M. (2002). *ApJ*, 566:L85.

Bildsten, L., Chakrabarty, D., Chiu, J., Finger, M. H., Koh, D. T., Nelson, R. W., Prince, T. A., et al. (1997). *ApJ*, 113:S367.

Binder, B., Williams, B. F., Kong, A. K. H., Gaetz, T. J., Plucinsky, P. P., Dalcanton, J. J., and Weisz, D. R. (2011). *ApJ*, 739:L51.

Bird, A. J., Coe, M. J., McBride, V. A., and Udalski, A. (2012). *MNRAS*, 423:3663.

Bonanos, A. Z., Castro, N., Macri, L. M., and Kudritzki, R. P. (2011). *ApJ*, 729:L9.

Borkowski, K. J., Hendrick, S. P., and Reynolds, S. P. (2006). *ApJ*, 652:1259.

Bozzo, E., Falanga, M., and Stella, L. (2008). *ApJ*, 683:1031.

Brandt, N. and Podsiadlowski, P. (1995). *MNRAS*, 274:461.

Caballero, I. and Wilms, J. (2012). *Memorie della Societa Astronomica Italiana*, 83:230.

Camilo, F., Ransom, S. M., Halpern, J. P., Reynolds, J., Helfand, D. J., Zimmerman, N., and Sarkissian, J. (2006). *Nature*, 422:892.

Camilo, F., Thorsett, S. E., and Kulkarni, S. R. (1994). *ApJ*, 421:L15.

Canuto, V. and Ventura, J. (1977). *FCPh*, 2:203.

Casares, J., Negueruela, I., Ribó, M., Ribas, I., Paredes, J. M., Herrero, A., and Simón-Daz, S. (2014). *Nature*, 505:378.

Chashkina, A. and Popov, S. B. (2012). *NA*, 17:594.

Chen, W., Qu, J. L., Zhang, S., Zhang, F., and Zhang, G. B. (2008). *CA&A*, 32:241.

Clark, G., Doxsey, R., Li, F., Jernigan, J. G., and van Paradijs, J. (1978). *ApJ*, 221:L37.

Clark, G., Li, F., and van Paradijs, J. (1979). *ApJ*, 227:54.

Coburn, W., Heindl, W. A., Gruber, D. E., Rothschild, R. E., Staubert, R., Wilms, J., and Kreykenbohm, I. (2001). *ApJ*, 552:738.

Coe, M. J., Bartlett, E. S., Bird, A. J., Haberl, F., Kennea, J. A., McBride, V. A., Townsend, L. J., and Udalski, A. (2015a). *MNRAS*, 447:2387.

Coe, M. J., Edge, W. R. T., Galache, J. L., and McBride, V. A. (2005). *MNRAS*, 356:502.

Coe, M. J., Finger, M., Bartlett, E. S., and Udalski, A. (2015b). *MNRAS*, 447:1630.

Coe, M. J., Haberl, F., Sturm, R., Bartlett, E. S., Hatzidimitriou, D., Townsend, L. J., Udalski, A., Mereghetti, S., and Filipovic, M. (2012). *MNRAS*, 424:282.

Coe, M. J., Haberl, F., Sturm, R., Pietsch, W., Townsend, L. J., Bartlett, E. S., Filipovic, M., et al. (2011). *MNRAS*, 414:3281.

Coe, M. J., Schurch, M., McBride, V. A., Corbet, R. H. D., Townsend, L. J., Udalski, A., and Galache, J. L. (2009). *MNRAS*, 394:2191.

Corbet, R. H. D. (1984). *A&A*, 141:91.

Corbet, R. H. D., Marshall, F. E., Coe, M. J., Laycock, S., and Handler, G. (2001). *ApJ*, 548:L41.

Daugherty, J. K. and Harding, A. K. (1986). *ApJ*, 309:362.

Davidson, K. and Ostriker, J. P. (1973). *ApJ*, 179:585.

Davies, R. E. and Pringle, J. E. (1981). *MNRAS*, 196:209.

de Oliveira, R. L., Motch, C., Haberl, F., Negueruela, I., and Janot-Pacheco, E. (2006). *A&A*, 454:265.

DeCesar, M. E., Boyd, P. T., Pottschmidt, K., Wilms, J., Suchy, S., and Miller, M. C. (2013). *ApJ*, 762:61.

Dickey, J. M. and Lockman, F. J. (1990). *ARA&A*, 28:215.

Doroshenko, V., Santangelo, A., Suleimanov, V., Staubert, R., Kreykenbohm, I., Ferrigno, C., and D., K. (2010a). *AIP Conf. Proc.*, 1248:155.

Doroshenko, V., Suchy, S., Santangelo, A., Staubert, R., Kreykenbohm, I., Rothschild, R., Pottschmidt, K., and Wilms, J. (2010b). *A&AL*, 515:1.

Dray, L. M. (2006). *MNRAS*, 370:2079.

Duncan, R. C. and Thompson, C. (1992). *ApJ*, 392:L9.

Ekşi, K. Y., Andaç, I. C., Çikintoğlu, S., Gençali, A. A., Güngör, C., and Öztekin, F. (2014). *MNRAS*, 448:L40.

Elsner, R. F. and Lamb, F. K. (1977). *ApJ*, 215:897.

Fu, L. and Li, X. D. (2012). *ApJ*, 757:171.

Galache, J. L., Corbet, R. H. D., Coe, M. J., Laycock, S., Schurch, M. P. E., Markwardt, C., Marshall, F. E., and Lochner, J. (2008). *ApJ*, 177:S189.

Galloway, D. K., Giles, A. B., Wu, K., and Greenhill, J. G. (2001). *MNRAS*, 325:419.

Gehrz, R. D., Hackwell, J. A., and Jones, T. W. (1974). *ApJ*, 191:675.

Ghosh, P. and Lamb, F. K. (1979). *ApJ*, 234:296.

Grebenev, S. A. (2010). *The Extreme sky: Sampling the Universe above 10 keV*, 96:60.

Grebenev, S. A., Lutovinov, A. A., Tsygankov, S. S., and Mereminskiy, I. A. (2013). *MNRAS*, 428:50.

Grimm, H. J., Gilfanov, M., and Sunyaev, R. (2003). *MNRAS*, 339:793.

Haberl, F. (1995). *A&A*, 296:685.

Haberl, F. (2007). *Ap&SS*, 308:181.

Haberl, F., Eger, P., and Pietsch, W. (2008). *A&A*, 489:327.

Hanuschik, R. W. (1989). *Ap&SS*, 161:63.

Heger, A., Fryer, C. L., Woosley, S. E., Langer, N., and Hartmann, D. H. (2003). *ApJ*, 591:288.

Heindl, W. A., Coburn, W., Gruber, D. E., Pelling, M. R., Rothschild, R. E., Wilms, J., Pottschmidt, K., and Staubert, R. (1999). *ApJ*, 521:L49.

Heindl, W. A., Coburn, W., Gruber, D. E., Rothschild, R. E., Kreykenbohm, I., Wilms, J., and Staubert, R. (2001). *ApJ*, 563:L35.

Hilditch, R. W., Howarth, I. D., and Harries, T. J. (2005). *MNRAS*, 357:304.

Ho, W. C. G., Klus, H., Coe, M. J., and Andersson, N. (2014). *MNRAS*, 437:3664.

Huang, S. S. (1972). *ApJ*, 171:549.

Ikhsanov, N. R. (2001a). *A&A*, 368:5.

Ikhsanov, N. R. (2001b). *A&A*, 375:944.

Ikhsanov, N. R. (2007). *MNRAS*, 375:698.

Ikhsanov, N. R. and Finger, M. H. (2012). *ApJ*, 753:1.

Ikhsanov, N. R., Likh, Y. S., and Beskrovnaya, N. G. (2014). *Astronomy Reports*, 58:376.

Illarionov, A. F. and Kompaneets, D. A. (1990). *MNRAS*, 247:219.

Illarionov, A. F. and Sunyaev, R. A. (1975). *A&A*, 39:185.

Kendziorra, E., Kretschmar, P., Pan, H. C., Kunz, M., Maisack, M., Staubert, R., Pietsch, W., Truemper, J., Efremov, V., and Sunyaev, R. (1994). *A&AL*, 291:31.

King, A. R. and Shaviv, G. (1984). *MNRAS*, 211:883.

Klus, H., Bartlett, E. S., Bird, A. J., Coe, M. J., Corbet, R. H. D., and Udalski, A. (2013). *MNRAS*, 428:3607.

Klus, H., Ho, W. C. G., Coe, M. J., Corbet, R. H. D., and Townsend, L. J. (2014). *MNRAS*, 437:3863.

Kluzniak, W. and Rappaport, S. (2007). *ApJ*, 671:1990.

Knigge, C., Coe, M. J., and Podsiadlowski, P. (2011). *Nature*, 479:372.

Kretschmar, P., Schönherr, G., Wilms, J., Nishimura, O., Kreykenbohm, I., Staubert, R., Klochkov, D., et al. (2010). *The Energetic Cosmos: from Suzaku to ASTRO-H*, 1:268.

Lai, D. (1996). *ApJ*, 466:L35.

Laycock, S., Corbet, R. H. D., Coe, M. J., Marshall, F. E., Markwardt, C., and Lochner, J. (2005). *ApJ*, 161:S96.

Li, X. (2010). *Sci China Phys Mech Astron*, 53:9.

Lipunov, V. M. (1992). *Astrophysics of Neutron Stars*, volume XIII. Springer-Verlag, Berlin.

Lutovinov, A., Revnivtsev, M., Gilfanov, M., et al. (2005). *A&A*, 444:821.

Maitra, C., Paul, B., and Naik, S. (2012). *MNRAS*, 420:2307.

Manchester, R. N., Hobbs, G. B., Teoh, A., and Hobbs, M. (2005). *AJ*, 129:1993.

Martin, R. G., Tout, C. A., and Pringle, J. E. (2009). *MNRAS*, 397:1563.

Massey, P. (2002). *ApJ*, 141:S81.

McBride, V. A., Coe, M. J., Negueruela, I., Schurch, M. P. E., and McGowan, K. E. (2008). *MNRAS*, 388:1198.

McBride, V. A., Wilms, J., Coe, M. J., Kreykenbohm, I., Rothschild, R. E., Coburn, W., Galache, J. L., Kretschmar, P., Edge, W. R. T., and Staubert, R. (2006). *A&A*, 451:267.

Mihara, T., Makishima, K., Kamijo, S., Ohashi, T., Nagase, F., Tanaka, Y., and Koyama, K. (1991). *ApJ*, 379:L61.

Mukerjee, K., Agrawal, P. C., Paul, B., et al. (2000). *A&A*, 353:239.

Munar-Adrover, P., Paredes, J. M., Ribó, M., Iwasawa, K., Zabalza, V., and Casares, J. (2014). *ApJ*, 786:L11.

Mytrophanov, I. G. and Tsygan, A. I. (1978). *ApJ*, 70:133.

Nagel, W. (1981a). *ApJ*, 251:278.

Nagel, W. (1981b). *ApJ*, 251:288.

Naik, S., Dotani, T., Terada, Y., Nakajima, M., Mihara, T., Suzuki, M., Makishima, K., et al. (2008). *ApJ*, 672:516.

Naik, S., Maitra, C., Jaisawal, G. K., and Paul, B. (2013). *ApJ*, 746:158.

Naik, S., Paul, B., Kachhara, C., and Vadawale, S. V. (2011). *MNRAS*, 413:241.

Nazé, Y. (2009). *IAUS*, 256:20.

Negueruela, I. (2010). *High Energy Phenomena in Massive Stars*, 422:57.

Negueruela, I. and Okazaki, A. T. (2000). *ASPC*, 214:713.

Negueruela, I. and Okazaki, A. T. (2001). *A&A*, 369:108.

Nomoto, K. (1984). *ApJ*, 277:791.

Nomoto, K. (1987). *ApJ*, 322:206.

Novikov, I. and Thorne, K. (1973). Astrophysics of black holes. In DeWitt, C. and DeWitt, B., editors, *Black Holes*. Gordon and Breach, Paris.

Okazaki, A. T., Bate, M. R., Ogilvie, G. I., and Pringle, J. E. (2002). *MNRAS*, 337:967.

Okazaki, A. T. and Negueruela, I. (2001). *A&A*, 377:161.

Pacini, F. (1967). *Nature*, 221:567.

Papitto, A., Torres, D. F., and Rea, N. (2012). *ApJ*, 756:188.

Parmar, A. N., White, N. E., and Stella, L. (1989). *ApJ*, 338:373.

Peacock, M. B., Maccarone, T. J., Kundu, A., and Zepf, S. E. (2002). *LEDA*, 0:0.

Pechenick, K. R., Ftaclas, C., and Cohen, J. M. (1983). *ApJ*, 274:846.

Pellizzoni, A., Pilia, M., Possenti, A., Fornari, F., Caraveo, P., Del Monte, E., Mereghetti, S., et al. (2009). *ApJ*, 691:1618.

Pizzolato, F., Colpi, M., De Luca, A., Mereghetti, S., and Tiengo, A. (2008). *ApJ*, 681:530.

Podsiadlowski, P., Langer, N., Poelarends, A. J. T., Rappaport, S., Heger, A., and Pfahl, E. (2004). *ApJ*, 612:1044.

Pons, J. A., Miralles, J. A., and Geppert, U. (2009). *A&A*, 496:207.

Postnov, K., Shakura, N. I., Kochetkova, A., and Hjalmarsdotter, L. (2011). *Extremesky*, 1:17.

Pottschmidt, K., Kreykenbohm, I., Wilms, J., Coburn, W., Rothschild, R. E., Kretschmar, P., McBride, V., Suchy, S., and Staubert, R. (2005). *ApJ*, 634:L97.

Pringle, J. E. (1996). *MNRAS*, 281:357.

Pringle, J. E. and Rees, M. J. (1972). *A&A*, 21:1.

Rajoelimanana, A. F., Charles, P. A., and Udalski, A. (2011). *MNRAS*, 413:1600.

Reig, P. (2011). *Ap&SS*, 332:1.

Reig, P., Fabregat, J., and Coe, M. J. (1997). *A&A*, 322:193.

Reig, P. and Nespoli, E. (2013). *A&A*, 551:1.

Reig, P., Torrejón, J. M., and Blay, P. (2012). *MNRAS*, 425:595.

Romano, P., Sidoli, L., et al. (2010). *Mem. SAIt.*, 81:332.

Russell, S. C. and Dopita, M. A. (1992). *APJ*, 384:508.

Schmidtke, P. C., Cowley, A. P., and Udalski, A. (2006). *ApJ*, 132:919.

Schonherr, G., Wilms, J., Kretschmar, P., Kreykenbohm, I., Santangelo, A., Rothschild, R., Coburn, W., and Staubert, R. (2007). *A&A*, 472:353.

Schurch, M., Udalski, A., and Coe, M. J. (2008). ATel, #1670.

Schurch, M. P. E. (2009). Doctoral dissertation, University of Southampton.

Shakura, N., Postnov, K., Kochetkova, A., and Hjalmarsdotter, L. (2013). *Physics-Uspekhi*, 56:321.

Shakura, N., Postnov, K., Kochetkova, A. Y., and Hjalmarsdotter, L. (2012). *MNRAS*, 420:216.

Shapiro, S. L. and Lightman, A. P. (1976). *ApJ*, 204:555.

Shrader, C. R., Sutaria, F. K., Singh, K. P., and Macomb, D. J. (1991). *ApJ*, 512:920.

Shvartsman, V. F. (1970). *IzRad*, 13:1852.

Soong, Y., Gruber, D. E., and Rothschild, R. (1987). *ApJ*, 319:L77.

Srinivasan, G. (2006). Neutron stars. In Meynet, G. and Schaerer, D., editors, *Stellar Remnants*. Springer Science & Business Media.

Stanimirović, S., Staveley-Smith, L., Dickey, J. M., Sault, R., and Snowden, S. L. (1999). *MNRAS*, 302:417.

Stella, L., White, N., and Rosner, R. (1986). *ApJ*, 308:669.

Sturm, R., Haberl, F., Pietsch, W., Coe, M. J., Mereghetti, S., La Palombara, N., Owen, R. A., and Udalski, A. (2012). *A&A*, 537:76.

Takata, J., Cheng, K. S., and Taam, R. E. (2012). *ApJ*, 745:100.

Tauris, T. M. and van den Heuvel, E. P. J. (2006). Formation and evolution of compact stellar x-ray sources. In Lewin, W. H. G. and van der Klis, M., editors, *Compact stellar X-ray sources*. Cambridge University Press, Cambridge.

Terada, Y., Mihara, T., Nakajima, M., Suzuki, M., Isobe, N., Makishima, K., Takahashi, H., et al. (2006). *ApJ*, 648:L139.

Thompson, C., Lyutikov, M., and Kulkarni, S. R. (2002). *ApJ*, 574:332.

Torres, D. F., Rea, N., Esposito, P., Li, J., Chen, Y., and Zhang, S. (2012). *ApJ*, 744:106.

Townsend, L. J., Coe, M. J., Corbet, R. H. D., and Hill, A. B. (2011a). *MNRAS*, 416:1556.

Townsend, L. J., Coe, M. J., Corbet, R. H. D., McBride, V. A., Hill, A. B., Bird, A. J., Schurch, M. P. E., et al. (2011b). *MNRAS*, 410:1813.

Townsend, L. J., Corbet, R. H. D., Coe, M. J., McBride, V. A., Hill, A. B., and Bird, A. J. (2009). ATel, #2202.

Townsend, L. J., Drave, S. P., Hill, A. B., Coe, M. J., Corbet, R. H. D., and Bird, A. J. (2013). *MNRAS*, 433:23.

Trümper, J., Kahabka, P., Ögelman, H., Pietsch, W., and Voges, W. (1986). *ApJ*, 300:L63.

Tsygankov, S. S., Krivonos, R. A., and Lutovinov, A. A. (2012). *MNRAS*, 421:2407.

Tsygankov, S. S., Lutovinov, A. A., Churrazov, E. M., and Sunyaev, R. A. (2006). *MNRAS*, 371:19.

van den Heuvel, E. P. J. (1975). *ApJ*, 198:L109.

Wang, Y. M. (1981). *A&A*, 102:36.

Wang, Y. M. and Frank, J. (1981). *ApJ*, 93:255.

Wang, Y. M. and Welter, G. L. (1981). *ApJ*, 102:97.

Waters, L. B. F. M., Coté, J., and Lamersv, H. J. G. L. M. (1987). *A&A*, 185:206.

White, N. E., Swank, J. H., and Holt, S. S. (1983). *ApJ*, 270:711.

Wilms, J., Allen, A., and McCray, R. (2000). *ApJ*, 542:914.

Woolf, N. J., Stein, W. A., and Strittmatter, P. A. (1970). *A&A*, 9:252.

Woosley, S. and Janka, T. (2005). *Nature Phys*, 1:147.

Wu, Y. X., Yu, W., Li, T. P., Maccarone, T. J., and Li, X. D. (2010). *ApJ*, 718:620.

Yamamoto, T., Mihara, T., Sugizaki, M., Nakajima, M., Makishima, K., and Sasano, M. (2014). *Publ. Astron. Soc. Jap.*, 66:59.

Yamamoto, T., Sugizaki, M., Mihara, T., Nakajima, M., Yamaoka, K., Matsuoka, M., Morii, M., and Makishima, K. (2011). *Publ. Astron. Soc. Jap.*, 63:S751.

Zamanov, R. K., Reig, P., Martí, J., Coe, M. J., Fabregat, J., Tomov, N. A., and Valchev, T. (2001). *A&A*, 367:884.

Zhang, F., Li, X. D., and Wang, Z. R. (2004). *ApJ*, 603:663.